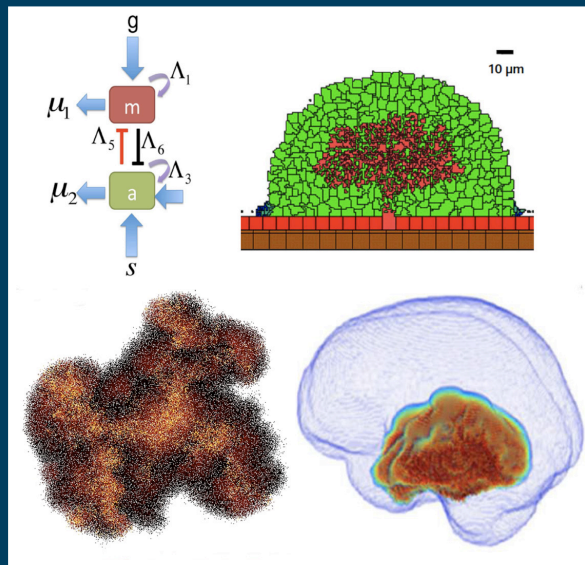


frontiers

RESEARCH TOPICS



COMPUTATIONAL MODELS IN ONCOLOGY: FROM TUMOR INITIATION TO PROGRESSION TO TREATMENT

Topic Editors

Katarzyna A. Rejniak and Heiko Enderling



frontiers

FRONTIERS COPYRIGHT STATEMENT

© Copyright 2007-2013
Frontiers Media SA.
All rights reserved.

All content included on this site, such as text, graphics, logos, button icons, images, video/audio clips, downloads, data compilations and software, is the property of or is licensed to Frontiers Media SA ("Frontiers") or its licensees and/or subcontractors. The copyright in the text of individual articles is the property of their respective authors, subject to a license granted to Frontiers.

The compilation of articles constituting this e-book, wherever published, as well as the compilation of all other content on this site, is the exclusive property of Frontiers. For the conditions for downloading and copying of e-books from Frontiers' website, please see the Terms for Website Use. If purchasing Frontiers e-books from other websites or sources, the conditions of the website concerned apply.

Images and graphics not forming part of user-contributed materials may not be downloaded or copied without permission.

Individual articles may be downloaded and reproduced in accordance with the principles of the CC-BY licence subject to any copyright or other notices. They may not be re-sold as an e-book.

As author or other contributor you grant a CC-BY licence to others to reproduce your articles, including any graphics and third-party materials supplied by you, in accordance with the Conditions for Website Use and subject to any copyright notices which you include in connection with your articles and materials.

All copyright, and all rights therein, are protected by national and international copyright laws.

The above represents a summary only. For the full conditions see the Conditions for Authors and the Conditions for Website Use.

ISSN 1664-8714

ISBN 978-2-88919-172-7

DOI 10.3389/978-2-88919-172-7

ABOUT FRONTIERS

Frontiers is more than just an open-access publisher of scholarly articles: it is a pioneering approach to the world of academia, radically improving the way scholarly research is managed. The grand vision of Frontiers is a world where all people have an equal opportunity to seek, share and generate knowledge. Frontiers provides immediate and permanent online open access to all its publications, but this alone is not enough to realize our grand goals.

FRONTIERS JOURNAL SERIES

The Frontiers Journal Series is a multi-tier and interdisciplinary set of open-access, online journals, promising a paradigm shift from the current review, selection and dissemination processes in academic publishing.

All Frontiers journals are driven by researchers for researchers; therefore, they constitute a service to the scholarly community. At the same time, the Frontiers Journal Series operates on a revolutionary invention, the tiered publishing system, initially addressing specific communities of scholars, and gradually climbing up to broader public understanding, thus serving the interests of the lay society, too.

DEDICATION TO QUALITY

Each Frontiers article is a landmark of the highest quality, thanks to genuinely collaborative interactions between authors and review editors, who include some of the world's best academicians. Research must be certified by peers before entering a stream of knowledge that may eventually reach the public - and shape society; therefore, Frontiers only applies the most rigorous and unbiased reviews.

Frontiers revolutionizes research publishing by freely delivering the most outstanding research, evaluated with no bias from both the academic and social point of view.

By applying the most advanced information technologies, Frontiers is catapulting scholarly publishing into a new generation.

WHAT ARE FRONTIERS RESEARCH TOPICS?

Frontiers Research Topics are very popular trademarks of the Frontiers Journals Series: they are collections of at least ten articles, all centered on a particular subject. With their unique mix of varied contributions from Original Research to Review Articles, Frontiers Research Topics unify the most influential researchers, the latest key findings and historical advances in a hot research area!

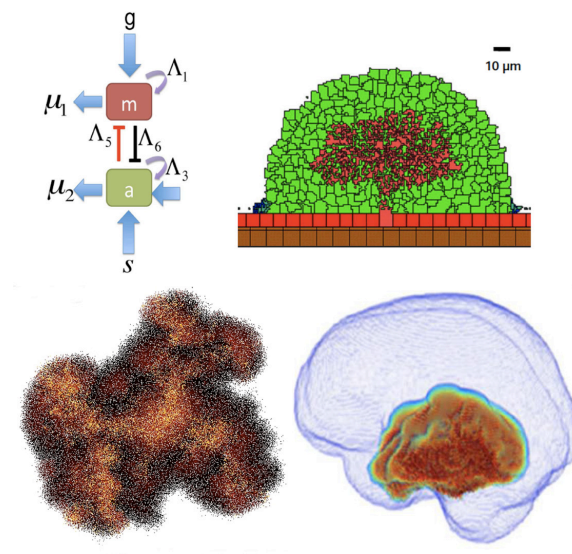
Find out more on how to host your own Frontiers Research Topic or contribute to one as an author by contacting the Frontiers Editorial Office: researchtopics@frontiersin.org

COMPUTATIONAL MODELS IN ONCOLOGY: FROM TUMOR INITIATION TO PROGRESSION TO TREATMENT

Topic Editors:

Katarzyna A. Rejniak, H. Lee Moffitt Cancer Center & Research Institute, USA

Heiko Enderling, Tufts University School of Medicine, St. Elizabeth's Medical Center, USA



Images of computational models of tumors discussed in this e-book; clockwise from top-left: Kim (2013), Steinkamp et al. (2013), Baldock et al. (2013), Enderling et al. (2013).

Cancer is one of the deadliest diseases of our time. Whilst the war on cancer has cost many millions of dollars, the mechanisms underlying its formation, progression, therapeutic cure or control are still not fully uncovered. An interdisciplinary effort that brings together clinicians, biologists, and quantitative scientists is demanded. Mathematical modeling and computational simulations bring to the table sophisticated tools for analyzing experimental data as well as for systematic, quantitative and multi-scale *in silico* experimentation. Taken together, such interdisciplinary approach promises to shed light on the underlying rules and/or complex interactions between tumor cells, tumor and stromal cells, as well as other components of the tumor microenvironment, and ultimately predict treatment outcomes.

In this research topic we will present the state-of-the-art in integrative cancer modeling (such as theoretical models based on biological or clinical data, and experimental results influenced by underlying mathematical and physical theories) and their applications to cancer biology and treatment. This collection of papers will showcase computational models addressing the most important current challenges in oncology, such as prognostic screening, metrics of tumor cell response to treatment, cancer cell mechanotransduction, cancer stem cell biology, metastatic cascade steps, and reciprocal co-evolution of tumors and their microenvironment. Quantitative and qualitative models included in this topic will discuss tumor initiation, development of pre-invasive tumors, transition from dormancy to malignancy, tumor angiogenesis, tumor cell signaling, complexity of the cellular, physical and chemical structure of the tumor microenvironment, and various models of anticancer treatment: chemo-, radio-, immuno-, hormone and adaptive therapies. This collection could then serve as an encyclopedic resource for the breadth of mathematical and computational techniques that can be applied to tumor modeling, including ordinary and partial differential equations models, individual-cell-based models, hybrid cellular automata models, bio-fluid approaches, game theory approaches, stochastic and multi-scale modeling.

Table of Contents

06 *Simulating Cancer: Computational Models in Oncology*

Heiko Enderling and Katarzyna Anna Rejniak

Part I: Subcellular Scale Mechanisms in Tumor Models

08 *Stochastic and Deterministic Models of Cellular p53 Regulation*

Gerald B. Leenders and Jack A. Tuszynski

24 *Compartment Model Predicts VEGF Secretion and Investigates the Effects of VEGF Trap in Tumor-Bearing Mice*

Stacey D Finley, Manjima Dhar and Aleksander S. Popel

45 *A Hybrid Model of the Role of VEGF Binding in Endothelial Cell Migration and Capillary Formation*

Harsh V. Jain and Trachette L. Jackson

60 *Genetic Diversity in Normal Cell Populations is the Earliest Stage of Oncogenesis Leading to Intra-Tumor Heterogeneity*

Cory L. Howk, Zachary Voller, Brandon B. Beck and Donghai Dai

74 *Stochastic Hypothesis of Transition from Inborn Neutropenia to AML: Interactions of Cell Population Dynamics and Population Genetics*

Marek Kimmel and Seth Corey

Part II: Mechanical Models of Tumor Progression

81 *Modeling the Mechanics of Cancer: Effect of Changes in Cellular and Extra-Cellular Mechanical Properties*

Parag Katira, Roger T. Bonnecaze and Muhammad H. Zaman

88 *Computational and Experimental Models of Cancer Cell Response to Fluid Shear Stress*

Michael J. Mitchell and Michael R. King

99 *Mathematical Modeling of Cancer Invasion: The Role of Membrane-Bound Matrix Metalloproteinases*

Niall E. Deakin and Mark A. J. Chaplain

108 *Properties of Tumor Spheroid Growth Exhibited by Simple Mathematical Models*

Dorothy I. Wallace and Xinyue Guo

117 *The Need for Integrative Computational Oncology: An Illustrated Example through MMP-Mediated Tissue Degradation*

Shannon Mumenthaler, Gianluca D'Antonio, Luigi Preziosi and Paul Macklin

Part III: Models of Cancer Stem Cells in Tumor Development and Treatment

121 Stem Cell Control, Oscillations, and Tissue Regeneration in Spatial and Non-Spatial Models

Ignacio A. Rodriguez-Brenes, Dominik Wodarz and Natalia L. Komarova

131 Cancer Stem Cells: A Minor Cancer Subpopulation that Redefines Global Cancer Features

Heiko Enderling, Lynn Hlatky and Philip Hahnfeldt

141 Mathematical Optimization of the Combination of Radiation and Differentiation Therapies for Cancer

Jeff W. N. Bachman and Thomas Hillen

Part IV: Models of Tumor-Environment Interactions

150 Cellular Potts Modeling of Tumor Growth, Tumor Invasion, and Tumor Evolution

András Szabó and Roeland M. H. Merks

162 Ovarian Tumor Attachment, Invasion, and Vascularization Reflect Unique Microenvironments in the Peritoneum: Insights from Xenograft and Mathematical Models

Mara P. Steinkamp, Kimberly Kanigel Winner, Suzy Davies, Carolyn Muller, Yong Zhang, Robert M. Hoffman, Abbas Shirinifard, Melanie Moses, Yi Jiang and Bridget S. Wilson,

180 Tumor Evolution in Space: The Effects of Competition Colonization Tradeoffs on Tumor Invasion Dynamics

Paul A. Orlando, Robert A. Gatenby and Joel S. Brown,

Part V: Models of Anticancer Therapies and Treatments

192 From Patient-Specific Mathematical Neuro-Oncology to Precision Medicine

A. L. Baldock, R. C. Rockne, A. D. Boone, M. L. Neal, A. Hawkins-Daarud, D. M. Corwin, C. A. Bridge, L. A. Guyman, A. D. Trister, M. M. Mrugala, J. K. Rockhill and K. R. Swanson

203 A Model of Dendritic Cell Therapy for Melanoma

Lisette DePillis, Angela Gallegos and Ami Radunskaya

217 The Role of Tumor Tissue Architecture in Treatment Penetration and Efficacy: An Integrative Study

Katarzyna A. Rejniak, Veronica Estrella, Tingan Chen, Allison S. Cohen, Mark C. Lloyd and David L. Morse

230 Regulation of Cell Proliferation and Migration in Glioblastoma: New Therapeutic Approach

Yangjin Kim

247 Modeling Tumor-Associated Edema in Gliomas During Anti-Angiogenic Therapy and Its Impact on Imageable Tumor

Andrea Hawkins-Daarud, Russell C. Rockne, Alexander R. A. Anderson and Kristin R. Swanson



Simulating cancer: computational models in oncology

Heiko Enderling¹ and Katarzyna Anna Rejniak^{2,3*}

¹ Center of Cancer Systems Biology, St. Elizabeth's Medical Center, Tufts University School of Medicine, Boston, MA, USA

² Integrated Mathematical Oncology, H. Lee Moffitt Cancer Center & Research Institute, Tampa, FL, USA

³ Department of Oncologic Sciences, College of Medicine, University of South Florida, Tampa, FL, USA

Edited by:

Lorenzo Galluzzi, Institut National de la Santé et de la Recherche Médicale, France

Reviewed by:

Andrei Zinovyev, Institut Curie, France

*Correspondence: kasia.rejniak@moffitt.org

Keywords: computational modeling, computational oncology, tumor development, tumor treatment, *in silico* cancer

Cancer is one of the deadliest diseases of our time. While the war on cancer has cost many billions of dollars, the mechanisms underlying tumor development, progression, and therapeutic cure or control are yet to be fully understood. An interdisciplinary effort that brings together clinicians and biologists with mathematical and computational modelers is therefore necessary. Mathematical modeling and computational simulations bring to the table sophisticated tools for analyzing experimental data as well as for systematic, quantitative, and multi-scale *in silico* experimentation. Taken together, such an interdisciplinary approach promises to shed light on the underlying rules of the intra-, inter-, and extracellular mechanisms behind complex tumor dynamics, with the ultimate aim to predict patient-specific treatment outcomes.

The papers in this Special Topic span a broad spectrum of cancer cell-related subjects from intracellular modifications in individual cells to complex interactions between tumor cells and tumor microenvironments to emerging behaviors of cell populations on the organ and whole body scale. Quantitative modeling has been applied to virtually every type of tumor. This collection includes papers on brain, ovarian, and colon cancers, as well as on melanomas, leukemias, sarcomas, and head and neck tumors. The models also addressed various stages of tumor development including its initiation, growth, invasion of the surrounding stroma, tumor cell migration, and intravascular transport, as well as metastatic colonization. Various types of anticancer treatments have been discussed in this Special Topic, including chemotherapy, radiotherapy, immunotherapy, and differentiation therapy. From a mathematical point of view, the models range from deterministic to stochastic, from continuous population dynamics to agent-based individual cell models, from fluid dynamics to Monte Carlo simulations and energy minimization models.

We divided the papers in this Special Topic into five categories. In the first, the subcellular mechanisms and their impact on a single cell and population-level heterogeneity are considered. Dynamics on the subcellular scale include intracellular gene modulations or extracellular diffusion of soluble factors. Leenders and Tuszyński (1) discuss both stochastic and deterministic models of p53 protein regulation that play a crucial role in cellular stress and DNA damage response. Kimmel and Corey (2) show that large variations in the timing of transitions from neutropenia to acute myeloid leukemia can be explained by stochasticity in cell driver mutations. Howk et al. (3) use a single cell model of two-hit mutations of normal cells into endometrial cancer cells to predict the frequency of cancer

stem cells in endometrial cancer. Jain and Jackson (4) present a hybrid model that simulates the dynamics of vascular endothelial growth factor (VEGF) diffusion and its binding to endothelial cell receptors, which triggers endothelial cell activation and polarization during angiogenesis. Finley et al. (5) consider another angiogenesis model centered on VEGF and its molecular interactions that has been calibrated to experimental data and shows that *in vivo* VEGF secretion rates are significantly lower than most reported *in vitro* measurements, which has profound implications for anti-angiogenic treatment.

The second class of papers contains mechanical models of tumor invasion that are influenced by both the physical forces and chemical factors necessary to degrade the host tissue. Deakin and Chaplain (6) present a mathematical model focusing on both soluble and membrane-bound metalloproteinases (MMPs) and their relative role in the degradation of highly dense collagen structures and cross-linked fibers. Mumenthaler et al. (7) discuss an integrative experimental–computational approach to understand MMP-mediated tissue degradation. The fluid-generated forces exerted on the cell either by the interstitial fluid or shear stress in the blood circulation are reviewed by Mitchell and King (8) from both experimental and computational perspectives. Katira et al. (9) discuss interdependence of mechanical and biological pathways within the cell and how intracellular and environmental mechanical properties, such as stiffness and adhesivity, lead to changes in cell behavior, including transformation into malignancy. Wallace and Guo (10) analyze mathematical models of avascular tumor growth and conditions under which the models reproduce the growth dynamics of *in vitro* spheroids.

The third group of studies investigates cancer stem cells. With experimental stem cell purification and reliable identification still in its infancy, mathematical models highlight the population-level dynamics resulting from different stem cell kinetics. Rodriguez-Brenes et al. (11) discuss homeostasis in stem cell lineages through tightly controlled feedback mechanisms that regulate stem cell proliferation and self-renewal. Enderling et al. (12) examine how tumors grow if the cancer population is fueled by a cancer stem cell, showing that tumors exhibit a variety of irregular morphologies and harbor stem cell fractions that vary by many orders of magnitude and evolve over time. Bachman and Hillen (13) investigate how conventional radiotherapy can be complemented by differentiation therapy that forces stem cells into differentiation to increase their sensitivity to radiation.

The next group of articles focuses on interactions between the tumor and its microenvironment. Szabó and Merks (14) discuss avascular and vascular tumor growth and evolution using the Cellular Potts model. Orlando et al. (15) examine tumor cell evolution at the tumor core and its invasive edge, focusing on the effects of colonization tradeoffs on tumor invasion dynamics. Steinkamp et al. (16) integrate *in vivo* xenograft mouse models and mathematical models to study tumor attachment, invasion, and vascularization in the ovary, showing that local factors and mesothelial lining features strongly influence invasion.

The final group of studies focuses on the use of quantitative models to improve treatment modalities. Patient-specific mathematical neuro-oncology approaches are reviewed by Baldock et al. (17). Kim (18) presents a mathematical model based on microRNAs that balance cell proliferation and migration in different microenvironmental conditions in glioblastoma, suggesting a post-surgery injection of chemoattractants and glucose to counteract the diffusive spread of residual cells. Hawkins-Daarud et al. (19) discuss a model of fluid accumulation in gliomas during anti-angiogenic therapy and discuss the implications of the environmental response to tumor growth on medical imaging. Rejniak et al. (20) present an integrative study examining penetration and efficacy of therapeutic agents in relation to tumor tissue architecture. DePillis et al. (21) use a model of dendritic cell therapy on melanoma, showing how dosage and schedule modifications enhance immunotherapy efficacy.

The images featured on page 2 of this e-book showcase computational models discussed in detail in this Special Topic. Clockwise from top left: a schematic of miR-451 activity in the model of Kim (18); a 2-D slice through the ovarian tumor simulated using the Potts model of Steinkamp et al. (16); a 3-D simulation of malignant glioma cells from Baldock et al. (17); cancer stem cell-driven tumor growth from Enderling et al. (12).

REFERENCES

- Leenders GB, Tuszyński JA. Stochastic and deterministic models of cellular p53 regulation. *Front Oncol* (2013) 3:64. doi: 10.3389/fonc.2013.00064
- Kimmel M, Corey S. Stochastic hypothesis of transition from inborn neutropenia to AML: interactions of cell population dynamics and population genetics. *Front Oncol* (2013) 3:89. doi: 10.3389/fonc.2013.00089
- Howk CL, Voller Z, Beck BB, Dai D. Genetic diversity in normal cell populations is the earliest stage of oncogenesis leading to intra-tumor heterogeneity. *Front Oncol* (2013) 3:61. doi: 10.3389/fonc.2013.00061
- Jain HV, Jackson TL. A hybrid model of the role of VEGF binding in endothelial cell migration and capillary formation. *Front Oncol* (2013) 3:102. doi: 10.3389/fonc.2013.00102
- Finley SD, Dhar M, Popel AS. Compartment model predicts VEGF secretion and investigates the effects of VEGF Trap in tumor-bearing mice. *Front Oncol* (2013) 3:196. doi: 10.3389/fonc.2013.00196
- Deakin NE, Chaplain MAJ. Mathematical modeling of cancer invasion: the role of membrane-bound matrix metalloproteinases. *Front Oncol* (2013) 3:70. doi: 10.3389/fonc.2013.00070
- Mumenthaler SM, D'Antonio G, Preziosi L, Macklin P. The need for integrative computational oncology: an illustrated example through MMP-mediated tissue degradation. *Front Oncol* (2013) 3:194. doi: 10.3389/fonc.2013.00194
- Mitchell MJ, King MR. Computational and experimental models of cancer cell response to fluid shear stress. *Front Oncol* (2013) 3:44. doi: 10.3389/fonc.2013.00044
- Katira P, Bonnacaze RT, Zaman MH. Modeling the mechanics of cancer: effect of changes in cellular and extra-cellular mechanical properties. *Front Oncol* (2013) 3:145. doi: 10.3389/fonc.2013.00145
- Wallace DI, Guo X. Properties of tumor spheroid growth exhibited by simple mathematical models. *Front Oncol* (2013) 3:51. doi: 10.3389/fonc.2013.00051
- Rodriguez-Brenes IA, Wodarz D, Komarova NL. Stem cell control, oscillations, and tissue regeneration in spatial and non-spatial models. *Front Oncol* (2013) 3:82. doi: 10.3389/fonc.2013.00082
- Enderling H, Hlatky L, Hahnfeldt P. Cancer stem cells: a minor cancer subpopulation that redefines global cancer features. *Front Oncol* (2013) 3:76. doi: 10.3389/fonc.2013.00076
- Bachman JWN, Hillen T. Mathematical optimization of the combination of radiation and differentiation therapies for cancer. *Front Oncol* (2013) 3:52. doi: 10.3389/fonc.2013.00052
- Szabó A, Merks RMH. Cellular potts modeling of tumor growth, tumor invasion, and tumor evolution. *Front Oncol* (2013) 3:87. doi: 10.3389/fonc.2013.00087
- Orlando PA, Gatenby RA, Brown JS. Tumor evolution in space: the effects of competition colonization tradeoffs on tumor invasion dynamics. *Front Oncol* (2013) 3:doi: 10.3389/fonc.2013.00045
- Steinkamp MP, Winner KK, Davies S, Muller C, Zhang Y, Hoffman RM, et al. Ovarian tumor attachment, invasion, and vascularization reflect unique microenvironments in the peritoneum: insights from xenograft and mathematical models. *Front Oncol* (2013) 3:97. doi: 10.3389/fonc.2013.00097
- Baldock AL, Rockne RC, Boone AD, Neal ML, Hawkins-Daarud A, Corwin DM, et al. From patient-specific mathematical neuro-oncology to precision medicine. *Front Oncol* (2013) 3:62. doi: 10.3389/fonc.2013.00062
- Kim Y. Regulation of cell proliferation and migration in glioblastoma: new therapeutic approach. *Front Oncol* (2013) 3:53. doi: 10.3389/fonc.2013.00053
- Hawkins-Daarud A, Rockne RC, Anderson ARA, Swanson KR. Modeling tumor-associated edema in gliomas during anti-angiogenic therapy and its impact on imageable tumor. *Front Oncol* (2013) 3:66. doi: 10.3389/fonc.2013.00066
- Rejniak KA, Estrella V, Chen T, Cohen AS, Lloyd MC, Morse DL. The role of tumor tissue architecture in treatment penetration and efficacy: an integrative study. *Front Oncol* (2013) 3:111. doi: 10.3389/fonc.2013.00111
- DePillis L, Gallegos A, Radunskaya A. A model of dendritic cell therapy for melanoma. *Front Oncol* (2013) 3:56. doi: 10.3389/fonc.2013.00056

Received: 09 August 2013; accepted: 27 August 2013; published online: 13 September 2013.
Citation: Enderling H and Rejniak KA (2013) Simulating cancer: computational models in oncology. *Front. Oncol.* 3:233. doi: 10.3389/fonc.2013.00233

This article was submitted to *Molecular and Cellular Oncology*, a section of the journal *Frontiers in Oncology*.

Copyright © 2013 Enderling and Rejniak. This is an open-access article distributed under the terms of the Creative Commons Attribution License (CC BY). The use, distribution or reproduction in other forums is permitted, provided the original author(s) or licensor are credited and that the original publication in this journal is cited, in accordance with accepted academic practice. No use, distribution or reproduction is permitted which does not comply with these terms.



Stochastic and deterministic models of cellular p53 regulation

Gerald B. Leenders and Jack A. Tuszynski *

Department of Physics, University of Alberta, Edmonton, AB, Canada

Edited by:

Katarzyna A. Rejniak, H. Lee Moffitt
Cancer Center and Research Institute,
USA

Reviewed by:

Natalia Komarova, University of
California Irvine, USA
Harsh Jain, Florida State University,
USA

*Correspondence:

Jack A. Tuszynski, Department of
Physics, University of Alberta, 3-336,
Cross Cancer Institute, 11560
University Avenue, Edmonton, AB
T6G1Z2, Canada.
e-mail: jackt@ualberta.ca

The protein p53 is a key regulator of cellular response to a wide variety of stressors. In cancer cells inhibitory regulators of p53 such as MDM2 and MDMX proteins are often overexpressed. We apply *in silico* techniques to better understand the role and interactions of these proteins in a cell cycle process. Furthermore we investigate the role of stochasticity in determining system behavior. We have found that stochasticity is able to affect system behavior profoundly. We also derive a general result for the way in which initially synchronized oscillating stochastic systems will fall out of synchronization with each other.

Keywords: p53, cell cycle, cancer, stochastic modeling, deterministic modeling, desynchronization

INTRODUCTION

Among the vast number of mechanisms utilized by cancer cells to sustain cell division, the inactivation of the essential tumor suppressor and transcription factor p53 is one of the most frequent and effective strategies. Therefore, restoring the activity of the p53-signaling pathway is currently one of the most promising therapeutic strategies for fighting this disease (Levine and Oren, 2009).

In normal cells, p53 plays a central role in the regulation of the cell cycle, apoptosis, DNA repair, and senescence (Teodoro et al., 2007); p53 responds to cellular stress, such as hypoxia or DNA damage, by accumulating in the nucleus, regulating the expression of target genes, and activating/inactivating various pathways in order to maintain the normal function of the cell (Maltzman and Czyzyk, 1984; Kastan et al., 1991; Graeber et al., 1994). Indeed, it appears that whenever the integrity of a cell's genetic code is threatened, p53 is there to protect it. This conclusion has led p53 to be called the guardian of the genome (Lane, 1992).

However, the p53-signaling pathway is inoperative in almost all types of human cancer; factors that inactivate p53 specifically include genetic mutations or deletions (Feki and Irminger-Finger, 2004), defective post-translational modifications, and interactions with its main endogenous inhibitors, MDM2 (Momand et al., 1998) and MDMX (Shvarts et al., 1996). Excitingly, a number of these tumors have been shown to have a less invasive phenotype upon restoration of p53 activity (Olivier et al., 2002; Ventura et al., 2007; Suad et al., 2009; Mandinova and Lee, 2011).

With the cost of drug development on the scale of hundreds of millions to billions of dollars per new drug entity – and rising – there is strong need to look for any possible acceleration and improvement to the efficiency and accuracy of the development process (Paul et al., 2010). Thanks to the increasing computing power available to researchers, it is now becoming affordable and practical to attempt to use *in silico* models to improve the

development process. One way to do this is to improve the ability of researchers to select appropriate proteins, or interactions between proteins, as targets for drug development by better understanding their function in protein interaction networks.

The purpose of this study is to gain new insights into the functioning of p53, a central protein in cell cycle regulation. A simple model of p53 oscillations in response to ionizing radiation is presented. Additionally, the behavior of stochastic and deterministic representations of the same model system is compared.

CELL CYCLE

The protein p53 is a regulator of the cell cycle and cell fate. Under normal conditions, a cell will normally progress through several stages. In the G1 phase (first gap phase) the cell grows in size to prepare for DNA synthesis. After G1, the cell moves into S phase (synthesis phase), during which new DNA is synthesized. Cells that are not replicating can also leave G1 and enter the G0 phase, a state in which they do not grow, and can remain quiescent indefinitely. Next comes the G2 phase (second gap phase), where cells grow further and complete their final preparations for mitosis. Mitosis then occurs and the cycle can begin anew (Lodish et al., 2008). A damaged cell may need to halt its cycle or even self-destruct in a process called apoptosis. Apoptosis is necessary for normal development and homeostasis of multicellular organisms, and is also a desirable outcome for cancer cells during cancer chemotherapy.

In order to ensure that the process of cell division is carefully regulated, the cell has a number of checkpoints. These checkpoints are conditions that a cell must meet in order to progress in the cell cycle. For example, one checkpoint in G1 ensures that a cell has grown sufficiently in size to move into S phase and replicate its DNA. Another checkpoint that occurs in G1 is mediated by the protein p53: when DNA is damaged, p53 halts the cell cycle until the damage is repaired; this prevents the cell from trying

to duplicate the damaged DNA. When p53 is inactivated, this checkpoint no longer functions. A cell attempting to duplicate damaged DNA is likely to accumulate mutations (Alberts et al., 1994). **Figure 1** diagrams the relevance of p53 to the cell cycle.

p53

The protein p53 responds to many stressors including ultraviolet light (Maltzman and Czyzyk, 1984), ionizing radiation (Kastan et al., 1991), hypoxia, heat (Graeber et al., 1994), improper cell adhesion (Nigro et al., 1997), ribonucleotide depletion (Linke et al., 1996), and infection by influenza (Turpin et al., 2005). Some viral proteins are known to interact with p53, for example hepatitis B virus HBx protein (Truant et al., 1995) and the large T antigen of simian virus 40 (Dobbelstein and Roth, 1998). The protein p53 has been demonstrated to induce cell cycle arrest, senescence, and apoptosis, with the specific outcome dependent on the extent and type of stress, and the genetic background of the cell (Vousden and Lu, 2002). The expression of p53 is tightly regulated by the cell (Sugrue et al., 1997; Lodish et al., 2008). In order to help it execute its various functions p53 is post-translationally modified at many sites to determine its response (Meek and Anderson, 2009; Dai and Gu, 2010). The protein p53 transcriptionally regulates numerous genes, with a pattern that varies depending on the type of stress and the cell type (Zhao et al., 2000). In addition to its transcriptional activity, p53 plays a transcription-independent role in apoptosis by binding to several anti-apoptotic proteins (Mihara et al., 2003).

The protein p53 is known to be mutated in approximately 50% of human tumors (Soussi and Wiman, 2007; Brown et al., 2009; Freed-Pastor and Prives, 2012). In addition, in tumors with wild type p53 it is common for p53 expression to be misregulated. For example, proteins that have a part in downregulating p53, such as MDM2 and MDMX, are commonly overexpressed in human tumors (Momand et al., 1998; Danovi et al., 2004). Furthermore, it has been demonstrated that restoration of p53 function can cause tumors to regress *in vivo* (Ventura et al., 2007). The importance of p53-signaling in cancer progression, and its therapeutic implications, have been investigated in previous mathematical models (Gammack et al., 2001; Perfahl et al., 2011), which highlights further our study.

Note that simply removing the limitations on a cell imposed by p53 is not enough for it to become cancerous; for a cell to become cancerous it must accumulate multiple hallmarks including: self-sufficiency in growth signals, insensitivity to anti-growth signals, limitless replicative potential, sustained angiogenesis, and the ability to migrate to other tissues (Hanahan and Weinberg, 2011). When such traits accumulate in a cell lacking functional p53, the probability of a cell becoming cancerous rises (Alberts et al., 1994).

MDM2

The protein MDM2 is a key player in the regulation of p53 (Bond et al., 2005) and it has been found that MDM2 is commonly amplified in human cancers (Momand et al., 1998). MDM2 has been shown to be an E3 ubiquitin ligase for p53 (Honda et al., 1997). This means that MDM2 can mark p53 for degradation by the proteasome. As such, amplification of MDM2 leads to reduced

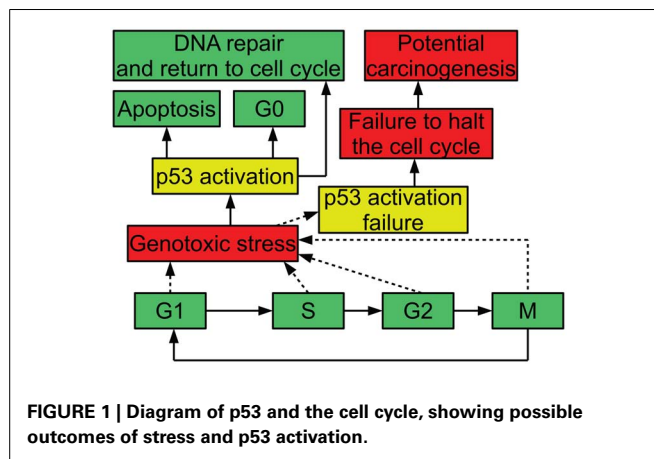


FIGURE 1 | Diagram of p53 and the cell cycle, showing possible outcomes of stress and p53 activation.

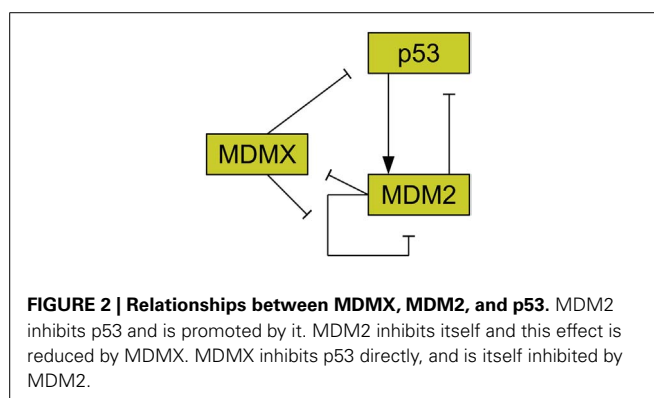


FIGURE 2 | Relationships between MDMX, MDM2, and p53. MDM2 inhibits p53 and is promoted by it. MDM2 inhibits itself and this effect is reduced by MDMX. MDMX inhibits p53 directly, and is itself inhibited by MDM2.

p53 levels (Haupt et al., 1997; Kubbutat et al., 1997). MDM2 production is also induced by p53, forming a feedback loop (Barak et al., 1993). **Figure 2** illustrates the interactions of MDM2 with p53. Additionally, MDM2 helps to regulate itself by autoubiquitination, meaning it marks itself for degradation by the proteasome (Fang et al., 2000). MDM2 possesses a nuclear localization signal, which is a structure on the protein that induces the cell to import the protein into the cell nucleus (Chen et al., 1995). MDM2 also has a cryptic nucleolar localization signal, which flags the protein for localization to the nucleolus, but only when MDM2 binding to another molecule changes the conformation of the signaling region (Lohrum et al., 2000).

In 2004 several small molecule inhibitors for the p53-MDM2 interaction were discovered (Vassilev et al., 2004). One of these inhibitors, Nutlin-3, was in Phase I clinical trials for retinoblastoma (Secchiero et al., 2011). Nutlins may also have some p53-independent effects, and these may be related to MDM2. It has been shown in some cell lines that MDM2 is upregulated by hypoxia independently of p53 (Gillespie, 2007). Furthermore, it has been shown that Nutlin-3 can radio-sensitize hypoxic cells that are p53 null, although it has a greater effect on cells with wild type p53 (Supiot et al., 2008). Additionally, Nutlin-3 has been shown to bind to several anti-apoptotic proteins other than MDM2, further complicating any analysis of its effects (Ha et al., 2011). MDM2 inhibitors bind to the protean competitively and occlude the binding site with p53 (Barakat et al., 2010). To the

best of our knowledge Nutlins do not alter the autoubiquitination properties of MDM2.

MDMX

Another important regulator of p53 is MDMX, a homolog of MDM2 (Shvarts et al., 1996; Finch et al., 2002). MDMX is commonly overexpressed in tumors, and its upregulation has been shown to promote tumor formation (Danovi et al., 2004). Unlike MDM2, however, MDMX expression is not induced by DNA damage (Shvarts et al., 1996). MDMX binds to both MDM2 (Sharp et al., 1999) and p53 (Shvarts et al., 1996). MDMX binding to MDM2 inhibits MDM2 autoubiquitination (Okamoto et al., 2009). Furthermore, MDM2 ubiquitinates MDMX (De Graaf et al., 2003). The interaction of MDMX and p53 has been shown to inhibit p53 activity (Marine et al., 2007). **Figure 2** schematically depicts the relationships between p53, MDM2, and MDMX. MDMX possesses a cryptic nuclear localization signal (LeBron et al., 2006), so it can only reach the nucleus while bound to other proteins. MDMX is normally located primarily in the cytoplasm (Gu et al., 2002).

Small molecule inhibitors of MDMX have only recently been discovered (Reed et al., 2010). Although initial results show some efficacy against cancers with upregulated MDMX in cell culture (Wang et al., 2011), more work will need to be done to show whether or not they will be active *in vivo*, as well as whether or not it is the MDMX interaction or some off-target interaction that is causing the effect.

UPSTREAM REGULATORS

There are many feedback loops known to affect p53, and the behavior of the p53 system is mediated by a number of upstream regulators (Harris and Levine, 2005). For example, the protein ATM is activated in response to ionizing radiation (Bakkenist and Kastan, 2003). Active ATM phosphorylates p53 (Banin et al., 1998), MDM2 (Maya et al., 2001), and Chk2 (Matsuoka et al., 2000). A related protein, ATR, phosphorylates p53 in response to single strand breaks in DNA (Tibbetts et al., 1999). Chk2 along with Chk1 also phosphorylate p53 (Shieh et al., 2000). These phosphorylations disrupt the ability of MDM2 to affect p53 (Zhang et al., 1998; Chehab et al., 2000; Maya et al., 2001).

OTHER FEEDBACKS

Aside from the MDM2 loop, there are other feedbacks affecting p53, although many of these involve also MDM2. The ARF protein is known to bind to MDM2 and promote its degradation (Zhang et al., 1998). ARF causes both MDM2 and MDMX to be localized to the nucleolus (Weber et al., 1999; Jackson et al., 2001). ARF is negatively regulated by p53 in a complex manner, thus forming a feedback loop (Stott et al., 1998; Lowe and Sherr, 2003). MDM2 activity becomes enhanced by a feedback in which p53 upregulates cyclin G, which then forms a complex with PP2A phosphatase. This complex then dephosphorylates MDM2, removing the inhibition caused by the phosphorylation effect (Harris and Levine, 2005). The Wip1 protein is induced by p53 and is able to modify ATM and Chk2, deactivating these proteins, and thus resulting in a stronger interaction between p53 and MDM2 (Fiscella et al., 1997; Fujimoto et al., 2006; Shreeram et al., 2006). Pirh2 has a

more direct feedback with p53. Like MDM2, Pirh2 and COP1 both ubiquitinate p53 and are upregulated by p53 (Leng et al., 2003; Dornan et al., 2004).

PROTEIN LEVEL OSCILLATIONS?

Lahav et al. (2004), Geva-Zatorsky et al. (2006), and Geva-Zatorsky et al. (2010) all directly observed sustained oscillations of p53 and MDM2 levels in the nuclei of individual cells. It is worth noting, however, that these single cell studies used MCF-7 cells. MCF-7 cells were initially used to study p53 because they exhibit wild type p53 (Lahav et al., 2004). Unfortunately, the MCF-7 cell line has a mutation in an MDM2 intron causing upregulation of MDM2 (Hu et al., 2007), lacks ARF (Stott et al., 1998), and possesses amplified MDMX (Danovi et al., 2004). Because of this, any assumption that any wild type cell would behave similarly to an MCF-7 cell with respect to p53 regulation is questionable at best. Unfortunately, there are no similar single cell studies of non-tumorigenic cell lines at the time of writing this paper. Also of note is the finding by Batchelor et al. (2011) that MCF-7 cells respond differently to damage induced by ultraviolet light than they do to double-strand breaks induced by gamma radiation or radiomimetic drugs. Geva-Zatorsky et al. (2006) also pointed out that undamped oscillations of p53 levels may appear damped in studies of cell populations due to the individual cells falling out of sync with each other. Damped oscillations have been observed in populations of non-tumorigenic cell lines, for example in entire mice (Hamstra et al., 2006).

PREVIOUS MODELING WORK

A number of models of p53 response to DNA damage have been proposed in the past. These models are based on a variety of approaches and serve a number of functions. Some basic models use built-in time delays on p53 induction of MDM2 transcription, such as some of the models developed by Geva-Zatorsky et al. (2006). In contrast, the model presented by Lev Bar-Or et al. (2000) used coupled differential equations to create time delay effects. There are advantages and disadvantages to each of these approaches. In a real cell, proteins are not produced instantly in response to a promoter. Both transcription and translation processes take time, and transport of the mRNA and the protein to the cytoplasm does not happen instantaneously. An explicit time delay deals with this problem directly, but may be more difficult to analyze than coupled equations. It also adds to the complexity of any computer algorithm made for stochastic simulations. A set of coupled equations, on the other hand, will start to show effects of induced protein production in the protein levels instantaneously, but the effect will be very small until some time has passed. In a stochastic system the protein levels are quantized and instead of instantaneous effects there is simply a small but non-zero possibility of instantaneous effects. In both the stochastic and deterministic cases adding more steps in the form of more coupled equations makes the system both more realistic and more computationally intensive. Another factor to consider is that p53 induces the transcription of MDM2 mRNA, and that mRNA is active for a time. Because of this, the actual rate of MDM2 production is dependent on a weighted average of past p53 levels rather than p53 levels at some specific time in the past. Using a

single delayed p53 term to describe MDM2 production is therefore problematic. One way around this problem is to use a delay term for the production of the MDM2 mRNA rather than the MDM2 protein, as was done by Cai and Yuan (2009). Ma et al. (2005) investigated the number of p53 pulses that occur in response to DNA double-strand breaks using a model made from three linked modules, simulating DNA repair, ATM activation, and the p53-MDM2 feedback loop. Linking together multiple systems like this, in particular linking to systems that can be easily perturbed experimentally, may be a good way to develop models that are straight-forward to test. Batchelor et al. (2008) proposed a model based on abstracted signal and inhibitor systems interacting with MDM2 as well as active and inactive p53. This model was created to investigate the possible effects of ATM, CHK2, and WIP1 on p53 behavior. They included an equation for an input signal that converted p53 from an inactive form to an active form, and a p53 induced inhibitor that reduced the effects of the signal. There have also been past efforts to look at stochastic models of the p53 regulatory system. Cai and Yuan (2009) modeled p53-MDM2 and MDMX interactions and analyzed some of the effects of intrinsic noise. Their model has MDM2 mRNA being produced with a time delay. It also includes ubiquitinated states of proteins and a deubiquitination term, rather than just assuming all ubiquitinated proteins are degraded. Puszyński et al. (2008) developed a complex stochastic model of p53 behavior aimed at showing how

stochastic effects lead to variability of cell fate in a bistable model. Their model includes a cytoplasmic compartment and a nuclear compartment, although p53 is not included in their cytoplasmic compartment. In addition to the negative feedback of MDM2 and p53 they include a positive feedback involving a series of events that lead to MDM2 being sequestered in the cytoplasm where it can no longer degrade p53.

Table 1 summarizes the key differences between the models. Ultimately, the differences in the models have as much, if not more, to do with differences in what the researchers were trying to investigate, rather than with differing assumptions about p53 behavior.

MATERIALS AND METHODS

THE MODEL

Since it has been observed that stochastic effects can cause a population of cells that undergo undamped oscillations to appear as if they were undergoing damped oscillations (Lahav et al., 2004; Geva-Zatorsky et al., 2006), it is interesting to compare a stochastic model of cell behavior to a deterministic one. By using both stochastic and deterministic versions of the same model it will be possible to look at the process of desynchronization between cells, which causes oscillations to appear damped, and to search for any other effects by which stochasticity could influence the system. As we shall see later, further investigation revealed several unexpected ways in which stochasticity influenced the system.

Table 1 | Key features of various models of p53 behavior.

Model	Stochasticity	MDMX	Compartments	Time delayed equations	Stress signal	Other notes
Geva-Zatorsky et al. (2006)						These models do not have saturable MDM2 production
Model 1	Limited noise	No	No	No	No	Linear Model
Model 2	Limited noise	No	No	No	No	
Model 3	Limited noise	No	No	Yes	No	Linear Model
Model 4	Limited noise	No	No	No	No	
Model 5	Limited noise	No	No	No	No	Linear Model
Model 6	Limited noise	No	No	Yes	Yes	
Lev Bar-Or et al. (2000)	None	No	No	No	Yes	Stress is abstract and gets repaired
Ma et al. (2005)	In the stress and repair modules only	No	No	Yes	Yes	Complex stress and repair modules
Batchelor et al. (2008)	No	No	No	Yes	Yes	p53 promotes an inhibitor of the stress signal
Cai and Yuan (2009)	Yes	Yes	No	Yes	No	Includes phosphorylated proteins
Puszyński et al. (2008)	Yes	No	Yes, but not for p53	No	Yes	Includes many other proteins
Our model	Stochastic and non-stochastic versions were implemented	No	Only for MDM2	No	No	Details in Section “Materials and Methods”

In this model p53 induces the transcription of MDM2 mRNA in the nucleus; there are three steps between induced transcription of MDM2 by p53 and the arrival of MDM2 proteins in the cell nucleus. Induced transcription is assumed to be proportional to $[p53]/(K_D^{1.8} + [p53]^{1.8})$, as was seen in the binding properties found by Weinberg et al. (2005). MDM2 mRNA is also produced at a basal rate. After being produced in the nucleus, the MDM2 mRNA proceeds to the cytoplasm, where it is translated and eventually decays. Even though mRNA from MDM2's different promoter regions are translated at different rates, they are treated as one species. Because the two types of mRNA are assumed to decay at the same rate, this amounts to absorbing the difference in translation rates into the mRNA production rates. Cytoplasmic MDM2 moves to the nucleus at a constant rate, and all other behaviors that cytoplasmic MDM2 could exhibit are ignored in this model. ARF was given constant production and degradation rates. Once in the nucleus, MDM2 can become bound to ARF, which removes both proteins from the system. Additionally, MDM2 autoubiquitinates, which is a process that also removes it from the system. **Figure 3** provides a schematic diagram of this system.

Using the principle of mass-action and the saturable transcription kinetics mentioned above, the system's behavior can be mathematically described in terms of a system of differential equations. In addition to all the chemical reactions in **Figure 3** the system of differential equations includes the production and degradation of p53, basal transcription of MDM2 mRNA, decay of cytoplasmic RNA, decay of ARF, and production of ARF. The equations are as follows:

$$\begin{aligned}\frac{d[p53]}{dt} &= k_p - k_1 [p53] [MDM2_{nuclear}] - d_p [p53] \\ \frac{d[RNA_{nuclear}]}{dt} &= k_m + k_2 \frac{[p53]^{1.8}}{K_D^{1.8} + [p53]^{1.8}} - k_0 [RNA_{nuclear}] \\ \frac{d[RNA_{cytoplasmic}]}{dt} &= k_0 [RNA_{nuclear}] - d_{rc} [RNA_{cytoplasmic}] \\ \frac{d[MDM2_{cytoplasmic}]}{dt} &= k_T [RNA_{cytoplasmic}] \\ &\quad - k_i [MDM2_{cytoplasmic}] \\ \frac{d[MDM2_{nuclear}]}{dt} &= k_i [MDM2_{cytoplasmic}] \\ &\quad - d_{mn} [MDM2_{cytoplasmic}]^2 \\ &\quad - k_3 [MDM2_{nuclear}] [ARF] \\ \frac{d[ARF]}{dt} &= k_a - d_a [ARF] - k_3 [MDM2_{nuclear}] [ARF]\end{aligned}$$

with k_p being the production rate of p53, k_1 being the rate at which MDM2 ubiquitinates p53, and d_p being the rate of MDM2-independent p53 degradation. Here, k_m is the rate of p53-independent MDM2 mRNA production, k_2 is the maximum rate of p53-dependent MDM2 mRNA production, K_D is the dissociation constant for p53 on the MDM2 promoter region, and k_0 is the rate of MDM2 mRNA transport to the nucleus. In the equations above, d_{rc} is the decay rate of MDM2 mRNA in the cytoplasm, k_T is the translation rate for MDM2 mRNA, and k_i is the rate of

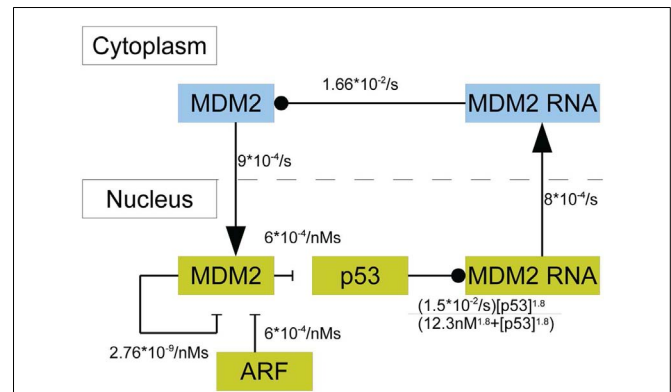


FIGURE 3 | A schematic of the model of p53 including MDM2 sequestration by ARF. The blue boxes denote molecular species in the cytoplasm. The yellow boxes indicate molecular species in the nucleus. Arrows denote movement between compartments, barred lines indicate degradation, and circles indicate inducing production.

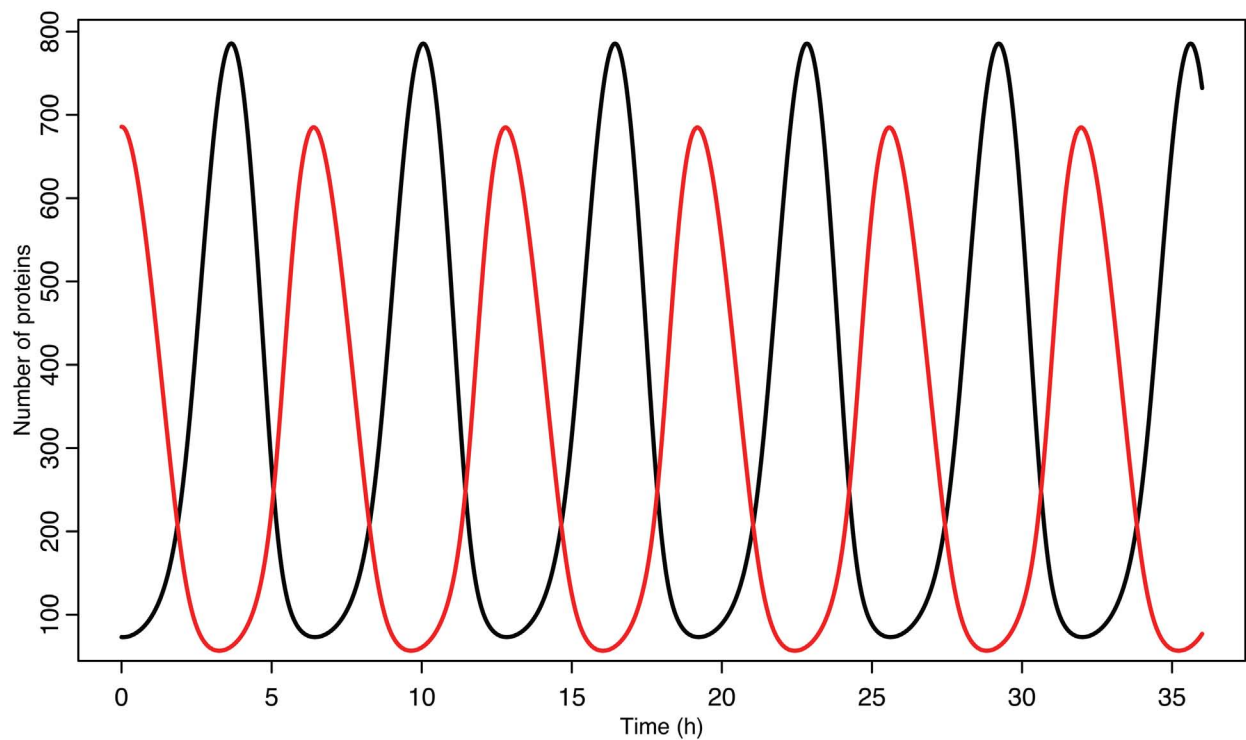
nuclear localization for MDM2. MDM2 autoubiquitination happens at the rate d_{mn} and MDM2 binds to ARF at the rate k_3 . Lastly, ARF is produced at the rate k_a and degraded at the rate d_a . The binding properties of p53 and the MDM2 promoter have been investigated experimentally by Weinberg et al. (2005), who showed that the appropriate Hill coefficient for the Hill function is 1.8.

A list of the values used for these parameters can be found in **Table 2**. The initial conditions were chosen by letting the system run until it settled into a stable limit cycle and then by using the values for the time when nuclear MDM2 levels were at a maximum.

Experimental observations of the p53-MDM2 feedback loop have found periods of oscillations between 4 and 7 h (Geva-Zatorsky et al., 2006, 2010). Due to scarcity of experimentally verified data, most of parameters in the model were chosen by hand in order to produce oscillations with a similar period. Some of the parameters were constrained by experimental data. K_D was found to be 12.3 nM by Weinberg et al. (2005). Some experimental results suggested that the half-life for MDM2 mRNA should be in the range of 1–2 h (Hsing et al., 2000; Mendrysa et al., 2001), so this constrained our choice of the decay rate. The MDM2 translation rate, k_T , was assumed to be one protein per mRNA molecule per minute, approximately the value estimated by Cai and Yuan (2009). The transport rate for MDM2 mRNA was constrained to be in the range of 5–40 min, based on Mor et al. (2010). The half-life of the ARF protein, d_a , was chosen to be 6 h based on Kuo et al. (2004). Complex formation rates were assumed to be 6×10^{-4} /nMs, a reasonable rate for protein–protein interactions (Northrup and Erickson, 1992). It was further assumed that the p53-MDM2 interaction would always result in p53 degradation. MDM2-independent p53 turnover was assumed to give a half-life of 10 h for the p53 protein; this is essentially negligible in this model, but this term was included in the model so that a bifurcation value could be calculated for it. Cytoplasmic volume was assumed to be $1000 \mu\text{m}^3$ with a nuclear volume of $100 \mu\text{m}^3$. The values for p53 production, ARF production, basal MDM2 mRNA production, p53 induced

Table 2 | Parameters used in the model.

Parameter	Description	Value	Value (alternate expression)
k_p	p53 Production	0.5 proteins/s	$8.30 \times 10^{-3}/\text{nM s}$
k_1	MDM2 dependent p53 degradation	$9.963 \times 10^{-6}/\text{s}$	$6 \times 10^{-4}/\text{nM s}$
d_p	p53 Decay	$1.925 \times 10^{-5}/\text{s}$	10 h half-life
k_m	p53-Independent MDM2 production	$1.5 \times 10^{-3} \text{ RNA/s}$	1 RNA per 666 s
k_2	p53-Dependent MDM2 production	$1.5 \times 10^{-2}/\text{s}$	Maximum of 1 RNA per 66 s
K_D	Dissociation constant	740 proteins	12.3 nM
k_0	RNA transport from nucleus to cytoplasm	$8.0 \times 10^{-4}/\text{s}$	14.4 min for half the proteins to move
d_{rc}	MDM2 mRNA decay in cytoplasm	$1.444 \times 10^{-4}/\text{s}$	1 h 20 min half-life
k_T	Transcription rate	$1.66 \times 10^{-2} \text{ proteins/s}$	One protein per RNA per min
k_i	Protein transport from cytoplasm to nucleus	$9.0 \times 10^{-4}/\text{s}$	12.4 min for half the proteins to move
d_{mn}	MDM2 autoubiquitination	$1.66 \times 10^{-7}/\text{s}$	$2.76 \times 10^{-9}/\text{nM s}$
k_a	ARF production	0.5 proteins/s	$8.30 \times 10^{-3}/\text{nM s}$
d_a	ARF decay	$3.209 \times 10^{-5}/\text{s}$	6 h half-life
k_3	MDM2-ARF complex formation rate	$9.963 \times 10^{-6}/\text{s}$	$6 \times 10^{-4}/\text{nM s}$

**FIGURE 4 | p53 and MDM2 oscillating in the deterministic model.** p53 is in black, MDM2 is in red.

MDM2 mRNA production, MDM2 nuclear import, and MDM2 autoubiquitination were unknown. These unknown parameters were chosen manually in order to produce oscillations similar to the ones observed in experiments on single cells. Although only one set of parameters was produced for this model, the choice is certainly not unique given the somewhat loose selection criteria. The model produces oscillations with a period of 6.4 h as can

be seen in **Figure 4**. Bifurcation points for the model are listed in **Table 3**. The bifurcation points were found numerically using Matlab (MathWorks, Inc.).

STOCHASTIC SIMULATION ALGORITHM

The Gillespie algorithm is one of the most commonly used methods of stochastic simulation (Gillespie, 1977). The Gillespie

Table 3 | Bifurcation points in the deterministic model.

Parameter	Bifurcation value	Oscillatory behavior
k_p	0.215/s	Undamped: $0.215 \leq k_p \leq 1.462$
k_p	1.462/s	Damped: $k_p \leq 0.215 \cup k_p \geq 1.462$
k_1	2.903×10^{-6} /s	Undamped: $2.903 \times 10^{-6} \leq k_1 \leq 1.834 \times 10^{-5}$
k_1	1.834×10^{-5} /s	Damped: $k_1 \leq 2.903 \times 10^{-6} \cup k_1 \geq 1.834 \times 10^{-5}$
d_p	4.237×10^{-4} /s	Undamped: $d_p \leq 4.237 \times 10^{-4}$
k_m	2.788×10^{-3} /s	Undamped: $k_m \leq 2.788 \times 10^{-3}$
k_2	7.501×10^{-3} /s	Undamped: $7.501 \times 10^{-3} \leq k_2 \leq 0.118$
k_2	0.118/s	Damped: $k_2 \leq 7.501 \times 10^{-3} \cup k_2 \geq 0.118$
K_D	253.083	Undamped: $253.083 \leq K_D \leq 1723.058$
K_D	1723.058	Damped: $K_D \leq 253.083 \cup K_D \geq 1723.058$
k_0	7.010×10^{-6} /s	Undamped: $7.010 \times 10^{-6} \leq k_0 \leq 6.160 \times 10^{-3}$
k_0	6.160×10^{-3} /s	Damped: $k_0 \leq 7.010 \times 10^{-6} \cup k_0 \geq 6.160 \times 10^{-3}$
d_{rc}	8.714×10^{-5} /s	Undamped: $8.714 \times 10^{-5} \leq d_{rc} \leq 2.704 \times 10^{-4}$
d_{rc}	2.704×10^{-4} /s	Damped: $d_{rc} \leq 8.714 \times 10^{-5} \cup d_{rc} \geq 2.704 \times 10^{-4}$
k_T	8.760×10^{-3} /s	Undamped: $8.760 \times 10^{-3} \leq k_T \leq 2.936 \times 10^{-2}$
k_T	2.936×10^{-2} /s	Damped: $k_T \leq 8.760 \times 10^{-3} \cup k_T \geq 2.936 \times 10^{-2}$
k_i	6.845×10^{-6} /s	Undamped: $6.845 \times 10^{-6} \leq k_i \leq 1.559 \times 10^{-2}$
k_i	1.559×10^{-2} /s	Damped: $k_i \leq 6.845 \times 10^{-6} \cup k_i \geq 1.559 \times 10^{-2}$
d_{mn}	1.251×10^{-6} /s	Undamped: $d_{mn} \leq 1.251 \times 10^{-6}$
k_a	0.324/s	Undamped: $0.324 \leq k_a \leq 0.963$
k_a	0.963/s	Damped: $k_a \leq 0.324 \cup k_a \geq 0.963$
d_a	2.088×10^{-3} /s	Undamped: $d_a \leq 2.088 \times 10^{-3}$
k_3	5.866×10^{-6} /s	Undamped: $k_3 \geq 5.866 \times 10^{-6}$

algorithm has the advantage of being exact, unfortunately, it is also computationally expensive. In order to conduct our investigation we chose to instead use an approximate simulation, because the Gillespie algorithm is too slow for the required complexity and number of simulation runs.

The algorithm we created was based on the concepts of a finite difference integrator. In a finite difference integrator a system of differential equations is evaluated by first calculating each of the

derivatives at a point in time, then multiplying them by the time step size, and finally updating each of the variables by the corresponding amount. In our algorithm, rather than being evaluated as a single set of derivatives each chemical reaction is evaluated separately. When the simulation evaluates a chemical reaction, the first step is to use the law of mass-action and the average of the current chemical concentrations, and their concentrations after the last time the reaction was evaluated, to find an expectation value for the number of times the reaction will occur during this time step. Next, the expectation value for the number of times the reaction will occur is set as the expectation value for a Poisson random number generator and the result is the number of times the reaction will actually occur during that time step. This gives the algorithm a strong resemblance to the well known tau leap method (Gillespie, 2007), in which Poisson random numbers are used in combination with the Gillespie algorithm to improve efficacy. In order to improve efficiency while preserving accuracy in our algorithm, an adaptive time step is used. The program evaluates each reaction 0.5^N times per simulated second, with N chosen such that the expectation value for a particular evaluation of a reaction is lower than a preset threshold multiplied by the quantity of the chemical molecules involved. In this way parts of the system that are changing rapidly are evaluated with a low enough time step to prevent numerical errors, without needing to waste additional computations on the slower reactions.

Figure 5 shows some examples of individual simulation runs for this model. The stochastic nature of the simulation leads to a number of interesting differences arising from the desynchronization of the individual model runs as well as from applying a distribution of p53 values into the non-linear function for MDM2 production.

RESULTS

DESYNCHRONIZATION IN GENERAL

In order to understand how the individual stochastic realizations of our model fall out of synch with each other let us first consider how stochastic systems may fall out of synchronization in general. An experiment averaging protein levels across many cells is analogous to looking at the average of many runs of a stochastic system. As such, it is interesting to consider how aggregate average behavior differs from the behavior of individual model runs. A given run of the stochastic model will not necessarily just be equal to the deterministic model plus noise. At any given step the stochastic model's variables depend on the values of the variables at the previous time step. For a periodic model this will result not only in noise moving variables up and down but also in random stepping forwards and backwards of the model's phase. Consequently, an ensemble of model runs will fall out of synchronization over time. Imagine for simplicity a stochastic model based on a deterministic model with a variable given by $A \sin(\omega t + \varphi)$. In the stochastic model random chance continuously moves each run in the ensemble toward or away from the next peak. Considering the central limit theorem applied over a large number of runs, one would then expect the distribution of timing of the peak in individual runs to approach a normal distribution. If all the runs are initialized from the same starting point, then the amplitude of the mean will not

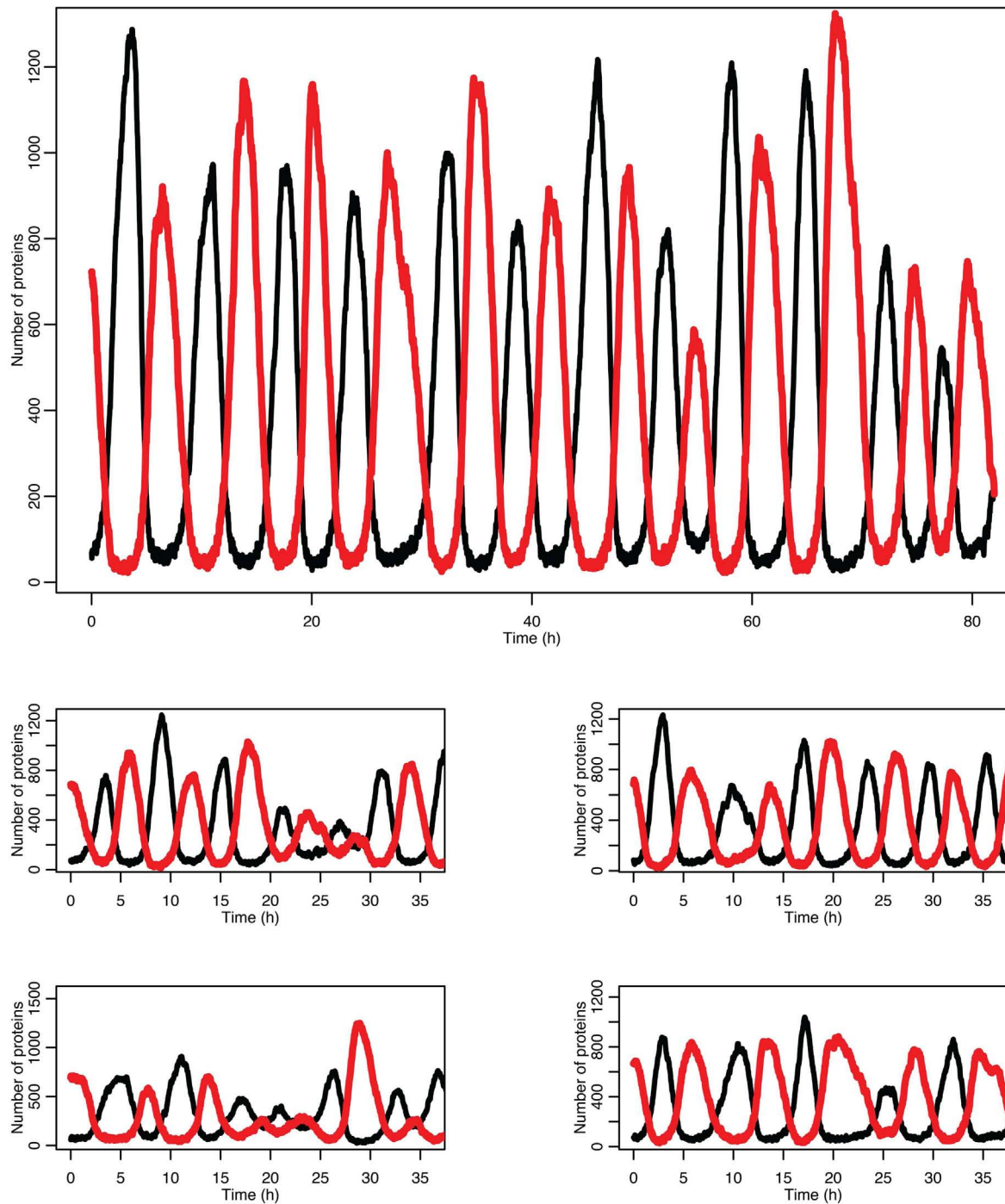


FIGURE 5 | Examples of time courses in the stochastic model. p53 is in black and MDM2 is in red.

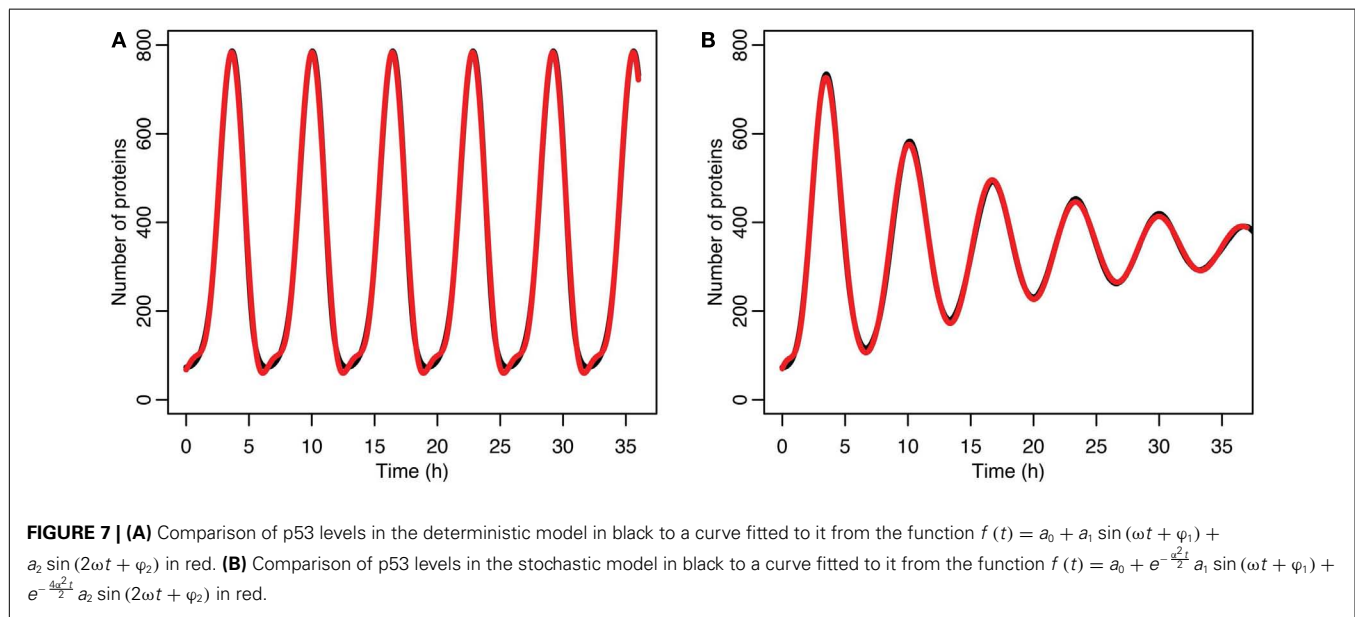
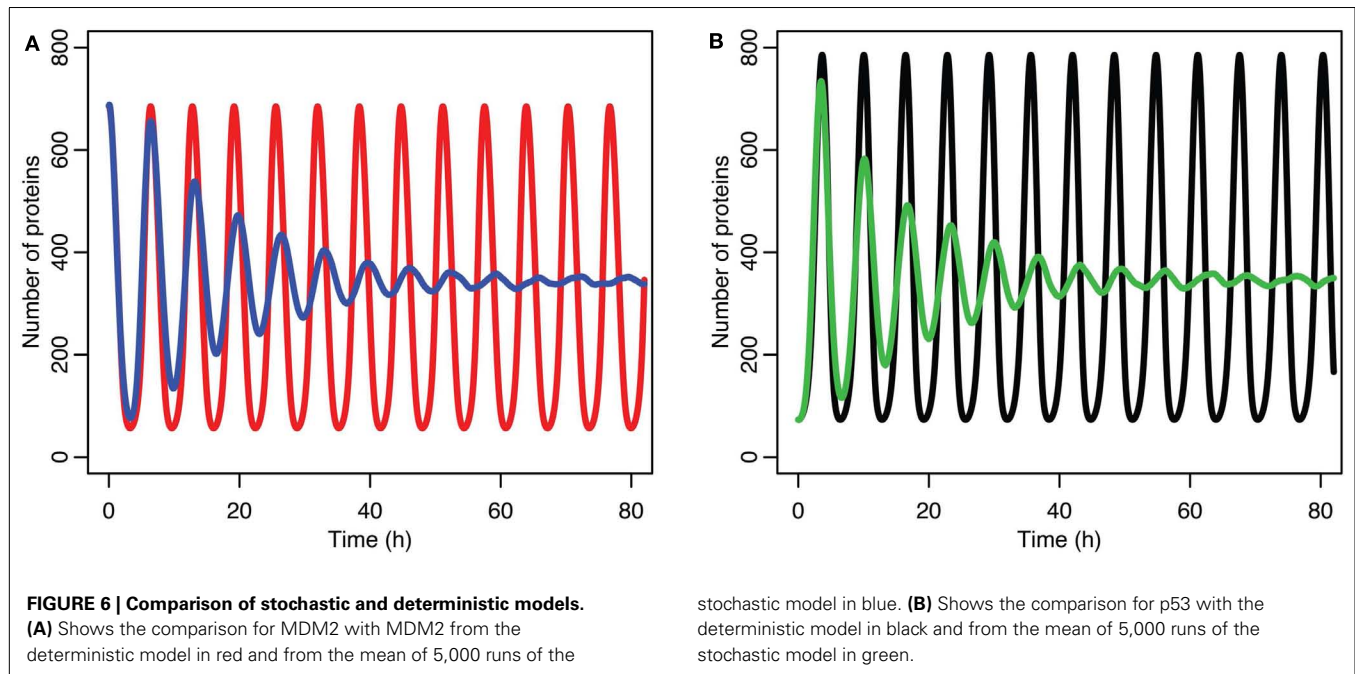
be $A \sin(\omega t + \varphi)$ but rather it will be

$$A \int_{-\infty}^{\infty} \frac{1}{\sigma\sqrt{2\pi}} e^{-\frac{t'^2}{2\sigma^2}} \sin(\omega t + \varphi + \omega t') dt'$$

because the timing of each run will be shifted with a Gaussian weighting given to the shift. Since the width of the distribution

will increase proportionally to the square root of time, the standard deviation σ can be expanded as $\alpha\sqrt{t}$, where α is a parameter related to the rate of desynchronization. This integral then works out to be

$$A e^{-\frac{\omega^2 \alpha^2 t}{2}} \sin(\omega t + \varphi)$$



Consider a 2π periodic function that is integrable on the interval from $-\pi$ to π . This function could be expressed as a Fourier series such that

$$f(t) = \frac{a_0}{2} + \sum_{n=1}^{\infty} [a_n \cos(nt) + b_n \sin(nt)]$$

or equivalently

$$f(t) = \frac{a_0}{2} + \sum_{n=1}^{\infty} \left[a_n \sin\left(nt + \frac{\pi}{2}\right) + b_n \sin(nt) \right]$$

Applying the result above we find that the function will be changed by desynchronization to become

$$f'(t) = \frac{a_0}{2} + \sum_{n=1}^{\infty} \left[a_n \sin\left(nt + \frac{\pi}{2}\right) + b_n \sin(nt) \right] e^{-\frac{n^2 \alpha^2 t}{2}}$$

Since the decay is proportional to the square of the frequency, any function will rapidly take on the appearance of a single decaying sine-function curve as time progresses.

DESYNCHRONIZATION IN THE STOCHASTIC MODEL

The damping caused by desynchronization in the stochastic model can be seen in **Figure 6**. The deterministic and stochastic systems can be compared by fitting a curve to the time series for p53. Specifically:

$$f(t) = a_0 + a_1 \sin(\omega t + \varphi_1) + a_2 \sin(2\omega t + \varphi_2)$$

for the deterministic model, and

$$f(t) = a_0 + e^{-\frac{\alpha^2 t}{2}} a_1 \sin(\omega t + \varphi_1) + e^{-\frac{4\alpha^2 t}{2}} a_2 \sin(2\omega t + \varphi_2)$$

for the stochastic model. **Table 4** lists the parameter estimates for the deterministic model as well as 95% confidence intervals for the stochastic model. **Figure 7** shows graphs of the functions and their best fits. The best fit was determined by using least squares regression on the mean p53 values from 5,000 instances of the stochastic

model. The upper and lower bounds were found by using bootstrapping on the 5,000 instances that were used to compute the best fit. The 95% confidence intervals for the amplitude and phase of the second sine curve ended up being very large due to the curve fitting function jumping between local minima. To ensure that the algorithm was being run at a high enough numerical precision, an additional 5,000 instances were generated with the acceptable error parameter in the code selected to equal 10 times the value used in this analysis. The resulting new confidence intervals were compared to the ones from the higher accuracy runs. In all cases significant overlap of the intervals was found, suggesting that the acceptable error was set low enough in the high accuracy runs to result in only negligible deviations from an exact solution.

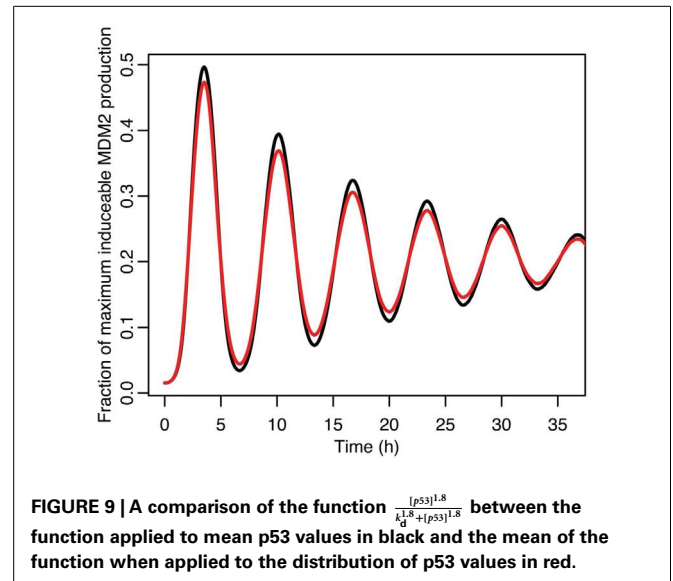
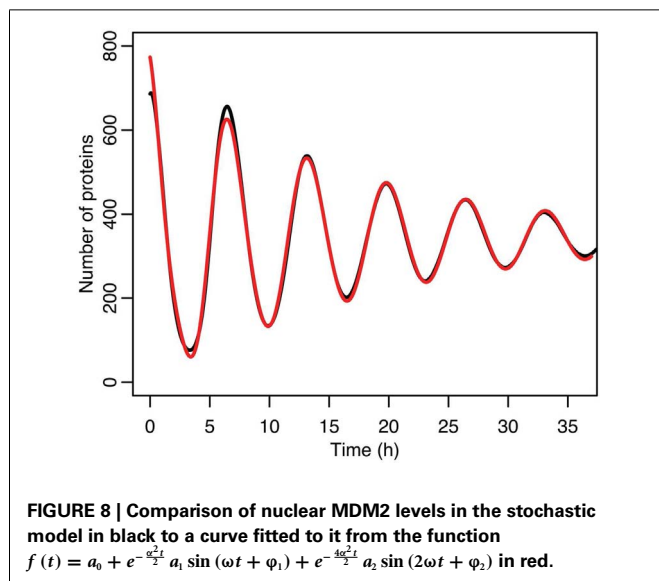
The differences between the stochastic model's behavior and the deterministic model's behavior are statistically significant. Most striking is that the frequency of the oscillations was changed by stochastic effects. The same analysis has been done on nuclear

Table 4 | Comparisons of the parameters found when fitting the deterministic model's p53 levels to the function $f(t) = a_0 + a_1 \sin(\omega t + \varphi_1) + a_2 \sin(2\omega t + \varphi_2)$ and the stochastic model's p53 levels to the function $f(t) = a_0 + e^{-\frac{\alpha^2 t}{2}} a_1 \sin(\omega t + \varphi_1) + e^{-\frac{4\alpha^2 t}{2}} a_2 \sin(2\omega t + \varphi_2)$.

	Parameters fitted to deterministic model	Parameters fitted to stochastic model	Lower bound for stochastic parameters	Upper bound for stochastic parameters
α	N/A	21.8/s ^{1/2}	21.2/s ^{1/2}	22.5/s ^{1/2}
ω	2.73×10^{-4} /s	2.63×10^{-4} /s	2.62×10^{-4} /s	2.64×10^{-4} /s
A_0	332	346	345	347
A_1	-348	-396	-406	-388
f_1	1.21	1.40	1.38	1.43
A_2	105	136	-136	144
f_2	0.633	-1.16	-36.6	13.6

Table 5 | Comparisons of the parameters found when fitting the deterministic model's nuclear MDM2 levels to the function $f(t) = a_0 + a_1 \sin(\omega t + \varphi_1) + a_2 \sin(2\omega t + \varphi_2)$ and the stochastic model's nuclear MDM2 levels to the function $f(t) = a_0 + e^{-\frac{\alpha^2 t}{2}} a_1 \sin(\omega t + \varphi_1) + e^{-\frac{4\alpha^2 t}{2}} a_2 \sin(2\omega t + \varphi_2)$.

	Parameters fitted to deterministic model	Parameters fitted to stochastic model	Lower bound for stochastic parameters	Upper bound for stochastic parameters
α	N/A	20.7/s ^{1/2}	20.2/s ^{1/2}	21.3/s ^{1/2}
ω	2.73×10^{-4} /s	2.63×10^{-4} /s	2.62×10^{-4} /s	2.63×10^{-4} /s
A_0	302	345	343	346
A_1	-314	-372	-379	-365
f_1	-1.72	-1.49	-1.51	-1.47
A_2	-71	-78.5	-82.8	-74.6
f_2	-1.73	-0.80	-0.87	-0.73

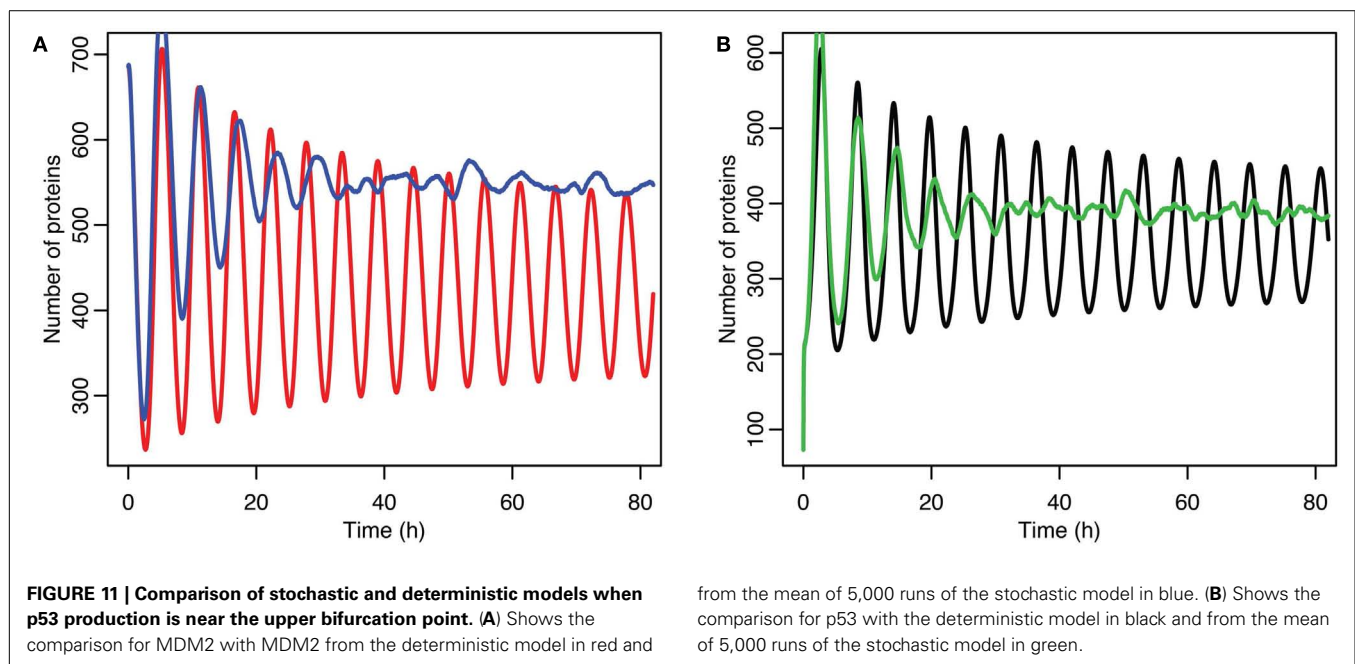
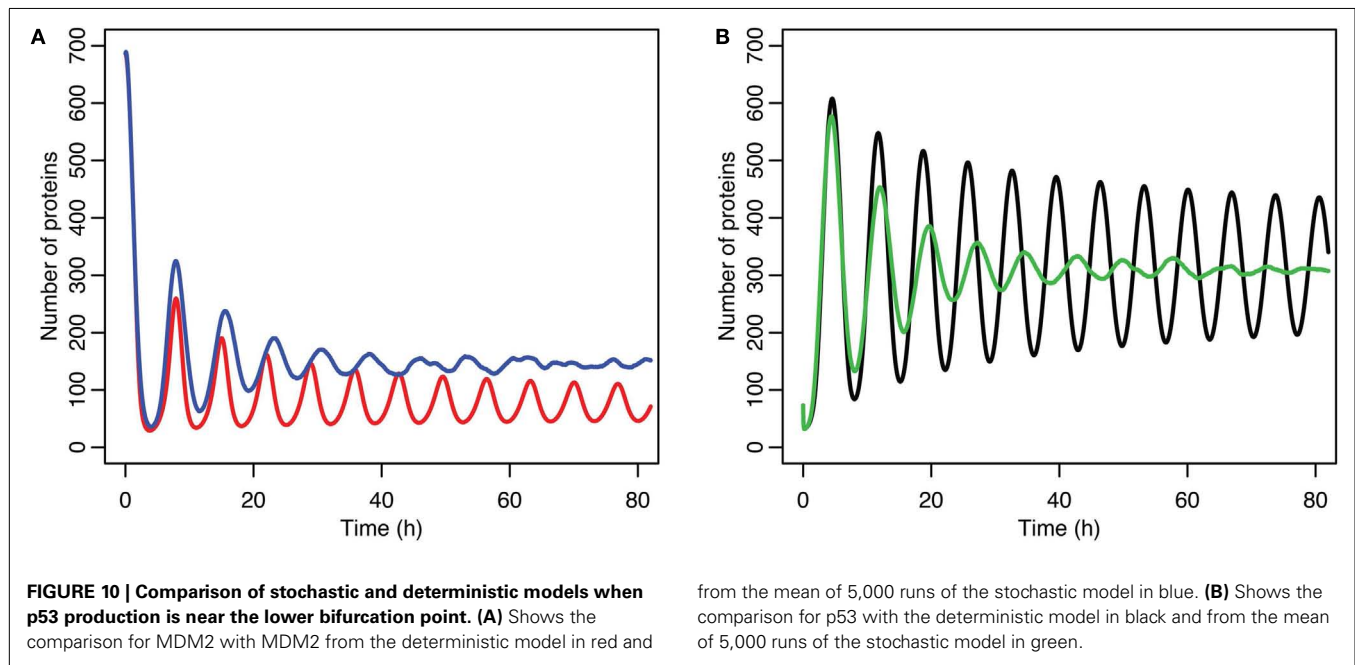


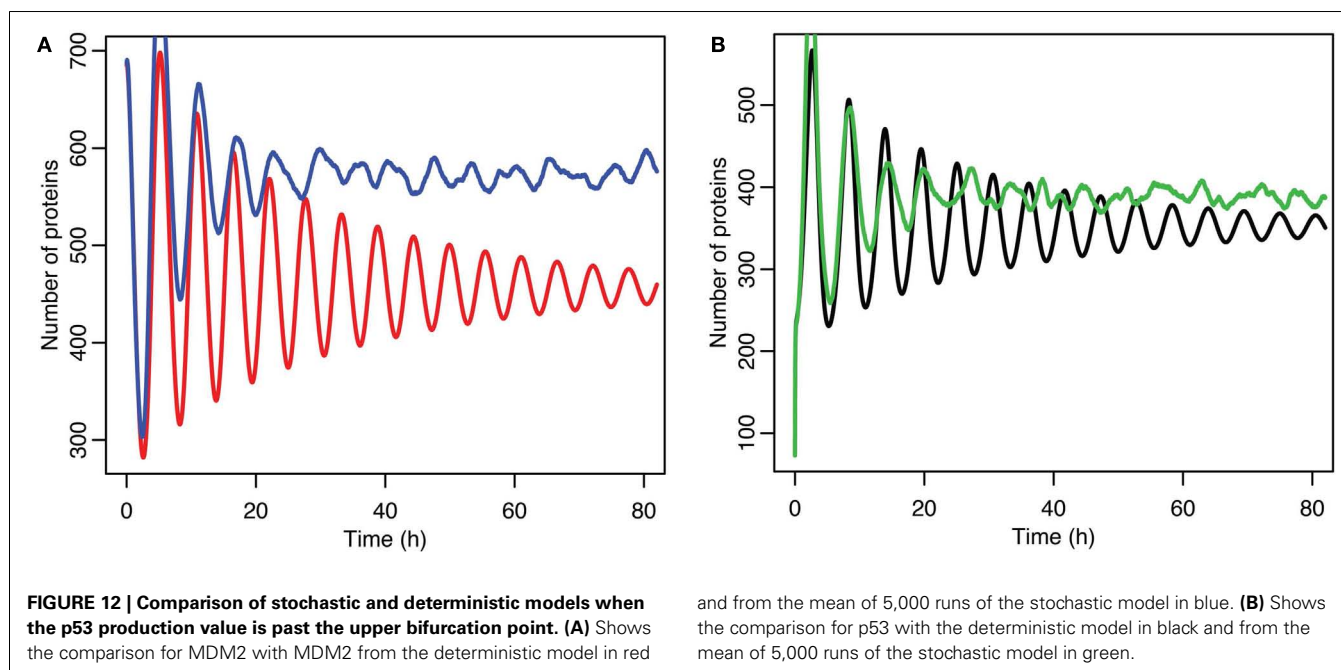
MDM2 levels, which can be seen in **Figure 8** and **Table 5**. The discrepancy between the fitted curve for MDM2 levels and the levels from the simulation hints at another difference between stochastic and deterministic systems, which will be discussed below. It is also worth noting that this stochastic model only considers the differences between cells due to noise in a few chemical reactions. In a real cell there would be many more factors contributing to desynchronization. Even simply adding mRNA for the p53 and ARF included in this model raises the desynchronization parameter a from 21.8 to $23.5 \text{ s}^{-1/2}$ (a mean of 30 mRNA molecules was used for this simulation). Additionally, differences in

cell volume would increase desynchronization by altering protein concentrations between cells.

CHANGES DUE TO NON-LINEAR EFFECTS

The mean of a stochastic ensemble for the stochastic model deviates from the deterministic model not just from desynchronization but also due to non-linear effects. For a non-linear function applied to a distribution of inputs, the mean of the function will not necessarily be equal to the function of the mean. In other words, as is well known in statistics, the following is usually true: $\langle f(x) \rangle \neq f(\langle x \rangle)$, unless f is a linear function of x .



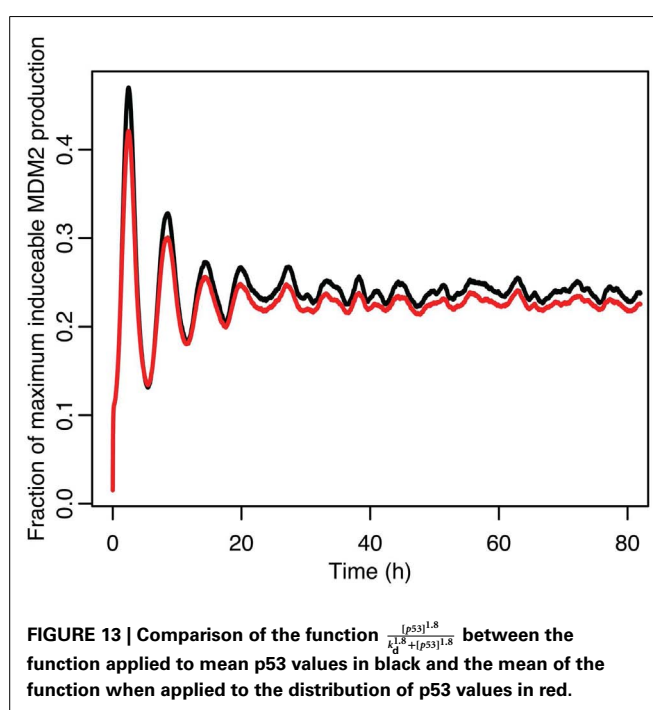


Production of MDM2 mRNA in this model is clearly non-linear because it is proportional to $f(p53) = \frac{[p53]^{1.8}}{k_d^{1.8} + [p53]^{1.8}}$. **Figure 9** compares the function of the mean to the mean of the function for this case. Mean MDM2 values in the stochastic model are determined by $\langle f(p53) \rangle$ (the red curve in **Figure 9**) which has a different amplitude than $f(\langle p53 \rangle)$ (the black curve in **Figure 9**). This discrepancy causes the behavior of the system to change relative to the deterministic case, which only has mean p53 values. This is also the most likely source of the discrepancy between the fitted curve in **Figure 8** and the actual levels of MDM2. With production that behaves differently, the initial conditions in the simulation would not have represented a point on the limit cycle for MDM2 levels. As a consequence, the system would have been moving toward the limit cycle at the same time as it was desynchronizing. The simple fitted curve cannot possibly account for this, which is why it did not fit well. p53 levels would also have been affected by this but this does not seem to have been a large enough effect to be readily noticeable on the graph.

Although the effect on the amplitude of the oscillations with the original parameters was relatively small, amounting to approximately 5%, the non-linear effects can be larger in other situations. Consider the case when the p53 production rate is set near to the lower bifurcation point, as shown in **Figure 10**. In this case the mean level of MDM2 from the stochastic model ends up being higher than the maximum amplitude of the oscillations in the deterministic model. A similar phenomenon occurs when p53 production is near the upper bifurcation point as is shown in **Figure 11**.

EXCURSIONS FROM THE MEAN

Stochastic effects continue to play an interesting role in the system's behavior even as we move past the upper bifurcation point,



so that the deterministic model exhibits damped oscillations. For **Figures 12–14**, p53 production was set to 1.6, putting the system into the realm of damped oscillations. In **Figure 12** we can see that as the oscillations decay, the MDM2 levels settle in at a value significantly higher in the stochastic model than the deterministic one. From **Figure 13** we can see that the non-linear effects of variable p53 levels are still altering behavior, but something more is occurring this time. In **Figure 12B** we see that mean p53 levels are settling in at a level higher in the stochastic model than in

the deterministic one. This seems strange in light of the higher MDM2 levels but **Figure 14** shows the reason. The stochastic nature of the system is sufficient to cause significant excursions from the mean even though the oscillations should be decaying. Some of the oscillations that occur later on are even larger than the initial pulse. Similar behavior has been observed in other stochastic models such as the one presented in McKane and Newman (2005), but has not been previously observed in a model of the p53 system.

DISCUSSION

The stochastic work we present in this paper differs from previous modeling efforts in that its goal is primarily to compare the behavior of stochastic and deterministic realizations of the same model. This requires only a simple model; therefore much of the complexity of the p53 system can be ignored. Since the model presented in this work is not aimed at addressing DNA repair, or dealing with the problem of variable damage being done, it does not include such systems. The model presented here also differs

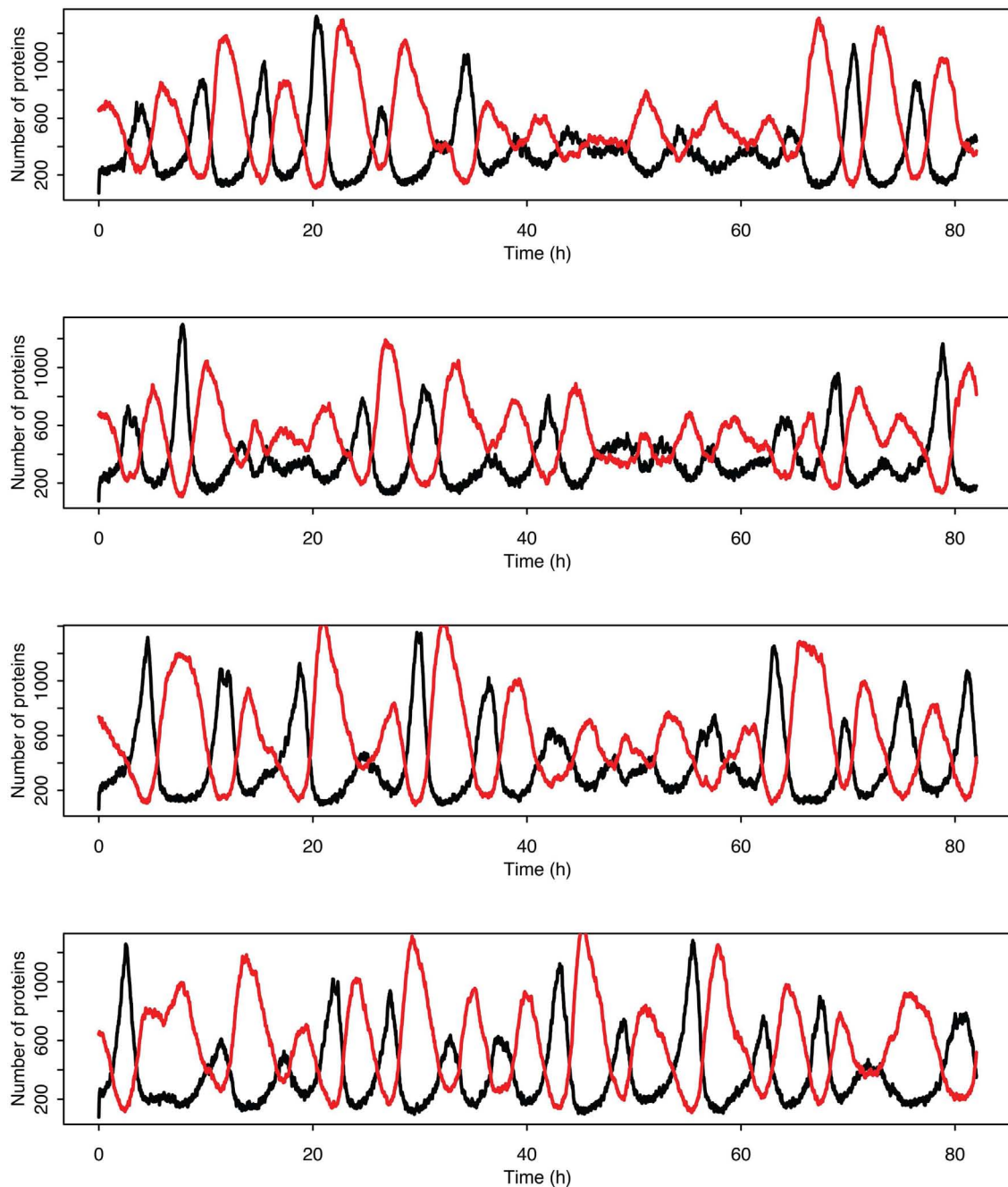


FIGURE 14 | Examples of individual stochastic realizations when p53 production is past the upper bifurcation point. p53 is in black MDM2 is in red.

from the previous models in a few other ways. Unlike in other models, MDM2 autoubiquitination was assumed to happen at a rate proportional to the square of MDM2 concentration. Given that MDM2 forms heterodimers with MDMX (Sharp et al., 1999), that MDMX inhibits MDM2 autoubiquitination (Okamoto et al., 2009), and that MDM2 ubiquitinates MDMX (De Graaf et al., 2003), it seems likely that one MDM2 molecule is ubiquitinating a second MDM2 molecule.

The work on the deterministic and stochastic models presented here demonstrates that the effects of stochasticity on the behavior of genetic regulatory networks cannot be dismissed without careful consideration. In our system stochastic effects altered every aspect of system behavior. In addition to desynchronization leading to the appearance of decaying oscillations, the amount of MDM2 in the system increased and the period of the oscillations changed. The changes in MDM2 levels became more obvious when p53 production was near bifurcation points. When the system was put into a state with decaying oscillations, the quantity of MDM2 still remained above that in the deterministic model, showing that stochasticity still alters behavior as the system is near a steady state. Furthermore, stochastic systems will not necessarily undergo damped oscillations even when assigned parameters that would cause damped oscillations in a deterministic system. Instead, they may show sporadic oscillation-like excursions from the mean behavior. It would seem then that even for cells in a steady state, the distribution of protein levels across a population and over time could wreak havoc with attempts to model cell behavior. This has implications for researchers wishing to model cell-level processes, as systematic errors could occur in deterministic models with no obvious way to compensate for them. As computers and algorithms improve, it may be the case that simply moving to stochastic modeling of cell populations will become the most practical solution.

The demonstration that stochasticity can be relevant is very general, but it was also shown that the magnitude of the effects could vary significantly between systems. The effect on mean protein levels could be around 5%, as in the original parameter set, or around 50%, as in some of the parameter sets with differing p53 levels. The obvious way to experimentally test the relevance

of stochasticity on any given system is by comparing data from cell populations to data from individual cells. Such experimental comparisons were, after all, the inspiration for investigating stochasticity in this system in the first place. The difference between a stochastic model and a deterministic one with different parameters are not likely to be obvious from population data, even if the effects of stochasticity are expected to be large. Testing the details of stochastic models will require investigating the behavior of individual cells. Of course, stochasticity is not the only factor that could drive individual cells to different behaviors. Factors such as differences in cell size, different cell cycle stages, and non-uniform distributions of components in cell culture medium could all alter behavior on the scale of single cells. Untangling these effects is potentially a fruitful area for future research.

A valuable way of expanding the utility of our model would be to link it to other models of related processes. The DNA repair and damage detection modules in Ma et al. (2005) would be a good example of this. Once one system is sufficiently well understood, it would be possible to begin analyzing how altering it changes connected systems, or conversely, how changing connected systems alters it. This could allow one to study downstream drug effects. For that kind of work it would likely be best to start as far upstream as possible, in order to facilitate the experimental control of inputs. For example, for the p53 system it would make sense to start with a model that quantifies the damage ionizing radiation causes to DNA and other cellular systems, because the level of radiation a cell is exposed to can be controlled in the lab. Then, once that is modeled accurately, one could study the DNA damage detection systems, and finally the p53 response. Repeating this process for other forms of damage, like for example ultraviolet light, could bring insight into the system's behavior.

ACKNOWLEDGMENTS

We would like to thank Marion Poirel for her assistance with the deterministic model, Brian Dupuis for his advice on statistics and programming in R, Dr. Krzysztof Puszyński for insightful comments on the Gillespie algorithm, Philip Winter for assistance editing the paper, and NSERC for funding support.

REFERENCES

- Alberts, B., Bray, D., Lewis, J., Raff, M., Roberts, K., and Watson, J. D. (1994). *Molecular Biology of the Cell*, 3rd Edn. New York: Garland Publishing Inc.
- Bakkenist, C. J., and Kastan, M. B. (2003). DNA damage activates ATM through intermolecular autophosphorylation and dimer dissociation. *Nature* 421, 499–506.
- Banin, S., Moyal, L., Shieh, S., Taya, Y., Anderson, C. W., Chessa, L., et al. (1998). Enhanced phosphorylation of p53 by ATM in response to DNA damage. *Science* 281, 1674–1677.
- Barak, Y., Juven, T., Haffner, R., and Oren, M. (1993). mdm2 expression is induced by wild type p53 activity. *EMBO J.* 12, 461–468.
- Barakat, K., Mane, J., Friesen, D., and Tuszyński, J. (2010). Ensemble-based virtual screening reveals dual-inhibitors for the p53-MDM2/MDMX interactions. *J. Mol. Graph. Model.* 28, 555–568.
- Batchelor, E., Loewer, A., Mock, C., and Lahav, G. (2011). Stimulus-dependent dynamics of p53 in single cells. *Mol. Syst. Biol.* 7, 488.
- Batchelor, E., Mock, C. S., Bhan, I., Loewer, A., and Lahav, G. (2008). Recurrent initiation: a mechanism for triggering p53 pulses in response to DNA damage. *Mol. Cell* 30, 277–289.
- Bond, G. L., Hu, W., and Levine, A. J. (2005). MDM2 is a central node in the p53 pathway: 12 years and counting. *Curr. Cancer Drug Targets* 5, 3–8.
- Brown, C. J., Lain, S., Verma, C. S., Fersht, A. R., and Lane, D. P. (2009). Awakening guardian angels: drug-gating the p53 pathway. *Nat. Rev. Cancer* 9, 862–873.
- Cai, X., and Yuan, Z.-M. (2009). Stochastic modeling and simulation of the p53-MDM2/MDMX loop. *J. Comput. Biol.* 16, 917–933.
- Chehab, N. H., Malikzay, A., Appel, M., and Halazonetis, T. D. (2000). Chk2/hCds1 functions as a DNA damage checkpoint in G(1) by stabilizing p53. *Genes Dev.* 14, 278–288.
- Chen, J., Lin, J., and Levine, A. J. (1995). Regulation of transcription functions of the p53 tumor suppressor by the mdm-2 oncogene. *Mol. Med.* 1, 142–152.
- Dai, C., and Gu, W. (2010). p53 post-translational modification: deregulated in tumorigenesis. *Trends Mol. Med.* 16, 528–536.
- Danovi, D., Meulmeester, E., Pasini, D., Migliorini, D., Capra, M., Frenk, R., et al. (2004). Amplification of Mdmx (or Mdm4) directly contributes to tumor formation by inhibiting p53 tumor suppressor activity. *Mol. Cell Biol.* 24, 5835–5843.
- De Graaf, P., Little, N. A., Ramos, Y. F. M., Meulmeester, E., Lettewboer, S. J. F., and Jochemsen, A. G. (2003). Hdmx protein stability is regulated by the ubiquitin ligase activity of Mdm2. *J. Biol. Chem.* 278, 38315–38324.

- Dobbelstein, M., and Roth, J. (1998). The large T antigen of simian virus 40 binds and inactivates p53 but not p73. *J. Gen. Virol.* 79 (Pt 12), 3079–3083.
- Dornan, D., Wertz, I., Shimizu, H., Arnott, D., Frantz, G. D., Dowd, P., et al. (2004). The ubiquitin ligase COP1 is a critical negative regulator of p53. *Nature* 429, 86–92.
- Fang, S., Jensen, J. P., Ludwig, R. L., Vousden, K. H., and Weissman, A. M. (2000). Mdm2 is a RING finger-dependent ubiquitin protein ligase for itself and p53. *J. Biol. Chem.* 275, 8945–8951.
- Feki, A., and Irminger-Finger, I. (2004). Mutational spectrum of p53 mutations in primary breast and ovarian tumors. *Crit. Rev. Oncol. Hematol.* 52, 103–116.
- Finch, R. A., Donoviel, D. B., Potter, D., Shi, M., Fan, A., Freed, D. D., et al. (2012). mdmX is a negative regulator of p53 activity in vivo. *Cancer Res.* 62, 3221–3225.
- Fiscella, M., Zhang, H., Fan, S., Sakaguchi, K., Shen, S., Mercer, W. E., et al. (1997). Wip1, a novel human protein phosphatase that is induced in response to ionizing radiation in a p53-dependent manner. *Proc. Natl. Acad. Sci. U.S.A.* 94, 6048–6053.
- Freed-Pastor, W. A., and Prives, C. (2012). Mutant p53: one name, many proteins. *Genes Dev.* 26, 1268–1286.
- Fujimoto, H., Onishi, N., Kato, N., Takekawa, M., Xu, X. Z., Kosugi, A., et al. (2006). Regulation of the antioncogenic Chk2 kinase by the oncogenic Wip1 phosphatase. *Cell Death Differ.* 13, 1170–1180.
- Gammack, D., Byrne, H. M., and Lewis, C. E. (2001). Estimating the selective advantage of mutant p53 tumour cells to repeated rounds of hypoxia. *Bull. Math. Biol.* 63, 135–166.
- Geva-Zatorsky, N., Dekel, E., Batchelor, E., Lahav, G., and Alon, U. (2010). Fourier analysis and systems identification of the p53 feedback loop. *Proc. Natl. Acad. Sci. U.S.A.* 107, 13550–13555.
- Geva-Zatorsky, N., Rosenfeld, N., Itzkovitz, S., Milo, R., Sigal, A., Dekel, E., et al. (2006). Oscillations and variability in the p53 system. *Mol. Syst. Biol.* 2, 2006.0033.
- Gillespie, D. T. (1977). Exact stochastic simulation of coupled chemical reactions. *J. Phys. Chem.* 81, 2340–2361.
- Gillespie, D. T. (2007). Stochastic simulation of chemical kinetics. *Annu. Rev. Phys. Chem.* 58, 35–55.
- Graeber, T. G., Peterson, J. F., Tsai, M., Monica, K., Fornace, A. J., Jr, and Giaccia, A. J. (1994). Hypoxia induces accumulation of p53 protein, but activation of a G1-phase checkpoint by low-oxygen conditions is independent of p53 status. *Mol. Cell. Biol.* 14, 6264–6277.
- Gu, J., Kawai, H., Nie, L., Kitao, H., Wiederschain, D., Jochemsen, A. G., et al. (2002). Mutual dependence of MDM2 and MDMX in their functional inactivation of p53. *J. Biol. Chem.* 277, 19251–19254.
- Ha, J.-H., Won, E.-Y., Shin, J.-S., Jang, M., Ryu, K.-S., Bae, K.-H., et al. (2011). Molecular mimicry-based repositioning of nutlin-3 to anti-apoptotic Bcl-2 family proteins. *J. Am. Chem. Soc.* 133, 1244–1247.
- Hamstra, D. A., Bhojani, M. S., Griffin, L. B., Laxman, B., Ross, B. D., and Rehmtulla, A. (2006). Real-time evaluation of p53 oscillatory behavior in vivo using bioluminescent imaging. *Cancer Res.* 66, 7482–7489.
- Hanahan, D., and Weinberg, R. A. (2011). Hallmarks of cancer: the next generation. *Cell* 144, 646–674.
- Harris, S. L., and Levine, A. J. (2005). The p53 pathway: positive and negative feedback loops. *Oncogene* 24, 2899–2908.
- Haupt, Y., Maya, R., Kazaz, A., and Oren, M. (1997). Mdm2 promotes the rapid degradation of p53. *Nature* 387, 296–299.
- Honda, R., Tanaka, H., and Yasuda, H. (1997). Oncoprotein MDM2 is a ubiquitin ligase E3 for tumor suppressor p53. *FEBS Lett.* 420, 25–27.
- Hsing, A., Faller, D. V., and Vaziri, C. (2000). DNA-damaging aryl hydrocarbons induce Mdm2 expression via p53-independent post-transcriptional mechanisms. *J. Biol. Chem.* 275, 26024–26031.
- Hu, W., Feng, Z., Ma, L., Wagner, J., Rice, J. J., Stolovitzky, G., et al. (2007). A single nucleotide polymorphism in the MDM2 gene disrupts the oscillation of p53 and MDM2 levels in cells. *Cancer Res.* 67, 2757–2765.
- Jackson, M. W., Lindstrom, M. S., and Berberich, S. J. (2001). MdmX binding to ARF affects Mdm2 protein stability and p53 transactivation. *J. Biol. Chem.* 276, 25336–25341.
- Kastan, M. B., Onyekwere, O., Sidransky, D., Vogelstein, B., and Craig, R. W. (1991). Participation of p53 protein in the cellular response to DNA damage. *Cancer Res.* 51, 6304–6311.
- Kubbutat, M. H., Jones, S. N., and Vousden, K. H. (1997). Regulation of p53 stability by Mdm2. *Nature* 387, 299–303.
- Kuo, M.-L., Den Besten, W., Bertwistle, D., Roussel, M. F., and Sherr, C. J. (2004). N-terminal polyubiquitination and degradation of the Arf tumor suppressor. *Genes Dev.* 18, 1862–1874.
- Lahav, G., Rosenfeld, N., Sigal, A., Geva-Zatorsky, N., Levine, A. J., Elowitz, M. B., et al. (2004). Dynamics of the p53-Mdm2 feedback loop in individual cells. *Nat. Genet.* 36, 147–150.
- Lane, D. P. (1992). p53, guardian of the genome. *Nature* 358, 15–16.
- LeBron, C., Chen, L., Gilkes, D. M., and Chen, J. (2006). Regulation of MDMX nuclear import and degradation by Chk2 and 14-3-3. *EMBO J.* 25, 1196–1206.
- Leng, R. P., Lin, Y., Ma, W., Wu, H., Lemmers, B., Chung, S., et al. (2003). Pirh2, a p53-induced ubiquitin-protein ligase, promotes p53 degradation. *Cell* 112, 779–791.
- Lev Bar-Or, R., Maya, R., Segel, L. A., Alon, U., Levine, A. J., and Oren, M. (2000). Generation of oscillations by the p53-Mdm2 feedback loop: a theoretical and experimental study. *Proc. Natl. Acad. Sci. U.S.A.* 97, 11250–11255.
- Levine, A. J., and Oren, M. (2009). The first 30 years of p53: growing ever more complex. *Nat. Rev. Cancer* 9, 749–758.
- Linke, S. P., Clarkin, K. C., Di Leonardo, A., Tsou, A., and Wahl, G. M. (1996). A reversible, p53-dependent G0/G1 cell cycle arrest induced by ribonucleotide depletion in the absence of detectable DNA damage. *Genes Dev.* 10, 934–947.
- Lodish, H., Berk, A., Kaiser, C. A., Kriger, M., Scott, M. P., Bretscher, A., et al. (2008). *Molecular Cell Biology*. New York: W. H. Freeman and Company.
- Lohrum, M. A., Ashcroft, M., Kubbutat, M. H., and Vousden, K. H. (2000). Identification of a cryptic nucleolar-localization signal in MDM2. *Nat. Cell Biol.* 2, 179–181.
- Lowe, S. W., and Sherr, C. J. (2003). Tumor suppression by Ink4a-Arf: progress and puzzles. *Curr. Opin. Genet. Dev.* 13, 77–83.
- Ma, L., Wagner, J., Rice, J. J., Hu, W., Levine, A. J., and Stolovitzky, G. A. (2005). A plausible model for the digital response of p53 to DNA damage. *Proc. Natl. Acad. Sci. U.S.A.* 102, 14266–14271.
- Maltzman, W., and Czyzyk, L. (1984). UV irradiation stimulates levels of p53 cellular tumor antigen in non-transformed mouse cells. *Mol. Cell. Biol.* 4, 1689–1694.
- Mandinova, A., and Lee, S. W. (2011). The p53 pathway as a target in cancer therapeutics: obstacles and promise. *Sci. Transl. Med.* 3, 64rv1.
- Marine, J.-C. W., Dyer, M. A., and Jochemsen, A. G. (2007). MDMX: from bench to bedside. *J. Cell. Sci.* 120, 371–378.
- Matsuoka, S., Rotman, G., Ogawa, A., Shiloh, Y., Tamai, K., and Elledge, S. J. (2000). Ataxia telangiectasia-mutated phosphorylates Chk2 in vivo and in vitro. *Proc. Natl. Acad. Sci. U.S.A.* 97, 10389–10394.
- Maya, R., Balass, M., Kim, S. T., Shkedy, D., Leal, J. F., Shifman, O., et al. (2001). ATM-dependent phosphorylation of Mdm2 on serine 395: role in p53 activation by DNA damage. *Genes Dev.* 15, 1067–1077.
- McKane, A. J., and Newman, T. J. (2005). Predator-prey cycles from resonant amplification of demographic stochasticity. *Phys. Rev. Lett.* 94, 218102.
- Meek, D. W., and Anderson, C. W. (2009). Posttranslational modification of p53: cooperative integrators of function. *Cold Spring Harb. Perspect. Biol.* 1, a000950.
- Mendrysa, S. M., McElwee, M. K., and Perry, M. E. (2001). Characterization of the 5' and 3' untranslated regions in murine mdm2 mRNAs. *Gene* 264, 139–146.
- Mihara, M., Erster, S., Zaika, A., Petrenko, O., Chittenden, T., Pancoska, P., et al. (2003). p53 has a direct apoptogenic role at the mitochondria. *Mol. Cell* 11, 577–590.
- Momand, J., Jung, D., Wilczynski, S., and Niland, J. (1998). The MDM2 gene amplification database. *Nucleic Acids Res.* 26, 3453–3459.
- Mor, A., Suliman, S., Ben-Yishay, R., Yunger, S., Brody, Y., and Shav-Tal, Y. (2010). Dynamics of single mRNP nucleocytoplasmic transport and export through the nuclear pore in living cells. *Nat. Cell Biol.* 12, 543–552.
- Nigro, J. M., Aldape, K. D., Hess, S. M., and Tlsty, T. D. (1997). Cellular adhesion regulates p53 protein levels in primary human keratinocytes. *Cancer Res.* 57, 3635–3639.
- Northrup, S. H., and Erickson, H. P. (1992). Kinetics of protein-protein association explained by Brownian dynamics computer simulation. *Proc. Natl. Acad. Sci. U.S.A.* 89, 3338–3342.
- Okamoto, K., Taya, Y., and Nakagama, H. (2009). Mdmx enhances p53 ubiquitination by altering the substrate preference of the Mdm2 ubiquitin ligase. *FEBS Lett.* 583, 2710–2714.
- Olivier, M., Eeles, R., Hollstein, M., Khan, M. A., Harris, C. C., and Hainaut, P. (2002). The IARCp53 database: new online mutation

- analysis and recommendations to users. *Hum. Mutat.* 19, 607–614.
- Paul, S. M., Mytelka, D. S., Dunwiddie, C. T., Persinger, C. C., Munos, B. H., Lindborg, S. R., et al. (2010). How to improve R&D productivity: the pharmaceutical industry's grand challenge. *Nat. Rev. Drug Discov.* 9, 203–214.
- Perfahl, H., Byrne, H. M., Chen, T., Estrella, V., Alarcón, T., Lapin, A., et al. (2011). Multiscale modelling of vascular tumour growth in 3D: the roles of domain size and boundary conditions. *PLoS ONE* 6:e14790. doi:10.1371/journal.pone.0014790
- Puszynski, K., Hat, B., and Lipniacki, T. (2008). Oscillations and bistability in the stochastic model of p53 regulation. *J. Theor. Biol.* 254, 452–465.
- Reed, D., Shen, Y., Shelat, A. A., Arnold, L. A., Ferreira, A. M., Zhu, F., et al. (2010). Identification and characterization of the first small molecule inhibitor of MDMX. *J. Biol. Chem.* 285, 10786–10796.
- Secchiero, P., Bosco, R., Celeghini, C., and Zauli, G. (2011). Recent advances in the therapeutic perspectives of Nutlin-3. *Curr. Pharm. Des.* 17, 569–577.
- Sharp, D. A., Kratowicz, S. A., Sank, M. J., and George, D. L. (1999). Stabilization of the MDM2 oncoprotein by interaction with the structurally related MDMX protein. *J. Biol. Chem.* 274, 38189–38196.
- Shieh, S. Y., Ahn, J., Tamai, K., Taya, Y., and Prives, C. (2000). The human homologs of checkpoint kinases Chk1 and Cds1 (Chk2) phosphorylate p53 at multiple DNA damage-inducible sites. *Genes Dev.* 14, 289–300.
- Shreeram, S., Demidov, O. N., Hee, W. K., Yamaguchi, H., Onishi, N., Kek, C., et al. (2006). Wip1 phosphatase modulates ATM-dependent signaling pathways. *Mol. Cell* 23, 757–764.
- Shvarts, A., Steegenga, W. T., Riteco, N., Van Laar, T., Dekker, P., Bazuine, M., et al. (1996). MDMX: a novel p53-binding protein with some functional properties of MDM2. *EMBO J.* 15, 5349–5357.
- Soussi, T., and Wiman, K. G. (2007). Shaping genetic alterations in human cancer: the p53 mutation paradigm. *Cancer Cell* 12, 303–312.
- Stott, F. J., Bates, S., James, M. C., McConnell, B. B., Starborg, M., Brookes, S., et al. (1998). The alternative product from the human CDKN2A locus, p14(ARF), participates in a regulatory feedback loop with p53 and MDM2. *EMBO J.* 17, 5001–5014.
- Suad, O., Rozenberg, H., Brosh, R., Diskin-Posner, Y., Kessler, N., Shimon, L. J. W., et al. (2009). Structural basis of restoring sequence-specific DNA binding and transactivation to mutant p53 by suppressor mutations. *J. Mol. Biol.* 385, 249–265.
- Sugrue, M. M., Shin, D. Y., Lee, S. W., and Aaronson, S. A. (1997). Wild-type p53 triggers a rapid senescence program in human tumor cells lacking functional p53. *Proc. Natl. Acad. Sci. U.S.A.* 94, 9648–9653.
- Supiot, S., Hill, R. P., and Bristow, R. G. (2008). Nutlin-3 radiosensitizes hypoxic prostate cancer cells independent of p53. *Mol. Cancer Ther.* 7, 993–999.
- Teodoro, J. G., Evans, S. K., and Green, M. R. (2007). Inhibition of tumor angiogenesis by p53: a new role for the guardian of the genome. *J. Mol. Med.* 85, 1175–1186.
- Tibbetts, R. S., Brumbaugh, K. M., Williams, J. M., Sarkaria, J. N., Cliby, W. A., Shieh, S. Y., et al. (1999). A role for ATR in the DNA damage-induced phosphorylation of p53. *Genes Dev.* 13, 152–157.
- Truant, R., Antunovic, J., Greenblatt, J., Prives, C., and Cromlish, J. A. (1995). Direct interaction of the hepatitis B virus HBx protein with p53 leads to inhibition by HBx of p53 response element-directed transactivation. *J. Virol.* 69, 1851–1859.
- Turpin, E., Luke, K., Jones, J., Tumpey, T., Konan, K., and Schultz-Cherry, S. (2005). Influenza virus infection increases p53 activity: role of p53 in cell death and viral replication. *J. Virol.* 79, 8802–8811.
- Vassilev, L. T., Vu, B. T., Graves, B., Carvajal, D., Podlaski, F., Filipovic, Z., et al. (2004). In vivo activation of the p53 pathway by small-molecule antagonists of MDM2. *Science* 303, 844–848.
- Ventura, A., Kirsch, D. G., McLaughlin, M. E., Tuveson, D. A., Grimm, J., Lin-tault, L., et al. (2007). Restoration of p53 function leads to tumour regression in vivo. *Nature* 445, 661–665.
- Vousden, K. H., and Lu, X. (2002). Live or let die: the cell's response to p53. *Nat. Rev. Cancer* 2, 594–604.
- Wang, H., Ma, X., Ren, S., Buolamwini, J. K., and Yan, C. (2011). A small-molecule inhibitor of MDMX activates p53 and induces apoptosis. *Mol. Cancer Ther.* 10, 69–79.
- Weber, J. D., Taylor, L. J., Roussel, M. F., Sherr, C. J., and Bar-Sagi, D. (1999). Nucleolar Arf sequesters Mdm2 and activates p53. *Nat. Cell Biol.* 1, 20–26.
- Weinberg, R. L., Veprintsev, D. B., Bycroft, M., and Fersht, A. R. (2005). Comparative binding of p53 to its promoter and DNA recognition elements. *J. Mol. Biol.* 348, 589–596.
- Zhang, Y., Xiong, Y., and Yarbrough, W. G. (1998). ARF promotes MDM2 degradation and stabilizes p53: ARF-INK4a locus deletion impairs both the Rb and p53 tumor suppression pathways. *Cell* 92, 725–734.
- Zhao, R., Gish, K., Murphy, M., Yin, Y., Notterman, D., Hoffman, W. H., et al. (2000). Analysis of p53-regulated gene expression patterns using oligonucleotide arrays. *Genes Dev.* 14, 981–993.

Conflict of Interest Statement: The authors declare that the research was conducted in the absence of any commercial or financial relationships that could be construed as a potential conflict of interest.

Received: 08 November 2012; accepted: 08 March 2013; published online: 02 April 2013.

Citation: Leenders GB and Tuszyński JA (2013) Stochastic and deterministic models of cellular p53 regulation. *Front. Oncol.* 3:64. doi: 10.3389/fonc.2013.00064

This article was submitted to *Frontiers in Molecular and Cellular Oncology*, a specialty of *Frontiers in Oncology*.

Copyright © 2013 Leenders and Tuszyński. This is an open-access article distributed under the terms of the Creative Commons Attribution License, which permits use, distribution and reproduction in other forums, provided the original authors and source are credited and subject to any copyright notices concerning any third-party graphics etc.



Compartment model predicts VEGF secretion and investigates the effects of VEGF Trap in tumor-bearing mice

Stacey D. Finley*, Manjima Dhar and Aleksander S. Popel

Department of Biomedical Engineering, Johns Hopkins University School of Medicine, Baltimore, MD, USA

Edited by:

Katarzyna Anna Rejniak, H. Lee
Moffitt Cancer Center & Research
Institute, USA

Reviewed by:

Roya Khosravi-Far, Massachusetts
Institute of Technology, USA
Katie Bentley, Cancer Research UK,
UK

*Correspondence:

Stacey D. Finley, Department of
Biomedical Engineering, Johns
Hopkins University School of
Medicine, 720 Rutland Avenue,
Baltimore, MD 21205, USA
e-mail: sdfinley@jhu.edu

Angiogenesis, the formation of new blood vessels from existing vasculature, is important in tumor growth and metastasis. A key regulator of angiogenesis is vascular endothelial growth factor (VEGF), which has been targeted in numerous anti-angiogenic therapies aimed at inhibiting tumor angiogenesis. Systems biology approaches, including computational modeling, are useful for understanding this complex biological process and can aid in the development of novel and effective therapeutics that target the VEGF family of proteins and receptors. We have developed a computational model of VEGF transport and kinetics in the tumor-bearing mouse, which includes three-compartments: normal tissue, blood, and tumor. The model simulates human tumor xenografts and includes human (VEGF₁₂₁ and VEGF₁₆₅) and mouse (VEGF₁₂₀ and VEGF₁₆₄) isoforms. The model incorporates molecular interactions between these VEGF isoforms and receptors (VEGFR1 and VEGFR2), as well as co-receptors (NRP1 and NRP2). We also include important soluble factors: soluble VEGFR1 (sFlt-1) and α -2-macroglobulin. The model accounts for transport via macromolecular transendothelial permeability, lymphatic flow, and plasma clearance. We have fit the model to available *in vivo* experimental data on the plasma concentration of free VEGF Trap and VEGF Trap bound to mouse and human VEGF in order to estimate the rates at which parenchymal cells (myocytes and tumor cells) and endothelial cells secrete VEGF. Interestingly, the predicted tumor VEGF secretion rates are significantly lower (0.007–0.023 molecules/cell/s, depending on the tumor microenvironment) than most reported *in vitro* measurements (0.03–2.65 molecules/cell/s). The optimized model is used to investigate the interstitial and plasma VEGF concentrations and the effect of the VEGF-neutralizing agent, VEGF Trap (aflibercept). This work complements experimental studies performed in mice and provides a framework with which to examine the effects of anti-VEGF agents, aiding in the optimization of such anti-angiogenic therapeutics as well as analysis of clinical data. The model predictions also have implications for biomarker discovery with anti-angiogenic therapies.

Keywords: systems biology, mathematical model, computational model, angiogenesis, tumor xenograft model, anti-angiogenic therapy, cancer

INTRODUCTION

Angiogenesis is the formation of new blood capillaries from pre-existing vessels, and is a process involved in physiological function, such as exercise and wound healing, as well as disease conditions, including cancer, peripheral and coronary artery diseases, pre-eclampsia, and age-related macular degeneration (AMD). The vascular endothelial growth factor (VEGF) family is a key promoter of angiogenesis and vascular development. The VEGF family includes five ligands: VEGF-A, VEGF-B, VEGF-C, VEGF-D, and placental growth factor (PlGF). One of the most widely studied members is VEGF-A, commonly referred to as VEGF. Alternative splicing of VEGF produces different isoforms, including VEGF₁₂₁, VEGF₁₆₅, VEGF₁₈₉, and VEGF₂₀₆ in humans. Expressed rodent isoforms are one amino acid shorter than human isoforms; therefore, the subscripted number is one less. Additionally, there are VEGF_{xxx} isoforms, which have been shown to be endogenous anti-angiogenic species (1, 2). VEGF promotes angiogenesis by

binding to and activating its receptors VEGFR1 and VEGFR2, and co-receptors called neuropilins (NRPs). Signal transduction through the receptors promotes many cellular processes, including cell proliferation, migration, and survival (3). VEGFR1 and VEGFR2 are expressed on endothelial cells (ECs), cancer cells, and other cell types, including bone marrow-derived cells and neurons [see (4) for review]. NRPs are expressed on various cell types, including ECs, tumor cells, and muscle fibers (4).

Angiogenesis has been targeted to treat diseases characterized by reduced vascularization (“pro-angiogenic therapy”) (5, 6) or to inhibit the formation of new blood vessels in conditions leading to hypervascularization (“anti-angiogenic therapy”) (7, 8). Of particular importance is anti-angiogenic therapy targeting tumor vascularization. Bevacizumab (9) is a recombinant monoclonal antibody that neutralizes VEGF and is approved by the Food and Drug Administration to treat colorectal cancer, glioblastoma, kidney cancer, and non-small cell lung cancer. Aflibercept

(Regeneron) is a soluble decoy receptor approved to treat metastatic colorectal cancer and wet AMD. The drug is also in clinical trials to evaluate its anti-angiogenic effect on various forms of cancers (10). Aflibercept binds to VEGF more tightly than bevacizumab (11) and forms a 1:1 complex with VEGF and PlGF (12). In addition to therapies that target the VEGF ligand, several tyrosine kinase inhibitors (TKIs) have been developed to target phosphorylation of VEGF receptors, as well as other pro-angiogenic receptors including platelet-derived growth factor (PDGF) receptors and fibroblast growth factor (FGF) receptors (13, 14).

Systems biology approaches, including quantitative experimental methods and mathematical modeling, have been applied to study angiogenesis (15–17). Computational models complement experimental studies and can aid in the development and optimization of effective therapeutics (18). Despite extensive basic science and translational research to develop anti-angiogenic therapies, little is known about the drugs’ mechanism of action, how and why tumors become resistant to the treatment, or the patient population that can benefit most from these drugs. Identifying biomarkers that can be used to predict the patients whose tumors will respond favorably to anti-angiogenic treatment is of great interest (19–21). Computational approaches can shed light upon these issues by providing a framework to generate and test hypotheses related to VEGF kinetics and transport in the body (14, 22).

We have previously developed an experiment-based compartment model of VEGF distribution in non-tumor-bearing mice, which estimates the distribution of VEGF in the body (23). Additionally, the model was used to fit kinetic parameters and to predict the rate at which VEGF is secreted by muscle fibers, which is difficult to measure experimentally *in vivo*. In this work, we present an expanded model that includes a tumor compartment and incorporates several new features: EC secretion of VEGF, soluble factors that influence VEGF levels, and a dynamic tumor volume. These new elements lead to a more physiological model and incorporate experimental observations relevant to VEGF kinetics and transport in the whole body, which can be compared to experimental data. Thus, this work represents a significant expansion to our previous models (23–26). We first re-calibrate the two-compartment model (no tumor is present) using *in vivo* experimental data and estimate the rates at which VEGF is secreted by muscle fibers and ECs, as well as the clearance rates of unbound and complexed VEGF Trap, and the binding affinity of VEGF trap. We then fit the three-compartment model to available *in vivo* experimental data in order to estimate the rate of VEGF secretion by muscle fibers, ECs, and tumor cells. We demonstrate how the model can be applied to investigate the effect of neutralizing VEGF using VEGF Trap. These results contribute to our understanding of the efficacy of VEGF Trap in specific tumor types. We also estimate the concentrations of VEGF in different compartments, which can be validated experimentally.

RESULTS

RE-CALIBRATION OF TWO-COMPARTMENT MODEL CAPTURES DYNAMICS OF BOUND AND COMPLEXED VEGF TRAP

The previous two-compartment model simulating non-tumor-bearing mice (23) did not include EC secretion of VEGF or soluble

factors. Therefore, we first refit the expanded two-compartment model that includes these additional features in order to match *in vivo* experimental data (12). The fitting optimized the values of five parameters: VEGF secretion rate of muscle fibers (q_{VEGF}^{muscle}), VEGF secretion rate of ECs (q_{VEGF}^{EC}), clearance rate of VEGF Trap (c_A), clearance rate of the VEGF/VEGF Trap complex (c_{VA}), and dissociation constant of VEGF and VEGF Trap (K_d). As described in the methods, although the experimental protocol used by Rudge and coworkers utilizes subcutaneous administration of VEGF Trap, we simulate intravenous administration and assume 100% of the reported dose is administered. The fitting procedure allows us to estimate the values of the free parameters using *in vivo* experimental data.

The optimized parameter values are shown in Table 1, and all raw data from the optimization is given in File 1 in Supplementary Material. The optimized value of K_d is comparable to the reported *in vitro* measurement of 0.6 pM (11), providing confidence in the fitting procedure. The optimization predicts the muscle fibers secrete very little VEGF (0.002 molecules/cell/s), and the standard deviation of the optimized values is high. This suggests that the model is not sensitive to the value of (q_{VEGF}^{muscle}). To investigate this possibility, we varied muscle secretion from 0 to 0.02 molecules/cell/s and used the model to estimate the concentrations of unbound VEGF Trap and the mouse VEGF (mVEGF)/VEGF Trap complex. This sensitivity study revealed that increasing (q_{VEGF}^{muscle}) up to one order of magnitude does not significantly change the fit, as shown in Figure 1. These results indicate that there may not be sufficient data to determine VEGF secretion from muscle fibers. Specifically, it is difficult to separate the contribution of VEGF from muscle fibers, compared to ECs. This result is not specific to the data used here, but more generally that plasma measurements cannot be used to determine endogenous VEGF production from multiple sources.

SENSITIVITY ANALYSIS REVEALS MODEL PARAMETERS THAT INFLUENCE VEGF CONCENTRATIONS

In the three-compartment model, the values of several parameters are based on characterization of the human VEGF (hVEGF) system due to a lack of quantitative experimental measurements in mice. We previously investigated sensitivity to individual parameters, including vascular permeability, lymphatic drainage, and properties of the anti-VEGF agent (25). In that work, parameters

Table 1 | Estimated model parameters from optimization of two-compartment model.

Parameter	Units	Optimal value	Standard deviation
Normal secretion	Molecules/cell/s	0.002	0.003
EC secretion	Molecules/cell/s	0.057	0.004
Tumor secretion	Molecules/cell/s	N/A	N/A
Clearance of free VEGF Trap	s ⁻¹	1.3 × 10 ⁻⁵	2 × 10 ⁻⁷
Clearance of bound VEGF	s ⁻¹	2.5 × 10 ⁻⁶	2 × 10 ⁻⁷
Trap			
K _d of VEGF Trap	pM	0.29	0.011

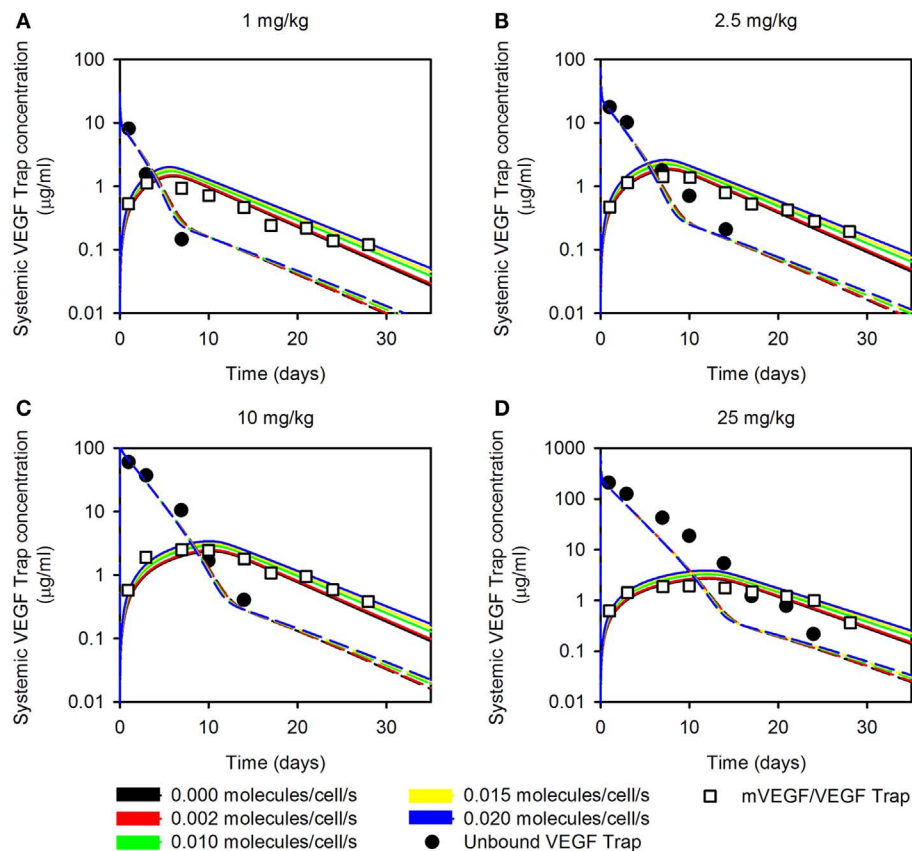


FIGURE 1 | Effect of varying muscle secretion in two-compartment model. The estimated plasma levels of free VEGF Trap (dashed lines) and mouse VEGF bound to VEGF Trap (solid lines) after a single intravenous injection of VEGF Trap at (A), 0.5 mg/kg; (B), 2.5 mg/kg; (C), 10 mg/kg; and (D),

25 mg/kg. The rate of VEGF secretion by muscle fibers is varied from 0 to 0.02 molecules/cell/s. Model results are compared to experimental measurements for free VEGF Trap (black circles) and mVEGF bound to VEGF Trap (white squares).

were varied one by one. Here, we perform a modular sensitivity analysis, where we investigate how variability in three sets of parameters (model inputs) influence mouse and hVEGF concentrations and sVEGFR1 levels in normal tissue, blood, and tumor (model outputs). Specifically, we investigated the effect of VEGF receptor expression, transport parameters, and kinetic parameters using the extended Fourier Amplitude Sensitivity Test (eFAST), as described in the Section “Materials and Methods.” Two indices provide an estimate of the sensitivity of the model output to model parameters. The first FAST index quantifies the variance of a model output with respect to the variance of each input. The total FAST index quantifies the variance of a model output with respect to the variances of each input and covariances between all combinations of inputs. If total FAST indices are larger than the first FAST indices, it means that the parameter is more important in combination with other parameters rather than individually.

The FAST indices for each set of model inputs are shown in Figure 2. When investigating the effect of tumor cell receptor expression, VEGF and sVEGFR1 concentrations are sensitive to the density of NRP co-receptors. Additionally, the level of VEGFR1 is an important determinant of hVEGF concentration in the tumor. In the transport module, the rate of lymphatic flow from normal

or tumor tissue in concert with other transport parameters is estimated to influence hVEGF levels in plasma and normal tissue. Soluble VEGFR1 concentrations, as well as mVEGF levels in plasma and normal tissue, are particularly sensitive to the permeability of the normal tissue to VEGF and VEGF/sVEGFR1 complexes. Individual parameters investigated in the kinetic module are predicted to influence VEGF and sVEGFR1 concentrations, rather than in combination with other kinetic parameters. VEGF and sVEGFR1 levels are particularly sensitive to VEGF₁₆₄ and VEGF₁₆₅ binding to NRP co-receptors and VEGF binding to VEGFR1. These results aid in our understanding of how uncertainty in the values of particular parameters influence the model output. Additionally, the sensitivity analysis provides quantitative data to support obtaining additional experimental measurements of specific parameters that significantly influence model outputs.

THE RATE OF VEGF SECRETION BY HUMAN TUMOR CELLS IS DEPENDENT ON THE TUMOR MICROENVIRONMENT

Tumor cells are a source of VEGF; however, there is a lack of *in vivo* data for VEGF secretion rates. Therefore, we have used *in vivo* experimental data on the plasma concentration of free VEGF Trap and VEGF Trap bound to mouse and hVEGF to determine VEGF

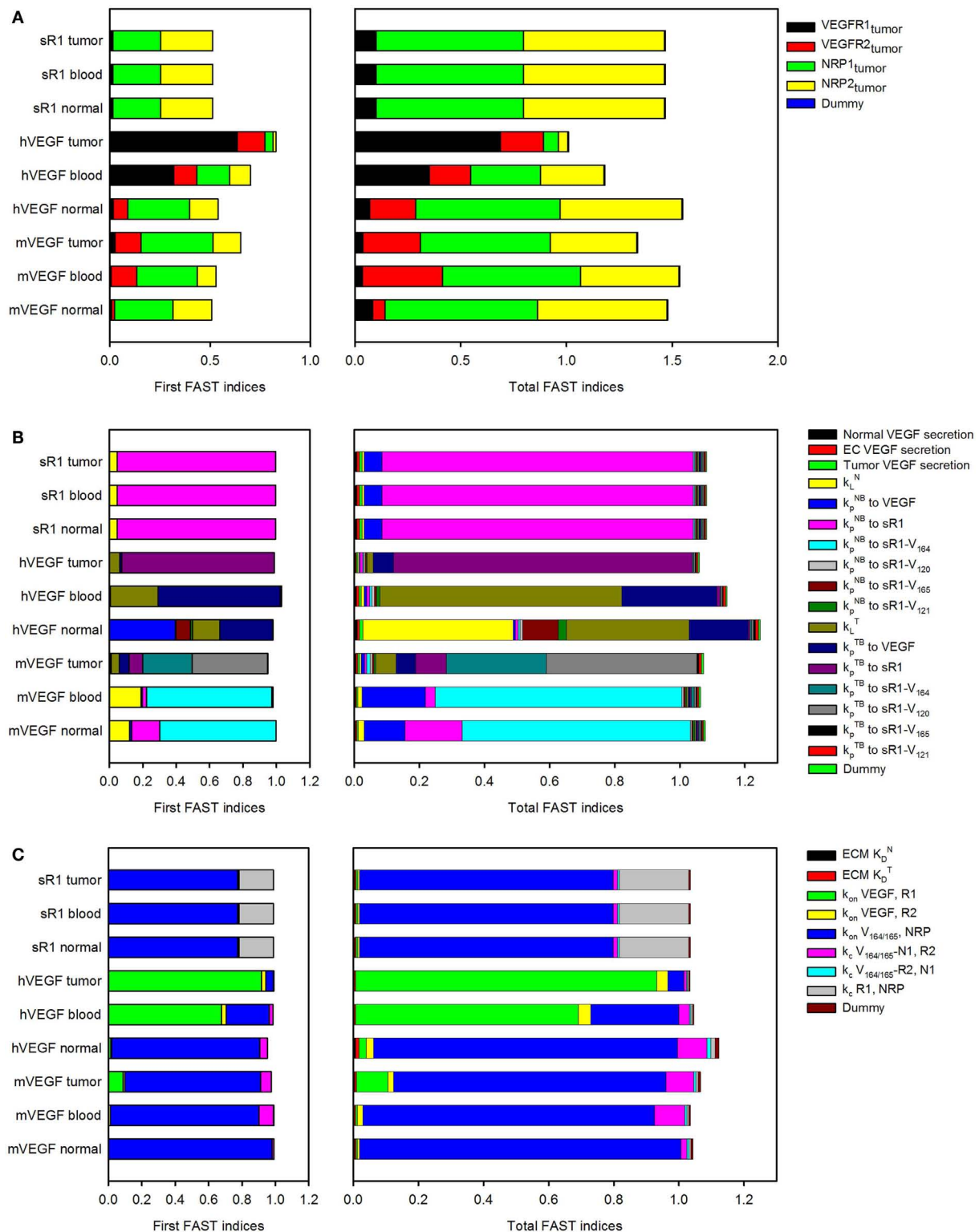


FIGURE 2 | Sensitivity indices of model parameters. The extended Fourier Amplitude Sensitivity Test (eFAST) was used to estimate the variance in the model output with respect to variance in individual model inputs (first FAST

indices) and covariances in combinations of model inputs (total FAST indices). A modular approach was used to investigate the sensitivity to **(A)**, tumor receptor expression; **(B)**, transport parameters; and **(C)**, kinetic parameters.

secretion rates in mice bearing human tumor xenografts. Here, we use the clearance rates of unbound and complexed VEGF Trap predicted in the two-compartment model and experimentally determined VEGF binding affinity. However, the VEGF secretion rates ($q_{\text{VEGF}}^{\text{muscle}}$, $q_{\text{VEGF}}^{\text{EC}}$, and tumor VEGF secretion, $q_{\text{VEGF}}^{\text{tumor}}$) were optimized to fit experimental data. We optimize the VEGF secretion rates since there is large variability in the predicted rate of muscle secretion obtained using the two-compartment model.

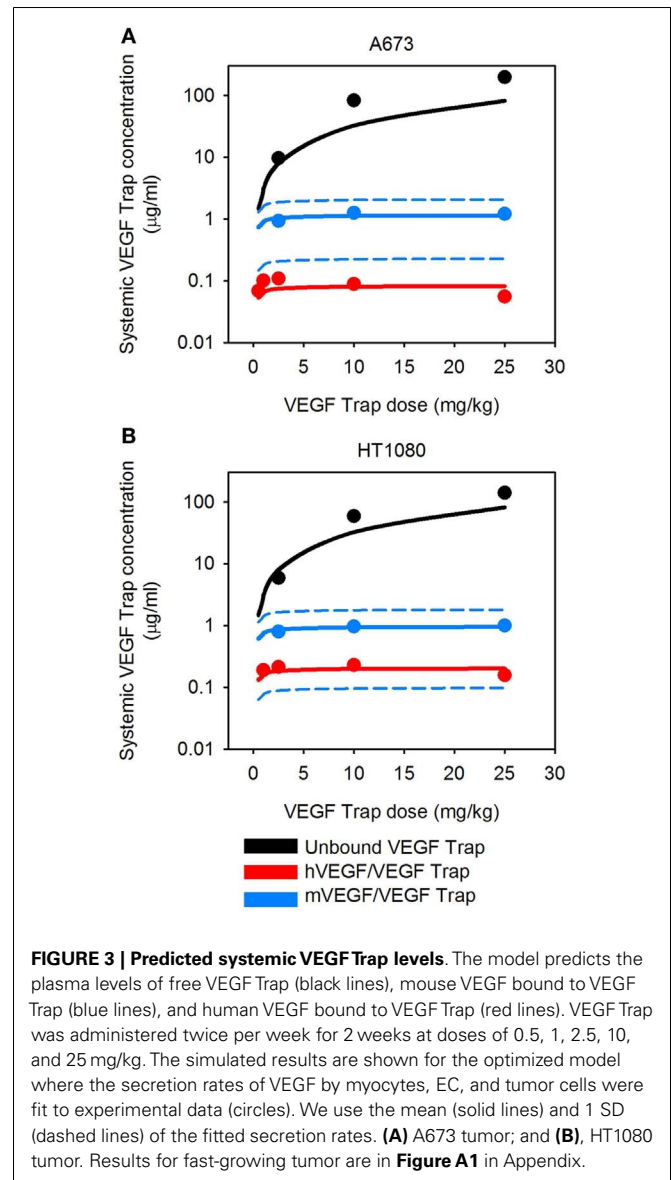
The VEGF secretion rates were predicted using the optimization algorithm, assuming the tumors follow either the average (baseline) or fast tumor growth profiles. We use data from Rudge et al. (12), where tumors were allowed to grow to $\sim 100 \text{ mm}^3$, and then the tumor-bearing mice were injected with VEGF Trap (“anti-VEGF”) twice weekly for 2 weeks. Various dosages of VEGF Trap were used, and the concentrations of free VEGF Trap and the mVEGF/VEGF Trap complex and hVEGF/VEGF Trap complex in the blood were measured. These measurements can be directly compared to model estimates where the anti-VEGF agent is administered intravenously. The optimized model provides a good fit to the experimental data, as shown in **Figure 3**. The average and standard deviation of the predicted VEGF secretion rates from the optimization runs are in **Figure 4** and **Table 2**, and File 1 in Supplementary Material contains the raw data.

CIRCULATING LEVELS OF VEGF TRAP AND HUMAN VEGF/VEGF TRAP COMPLEX AND MAXIMUM CONCENTRATION OF TOTAL VEGF TRAP VARY WITH DOSE

To our knowledge, the dynamic levels of free and complexed VEGF Trap in tumor-bearing mice have not been reported. These data are useful in elucidating the mechanism of action of VEGF Trap and to determine if the dosage is sufficient to neutralize VEGF secreted by the tumor. Therefore, we used the optimized model for A673 rhabdomyosarcoma human xenograft to predict the concentration profiles for free VEGF Trap and VEGF Trap bound to hVEGF (**Figure 5**). The level of VEGF Trap bound to hVEGF is more than an order of magnitude lower than the concentration of mVEGF complexed with VEGF Trap. This result is consistent with the finding that normal production of VEGF eclipses the production from tumors, as described by Rudge and co-authors (12). Additionally, the level of free VEGF Trap remains well above the level of the hVEGF/VEGF trap complex for up to 14 days. This indicates effective dosing, as the VEGF-neutralizing agent is able to neutralize all VEGF secreted by the tumor. The HT1080 fibrosarcoma tumor response is similar (data not shown).

VEGF TRAP IS PREDICTED TO DEplete UNBOUND VEGF IN THE BODY

The optimized model of a tumor-bearing mouse provides a framework with which to study the concentration of unbound VEGF before and after administration of VEGF Trap. As expected, endogenous levels of unbound VEGF are highest in the normal tissue and plasma, and the concentration of hVEGF is highest in the tumor, based on the source of mouse and hVEGF. Before any injection, mVEGF concentration is estimated to range from 0.17 to 1.47 pM in mice with A673 tumors, based on 1 SD above and below the average predicted VEGF secretion rates (**Table 3**). Unbound hVEGF in the tumor is estimated to be $\sim 0.5 \text{ pM}$. We also



present free VEGF concentration during twice-weekly injections of VEGF Trap at 2.5 mg/kg (**Figures 6A,B**). The model estimates that free VEGF in the body is first depleted before increasing slightly before the next injection. Thus, the model can be used to understand the effect of anti-VEGF agents on systemic and tissue levels of VEGF.

In addition to using the model to estimate the concentration of unbound VEGF, we have also determined the percentage of free VEGF in the form of VEGF₁₆₄ or VEGF₁₆₅. The isoform secretion ratio for VEGF₁₆₄:VEGF₁₂₀ in muscle is 92:8 and 90:10 in EC, and the secretion ratio for VEGF₁₆₅:VEGF₁₂₁ in tumor cells is 50:50, as described in the Section “Materials and Methods.” These ratios determine the fraction of VEGF₁₆₄ or VEGF₁₆₅ in the compartments; and, the fractions at which the isoforms are present change with time and drug dose. Here, we consider a dosage of 2.5 mg/kg. After the first anti-VEGF injection, the percentage of free mVEGF

in the form of VEGF₁₆₄ is ~90% in all compartments (**Figure 6C**, left). The percentage of hVEGF in the form of VEGF₁₆₅ in tumor is slightly lower than the percentage of VEGF₁₆₅ in normal tissue and plasma (44–49%, as compared to 55%; **Figure 6D**). These types of model predictions can aid in biomarker identification, as the concentration of specific VEGF isoforms may predict tumors that will respond to anti-VEGF treatment or other anti-angiogenic therapies.

We also apply the model to investigate the total levels of circulating VEGF in plasma. The soluble factors sVEGFR1 and α -2-macroglobulin (α 2M) bind to VEGF and contribute to circulating levels of VEGF. Thus, total circulating VEGF is comprised of free VEGF, VEGF bound to sVEGFR1, and α 2M-bound VEGF (both the native and active forms). VEGF bound to the VEGF Trap drug is also included. We again allow the tumors to reach a volume of 100 mm³ before simulating twice-weekly injections of VEGF Trap at varying doses. Before the first injection, the relative amounts of free, sVEGFR1-bound, and α 2M-bound circulating VEGF are 80, 4, and 16%, respectively. One day after the first injection of VEGF Trap, the composition of the circulating VEGF changes, depending on the drug dose (data not shown). If we consider a drug dose of 2.5 mg/kg, the relative amounts of free, sVEGFR1-bound, α 2M-bound, and VEGF Trap-bound VEGF are 0.6, 0.03, 5, and 94%, respectively. Thus, the VEGF Trap displaces the soluble factors bound to VEGF.

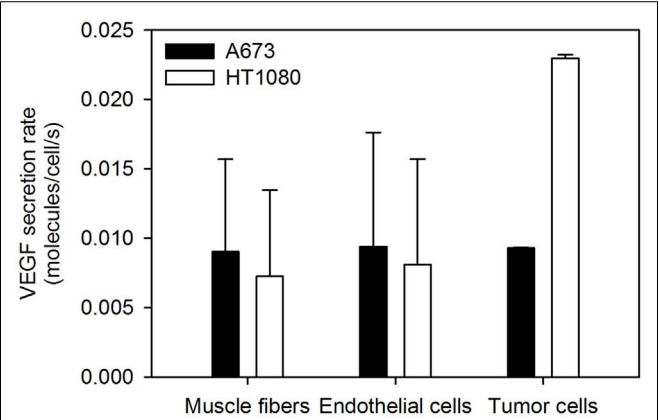


FIGURE 4 | Optimized VEGF secretion rates. The model parameters were optimized to fit experimental data, and the values of normal, EC, and tumor VEGF secretion rates were determined. The mean optimal secretion rates and standard deviation of 20 optimization runs are shown. Results for fast-growing tumors are in **Figure A2** in Appendix.

DISCUSSION

We have developed a compartment model of VEGF distribution in tumor-bearing mouse. The model incorporates tumor-specific properties, including the rate of tumor growth and VEGF secretion. We have used *in vivo* experimental data for the levels of free and bound VEGF Trap in mice bearing human tumor xenografts in order to predict the endogenous rate of VEGF secretion by myocytes and ECs and compared them to the predicted secretion rates in normal mice. We also predicted the rate at which cells from different human tumor xenografts secrete VEGF. To our knowledge, VEGF secretion rates can only be obtained from *in vitro* experiments and cannot be directly measured *in vivo*; however, VEGF concentrations that depend on the secretion rates can be measured experimentally, although such interstitial measurements are presently not available. Therefore, this work provides new insight into VEGF levels in a pre-clinical *in vivo* model of cancer. In addition, using the optimized model for tumor-bearing mice, we have estimated the concentration of VEGF in the mouse following administration of VEGF Trap, as well as the distribution of VEGF in mice and circulating levels of VEGF Trap and the VEGF/VEGF Trap complex. These results show that the concentration of free VEGF in the tumor depends on the tumor-specific properties such as the rate of tumor growth and the amount of VEGF secreted by tumor cells. Lastly, we used the predicted level of VEGF Trap and hVEGF/VEGF Trap complex to compare various dosages. The model predicted that all hVEGF originating from the tumor is neutralized at higher doses of the drug. This demonstrates an important application of the model: to incorporate tumor-specific properties and investigate the efficacy of different drug doses.

We used the two-compartment model to estimate VEGF secretion rates, clearance of free and bound VEGF Trap, and the binding affinity of VEGF Trap for normal mice. The value of binding affinity of VEGF Trap estimated by the model is comparable to the experimentally measured value (11). Additionally, the estimated EC secretion is comparable to the experimentally determined value of 0.028 molecules/cell/s (27). However, the predicted rate at which muscle cells secrete VEGF is very low, and varying this parameter over one order of magnitude does not significantly change the fit. In contrast, EC secretion can be specified and changing this parameter drastically influences the fit to experimental data (results not shown). These results may indicate that the rate of VEGF secretion from muscle and ECs cannot be simultaneously estimated using the available experimental data. That is, measurements of free and bound VEGF Trap in plasma do not allow us to distinguish how muscle and ECs contribute to VEGF levels. Additional experimental measurements such as interstitial levels of VEGF in

Table 2 | Estimated VEGF secretion rates from optimization of three-compartment model.

Tumor	Baseline tumor growth profile*			Fast growth profile		
	Normal	EC	Tumor	Normal	EC	Tumor
A673	0.011 ± 0.007	0.009 ± 0.008	0.009 ± 5 × 10 ⁻⁵	0.009 ± 0.006	0.009 ± 0.008	0.007 ± 4 × 10 ⁻⁵
HT1080	0.007 ± 0.006	0.008 ± 0.008	0.023 ± 3 × 10 ⁻⁴	0.007 ± 0.006	0.008 ± 0.008	0.017 ± 3 × 10 ⁻⁵

*Secretion rate is given in molecules/cell/s. We report the mean ± SD of the 20 optimization runs.

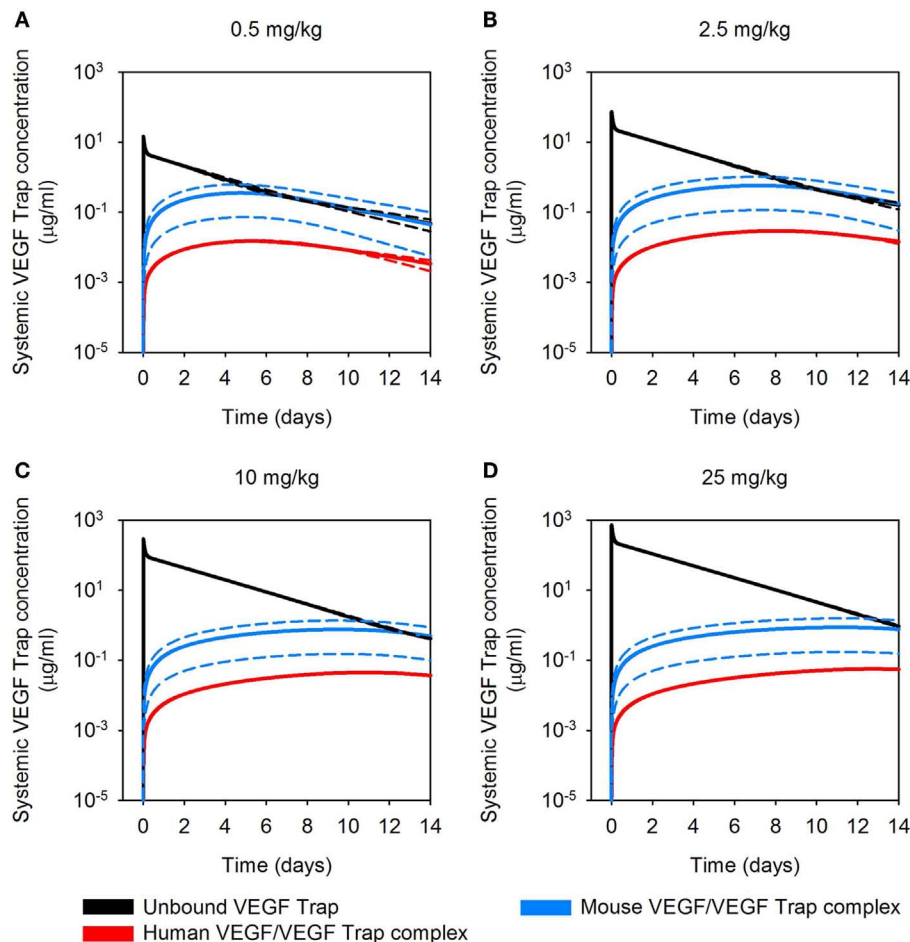


FIGURE 5 | Predicted concentration profiles of systemic VEGF Trap.

The optimized model was applied to predict the time course of free VEGF Trap (black), mouse VEGF bound to VEGF Trap (blue), and human VEGF bound to VEGF Trap (red) in the mouse plasma after a single intravenous

injection of VEGF Trap at (A), 0.5 mg/kg; (B), 2.5 mg/kg; (C), 10 mg/kg; and (D), 25 mg/kg in the A673 rhabdomyosarcoma human tumor xenograft. We use the mean (solid lines) and standard deviation (dashed lines) of the fitted secretion rates.

Table 3 | Estimated concentrations of free VEGF before VEGF Trap injection.

Tumor	Range of free VEGF (pM)*					
	Mouse			Human		
	Normal	Plasma	Tumor	Normal	Plasma	Tumor
A673	0.17–1.47	0.04–0.61	0.002–0.02	5.03×10^{-5} – 5.30×10^{-5}	1.18×10^{-3} – 1.20×10^{-3}	0.49–0.50
HT1080	0.07–1.27	0.02–0.54	0.001–0.02	1.26×10^{-4} – 1.34×10^{-4}	2.95×10^{-3} – 3.05×10^{-3}	1.23–1.26

*Calculated using (mean \pm SD).

skeletal muscle are needed in order to predict VEGF secretion by muscle fibers with confidence. Currently, interstitial VEGF concentrations are only available in human tissue (28–33); however, similar studies in mice are of great interest.

We found that fitted parameters from normal mice were not sufficient to match the levels of unbound and complexed VEGF Trap in the model of tumor-bearing mice. We first attempted to

use the fitted parameters from the two-compartment model in the model of tumor-bearing mice and use *in vivo* experimental data to fit the rate of VEGF secretion from tumor cells. However, the model overestimated the amount of VEGF Trap complexed with mVEGF (results not shown). We are able to more closely fit the experimental data for the tumor-bearing mice by optimizing the three-compartment model independent of the optimized model for

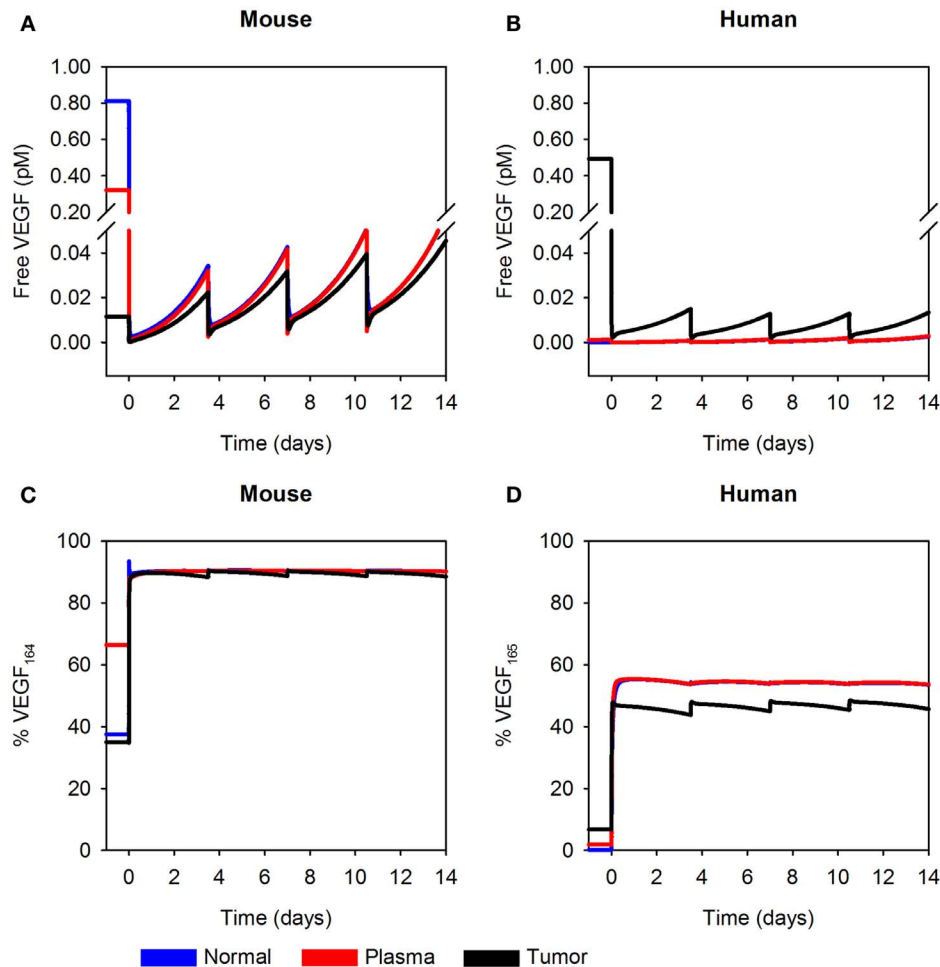


FIGURE 6 | Predicted concentration profiles of unbound VEGF. The optimized model was applied to predict the time course of free VEGF and the fraction of free VEGF in the form of VEGF₁₆₄ or VEGF₁₆₅ in normal tissue (blue), plasma (red), and tumor (black) twice-weekly

injection of VEGF Trap at 2.5 mg/kg. **(A)** Free mVEGF; **(B)**, free hVEGF; **(C)**, percentage of VEGF₁₆₄; and **(D)**, percentage of VEGF₁₆₅ in the A673 rhabdomyosarcoma human tumor xenograft. We use the mean of the fitted secretion rates.

normal mice. This indicates that endogenous VEGF secretion may be different in normal and tumor-bearing mice (Tables 1 vs 2). Experimental studies are needed to validate these results; however, evidence shows that VEGF secretion is reduced following administration of VEGF Trap (34) or other anti-angiogenic therapies (35–37).

The three-compartment model predicted that the *in vivo* tumor VEGF secretion rates needed to fit experimental data are lower than data obtained from *in vitro* measurements. *In vitro* experimental measurements of the VEGF secretion rate vary widely: 0.03–2.65 molecules/cell/s (38–41). We predicted that human tumors secrete VEGF at rates range ranging from 0.007 to 0.023 molecules/cell/s. Interestingly, there is little variability in the predicted tumor secretion rate, as indicated by the small standard deviation ($\sim 10^{-5}$ molecules/cell/s). Having experimental measurements of the plasma concentration of VEGF Trap bound to hVEGF (i.e., VEGF originating from the tumor) enables us to predict the rate at which the tumor secretes VEGF

in vivo. In this way, xenograft models are preferable to syngeneic tumor models, in which VEGF derived from tumor and other tissues are indistinguishable. Similarly, plasma measurements in human patients would not be sufficient to specify tumor VEGF. Thus, xenograft models provide unique insight into the effects of anti-angiogenic therapies and are relevant to human studies.

Tumor VEGF secretion is predicted to depend on the tumor microenvironment. HT1080 tumors are predicted to secrete ~ 2 -fold more VEGF than A673 tumors. Additionally, average- and fast-growing tumors are predicted to secrete different amounts of VEGF, where VEGF secretion in fast-growing tumors is slightly lower than that of tumors that grow at an average rate. To our knowledge, experimental data for VEGF secretion rates is limited to *in vitro* measurements. Therefore, the ability to use the model to determine the VEGF secretion from *in vivo* data and track and quantify normal and tumor VEGF are important features of the model.

Using the optimized model, it is possible to estimate VEGF concentrations in the mouse before and after VEGF Trap administration. In the model, we allowed the tumor to grow for 2 weeks before the VEGF Trap injection. Just before the injection, the estimated plasma VEGF levels are within the range of experimental measurements in mouse of 0.3–1.4 pM (42, 43). The model indicates that plasma VEGF depends on properties of the tumor, such as volume, a result that is validated by experimental evidence (44). Using the model, free VEGF in muscle interstitium is predicted to range from 0.2 to 1.5 pM. To our knowledge, interstitial VEGF in normal tissues has only been quantified in human samples. Interstitial muscle VEGF in humans ranges from 0.3 to 3 pM (28–33, 45). It is not clear how this concentration range varies across species. However, since the range of plasma VEGF measurements is similar between mice and humans, where human plasma VEGF is measured to be 0.4–3 pM (46), it is possible that interstitial VEGF is also comparable in mice and humans. Thus, our model results and predictions provide a framework to compare VEGF distribution in different species and can be experimentally validated. Additionally, we are able to predict the concentration of specific VEGF isoforms (i.e., the percentage of free VEGF in the form of VEGF₁₆₄ or VEGF₁₆₅, as compared to the shorter isoforms VEGF₁₂₀ or VEGF₁₂₁). These results may be useful in identifying predictive biomarkers for anti-VEGF treatment, where the level of VEGF₁₂₁ is being evaluated as a biomarker (47, 48). We also applied the model to estimate the relative contribution of sVEGFR1-bound and α 2M-bound VEGF to total circulating VEGF. The soluble factors compete with anti-VEGF agents; therefore, it is of interest to investigate the effect of sVEGFR1 on the response to anti-VEGF treatment. In this way, the model complements studies evaluating sVEGFR1 as a potential biomarker to predict resistance to anti-VEGF treatment (49).

We can also compare the estimated levels of plasma VEGF generated by the model following administration of VEGF Trap with experimental studies. *In vivo* studies of mice with breast tumor xenografts indicate the plasma VEGF is reduced following VEGF Trap treatment, particularly at the higher doses (34). Additionally, Hoff and coworkers report that VEGF Trap is able to bind all free VEGF 11 days after treatment in an experimental model of rat glioma (50). These studies support the computational model predictions. However, we are not aware of animal studies that provide the time course of VEGF and VEGF/VEGF Trap concentration, which is an important contribution of the model and can complement pre-clinical studies that investigate the efficacy of VEGF Trap.

We show that interstitial tumor VEGF levels depend on specific properties of the tumor. To our knowledge, there are no experimental measurements for interstitial tumor VEGF concentrations. However, a sampling of available experimental measurements of total VEGF in tumor tissue (free and bound VEGF, both intracellular and extracellular) reveals a wide range of values, depending on tumor type and size. File 1 in Supplementary Material shows a compilation of measurements of tumor VEGF for various tumor types. Experimental studies to measure free VEGF in tumor tissue in mouse models would provide much needed quantitative data to test and validate the model predictions presented here.

MODEL LIMITATIONS

We consider the model presented here to be a minimal model that accurately reproduces experimental data, both qualitatively and quantitatively. The model includes several assumptions, which may be addressed as quantitative data become available. For example, we assume the normal tissue is skeletal muscle, although other tissues and organs secrete and contain VEGF (51), but are not as well-characterized as muscle. We include two major VEGF isoforms (VEGF₁₂₀/VEGF₁₂₁ and VEGF₁₆₄/VEGF₁₆₅); however, other isoforms such as VEGF₁₈₈/VEGF₁₈₉ (52) and VEGF_{xxx}b (53, 54) also influence angiogenesis and may impact anti-VEGF therapies. Recent studies also show that other VEGF ligands and receptors contribute to angiogenesis (55–57), and the model can be expanded in the future to include these molecular species. Additionally, although platelets contain large amounts of VEGF and contribute to angiogenesis (58), we have not included them in the model as the rate and conditions under which they secrete or unload VEGF are unknown. We assume that as the tumor grows, the relative proportions of interstitial space, vascular volume, and tumor cells remain constant. However, experimental studies indicate that these proportions should change as the tumor grows (59). Finally, we have not included the effects of anti-VEGF treatment on tumor volume or vascular permeability. Pre-clinical studies show tumor growth inhibition and even regression of the tumor following anti-angiogenic therapy that targets VEGF. We have performed preliminary studies where the tumor volume is constant after 1 week of anti-VEGF treatment since experimental studies indicate that tumor growth is halted during 2 weeks of twice-weekly VEGF Trap injections (34). We found that the predicted tumor secretion rate is slightly larger when accounting for tumor growth stagnation. This is because the tumor is smaller and consists of fewer cells. Therefore, the amount of VEGF that must be secreted on a per cell basis in order to obtain a certain level of VEGF or VEGF/VEGF Trap complex is higher. Tumor permeability may decrease with anti-angiogenic therapy, as the tumor normalizes neovasculature and it begins to resemble normal vessels; however, we have not included that effect in the current model. In a human model of VEGF transport and kinetics, we considered “low” and “high” vascular permeability between the tumor and blood (22). Interestingly, the model predicts that tumor VEGF can increase above the pre-treatment level depending on properties of the tumor microenvironment, even when tumor permeability is high. Future computational studies may investigate the effect of anti-VEGF treatment on tumor volume and vascular permeability in greater detail.

CONCLUSION

The compartment model presented here provides a framework to investigate the action of VEGF-targeting agents for particular types of tumors. The physiologically based and experimentally validated model, based on currently available animal data, predicted the dynamic concentrations of molecular species and other biological parameters that are difficult to quantify experimentally. Thus, the model complements pre-clinical experiments, can aid in the development of agents that target VEGF and inhibit angiogenesis, and may be useful in evaluating biomarkers of anti-angiogenic therapies. The model can be extended to human patients; this is

particularly important since in 2012 aflibercept has been approved to treat metastatic colorectal cancer in humans (60).

MATERIALS AND METHODS

COMPUTATIONAL MODEL

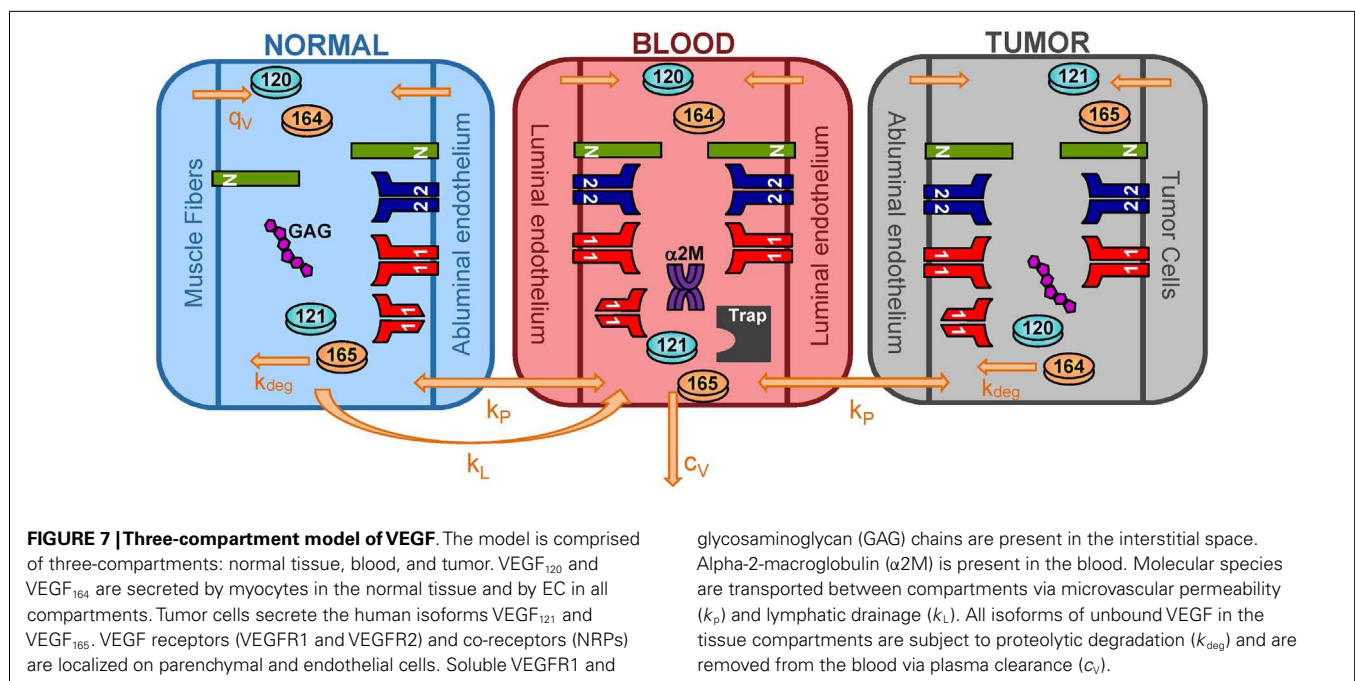
We have expanded the two-compartment model of VEGF distribution in the mouse (23) to include tumor tissue (“tumor compartment”). The model is illustrated in **Figure 7**. Geometric and kinetic parameters for the normal and blood compartments have been fully detailed in (23). By simulating a human tumor xenograft (tissue that grows from human cancer cells that have been injected into the mouse), we also incorporate hVEGF isoforms and cross-species reactions between ligands and receptors. Specifically, we include VEGF₁₂₁ and VEGF₁₆₅, which are secreted by tumor cells. The human isoforms can bind to human receptors present on tumor cells, as well as mouse receptors on endothelial surfaces in the body (normal and tumor EC) and muscle fibers in the normal compartment. Additionally, the mouse isoforms bind to mouse receptors on muscle fibers and ECs and human receptors on tumor cells. The model can also be adapted to simulate mouse syngeneic tumors, where the tumor cells secrete VEGF₁₂₀ and VEGF₁₆₄; in this case, only mVEGF is present in the model. In this work, however, we have focused on human tumors. The molecular interactions between VEGF and its receptors are illustrated in **Figure 8**.

In addition to introducing the tumor compartment, we include VEGF interactions with two soluble factors: soluble VEGFR1 (sVEGFR1) and α 2M and introduce VEGF secretion by ECs. Soluble VEGFR1 is secreted by ECs and transported throughout the body, enabling it to interact with VEGF in all compartments. The soluble factor α 2M is present in two forms: native and active (α 2M_{fast}) (61). Both forms are present at high concentrations (nanomolar to micromolar levels) (62), and due to

their size (720 kDa MW), we assume that both forms are confined to the blood compartment. The model predicts the levels of free VEGF in the tissue interstitium and in plasma. These soluble factors interfere with assays that measure VEGF concentration, making it difficult to distinguish between VEGF that is truly free versus VEGF that is bound to trapping molecules (63). Both sVEGFR1 and α 2M can sequester VEGF and reduce the levels of free VEGF. Therefore, it is important to include these factors in the model.

We have also included VEGF secretion by ECs, as experimental studies demonstrate that EC are a source of VEGF (64, 65). The luminal and abluminal endothelial surfaces secrete VEGF, and luminal secretion is predicted to be a major determinant of plasma VEGF. Due to EC secretion of VEGF, the compartments are relatively autonomous, since the concentration of VEGF in each compartment is determined primarily by the secretion rate in that compartment, as well as the microenvironmental variables of the compartment; however, transport between compartments is also important.

The model is described by 258 non-linear ordinary differential equations (ODEs), including 53 for the normal compartments, 126 for the blood, and 79 for the tumor compartment. In addition to the ODEs that describe how the species’ concentrations vary with time, we include an equation for the tumor volume, such that the model simulates VEGF distribution in tumor-bearing mice, immediately following inoculation of tumor cells. The initial tumor volume is 10^{-6} cm³. A sampling of experimental data for the volume of xenografts generated from MCF-7 and MDA-MB-231 breast cancer cells (66–74) reveals various growth profiles. We fit the data to exponential curves, accounting for a range of tumor growth profiles (**Figure 9**). The growth curves fit experimental data well, within the time scales used in the model (i.e., <6 weeks). In cases where the model is run for longer times, different growth



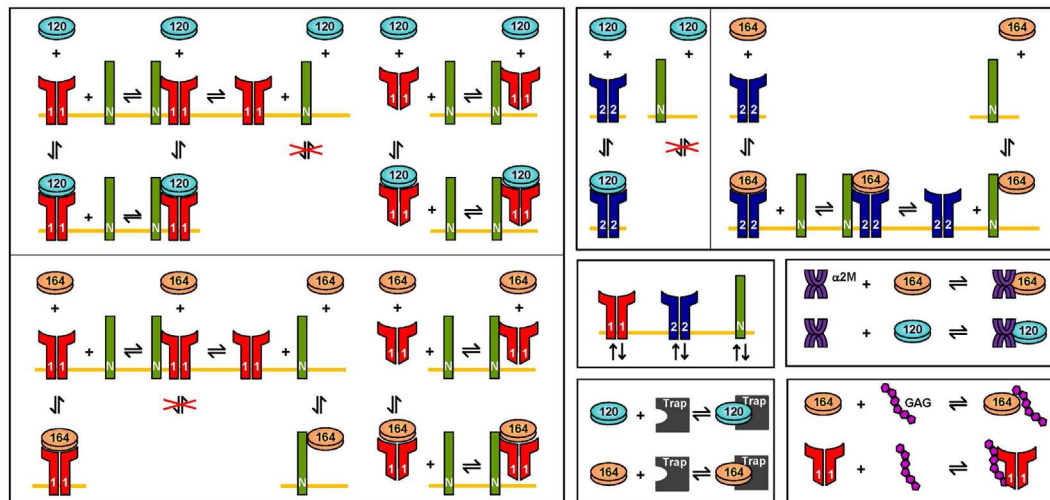


FIGURE 8 | Molecular interactions. The interactions of VEGF₁₂₀ and VEGF₁₆₄ are illustrated. VEGF₁₂₁ is involved in the same binding reactions as VEGF₁₂₀. Similarly, the interactions for VEGF₁₆₅ are the same as VEGF₁₆₄. Differences in the interactions of VEGF_{120/121}, as compared to VEGF_{164/165} are due to differential exon splicing.

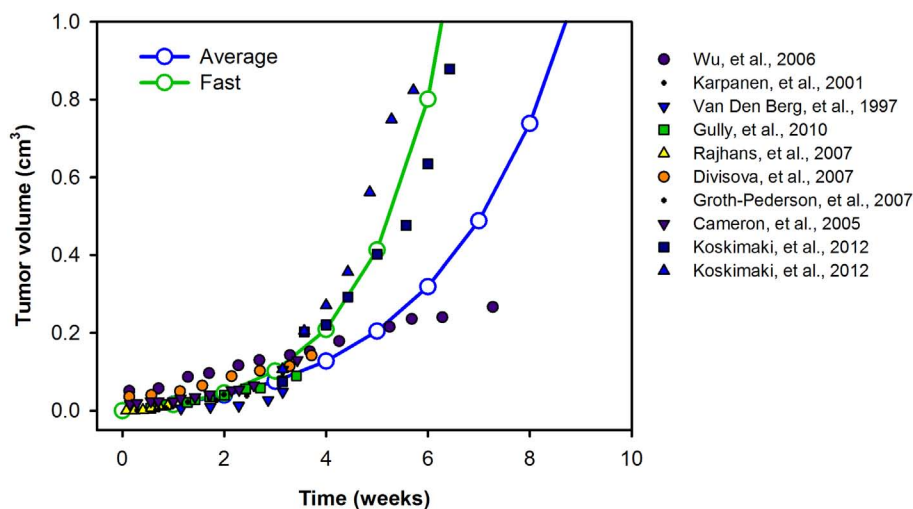


FIGURE 9 | Tumor growth profiles. We investigate the growth profiles of two categories of tumors: average- (blue) and fast-growing (green) tumors, based on available experimental data. The data are fit to exponential curves, and the growth equations are given in the File 2 in Supplementary Material.

curves should be used in order to capture the full range of tumor growth dynamics for the desired time scale. The complete set of equations, chemical reactions, and glossary of terms are given in File 2 in Supplementary Material.

SIMULATION OF ADMINISTRATION OF VEGF TRAP

Experimental studies utilize a subcutaneous injection of VEGF Trap (“anti-VEGF”); however, the authors of the experimental study state that the bioavailability of the drug is the same whether injected subcutaneously or intravenously (12). The current model does not include a subcutaneous compartment; therefore, we simulate an intravenous injection, which inherently assumes that all of

the drug appears in the blood. Injection lasts for 1 min (the duration does not affect the results, within limits) and is performed once the tumor reaches a particular volume, according to experimental methods described by Rudge et al. (12). Various doses of VEGF Trap are used, as reported by Rudge and coworkers (12) (0.5, 1, 2.5, 10, and 25 mg/kg).

SENSITIVITY ANALYSIS

In order to understand the impact of various parameters, we perform variance-based global sensitivity analyses using the eFAST (75). The eFAST method estimates the sensitivity of model outputs (i.e., VEGF concentration) with respect to variations in model

parameters. The three-compartment model is run multiple times with different parameter sets, where all parameters are varied from their baseline values. Variance for a parameter i is:

$$D_i = 2 \sum_{p=1}^{\infty} (A_{pj}^2 + B_{pj}^2)$$

where A_j and B_j are the Fourier coefficients of the cosine series and sine series, respectively, for the frequency, j , associated with the parameter i and include harmonics, p , of the base frequency. The total variance in the output is:

$$D_{\text{total}} = 2 \sum_{j=1}^{\infty} (A_j^2 + B_j^2)$$

The variances are used to estimate two indices that provide a measure the sensitivity: first-order FAST indices, S_i , and the total FAST indices, S_{Ti} . The first-order indices measure the local sensitivity and do not account for interactions with other parameters:

$$S_i = \frac{D_i}{D_{\text{total}}}$$

The Total FAST indices measure of global sensitivity and take into account second- and higher-order interactions between parameters. S_{Ti} are calculated by excluding the effects of the complementary set of other parameters:

$$S_{Ti} = 1 - \frac{D_{ci}}{D_{\text{total}}}$$

The eFAST method has been applied to systems biology models (76), and our laboratory has previously used the method to investigate the sensitivity of VEGFR2 signaling (77). In this work, we apply eFAST to investigate the sensitivity of steady state VEGF concentrations with respect to kinetic parameters, transport parameters, and receptor expression levels. We use Simlab 2.2 from Econometrics and Applied Statistics Unit EAS at the Joint Research Centre of the European Commission to implement eFAST.

NUMERICAL IMPLEMENTATION

The model equations were implemented in MATLAB using the SimBiology toolbox and were solved with the Sundials solver. The model is available in SBML format at: <http://www.jhu.edu/apopel/software.html>

PARAMETERS

Geometry

The geometric parameters for the tumor compartment are summarized in **Table A1** in Appendix. The tumor cells are assumed to have the same volume as the MCF-7 breast tumor cells, which have a mean diameter of $12 \mu\text{m}$ (78). A sphere of this diameter would have a volume and surface area of $905 \mu\text{m}^3$ and $452 \mu\text{m}^2$, respectively. However, since tumor cells are not spherical, we assume a dodecahedral cell of the same volume, which has a surface area of $497 \mu\text{m}^2$. The average luminal diameter of

capillaries in growing MCF-7 xenografts is $13.94 \mu\text{m}$ (79), and imaging of tumor vasculature supports this value (80). We assume an EC thickness of $0.5 \mu\text{m}$, which would yield a cylindrical cross-sectional area of $175 \mu\text{m}^2$ and an outer perimeter of $46.9 \mu\text{m}$. However, microvessels are not cylindrical. Therefore, to find the true perimeter, we used a relationship between total perimeter and total cross-sectional area in breast cancer capillaries, where the increase in perimeter is 23% (81, 82), yielding a capillary perimeter of $57.7 \mu\text{m}$.

The extracellular fluid volume fraction in the breast tumor xenografts has been shown to range from 33 to 76% (78). Another measurement reports the extracellular fluid volume in MCF-7 tumors to be 40% (83). We assume a value of 45%, which is divided into interstitial space and intravascular space. We set the volume fraction of intravascular space to be 10%, which is within the range of available experimental data (84–86). Given the capillary dimensions described above and an intravascular volume of 10%, the capillary density is calculated to be 655 capillaries/ mm^2 . Based on a cell thickness of $0.5 \mu\text{m}$, the volume occupied by the ECs of the microvessels is 1.5%. Cancer cells occupy the remaining tissue volume of 53.5%. The volume fractions of microvessels and tumor cells are then used to calculate the total surface area of all vessels and tumor cells per unit volume of tissue: $378 \text{ cm}^2 \text{ EC surface/cm}^3 \text{ tissue}$ and $2939 \text{ cm}^2 \text{ tumor cell surface/cm}^3 \text{ tissue}$.

The interstitial space is composed of extracellular matrix (ECM), and basement membranes associated with the microvessels (endothelial basement membrane, EBM) and tumor cells (parenchymal basement membrane, PBM). The thickness of the basement membranes is assumed to be 50 and 30 nm, for the EBM and PBM, respectively, yielding volume fractions of 0.0081 and $0.0015 \text{ cm}^3/\text{cm}^3 \text{ tissue}$. The remaining volume of the interstitial space is the ECM volume (34.04%).

Each region of the interstitial space can be represented as a porous medium that contains a solid fraction composed primarily of collagen that is unavailable to VEGF, and a fluid fraction that is accessible to VEGF. The size of the pores further limits the volume available for VEGF to diffuse. Therefore, the available volume in the ECM and basement membranes is calculated as the product of the volume, fluid fraction, and partition coefficient. The fluid fraction is the non-collagen fraction and is calculated by using the total collagen content in interstitial space. Given limited data for this measurement, we used 5%, the same value as in our previous models (24, 25, 87). The ratio of basement membrane collagen to total body collagen is assumed to be 0.3, which yields 0.0482 for the ratio of ECM collagen to total body collagen. The fluid fractions are then 0.7 for the basement membranes and 0.9318 for the ECM. The partition coefficient is the ratio of available fluid volume to interstitial fluid volume. We take 0.9 for the partition coefficient for the EBM (88), and the same value is used for the ECM and PBM, as it is difficult to distinguish basement membranes and the ECM (89). The available fluid volume for the ECM, EBM, and PBM are therefore 0.2916 , 9.720×10^{-4} , and $5.082 \times 10^{-3} \text{ cm}^3/\text{cm}^3 \text{ tissue}$, respectively.

Concentrations

Receptor densities and ECM binding site densities are listed in **Table A2** in Appendix. VEGFR1, VEGFR2, and NRP1 on the

luminal and abluminal surfaces of diseased EC surfaces and on tumor cells are based on quantitative flow cytometry measurements in ECs isolated from tumor tissue, as described in (25). We assume NRP2 surface concentration on tumor cells at the same level as NRP1.

Kinetics

To our knowledge, there are no data for the kinetics of mVEGF isoforms binding to glycosaminoglycan (GAG) chains or mouse receptors or cross-reactions between human and mouse isoforms and receptors. Therefore, we assume the kinetic rates for VEGF binding to and dissociation from receptors, co-receptors, and GAG chains in the ECM and basement membranes are the same as in our previous papers, based on experimental data (23–25, 87) and are given in **Table A3** in Appendix. We use experimental data from Papadopoulos (11) for the on and off rates of VEGF binding to VEGF Trap.

Transport

Transport parameters for VEGF, anti-VEGF, and the VEGF/anti-VEGF complex are listed in **Table A4** in Appendix. Parameters that govern transport between the normal and blood compartments are the same as in our previous model (23). Here, we explain specific transport parameters required for the addition of soluble factors sVEGFR1 and $\alpha 2M$ and the tumor compartment. As in the previous model, myocytes are a source of VEGF and secrete the VEGF isoforms VEGF₁₂₀ and VEGF₁₆₄ at a ratio of 8:92 (90, 91). Additionally, tumor cells secrete VEGF into the tumor interstitium at a ratio of 50:50 for VEGF₁₂₁:VEGF₁₆₅, based on experimental quantification of mRNA isoform expression levels (92–96). Here, we also consider VEGF secretion by EC. We set the secretion ratio of VEGF₁₂₀:VEGF₁₆₄ by EC to be 10:90, similar to the isoform ratio in muscle tissue, since to our knowledge, this ratio has not been determined experimentally. Additionally, we assume normal and tumor EC secrete the same amount of VEGF; tumor EC are a small fraction of the total EC in the body, thus this assumption should not affect VEGF distribution. The rates of VEGF secretion by muscle fibers, EC, and tumor cells are determined by parameter optimization, fitting to experimental data from Rudge and coworkers (12).

This expanded model includes soluble factors sVEGFR1 and $\alpha 2M$. ECs are a source of sVEGFR1, and the rates of secretion by normal EC was set to 6×10^{-3} molecules/cell/s. Similar to VEGF secretion, we assume that sVEGFR1 secretion rate is the same for tumor EC. At steady state, the model estimated the distribution of sVEGFR1 in the body to be 0.4, 2.1, and 0.04 pM in the normal, blood, and tumor compartments, respectively. The level of sVEGFR1 in the plasma is within the range of experimental measurements, which range from 1 to 10 pM (97, 98). The clearance of $\alpha 2M$ was set at $2.62 \times 10^{-3} \text{ min}^{-1}$, based on experimental measurements of the half-life, $t_{1/2}$ (99), using $\ln(2)/t_{1/2}$. The synthesis of $\alpha 2M$ was then estimated from mass balance at steady state, where the concentrations of native and active $\alpha 2M$ are 1.4 μM (62) and 14 nM, respectively. We assume that the concentration of active $\alpha 2M$ is 100-fold lower than that of the native form, based on experimental data for humans (100–102).

Molecular species are removed from the system via two mechanisms: plasma clearance and proteolytic degradation. The values of these parameters are in **Table A4** in Appendix. For the normal endothelium, the permeability to sVEGFR1 and VEGF/sVEGFR1 is calculated using an empirical relation between the Stokes–Einstein radius, a_E , and molecular weight [$a_E = 0.483 \times (\text{MW})^{0.386}$], the corresponding theoretical macro-molecular permeability-surface area product, PS (103), and the capillary surface area, S . Taking microvascular permeability as PS/ S , and the calculated value is on the order of 10^{-8} cm/s , between the normal and blood compartments. Since tumor vasculature is more permeable than normal microvessels (104), we assume that the microvascular permeability between the tumor and blood is an order of magnitude higher than permeability between normal and blood for both VEGF and the anti-VEGF or complex. Therefore, the permeability to VEGF is 4×10^{-7} and $3 \times 10^{-7} \text{ cm/s}$ for the anti-VEGF and VEGF/anti-VEGF complex. The permeability to sVEGFR1 and VEGF bound to sVEGFR1 is $1.5 \times 10^{-7} \text{ cm/s}$.

Parameter estimation

The estimation of the VEGF secretion by muscle fibers, ECs, and tumor cells was achieved using the “lsqnonlin” function in MATLAB, as previously described (23). This algorithm solves the non-linear least squares problem using the trust-region-reflective optimization algorithm (105, 106), minimizing the weighted sum of the squared residuals (WSSR):

$$\min \text{WSSR}(\theta) = \min \sum_{i=1}^n [W_i (C_{\text{experimental}, i} - C_{\text{simulation}, i}(\theta))]^2$$

where $C_{\text{experimental}, i}$ is the i th experimentally measured plasma concentration data point, $C_{\text{simulation}, i}(\theta)$ is the i th simulated plasma concentration at the corresponding time point, W_i is the weight taken to be $1/C_{\text{experimental}, i}$, and n is the total number of experimental measurements. The minimization is subject to the upper and lower bounds of the free parameters, θ .

The two-compartment model was used to determine the rate of VEGF secretion by muscle fibers and ECs (“normal” and “EC” secretion, respectively), clearance of free and bound VEGF Trap, dissociation constant of VEGF and VEGF Trap. These five free parameters were fit to experimental data for the concentration profiles of VEGF/VEGF Trap complex and unbound VEGF Trap in mice at different doses of VEGF Trap (12), with a total of 58 data points. The initial value of the secretion rates was generated within the lower and upper bounds of 1.5×10^{-6} and 2 molecules/cell/s, respectively. The lower bound corresponds to 10 pg/ml and was set based on the limit of detection of standard ELISA kits used to measure (63). The half-life of VEGF Trap in mouse serum has been reported as 72 h (107), which corresponds to a clearance rate of $1.6 \times 10^{-4} \text{ min}^{-1}$, assuming clearance rate is equal to $\ln(2)/\text{half-life}$. The upper and lower bounds of the clearance rates were one order of magnitude above and below this value, respectively. The upper and lower bounds for the dissociation constant were set to 0.25 and 5 pM, based on experimental data (11, 12). The baseline value of permeability of the normal tissue to VEGF Trap is $3 \times 10^{-8} \text{ cm/s}$, as described above, and the bounds were one order

of magnitude above and below this value. The optimal parameter values are reported as the mean and standard deviation of the 20 runs.

We used the three-compartment model to determine the rate at which VEGF is secreted by tumor cells (“tumor secretion”) and permeability of diseased tissue to free and complexed VEGF Trap. Tumor secretion was optimized to fit experimental data for the systemic VEGF Trap levels (free and complexed) reported by Rudge et al. (12). Experimental data for two human tumor xenografts (A673 rhabdomyosarcoma and HT1080 fibrosarcoma) were used separately; the total number of data points was 11 for A673 tumors and 10 for HT1080 tumors. Twenty runs were performed for each tumor, which either followed the average (baseline) or fast growth profile. This yields two conditions for each tumor type. The optimal secretion rates are reported as the mean and

standard deviation of the 20 runs and should be interpreted as a range of values, where the values are dependent on the tumor microenvironment, tumor type, and growth profile.

ACKNOWLEDGMENTS

The authors thank Phillip Yen, members of the Popel Lab and Dr. Feilim Mac Gabhann for helpful discussions. This work was supported by NIH grant R01 CA138264 (Aleksander S. Popel), NIH fellowship F32 CA154213 (Stacey D. Finley), and UNCF/Merck Postdoctoral Fellowship (Stacey D. Finley).

SUPPLEMENTARY MATERIAL

The Supplementary Material for this article can be found online at http://www.frontiersin.org/Molecular_and_Cellular_Oncology/10.3389/fonc.2013.00196/abstract

REFERENCES

- Rennel ES, Harper SJ, Bates DO. Therapeutic potential of manipulating VEGF splice isoforms in oncology. *Future Oncol* (2009) 5:703–12. doi:10.2217/fon.09.33
- Dokun AO, Annex BH. The VEGF165b “ICE-o-form” puts a chill on the VEGF story. *Circ Res* (2011) 109:246–7. doi:10.1161/CIRCRESAHA.111.249953
- Koch S, Tugues S, Li X, Gualandi L, Claesson-Welsh L. Signal transduction by vascular endothelial growth factor receptors. *Biochem J* (2011) 437:169–83. doi:10.1042/BJ20110301
- Olsson A-K, Dimberg A, Kreuger J, Claesson-Welsh L. VEGF receptor signalling – in control of vascular function. *Nat Rev Mol Cell Biol* (2006) 7:359–71. doi:10.1038/nrm1911
- Cao Y. Therapeutic angiogenesis for ischemic disorders: what is missing for clinical benefits? *Discov Med* (2010) 9:179–84.
- Roy RS, Roy B, Sengupta S. Emerging technologies for enabling proangiogenic therapy. *Nanotechnology* (2011) 22:494004. doi:10.1088/0957-4484/22/49/494004
- Al-Latayfeh M, Silva PS, Aiello LP. Antiangiogenic therapy for ischemic retinopathies. *Cold Spring Harb Perspect Med* (2012) 2:a006411. doi:10.1101/cshperspect.a006411
- Jayson GC, Hicklin DJ, Ellis LM. Antiangiogenic therapy – evolving view based on clinical trial results. *Nat Rev Clin Oncol* (2012) 9:297–303. doi:10.1038/nrclinonc.2012.8
- Genentech, Inc. *Avastin Prescribing Information*. (2011) [accessed September 2011]. Available from: <http://www.avastin.com/avastin/hcp/overview/about/dosing/index.html>
- Gaya A, Tse V. A preclinical and clinical review of aflibercept for the management of cancer. *Cancer Treat Rev* (2012) 38:484–93. doi:10.1016/j.ctrv.2011.12.008
- Papadopoulos N, Martin JD, Ruan Q, Rafique A, Rosconi MP, Shi E, et al. Binding and neutralization of vascular endothelial growth factor (VEGF) and related ligands by VEGF Trap, ranibizumab and bevacizumab. *Angiogenesis* (2012) 15:171–85. doi:10.1007/s10456-011-9249-6
- Rudge JS, Holash J, Hylton D, Russell M, Jiang S, Leidich R, et al. VEGF Trap complex formation measures production rates of VEGF, providing a biomarker for predicting efficacious angiogenic blockade. *Proc Natl Acad Sci U S A* (2007) 104:18363–70. doi:10.1073/pnas.0708865104
- Singh M, Ferrara N. Modeling and predicting clinical efficacy for drugs targeting the tumor milieu. *Nat Biotechnol* (2012) 30:648–57. doi:10.1038/nbt.2286
- Jain RK. Normalizing tumor microenvironment to treat cancer: bench to bedside to biomarkers. *J Clin Oncol* (2013) 31:2205–18. doi:10.1200/JCO.2012.46.3653
- Peirce SM. Computational and mathematical modeling of angiogenesis. *Microcirculation* (2008) 15:739–51. doi:10.1080/10739680802220331
- Qutub AA, Mac Gabhann F, Karagiannis ED, Vempati P, Popel AS. Multiscale models of angiogenesis. *IEEE Eng Med Biol Mag* (2009) 28:14–31. doi:10.1109/EMMB.2009.931791
- Stefanini MO, Qutub AA, Mac Gabhann F, Popel AS. Computational models of VEGF-associated angiogenic processes in cancer. *Math Med Biol* (2012) 29:85–94. doi:10.1093/imammb/dqq025
- Byrne HM. Dissecting cancer through mathematics: from the cell to the animal model. *Nat Rev Cancer* (2010) 10:221–30. doi:10.1038/nrc2808
- Young RJ, Reed MWR. Anti-angiogenic therapy: concept to clinic. *Microcirculation* (2012) 19:115–25. doi:10.1111/j.1549-8719.2011.00147.x
- Duda DG, Munn LL, Jain RK. Can we identify predictive biomarkers for antiangiogenic therapy of cancer using mathematical models? *J Natl Cancer Inst* (2013) 105:762–5. doi:10.1093/jnci/djt114
- Wehland M, Bauer J, Magnusson NE, Infanger M, Grimm D. Biomarkers for anti-angiogenic therapy in cancer. *Int J Mol Sci* (2013) 14:9338–64. doi:10.3390/ijms14059338
- Finley SD, Popel AS. Effect of tumor microenvironment on tumor VEGF during anti-VEGF treatment: systems biology predictions. *J Natl Cancer Inst* (2013) 105:802–11. doi:10.1093/jnci/djt093
- Yen P, Finley SD, Engel-Stefanini MO, Popel AS. A two-compartment model of VEGF distribution in the mouse. *PLoS ONE* (2011) 6:e27514. doi:10.1371/journal.pone.0027514
- Stefanini MO, Wu FTH, Mac Gabhann F, Popel AS. A compartment model of VEGF distribution in blood, healthy and diseased tissues. *BMC Syst Biol* (2008) 2:77. doi:10.1186/1752-0509-2-77
- Finley SD, Engel-Stefanini MO, Imoukhuede PI, Popel AS. Pharmacokinetics and pharmacodynamics of VEGF-neutralizing antibodies. *BMC Syst Biol* (2011) 5:193. doi:10.1186/1752-0509-5-193
- Finley SD, Popel AS. Predicting the effects of anti-angiogenic agents targeting specific VEGF isoforms. *AAPS J* (2012) 14:500–9. doi:10.1208/s12248-012-9363-4
- Chauhan VP, Stylianopoulos T, Martin JD, Popovic Z, Chen O, Kamoun WS, et al. Normalization of tumour blood vessels improves the delivery of nanomedicines in a size-dependent manner. *Nat Nanotechnol* (2012) 7:383–8. doi:10.1038/nnano.2012.45
- Gavin TP, Ruster RS, Carrithers JA, Zwetsloot KA, Kraus RM, Evans CA, et al. No difference in the skeletal muscle angiogenic response to aerobic exercise training between young and aged men. *J Physiol* (2007) 585:231–9. doi:10.1113/jphysiol.2007.143198
- Hellsten Y, Rufener N, Nielsen JJ, Hoier B, Krustup P, Bangsbo J. Passive leg movement enhances interstitial VEGF protein, endothelial cell proliferation, and eNOS mRNA content in human skeletal muscle. *Am J Physiol Regul Integr Comp Physiol* (2008) 294:R975–82. doi:10.1152/ajpregu.00677.2007
- Hansen-Algenstaedt N, Nielsen JJ, Saltin B, Hellsten Y. Exercise training normalizes skeletal muscle vascular endothelial growth factor levels in patients with essential hypertension. *J Hypertens* (2010) 28:1176–85. doi:10.1097/HJH.0b013e3283379120

31. Hoier B, Rufener N, Bojsen-Moller J, Bangsbo J, Hellsten Y. The effect of passive movement training on angiogenic factors and capillary growth in human skeletal muscle. *J Physiol* (2010) **588**:3833–45. doi:10.1113/jphysiol.2010.190439
32. Hoier B, Nordsborg N, Andersen S, Jensen L, Nybo L, Bangsbo J, et al. Pro- and anti-angiogenic factors in human skeletal muscle in response to acute exercise and training. *J Physiol* (2012) **590**:595–606. doi: 10.1113/jphysiol.2011.216135
33. Hoier B, Passos M, Bangsbo J, Hellsten Y. Intense intermittent exercise provides weak stimulus for VEGF secretion and capillary growth in skeletal muscle. *Exp Physiol* (2013) **98**:585–97. doi:10.1113/expphysiol.2012.067967
34. Le X-F, Mao W, Lu C, Thornton A, Heymach JV, Sood AK, et al. Specific blockade of VEGF and HER2 pathways results in greater growth inhibition of breast cancer xenografts that overexpress HER2. *Cell Cycle* (2008) **7**:3747–58. doi: 10.4161/cc.7.23.7212
35. Bjorndahl M, Cao R, Eriksson A, Cao Y. Blockage of VEGF-induced angiogenesis by preventing VEGF secretion. *Circ Res* (2004) **94**:1443–50. doi:10.1161/01.RES.0000129194.61747.bf
36. Kavitha CV, Agarwal C, Argawal R, Deep G. Asiatic acid inhibits pro-angiogenic effects of VEGF and human gliomas in endothelial cell culture models. *PLoS ONE* (2011) **6**:e22745. doi:10.1371/journal.pone.0022745
37. van der Bilt ARM, van Scheltinga AGTT, Timmer-Bosscha H, Schroder CP, Pot L, Kosterink JGW, et al. Measurement of tumor VEGF-A levels with 89Zr-bevacizumab PET as an early biomarker for the antiangiogenic effect of everolimus treatment in an ovarian cancer xenograft model. *Clin Cancer Res* (2012) **18**:6306–14. doi:10.1158/1078-0432.CCR-12-0406
38. Leith JT, Michelson S. Secretion rates and levels of vascular endothelial growth factor in clone A or HCT-8 human colon tumour cells as a function of oxygen concentration. *Cell Prolif* (1995) **28**:415–30. doi:10.1111/j.1365-2184.1995.tb00082.x
39. Rofstad EK, Halsor EF. Vascular endothelial growth factor, interleukin 9, platelet-derived endothelial cell growth factor, and basic fibroblast growth factor promote angiogenesis and metastasis in human melanoma xenografts. *Cancer Res* (2000) **60**:4932–8.
40. Pilch H, Schlenger K, Steiner E, Brockerhoff P, Knapstein P, Vaupel P. Hypoxia-stimulated expression of angiogenic growth factors in cervical cancer cells and cervical cancer-derived fibroblasts. *Int J Gynecol Cancer* (2001) **11**:137–42. doi:10.1046/j.1525-1438.2001.011002.137.x
41. Salnikov AV, Heldin N-E, Stuhr LB, Wiig H, Gerber H-P, Reed RK, et al. Inhibition of carcinoma cell-derived VEGF reduces inflammatory characteristics in xenograft carcinoma. *Int J Cancer* (2006) **119**:2795–802. doi:10.1002/ijc.22217
42. Sugimoto H, Hamano Y, Charytan D, Cosgrove D, Kieran M, Sudhakar A, et al. Neutralization of circulating vascular endothelial growth factor (VEGF) by anti-VEGF antibodies and soluble VEGF receptor 1 (sFlt-1) induces proteinuria. *J Biol Chem* (2003) **278**:12605–8. doi:10.1074/jbc.C300012200
43. Bocci G, Man S, Green SK, Francia G, Ebos JM, du Manoir JM, et al. Increased plasma vascular endothelial growth factor (VEGF) as a surrogate marker for optimal therapeutic dosing of VEGF receptor-2 monoclonal antibodies. *Cancer Res* (2004) **64**:6616–25. doi:10.1158/0008-5472.CAN-04-0401
44. Keyes KA, Mann L, Cox K, Treadway P, Iversen P, Chen Y-F, et al. Circulating angiogenic growth factor levels in mice bearing human tumors using Luminex Multiplex technology. *Cancer Chemother Pharmacol* (2003) **51**:321–7.
45. Rullman E, Rundqvist H, Wagsater D, Fischer H, Eriksson P, Sundberg CJ, et al. A single bout of exercise activates matrix metalloproteinase in human skeletal muscle. *J Appl Physiol* (2007) **102**:2346–51. doi: 10.1152/jappphysiol.00822.2006
46. Kut C, Mac Gabhann F, Popel AS. Where is VEGF in the body? A meta-analysis of VEGF distribution in cancer. *Br J Cancer* (2007) **97**:978–85. doi:10.1038/sj.bjc.6603923
47. Bernaards C, Hegde P, Chen D, Holmgren E, Zheng M, Jubb AM, et al. Circulating vascular endothelial growth factor (VEGF) as a biomarker for bevacizumab-based therapy in metastatic colorectal, non-small cell lung, and renal cell cancers: analysis of phase III studies. *J Clin Oncol* (2010) **28**:10519.
48. Sanmartin E, Jantus E, Blasco A, Sireira R, Caballero C, Gallach S, et al. Plasma levels of VEGF-A and VEGFR-2 in advanced NSCLC. *J Clin Oncol* (2010) **28**:10623.
49. Willett CG, Duda DG, di Tomaso E, Boucher Y, Ancukiewicz M, Sahani DV, et al. Efficacy, safety, and biomarkers of neoadjuvant bevacizumab, radiation therapy, and fluorouracil in rectal cancer: a multidisciplinary phase II study. *J Clin Oncol* (2009) **27**:3020–6. doi:10.1200/JCO.2008.21.1771
50. Hoff BA, Bhojani MS, Rudge J, Chenevert TL, Meyer CR, Galban S, et al. DCE and DW-MRI monitoring of vascular disruption following VEGF-Trap treatment of a rat glioma model. *NMR Biomed* (2011) **25**:935–42. doi:10.1002/nbm.1814
51. Zhang Q-X, Magover CJ, Mack CA, Budenbender KT, Ko W, Rosengart T. Vascular endothelial growth factor is the major angiogenic factor in omentum: mechanism of the omentum-mediated angiogenesis. *J Surg Res* (1997) **67**:147–54. doi:10.1006/jsre.1996.4983
52. Yuan A, Lin C-Y, Chou C-H, Shih C-M, Chen C-Y, Cheng H-W, et al. Functional and structural characteristics of tumor angiogenesis in lung cancers overexpressing different VEGF isoforms assessed by DCE- and SSCE-MRI. *PLoS ONE* (2011) **6**:e16062. doi: 10.1371/journal.pone.0016062
53. Woolard J, Wang W-Y, Bevan HS, Qiu Y, Morbidelli L, Pritchard-Jones RO, et al. VEGF165b, an inhibitory vascular endothelial growth factor splice variant: mechanism of action, in vivo effect on angiogenesis and endogenous protein expression. *Cancer Res* (2004) **64**:7822–35. doi:10.1158/0008-5472.CAN-04-0934
54. Bates DO, Catalano PJ, Symonds KE, Varey AHR, Ramani P, O'Dwyer PJ, et al. Association between VEGF splice isoforms and progression-free survival in metastatic colorectal cancer patients treated with bevacizumab. *Clin Cancer Res* (2012) **18**:6384–91. doi:10.1158/1078-0432.CCR-12-2223
55. Achen MG, Stacker SA. Vascular endothelial growth factor-D: signaling mechanisms, biology, and clinical relevance. *Growth Factors* (2012) **30**:283–96. doi:10.3109/0897194.2012.704917
56. Benedito R, Rocha SF, Woeste M, Zamykal M, Radtke F, Casanovas O, et al. Notch-dependent VEGFR3 upregulation allows angiogenesis without VEGF-VEGFR2 signalling. *Nature* (2012) **484**:110–4. doi:10.1038/nature10908
57. Chen JC, Chang YW, Hong CC, Yu YH, Su JL. The role of the VEGF-C/VEGFRs axis in tumor progression and therapy. *Int J Mol Med* (2012) **14**:88–107. doi:10.3390/ijms14010088
58. Battinelli EM, Markens BA, Italiano JE Jr. Release of angiogenesis regulatory proteins from platelet alpha granules: modulation of physiologic and pathologic angiogenesis. *Blood* (2011) **118**:1359–69. doi:10.1182/blood-2011-02-334524
59. Yankeelov TE, Lepage M, Chakravarthy A, Broome EE, Niernann KJ, Kelley MC, et al. Integration of quantitative DCE-MRI and ADC mapping to monitor treatment response in human breast cancer. *Magn Reson Imaging* (2007) **25**:1–13. doi:10.1016/j.mri.2006.09.006
60. Mitchell EP. Targeted therapy for metastatic colorectal cancer: role of aflibercept. *Clin Colorectal Cancer* (2012) **12**(2):73–85. doi:10.1016/j.clcc.2012.08.001
61. Barrett AJ, Starkey PM. The interaction of alpha 2-macroglobulin with proteinases. Characteristics and specificity of the reaction, and a hypothesis concerning its molecular mechanism. *Biochem J* (1973) **133**:709–24.
62. Webb DJ, Wen J, Lysiak JJ, Umans L, Van Leuven F, Gonias SL. Murine a-macroglobulins demonstrate divergent activities as neutralizers of transforming growth factor-b and as inducers of nitric oxide synthesis. *J Biol Chem* (1996) **271**:24982–8. doi:10.1074/jbc.271.40.24982
63. Jelkmann W. Pitfalls in the measurement of circulating vascular endothelial growth factor. *Clin Chem* (2001) **47**:617–23.
64. Lee S, Chen TT, Barber CL, Jordan MC, Murdock J, Desai S, et al. Autocrine VEGF signaling is required for vascular homeostasis. *Cell* (2007) **130**:691–703. doi:10.1016/j.cell.2007.06.054
65. dela Paz NG, Walshe TE, Leach L, Saint-Geniez M, D'Amore PA. Role of shear-stress-induced VEGF expression in endothelial cell survival. *J Cell Sci* (2012) **125**:831–43. doi:10.1242/jcs.084301

66. Van den Berg CL, Cox GN, Stroh CA, Hilsenbeck SG, Weng C-N, McDermott MJ, et al. Polyethylene glycol conjugated insulin-like growth factor binding protein 1 (IGFBP-1) inhibits growth of breast cancer in athymic mice. *Eur J Cancer* (1997) **33**:1108–13. doi: 10.1016/S0959-8049(97)00071-3
67. Karpanen T, Egeblad M, Karkkainen MJ, Kubo H, Yla-Herttuala S, Jaattela M, et al. Vascular endothelial growth factor C promotes tumor lymphangiogenesis and intralymphatic tumor growth. *Cancer Res* (2001) **61**:1786–90.
68. Cameron IL, Sun L-Z, Short N, Hardman WE, Williams CD. Therapeutic Electromagnetic Field (TEMF) and gamma irradiation on human breast cancer xenograft growth, angiogenesis and metastasis. *Cancer Cell Int* (2005) **5**:23. doi:10.1186/1475-2867-5-17
69. Divisova J, Kuitatse I, Lazard D, Weiss H, Vreeland F, Hadsell DL, et al. The growth hormone receptor antagonist pegvisomant blocks both mammary gland development and MCF-7 breast cancer xenograft growth. *Breast Cancer Res Treat* (2006) **98**(3):315–27. doi:10.1007/s10549-006-9168-1
70. Wu Y, Hooper AT, Zhong Z, Witte L, Bohlen P, Rafii S, et al. The vascular endothelial growth factor receptor (VEGFR-1) supports growth and survival of human breast carcinoma. *Int J Cancer* (2006) **119**:1519–29. doi:10.1002/ijc.21865
71. Groth-Pedersen L, Ostenfeld MS, Hoyer-Hansen M, Nylandsted J, Jaattela M. Vincristine induces dramatic lysosomal changes and sensitizes cancer cells to lysosome-destabilizing siramesine. *Cancer Res* (2007) **67**:2217–25. doi:10.1158/0008-5472.CAN-06-3520
72. Rajhans R, Nair S, Holden AH, Kumar R, Takmel RR, Vadlamudi RK. Oncogenic potential of the nuclear receptor coregulator proline-, glutamic acid-, leucine-rich protein 1/modulator of the nongenomic actions of the estrogen receptor. *Cancer Res* (2007) **67**:5505–12. doi:10.1158/0008-5472.CAN-06-3647
73. Gully CP, Zhang F, Chen J, Yeung JA, Valazquez-Torres G, Wang E, et al. Antineoplastic effects of an Aurora B kinase inhibitor in breast cancer. *Mol Cancer* (2010) **9**:42. doi:10.1186/1476-4598-9-42
74. Koskimaki JE, Rosca EV, Rivera CG, Lee E, Chen W, Pandey NB, et al. Serpin-derived peptides are antiangiogenic and suppress breast tumor xenograft growth. *Transl Oncol* (2012) **5**:92–7.
75. Saltelli A, Bolado R. An alternative way to compute Fourier amplitude sensitivity test (FAST). *Comput Stat Data Anal* (2008) **26**:445–60. doi:10.1016/S0167-9473(97)00043-1
76. Marino S, Hogue IB, Ray CJ, Kirschner DE. A methodology for performing global uncertainty and sensitivity analysis in systems biology. *J Theor Biol* (2008) **254**:178–96. doi:10.1016/j.jtbi.2008.04.011
77. Tan WH, Popel AS, Mac Gabhann F. Computational model of Gab1/2-dependent VEGFR2 pathway to Akt activation. *PLoS ONE* (2013) **8**:e67438. doi:10.1371/journal.pone.0067438
78. Paran Y, Bendel P, Margalit R, Degani H. Water diffusion in the different microenvironments of breast cancer. *NMR Biomed* (2004) **17**:170–80. doi:10.1002/nbm.882
79. Schaefer C, Schroeder M, Fuhrhop I, Viezens L, Otten J, Fiedler W, et al. Primary tumor dependent inhibition of tumor growth, angiogenesis, and perfusion of secondary breast cancer in bone. *J Orth Res* (2011) **29**:1251–8. doi:10.1002/jor.21402
80. Kim E, Stamatelos SK, Cebulla J, Bhujwalla ZM, Popel AS, Pathak AP. Multiscale imaging and computational modeling of blood flow in the tumor vasculature. *Ann Biomed Eng* (2012) **40**:2425–41. doi:10.1007/s10439-012-0585-5
81. Olewniczak S, Chosia M, Kwas A, Kram A, Domagala W. Angiogenesis and some prognostic parameters of invasive ductal breast carcinoma in women. *Pol J Pathol* (2002) **53**:183–8.
82. Olewniczak S, Chosia M, Kolodziej B, Kwas A, Kram A, Domagala W. Angiogenesis as determined by computerised image analysis and the risk of early relapse in women with invasive ductal breast carcinoma. *Pol J Pathol* (2003) **54**:53–9.
83. Hassid Y, Furman-Haran E, Margalit R, Eilam R, Degani H. Noninvasive magnetic resonance imaging of transport and interstitial fluid pressure in ectopic human lung tumors. *Cancer Res* (2006) **66**:4159–66. doi:10.1158/0008-5472.CAN-05-3289
84. Lewin M, Bredow S, Sergeev N, Marecos E, Bodganov A Jr, Weissleder R. In vivo assessment of vascular endothelial growth factor-induced angiogenesis. *Int J Cancer* (1999) **83**:798–802. doi:10.1002/(SICI)1097-0215(19991210)83:6<798:AID-IJC16>3.0.CO;2-W
85. Bogin L, Margalit R, Mispelter J, Degani H. Parametric imaging of tumor perfusion using flow- and permeability-limited tracers. *J Magn Reson Imaging* (2002) **16**:289–99. doi:10.1002/jmri.10159
86. Cao M, Liang Y, Shen C, Miller KD, Stantz KM. Developing DCE-CT to quantify intratumor heterogeneity in breast tumors with different angiogenic phenotype. *IEEE Trans Med Imaging* (2009) **28**:861–71. doi:10.1109/TMI.2008.2012035
87. Mac Gabhann F, Popel AS. Targeting neuropilin-1 to inhibit VEGF signaling in cancer: comparison of therapeutic approaches. *PLoS Comp Biol* (2006) **2**:e180. doi:10.1371/journal.pcbi.0020180
88. Yuan F, Krol A, Tong S. Available space and extracellular transport of macromolecules: effects of pore size and connectedness. *Ann Biomed Eng* (2001) **29**:1150–8. doi:10.1114/1.1424915
89. Hashizume H, Baluk P, Morikawa S, McLean JW, Thurston G, Roberge S, et al. Openings between defective endothelial cells explain tumor vessel leakiness. *Am J Pathol* (2000) **156**:1363–80. doi:10.1016/S0002-9440(10)65006-7
90. Ng YS, Rohan R, Sunday ME, Demello DE, D'Amore PA. Differential expression of VEGF isoforms in mouse during development and in the adult. *Dev Dyn* (2001) **220**:112–21. doi:10.1002/1097-0177(2000)9999:9999<::AID-DVDY1093>3.0.CO;2-D
91. Gustafsson T, Ameln H, Fischer H, Sundberg CJ, Timmons JA, Jansson E. VEGF-A splice variants and related receptor expression in human skeletal muscle following submaximal exercise. *J Appl Physiol* (2005) **98**:2137–46. doi:10.1152/japplphysiol.01402.2004
92. Cheung N, Wong MP, Yuen ST, Leung SY, Chung LP. Tissue-specific expression pattern of vascular endothelial growth factor isoforms in the malignant transformation of lung and colon. *Hum Pathol* (1998) **29**:910–4. doi:10.1016/S0046-8177(98)90195-2
93. Yuan A, Yu CJ, Luh KT, Lin FY, Kuo SH, Yang PC. Quantification of VEGF mRNA expression in non-small cell lung cancer using a real-time quantitative reverse transcription-PCR assay and a comparison with quantitative competitive reverse transcription-PCR. *Lab Invest* (2000) **2000**:11.
94. Stimpfl M, Tong D, Fasching B, Schuster E, Obermair A, Leodolter S, et al. Vascular endothelial growth factor splice variants and their prognostic value in breast and ovarian cancer. *Clin Cancer Res* (2002) **8**:2253–9.
95. Ljungberg B, Jacobsen J, Haggstrom-Rudolfsson S, Rasmuson T, Lindh G, Grankvist K. Tumor vascular endothelial growth factor (VEGF) mRNA in relation to serum VEGF protein levels and tumour progression in human renal cell carcinoma. *Urol Res* (2003) **31**:335–40. doi:10.1007/s00240-003-0346-x
96. Zygaki E, Tsaroucha EG, Kaklamani L, Lianidou ES. Quantitative real-time reverse transcription-PCR study of the expression of vascular endothelial growth factor (VEGF) splice variants and VEGF receptors (VEGFR-1 and VEGFR-2) in non-small cell lung cancer. *Clin Chem* (2007) **53**:1433–9. doi:10.1373/clinchem.2007.086819
97. Roland CL, Dineen SP, Lynn KD, Sullivan LA, Dellinger MT, Sadegh L, et al. Inhibition of vascular endothelial growth factor reduces angiogenesis and modulates immune cell infiltration of orthotopic breast cancer xenografts. *Mol Cancer Ther* (2009) **8**:1761–71. doi:10.1158/1535-7163.MCT-09-0280
98. Blankenberg FG, Levashova Z, Sarkar SK, Pizzonia J, Backer MV, Bacher JM. Noninvasive assessment of tumor VEGF receptors in response to treatment with pazopanib: a molecular imaging study. *Transl Oncol* (2010) **3**:56–64.
99. Hudson NW, Kehoe JM, Koo PH. Mouse alpha-macroglobulin. Structure, function, and a molecular model. *Biochem J* (1987) **248**:837–45.
100. Banks RE, Evans SW, Van Leuven F, Alexander D, McMahon MJ, Whicher JT. Measurement of the “fast” or complexed form of α_2 -macroglobulin in biological fluids using a sandwich enzyme immunoassay. *J Immunol Methods* (1990) **126**:13–20. doi:10.1016/0022-1759(90)90006-H

101. Zucker S, Lysik RM, Zarrabi MH, Fiore JJ, Strickland DK. Proteinase-alpha2 macroglobulin complexes are not increased in plasma of patients with cancer. *Int J Cancer* (1991) **48**:399–403. doi:10.1002/ijc.2910480316
102. Jespersen MH, Jensen J, Rasmussen LH, Ejlersen E, Møller-Petersen J, Sperling-Petersen HU. The reference range for complexed a2-macroglobulin human plasma: development of a new enzyme linked in immunosorbent assay (ELISA) for quantitation of complexed a2-macroglobulin. *Scand J Clin Lab Invest* (1993) **53**:639–48. doi:10.1080/00365519309092565
103. Garlick DG, Renkin EM. Transport of large molecules from plasma to interstitial fluid and lymph in dogs. *Am J Physiol* (1970) **219**:1595–605.
104. Goel S, Duda DG, Xu L, Munn LL, Boucher Y, Fukumura D, et al. Normalization of the vasculature for treatment of cancer and other diseases. *Physiol Rev* (2011) **91**:1071–121. doi:10.1152/physrev.00038.2010
105. Coleman TF, Li Y. On the convergence of reflective Newton methods for large-scale nonlinear minimization subject to bounds. *Math Program* (1994) **67**:189–224. doi:10.1007/BF01582221
106. Coleman TF, Li Y. An interior, trust region approach for nonlinear minimization subject to bounds. *SIAM J Optim* (1996) **6**:418–45. doi:10.1137/0806023
107. Wachsberger PR, Burd R, Cardi C, Thakur M, Daskalakis C, Holash J, et al. VEGF trap in combination with radiotherapy improves tumor control in u87 glioblastoma. *Int J Radiat Oncol Biol Phys* (2007) **67**:1526–37. doi:10.1016/j.ijrobp.2006.11.011
108. Hall JE. The circulation. In: Hall JE, editor. *Guyton and Hall Textbook of Medical Physiology*. 12th ed. Philadelphia, PA: W.B. Saunders Company (2011). p. 177–90.
109. Baluk P, Morikawa S, Haskell A, Mancuso M, McDonald DM. Abnormalities of basement membrane on blood vessels and endothelial sprouts in tumors. *Am J Pathol* (2003) **163**:1801–15. doi:10.1016/S0002-9440(10)63540-7
110. Bhattacharjee G, Asplin IR, Wu SM, Gawdi G, Pizzo SV. The conformation-dependent interaction of alpha-2-macroglobulin with vascular endothelial growth factor. *J Biol Chem* (2000) **275**:26806–11.
111. Fuh G, Garcia KC, de Vos AM. The interaction of neuropilin-1 with vascular endothelial growth factor and its receptor flt-1. *J Biol Chem* (2000) **275**:26690–5.
112. Folkman J. Angiogenesis in cancer, vascular rheumatoid and other disease. *Nat Med* (1995) **1**:27–31. doi:10.1038/nm0195-27
113. Wu FTH, Stefanini MO, MacGabhann F, Popel AS. A compartment model of VEGF distribution in humans in the presence of soluble VEGF receptor-1 acting as a ligand trap. *PLoS ONE* (2009) **4**:e5108. doi:10.1371/journal.pone.0005108
114. Imber MJ, Pizzo SV. Clearance and binding of two electrophoretic “fast” forms of human alpha-2-macroglobulin. *J Biol Chem* (1981) **256**:8134–9.

Conflict of Interest Statement: The authors declare that the research was conducted in the absence of any commercial or financial relationships that could be construed as a potential conflict of interest.

Received: 21 December 2012; accepted: 13 July 2013; published online: 30 July 2013.
Citation: Finley SD, Dhar M and Popel AS (2013) Compartment model predicts VEGF secretion and investigates the effects of VEGF Trap in tumor-bearing mice. *Front. Oncol.* **3**:196. doi: 10.3389/fonc.2013.00196

This article was submitted to *Frontiers in Molecular and Cellular Oncology*, a specialty of *Frontiers in Oncology*. Copyright © 2013 Finley, Dhar and Popel. This is an open-access article distributed under the terms of the Creative Commons Attribution License (CC BY). The use, distribution or reproduction in other forums is permitted, provided the original author(s) or licensor are credited and that the original publication in this journal is cited, in accordance with accepted academic practice. No use, distribution or reproduction is permitted which does not comply with these terms.

APPENDIX

Table A1 | Geometric parameters.

	Value	Units	Reference
CANCER CELLS			
Tumor cell external diameter	12	μm	Paran et al. (78)
Volume of one cell	905	μm^3	Calculated (see manuscript)
Surface area of one cell	497	μm^2	Calculated (see manuscript)
MICROVESSELS			
Average luminal diameter	13.9	μm	Schaefer et al. (79)
Endothelial cell thickness	0.5	μm	Based on normal microvessels (108)
Average external diameter	14.9	μm	Calculated (see manuscript)
Cross-sectional area of one vessel	175.3	μm^2	Calculated (see manuscript)
Perimeter of one vessel	57.7	μm	Calculated (see manuscript)
Capillary density	655	Capillaries/ mm^2	Calculated (see manuscript)
VOLUME FRACTIONS			
Interstitial space	35.0%	cm^2/cm^3 tissue	Based on (78, 83)
Cancer cells	53.5%	cm^2/cm^3 tissue	Calculated (see manuscript)
Microvessels of which intravascular space	11.5%	cm^2/cm^3 tissue	Calculated (see manuscript)
	10.0%	cm^2/cm^3 tissue	Based on (84–86)
SURFACE AREAS			
Tumor cells	2939	cm^2/cm^3 tissue	Calculated (see manuscript)
Microvessels	378	cm^2/cm^3 tissue	Calculated (see manuscript)
BASEMENT MEMBRANES (BM)			
Thickness of tumor cell BM	30	nm	Based on (109)
Basement membrane volume (tumor cells) of which available to VEGF	0.00807	cm^3/cm^3	Calculated (see manuscript)
	0.00508	cm^3/cm^3 tissue	Calculated (see manuscript)
Thickness of microvessel BM	50	nm	Based on (109)
Basement membrane volume (microvessels) of which available to VEGF	0.00154	cm^3/cm^3 tissue	Calculated (see manuscript)
	0.000972	cm^3/cm^3 tissue	Calculated (see manuscript)
Extracellular matrix volume of which available to VEGF	0.3375	cm^3/cm^3 tissue	Calculated (see manuscript)
	0.2892	cm^3/cm^3 tissue	Calculated (see manuscript)

Table A2 | Concentrations in tumor compartment.

	Value	Units
VEGFR1		
Luminal EC	3750	Dimers/EC
Abluminal EC	3750	Dimers/EC
Tumor	1100	Dimers/TC
VEGFR2		
Luminal EC	300	Dimers/EC
Abluminal EC	300	Dimers/EC
Tumor	550	Dimers/TC
NRP1		
Luminal EC	39,748	Dimers/EC
Abluminal EC	39,748	Dimers/EC
Tumor	39,500	Dimers/TC
NRP2		
Tumor	39,500	Dimers/TC
ECM binding density	0.75	μM
EBM binding density	13	μM
PBM binding density	13	μM

EC, endothelial cell; TC, tumor cell.

Table A3 | Kinetic parameters.

	Value	Unit	Reference
VEGF BINDING TO VEGFR1			
k_{on}	3×10^7	$M^{-1} s^{-1}$	Mac Gabhann and Popel (87), Stefanini et al. (24)
k_{off}	10^{-3}	s^{-1}	Mac Gabhann and Popel (87), Stefanini et al. (24)
K_d	33	pM	Mac Gabhann and Popel (87), Stefanini et al. (24)
VEGF BINDING TO VEGFR2			
k_{on}	10^7	$M^{-1} s^{-1}$	Mac Gabhann and Popel (87), Stefanini et al. (24)
k_{off}	10^{-3}	s^{-1}	Mac Gabhann and Popel (87), Stefanini et al. (24)
K_d	100	pM	Mac Gabhann and Popel (87), Stefanini et al. (24)
VEGF BINDING TO NRP1			
k_{on}	3.2×10^6	$M^{-1} s^{-1}$	Mac Gabhann and Popel (87), Stefanini et al. (24)
k_{off}	10^{-3}	s^{-1}	Mac Gabhann and Popel (87), Stefanini et al. (24)
K_d	312.5	pM	Mac Gabhann and Popel (87), Stefanini et al. (24)
VEGF BINDING TO GAGs			
k_{on}	4.20×10^5	$M^{-1} s^{-1}$	Mac Gabhann and Popel (87), Stefanini et al. (24)
k_{off}	10^{-2}	s^{-1}	Mac Gabhann and Popel (87), Stefanini et al. (24)
K_d	24	pM	Mac Gabhann and Popel (87), Stefanini et al. (24)
COUPLING OF NRP1 AND VEGFR1			
k_c	10^{14}	$(mol/cm^2)^{-1} s^{-1}$	Mac Gabhann and Popel (87), Stefanini et al. (24)
k_{off}	10^{-2}	s^{-1}	Mac Gabhann and Popel (87), Stefanini et al. (24)
COUPLING OF NRP1 AND VEGFR2			
$k_{cV165R2, N1}$	3.1×10^{13}	$(mol/cm^2)^{-1} s^{-1}$	Mac Gabhann and Popel (87), Stefanini et al. (24)
$k_{offV165R2, N1}$	10^{-3}	s^{-1}	Mac Gabhann and Popel (87), Stefanini et al. (24)
$k_{cV165N1, R2}$	10^{14}	$(mol/cm^2)^{-1} s^{-1}$	Mac Gabhann and Popel (87), Stefanini et al. (24)
$k_{offV165N1, R2}$	10^{-3}	s^{-1}	Mac Gabhann and Popel (87), Stefanini et al. (24)
VEGFR INTERNALIZATION			
k_{int}	2.8×10^{-4}	s^{-1}	Mac Gabhann and Popel (87), Stefanini et al. (24)
VEGF₁₂₁ BINDING TO ANTI-VEGF			
k_{on}	3.75×10^8	$M^{-1} s^{-1}$	Calculated
k_{off}	1.35×10^{-5}	s^{-1}	Papadopoulos et al. (11)
K_d	0.36	pM	Papadopoulos et al. (11)
VEGF₁₆₅ BINDING TO ANTI-VEGF			
k_{on}	4.10×10^7	$M^{-1} s^{-1}$	Calculated
k_{off}	2.01×10^{-5}	s^{-1}	Papadopoulos et al. (11)
K_d	0.49	pM	Papadopoulos et al. (11)
VEGF₁₂₀ BINDING TO ANTI-VEGF			
k_{on}	2.15×10^7	$M^{-1} s^{-1}$	Calculated
k_{off}	1.23×10^{-5}	s^{-1}	Papadopoulos et al. (11)
K_d	0.572	pM	Papadopoulos et al. (11)
VEGF₁₆₄ BINDING TO ANTI-VEGF			
k_{on}	2.80×10^7	$M^{-1} s^{-1}$	Calculated
k_{off}	1.64×10^{-5}	s^{-1}	Papadopoulos et al. (11)
K_d	0.586	pM	Papadopoulos et al. (11)
VEGF BINDING TO $\alpha 2M$			
k_{on}	25	$M^{-1} s^{-1}$	Calculated
k_{off}	10^{-4}	s^{-1}	Assumed
K_d	4.0	μM	Bhattacharjee et al. (110)
VEGF BINDING TO $\alpha 2M_{FAST}$			
k_{on}	2.4×10^2	$M^{-1} s^{-1}$	Calculated
k_{off}	10^{-4}	s^{-1}	Assumed
K_d	0.42	μM	Bhattacharjee et al. (110)

(Continued)

Table A3 | Continued

	Value	Unit	Reference
sVEGFR1 BINDING TO VEGF			
k_{on}	3×10^7	$M^{-1} s^{-1}$	Assumed, based on VEGF binding to VEGFR1
k_{off}	10^{-3}	s^{-1}	Assumed
K_d	33	pM	Assumed
sVEGFR1 BINDING TO NRP1			
k_{on}	5.6×10^6	$M^{-1} s^{-1}$	Calculated
k_{off}	10^{-2}	s^{-1}	Assumed, based on VEGFR1 coupling to NRP1
K_d	1.8	nM	Fuh et al. (111)
sVEGFR1 BINDING TO GAGs			
k_{on}	4.20×10^5	$M^{-1} s^{-1}$	Assumed, based on VEGF ₁₆₅ binding to GAG
k_{off}	10^{-2}	s^{-1}	Assumed
K_d	24	pM	Assumed

Table A4 | Transport parameters.

	Value	Unit	Reference
PERMEABILITY BETWEEN NORMAL AND BLOOD			
VEGF	4.0×10^{-8}	cm/s	Stefanini et al. (24)
Anti-VEGF and VEGF/anti-VEGF complex	3.0×10^{-8}	cm/s	Stefanini et al. (24)
Soluble VEGFR1	1.5×10^{-8}	cm/s	Calculated, see text
Soluble VEGFR1/VEGF complex	1.5×10^{-8}	cm/s	Calculated, see text
PERMEABILITY BETWEEN TUMOR AND BLOOD			
VEGF	4.0×10^{-7}	cm/s	Assumed, see text
Anti-VEGF and VEGF/anti-VEGF complex	3.0×10^{-7}	cm/s	Assumed, see text
Soluble VEGFR1	1.5×10^{-7}	cm/s	Assumed, see text
Soluble VEGFR1/VEGF complex	1.5×10^{-7}	cm/s	Assumed, see text
CLEARANCE			
VEGF	2.3×10^{-1}	min^{-1}	Folkman (112)
Anti-VEGF	8.9×10^{-4}	min^{-1}	Yen et al. (23)
VEGF/anti-VEGF complex	2.8×10^{-4}	min^{-1}	Yen et al. (23)
Soluble VEGFR1	3.0×10^{-4}	min^{-1}	Wu et al. (113)
Soluble VEGFR1/VEGF complex	3.0×10^{-4}	min^{-1}	Wu et al. (113)
Alpha-2-macroglobulin ($\alpha 2M$)	2.6×10^{-3}	min^{-1}	Hudson et al. (99)
$\alpha 2M$ /VEGF complex	2.6×10^{-3}	min^{-1}	Assumed, based on $\alpha 2M$
$\alpha 2M$ /VEGF/anti-VEGF complex	2.6×10^{-3}	min^{-1}	Assumed, based on $\alpha 2M$
Activated alpha-2-macroglobulin ($\alpha 2M_{fast}$)	2.4×10^{-1}	min^{-1}	Imber and Pizzo (114)
$\alpha 2M$ /VEGF complex	2.6×10^{-3}	min^{-1}	Assumed, based on $\alpha 2M_{fast}$
DEGRADATION			
Soluble VEGFR1	1.2×10^{-2}	min^{-1}	Assumed based on VEGF
Soluble VEGFR1/VEGF complex	1.2×10^{-2}	min^{-1}	Assumed based on VEGF
SYNTHESIS			
Alpha-2-macroglobulin	1.8×10^{10}	Molecules/cm ³ tissue/s	Calculated, see text
Activated alpha-2-macroglobulin	1.6×10^{10}	Molecules/cm ³ tissue/s	Calculated, see text

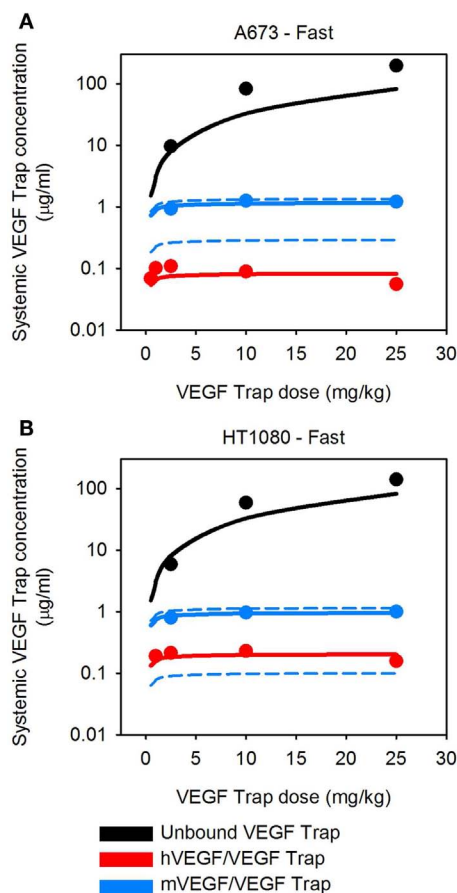


FIGURE A1 | Predicted systemic VEGF Trap levels for fast-growing tumors. The model predicts the plasma levels of free VEGF Trap (black lines), mouse VEGF bound to VEGF Trap (blue lines), and human VEGF bound to VEGF Trap (red lines) for fast-growing tumors. VEGF Trap was administered twice per week for 2 weeks at doses of 0.5, 1, 2.5, 10, and 25 mg/kg. The simulated results are shown for the optimized model where the secretion rates of VEGF by myocytes, EC, and tumor cells were fit to experimental data (circles). We use the mean (solid lines) and 1 SD (dashed lines) of the fitted secretion rates. **(A)** A673 tumor; and **(B)** HT1080 tumor.

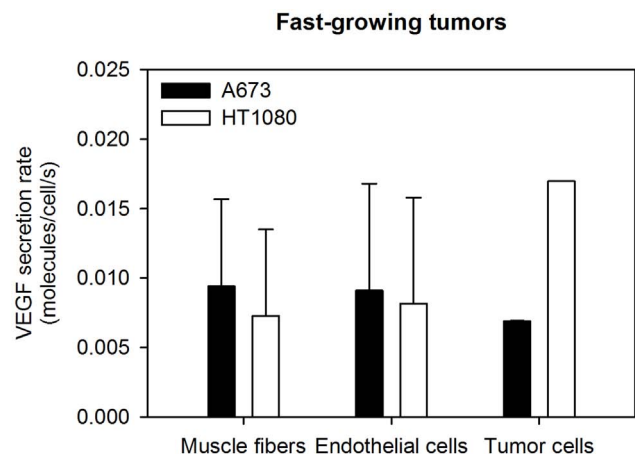


FIGURE A2 | Optimized VEGF secretion rates. The model parameters were optimized to fit experimental data, and the values of normal, EC, and tumor VEGF secretion rates were determined. The mean optimal secretion rates and standard deviation of 20 optimization runs for fast-growing tumors are shown.



A hybrid model of the role of VEGF binding in endothelial cell migration and capillary formation

Harsh V. Jain^{1*} and Trachette L. Jackson²

¹ Department of Mathematics, Florida State University, Tallahassee, FL, USA

² Department of Mathematics, University of Michigan, Ann Arbor, MI, USA

Edited by:

Heiko Enderling, Tufts University
School of Medicine, USA

Reviewed by:

Juan C. Chimal, Instituto Politécnico
Nacional, Mexico
Xiaoming Zheng, Central Michigan
University, USA

*Correspondence:

Harsh V. Jain, Department of
Mathematics, Florida State University,
208 Love Bldg, 1017 Academic Way,
Tallahassee, FL 32306, USA.
e-mail: hjain@fsu.edu

Vascular endothelial growth factor (VEGF) is the most studied family of soluble, secreted mediators of endothelial cell migration, survival, and proliferation. VEGF exerts its function by binding to specific tyrosine kinase receptors on the cell surface and transducing the effect through downstream signaling. In order to study the influence of VEGF binding on endothelial cell motion, we develop a hybrid model of VEGF-induced angiogenesis, based on the theory of reinforced random walks. The model includes the chemotactic response of endothelial cells to angiogenic factors bound to cell-surface receptors, rather than approximating this as a function of extracellular chemical concentrations. This allows us to capture biologically observed phenomena such as activation and polarization of endothelial cells in response to VEGF gradients across their lengths, as opposed to extracellular gradients throughout the tissue. We also propose a novel and more biologically reasonable functional form for the chemotactic sensitivity of endothelial cells, which is also governed by activated cell-surface receptors. This model is able to predict the threshold level of VEGF required to activate a cell to move in a directed fashion as well as an optimal VEGF concentration for motion. Model validation is achieved by comparison of simulation results directly with experimental data.

Keywords: mathematical model, angiogenesis, VEGF binding dynamics, endothelial cell migration, hybrid modeling

1. INTRODUCTION

Motility – random, directed, and collective – is a fundamental property of cells. Coordinated cellular motion leads to all physiological tissue patterns, a consequence of integration across multiple temporal and spatial scales. However, when this integration is aberrant, the properties that emerge lead to a critical bifurcation point in cancer progression: angiogenesis. Angiogenesis, the formation of new blood vessels from pre-existing ones, provides the necessary blood supply for the growth and nourishment of solid tumors beyond a few millimeters in diameter (Hanahan and Weinberg, 2000; Augustin et al., 2009). Tumor angiogenesis is associated with an extremely complex, yet well-ordered series of events at the center of which is the enhanced replicative potential and motility of endothelial cells (ECs) that line the inner surface of blood vessels (Folkman, 1985; Hanahan and Weinberg, 2000).

The multistep process associated with successful angiogenesis can be summarized as EC degradation of the adjacent basement membrane, migration (sprouting), proliferation, alignment, tube formation, branching that increases near the tumor leading to a brush-border, anastomosis (fusion of vessels), synthesis of new basement membrane, recruitment of parenchymal cells, network remodeling, and a return to quiescence (Folkman, 1985; Yancopoulos et al., 2000; Conway et al., 2001; Augustin et al., 2009). Precise coordination and integration of molecular, cellular, and tissue level interactions is required for angiogenesis to be successful from initiation to stabilization of a functional vascular plexus.

Under conditions of hypoxia, tumor cells induce angiogenesis by releasing a wide variety of polypeptide angiogenic factors that

stimulate EC activation, survival, proliferation, migration, and maturation. Members of the vascular endothelial growth factor (VEGF) family have been identified as the predominant amongst these angiogenic factors that regulate EC phenotype (Yancopoulos et al., 2000; Jain, 2002; Ferrara, 2004; Hicklin and Ellis, 2005). VEGF has been implicated across a range of human cancer and preclinical studies have shown that VEGF stimulates survival of existing vessels, promotes new vessel growth, and contributes to vascular abnormalities such as tortuosity and hyperpermeability. The angiogenic effects of the VEGF pathway are primarily initiated through the interaction of VEGFA and its natural, endothelial cell specific receptor, VEGFR2, which is up-regulated during angiogenesis (Neufeld et al., 1999; McMahon, 2000; Conway et al., 2001). Dimerization and activation of VEGFR2 results in mitogenic, chemotactic, and prosurvival signals (Nor et al., 1999; Ferrara et al., 2003; Ferrara, 2004), which help to determine endothelial cell phenotype.

The various steps of the angiogenic cascade require endothelial cells to take on spatio-temporally varying phenotypes; that is, at any given time and at any specific spatial location within a developing sprout, ECs can have a proliferative, migratory, or quiescent phenotype. For example, tip cells are highly migratory and lead the extending sprout through the extracellular matrix (ECM), whereas stalk cells, which form the vessel lumen and recruit support cells, can be either proliferative or quiescent. It has been shown that endothelial cells compete for the tip cell position through relative levels of VEGF-receptors (Jakobsson et al., 2010). While much is known about the sequential morphogenetic processes required for

angiogenesis and the growth factors that drive it, far less is known about how cellular and molecular mechanisms are coordinated to control cell motility decisions and phenotype choices. In order to advance the understanding and manipulating of the processes that occur during angiogenesis, it is critical to understand how individual cells interpret the biochemical signals that come from their unique microenvironment.

For decades, mathematical models have been employed to help address some of the pressing questions associated with tumor angiogenesis. As discussed in detail in Jackson and Zheng (2010), Zheng et al. (2013), existing models of tumor-induced angiogenesis can be characterized as continuous approaches (Balding and McElwain, 1985; Byrne and Chaplain, 1995, 1996; Anderson and Chaplain, 1998a,b; Holmes and Sleeman, 2000; Levine et al., 2001; Arakelyan et al., 2002; Sleeman and Wallis, 2002; Manousaki, 2003; Plank and Sleeman, 2003, 2004; Plank et al., 2004; Levine and Nilsen-Hamilton, 2006; Schugart et al., 2008; Billy et al., 2009; Xue et al., 2009; Travasso et al., 2011), wherein cells are assumed to have a continuous distribution; discrete or hybrid models (Stokes and Lauffenburger, 1991; Anderson and Chaplain, 1998b; Tong and Yuan, 2001; Plank and Sleeman, 2003, 2004; Sun et al., 2005; Bartha and Rieger, 2006; Gevertz and Torquato, 2006; Frieboes et al., 2007; Milde et al., 2008; Capasso and Morale, 2009; Owen et al., 2009; Perfahl et al., 2011), wherein cells are modeled as individual agents and diffusible chemicals are modeled as a continuum; and cell-based formulations (Peirce et al., 2004; Bauer et al., 2007; Bentley et al., 2009; Qutub and Popel, 2009; Wcislo et al., 2009; Jackson and Zheng, 2010; Liu et al., 2011) wherein explicit incorporation of different properties of individual cells allows collective behavior of cell clusters to be predicted from the behavior and interactions of individual cells. Reviews of these models that appeared in or before 2009 can be found in Mantzaris et al. (2004), Peirce (2008), Qutub et al. (2009). However, these models suffer from the following limitations. Continuum descriptions of biological motion such as chemotaxis are derived by averaging quantities such as cellular and vascular densities, and therefore apply to the macroscopic behavior of a large number of cells. However, the initial stages of new capillary development requires only a small number of cells in a highly discrete arrangement, which is better described by treating cells as individual agents. Further, even when a hybrid or cell-based approach has been adopted, endothelial cell movement, and/or microvessel formation speed and direction is typically assumed to depend on extracellular chemokine concentrations, whereas it is known that cells integrate the chemical signal via receptors on their surfaces in order to make behavioral decisions (Nor et al., 1999; Ferrara et al., 2003; Ferrara, 2004).

In order to study the influence of VEGF binding on EC motion, we develop here a hybrid model of VEGF-induced angiogenesis that is based on the theory of reinforced random walks. We will include in our model, the chemotactic response of endothelial cells to angiogenic factors bound to cell-surface receptors, rather than approximating this as a function of extracellular chemical concentrations. This will allow us to capture biologically observed phenomena such as the activation and polarization of endothelial cells in response to VEGF gradients across their lengths. We will also propose a novel and more biologically reasonable functional

form for the chemotactic sensitivity of cells, which is also governed by activated cell-surface receptors.

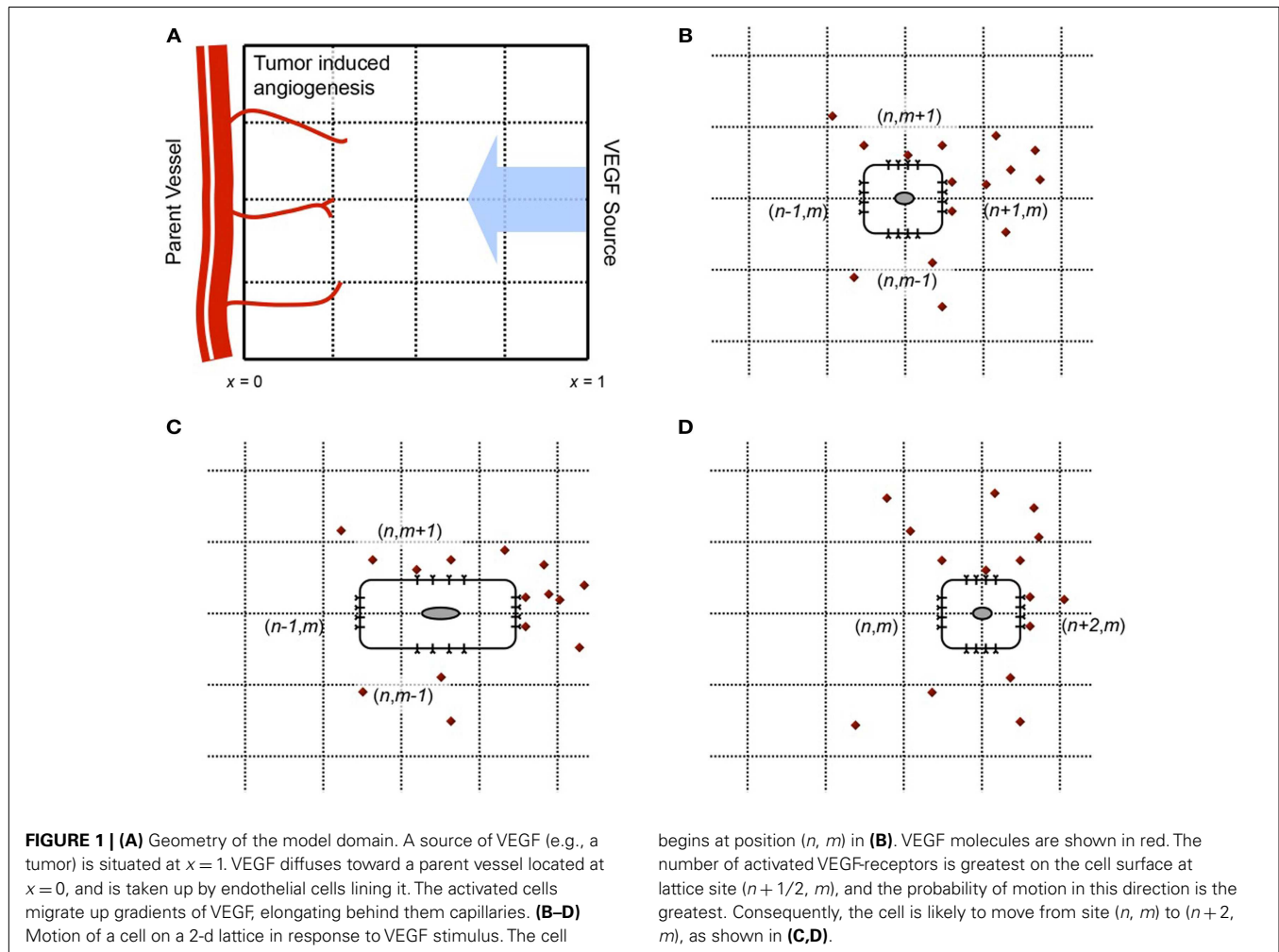
In the sections that follow, we will first develop a model to describe the motion of a single EC that has a tip cell phenotype. The motion of an EC across a 1 mm^2 domain will be simulated, and average time taken by the cell to reach the tumor (VEGF source) computed as a function of source strength. We will then extend this model to study the early stages of blood vessel formation and sprout extension. In particular, we will capture the following growth pattern of developing sprouts, typically observed in experiments. Sprouts arising from parent vessels are observed to grow parallel to each other initially (Pawelitz and Knierim, 1989), with anastomoses between tip cells and stalk cells, or between two tip cells observed to occur a certain distance into the stroma. As the developing vessels near the source of chemoattractants, new sprouts emerge in a process called sprout branching, which increases with proximity to the source. This has been described as a “brush-border” effect (Muthukkaruppan et al., 1982; Sholley et al., 1984). We will also investigate the effect on vascular development of the source strength of VEGF. Model validation will follow from a qualitative comparison of simulations with experimental data on neovascularization of the rat cornea taken from Sholley et al. (1984).

2. MATERIALS AND METHODS

2.1. MODEL DEVELOPMENT: SINGLE CELL MOTION UNDER THE INFLUENCE OF VEGF

A vital characteristic of all cells is their ability to sense their environment and respond to it, such as motion toward or away from an external, chemical stimulus. The response of endothelial cells to a chemokine like VEGF involves the following two major steps that a mathematical description of this process needs to account for: (i) detection of the signal (via gradient of bound VEGF to cell-surface receptors) and (ii) transduction of the external signal into an internal signal that controls the pattern of movement (Mantzaris et al., 2004). The theory of reinforced random walks, where a master equation governing cell movement is derived directly from the governing biology, as opposed to discretizing a continuous equation of macroscopic motion, provides a natural framework for modeling the movement of individual endothelial cells that initiate vascular sprout development. We remark that for simplicity, the effects of the extracellular matrix on EC motion are not explicitly considered at this time so that the cell is assumed to migrate on a homogeneous and isotropic medium. Further, on the time-scale of interest, cell proliferation, and death are assumed to be negligible.

We begin our model development by first simulating a single EC moving under the influence of VEGF. The EC is interpreted as a (biased) random walker that adapts its motility decisions under the influence of activated VEGF-receptors on its surface. We consider a 2-dimensional spatial domain, with a tumor located at $x = 1$ serving as the source of VEGF, and a parent vessel located at $x = 0$ providing individual ECs to begin sprout development, as shown in Figure 1A. The tumor secretes VEGF under the condition of hypoxia, which diffuses toward the parent vessel. VEGF is taken up by cells lining the parent vessel, transforming them into sprout tip cells. These migrate up its chemical gradient, pulling behind them the developing capillaries. The principal dynamics that we wish to



capture with the model are the binding and uptake of VEGF by the sprout tip cells, the subsequent activation of cell-surface receptors, and the chemotactic response of the cells to this stimulation. To our knowledge, this level of molecular detail has not been implemented previously in a model of tumor-induced angiogenesis.

The cell is located initially at spatial position $x = 0, y = 0.5$, and will move in response to a local, cellular gradient of VEGF, which has its source at $x = 1$. A schematic of this process is shown in **Figures 1B–D**. Following Plank et al. (Plank and Sleeman, 2003; Plank et al., 2003, 2004), we base our spatial discretization on purely biological considerations. As per the approach developed in Plank and Sleeman (2003), Plank et al. (2003), Plank et al. (2004), Othmer and Stevens (1997), the following master equation is used to describe a biased random walk (in two dimensions) of the endothelial cell, moving under the influence of VEGF in its local environment:

$$\begin{aligned} \frac{\partial p_{n,m}}{\partial t} = & \hat{T}_{n-1,m}^{H+}(W) p_{n-1,m} + \hat{T}_{n+1,m}^{H-}(W) p_{n+1,m} \\ & + \hat{T}_{n,m-1}^{V+}(W) p_{n,m-1} + \hat{T}_{n,m+1}^{V-}(W) p_{n,m+1} \\ & - \left(\hat{T}_{n,m}^{H+}(W) + \hat{T}_{n,m}^{H-}(W) + \hat{T}_{n,m}^{V+}(W) \right. \\ & \left. + \hat{T}_{n,m}^{V-}(W) \right) p_{n,m}. \end{aligned} \quad (1)$$

Here, $p_{n,m}(t)$ describes the probability that a cell is at site (n, m) , at time t . $\hat{T}_{n,m}^{H\pm}(\cdot)$, and $\hat{T}_{n,m}^{V\pm}(\cdot)$ are the transition probabilities per unit time for a one step horizontal jump to $(n \pm 1, m)$, or a one step vertical jump to $(n, m \pm 1)$ respectively. The vector W gives the concentration of the chemoattractant C , at the lattice sites. In order for the master equation to translate to the standard diffusion-chemotaxis equation for cell movement in the continuum limit, it is assumed that the dependence of transition rates at lattice site (n, m) is localized to chemoattractant concentration at sites $(n \pm 1/2, m)$ and $(n, m \pm 1/2)$. This is reasonable, since we may think of a cell present at lattice site (n, m) , with its boundaries extending to half the lattice length. The cell can therefore sense the chemical concentrations at these half-lattice sites, and make a decision where to move, as illustrated in **Figures 1B–D**. Under these assumptions, $W = (\dots, C_{-n-1/2,m}, C_{-n,m}, C_{-n+1/2,m}, C_{-n+1,m}, \dots)$.

The mean waiting time at the (n, m) th site is given by $1 / \left(\hat{T}_{n,m}^{H+}(W) + \hat{T}_{n,m}^{H-}(W) + \hat{T}_{n,m}^{V+}(W) + \hat{T}_{n,m}^{V-}(W) \right)$. We make the assumption that the decision of where to move in space is independent of the decision when to move in time. Mathematically, this is equivalent to setting

$$\hat{T}_{n,m}^{H+}(W) + \hat{T}_{n,m}^{H-}(W) + \hat{T}_{n,m}^{V+}(W) + \hat{T}_{n,m}^{V-}(W) = k. \quad (2)$$

That is to say, the cell makes a decision to move (or to stay still) after a constant amount of time, k . One way to satisfy these assumptions is the following choice of transition probabilities, as made by Othmer and Stevens (1997):

$$\begin{aligned}\mathcal{T}_{n,m}^{H\pm} &= \frac{1}{k} \frac{\tau(C_{n\pm 1/2,m})}{\tau(C_{n+1/2,m}) + \tau(C_{n-1/2,m}) + \tau(C_{n,m+1/2}) + \tau(C_{n,m-1/2})}, \\ \mathcal{T}_{n,m}^{V\pm} &= \frac{1}{k} \frac{\tau(C_{n,m\pm 1/2})}{\tau(C_{n+1/2,m}) + \tau(C_{n-1/2,m}) + \tau(C_{n,m+1/2}) + \tau(C_{n,m-1/2})}\end{aligned}\quad (3)$$

for some function $\tau(C)$ of the chemoattractant. The choice of the functional form for $\tau(C)$ is based on the particular form of the chemotactic sensitivity desired, and is explained in the following section. A grid of mesh size h is chosen, thereby fixing $x = nh$. Passing to the continuum limit $h \rightarrow 0$ and $1/4k \rightarrow \infty$ such that $h^2/4k = D_p$, where D_p is the diffusion coefficient of ECs, Othmer and Stevens (1997) show that the master equation (1) translates to the familiar diffusion-chemotaxis equation (4), for cell motion.

$$\frac{\partial p}{\partial t} = D_p \Delta p - \nabla \cdot (p \chi(C) \nabla C), \quad (4)$$

where the chemotactic sensitivity $\chi(C) = D_p (\ln \tau(C))'$. To get a completely discretized model of the motion of the cell, the time derivative of p in equation (1) is approximated by a simple forward difference scheme, with k as the time step, given by

$$k = \frac{h^2}{4D_p}. \quad (5)$$

A diagrammatic representation of the motion of the cell is shown in **Figure 1**. The cell starts out at time t at the lattice site (n, m) (**Figure 1B**). Endothelial cells are large enough to detect gradients of chemoattractants across their length, which is typically $20 \mu\text{m}$ (Vadapalli et al., 2000). In contrast to existing models of cellular chemotaxis, in which cells typically respond to free, extracellular chemokine concentrations, or their gradients in the surrounding tissue, the model developed here will capture the response of ECs to VEGF that is bound to cell-surface receptors. VEGF-VEGFR2 binding is known to be the signal that initiates endothelial motility, therefore incorporating this molecular response is important for a realistic description of cell motion.

The cell detects *bio-available* VEGF by taking it up at the half-lattice sites (**Figure 1B**). The model will thus make the crucial distinction between VEGF that is free to bind to the cell, versus VEGF that might be sequestered in the underlying extracellular matrix, unavailable to the cell. Based on the numbers of activated receptors at its four sides, the cell becomes polarized and attains a bias in a particular direction. It correspondingly elongates in this direction (**Figure 1C**). Finally, the rear of the cell detaches from the underlying matrix and contracts, and the cell has now moved to the site $(n+1, m)$ (**Figure 1D**). We remark that it has been observed experimentally that ECs may respond to chemoattractant concentration differences of as small as 2% across their length,

frequently at concentrations at which molecular fluctuations are significant (Mantzaris et al., 2004). In our model, fluctuations of the order of 100 molecules of VEGF per cell are significant enough to alter its polarization, and hence its direction of motion.

2.2. A NOVEL CHEMOTACTIC SENSITIVITY FUNCTION

An important difference that sets this model apart from those preceding it, is the choice of the chemotactic sensitivity function $\chi(C)$. Various choices have been proposed thus far in the modeling literature for $\chi(C)$, for a review of the most commonly used functional forms (see Ford and Lauffenburger, 1991). The simplest choice is to assume that the chemotactic sensitivity is constant, $\chi(C) = \chi_0$ (Keller and Segel, 1971a,b). However, this implies that the chemotactic sensitivity is unchanging in the presence of the chemoattractant, and does not account for the desensitization of cells which has been experimentally observed to occur in regions of high chemokine concentrations (Kuppuswamy and Pike, 1989; Wang et al., 2000; Kurt et al., 2001). To overcome this, Lapidus and Schiller (1976), and later Murray (2003) used the functional form $\chi(C) = \chi_0/(K+C)^2$, also known as the receptor-kinetic law. This has the advantage that it is able to account for the desensitization of receptors when c is large. Yet another popular phenomenological choice is $\chi(C) = \chi_0/(K+C)$, where K is the dissociation constant of the chemokine binding to the receptors (Balding and McElwain, 1985; Anderson and Chaplain, 1998b; Plank et al., 2003).

Although the choices mentioned above have been widely used in the angiogenesis literature, there are a few biological issues that these choices do not address. Firstly, they indicate that when no chemokine is present at a site, the chemotactic sensitivity is the greatest, and that the sensitivity decreases as chemokine concentrations increase. However, there is experimental evidence which points toward the existence of a minimum threshold level of chemical stimulus required for the cell-surface receptors to become activated, and for the cell to start moving in a directed fashion (Favier et al., 2006; Liu et al., 2006). This threshold has been incorporated in the cell-based model of tumor angiogenesis by Bauer et al. (2007). Secondly, the above functions do not account for the fact that the amount of chemokine required to desensitize cells depends on the concentration of cells present at the lattice site. For instance, while 10 fg of VEGF is enough to desensitize a single EC, it is not enough for 10 cells. Finally, for an external chemical signal to elicit a chemotactic response from a cell, it needs to be detected by the cell, and transduced into an internal signal controlling cell motion. Neutrophils have been shown to sense chemical gradients of 1% across their lengths, under optimal conditions (Wang et al., 2004; Levine et al., 2006), while this number can be as low as 0.1% for axons (Wang et al., 2004). In general, eukaryotic cells are reported to be able to polarize and migrate in a directed fashion in alignment with chemical gradients of about 2% across their lengths (Franz et al., 2002). It is therefore biologically more reasonable to assume that the chemotactic response of cells is dependent on the gradients of activated receptor complexes formed on the cell surface when the chemokine binds to its receptors, rather than gradients of free chemokine concentration throughout the tissue.

To address these concerns, we propose that the chemotactic sensitivity function should in fact be a function of the activated

receptor concentration, A . In this case, equation (4) for the motion of a cell in 2 dimensions transforms to the following:

$$\frac{\partial p}{\partial t} = D_p \Delta p - \nabla \cdot (\chi(A) p \nabla A). \quad (6)$$

Correspondingly, the transition probabilities in equation (1) will now be functions of concentration of activated receptor complexes on the cell surface a and not extracellular VEGF. That is,

$$\begin{aligned} \mathcal{T}_{n,m}^{H\pm} &= \frac{1}{k} \frac{\tau(A_{n\pm 1/2,m})}{\tau(A_{n+1/2,m}) + \tau(A_{n-1/2,m}) + \tau(A_{n,m+1/2}) + \tau(A_{n,m-1/2})}, \\ \mathcal{T}_{n,m}^{V\pm} &= \frac{1}{k} \frac{\tau(A_{n,m\pm 1/2})}{\tau(A_{n+1/2,m}) + \tau(A_{n-1/2,m}) + \tau(A_{n,m+1/2}) + \tau(A_{n,m-1/2})}. \end{aligned} \quad (7)$$

We have to add equations for the binding of chemokine to their cell-surface receptors, which will need to be solved wherever a cell is present (see Section 2.3). Biologically, the chemotactic sensitivity $\chi(A)\nabla A$ can be interpreted by breaking it down as follows: a velocity $\chi(A)$ imparted to the cell due to the presence of bound chemokine on its surface, and a gradient ∇A which governs the direction of motion. This gradient simply means that the cell is able to sense the amount of chemokine bound to its various faces, and is correspondingly able to align itself for motion in this direction. Therefore, a is in fact taken to be the amount of activated receptors *per cell face*. We choose a velocity function that satisfies the requirements that there can be no chemotaxis in the absence of a signal, and that the cell gets desensitized in the presence of excess signal. One such functional form is:

$$\chi(A) = \chi_0 A e^{-A/K}. \quad (8)$$

The maximum of this function occurs at $A = K$, while its maximum value is given by $\chi_0 K e^{-1}$. In order for this choice to be consistent with the discrete formulation, the function $\tau(A)$, from equation (3) must be taken as follows;

$$\tau(A) = \exp \left[\frac{\chi_0 K}{D_p} (K - (K + A) e^{-A/K}) \right]. \quad (9)$$

The parameters χ_0 and K are unknown in our model formulation, and would ideally be determined from experimental observations. K specifies the fractional occupancy of the receptors on the cell surface at which its chemotactic response is the greatest, while χ_0 determines the maximum value of this response. Here, values of these parameters are chosen to produce biologically realistic simulation results. **Figure 2B** plots the chemotactic sensitivity equations (8) as a function of the fraction of activated receptors on a cell face, for a particular choice of K and χ_0 . We can see that at zero fractional activation, the cell remains inactive. The sensitivity peaks at 5% fractional activation of receptors, and decays thereafter. Also shown for comparison are the receptor-kinetic law, and constant chemotactic sensitivity.

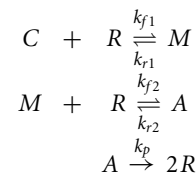
2.3. VEGF-VEGFR2 BINDING DYNAMICS

We now describe the equations governing the rates of change of the concentrations of free VEGF (C), free VEGFR2 (R), VEGF-VEGFR2 monomers (M), and activated VEGF-VEGFR2 dimer complexes (A). Beginning with free VEGF, we assume that the processes of diffusion and natural decay dominate the dynamics, which are represented by the reaction-diffusion equation:

$$\frac{\partial C}{\partial t} = D_c \Delta C - \alpha_c C - f(p) C. \quad (10)$$

Here, D_c is the diffusion coefficient of VEGF, and α_c is its rate of decay in tissue. The uptake of VEGF by the migrating EC has also been accounted for via the term $f(p)C$, which is derived in the following discussion. As in Anderson and Chaplain (1998b), a line source of tumor cells is assumed at $x = 1$ that produces VEGF at a constant rate, so that $C(1, y, t) = C_0$. At each of the remaining domain boundaries $x = 0$ and $y = 0, 1$, a no-flux condition is imposed on free VEGF. **Figure 2A** shows the distribution of VEGF, expressed in non-dimensional terms, as determined by equation (10) across the domain.

At each half-lattice site surrounding a site occupied by an EC, free extracellular VEGF (C) binds to free cell-surface receptors, VEGFR2 (R), to form activated dimerized receptor complexes (A). Following Jain et al. (2008), we assume ligand-induced dimerization to be the dominant mechanism by which VEGF activates VEGFR2, as represented by the following chemical reactions:



the rates of forward reactions are indicated above the reaction arrows, while those of reverse reactions are indicated below the reaction arrow.

This reaction diagram can be converted to the following system of differential equations using principles of mass balance:

$$\frac{dC}{dt} = -2\eta_1 k_{f1} CR + \eta_2 k_{r1} M, \quad (11)$$

$$\frac{dR}{dt} = -2k_{f1} CR + \eta_3 k_{r1} M - k_{f2} MR + 2\eta_4 k_{r2} A + 2\eta_4 k_p A, \quad (12)$$

$$\frac{dM}{dt} = 2\eta_5 k_{f1} CR + k_{r1} M - \eta_5 k_{f2} MR + 2\eta_6 k_{r2} A, \quad (13)$$

$$\frac{dA}{dt} = \eta_7 k_{f2} MR - 2k_{r2} A - k_p A. \quad (14)$$

The multiplicative factor 2 in some of the equations accounts for the possibility that there may be two ways for that product to form. The constants η_i represent the ratios of weights of different molecules and have been introduced to express chemical concentrations in units of pg/mm^3 . The values of these constants are given in **Table 1** and have been estimated from Ferrara et al. (2003), Stewart et al. (2003).

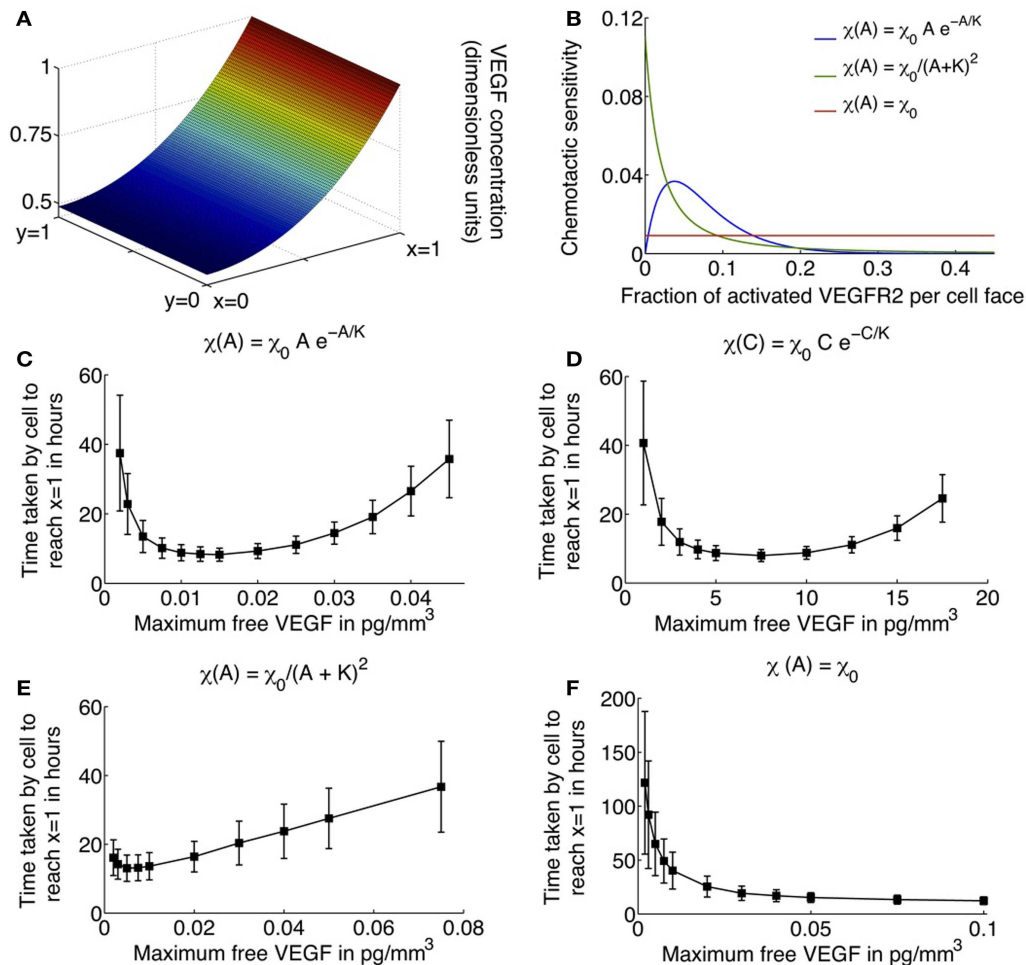


FIGURE 2 | (A) Typical profile of unbound VEGF, the source of which is located at $x = 1$. **(B)** Various choices for the chemotactic sensitivity of an endothelial cell to VEGF bound to its surface receptors, as a function of the fraction of activated VEGFR2 per cell face. **(C–F)** Average migration times (in hours) for a single cell to travel across a $1 \text{ mm} \times 1 \text{ mm}$ domain as a function of increasing the maximum free VEGF concentration at a lattice site, for various choices of the chemotactic sensitivity function. Cells are

assumed to respond to activated VEGFR2 on their surfaces, with chemotactic sensitivity taken as: **(C)** as proposed in equation (8); **(D)** cells are assumed to respond to free VEGF with chemotactic sensitivity as defined in equation (8) with activated receptor concentration A replaced by free VEGF concentration C ; **(E)** receptor-kinetic law, for which $\tau(A) = e^{\chi_0 A/(K D_p(K+A))}$, $\chi_0 = 0.4416 \text{ (pg/mm}^3 \text{) mm}^2/\text{h}$, $K = 2 \text{ pg/mm}^3$; and **(F)** constant, $\chi_0 = 0.0046 \text{ mm}^2/(\text{pg/mm}^3 \text{)h}$.

Since EC migration and sprout elongation occurs on a time-scale of several hours to days, and the biochemical reactions equations (11–14) occur on a time-scale of several seconds to minutes, we assume that the VEGF-receptor complex concentrations M and A are at quasi steady state. This is equivalent to setting the left hand sides of equations (13) and (14) to zero, and solving for M and A . Further, by conservation of total receptor number, we have $R + \eta_3 M + 2\eta_4 A = R_f N$, where R_f is the total number of receptors per EC face and N is the number of ECs ($N = 1$ in the case of single cell migration, and $N =$ the total number of tip cells in the case of capillary formation). We therefore deduce that at quasi steady state,

$$A = \frac{-2\alpha\delta - \gamma + \theta\beta + \sqrt{(2\alpha\delta + \gamma - \theta\beta)^2 + 4\alpha\beta(\eta_4 + \delta)(\theta - \alpha)}}{2\beta(\eta_4 + \delta)}, \quad (15)$$

where,

$$\alpha = \frac{k_{r1} R_f}{2k_{f1} C + k_{r1}}, \quad \beta = \frac{\eta_4 (k_p - 2k_{r1})}{2k_{f1} C + k_{r1}},$$

$$\gamma = \frac{2k_{r2} + k_p}{\eta_5 \eta_7 k_{f2}} \quad \delta = \eta_4 + \beta, \quad \theta = R_f N. \quad (16)$$

In all that follows, equation (15) will be used to estimate the concentration of activated VEGF-VEGFR2 dimers in the domain. Adding equations (12) and (14) and substituting in equation (11) gives the following equation for the uptake of VEGF by ECs:

$$\frac{dC}{dt} = -\eta_0 k_p A. \quad (17)$$

Therefore, in equation (10) the cellular uptake function $f(p)C = -\eta_0 k_p A I(p)$, where $I(p)$ is an indicator function that has

Table 1 | Parameter values relating to the molecular weights of VEGF and VEGFR2.

Parameter	Value	Units
η_0	0.1101	pg VEGF per pg VEGFR2-VEGF-VEGFR2
η_1	0.2250	pg VEGF per pg VEGFR2
η_2	0.1837	pg VEGF per pg VEGFR2-VEGF
η_3	0.8163	pg VEGFR2 per pg VEGFR2-VEGF
η_4	0.4494	pg VEGFR2 per pg VEGFR2-VEGF-VEGFR2
η_5	1.2250	pg VEGFR2-VEGF per pg VEGFR2
η_6	0.5506	pg VEGFR2-VEGF per pg VEGFR2-VEGF-VEGFR2
η_7	2.2250	pg VEGFR2-VEGF-VEGFR2 per pg VEGFR2

a value of 1 at half-lattice sites where EC boundaries are present and is zero otherwise. Observing that $\eta_0 k_p \ll \alpha_C$ (see parameter values in **Table 2**), we make a final simplifying assumption that due to the constant production and rapid diffusion of extracellular VEGF, cellular uptake will not significantly effect its concentration, that is, $f(p)C$ is neglected. Thus, the equation governing free VEGF dynamics is taken to be

$$\frac{\partial C}{\partial t} = D_c \Delta C - \alpha_C C. \quad (18)$$

2.3.1. Summary of model equations

The principle variables in our model are: $p(n, m, t)$, the probability that a cell occupies lattice site (n, m) at time t ; $C(x, y, t)$, the concentration of free VEGF at position (x, y) and at time t in pg per lattice site volume, where each lattice site has a height of 1 mm and a base equal to the surface area of a cell; $R(i, j, t)$, the concentration of free VEGFR2 at half-lattice sites (i, j) and at time t in pg per lattice site volume; $M(i, j, t)$, the concentration of VEGF-VEGFR2 monomers at half-lattice sites (i, j) and at time t in pg per lattice site volume; and $A(i, j, t)$, the concentration of free activated VEGFR2-VEGF-VEGFR2 dimers at half-lattice sites (i, j) and at time t in pg per lattice site volume. We remark that R , M , and A can only take positive values at neighboring half-lattice sites where a cell is present, and are 0 otherwise. Equations (1), (7), and (9) that describe the biased random walk of a cell under the influence of activated VEGF-receptors have already been discussed. The following conditions are imposed on the transition probabilities for cell motion as described by equation (1) to ensure that no cell exits the domain:

$$\mathcal{T}_{1,m}^{H-}(\cdot) = \mathcal{T}_{N_s+1,m}^{H+}(\cdot) = \mathcal{T}_{n,1}^{V-}(\cdot) = \mathcal{T}_{n,N_s+1}^{V+}(\cdot) = 0. \quad (19)$$

Here, $N_s = 1/h$, h being the lattice size so that $1 \leq n, m \leq N_s + 1$.

2.4. PARAMETER ESTIMATION

A list of parameter values and sources is given in **Table 2**. The random motility coefficient of endothelial cells has been estimated to lie within the range 7.2×10^{-4} – 7.2×10^{-3} mm²/h (Anderson and Chaplain, 1998b). Consequently, intermediate value of 1.44×10^{-4} mm²/h is assumed. The rates $k_r l$ and $k_f l$ are chosen to ensure that the equilibrium disassociation constant $k_D = k_r l / k_f l$

has a value of 30.375 pg/mm³ (Wang et al., 2002). VEGF binding is known to induce receptor aggregation; therefore, as in Jain et al. (2008) we assume that the rate of formation of a dimerized VEGF-VEGFR2 complex is greater than the rate of formation of a monomer VEGF-VEGFR2 (that is, $k_f 2 (k_f l)$). Further, because the dimerized complex A is the signaling form of VEGFR2, it is reasonable to assume that A is more stable than the monomer complex M , that is, $k_r 2 = k_r l$. The size h of the lattice on which the cell moves is taken to be 20 μ m, since typical microvascular endothelial cell volume is about 400 μ m (Vadapalli et al., 2000), while its thickness is about 1 μ m (Levine et al., 2002). Finally, the parameters χ_0 and K relating to chemotactic sensitivity are chosen to reproduce cell motion and capillary formation profiles that are biologically realistic.

2.5. METHOD OF SIMULATION

The time interval over which the movement of the cell is simulated, is divided into subintervals of length k , given by the mean waiting time of the cell at any lattice site. The cell moves on a lattice of step-size h . Activated VEGFR2 concentrations are calculated at half-lattice sites, neighboring a site where the cell is currently situated. The method of simulation of cell movement is based on that described in Plank et al. (2003). Briefly, at each time step, the movement of the cell is simulated according to the master equation (1), with the probabilities of moving up, down, left, and right calculated according to equation (3). Equation (9) quantifies the dependence of the transition probabilities on the levels of activated VEGFR2 on each cell face as given by equation (15). The full interval $[0, 1]$ is divided into five subintervals, each of length proportional to the probabilities of moving or staying still. A random number q lying within this interval is generated, and depending on the sub-interval in which it lies, the cell either executes a motion in the corresponding direction or stays stationary. Thus, the cell moves left if $q \in [0, \mathcal{T}_{n,m}^{H-})$, moves right if $q \in [\mathcal{T}_{n,m}^{H-}, \mathcal{T}_{n,m}^{H+})$, and so on.

The results of the single cell motion model are discussed in Section 3.1.

2.6. ADAPTATION OF SINGLE CELL MOTION MODEL TO SIMULATE CAPILLARY FORMATION

To simulate capillary formation in response to a VEGF stimulus from a tumor source, we modify the single cell motion model described above as follows. As mentioned earlier, we motivate our model of capillary formation by the experiments of Sholley et al. (1984) wherein inflammatory neovascularization of the rat cornea was induced by cauterization using silver nitrate and levels of EC proliferation and degree of vascular profusion measured periodically. From these experiments, the average rate of sprout extension into the cornea is estimated to be 0.26 mm/day or 0.78 mm in 3 days. In our model, we do not account for vessel maturation; a process that typically occurs after 3 days of vessel formation. Consequently, we simulate vessel growth for lengths ≤ 0.78 mm. With this constraint, a parent vessel, from which sprout tips will migrate toward the tumor, is assumed at $x = 0.22$ mm. As in the single cell model, a line of tumor cells is assumed at $x = 1$, providing a constant source of VEGF. For ease of computations, the domain size is reduced to 0.5 mm in the y -direction, and initially 4 sprouts are

Table 2 | List of parameter values for single cell motion.

Parameter	Value	Units	Reference
D_p	1.44×10^{-4}	mm ² /h	See text
D_c	3.60×10^{-1}	mm ² /h	Mac Gabhann and Popel (2005)
α_c	0.65	Per hour	Serini et al. (2003)
k_{f1}	1.69	Per (pg VEGF/mm ³)/h	Wang et al. (2002)
k_{r1}	0.02	Per hour	Wang et al. (2002)
k_{f2}	$k_{f1} \times 100$	Per (pg VEGF-VEGFR2/mm ³)/h	See text
k_{r2}	$k_{r1}/100$	Per hour	See text
k_p	0.6667	Per hour	Wang et al. (2002)
R_f	0.02	pg receptors per cell face	Stewart et al. (2003), Mac Gabhann and Popel (2004)
h	0.02	mm	Vadapalli et al. (2000), Levine et al. (2002)
k	0.07	Hours	See equation (5)
χ_0	0.05	mm ² per hour per (pg/mm ³) ⁻¹	See text
K	2.00	pg/mm ³	See text

assumed to have formed along the parent vessel at $y = 0.1, 0.2, 0.3$, and 0.4 mm.

It is known that specialized ECs situated at the tips of the sprouts, called tip cells, are activated by, and respond to VEGF, by chemotactic migration (Hangai et al., 2002; Gerhardt et al., 2003). We therefore keep track of these leading cells in our simulations. As a tip cell moves, it pulls behind it a developing vessel. Hence, receptors on its tail are made unavailable for binding VEGF at any given time. This eliminates the possibility for the tip cell to back-track. By keeping track of all the lattice sites a tip cell visits, we know the location of the newly formed vessel behind it.

The processes of branch formation and anastomoses formation of loops by capillary sprouts are also included explicitly in our model. At each time step, as the tip cells migrate under the influence of VEGF, probabilities of motion to adjacent lattice sites are calculated. Anastomoses between the tip cell and a sprout may occur if a sprout is present at a site which the tip cell wants to move to. We assume that the probability of tip cell loss as a result of such an event is 1%. Likewise, as in Anderson and Chaplain (1998b), it is assumed that if another tip cell is encountered at a site, only one of these cells continues to grow (with a probability 99%), while the rest of the time, a loop is created with the loss of both cells.

Sholley et al. (1984) have demonstrated that sprout extension cannot occur in the absence of mitosis. While we do not explicitly model cell division, the dependence of capillary extension on it is accounted for in the processes of capillary elongation and branch formation as follows. The proliferation of cells is known to be regulated by total concentration of activated cell-surface receptors (Gerhardt et al., 2003). Thus, in our model, the tip cell integrates the total VEGF bound to it and sprout extension via tip cell motion, and branch formation is only possible if there are enough activated VEGFR2 on its surface. The effect of proliferation on tip cell motion is simulated by introducing a scaling factor of $P_m(A_t)$ that multiplies the movement probabilities of each cell, where A_t is the total concentration of activated VEGFR2 on the cell. P_m is assumed to be a positive, increasing, and saturating function of A_t , with a saturating value of 1. Thus, for small values of A_t , the probability of capillary extension will be ~ 0 due to an insufficient proliferation

stimulus. Here, we take $P_m(A_t) = 1/(1 + \mu_m e^{-A_t})$ which is plotted as a function of the fraction of total activated VEGFR2 per tip cell in **Figure 5D**.

We further assume that the generation of new sprouts occurs only from existing sprout tips. This is in keeping with the fact that there is a region of proliferating cells just behind the tip cell (Sholley et al., 1984), which could give rise to new branches. As in the case for P_m , the branching probability P_b is also taken to be an increasing and saturating function of A_t . This will result in the creation of the brush-border effect. Similar rules for branching have been applied previously by Anderson and Chaplain (1998b). Here, we take $P_b(A_t) = 1/(\mu_b 1 + e^{-\mu_b 2(A_t - A_0)})$ which is plotted as a function of the fraction of total activated VEGFR2 per tip cell in **Figure 5D**.

2.6.1. Parameter estimation for capillary formation model

A list of parameter values that are different or new in the capillary formation model is given in **Table 3**. For consistency with the single cell model, we keep the time step-size k unchanged at 0.07 h. Further, the diffusion rate of a tip cell, say D_t , has been estimated to be much smaller than the diffusion rate D_p of an individual EC (Anderson and Chaplain, 1998b; Levine et al., 2001). Therefore, the lattice size h for the capillary model needs to be altered accordingly. Equation (5) is used to estimate $h = \sqrt{4kD_t} \approx 0.001$ mm. Finally, the parameters μ_m , μ_{b1} , μ_{b2} , and A_0 relating to the movement probability and branching probability are chosen to reproduce capillary formation profiles that are biologically realistic.

2.6.2. Simulation methodology for capillary formation model

The simulation methodology is similar to that of single cell motion described in section 2.5, with the additional computation of accounting for branching and anastomoses for each tip cell, and at each time step. Briefly, in addition to generating a random number q_b which is used to determine the direction of tip cell motion, two further random numbers are generated (q_a and q_b) by uniformly sampling the interval $[0, 1]$. We use q_a to determine whether or not anastomoses occurs, and q_b is used to determine whether a new branch forms, in accordance with the rules described above.

Table 3 | List of parameter values for capillary formation.

Parameter	Value	Units	Reference
D_t	3.60×10^{-6}	mm^2/h	(Levine et al., 2001)
h	0.001	mm	See text
k	0.07	Hours	See text
μ_m	300	Dimensionless	See text
μ_{b1}	30	Dimensionless	See text
μ_{b2}	0.25	per pg VEGFR2-VEGF-VEGFR2/ mm^3	See text
A_0	40	pg VEGFR2-VEGF-VEGFR2/ mm^3	See text

The results of the capillary formation simulation are discussed in Section 3.2.

3. RESULTS

3.1. SINGLE CELL MOTION

Simulations of the system governing a single endothelial cell migrating up a gradient of VEGF, as described by equations (1), (7), (9), and (15), were run in two dimensions, with unbound VEGF profile described by equation (18). The average time in hours it takes for the cell to travel across the domain is plotted in **Figures 2C–F**, as a function of C_0 , the maximum free VEGF concentration at a lattice site, for various possible choices of the chemotactic sensitivity function $\chi(\cdot)$. Standard deviations and average times are computed over 500 runs of the model.

Figures 2C,E,F depict the cases when $\chi(\cdot)$ is assumed to be a function of activated VEGFR2 on the cell surface. When $\chi(\cdot)$ is as defined in equation (8), the model captures the existence of a minimum level of VEGF stimulus required for directed cell motion, as well as desensitization of VEGFR2 at high VEGF concentrations (see **Figure 2C**). As C_0 increases from 0.002 pg/mm^3 , the average EC migration time is observed to first decrease and then increase, attaining a minimum of 8.23 h at $C_0 = 0.015 \text{ pg/mm}^3$. A typical cellular trajectory is plotted in **Figure 3C** for this optimal value of C_0 , and the corresponding movement probabilities at any lattice site are plotted in **Figure 3D**. Note that since the VEGF profile is invariant along the y -direction, the movement probabilities are also invariant along this axis – they only vary as x varies. The probabilities show a large bias toward stepping to the right, while steps to the left are very unlikely to occur. This is because: (i) the chemokine gradient across the cell length has an average value of 1.32%, over the entire domain, which lies within the reported value of 1–2% at which eukaryotic cells become polarized; and (ii) the fraction of activated receptors on any cell face is sufficiently large, with an average value of 9%, over the entire domain.

As C_0 is decreased below 0.015, the average migration time is predicted to increase exponentially. For instance, when $C_0 = 0.002 \text{ pg/mm}^3$, the average migration time is predicted to be 37.46 h, and the cell exhibits a high degree of randomness in its motion, as evident from a typical cellular trajectory shown in **Figure 3A**. The corresponding movement probabilities at any lattice site plotted in **Figure 3B** show that a definite bias is apparent for motion to the right only close to $x = 1$. This is because the fraction of activated VEGFR2 on any cell face is very low, with a

maximum of < 2%, even though the chemokine gradient across the cell length has an average value of 1.46%. Thus, the model is able to account for the fact that if chemokine concentrations are too low, cell-surface receptors do not achieve a sufficient degree of activation.

As C_0 is increased beyond its optimal value of 0.015– 0.08 pg/mm^3 , the model replicates the desensitization effect which has been observed to occur when receptors are over-exposed to chemokines. It now takes the cell an average of 35.77 h to migrate across the domain. From **Figure 3E**, we observe that typical cell trajectories exhibit a large degree of random motion. Now, activated receptor gradients across the cell have an average value of only 1%. Further, the fraction of activated receptors that vary between 18 and 34% across the domain so that the negative exponential in equation (8) dominates resulting in a very slight bias of movement to the right (see **Figure 3F**).

For comparison, we also consider the cases where $\chi(A) = \chi_0/(K + A)^2$ or the receptor-kinetic law and when $\chi(A) = \text{constant} = \chi_0$. As can be seen from **Figure 2E**, while the receptor-kinetic law captures the desensitization of VEGFR2 at high concentrations of VEGF, the cell still displays a high degree of directed motion for very low values of C_0 . For instance, when $C_0 = 0.002 \text{ pg/mm}^3$ the average migration time is as low as 16.08 h as compared to 37.46 h in the earlier case. In contrast, the existence of a minimum activation threshold for VEGF is predicted by assuming $\chi(A) = \chi_0$, as evident from **Figure 2F**. However, this model is unable to capture receptor desensitization at high values of C_0 , and in fact, the average migration time is predicted to decrease monotonically with C_0 .

Finally, for illustration purposes, we also consider the case when $\chi(\cdot)$ has the same qualitative properties as in equation (8), but the cell now responds to free VEGF rather than activated VEGFR2, that is, $\chi(C) = \chi_0 C e^{-C/K}$ (see **Figure 2D**). While the graph is qualitatively similar to **Figure 2C**, the fastest migration of the EC across the domain is occurs at $C_0 = 7.5 \text{ pg/mm}^3$. This is biologically implausible since for such high receptor activation levels, the fraction of activated VEGFR2 on any cell face > 0.97 throughout the domain, and the cell should be completely desensitized to the chemical gradient around it.

3.1.1. Effect of receptor expression level on cell migration

An important parameter in our simulations of EC migration is R_T , the expression level of VEGFR2 per cell. This is known to be highly variable across cell lines, and it is even possible to find different values for R_T for the same cell line. We therefore conduct a sensitivity analysis on the migration times of an EC across the domain as R_T is varied, the results of which are graphed in **Figure 4**. For the baseline simulations discussed earlier, a value of $R_T = 230,000$ receptors per cell or 0.08 pg/cell (Stewart et al., 2003; Mac Gabhann and Popel, 2004) was used (see **Figures 2 and 3**). We now simulate the effect on cell migration of increasing R_T from a minimum of 46,000 to a maximum of 1,115,000 receptors per cell for various values of C_0 , the maximum free VEGF concentration at a lattice site. For each of the cases when $R_T = 115,000$ (**Figure 4B**), $R_T = 230,000$ (**Figure 2C**), $R_T = 460,000$ (**Figure 4C**), and $R_T = 1,150,000$ (**Figure 4D**), the average migration time of the EC is predicted to first decrease and then increase, as C_0

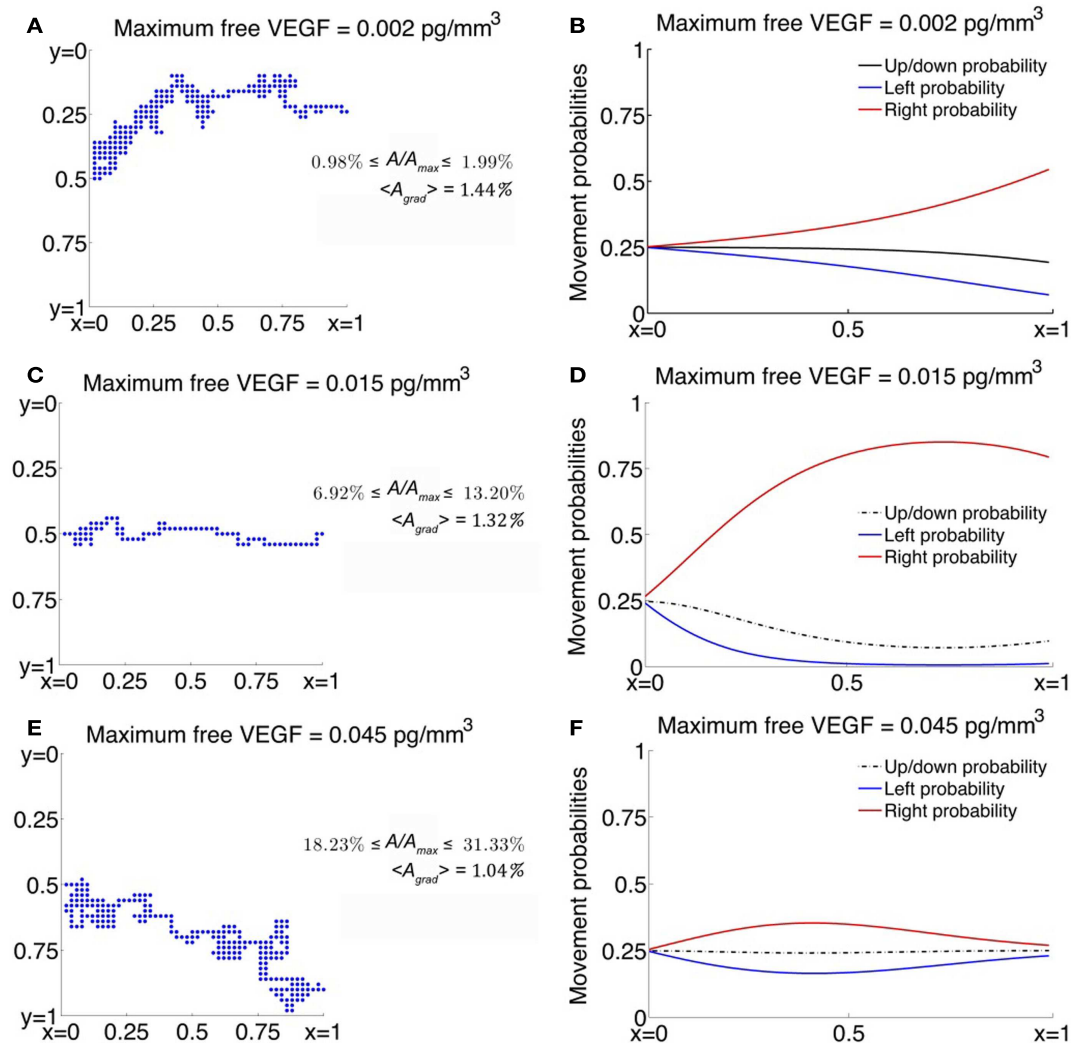


FIGURE 3 | (A,C,E) Typical trajectories of a cell migrating across a 2-dimensional domain under the influence of VEGF. Here, A represents the concentration of activated VEGFR2 per cell face and A_{max} represents the maximum value A can take so that A/A_{max} is the fraction of activated VEGFR2

per cell face expressed here as a percentage, and $\langle A_{grad} \rangle$ represents the gradient of A across a cell length, averaged over the entire domain. **(B,D,F)** Corresponding movement probabilities for various values of maximum VEGF concentration.

is increases. Thus, for a large range of values of R_T , the model captures the existence of an activation threshold of VEGFR2, and their desensitization when exposed to high VEGF concentrations. However, when R_T is very low (46,000/cell, **Figure 4A**), receptor desensitization is not predicted. This is possibly due to a high value of the parameter K , which is held fixed in all our simulations. As can be seen from equation (8), K determines the concentration of activated VEGFR2 per cell face at which the chemotactic sensitivity $\chi(A)$ is maximum.

Next, as can be seen from a plot of fastest migration times versus receptor expression in **Figure 4E**, the EC migrates more rapidly across the domain as R_T increases. The fastest migration time is predicted to be 8.25 h, for $R_T \geq 460,000/\text{cell}$. Interestingly, the maximum free VEGF concentration at which EC migration is fastest decreases with increasing R_T (**Figure 4F**). Thus receptor over-expression is predicted to lower the activation threshold

for ECs, possibly because gradients of activated VEGFR2 become more pronounced across the cell.

3.2. CAPILLARY FORMATION

Simulations of the system governing capillary network formation under the influence of VEGF, described in section 2.6, were run in two dimensions. Averages and standard deviations of all observed quantities were calculated from 100 runs of the model.

The first case considered is when the sprout tips move across the domain in the least amount of time. This occurs when the maximum concentration of unbound VEGF $C_0 = 0.015 \text{ pg/mm}^3$, as deduced from the single cell simulations. The results from a typical simulation are shown in **Figure 5A**. We begin with 4 initially formed sprout tips at $x = 0.22 \text{ mm}$. As the tip cells migrate across the domain, they lay down behind them capillary sprouts. As the vascular network penetrates deeper into the stroma, branching is

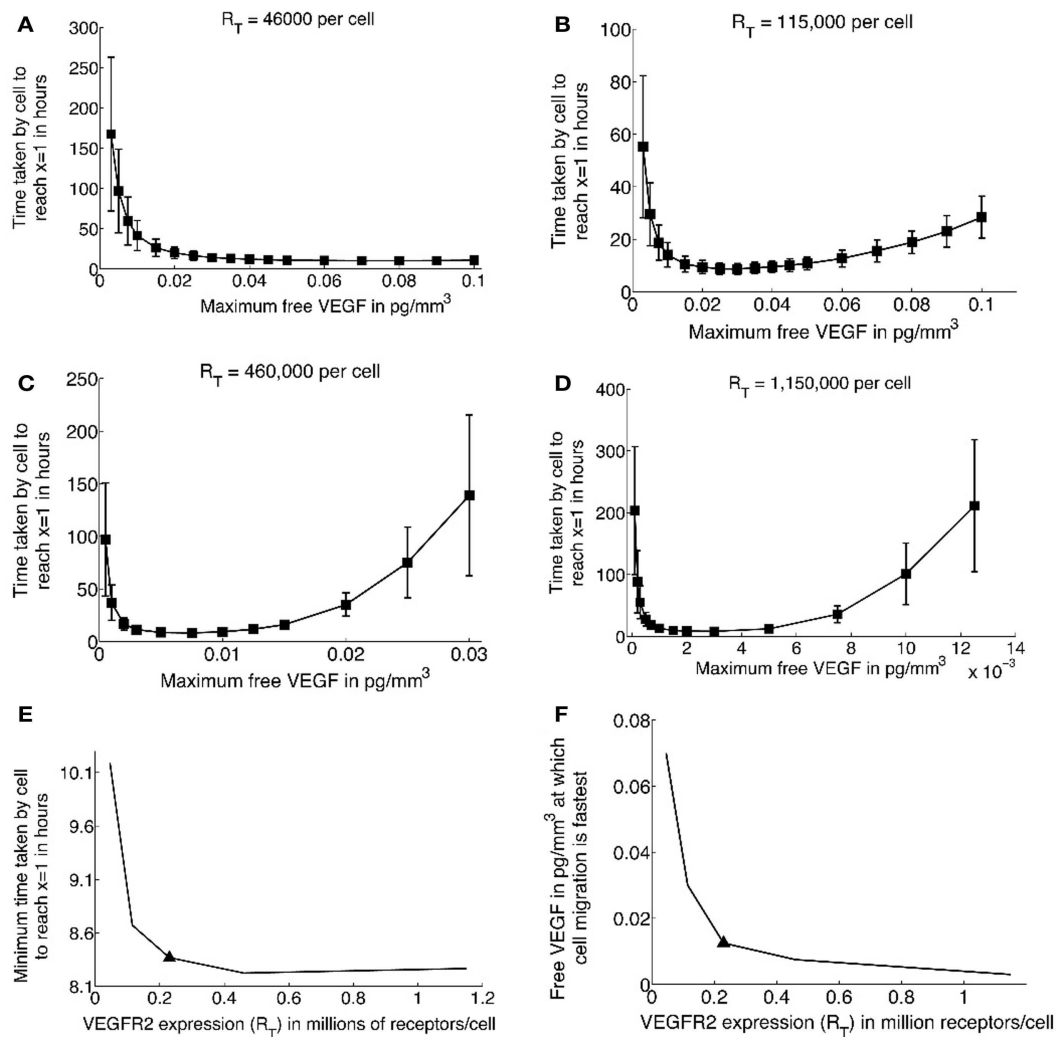


FIGURE 4 | (A–D) Average migration times (in hours) for a single cell to travel across a $1 \text{ mm} \times 1 \text{ mm}$ domain as a function of increasing the maximum free VEGF concentration at a lattice site, for different values of R_T , the total number of VEGFR2 per cell. Baseline simulations correspond to $R_T = 230,000/\text{cell}$, and are shown in **Figure 2C**. **(E)** Minimum migration

time for a single cell to cross the domain as a function of increasing R_T , solid triangle corresponds to baseline simulations. **(F)** The maximum free VEGF concentration at a lattice site (C_0) at which cell migration is fastest, as a function of increasing R_T , solid triangle corresponds to baseline simulations.

observed to occur leading to the brush-border effect. The model predicts that it takes on average 1170 ± 27 steps or 3.38 ± 0.08 days for the vasculature to reach the tumor source at $x = 1 \text{ mm}$. Our model is validated by the experiments in Sholley et al. (1984) where the vascular sprouts traveled the same distance in 3 days. Further validation follows by observing that the vascular networks generated by our model are qualitatively similar to those observed by Sholley et al. (1984).

Next, the effects of low (0.005 pg/mm^3) and high (0.030 pg/mm^3) maximum VEGF concentrations on vascular formation are investigated. As remarked earlier, we do not model vessel maturation, which is typically observed after ~ 3 days of vessel formation. Model simulations are run for a maximum of 1170 time steps and the average degree of vascular penetration into the stroma, along with the fraction of sprouts that remain

viable (that is, have at least one active tip cell) at the end of this time is computed. When $C_0 = 0.005 \text{ pg/mm}^3$, the average lengths of sprouts formed is predicted to be $0.2 \pm 0.1 \text{ mm}$, with only 40% of the initial sprouts still viable after 1170 time steps. Sprouts that remain viable after 1170 time steps extend a greater distance ($0.4 \pm 0.03 \text{ mm}$) into the stroma. However, these display virtually no branching, with the average number of branches per sprout only 1.1 ± 0.4 . **Figure 5B** shows the results of a typical simulation. As can be seen, there has been no branching and all but the first sprout have anastomosed with themselves to form closed loops. This is due to an insufficient bias to move forwards, coupled with a low value of the scaling factor P_m (see section 2.6).

Finally, when $C_0 = 0.030 \text{ pg/mm}^3$, the average lengths of sprouts formed after 1170 time steps is predicted to be $0.6 \pm 0.1 \text{ mm}$. As can be seen from a typical simulation shown

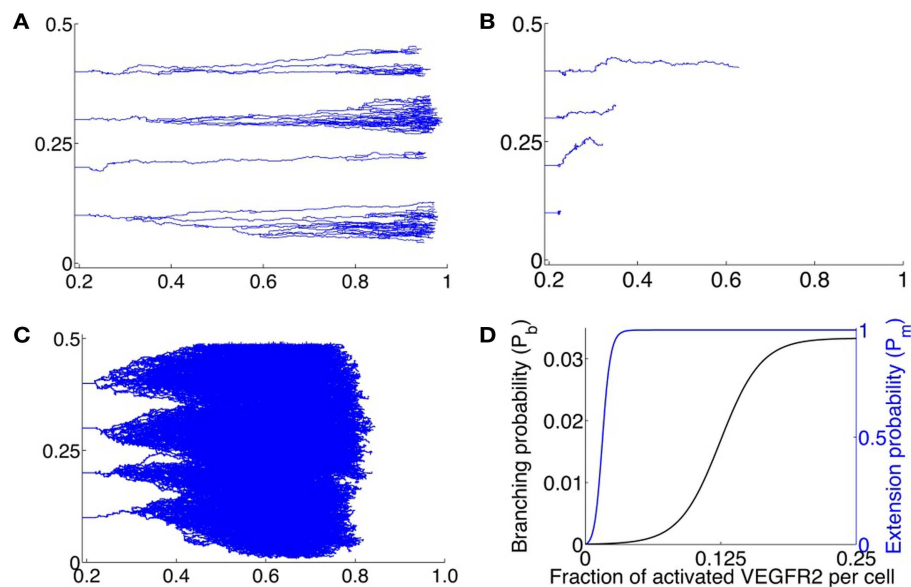


FIGURE 5 | (A–C) Typical vascular networks formed by 4 initial sprouts located along $x = 0.22$ at positions $y = 0.1, 0.2, 0.3, 0.4$; x being plotted along the abscissa and y along the ordinate – migrating across a 2-dimensional domain under the influence of VEGF for various values of C_0 , the maximum VEGF concentration per lattice site. **(A)** Optimal VEGF concentration, $C_0 = 0.015$ pg/lattice volume. The bias of movement is overwhelmingly in the forward direction. Branching and anastomoses are observed to occur as the vasculature penetrates deeper into the stroma. The resulting networks are qualitatively similar to those observed experimentally in Sholley et al. (1984). **(B)** $C_0 = 0.005$ pg/lattice volume. The amount of VEGF is too low to induce

proliferation or polarization of the tip cell, leading to a poorly developed and stunted vasculature that does not reach the VEGF source within the time frame of simulations (3 days). **(C)** $C_0 = 0.030$ pg/lattice volume. Due to a high VEGF concentration, over-stimulation of endothelial cells occurs, and extensive branching, anastomoses and lateral movement of the tip cell is observed. Due to excessive lateral movement, the vasculature that does not reach the VEGF source within the time frame of simulations (3 days). **(D)** Assumed branching probability P_b of the migrating tip cell (black curve), and assumed extension probability P_m of the capillary (blue curve), expressed as functions of total fraction of activated VEGFR2 per cell.

in **Figure 5C**, extensive branching and anastomoses are observed. Given the density of vessel branches, it is reasonable to expect that several of these may fuse into one another resulting in thicker and more dilated vessels, which is a morphology consistent with vascular hyperplasia, as seen in Lee et al. (2005). The higher VEGF concentration implies that the vessels have a weaker bias for forward motion, and lateral movement of vessels as well as movement against the gradient of VEGF are observed to occur. These phenomenon have been observed *in vivo*, and have been numerically simulated previously (Anderson and Chaplain, 1998b; Plank and Sleeman, 2004; Sun et al., 2005; Zheng et al., 2013).

4. CONCLUSION

We have developed a hybrid model of cellular chemotaxis and capillary formation under the influence of VEGF. The migrating cell, whether by itself or as the tip cell “pulling” behind it a developing sprout, was treated as an agent. Its movement was simulated stochastically with movement probabilities based on the theory of biased random walks. On the other hand, due to its fast diffusion coefficient, VEGF dynamics were governed by a continuum reaction-diffusion equation. Using this approach, we first simulated the motion of a single cell on a two-dimensional grid, following the gradient of VEGF laid down by a constant source. Next, our model was adapted to simulate the formation of new vessels from pre-formed sprouts along a parent vessel, also under the influence of a constant source of VEGF, such

as a tumor. Events such as branching and anastomoses, which are observed to occur *in vivo*, were incorporated explicitly in the model. The rate of vessel formation closely matched that observed experimentally (Sholley et al., 1984) under an optimal VEGF concentration. Additionally, as the forming vessels neared the VEGF source, a brush-border effect due to increased branching was predicted, thus proving both quantitative and qualitative validation of our approach. Using this framework, we also tested the effects of excessive as well as low levels of VEGF signaling on vascular development. Insufficient chemotactic and mitotic cues from VEGF resulted in stunted and solitary vessels, while an over-stimulation induced a high degree of branching and lateral movement.

An important difference that sets our model apart from similar hybrid models of chemotaxis is the inclusion of a molecular level detail of interaction between VEGF and its cell-surface receptor VEGFR2, the activation of which polarizes the cell and induces directed motion. This has been observed experimentally as well – endothelial cells respond to gradients of chemokines across their lengths, rather than to free chemokine concentrations. These gradients have been shown to be between 1 and 2%, which was seen in the numerical simulations as well, thus validating our model. Crucially, a chemotaxis sensitivity function was proposed that incorporated biological detail hitherto ignored by commonly used sensitivity functions currently. The model could thus capture realistic dynamics, such as the requirement of a minimum activation

level of cell-surface receptors and receptor desensitization in high concentrations of VEGF.

Angiogenesis, both physiological and pathological, is a highly complex process, and understanding its mechanisms can lead to significant breakthroughs in the treatment of diseases such as cancer that depend on it. To this end, it is vital that modeling efforts keep up with current advances in experimentation. Our model provides such a framework, in which it is easy to build in biochemical and biomechanical forces guiding vessel formation. In fact, a number of highly detailed and complex hybrid models of vascular tumor growth have recently been proposed (Frieboes et al., 2007; Owen et al., 2009; Perfahl et al., 2011) and a significant strength of our model is that it can easily be incorporated into these. The inclusion of greater biological detail would only increase confidence in the predictive power of such models.

In addition, a number of refinements of the model proposed here are under active consideration. For instance, EC response to cell-surface bound VEGF has already been explicitly included. However, for the ease of computation, certain simplifying assumptions were made. Most notably, activated VEGFR2 were assumed to be in quasi steady state. Further, only the tip cell was tracked, while VEGF uptake by stalk cells was ignored. Cell death was also omitted, while the processes of cell proliferation, branching, and anastomoses were included phenomenologically. We plan to

extend this model by relaxing some of these assumptions. Lattice-based models of angiogenesis face the criticism that the capillary networks generated by them are artificial to a certain extent, as they are forced to follow the lattice used to discretize the model. A first step would therefore be to develop a lattice-free version of our model of capillary formation, in which the ECs move without geometric constraints. Such models have been applied to capillary formation previously (Plank and Sleeman, 2004; Frieboes et al., 2007).

Other model refinements include incorporation of the relation between extra cellular matrix or ECM and vascular morphology. ECs require the ECM to gain traction in order to move. To facilitate their migration, ECs also secrete proteolytic enzymes such as matrix metalloproteinases (MMPs), that degrade collagen and elastin and clear a path for the ECs to follow. As ECs interact with the matrix, they also cause the release of matrix bound angiogenic factors such as VEGF, which are then available to induce further pro-angiogenic activity (Mantzaris et al., 2004). Further, pericytes, macrophages, and angiopoietins are also important determinants of developing vascular morphology and maturation (Levine et al., 2000; Plank and Sleeman, 2003), and need to be considered explicitly. The framework presented here is highly flexible, and would allow for the inclusion of the above processes, grounding it further in biology, and enhancing its usefulness as a tool to understanding the process of angiogenesis.

REFERENCES

- Anderson, A. R. A., and Chaplain, M. A. J. (1998a). A mathematical model for capillary network formation in the absence of endothelial cell proliferation. *Appl. Math. Lett.* 11, 109–114.
- Anderson, A. R. A., and Chaplain, M. A. J. (1998b). Continuous and discrete mathematical models of tumor-induced angiogenesis. *Bull. Math. Biol.* 60, 857–900.
- Arakelyan, L., Vainstein, V., and Agur, Z. (2002). A computer algorithm describing the process of vessel formation and maturation, and its use for predicting the effects of anti-angiogenic and anti-maturation therapy on vascular tumor growth. *Angiogenesis* 5, 203–214.
- Augustin, H. G., Koh, G. Y., Thurston, G., and Alitalo, K. (2009). Control of vascular morphogenesis and homeostasis through the angiopoietin-tie system. *Nat. Rev. Mol. Cell Biol.* 10, 165–177.
- Balding, D., and McElwain, D. L. S. (1985). A mathematical model of tumor-induced capillary growth. *J. Theor. Biol.* 114, 53–73.
- Bartha, K., and Rieger, H. (2006). Vascular network remodeling via vessel cooption, regression and growth in tumors. *J. Theor. Biol.* 21, 903–918.
- Bauer, A., Jackson, T., and Jiang, Y. (2007). A cell-based model exhibiting branching and anastomosis during tumor-induced angiogenesis. *Biophys. J.* 92, 3105.
- Bentley, K., Mariggi, G., Gerhardt, H., and Bates, P. A. (2009). Tip-ping the balance: robustness of tip cell selection, migration and fusion in angiogenesis. *PLoS Comput. Biol.* 5:e1000549. doi:10.1371/journal.pcbi.1000549
- Billy, F., Ribba, B., Saut, O., Morre-Trouilhet, H., Colin, T., Bresch, D., et al. (2009). A pharmacologically based multiscale mathematical model of angiogenesis and its use in investigating the efficacy of a new cancer treatment strategy. *J. Theor. Biol.* 260, 545–562.
- Byrne, H. M., and Chaplain, M. A. J. (1995). Mathematical models for tumour angiogenesis: numerical simulations and nonlinear wave solutions. *Bull. Math. Biol.* 57, 461–486.
- Byrne, H. M., and Chaplain, M. A. J. (1996). Explicit solutions of a simplified model of capillary sprout growth during tumor angiogenesis. *Appl. Math. Lett.* 9, 69–74.
- Capasso, V., and Morale, D. (2009). Stochastic modelling of tumour-induced angiogenesis. *J. Math. Biol.* 58, 219–233.
- Conway, E. M., Collen, D., and Carmeliet, P. (2001). Molecular mechanisms of blood vessel growth. *Cardiovasc. Res.* 49, 507–521.
- Favier, B., Alam, A., Barron, P., Bonnin, J., Laboudie, P., Fons, P., et al. (2006). Neuropilin-2 interacts with VEGFR-2 and VEGFR-3 and promotes human endothelial cell survival and migration. *Blood* 108, 1243–1250.
- Ferrara, N. (2004). Vascular endothelial growth factor: basic science and clinical progress. *Endocr. Rev.* 25, 581–611.
- Ferrara, N., Gerber, H. P., and LeCouter, J. (2003). The biology of VEGF and its receptors. *Nat. Med.* 9, 669–676.
- Folkman, J. (1985). Tumor angiogenesis. *Adv. Cancer Res.* 43, 175–203.
- Ford, R. M., and Lauffenburger, D. A. (1991). Analysis of chemotactic bacterial distributions in population migration assays using a mathematical model applicable to steep or shallow attractant gradients. *Bull. Math. Biol.* 53, 721–749.
- Franz, C. M., Jones, G. E., and Ridley, A. J. (2002). Cell migration in development and disease. *Dev. Cell* 2, 153–158.
- Frieboes, H. B., Lowengrub, J. S., Wise, S., Zheng, X., Macklin, P., Bearer, E. L., et al. (2007). Computer simulation of glioma growth and morphology. *Neuroimage* 37, 59–70.
- Gerhardt, H., Golding, M., Frutiger, M., Lundkvist, A., Ruhrberg, C., Abramsson, A., et al. (2003). VEGF guides angiogenic sprouting utilizing endothelial tip cell filopodia. *J. Cell Biol.* 161, 2263–1167.
- Gevertz, J. L., and Torquato, S. (2006). Modeling the effects of vasculature evolution on early brain tumor growth. *J. Theor. Biol.* 243, 517–531.
- Hanahan, D., and Weinberg, R. A. (2000). The hallmarks of cancer. *Cell* 100, 57–70.
- Hangai, M., Kitaya, N., Xu, J., Chan, C. K., Kim, J. J., Werb, Z., et al. (2002). Matrix metalloproteinase-9-dependent exposure of a cryptic migratory control site in collagen is required before retinal angiogenesis. *Am. J. Pathol.* 161, 1429–1437.
- Hicklin, D. J., and Ellis, L. M. (2005). Role of the vascular endothelial growth factor pathway in tumor growth and angiogenesis. *J. Clin. Oncol.* 23, 1011–1027.
- Holmes, M. J., and Sleeman, B. D. (2000). A mathematical model of tumour angiogenesis incorporating cellular traction and viscoelastic effects. *J. Theor. Biol.* 202, 95–112.
- Jackson, T. L., and Zheng, X. (2010). A multiscale model of cell elongation, proliferation and maturation during angiogenesis. *Bull. Math. Biol.* 72, 830–868.
- Jain, H. V., Nor, J. E., and Jackson, T. L. (2008). Modelling the VEGF-Bcl-2-CXCL8 pathway in intra-tumoral angiogenesis. *Bull. Math. Biol.* 70, 89–117.

- Jain, R. K. (2002). Tumor angiogenesis and accessibility: role of vascular endothelial growth factor. *Semin. Oncol.* 29(Suppl. 16), 3–9.
- Jakobsson, L., Franco, C. A., Bentley, K., Collins, R. T., Ponsioen, B., Aspalter, I. M., et al. (2010). Endothelial cells dynamically compete for the tip cell position during angiogenic sprouting. *Nat. Cell Biol.* 12, 943–953.
- Keller, E. F., and Segel, L. A. (1971a). Models of chemotaxis. *J. Theor. Biol.* 30, 225–234.
- Keller, E. F., and Segel, L. A. (1971b). Traveling bands of chemotactic bacteria: a theoretical analysis. *J. Theor. Biol.* 30, 235–248.
- Kuppuswamy, D., and Pike, L. J. (1989). Ligand-induced desensitization of 125I-epidermal growth factor internalization. *J. Biol. Chem.* 264, 3357–3363.
- Kurt, R. A., Baher, A., Wisner, K. P., Tackitt, S., and Urba, W. J. (2001). Chemokine receptor desensitization in tumor-bearing mice. *Cell. Immunol.* 207, 81–88.
- Lapidus, I. R., and Schiller, R. (1976). A model for the chemotactic response of a bacterial population. *Biophys. J.* 16, 779–789.
- Lee, S., Jilani, S. M., Nikolova, G. V., Carpizo, D., and Iruela-Arispe, M. L. (2005). Processing of VEGF-A by matrix metalloproteinases regulates bioavailability and vascular patterning in tumors. *J. Cell Biol.* 169, 681–691.
- Levine, H., Kessler, D. A., and Rappe, W. J. (2006). Directional sensing in eukaryotic chemotaxis: a balanced inactivation model. *Proc. Natl. Acad. Sci. U.S.A.* 103, 9761–9766.
- Levine, H. A., and Nilsen-Hamilton, M. (2006). “Angiogenesis – a biochemical/mathematical perspective,” in *Tutorials in Mathematical Biosciences III, Number 1872 in Lecture Notes in Mathematics*, Chap. 2, ed. A. Friedman (Heidelberg: Springer), 65.
- Levine, H. A., Pamuk, S., Sleeman, B. D., and Nilsen-Hamilton, M. (2001). Mathematical modeling of capillary formation and development in tumor angiogenesis: penetration into the stroma. *Bull. Math. Biol.* 63, 801–863.
- Levine, H. A., Sleeman, B. D., and Nilsen-Hamilton, M. (2000). A mathematical model for the roles of pericytes and macrophages in the initiation of angiogenesis. I. The role of protease inhibitors in preventing angiogenesis. *Math. Biosci.* 168, 77–115.
- Levine, H. A., Tucker, A. L., and Nilsen-Hamilton, M. (2002). A mathematical model for the role of cell signal transduction in the initiation and inhibition of angiogenesis. *Growth Factors* 20, 155–175.
- Liu, G., Qutub, A., Vempati, P., Mac Gabhann, F., and Popel, A. (2011). Module-based multiscale simulation of angiogenesis in skeletal muscle. *Theor. Biol. Med. Model.* 8, 6.
- Liu, Y., McCarthy, J., and Ladisch, S. (2006). Membrane ganglioside enrichment lowers the threshold for vascular endothelial cell angiogenic signaling. *Cancer Res.* 66, 10408–10414.
- Mac Gabhann, F., and Popel, A. S. (2004). Model of competitive binding of vascular endothelial growth factor and placental growth factor to VEGF receptors on endothelial cells. *Am. J. Physiol. Heart Circ. Physiol.* 286, H153–H154.
- Mac Gabhann, F., and Popel, A. S. (2005). Differential binding of VEGF isoforms to VEGF receptor 2 in the presence of neuropilin-1: a computational model. *Am. J. Physiol. Heart Circ. Physiol.* 288, H2851–60.
- Manoussaki, D. (2003). A mechanochemical model of angiogenesis and vasculogenesis. *Esaim Math. Model. Numer. Anal.* 37, 581–599.
- Mantzaris, N., Webb, S., and Othmer, H. G. (2004). Mathematical modeling of tumor-induced angiogenesis. *J. Math. Biol.* 49, 111–187.
- McMahon, G. (2000). VEGF receptor signaling in tumor angiogenesis. *Oncologist* 5(Suppl. 1), 3–10.
- Milde, F., Bergdorf, M., and Koumoutsakos, P. (2008). A hybrid model for three-dimensional simulations of sprouting angiogenesis. *Biophys. J.* 95, 3146–3160.
- Murray, J. D. (2003). *Mathematical Biology II: Spatial Models and Biomedical Applications*. New York: Springer-Verlag.
- Muthukkaruppan, V. R., Kubai, L., and Auerbach, R. (1982). Tumor-induced neovascularization in the mouse eye. *J. Natl. Cancer Inst.* 69, 699–708.
- Neufeld, G., Cohen, T., Gengrinovitch, S., and Poltorak, Z. (1999). Vascular endothelial growth factor (VEGF) and its receptors. *FASEB J.* 13, 9–22.
- Nor, J. E., Christensen, J., Mooney, D. J., and Polverini, P. J. (1999). Vascular endothelial growth factor (VEGF)-mediated angiogenesis is associated with enhanced endothelial cell survival and induction of Bcl-2 expression. *Am. J. Pathol.* 154, 375–384.
- Othmer, H. G., and Stevens, A. (1997). Aggregation, blowup and collapse: the ABC's of generalized taxis in reinforced random walks. *SIAM J. Appl. Math.* 57, 1044–1081.
- Owen, M. R., Alarcon, T., Maini, P. K., and Byrne, H. M. (2009). Angiogenesis and vascular remodelling in normal and cancerous tissues. *J. Math. Biol.* 58, 689–721.
- Pawletz, N., and Knierim, M. (1989). Tumor-related angiogenesis. *Crit. Rev. Oncol. Hematol.* 9, 197–242.
- Peirce, S. M. (2008). Computational and mathematical modeling of angiogenesis. *Microcirculation* 15, 739–751.
- Peirce, S. M., Van Gieson, E. J., and Skalak, T. C. (2004). Multicellular simulation predicts microvascular patterning and in silico tissue assembly. *FASEB J.* 18, 731–733.
- Perfahl, H., Byrne, H. M., Chen, T., Estrella, V., Alarcon, T., Lapin, A., et al. (2011). Multiscale modelling of vascular tumour growth in 3D: the roles of domain size and boundary conditions. *PLoS ONE* 6:e14790. doi:10.1371/journal.pone.0014790
- Plank, M. J., and Sleeman, B. D. (2003). A reinforced random walk model of tumor angiogenesis and anti-angiogenesis strategies. *IMA J. Math. Appl. Med. Biol.* 20, 135–181.
- Plank, M. J., and Sleeman, B. D. (2004). Lattice and non-lattice models of tumour angiogenesis. *Bull. Math. Biol.* 66, 1785–1819.
- Plank, M. J., Sleeman, B. D., and Jones, P. F. (2003). A mathematical model of an in vitro experiment to investigate endothelial cell migration. *J. Theor. Med.* 4, 251–207.
- Plank, M. J., Sleeman, B. D., and Jones, P. F. (2004). A mathematical model of tumour angiogenesis, regulated by vascular endothelial growth factor and the angiopoietins. *J. Theor. Biol.* 229, 435–454.
- Qutub, A. A., Mac Gabhann, F., Karagiannis, E. D., Vempati, P., and Popel, A. S. (2009). Multiscale models of angiogenesis. *IEEE Eng. Med. Biol. Mag.* 28, 14–31.
- Qutub, A. A., and Popel, A. S. (2009). Elongation, proliferation & migration differentiate endothelial cell phenotypes and determine capillary sprouting. *BMC Sys. Biol.* 3:13. doi:10.1186/1752-0509-3-13
- Schugart, R. C., Friedman, A., Zhao, R., and Sen, C. K. (2008). Wound angiogenesis as a function of tissue oxygen tension: a mathematical model. *Proc. Natl. Acad. Sci. U.S.A.* 105, 2628–2633.
- Serini, G., Ambrosi, D., Giraudo, E., Gamba, A., Preziosi, L., and Bus-solino, F. (2003). Modeling the early stages of vascular network assembly. *EMBO J.* 22, 1771–1779.
- Sholley, M. M., Ferguson, G. P., Seibel, H. R., Montour, J. L., and Wilson, J. D. (1984). Mechanisms of neovascularization. vascular sprouting can occur without proliferation of endothelial cells. *Lab. Invest.* 51, 624–634.
- Sleeman, B. D., and Wallis, I. P. (2002). Tumour induced angiogenesis as a reinforced random walk: modeling capillary network formation without endothelial cell proliferation. *Math. Comput. Model.* 36, 339–358.
- Stewart, M., Turley, H., Cook, N., Pezzella, F., Pillai, G., Ogilvie, D., et al. (2003). The angiogenic receptor KDR is widely distributed in human tissues and tumours and relocates intracellularly on phosphorylation. *Histopathology* 43, 33–39.
- Stokes, C. L., and Lauffenburger, D. A. (1991). Analysis of the roles of microvessel endothelial cell random mobility and chemotaxis in angiogenesis. *J. Theor. Biol.* 152, 377–403.
- Sun, S., Wheeler, M. F., Obeyesekere, M., and Patrick, C. (2005). A deterministic model of growth factor-induced angiogenesis. *Bull. Math. Biol.* 67, 313–337.
- Tong, S., and Yuan, F. (2001). Numerical simulations of angiogenesis in the cornea. *Microvasc. Res.* 61, 14–27.
- Travasso, R. D. M., Corvera Poiré, E., Castro, M., Rodríguez-Manzanique, J. C., and Hernández-Machado, A. (2011). Tumor angiogenesis and vascular patterning: a mathematical model. *PLoS ONE* 6:e19989. doi:10.1371/journal.pone.0019989
- Vadapalli, A., Pittman, R. N., and Popel, A. S. (2000). Estimating oxygen transport resistance of the microvascular wall. *Am. J. Physiol. Heart Circ. Physiol.* 279, 657–671.
- Wang, D., Donner, D. B., and Warren, R. S. (2000). Homeostatic modulation of cell surface KDR and Flt1 expression and expression of the vascular endothelial cell growth factor (VEGF) receptor mRNAs by VEGF. *J. Biol. Chem.* 275, 15905–15911.
- Wang, D., Lehman, R. E., Donner, D. B., Matli, M. R., Warren, R. S., and Welton, M. L. (2002). Expression and endocytosis of VEGF and its receptors in human colonic vascular endothelial cells. *Am. J. Physiol. Gastrointest. Liver Physiol.* 282, G1088–G1096.
- Wang, S. J., Saadi, W., Lin, F., Minh-Canh Nguyen, C., and Li Jeon, N. (2004). Differential effects of EGF

- gradient profiles on MDA-MB-231 breast cancer cell chemotaxis. *Exp. Cell Res.* 300, 180–189.
- Wcislo, R., Dzwiniel, W., Yuen, D., and Dudek, A. (2009). A 3-D model of tumor progression based on complex automata driven by particle dynamics. *J. Mol. Model.* 15, 1517–1539.
- Xue, C., Friedman, A., and Sen, C. K. (2009). A mathematical model of ischemic cutaneous wounds. *Proc. Natl. Acad. Sci. U.S.A.* 106, 16782–16787.
- Yancopoulos, G. D., Davis, S., Gale, N. W., Rudge, J. S., Wiegand, S. J., and Holash, J. (2000). Vascular-specific growth factors and blood vessel formation. *Nature* 407, 242–248.
- Zheng, X., Koh, G. Y., and Jackson, T. L. (2013). A continuous model of angiogenesis: initiation, extension, and maturation of new blood vessels modulated by vascular endothelial growth factor angiopoietins, platelet-derived growth factor- β , and pericytes. *Discrete Continuous Dyn. Syst. Ser. B*, 18, 1109–1154.
- Conflict of Interest Statement:** The authors declare that the research was conducted in the absence of any commercial or financial relationships that could be construed as a potential conflict of interest.
- Received: 15 January 2013; paper pending published: 15 February 2013; accepted: 11 April 2013; published online: 10 May 2013.*
- Citation: Jain HV and Jackson TL (2013) A hybrid model of the role of VEGF binding in endothelial cell migration and capillary formation. Front. Oncol. 3:102. doi: 10.3389/fonc.2013.00102*
- This article was submitted to Frontiers in Molecular and Cellular Oncology, a specialty of Frontiers in Oncology. Copyright © 2013 Jain and Jackson. This is an open-access article distributed under the terms of the Creative Commons Attribution License, which permits use, distribution and reproduction in other forums, provided the original authors and source are credited and subject to any copyright notices concerning any third-party graphics etc.*



Genetic diversity in normal cell populations is the earliest stage of oncogenesis leading to intra-tumor heterogeneity

Cory L. Howk^{1†}, Zachary Voller², Brandon B. Beck¹ and Donghai Dai^{1*}

¹ Department of Obstetrics and Gynecology, University of Iowa, Iowa City, IA, USA

² Department of Mathematics, Iowa State University, Ames, IA, USA

Edited by:

Heiko Enderling, Tufts University
School of Medicine, USA

Reviewed by:

Jacob G. Scott, H. Lee Moffitt Cancer
Center and Research Institute, USA
Irina Kareva, Tufts University School of
Medicine, USA

*Correspondence:

Donghai Dai, Department of
Obstetrics and Gynecology,
University of Iowa, Rm 3234, Bldg
MERF, 375 Newton Rd, Iowa City, IA,
USA.
e-mail: donghai-dai@uiowa.edu

†Present address:

Cory L. Howk, Department of
Mathematics and Computer Science,
Western Carolina University,
Cullowhee, NC, USA.

Random mutations and epigenetic alterations provide a rich substrate for microevolutionary phenomena to occur in proliferating epithelial tissues. Genetic diversity resulting from random mutations in normal cells is critically important for understanding the genetic basis of oncogenesis. However, evaluation of the cell-specific role of individual (epi-)genetic alterations in living tissues is extremely difficult from a direct experimental perspective. For this purpose, we have developed a single cell model to describe the fate of every cell in the uterine epithelium and to simulate occurrence of the first cancer cell. Computational simulations have shown that a baseline mutation rate of two mutations per cell division is sufficient to explain sporadic endometrial cancer as a rare evolutionary consequence with an incidence similar to that reported in SEER data. Simulation of the entire oncogenic process has allowed us to analyze the features of the tumor-initiating cells and their clonal expansion. Analysis of the malignant features of individual cancer cells, such as de-differentiation status, proliferation potential, and immortalization status, permits a mathematical characterization of malignancy at the single cell level and a comparison of intra-tumor heterogeneity between individual tumors. We found, under the conditions specified, that cancer stem cells account for approximately 7% of the total cancer cell population. Therefore, our mathematical modeling describes the genetic diversity and evolution in a normal cell population at the early stages of oncogenesis and characterizes intra-tumor heterogeneity. This model has explored the role of accumulation of a large number of genetic alterations in oncogenesis as an alternative to traditional biological approaches emphasizing the driving role of a small number of genetic mutations. A quantitative description of the contribution of a large set of genetic alterations will allow the investigation of the impact of environmental factors on the growth advantage of and selection pressure on individual cancer cells for tumor progression.

Keywords: evolution, oncogenesis, genetic mutation, endometrial cancer, fitness, phylogenetic analysis, tumor heterogeneity, mathematical modeling

INTRODUCTION

An evolutionary model has been established to describe the entire process of tumor development in colorectal cancer with detailed molecular mechanisms for the stepwise oncogenic progression driven by sequential accumulation of several genetic mutations (Fearon and Vogelstein, 1990; Jones et al., 2008a). However, in our view, this model can be expanded to understand evolution among a population of normal cells in the uterine epithelium with inclusion of random mutations. Several studies have estimated the mutation rates in normal cells to be around 10^{-7} per cell per generation (for a specific gene) through measurement of the frequency of mutations in the gene in proliferating cells (Elmore et al., 1983; Araten et al., 2005). The more accurate estimates are done in a living tissue and a rate of $\approx 5\text{--}10 \times 10^{-10}$ mutations per base pair per cell per generation is reported (Jones et al., 2008a). This rate can be approximately translated into about two to three mutations per cell per division. This reported mutation rate of two to three random mutations per cell per generation would produce billions of

mutations in the proliferating uterine epithelial tissue and may be sufficient to explain the large number of genetic mutations uncovered in human tumors (Gallo et al., 2012; Kuhn et al., 2012; Liang et al., 2012). Interestingly, these studies have not found a significant difference in the mutation rate between normal and transformed cells (Elmore et al., 1983; Araten et al., 2005; Jones et al., 2008a), indicating that the genetic diversity universally reported in cancer cell populations may be present in normal cell populations as well, serving as fertile ground for evolution at the earliest stage of oncogenesis. Therefore, genetic mutations in normal cells can provide significant genetic diversity for subsequent selection, allowing for a unique, albeit extremely rare, consequence: a cell may escape the typical fate of normal cells and become immortalized.

However, the process of evolution in a normal cell population is rarely a popular cancer research subject. Normal cells in a tissue are often not considered to harbor any dysfunctional mutations nor are they considered to demonstrate any phenotype commonly seen in cancer. Furthermore, any suggestion that

minor random mutations are sufficient for oncogenesis in some cancers may be seen as a contradiction to the genetic theory that certain notable genetic mutations and oncogenic pathways are the driving forces for tumor development. These seeming contradictions can be reconciled by considering that a significantly larger number of pathways than was commonly believed are present in well-developed tumors (Jones et al., 2008b), meaning that the genetic slot machine for transformation of an individual cell has many reels. Phenotypically normal cells, with no apparent growth advantage, may quietly harbor multiple accumulated alterations in multiple pathways before transformation by a single major mutation or by minor mutations in remaining key pathways. While the chance of complete transformation of an individual cell may be negligible, genetic diversity represents the non-negligible collective chances of many individual cells, each with a particular set of mutations after a number of generations with a steady mutation rate.

The appearance of the first cancer cell, the tumor-initiating cancer cell (TICC) which propagates to form the entire cancer cell population in a tumor, seems to be an extremely rare occurrence. For instance, endometrial cancer incidence is about 6 per 100,000 women at reproductive age according to the SEER database (2008, female, all races, <50 years) and the peak cell number in the uterine epithelium is several billion with monthly turnover, which gives an approximate probability of the occurrence of the TICC of less than 5×10^{-15} per normal cell per year. This manuscript, utilizing mathematical modeling and numerical simulation, tests whether the baseline mutation rate in a normal cell population, such as the uterine epithelium, is sufficient for the rare occurrence of a TICC. Simulation of the longitudinal and prospective process of tumor initiation and development, including following the evolution of individual normal cell lines in the uterine epithelium, has allowed us to describe the clonal progression of a TICC into a clinically detectable tumor.

MATERIALS AND METHODS

The goal of this manuscript is to explore whether the baseline mutation rate in a normal endometrial cell population is sufficient to explain endometrial cancer incidence. We will also explore whether description of the fate of every single cell in our model can demonstrate in sufficient detail the development of heterogeneity within the mass, and the corresponding properties of the ancestor cells of endometrial tumors. This is analyzed through numerical simulations of a recently published model for the proliferation of uterine epithelial cells (Dai et al., 2011).

OUTLINE OF CELL PROPAGATION

The mathematical model under consideration views the proliferation of epithelial cells in terms of a continuous-time bifurcating process. The simulation begins with an initial progenitor cell. The time required for the cell to either divide or die is governed by a set of equations describing various properties of the cell (Eqs 1–7, individual variables are described in **Tables 1** and **2**). In the event of division, the daughter cells inherit their properties from the parent cell, with the quantitative values of the properties subject to stochastic variation. We then follow the fates of each daughter cell, which follow Eqs 1–7 independently. The cells

are simultaneously viewed as traversing a differentiation pathway, with each cell existing along a spectrum from progenitor cell to a fully differentiated descendant clone typically seen in the uterine epithelium (Dai et al., 2011). Therefore the cell's properties are also influenced due to this "biological progression." The size of the uterine epithelium is determined by the total number of descendant cells existing at time t . The fate of each individual constituent cell is calculated through Monte Carlo simulation.

Cell cycle status value:

$$c(t) = \int_{t_n}^t \alpha(s) ds, \text{ where } t_n \text{ denote the cell's birth time} \quad (1)$$

Programmed proliferation potential:

$$\alpha_p(t) = \frac{1}{7} (10 - g(t)) g(t) \quad (2)$$

Programmed differentiation coefficient:

$$k_p(t) = 3.78 \left[1 - e^{-0.4 \cdot g(t)} \right] + 0.03g(t) \quad (3)$$

$$\text{Generation number: } g(t) = 1 + \text{floor} \left(\int_0^t |\alpha(s)| ds \right) \quad (4)$$

$$\text{Resistance potential: } r(t) = k(t) (\alpha_p(t) - \alpha(t)) \quad (5)$$

$$\text{Differentiation coefficient: } k(t) = k_p(t) + \sum_{i=1}^n m_i \quad (6)$$

$$\text{Proliferation potential rate of change: } \frac{d\alpha}{dt} = r(t) + \beta(t) \quad (7)$$

The cell cycle status $c(t)$ of a cell, governed by the cell's growth rate (proliferation potential) $\alpha(t)$, denotes the progression toward apoptosis (death) or division (bifurcation) in the branching process. When a cell is born at a time t_n , this value is 0. If $c(t^*) = 1$ for some $t^* > t_n$, the cell undergoes division into two daughter cells, while if $c(t^*) = -1$ for some $t^* > t_n$, the cell undergoes apoptosis. This measurement of cell cycle status is related to $P(t) = 2^{\int_{t_n}^t \alpha(s) ds}$, the solution of the differential equation for doubling of a population, $dP/dt = \ln(2)\alpha(t)P$. However, we utilize the measurement $c(t)$ since, in the above mathematical system, we are considering the fate of a single cell instead of a population.

Equations 2–4 describe a hypothetical trajectory (fate) of a single cell which is genetically determined and automatically proceeds along cellular time, g , free of any perturbing influence, such as genetic alterations and environmental factors. Equations 2 and 3 describe the parallel process of a cell's proliferation $[\alpha_p(t)]$ and differentiation $[k_p(t)]$. Equation 4 represents cellular time (g , generation), which is determined by factors related to cell division such as telomere length, and depends on physical time (t , in months, and related to patient age). Equations 5–7 incorporate the hypothetical trajectory, perturbations from it, and resistance to these perturbations as part of homeostasis. Additional explanation of the rationale of these equations were provided previously (Dai et al., 2011).

OUTLINE OF CELL PROPERTIES

Each cell's status is described by four quantities: proliferation potential (α), differentiation coefficient (k), resistance potential

Table 1 | Terms for hypothetical cellular growth of a single cell.

Term	Definition	Unit	Description
$c(t)$	Measurement of the status of cell cycle of a cell with a numerical value between -1 and $+1$	Cycle	The status of a cell cycle is provided with a numerical value in order to describe the quantitative progression of cell proliferation. A cell cycle exists between two endpoints: death and birth (of two daughter cells). In either case, the cell ceases to exist. A cell divides if $c(t) = 1$, dies if $c(t) = -1$, for some $t > t_n$, where t_n is the time that the cell was born
$N(t)$	Size of a tissue or a mass at time t	Cell	The total number of cells in a tissue or a mass at time t with summation of the value of all individual cells. A clone is comprised of all descendant cells from a progenitor cell borne from asymmetrical division of a tissue stem cell
t	Physical time, as it relates to patient age and menstrual cycle	Month	It is the physical time and can be assigned with a unit of day, month, or year. We assume that 1 year = 12 months and 1 month = 30 days for convenience
$\alpha_p(t)$	(Programed) proliferation potential (Eq. 2)	Cycles/month	Programed rate of a cell's multiplication according to the cell's progression in clonal development (progression of generations) and expressed as the number of cell cycles per unit time
$k_p(t)$	(Programed) differentiation coefficient (Eq. 3)	1/month	Measurement of a cell's differentiation status, commonly with a range from 0 to K_{\max} (a tissue specific constant)
$g(t)$	Generation number (Eq. 4)	Cycle	Measurement of lineage progression in a clone and cellular senescence. A daughter cell assumes a new generation value of $g + 1$ with g as the parent generation number. It has the same unit as the cell cycle. It represents how a cell perceives senescence, and is determined by its cellular mechanism, for instance by telomere length. Although $g(t)$ and division (d) synchronize most of time, there is a possibility that they may differ. For instance, active telomerase may maintain telomere length after many divisions

These terms are for cells living under conditions free of any genetic insults and environmental influences, a hypothetical scenario used as a frame of reference to study the effect of genetic and environmental factors on cell growth.

Table 2 | Terms for the growth of a single cell.

Term	Definition	Unit	Description
m_i	Mutational coefficient (Eq. 6)	1/month	Quantifies the effect of each genetic alteration on a cell's ability to maintain differentiation status, $k(t)$
$\alpha(t)$	Proliferation potential (Eq. 7)	Cycles/month	A measurement of the number of completed cell cycle per unit time. A cell's proliferation potential is the function of resistance potential (r) and environmental stimulation (β) over time (t) in Eq. 7, indicating the pace of cell cycling under influence. Therefore, cell death induced by anti-growth signals can be simulated by a negative α induced by a negative β over time
$k(t)$	Differentiation coefficient (Eq. 6)	1/month	Measurement of a cell's differentiation status under influence as the sum of programmed differentiation coefficient and mutational effect
$r(t)$	Resistance potential (Eq. 6)	Cycles/month ²	Measurement of a cell's inherent ability to adhere to the development program by restoring $\alpha(t)$ to $\alpha_p(t)$ which will lead to the control of cell number and progression of differentiation
$\beta(t)$	Environmental coefficient (Eq. 7)	Cycles/month ²	All environmental factors affecting cell multiplication. Hormonal stimulation on cell proliferation is an example

These terms are for experimental measurement of (clonal) cellular growth under our experimental observations with genetic insults and under environmental influences.

(r), and generation number (g). A cell lineage begins with the birth of an initial progenitor cell at time $t = 0$. Its physical position within the lineage is given by the number of divisions the cell is removed from the initial progenitor cell (d). An alternate measurement of progression is used to measure a cell's biological

progression along the differentiation pathway (g). This parameter may be viewed as a measurement of how a cell perceives the passage of time, which may not necessarily sync with the number of divisions its lineage has undergone. Progression of a cell's g value is accompanied by the gain of additional mutations and

a corresponding alteration in α_p and k_p , which denote behaviors inherent to position along the differentiation pathway (Table 1).

An individual cell's proliferation potential is denoted by $\alpha(t)$, and is distinguished from its programmed rate that is inherent to its position along the differentiation pathway [$\alpha_p(t)$]. The cell has a draw toward this inherent rate which is reflected by $d\alpha/dt \propto \alpha_p(t) - \alpha(t)$, but may be influenced by other environmental effects (such as hormones). The strength of this restorative force is defined by the cell's differentiation coefficient (k). Cells early in the lineage have a limited ability, due to their similarity with the initial progenitor cell, to maintain homeostasis with respect to properties inherent to the differentiation pathway. Conversely, this ability is increased, consistent with their similarity to the fully differentiated cell type, for cells late in the lineage. This idealized restorative strength is denoted k_p and is inherent to a cell's position along the pathway. Mutations alter this ability, resulting in the cell's k -value. The cell's resistance potential (r) defines its ability to resist deviations from normal proliferative behavior, and cells early in the pathway have a weak resistance to alterations in proliferative behavior, while those later in the pathway will have a strong resistance, provided there are few strong mutations affecting the cell. A more thorough description of these terms has been provided previously (Dai et al., 2011).

ENVIRONMENTAL AND MUTATIONAL EFFECTS

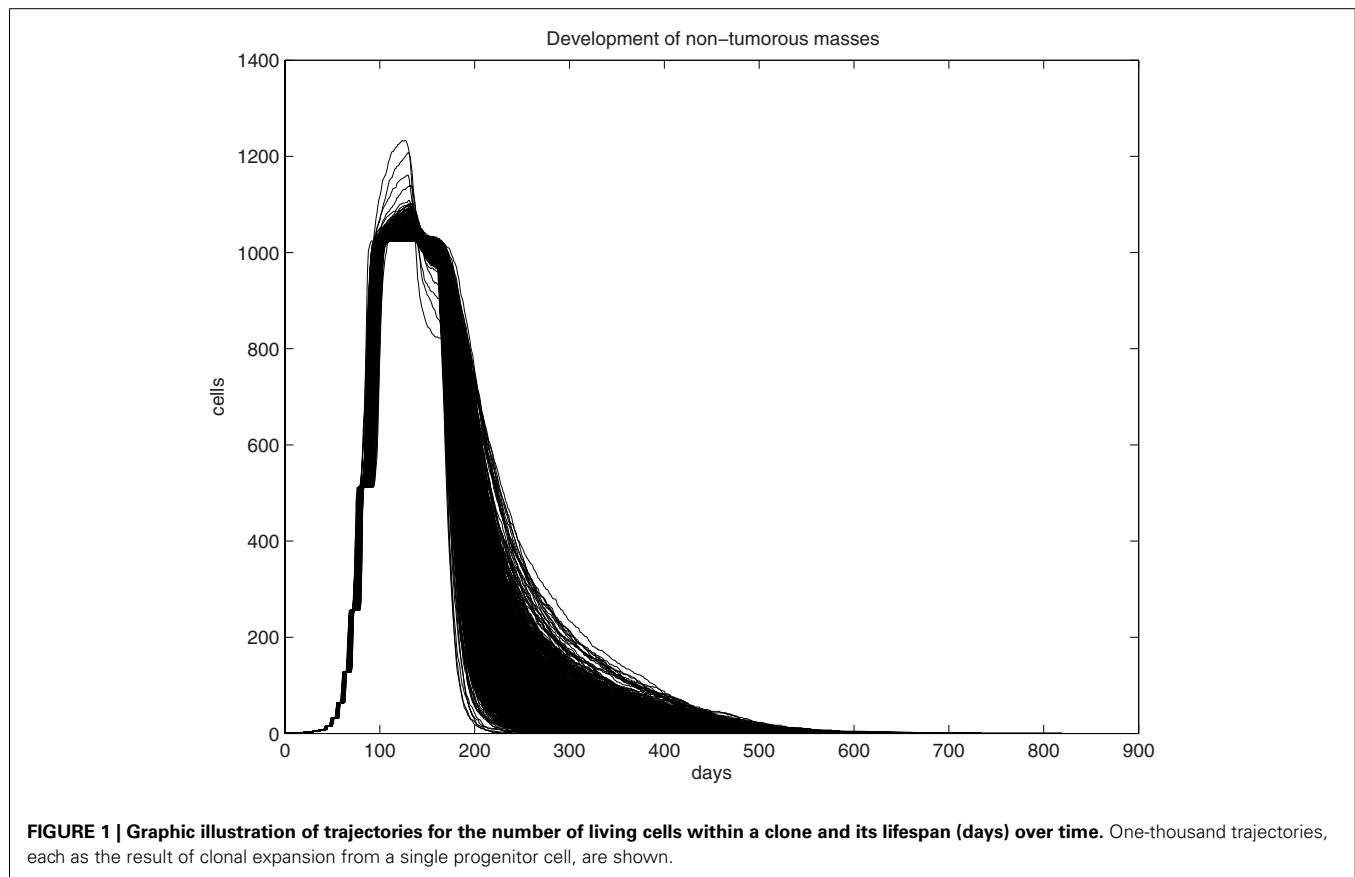
Simulations are performed with $\beta \sim N(5, 0.5^2)$ to represent relatively low hormone level with constant mean ($\mu = 5$) and SD = 0.5

to indicate a slight variation of hormone levels among individual cells, consistent with a typical postmenopausal hormone level. A fixed and typical mean β value allows us to focus on the role of genetic diversity (accumulation of m ; in an individual cell) among the population. The importance of overexposure of estrogen, and other environmental factors in endometrial oncogenesis will be reported in separate manuscripts. We also assume two mutations per cell division in accordance with the hypothesis under consideration. As a consequence of evolution in epithelial cells due to immortalization and de-differentiation, a clinically detectable tumor is defined as a mass of at least 10^6 cells derived from an initial progenitor cell. In this early exploration of the model, the initial progenitor cells within the uterine epithelium are assumed identical and independently follow the seven equations.

RESULTS

CELLULAR PROLIFERATION AND DIFFERENTIATION IN THE UTERINE EPITHELIUM

We first examine the clonal expansion from a progenitor cell in order to understand the life cycle of epithelial cells in the uterine epithelium. Simulations are initiated with an initial progenitor cell born through asymmetric division or differentiation of a tissue stem cell. The clone is allowed to proliferate until it dies out. The size curve of each clone over time for a single progenitor cell is fairly consistent, however, as can be seen from 1,000 randomly selected trajectories generated through simulation of the fate of 10^6 progenitor cells (Figure 1). We find that the peak size



of each clone ranges from 1,024 to 1,277 cells, with a median value of 1,033.5 cells and a standard deviation of 16.2. This can be interpreted both as the typical fate of a clone spawned from each progenitor cell and is the common physiological scenario. Thus, for any cell and any clone, their lifespan is limited and they follow a predictable course and fate. One feature of tissue homeostasis, interpreted as the maintenance of a relatively stable cell number, is largely accomplished by the balance between two mechanisms, the constant commitment of tissue stem cells to produce new cells and the limited lifespan (number of generations) of individual cells to allow cell death. Thus, a significant extension of a cell's lifespan and a substantial expansion of its descendant size beyond the typical physiological range will disrupt tissue homeostasis and serve as an early step of oncogenesis. Analysis of simulations on 10^6 progenitor cells has shown that the lifespan of the clones was found to have a wider range, varying between 205 and 901 days, with a median of 576 days and a standard deviation of 67.5, a significant extension from the observation in **Figure 1**. Immortalization will be expected if the simulation involves a significantly larger population.

Indeed, a further analysis of the fates of 305,505,000 progenitor cells resulted in the detection of 8 tumors, translated

into an endometrial cancer incidence of 94 tumors per 100,000 menopausal women, similar to the epidemiological data of 78 per 100,000 women based on the 2008 SEER database for all races of age ≥ 50 . This also yielded an empirical probability of 2.61862×10^{-8} [95% confidence interval (1.13053×10^{-8} , 5.15998×10^{-8})] that a progenitor cell will spawn a primary tumor under the experimental conditions. Our simulation has shown the progression from common physiological tissue regeneration (in 10^3 randomly selected progenitor cells) to partial immortalization (in 10^6 progenitor cells) and the occurrence of neoplasm (in 3×10^8 progenitor cells), demonstrating oncogenesis as a seemingly rare stochastic event which occurs only in a sufficiently large number of simulations under specific environmental (hormone) conditions. More importantly, this experiment indicates that a random mutation rate of two per cell division may be sufficient for sporadic endometrial cancer.

PHYLOGENETIC TREE ANALYSIS

A unique ID is assigned to each cell born during the lifespan of the clone. The cell passes information about its lineage to each daughter cell after division by assigning the daughter cell the ID $10x + i$, where x is the ID of the parent and i is either 1 or 2,

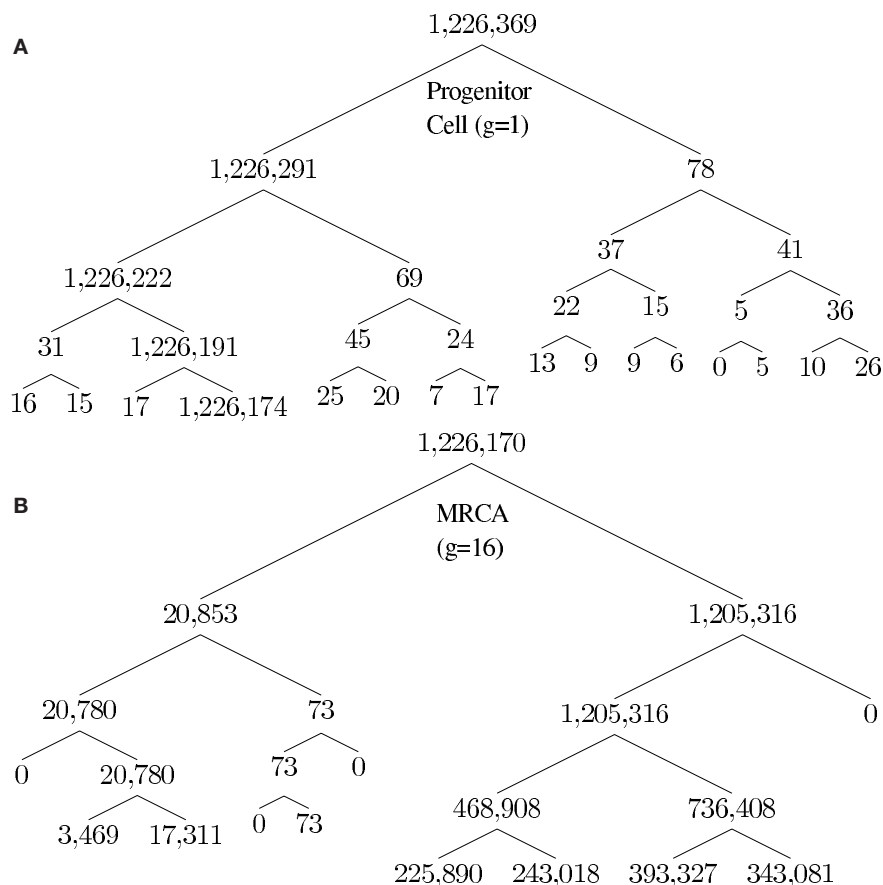


FIGURE 2 | Phylogenetic tree for illustration of lineage relationship during the earliest stage of oncogenesis. The number indicates the size of descendants in the tumor from the cells (nodes). **(A)** The lineage map

formed within the first five divisions; **(B)** a subset of the phylogenetic tree, centered on the most recent common ancestor (MRCA) of the tumor of generation 16.

unique to each daughter. **Figure 2** shows how a tumor arises from a clone. **Figure 2A** shows the number of descendants from each cell in the first five generations starting from a progenitor, which eventually give rise to the most recent common ancestor (MRCA) of a tumor, where division 1 denotes the birth of the progenitor cell through an asymmetric division of a stem cell. Note that there is one dominant branch with more than 10^6 descendants, whereas other branch points have few descendants (the node with 78 descendant cells in the tumor), which coexist with the tumor and survive longer than a typical normal cell because of slow progression in the completion of senescence (and cell death) due to a low α value. Cell feature analysis shows that they have a high k -value (still differentiated) and are not immortalized since their generation number is less than 12 [see Cells within the tumor that are not descendant from MRCA(0.995) in Appendix]. **Figure 2B** shows the MRCA of the tumor at generation 16 with subsequent divisions demonstrating different lineages with varying descendant sizes. Thus, there is remarkable clonal heterogeneity in that the number of descendant cells varies substantially in different branches.

THE PHENOTYPIC HETEROGENEITY OF THE TUMOR-INITIATING CANCER CELLS

The heterogeneity of a tumor during its clonal development was analyzed by considering distributional information aggregated from 74 tumors generated through this mathematical model. The heterogeneous features in individual cells are described based on three criteria: the immortalization status by generation number g , proliferation status by proliferation potential α , and differentiation status by differentiation coefficient k . The median time required to form masses of size 10^6 cells was found to be approximately 270 days.

We utilized a phylogenetic analysis of each tumor in order to examine the development of endometrial cancer. The MRCA of $x \times 100\%$ of the mass of 10^6 cells will be denoted by MRCA(x). We first considered the number of divisions between the MRCA(x) and the initial progenitor cell. The lifespan typical for a normal cell clone is commonly estimated to be between 10 and 12 divisions, where cells would reach the fully differentiated cell type and enter senescence. Some cells, as our analysis shows, remain in the process of their senescence for some time before their death. Data for MRCA(x) from the 74 tumors is presented in **Table 3**. MRCA(1) is found to be 1 division for each mass, however MRCA(0.999) and MRCA(0.995) jump to a median of 16.7 and 17.2 divisions, respectively, which indicates the immortalization (**Table 3A**).

The phenotype of MRCA(x) can be further defined by the values for its proliferation potential (α) and its differentiation coefficient (k) in addition to the generation number in **Table 3A**. Data for these values are provided in **Tables 3B,C**, respectively. The evolution of low k -values is the underlying mechanism of uncontrolled tumor growth due to loss of differentiation, as this parameter defines the differentiation status of a cell. As this value decreases, the cell becomes more susceptible to any external stimulation such as hormones. The MRCA for all cancer cells in a tumor must be a cancer cell if, as we assume based on consensus in the literature, cancer is monoclonal in origin (Weinberg, 2007; Hanahan and Weinberg, 2011). We define, based on the

Table 3 | (A) d For MRCA(x); (B) α for MRCA(x); and (C) k for MRCA(x).

MRCA(x)	Median	SD	Min	Max
(A)				
1	1	0	1	1
0.999	16.70	2.36	9	22
0.995	17.20	2.09	11	22
0.99	17.30	2.05	11	22
0.95	18.18	2.34	13	23
0.90	18.72	1.99	14	23
0.80	19.04	2.18	14	24
0.70	19.62	2.35	14	25
0.60	20.22	2.41	14	27
0.50	21.18	2.43	15	28
(B)				
1	2.95	0.004	2.80	3.09
0.999	3.43	1.25	1.13	5.95
0.995	3.66	1.41	1.13	6.26
0.99	3.73	1.41	1.13	6.26
0.95	4.23	1.22	1.66	7.39
0.90	4.49	1.39	1.66	7.39
0.80	4.65	1.49	1.66	7.39
0.70	6.02	1.97	1.66	7.95
0.60	6.66	1.72	2.24	7.95
0.50	6.53	1.44	4.24	9.12
(C)				
1	1.90	0.015	1.65	2.24
0.999	0.23	0.05	0	1.43
0.995	0.18	0.03	0	0.90
0.99	0.17	0.03	0	0.90
0.95	0.11	0.02	0	0.76
0.90	0.08	0.01	0	0.30
0.80	0.07	0.01	0	0.30
0.70	0.07	0.01	0	0.30
0.60	0.05	0.005	0	0.30
0.50	0.03	0.002	0	0.27

analysis of the formation of 74 tumors, a TICC as a cell with the median properties of MRCA(0.995). Although there is substantial heterogeneity in the phenotypes among MRCA(0.995)s, these cells are immortalized with generation number g between 11 and 22, proliferative with α between 1.1 and 6.3, and most important of all, de-differentiated with k between 0 and 0.9. We define a typical TICC as a cancer cell with the following median features: $k = 0.18$, $\alpha = 3.66$, $g = 17$. Consequently, we define a typical tumor-initiating cancer stem cell (TICSC) as a TICC with completely undifferentiated status: $k = 0$, $\alpha = 3.66$, $g = 17$. Using the features of a typical TICC, simulation of the fate of 10,300 TICC showed a 71.7% probability that they will spawn a tumor, while the corresponding TICSC had roughly a 94% probability.

DISTRIBUTIONAL ANALYSIS OF THE HETEROGENEITY OF A TUMOR FORMED BY A TICC

The primary tumor formed from a TICC is a heterogeneous mass of cells. Continuous proliferation of cancer cells have resulted

in the accumulation of an increasing number of genetic mutations and produced a cancer cell population with an enormous genetic diversity, which will drive further tumor evolution and progression. This genotypic and phenotypic variability increases the difficulty for a therapeutic intervention, such as targeted therapies aiming at a specific genetic alteration, to kill all cancer cells. A distributional analysis of a single tumor formed from a TICC was performed in order to analyze the spectrum of phenotypes and overall properties of the tumor. **Table 4** describes the division number d of each cell within the clinically detectable mass, that is, the number of divisions that have passed between the cell and the initial progenitor cell. Note that most cells possess at least $d = 30$, with a median value of $d = 44$, indicating that almost all cancer cells in a tumor are immortalized.

The intra-tumor heterogeneity is also illustrated by the distribution of k -values within the mass. A terminally differentiated cell will typically have a $k \approx 4.0$, indicating a strong capability to maintain homeostasis. However, **Table 5** shows that the median k -value within the mass is only 0.3, with no values above 1.7, illustrating the de-differentiation (malignant transformation) that the cells have undergone. Interestingly, there are approximately 7% of cancer cells with $k = 0$, indicating that they are completely undifferentiated, and are the cancer stem cell portion in the tumor (see Evolution of low k -values in the mass in Appendix). Finally, we consider the heterogeneity in cell proliferation through analysis of the distribution of proliferation potential among cancer cells within the mass in **Table 6**. We observe that 98% of cells are proliferative [$\alpha(t) > 0$], with a median value of $\alpha = 10.3$.

ANALYSIS OF THE MEDIAN PROPERTIES OF TUMORS FORMED BY TICC AND TICSCs

We extend the above analysis to 500 tumors generated from TICC. The median properties of each tumor are recorded, and the distribution of these values is then analyzed. **Table 7A** lists statistical information for the median properties of the 500 tumors produced by TICC, with corresponding histograms presented in the **Figures A3(A)–(C)** in Appendix. Based on this information, we define a median cancer cell (MCC) in a clinically detectable tumor as a cell with the properties: $k = 0.295$, $\alpha = 10.3$, $g = 45$.

The tumors appear to be very similar with respect to median proliferation potentials and division numbers, both of which have statistical properties similar to normal distributions. However, the distribution of median k -values deserves more attention. Whereas most tumors had median k -values similar to the single TICC tumor examined above (median and mean of k around 0.3), some of the median values are significantly lower, approaching $k = 0$. These tumors are poorly differentiated and particularly aggressive, with the capability to undergo rapid proliferation when receiving environmental stimulation conducive to growth. For the purpose of controlled comparison, we define a median cancer stem cell (MCSC) in a clinically detectable tumor as a MCC with a completely undifferentiated feature: $k = 0$, $\alpha = 10.3$, $g = 45$.

A similar analysis was performed on 500 tumors spawned from TICSCs, with distributions for the median properties presented in **Table 7B** and illustrated as histograms in the **Figures A4(A)–(C)** in Appendix.

COMPARISON OF THE MEDIAN PROPERTIES OF TUMORS AMONG THOSE FORMED BY A TICC VS. TICSC

The types of distributions derived from the median properties from the 500 tumors are unknown. However, the non-parametric two-sample Kolmogorov–Smirnov test (Hollander and Wolfe, 1999) can be utilized to examine whether the empirical distributions of a specific property are statistically equivalent among primary tumors formed from either a TICC or TICSC.

The distributions of median values of k , α , and d among tumors formed by TICC were tested against the corresponding distributions among tumors formed from TICSCs. In each case, we find that the null hypothesis can be rejected to at least a 99% confidence (α : $p = 0.00428$, k : $p = 1.3 \times 10^{-157}$, d : $p = 9.5 \times 10^{-17}$). We conclude that a qualitative difference exists between tumors formed from a cancer cell as compared to those formed from a cancer stem cell. However, it should be noted that the median of the median properties appear to be similar for the primary tumors regardless of whether they were spawned from a TICC or TICSC.

DISCUSSION

Carcinogenesis as an evolutionary consequence can be viewed as the result of environmental selection among billions of genetically

Table 4 | d -Value cdf for cancer cells in a clinically detectable tumor.

d_0	28	30	32	34	36	38	40
$\Pr(d \leq d_0)$	1.34E–5	8.81E–5	6.28E–4	2.89E–3	1.18E–2	4.11E–2	0.126
d_0	41	42	43	44	45	46	47
$\Pr(d \leq d_0)$	0.207	0.328	0.489	0.673	0.818	0.927	0.993

Table 5 | k -Value cdf for cancer cells in a clinically detectable tumor.

k_0	0	0.1	0.2	0.3	0.4	0.5	0.6	0.7	0.8
$\Pr(k \leq k_0)$	0.0695	0.210	0.351	0.500	0.641	0.762	0.857	0.922	0.962
k_0	0.9	1.0	1.1	1.2	1.3	1.4	1.5	1.6	1.7
$\Pr(k \leq k_0)$	0.984	0.994	0.998	0.9994	0.99986	0.99996	0.999991	0.999999	1

Table 6 | α -Value cdf for cancer cells in a clinically detectable tumor.

α_0	-7.5	-5	-2.5	0	2
$\Pr(\alpha \leq \alpha_0)$	8.33E-5	1.50E-3	6.25E-3	1.91E-2	4.26E-2
α_0	4	5	6	7	8
$\Pr(\alpha \leq \alpha_0)$	8.72E-2	0.120	0.163	0.216	0.280
α_0	9	10	11	12	13
$\Pr(\alpha \leq \alpha_0)$	0.359	0.451	0.556	0.669	0.784
α_0	14	15	16	17	18
$\Pr(\alpha \leq \alpha_0)$	0.883	0.954	0.989	0.9992	1

Table 7 | Properties of the distributions of median values of cancer cells among 500 tumors derived from (A) TICC and (B) TICSC.

Property	Median	Mean	SD	Skewness	Kurtosis
(A)					
k	0.295	0.271	0.0672	-2.34	6.87
α	10.3	10.326	0.236	7.10E-4	3.15
d	45	44.978	1.90	0.484	2.96
(B)					
k	0.31	0.297	0.0469	-4.13	18.72
α	10.4	10.36	0.207	0.0835	3.42
d	43	43.92	1.79	1.63	7.39

diverse cells in a tissue. Theoretical approaches have the unique strength of modeling the behavior of individual cells in a tissue and to construct the landscape of a dynamic and diverse cell population in order to identify and define a much smaller spectrum of cancer cells. This prospective strategy is necessary and should be complementary to the common biological approach to characterize the decisive role of a single or a few genetic alterations.

We have developed a mathematical model to simulate evolution in an epithelial tissue with an individual cell as the basic member and the entire tissue as the population. This model is unique in that it assigns quantitative value (due to varying m_i) to genetic features in each individual cell and a quantitative value (α) of growth advantage translated from combined effect of genetic features $\left(\sum_{i=1}^n m_i\right)$ and environmental factors (β) in a single cell at a given time. Hormone level (β), the dominant environmental factor in uterine epithelium, is fixed at a level typical for the majority of menopausal women. The influence of these environmental factors will be further explored in a future manuscript.

Our simulations have shown that a rate of two random mutations per cell division has the potential to provide sufficient genetic diversity for enabling evolution among the simulated uterine epithelial cells. The rare event of immortalization and malignant transformation is observed when the simulation has been performed for a sufficiently large number of progenitor cells with the resultant cancer incidence comparable to the level found in epidemiological data. Our model of normal cells in the uterine epithelium gives phylogenetic context to the clonal progression of a TICC into a clinically detectable tumor and, more generally, simulates the longitudinal and prospective process of tumor development, including evolution in a normal cell population, the birth

of the TICC and formation of a tumor. Cancer cells and cancer stem cells are defined based on their major features which distinguish them from normal (non-cancer) cells such as the status of de-differentiation (k -value), uncontrolled proliferation (α value), and immortalization (g value). Since all these three criteria are quantitatively expressed, a meaningful definition of cancer cells and cancer stem cells at the single cell level and of a tumor at the clinical level can be derived by their probability to form a tumor and a metastatic lesion in defined environmental conditions. The empirical and pathological terms of benign tumor, precancerous lesion, well-differentiated tumor (good outcome), and poorly differentiated cancer can be quantitatively and progressively described by the probability for tumor progression and development of metastatic diseases under a specific genetic and environmental set of conditions. Furthermore, interaction of genetic factors (m_i) and environmental factors (β) can be quantitatively studied along a timeline to determine their combined effect (probability) on tumor development. Additionally, our model is built upon the description of single cells, and can thus be used to describe intra-tumor heterogeneity based upon features of individual cells. Description of cell-specific features is important to understand the heterogeneous nature of a tumor and to identify the cells with the greatest potential for metastasis. While the difference in heterogeneity between tumors can be described statistically as we did in Section “Comparison of the Median Properties of Tumors Among Those Formed by a TICC vs. TICSC,” documentation of the features of individual cells, such as immortalization, proliferation, and de-differentiation, also allows investigation of the malignant potential of individual cells, for instance, to investigate the difference in metastatic potential between a cancer stem cell and a non-stem cancer cell.

This manuscript is primarily focused on the understanding of genetic diversity in evolution. The important role of environmental factors in the selection of cells with fitness has not been presented, and remains a relevant subject for this model. Additionally, our model remains a single cell model which should be further developed to include terms to address cell-cell interactions and the role of tissue structure. For instance, angiogenesis and the molecular mechanisms underlying migration of cancer cells from the primary tumor are extremely important factors to determine cancer cell migration dynamics and the efficacy of metastasis.

Taken together, our model has provided a novel approach to demonstrate genetic diversity and evolutionary dynamics in a normal cell population at the earliest stage of oncogenesis. Cell-specific description of genotypes and phenotypes has also provided a potentially powerful tool to quantitatively analyze and understand the evolutionary process in tumor development.

ACKNOWLEDGMENTS

The authors would like to thank Ben Rogers, David Eichmann, and the Institute for Clinical and Translational Science (ICTS) at the University of Iowa Carver College of Medicine for the generous use of computing resources. This work was partially supported by the University of Iowa Department of Obstetrics and Gynecology Basic Research Fund.

REFERENCES

- Araten, D. J., Golde, D. W., Zhang, R. H., Thaler, H. T., Gargiulo, L., Notaro, R., et al. (2005). A quantitative measurement of the human somatic mutation rate. *Cancer Res.* 65, 8111–8117.
- Dai, D., Beck, B. B., Wang, X., Howk, C., and Li, Y. (2011). Quantitative interpretation of a genetic model of carcinogenesis using computer simulations. *PLoS ONE* 6:e16859. doi:10.1371/journal.pone.0016859
- Elmore, E., Kakunaga, T., and Barrett, J. C. (1983). Comparison of spontaneous mutation rates of normal and chemically transformed human skin fibroblasts. *Cancer Res.* 43, 1650–1655.
- Fearon, E. R., and Vogelstein, B. (1990). A genetic model for colorectal tumorigenesis. *Cell* 61, 759–767.
- Gallo, M. L., O'Hara, A. J., Rudd, M. L., Urlick, M. E., Hansen, N. F., O'Neil, N. J., et al. (2012). Exome sequencing of serous endometrial tumors identifies recurrent somatic mutations in chromatin-remodeling and ubiquitin ligase complex genes. *Nat. Genet.* 44, 1310–1315.
- Hanahan, D., and Weinberg, R. A. (2011). Hallmarks of cancer: the next generation. *Cell* 144, 646–674.
- Hollander, M., and Wolfe, D. A. (1999). *Nonparametric Statistical Methods*. New York: Wiley-Interscience.
- Jones, S., Chen, W. D., Parmigiani, G., Diehl, F., Beerewinkel, N., Antal, T., et al. (2008a). Comparative lesion sequencing provides insights into tumor evolution. *Proc. Natl. Acad. Sci. U.S.A.* 105, 4283–4288.
- Jones, S., Zhang, X., Parsons, D. W., Lin, J. C., Leary, R. J., Angenendt, P., et al. (2008b). Core signaling pathways in human pancreatic cancers revealed by global genomic analyses. *Science* 321, 1801–1806.
- Kuhn, E., Wu, R. C., Guan, B., Wu, G., Zhang, J., Wang, Y., et al. (2012). Identification of molecular pathway aberrations in uterine serous carcinoma by genome-wide analyses. *J. Natl. Cancer Inst.* 104, 1503–1513.
- Liang, H., Cheung, L. W., Li, J., Ju, Z., Yu, S., Stemke-Hale, K., et al. (2012). Whole-exome sequencing combined with functional genomics reveals novel candidate driver cancer genes in endometrial cancer. *Genome Res.* 22, 2120–2129.
- Weinberg, R. A. (2007). “The nature of cancer,” in *The Biology of Cancer*, ed. R. A. Weinber (New York: Garland Science), 25–56.
- Conflict of Interest Statement:** The authors declare that the research was conducted in the absence of any commercial or financial relationships that could be construed as a potential conflict of interest.

Received: 01 November 2012; accepted: 07 March 2013; published online: 05 April 2013.

Citation: Howk CL, Voller Z, Beck BB and Dai D (2013) Genetic diversity in normal cell populations is the earliest stage of oncogenesis leading to intra-tumor heterogeneity. *Front. Oncol.* 3:61. doi: 10.3389/fonc.2013.00061

This article was submitted to *Frontiers in Molecular and Cellular Oncology*, a specialty of *Frontiers in Oncology*.

Copyright © 2013 Howk, Voller, Beck and Dai. This is an open-access article distributed under the terms of the Creative Commons Attribution License, which permits use, distribution and reproduction in other forums, provided the original authors and source are credited and subject to any copyright notices concerning any third-party graphics etc.

APPENDIX

RESULTS

Cells within the tumor that are not descendant from MRCA(0.995)

There are a few cells remaining in the developed tumor that are descendant from early branch points during the development of the mass (**Figure A1(A)** in manuscript). All other cells are from the main branch forming the tumor, with the branch point spawning the tumor found to be MRCA(0.995). Among the 74 tumors under analysis, the number of cells not emanating from the main branch was found to range from 38 to 728, with a median value of 244.824. These cells have undergone between 11 and 12 divisions, with a median of 11.0196 (**Figure A1(A)**). Their k -values are quite high (**Figure A1(B)**), and values range from 2.64 to 4.45, with a median of 3.37. These cells are following the inherent physiological lifespan, and are near the point of senescence. They are undergoing or preparing to undergo apoptosis. This is evidenced by their proliferation potentials (**Figure A1(C)**) which ranges from -3.37 to 0.164 with a median value of -0.44 . These “remnant” cells are

still following the normal status of development and will soon die out.

Evolution of low k -values in the mass

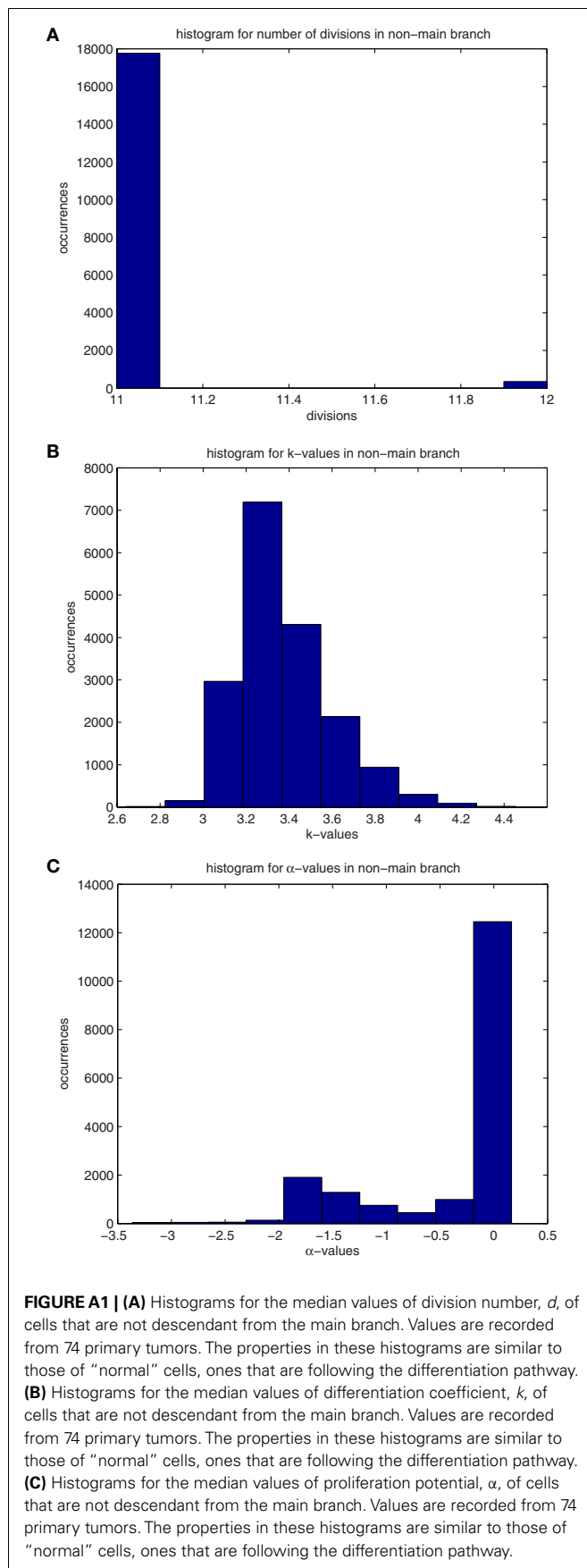
The evolution of low k -values within the mass as it develops is illustrated by quantile plots in **Figure A2**, where the quantiles are determined based on the proportion of the tumor with these low k -values at the time the mass reaches 106 cells. After these low k -values appear, they quickly (over a period of approximately 1 month) form subpopulations comprising roughly 25% of the mass. This evolution is likely occurring within the dominant subpopulation that is driving the formation of the tumor. We find that roughly 7% of the mass will comprise cells with $k = 0$, cells that have lost all draw toward behavior inherent to the pathway and thus have stem cell-like behavior, with approximately 13% having $k < 0.033$ and 18% having $k < 0.067$. Moreover, the dynamic nature of the composition of the tumor during its early development is illustrated in **Figure A2**.

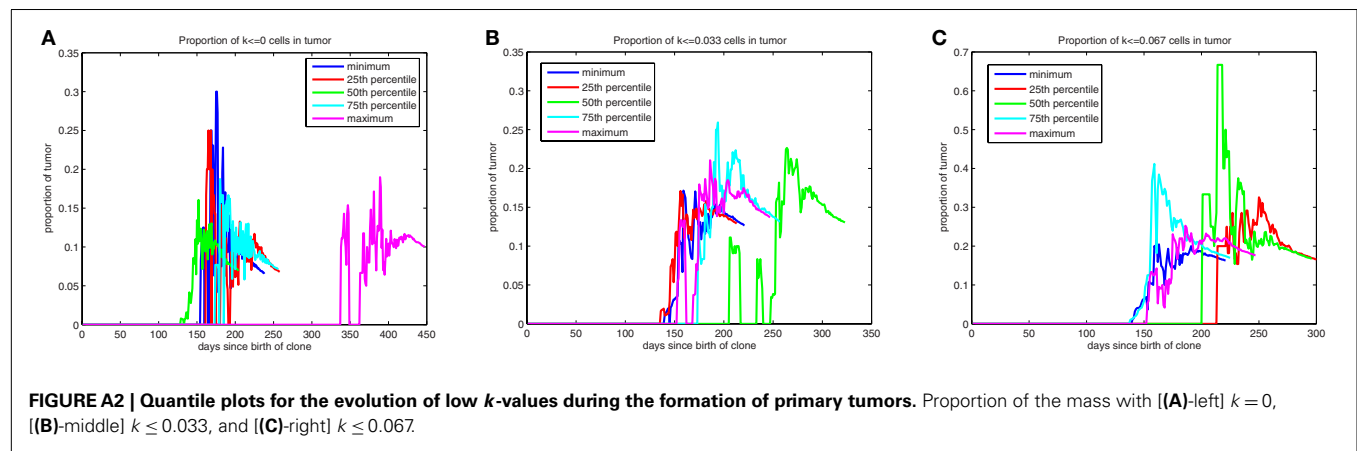
Table A1 | Data for the max sizes of masses that eventually die out.

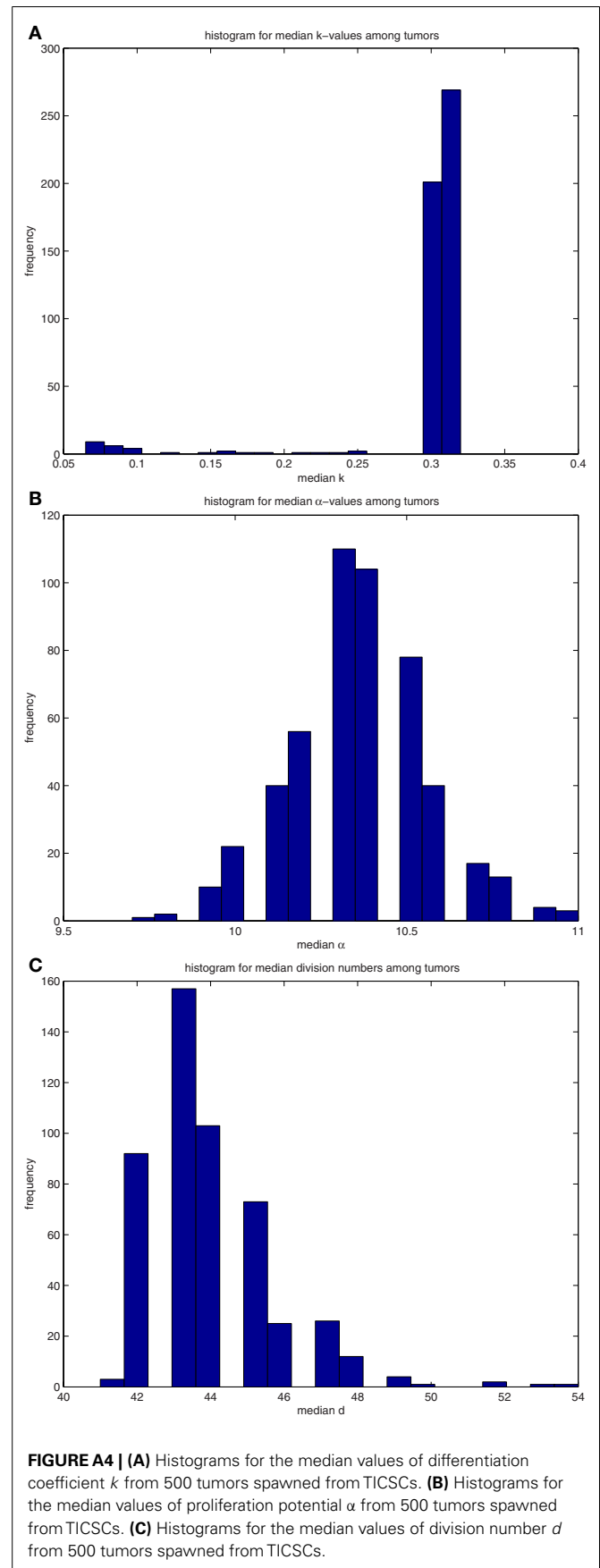
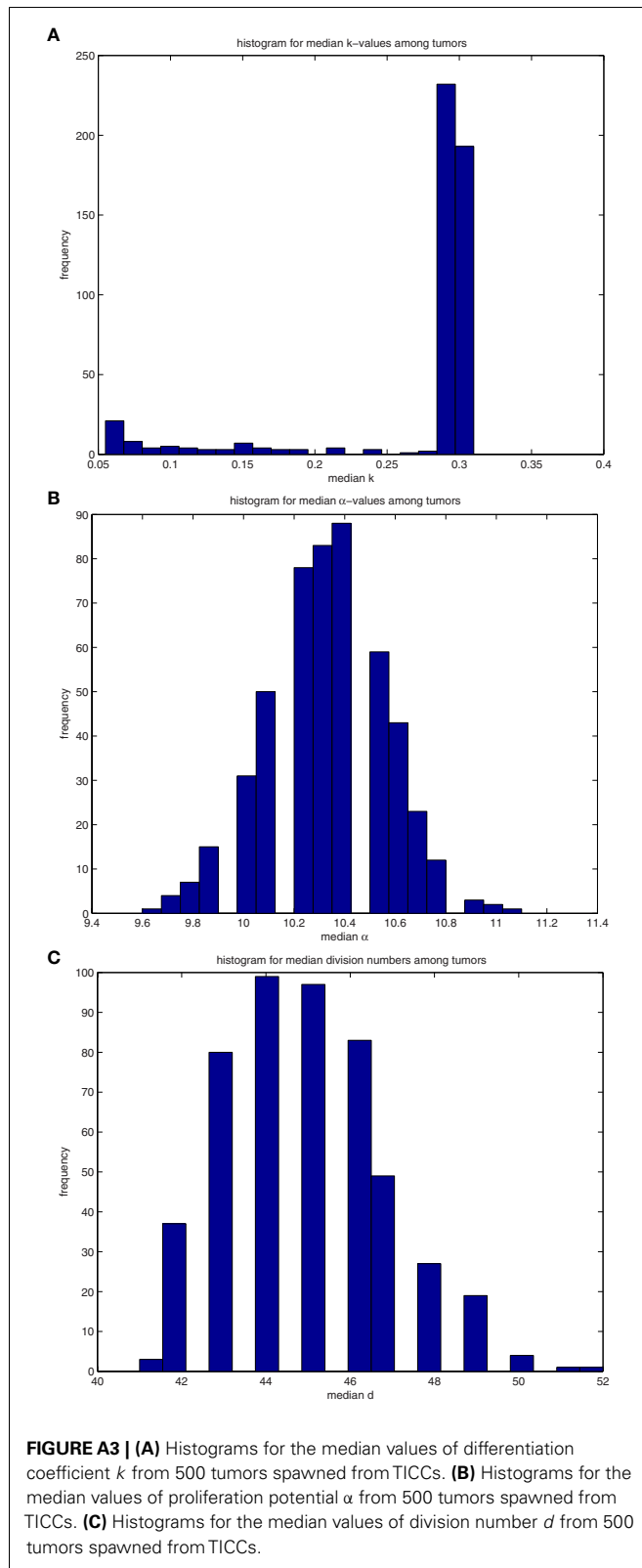
Experiment	Median	Mean	SD	Skewness	Kurtosis
A	5	16496.5	83716.5	6.78706	52.5286
B	5	13981.3	75298.7	7.90778	75.1809
C	5865	123907	220817	2.04835	6.35482

Table A2 | Proportion of masses with max sizes surpassing thresholds.

Experiment	10 K	50 K	100 K	200 K	300 K	400 K	500 K	600 K	700 K	800 K	900 K
A	0.092	0.053	0.042	0.024	0.02	0.015	0.013	0.008	0.005	0.001	0
B	0.08	0.05	0.038	0.023	0.014	0.01	0.009	0.005	0.003	0.002	0.002
C	0.47	0.35	0.287	0.211	0.157	0.122	0.094	0.069	0.042	0.025	0.01









Stochastic hypothesis of transition from inborn neutropenia to AML: interactions of cell population dynamics and population genetics

Marek Kimmel^{1,2*} and Seth Corey^{3,4}

¹ Department of Statistics, Rice University, Houston, TX, USA

² Department of Bioengineering, Rice University, Houston, TX, USA

³ Department of Pediatrics, Feinberg School of Medicine, Northwestern University, Chicago, IL, USA

⁴ Department Cell and Molecular Biology, Feinberg School of Medicine, Northwestern University, Chicago, IL, USA

Edited by:

Heiko Enderling, Tufts University
School of Medicine, USA

Reviewed by:

Stephan Von Gunten, University of
Bern, Switzerland

Rainer K. Sachs, University of
California at Berkeley, USA

*Correspondence:

Marek Kimmel, Department of
Statistics, Rice University, 6100 Main
Street, Houston, TX 77005, USA.
e-mail: kimmel@rice.edu

We present a stochastic model of driver mutations in the transition from severe congenital neutropenia to myelodysplastic syndrome to acute myeloid leukemia (AML). The model has the form of a multitype branching process. We derive equations for the distributions of the times to consecutive driver mutations and set up simulations involving a range of hypotheses regarding acceleration of the mutation rates in successive mutant clones. Our model reproduces the clinical distribution of times at diagnosis of secondary AML. Surprisingly, within the framework of our assumptions, stochasticity of the mutation process is incapable of explaining the spread of times at diagnosis of AML in this case; it is necessary to additionally assume a wide spread of proliferative parameters among disease cases. This finding is unexpected but generally consistent with the wide heterogeneity of characteristics of human cancers.

Keywords: severe congenital neutropenia, myelodysplastic syndrome, acute myeloid leukemia, branching process, driver mutations, clonal evolution

INTRODUCTION

Granulocytes are essential for host defense and survival. Their importance is apparent in severe congenital neutropenia (SCN). Life-threatening infections in children with SCN can be avoided through the use of recombinant granulocyte colony-stimulating factor (G-CSF). However, SCN often transforms into secondary myelodysplastic syndrome (sMDS) and then into secondary acute myeloid leukemia (sAML). A great unresolved clinical question is whether chronic, pharmacological doses of G-CSF contribute to this transformation (Glaubach and Corey, 2012). A number of epidemiological clinical trials have demonstrated a strong association between exposure to G-CSF and sMDS/sAML (Dong et al., 1995; Donadieu et al., 2005; Rosenberg et al., 2006; Germeshausen et al., 2007; Carlsson et al., 2012). Mutations in the distal domain of the G-CSF Receptor (G-CSFR) have been isolated from patients with SCN who developed sMDS/sAML or patients with *de novo* MDS (Beekman and Touw, 2010). Most recently, clonal evolution over approximately 20 years was documented in a patient with SCN who developed sMDS/sAML (Beekman et al., 2012). Clonal evolution of a sick hematopoietic progenitor cell in SCN involves perturbations in proximal and distal signaling networks triggered by a mutant G-CSFR. Transition from SCN → sMDS → sAML involves chance mechanisms such as mutations, drift and transcription, and receptor noise, which require that stochastic models are needed (Whitchard et al., 2010).

In the present paper we use stochastic modeling to understand the wide range of times at which the transition to sAML occurs. We develop a model in the form of a multitype branching process, which allows one tying population genetics and

population dynamics aspects of the transition from SCN to sMDS to sAML, and validating it against existing evidence. Branching processes have been used widely to model mutation, selection, and drift processes in populations of variable size, to which the classical Wright–Fisher model does not apply (Cyran and Kimmel, 2010). We adopted approach similar to that developed in Nowak's group (Bozic et al., 2010), modified to bring out stochastic time intervals between successive driver mutations.

The model we developed allows predicting the time at transition to sAML given the probability of each successive driver mutation, the number of mutations needed, and the proliferative potential of each successive mutated clone of hemopoietic stem cells. We can then compare these times to observed distribution of times at transition. As documented in the paper, the outcome is intriguing: stochasticity inherent in the mutation process is insufficient to explain the wide distribution of times at transition (ranging from 1 to 38; **Table 1**). Additional factors are required, one of which may be a wide interpatient spread of proliferative potential of the mutant clones.

POPULATION GENETICS AND POPULATION DYNAMICS MODEL OF THE SCN → sMDS → sAML TRANSITION

Missense, nonsense, and frameshift mutations, and dysregulated alternative splicing in G-CSFR have been isolated in patients with MDS/AML. In the study of Beekman et al. (2012), nonsense and missense mutations in G-CSFR arose during the course of the disease. In the model we envision, population genetics, and population dynamics of proliferating bone marrow cells are closely intertwined.

Table 1 | Summary of life histories of patients transitioning from severe congenital neutropenia (SCN) to secondary myelodysplastic syndrome (sMDS) to secondary acute myeloid leukemia (sAML) (Walter et al., 2012).

Phase of disease	Age at diagnosis (years)	Number of co-existing mutations
SCN	0–0.5	1*
MDS	1–12	1–3 \pm chromosomal loss or gain**
AML	2–38	1–9 \pm chromosomal loss or gain***

*ELANE, HAX1, G6PC, WAS, CSF3R.

**GCSF3R, ZC3H18, LLGL2; RAS \pm monosomy 7.

***RUNX1, ASXL1, p300, CEBA, CSF3R, MGA, SUZ12, LAMB, FBXO18, CCDC15, \pm monosomy 7, trisomy 21.

POPULATION GENETICS PERSPECTIVE

Proliferating healthy cells in the bone marrow mutate at random times, possibly influenced by super-pharmacological doses of GCSF. A summary of possible mutations and their consequences for proliferation dynamics of granulocyte precursors is depicted in **Figure 1**. GCSF signaling occurs through its cognate receptor, GCSFR. It involves both proximal signaling networks consisting of signaling molecules such as Lyn, Jak, STAT, Akt, and ERK, and distal gene regulatory networks consisting of transcription factors. Together, these signaling networks promote proliferation, survival, and differentiation. In patients with SCN, the earliest known mutation to contribute to transformation to secondary MDS or AML is a nonsense mutation in the GCSFR gene. This mutation leads to a truncated receptor, GCSR delta 715 (Glaubach and Corey, 2012, and reference therein).

It follows from a simple calculus of mutation events that as long as the cell population size is kept in check, the rate at which new mutant clones appear in the population is rather low. When the population expands, new mutant clones arise faster (see further on).

In our model we take the view that carcinogenesis is driven by a succession of small-scale (e.g., point) mutations in specific loci. Other viewpoints (epigenetic effects, karyotypic alterations, intercellular interactions, etc.) have been suggested. In treatment-related MDS some drugs (e.g., many alkylating agents) induce t-MDS primarily via large scale alterations that lead to karyotypic instability (Bhatia, 2011).

POPULATION DYNAMICS PERSPECTIVE

Limited mutation load at the SCN phase causes neutropenia and fluctuations of cell population size. With time, accumulation of driver mutations causes expansion of mutant clones, which however are not yet expanding at a dramatic rate. At some point in time, mutations accumulate sufficiently to cause a major change in the proliferation law and the now malignant cell population starts rapidly expanding.

Our model is based on the following hypotheses (**Figure 2**):

1. At the time of diagnosis of SCN, GCSF therapy is initiated, which induces an initial series of X driver mutations, occurring at random times.

2. The X -th mutation causes transition to the MDS, during which further Y mutations occur.
3. After $X + Y$ mutations, the AML stage begins, during which the subsequent mutant clone grow at increasing rate, which in turn shortens times at which still new mutations appear.

In the model, the increasing proliferation rate of successive mutant clones causes acceleration of growth of the malignant bone marrow stem cell population, which shortens the time interval to appearance of new clones, which in turns increases proliferation rate, and so forth; this results in a positive feedback. As we will see, the stochastic nature of the process (the times to appearance of each next mutant are random) causes a spread of the timing of the subsequence mutations, particularly the first X mutations during the SCN phase. This may result in the transition to MDS not manifesting itself for a very long time in a fraction of cases.

ROLE OF STOCHASTIC DYNAMICS IN THE MODEL

We explain some other intuitions underlying the model. For a new subclone, stochastic theory is used to estimate extinction probability, with extinction after more than a few cell generations being negligible in view of the growth advantage of the new clone. However the time at which the next mutation occurs in a cell clone is also stochastic and it is as a rule more dispersed for the slower-growing clones. Therefore the time to reaching the threshold number of bone marrow stem cells (which in our model defines the time at sAML diagnosis), is a random variable. One of the questions we ask is if dispersion of this time matches the wide distribution of the times at diagnosis (Rosenberg et al., 2010).

MATERIALS AND METHODS

MATHEMATICS OF THE MODEL

The population-genetic effect of population size-dependent accumulation of mutations occurs as a natural consequence of the proliferation law in the form of a multitype Galton–Watson branching process:

1. Consecutively arising surviving mutant clones are numbered with the index k , ranging from 1 to K ; time interval between the appearance of the k -th and $k + 1$ -st surviving mutant clones is denoted by τ_k . k -th mutant cells have accumulated k driver mutations (assuming the clone in SCN bone marrow at diagnosis has a single cell with one driver mutation, which seems a defensible idealization).
2. All clones expand as Galton–Watson branching processes (see further on). Cell life length is constant and equal to T , and at that time the cell either produces two progeny with probability b_k (cell type k) or dies (or becomes quiescent or differentiated, which does not make a difference for disease dynamics) with probability $1 - b_k$.
3. A cell of type k can mutate upon its birth (for definiteness) to type $k + 1$ with probability u .

These three rules allow one derive the probability distributions of time intervals τ_k , probabilities of survival of each clone, and expected growth laws of each clone. Mathematical details follow from the theory of Galton–Watson branching process; see for example the monograph by Kimmel and Axelrod (2002).

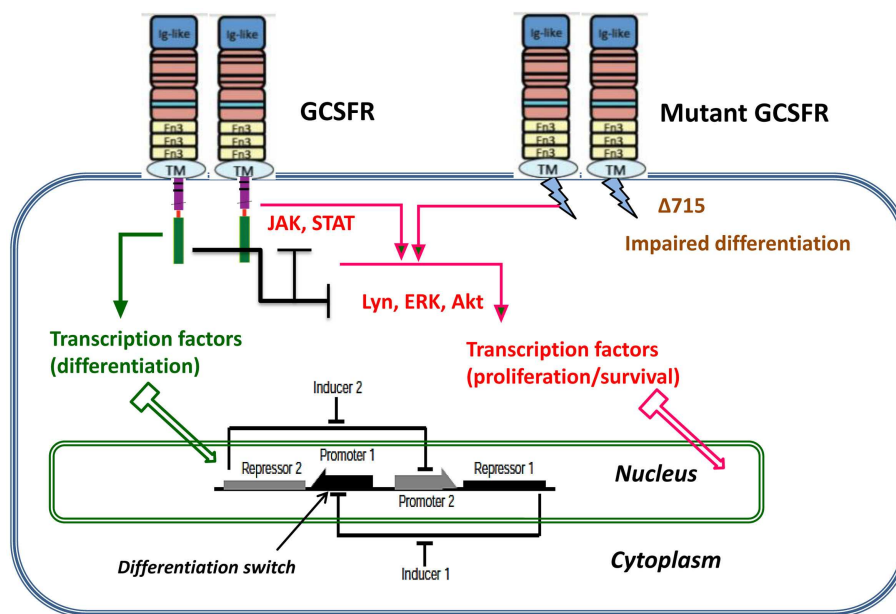


FIGURE 1 | Dynamic stochastic model of impaired differentiation in granulocyte precursors. GCSF signaling occurs through its cognate receptor, GCSFR. It involves both proximal signaling networks consisting of signaling molecules such as Lyn, Jak, STAT, Akt, and ERK, and distal gene regulatory networks consisting of transcription factors. Together,

these signaling networks promote proliferation, survival, and differentiation. In patients with severe congenital neutropenia, the earliest known mutation to contribute to transformation to secondary MDS or AML is a nonsense mutation in the GCSFR gene. This mutation leads to a truncated receptor, GCSFR delta 715.

We assume that cell division is effective with probability b , i.e., the probability generating function (pgf) of the number of progeny cells per parent cell has the form $f(s) = bs^2 + (1 - b)$. The extinction probability q is the smaller solution of the equation $q = f(q)$, which is less than 1 if the process is supercritical. In our case,

$$q = bq^2 + (1 - b) \Rightarrow q = (b^{-1} - 1); \quad b \in (0.5, 1]. \quad (1)$$

Similarly, the expected number of progeny of a cell is equal to $f'(1) = 2b$, hence the expected number of cells at time t is equal to $N(t) = (2b)^{(t/T)}$, which yields the value of λ

$$\exp(\lambda t) = (2b)^{(t/T)} \Rightarrow \lambda = \ln(2b)/T. \quad (2)$$

We will use “continuous” time t for notational convenience. However, we consider generations of cells dividing at discrete times $t_i = iT$, where T is the average cell cycle time. As it is known, the expected (mean) growth law in the Galton–Watson process has the form

$$E[\text{\# cells, at time } t, \text{ in a clone started at time } t_0] \stackrel{\text{def}}{=} [N(t) = \exp(\lambda(t - t_0))], \text{ as } t \rightarrow \infty. \quad (3)$$

To determine the distribution of time to a mutation creating a new non-extinct clone, we consider a newborn cell. In this cell, mutation may occur with probability u , and if the extinction probability of the mutant clone is q' , then the probability that the cell does not produce a new mutant clone is equal

to $1 - u(1 - q')$. Until time $t_i = iT$, approximately $\sum_{j=0}^i N(t_j) = N(t_0) (\exp(\lambda T)^{i+1} - 1) (\exp(\lambda T) - 1)^{-1}$ new cells are born, and assuming independence, we obtain

$$\begin{aligned} \Pr[\text{no mutant initiating nonextinct clone appears until time } t_i = iT] \\ &= \Pr[\tau =: \text{time to nearest nonextinct mutant clone} > t_i = iT] \\ &= (1 - u(1 - q'))^{\sum_{j=0}^i N(t_j)} \\ &= (1 - u(1 - q'))^{N(t_0) \frac{\exp(\lambda T)^{i+1} - 1}{\exp(\lambda T) - 1}} = a^{d(\exp(\lambda T) - 1)}. \end{aligned} \quad (4)$$

where, for the k -th mutant population

$$\begin{aligned} a &= (1 - (1 - q_{k+1}) u_k) = (1 - u_k (2b_{k+1} - 1) / b_{k+1}), \\ c &= \lambda_k = \ln(2b_k) / T, \\ d &= (\exp(\lambda_k T) - 1)^{-1} = (2b_k - 1)^{-1}. \end{aligned}$$

Since the distribution tail of random variable τ_k has the form

$$\Pr[\tau_k > \tau] = a^{d(\exp(\lambda_k \tau) - 1)} = \exp(-\ln(a^{-1}) d (\exp(\lambda_k \tau) - 1)).$$

it can be algorithmically generated using the inverse tail method

$$\tau_k = c^{-1} \ln(\ln r / (d \ln a) + 1), \quad (5)$$

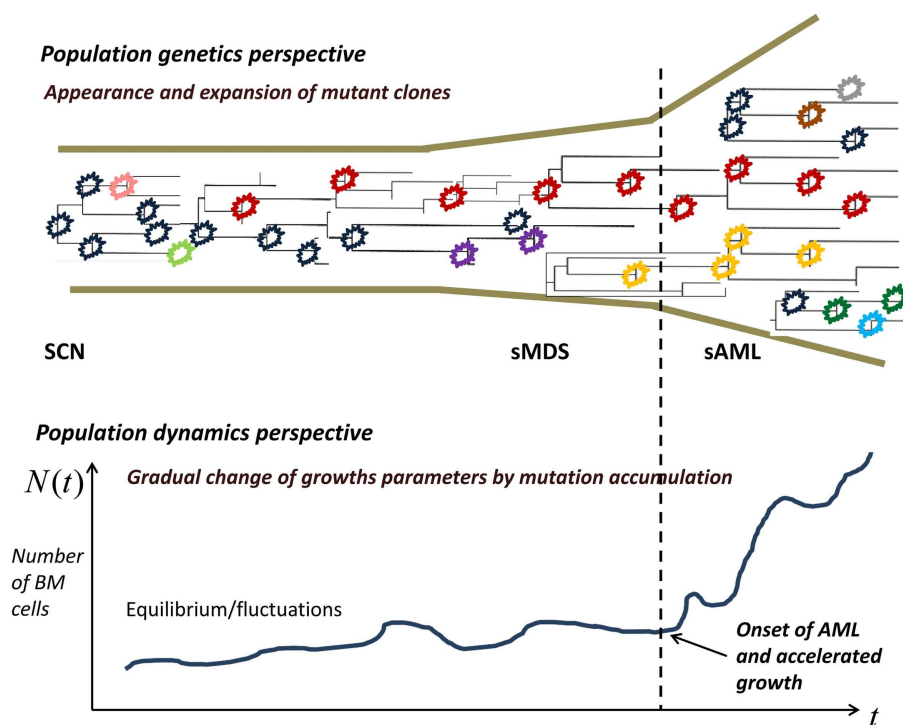


FIGURE 2 | Proliferating healthy cells in the bone marrow mutate at random times, possibly influenced by super-pharmacological doses of G-CSF. As long as the cell population size is kept in check, genetic drift, and selection remove many of the mutants, whereas some mutants

persist. When the population expands, new mutant clones become more easily established. At some point, a qualitative change in the proliferation rate occurs and the now malignant cell population starts rapidly expanding.

where r is a pseudo-random number uniformly distributed from 0 to 1. In this framework, a sample path of the number of cells in the k -th mutant clone (which contains cells with k mutations accumulated) is equal to

$$N_k(t) = \begin{cases} 0 & t \leq \sum_{j=1}^{k-1} \tau_j \\ \exp\left(\lambda_k \left(t - \sum_{j=1}^{k-1} \tau_j\right)\right) & \text{otherwise} \end{cases} \quad (6)$$

The derivations presented are quite similar to those of Bozic et al. (2010), except that in that paper, expected times $E(\tau_k)$ to the next mutation have been used. Here, we are interested in exposing stochastic variability in the time course of the SNC \rightarrow sMDS \rightarrow sAML transition. Another refinement would be to use distributions of cell counts instead of expected values $N_k(t)$. This would result in serious computational problems, arguably without much impact on the results.

MODELING THE SNC \rightarrow sMDS \rightarrow sAML TRANSITION

Equations 1 and 2 allow generating realizations of times to successive driver mutations under different values of mutation rates and proliferative characteristics of the mutant clones. We make the following assumptions:

1. Transition to sMDS requires one or two somatic driver mutations, whereas the transition to sAML requires at least three somatic driver mutations (cf. Table 1).

2. Diagnosis of sAML requires presence of 10^4 leukemic HSC. For details of computations leading to this estimate, see further on.
3. Successive mutant clones have increasing proliferative potential. We assume a power law for the coefficients b_i , which seems to lead to fits that do not contradict data:

$$b_i = \min(0.5 + A(\epsilon + (i-1)^\kappa), 1), \quad (7)$$

where coefficients A , ϵ , and κ are considered further on.

4. As it will be seen, it is necessary to assume that the coefficients A be generated from a probability distribution instead of assuming a constant value. We assume the distribution function $F_A(a)$ selected so that the times of at diagnosis of sAML fit available statistics (for details see further on).

ESTIMATE OF THE NUMBER OF LEUKEMIC CELLS

We carried out computations based on two literature sources and then used rounding to the nearest order of magnitude to obtain a working threshold number of the leukemic initiating cells (LIC) (Bonnet and Dick, 1997). In both cases we assume that the volume of human bone marrow is equal to $V = 1700$ ml and that LIC cells constitute a fraction $\psi = 10^{-6}$ of leukemic bone marrow mono-nucleated cells (BMMNC). We also assume that in sAML, fraction $\rho = 0.8$ of BMMNC is constituted by leukemic cells.

Estimate 1

Dedeeiya et al. (2012) provide an estimate of the number of BNNMC per 1 ml $B = 3.67 \times 10^6$. This results in an estimate of the number L of LIC cells in the entire bone marrow $L = \rho \times \psi \times V \times B = 4991$ cells.

Estimate 2

Bender et al. (1994) provide estimates of B in the range from 3.02×10^6 to 4.71×10^6 . This results in $L = 4107 \div 5535$ cells. These estimates are remarkably consistent. Rounding to the nearest order of magnitude results in a working estimate of $L = 10^4$ cells.

TIME AT DIAGNOSIS OF sAML AND DISTRIBUTION OF PARAMETER A

Under given values of parameters κ and ε as well as mutation rates u_k , the time at diagnosis of sAML, defined as the time T from initiation of GCSF treatment such that

$$\sum_k N_k(T) = L$$

depends on parameter A according to an approximate power law

$$T = f(A) = \exp(\alpha) A^\beta,$$

where $\beta < 0$. This dependence, which was obtained via simulation studies (not shown), allows finding the distribution of A that leads to a clinically observed distribution of the time of sAML diagnosis according to the following expression for distribution tails

$$\bar{F}_A(a) = 1 - \bar{F}_T(f(a)),$$

where $\bar{F}_T(t) = \Pr[T > t]$ is the tail of the distribution of time T . This in turn allows generating pseudo-random realizations of A according to the expression

$$A = f^{-1}(\bar{F}_T^{-1}(R)) = (\exp(-\alpha) \bar{F}_T^{-1}(R))^{1/\beta}, \quad (8)$$

where R is a pseudo-random number from the uniform distribution on the $(0, 1)$ interval.

We need to approximate the tail of the distribution of the time at diagnosis of sAML. A recent source is the paper by Rosenberg et al. (2010). These authors reported results of a prospective study of 374 SCN patients, and included estimates of hazard rates and cumulative probability of sMDS/sAML as a function of time after GCSF treatment. Hazard rate grows for the first 5 years and then plateaus. To simplify computations we adopted a piecewise constant estimate of the hazard rate $h_T(t)$

$$h_T(t) = \begin{cases} 0.01 & t \in [0, 3) \\ 0.02 & t \in [3, \infty) \end{cases}$$

with time in years. Comparing with Figure 1A in Rosenberg et al. (2010) we see that $h_T(t)$ remains within the confidence band computed based on the prospective study. Using the expression

$$\bar{F}_T(t) = \exp\left(-\int_0^t h_T(\tau) d\tau\right)$$

and inverting the tail function $\bar{F}_T(t)$ we complete the derivation of expression Eq. 8 (elementary details not shown).

OVERVIEW OF PARAMETER ESTIMATION

The form of expression Eq. 8 and plausible estimates of parameters κ and ε as well as of mutation rates u_k , are difficult to be uniquely determined with the data available at the present time. We used the following heuristic procedure:

1. Driver mutation rates increase from the reference value by a factor of 5, starting mutation 3, so that $u_{1,2} = u$ but $u_{3,4,5} = 5u$. The increase is needed for the later mutations to occur in quick succession, so that mutation 3 occurs before $\sum_k N_k(T) > L$, with $L = 10^4$ being a relatively low value.
2. Reference driver mutation rate had to be set equal to 0.00034, 10 times higher than the value estimated by Bozic et al. (2010). This is required for enough mutations to accumulate before the threshold time T .
3. Proliferation rate increases as power κ of the mutation number, value $\kappa = 2$ provides sufficient acceleration to explain relative rapidity of the AML stage. The offset parameter $\varepsilon = 0.02$ keeps proliferation rate before mutation 1 sufficiently low.
4. Once estimates of parameters u_k , κ , and ε are obtained, estimates of the power law parameters α and β are determined by a simulation study, and the generator of random parameter A is obtained via expression Eq. 8.

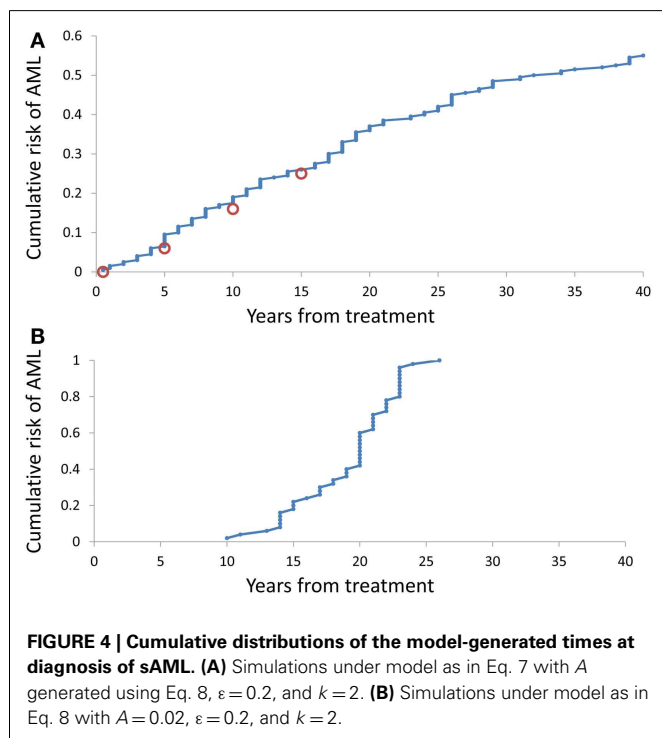
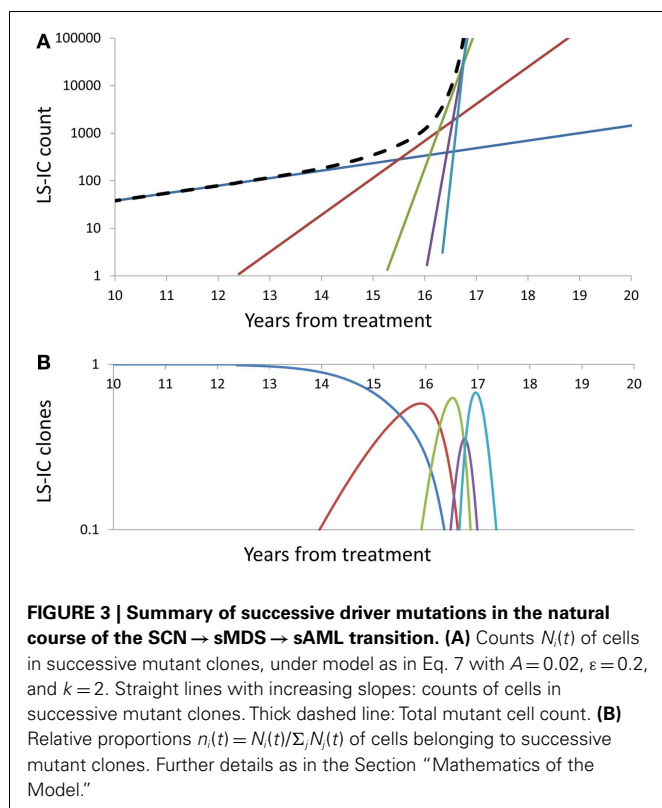
RESULTS**SIMULATED COURSE OF DISEASE**

Figure 3 depicts the impact of successive driver mutations on the natural course of the SCN \rightarrow sMDS \rightarrow sAML transition. Figure 3A depicts counts $N_i(t)$ of cells in successive mutant clones as a function of time, under model as in Eq. 7 with $A = 0.005$, $\varepsilon = 0.02$, and $\kappa = 2$. Straight lines with increasing slopes are counts of cells in successive mutant clones. We observe that the time intervals separating the origins of successive clones are decreasing with each mutation event. Thick dashed line represents the total mutant cell count. It is also interesting to observe that clones with increasing numbers of mutations dominate transiently, until they are replaced by other clones with higher proliferative capacity (selective value). Figure 3B depicts relative proportions $n_i(t) = N_i(t)/\sum_j N_j(t)$ of cells belonging to successive mutant clones.

TIME AT sAML DIAGNOSIS

It is somewhat surprising that under any combination of coefficients A and k , the range of simulated times at sAML diagnosis is rather narrow. Figure 4B depicts ranked simulated times at sAML diagnosis under model as in Eq. 7 with $A = 0.005$, $\varepsilon = 0.02$, and $\kappa = 2$. Spread of these values is narrow, with interquartile range between 15 and 21. Systematic simulation experiments demonstrate that this is the case for a wide range of A and κ parameter values. This outcome is in contrast to the wide spread of times at diagnosis summarized in Table 1 and that based on Rosenberg et al. (2010).

Simulation-estimation experiment outlined in the Methods demonstrates that distribution of simulated times (counting from initiation of GCSF treatment) at sAML (Rosenberg et al., 2010) is reproduced by our model. Figure 4A cumulative distribution



of the times at sAML diagnosis under model as in Eq. 7 with $\kappa = 2$, $\epsilon = 0.02$, and A generated from the distribution in Eq. 8 with $\alpha = -0.655$ and $\beta = -0.912$.

CONCLUSION

The process of development and replacement of leukemic clones is influenced by the processes of genetic drift and selection (Walter et al., 2012). These forces are usually analyzed by geneticists in the framework of the Wright–Fisher or coalescent model (see Discussion and references in Cyran and Kimmel, 2010). However, in the case of expanding cell clones, the more appropriate population process seems to be one of the types of branching processes; in our case, the Galton–Watson process (Kimmel and Axelrod, 2002). In the particular version of the multitype Galton–Watson process that we use, genetic drift’s mechanism is the loss of variants through extinction and selection is embodied in the principle that each next surviving clone is proliferating faster (has greater fitness).

A characteristic feature of human cancers is very wide heterogeneity with respect to extent of involvement, genotype and rate of progression, and spread (Michor et al., 2004; Hanahan and Weinberg, 2011). This is in contrast to induced animal tumors, which are relatively uniform. Secondary AML, resulting from a transition from SCN via myelodysplastic syndrome, is not an exception, with onset varying from 1 to 38 years of age and with wide variability of mutational background (Table 1). It is interesting, and we consider it a major result, that such spread of the age of onset is not due solely to stochastic nature of mutation-driven transitions, but it requires a large variability in proliferative potential from one disease case to another. Also, this distribution of coefficient A , which parameterizes the proliferative potential, is right-skewed, with slowly evolving (low- A) clones prevailing. This provides a testable hypothesis about distribution of proliferating rates in leukemic stem cell clones.

The model presented in this paper addresses certain aspects of the SNC → sMDS → sAML transition. Among other, although we might derive an expression relating the number of driver (selective) mutations to the corresponding count of accumulated passenger (neutral) mutations (similarly as it was done in Bozic et al. (2010), we do not have at our disposal sequencing data to validate such an expression. Also, we do not attempt here to fit the distribution of the age at diagnosis of the sMDS, since we are missing data on individual life histories, which would involve somatic mutation as well as sequencing data.

From the mathematical point of view, the current model is also somewhat simplified. It considers each new mutation to provide more selective advantage to the arising clone. This is in apparent disagreement with the recent observation of Beekman et al. (2012), of mutations which appear at the sMDS stage and disappear at the sAML stage. The linear structure of mutation confers desirable simplicity to modeling but is not necessarily realistic. In the framework of multitype branching processes and special processes such as Griffiths and Pakes branching infinite allele model (Griffiths and Pakes, 1988; Kimmel and Mathaas, 2010), more complicated scenarios can be gaged.

ACKNOWLEDGMENTS

Marek Kimmel was supported by the CPRIT grant RP101089 and by DEC-2012/04/A/ST7/00353 grant from the National Science Center (Poland). Seth Corey was supported by RO1-CA108992.

REFERENCES

- Beekman, R., and Touw, I. P. (2010). G-CSF and its receptor in myeloid malignancy. *Blood* 115, 5131–5136.
- Beekman, R., Valkhof, M. G., Sanders, M. A., van Strien, P. M., Haanstra, J. R., Broeders, L., et al. (2012). Sequential gain of mutations in severe congenital neutropenia progressing to acute myeloid leukemia. *Blood* 119, 5071–5077.
- Bender, J. G., Unverzagt, K., Walker, D. E., Lee, W., Smith, S., Williams, S., et al. (1994). Phenotypic analysis and characterization of CD34+ cells from normal human bone marrow, cord blood, peripheral blood, and mobilized peripheral blood from patients undergoing autologous stem cell transplantation. *Clin. Immunol. Immunopathol.* 70, 10–18.
- Bhatia, S. (2011). Role of genetic susceptibility in development of treatment-related adverse outcomes in cancer survivors. *Cancer Epidemiol. Biomarkers Prev.* 20, 2048–2067.
- Bonnet, J., and Dick, J. (1997). Human acute myeloid leukemia is organized as a hierarchy that originates from a primitive hematopoietic cell. *Nat. Med.* 3, 730–737.
- Bozic, I., Antal, T., Ohtsuki, H., Carter, H., Kim, D., Chen, S., et al. (2010). Accumulation of driver and passenger mutations during tumor progression. *Proc. Natl. Acad. Sci. U.S.A.* 107, 18545–18550.
- Carlsson, G., Fasth, A., Berglöf, E., Lagerstedt-Robinson, K., Nordenskjöld, M., Palmblad, J., et al. (2012). Incidence of severe congenital neutropenia in Sweden and risk of evolution to myelodysplastic syndrome/leukaemia. *Br. J. Haematol.* 158, 363–369.
- Cyran, K. A., and Kimmel, M. (2010). Alternatives to the Wright-Fisher model: the robustness of mitochondrial Eve dating. *Theor. Popul. Biol.* 78, 165–172.
- Dedeepiya, V. D., Rao, Y. Y., Jayakrishnan, G. A., Parthiban, J. K., Baskar, S., Manjunath, S. R., et al. (2012). Index of CD34+ cells and mononuclear cells in the bone marrow of spinal cord injury patients of different age groups: a comparative analysis. *Bone Marrow Res.* 2012, 787414.
- Donadieu, J., Leblanc, T., Bader, M., eunierB., Barkaoui, M., Fenneteau, O., Bertrand, Y., et al. (2005). Analysis of risk factors for myelodysplasias, leukemias and death from infection among patients with congenital neutropenia. Experience of the French Severe Chronic Neutropenia Study Group. *Haematologica* 90, 45–53.
- Dong, F., Brynes, R. K., Tidow, N., Welte, K., Lowenberg, B., and Touw, I. P. (1995). Mutations in the gene for the granulocyte colony-stimulating-factor receptor in patients with acute myeloid leukemia preceded by severe congenital neutropenia. *N. Engl. J. Med.* 333, 487–493.
- Germeshausen, M., Ballmaier, M., and Welte, K. (2007). Incidence of CSF3R mutations in severe congenital neutropenia and relevance for leukemogenesis: results of a long-term survey. *Blood* 109, 93–99.
- Glaubach, T., and Corey, S. J. (2012). From famine to feast: sending out the clones. *Blood* 119, 5063–5064.
- Griffiths, R. C., and Pakes, G. (1988). An infinite-alleles version of the simple branching process. *Adv. Appl. Probab.* 20, 489–524.
- Hanahan, D., and Weinberg, R. A. (2011). Hallmarks of cancer: the next generation. *Cell* 144, 646–674.
- Kimmel, M., and Axelrod, D. E. (2002). *Branching Processes in Biology*. New York: Springer.
- Kimmel, M., and Mathaes, M. (2010). Modeling neutral evolution of Alu elements using a branching process. *BMC Genomics* 11(Suppl. 1), S11. doi:10.1186/1471-2164-11-S1-S11
- Michor, F., Iwasa, Y., and Nowak, M. A. (2004). Dynamics of cancer progression. *Nat. Rev. Cancer* 4, 197–205.
- Rosenberg, P. S., Alter, B. P., Bolyard, A. A., Bonilla, M. A., Boxer, L. A., Cham, B., et al. (2006). The incidence of leukemia and mortality from sepsis in patients with severe congenital neutropenia receiving long-term G-CSF therapy. *Blood* 107, 4628–4635.
- Rosenberg, P. S., Zeidler, C., Bolyard, A. A., Alter, B. P., Bonilla, M. A., Boxer, L. A., et al. (2010). Stable long-term risk of leukaemia in patients with severe congenital neutropenia maintained on G-CSF therapy. *Br. J. Haematol.* 150, 196–199.
- Walter, M. J., Shen, D., Ding, L., Shao, J., Koboldt, D. C., Chen, K., et al. (2012). Clonal architecture of secondary acute myeloid leukemia. *N. Engl. J. Med.* 366, 1090–1098.
- Whichard, Z. L., Sarkar, C. A., Kimmel, M., and Corey, S. J. (2010). Hematopoiesis and its disorders: a systems biology approach. *Blood* 115, 2339–2347.

Conflict of Interest Statement: The authors declare that the research was conducted in the absence of any commercial or financial relationships that could be construed as a potential conflict of interest.

Received: 15 January 2013; accepted: 02 April 2013; published online: 29 April 2013.

Citation: Kimmel M and Corey S (2013) Stochastic hypothesis of transition from inborn neutropenia to AML: interactions of cell population dynamics and population genetics. *Front. Oncol.* 3:89. doi: 10.3389/fonc.2013.00089

This article was submitted to *Frontiers in Molecular and Cellular Oncology*, a specialty of *Frontiers in Oncology*.

Copyright © 2013 Kimmel and Corey. This is an open-access article distributed under the terms of the Creative Commons Attribution License, which permits use, distribution and reproduction in other forums, provided the original authors and source are credited and subject to any copyright notices concerning any third-party graphics etc.



Modeling the mechanics of cancer: effect of changes in cellular and extra-cellular mechanical properties

Parag Katira¹, Roger T. Bonnecaze¹ and Muhammad H. Zaman^{2*}

¹ McKetta Department of Chemical Engineering, The University of Texas at Austin, Austin, TX, USA

² Department of Biomedical Engineering, Boston University, Boston, MA, USA

Edited by:

Katarzyna Anna Rejniak, H. Lee
Moffitt Cancer Center & Research
Institute, USA

Reviewed by:

Paul Macklin, University of Southern
California, USA
Yi Jiang, Los Alamos National
Laboratory, USA

*Correspondence:

Muhammad H. Zaman, Department
of Biomedical Engineering, Boston
University, 38 Cummington Street,
Boston, MA 02215, USA
e-mail: zaman@bu.edu

Malignant transformation, though primarily driven by genetic mutations in cells, is also accompanied by specific changes in cellular and extra-cellular mechanical properties such as stiffness and adhesivity. As the transformed cells grow into tumors, they interact with their surroundings via physical contacts and the application of forces. These forces can lead to changes in the mechanical regulation of cell fate based on the mechanical properties of the cells and their surrounding environment. A comprehensive understanding of cancer progression requires the study of how specific changes in mechanical properties influences collective cell behavior during tumor growth and metastasis. Here we review some key results from computational models describing the effect of changes in cellular and extra-cellular mechanical properties and identify mechanistic pathways for cancer progression that can be targeted for the prediction, treatment, and prevention of cancer.

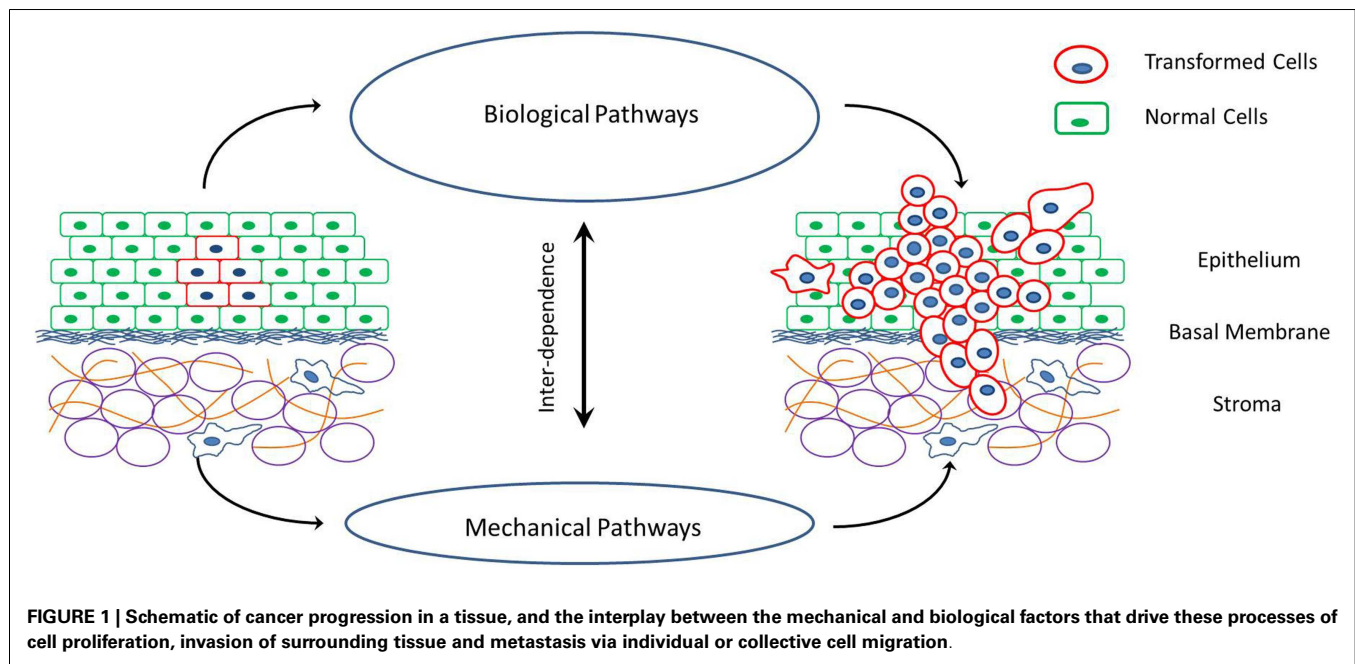
Keywords: cancer modeling, mechanical forces, cell-material interactions, cell-cell interaction, review

INTRODUCTION

Cancer is a disease rooted in the dis-regulation of cellular signaling pathways that control cell proliferation and apoptosis. This is generally caused by mutations in genes that express key proteins involved in these biochemical reactions. However, cancer is also accompanied by specific changes in the mechanical properties of cells and their surrounding extra-cellular environment (Figure 1). For example, cancerous cells are less stiff compared to their healthy counter parts (Suresh, 2007). This decrease in cell stiffness with malignant transformation has been observed in a variety of cancers such as breast cancer, lung cancer, renal cancer, prostate cancer, oral cancer, skin cancer, and so on (Guck et al., 2005; Cross et al., 2007; Suresh, 2007; Remmerbach et al., 2009; Fuhrmann et al., 2011; Jonas et al., 2011; Plodinec et al., 2012). Furthermore, the decrease in cell stiffness seems to be greater in cells with higher malignancy and metastatic potential (Swaminathan et al., 2011). Cancerous cells also have increased acto-myosin cortex contractility as compared to corresponding healthy cells (Jonas et al., 2011; Kraning-Rush et al., 2012). This has been observed in response to the stretching of cells by external stimuli. Apart from the cortex stiffness and contractility, cancerous cells also undergo changes in their ability to physically bind to their neighbors and the surrounding extra-cellular elements at different stages of cancer progression (Paredes et al., 2005; Ribeiro et al., 2010a,b). This is caused by the up or down regulation of specific adhesion proteins on the cell surface and affect the growth rate, shape, and invasiveness of tumors. Accompanying the changes in cellular mechanical properties are also some very specific changes in the mechanical properties of the extra-cellular environment. Tumors with high invasive potentials have a stiff extra-cellular environment (Erler and Weaver, 2009; Levental et al., 2009). The tumor extra-cellular environment consists primarily of fibrous tissue made up of collagen fibers. With malignant transformation of cells, an increase

in the cross-linking of these fibers and a consequent stiffening of the extra-cellular matrix (ECM) environment has been observed (Erler et al., 2006). Once again this observation is common for a variety of cancers. Also, with the advent of metastasis and the invasion of the extra-cellular environment by cells of a growing tumor, the fibers in the ECM undergo extensive remodeling in terms of degradation, re-polymerization, and alignment (Alini and Losa, 1991; Vijayagopal et al., 1998; Zhang et al., 2003; Yang et al., 2004; Paszek et al., 2005; Vader et al., 2009). This realignment of ECM fibers and strain-induced stretching can alter the ECM mechanical properties as shown by Stein et al. (2011).

There is an increasing interest in the mechanics of cancer progression with an aim to identify mechanistic pathways that can be targeted for the prediction, treatment, and even prevention of cancer. With this in mind it is important to understand the effect of these peculiar changes in cellular and extra-cellular mechanical properties on tumor growth and metastatic potential. The potential influence of mechanical property changes on cell behavior during cancer progression has been discussed in recent commentaries and insight articles (Peyton et al., 2007; Kumar and Weaver, 2009; Fritsch et al., 2010). The underlying idea is that mechanical forces acting on cells can regulate signaling pathways responsible for cell death, division, differentiation, and migration (Assoian and Klein, 2008; Chen, 2008; Mammoto and Ingber, 2009; Nelson and Gleghorn, 2012; West-Foyle and Robinson, 2012). Changes in cellular and extra-cellular mechanical properties during malignant transformation potentially alter the forces acting on cells and thus influence morphogenetic evolution, proliferation, and invasion of cancer cells (Huang and Ingber, 2005; Lopez et al., 2008). It would be desirable to quantify this effect of mechanical properties on collective cell behavior in *in vivo* and *in vitro* multi-cellular systems. However, the presence of various other biological factors influencing cell behavior, as well as the complex interplay between



the biological and mechanical factors makes it extremely difficult to isolate the effects of mechanical interactions. Computational modeling is an extremely useful tool in such conditions, where the effect of individual parameters can be studied and there is unlimited control on the parameter space.

Computational models can be developed to observe specific effects at various length scales ranging from the molecular to the macroscopic level, and these observations can then be integrated to obtain a complete picture of a specific process. Models have indeed been used extensively in understanding various aspects of cancer progression. Different models focusing on different aspects of cancer, such as effect of genetic heterogeneity, phenotypic evolution, biochemical interactions between cells and their surroundings, chemical and nutrient gradients, external forces, and mechanical interaction between cells, their neighbors, and the ECM can be found in literature. These models vary from being continuum based models of two evolving spatial domains representing the tumor mass and its environment to being discrete models where individual cells interacting with each other and the surroundings describe the system being simulated. A recent trend is to adopt a hybrid approach to incorporate the advantages of both continuum and discrete models into one, with a continuum description for the main tumor mass, and a discrete individual cell approach for tumor-environment interactions. The various modeling approaches have been reviewed in these references (Galle et al., 2006; Sanga et al., 2007; Byrne and Drasdo, 2009; Stolarska et al., 2009; Rejniak and McCawley, 2010; Deisboeck et al., 2011; Frieboes et al., 2011; Kam et al., 2012) and many others. Here we discuss some of these models, and a few other recent ones that examine the role of mechanics in tumor growth and invasion.

The goal of this review is to summarize the effects that changes in mechanical properties of cells and their surroundings have on tumor growth and metastasis as understood from computational models. There are a lot of models that incorporate some

form of mechanical interaction between its elements, and many of them are progressions or off-shoots of previous models focusing more on the biochemical aspects of cancer progression. Hence, we shall focus only on key results regarding the influence of mechanical interactions rather than delve into the details of the model development process. With this information, we hope to display the importance of mechanistic models in identifying novel pathways of cancer progression, and direct the reader to more detailed sources on models interesting to them. **Table 1** lists the specific changes in cellular and extra-cellular mechanical properties discussed here, experiments describing these changes and the corresponding observations on tumor cell behavior, as well as models that describe potential mechanisms connecting the two.

CHANGES IN EXTRA-CELLULAR MECHANICAL PROPERTIES

The extra-cellular environment of a carcinoma consists of surrounding healthy cells, a dense layer of fibrous basal membrane, and the surrounding stroma mainly comprised of fibrous matrix, adipocytes, and fibroblasts (Hogg et al., 1983). A growing tumor needs to push against this extra-cellular environment as it grows. Thus, intuitively, the stiffer the extra-cellular environment is, the less it deforms against the pressure applied by the growing tumor, restricting tumor size. This phenomenon was demonstrated experimentally by Helmlinger et al. (1997) and more recently by Cheng et al. (2009). Computationally this has been reproduced with varying levels of agreement by a variety of models (Chen et al., 2001; Ambrosi and Mollica, 2004; Drasdo and Hohme, 2005; Gevertz et al., 2008; Basan et al., 2009; Torquato, 2011; Montel et al., 2012; Ciarletta et al., 2013; Kim and Othmer, 2013) irrespective of model type (continuum, discrete, hybrid) and mechanism (growth retardation by formation of a necrotic core due to lack of nutrients, or by contact inhibition from increased packing density of growing cells, or both).

Table 1 | Some specific changes in cellular and extra-cellular mechanical properties, observations from experiments and computational models.

Experimental observations	Model predictions
Extra-cellular mechanical properties	
Matrix stiffening (effect of increased density, cross-linking) (Paszek et al., 2005; Levental et al., 2009)	Increased cell proliferation driven by heterogeneity in ECM mechanical properties, protrusions along high density gradients (Macklin and Lowengrub, 2007; Rubenstein and Kaufman, 2008; Anderson et al., 2009; Macklin et al., 2009)
Matrix re-organization (effect of degradation and realignment) (Wolf et al., 2007; Friedl and Wolf, 2008)	Cell Proliferation driven by matrix degradation through the expression of MMPs and along realigned matrix fibers (Franks et al., 2005; Painter, 2009; Givero et al., 2010; D'Antonio et al., 2013)
Cellular mechanical properties	
Increase in cell compliance or deformability (Cross et al., 2007; Fritsch et al., 2010; Jonas et al., 2011)	Tumorigenesis and increased malignancy, (Katira et al., 2012). Increased migration through porous ECM (Zaman, 2006; Zaman et al., 2007; Scianna and Preziosi, 2013)
Changes in cell adhesivity (Paredes et al., 2005; Ribeiro et al., 2010b)	Changes in tumor morphology, growth rates, and metastatic potential (Byrne and Chaplain, 1996; Armstrong et al., 2006; Ramis-Conde et al., 2008b; Frieboes et al., 2010; Rejniak et al., 2010; Katira et al., 2012)
Increase in cell contractility (Jonas et al., 2011; Kraning-Rush et al., 2012)	Increased migration rates and rigidity sensing (Moreo et al., 2008; Brodland and Veldhuis, 2012)

However, it is now known that the extra-cellular environment surrounding a tumor stiffens as the cells transform from normal to malignant to metastatic, and this transformation promotes cancer progression rather than arrests it (Paszek et al., 2005; Erler and Weaver, 2009; Klein et al., 2009; Levental et al., 2009; Ulrich et al., 2009). The models described above in their base form do not support this possibility. To explain the growth and metastasis of tumors against a dense, stiff, low porosity extra-cellular environment, models incorporating cell-ECM interactions are required. The continuum model described by Macklin and Lowengrub (2007) suggests that the aggressiveness of tumors growing in denser, stiffer environments that restrict cell mobility arises from increased shape instabilities during tumor growth and the formation of invasive finger-like morphologies. On the other hand, Franks et al. (2005) have suggested that tumor growth in a harsh environment like the one described above can lead to cell morphogenesis and progression toward a more malignant phenotype expressing high level of matrix degrading proteins (MMPs). These MMPs can then degrade the stiff, cross-linked ECM, weakening it. The growing tumor can then push against these weaker sections to grow as shown by D'Antonio et al. (2013). Chaplain et al. (2006) also incorporate a more active role of cell-ECM interactions in altering cell proliferation and migration rates to explain the growth of solid tumors against stiff extra-cellular environments. Their model focuses solely on mechanistic factors influencing tumor growth and incorporates the increase in ECM fiber density (Christensen, 1992; Kauppila et al., 1998; Brown et al., 1999) as well as changes in ECM degradation rates observed with malignant transformation (Clark et al., 2007; Alexander et al., 2008; Rizki et al., 2008). Increased ECM density facilitates cell proliferation as well as cell migration up to a certain extent (Zaman et al., 2006; Alexander et al., 2008). Increased MMP activity and corresponding degradation of the ECM also promotes cell migration through a dense ECM up to a certain extent (Erler and Weaver, 2009; Harjanto and Zaman, 2010). The effect of ECM density and cross-linking

on cell invasiveness via the formation of invadopodia has been computationally modeled by Enderling et al. (2008). The effect of ECM degradation via the action of MMPs and resulting cell invasion has been modeled by Givero et al. (2010). Based on the balance between the ECM fiber deposition and MMP degradation rates, as well as the spatial distribution of these factors in the tissue, various regimes of tumor growth, arrest, and invasion are possible. The heterogeneity arising in the tissue environment in terms of ECM density and stiffness because of these interactions can give rise to different morphologies for a growing tumor (Anderson et al., 2006; Frieboes et al., 2007; Gerlee and Anderson, 2008; Macklin and Lowengrub, 2008; Macklin et al., 2009; Trucu et al., 2013). Another model useful for studying the effect of ECM structure is described by Rubenstein and Kaufman (2008) where cell fate decisions are influenced by the neighboring elements and the overall interaction energy of the multi-cellular system. This allows for cell-cell as well as cell-ECM interactions to influence cell behavior and different collective phenomena can be observed based on the interaction rules. The model shows similar results as the described above, with increased cell proliferation near the densest ECM regions. Apart from cell proliferation and increased motility, changes in ECM structure can also impart directionality to the cells emanating from a growing tumor as shown computationally by Painter (2009). This is made possible through a mechanism known as contact guidance (Dunn and Heath, 1976; Guido and Tranquillo, 1993) where cells migrate along the length of ECM fibers. Thus, formation of aligned ECM fiber bundles can influence directed cell motility into the surrounding tissue.

CHANGES IN CELLULAR MECHANICAL PROPERTIES

Cells undergo very specific changes in their mechanical properties along with malignant transformation, just as the extra-cellular environment does. One particular change is the decrease in the stiffness of cells, or in other words, an increase in the compliance or deformability of cells. This has been observed for many

different cancers. Furthermore, increased deformability of cells corresponds to higher malignancy and metastatic potential. This change in the mechanical property of cells complements that of the extra-cellular environment, which gets stiffer with increased malignancy. Using computational modeling Katira et al. (2012) have shown that decrease in cell stiffness can have a similar effect on cell proliferation rates as increase in the stiffness of the surroundings do (Klein et al., 2009). The model by Katira et al. incorporates the mechanical regulation of cell fate driven by changes in cell shape, and suggests that for cell clusters larger than a threshold size, the decrease in cell stiffness can drive uncontrolled growth and evasion of apoptosis in cells. While there are a number of other factors that influence cell proliferation, this seems to be a mechanistic pathway that aids tumor growth. The effect of changes in cell stiffness has also been studied by Drasdo and Hoehme (2012), where they look at the mechanical interactions between cells and a granular surrounding medium. Apart from tumor growth, the decrease in stiffness of cells has been shown to influence their ability to navigate tight turns during cell migration (Park et al., 2005; Lautenschlager et al., 2009). While the effect of this on cell migration during metastasis through the ECM is unknown, a potential increase in mobility can be predicted based on the models described in (Zaman et al., 2007; Scianna and Preziosi, 2013).

Apart from the lowering of cell stiffness, cells undergo changes in their binding ability with other cancer cells, normal cells, and the extra-cellular environment. These changes vary with cell phenotype and can be different at different stages of cancer progression. Also, their effects on tumor growth can vary based on the size and morphology of the tumor and the tumor-environment. For example studies have shown increased malignancy but non-invasiveness in tumors with increased P-cadherin binding between the cells (Van Marck et al., 2005). On the other hand studies have shown tumor growth arrest with increased E-cadherin binding. Other results have also shown increase in malignancy with decreased E-cadherin mediated adhesion (Bryan et al., 2008), while in still other cases the initiation of metastasis is driven by hypoxia induced loss of binding (Behrens et al., 1989; Finger and Giaccia, 2010). The effect of changes in cell adhesion has been studied in a lot of different modeling works (Drasdo and Hohme, 2005; Armstrong et al., 2006; Anderson et al., 2009; Bearer et al., 2009; Frieboes et al., 2010; Katira et al., 2012). One of the early models describing the effect of cell–cell adhesion on tumor growth is by Byrne and Chaplain (1996). The model balances the internal pressure of a growing tumor to the surface tension which is a function of the cell–cell adhesion. Thus changes in adhesion energies can drive

instabilities in the contour profile of the growing tumor and result in finger-like extensions, representing metastasis. A model specifically suited for analyzing the effect of multiple changes occurring in the expression of cell-surface proteins that regulate cell–cell and cell-ECM interactions is the IBCell model described by Rejniak et al. (2010). The model describes cell behavior in terms of growth, phenotypic evolution, and apoptosis as a function of all the interactions it has with its neighbors and the different levels of surface proteins it is expressing at the time. This enables the prediction of a variety of different phenomena arising during malignant transformation and tumor growth. In principal this model is similar to the Rubenstein model mentioned previously, however the focused application described has been on the effect of changes in expressed cell-surface receptors and mechanical interactions between cells. Ramis-Conde et al. (2008a,b) describe a slightly different model focusing on the cadherin-catenin biochemical pathway and its effect on mechanical interaction between cells. The detachment of the cadherin bonds triggers the *wnt*-signaling pathway, and the model is able to predict epithelial to mesenchymal transition and cell migration toward a particular signal source.

FUTURE DIRECTIONS

There are a number of models that describe the mechanics of cancer and the effect of specific changes in cellular and extra-cellular properties. However, it is necessary to combine these models focusing on different aspects of cell–cell and cell-ECM mechanical interactions into a unified theory of cancer progression. This comprehensive understanding of all the mechanical aspects is required in order to predict clinically observed tumor growth and metastasis, and decouple the mechanics from the biology. The idea that a select few changes in cellular and extra-cellular mechanical properties can promote the growth of a malignant phenotype of cancer is intriguing. As depicted in **Figure 1**, there is a strong interplay between biological and mechanical factors involved in cancer progression, with each one influencing the other. This opens up the possibility of mechanical regulation and manipulation of cell behavior to alter cancer outcome. Researchers can develop tools to predict and treat cancer that are focused on rectifying the few mechanical property changes (for examples refer to Lekka et al., 2001; Cross et al., 2011) as compared to vast number of heterogeneous genetic and epigenetic factors associated with cancer progression (Swanton et al., 2011; Visvader, 2011).

ACKNOWLEDGMENTS

The authors would like to acknowledge the support from National Institutes of Health (R01CA132633) to Muhammad H. Zaman.

REFERENCES

- Alexander, N. R., Branch, K. M., Parekh, A., Clark, E. S., Lwueke, L. C., Guelcher, S. A., et al. (2008). Extracellular matrix rigidity promotes invadopodia activity. *Curr. Biol.* 18, 1295–1299. doi:10.1016/j.cub.2008.07.090
- Alini, M., and Losa, G. A. (1991). Partial characterization of proteoglycans isolated from neoplastic and nonneoplastic human breast tissues. *Cancer Res.* 51, 1443–1447.
- Ambrosi, D., and Mollica, F. (2004). The role of stress in the growth of a multicell spheroid. *J. Math. Biol.* 48, 477–499. doi:10.1007/s00285-003-0238-2
- Anderson, A. R. A., Rejniak, K. A., Gerlee, P., and Quaranta, V. (2009). Microenvironment driven invasion: a multiscale multimodel investigation. *J. Math. Biol.* 58, 579–624. doi:10.1007/s00285-008-0210-2
- Anderson, A. R. A., Weaver, A. M., Cummings, P. T., and Quaranta, V. (2006). Tumor morphology and phenotypic evolution driven by selective pressure from the microenvironment. *Cell* 127, 905–915. doi:10.1016/j.cell.2006.09.042
- Armstrong, N. J., Painter, K. J., and Sherratt, J. A. (2006). A continuum approach to modelling cell-cell adhesion. *J. Theor. Biol.* 243, 98–113. doi:10.1016/j.jtbi.2006.05.030
- Assoian, R. K., and Klein, E. A. (2008). Growth control by intracellular tension and extracellular stiffness. *Trends Cell Biol.* 18, 347–352. doi:10.1016/j.tcb.2008.05.002

- Basan, M., Risler, T., Joanny, J. F., Sastre-Garau, X., and Prost, J. (2009). Homeostatic competition drives tumor growth and metastasis nucleation. *HFSP J.* 3, 265–272. doi:10.2976/1.3086732
- Bearer, E. L., Lowengrub, J. S., Frieboes, H. B., Chuang, Y. L., Jin, F., Wise, S. M., et al. (2009). Multiparameter computational modeling of tumor invasion. *Cancer Res.* 69, 4493–4501. doi:10.1158/0008-5472.CAN-08-3834
- Behrens, J., Mareel, M. M., Vanroy, F. M., and Birchmeier, W. (1989). Dissecting tumor-cell invasion – epithelial-cells acquire invasive properties after the loss of uvomorulin-mediated cell cell-adhesion. *J. Cell Biol.* 108, 2435–2447. doi:10.1083/jcb.108.6.2435
- Brodland, G. W., and Veldhuis, J. H. (2012). The mechanics of metastasis: insights from a computational model. *PLoS ONE* 7:e44281. doi:10.1371/journal.pone.0044281
- Brown, L. F., Guidi, A. J., Schnitt, S. J., Van De Water, L., Iruela-Arispe, M. L., Yeo, T. K., et al. (1999). Vascular stroma formation in carcinoma in situ, invasive carcinoma, and metastatic carcinoma of the breast. *Clin. Cancer Res.* 5, 1041–1056.
- Bryan, R. T., Atherfold, P. A., Yeo, Y., Jones, L. J., Harrison, R. F., Wallace, D. M. A., et al. (2008). Cadherin switching dictates the biology of transitional cell carcinoma of the bladder: ex vivo and in vitro studies. *J. Pathol.* 215, 184–194. doi:10.1002/path.2346
- Byrne, H., and Drasdo, D. (2009). Individual-based and continuum models of growing cell populations: a comparison. *J. Math. Biol.* 58, 657–687. doi:10.1007/s00285-008-0212-0
- Byrne, H. M., and Chaplain, M. A. J. (1996). Modelling the role of cell-cell adhesion in the growth and development of carcinoma. *Math. Comput. Model.* 24, 1–17. doi:10.1016/S0895-7177(96)00174-4
- Chaplain, M. A. J., Graziano, L., and Preziosi, L. (2006). Mathematical modelling of the loss of tissue compression responsiveness and its role in solid tumour development. *Math. Med. Biol.* 23, 197–229. doi:10.1093/imammb/dql009
- Chen, C. S. (2008). Mechanotransduction – a field pulling together? *J. Cell. Sci.* 121, 3285–3292. doi:10.1242/jcs.023507
- Chen, C. Y., Byrne, H. M., and King, J. R. (2001). The influence of growth-induced stress from the surrounding medium on the development of multicell spheroids. *J. Math. Biol.* 43, 191–220. doi:10.1007/s002850100091
- Cheng, G., Tse, J., Jain, R. K., and Munn, L. L. (2009). Micro-environmental mechanical stress controls tumor spheroid size and morphology by suppressing proliferation and inducing apoptosis in cancer cells. *PLoS ONE* 4:e4632. doi:10.1371/journal.pone.0004632
- Christensen, L. (1992). The distribution of fibronectin, laminin and tetranectin in human breast-cancer with special attention to the extracellular-matrix. *APMIS* 100, 1–39.
- Ciarletta, P., Ambrosi, D., Maugin, G. A., and Preziosi, L. (2013). Mechano-transduction in tumour growth modelling. *Eur. Phys. J. E Soft Matter* 36, 1–9. doi:10.1140/epje/i2013-13023-2
- Clark, E. S., Whigham, A. S., Yarbrough, W. G., and Weaver, A. M. (2007). Cortactin is an essential regulator of matrix metalloproteinase secretion and extracellular matrix degradation in invadopodia. *Cancer Res.* 67, 4227–4235. doi:10.1158/0008-5472.CAN-06-3928
- Cross, S. E., Jin, Y. S., Lu, Q. Y., Rao, J. Y., and Gimzewski, J. K. (2011). Green tea extract selectively targets nanomechanics of live metastatic cancer cells. *Nanotechnology* 22, doi:10.1088/0957-4484/22/21/215101
- Cross, S. E., Jin, Y. S., Rao, J., and Gimzewski, J. K. (2007). Nanomechanical analysis of cells from cancer patients. *Nat. Nanotechnol.* 2, 780–783. doi:10.1038/nnano.2007.388
- D'Antonio, G., Macklin, P., and Preziosi, L. (2013). An agent-based model for elasto-plastic mechanical interactions between cells, basement membrane and extracellular matrix. *Math. Biosci. Eng.* 10, 75–101. doi:10.3934/mbe.2013.10.75
- Deisboeck, T. S., Wang, Z. H., Macklin, P., and Cristini, V. (2011). Multiscale cancer modeling. *Annu. Rev. Biomed. Eng.* 13, 127–155. doi:10.1146/annurev-bioeng-071910-124729
- Drasdo, D., and Hoehme, S. (2012). Modeling the impact of granular embedding media, and pulling versus pushing cells on growing cell clones. *New J. Phys.* 14:055025. doi:10.1088/1367-2630/14/5/055025
- Drasdo, D., and Hohme, S. (2005). A single-cell-based model of tumor growth in vitro: monolayers and spheroids. *Phys. Biol.* 2, 133–147. doi:10.1088/1478-3975/2/3/001
- Dunn, G. A., and Heath, J. P. (1976). New hypothesis of contact guidance in tissue-cells. *Exp. Cell Res.* 101, 1–14. doi:10.1016/0014-4827(76)90405-5
- Enderling, H., Alexander, N. R., Clark, E. S., Branch, K. M., Estrada, L., Crooke, C., et al. (2008). Dependence of invadopodia function on collagen fiber spacing and cross-linking: computational modeling and experimental evidence. *Biophys. J.* 95, 2203–2218. doi:10.1529/biophysj.108.133199
- Erler, J. T., Bennewith, K. L., and Giaccia, A. J. (2006). The role of lysyl oxidase in premetastatic niche formation. *Breast Cancer Res. Treat.* 100, S7–S7.
- Erler, J. T., and Weaver, V. M. (2009). Three-dimensional context regulation of metastasis. *Clin. Exp. Metastasis* 26, 35–49. doi:10.1007/s10585-008-9209-8
- Finger, E. C., and Giaccia, A. J. (2010). Hypoxia, inflammation, and the tumor microenvironment in metastatic disease. *Cancer Metastasis Rev.* 29, 285–293. doi:10.1007/s10555-010-9224-5
- Franks, S. J., Byrne, H. M., Underwood, J. C. E., and Lewis, C. E. (2005). Biological inferences from a mathematical model of comedo ductal carcinoma in situ of the breast. *J. Theor. Biol.* 232, 523–543. doi:10.1016/j.jtbi.2004.08.032
- Frieboes, H. B., Chaplain, M. A. J., Thompson, A. M., Bearer, E. L., Lowengrub, J. S., and Cristini, V. (2011). Physical oncology: a bench-to-bedside quantitative and predictive approach. *Cancer Res.* 71, 298–302. doi:10.1158/0008-5472.CAN-10-2676
- Frieboes, H. B., Jin, F., Chuang, Y. L., Wise, S. M., Lowengrub, J. S., and Cristini, V. (2010). Three-dimensional multispecies nonlinear tumor growth-II: tumor invasion and angiogenesis. *J. Theor. Biol.* 264, 1254–1278. doi:10.1016/j.jtbi.2010.02.036
- Frieboes, H. B., Lowengrub, J. S., Wise, S., Zheng, X., Macklin, P., Elaine, L. B. D., et al. (2007). Computer simulation of glioma growth and morphology. *Neuroimage* 37, S59–S70. doi:10.1016/j.neuroimage.2007.03.008
- Friedl, P., and Wolf, K. (2008). Tube travel: the role of proteases in individual and collective a cancer cell invasion. *Cancer Res.* 68, 7247–7249. doi:10.1158/0008-5472.CAN-08-0784
- Fritsch, A., Hockel, M., Kiessling, T., Nnetu, K. D., Wetzel, F., Zink, M., et al. (2010). Are biomechanical changes necessary for tumour progression? *Nat. Phys.* 6, 730–732. doi:10.1038/nphys1800
- Fuhrmann, A., Staunton, J. R., Nandakumar, V., Banyai, N., Davies, P. C. W., and Ros, R. (2011). AFM stiffness nanotomography of normal, metaplastic and dysplastic human esophageal cells. *Phys. Biol.* 8:015007. doi:10.1088/1478-3975/8/1/015007
- Galle, J., Aust, G., Schaller, G., Beyer, T., and Drasdo, D. (2006). Individual cell-based models of the spatial-temporal organization of multicellular systems – achievements and limitations. *Cytometry A* 69A, 704–710. doi:10.1002/cyto.a.20287
- Gerlee, P., and Anderson, A. R. A. (2008). A hybrid cellular automaton model of clonal evolution in cancer: the emergence of the glycolytic phenotype. *J. Theor. Biol.* 250, 705–722. doi:10.1016/j.jtbi.2007.10.038
- Gevertz, J. L., Gillies, G. T., and Torquato, S. (2008). Simulating tumor growth in confined heterogeneous environments. *Phys. Biol.* 5, 036010. doi:10.1088/1478-3975/5/3/036010
- Giverso, C., Scianna, M., Preziosi, L., Lo Buono, N., and Funaro, A. (2010). Individual cell-based model for in-vitro mesothelial invasion of ovarian cancer. *Math. Model. Nat. Phenom.* 5, 203–223. doi:10.1051/mmnp/20105109
- Guck, J., Schinkinger, S., Lincoln, B., Wottawah, F., Ebert, S., Romeyke, M., et al. (2005). Optical deformability as an inherent cell marker for testing malignant transformation and metastatic competence. *Biophys. J.* 88, 3689–3698. doi:10.1529/biophysj.104.045476
- Guido, S., and Tranquillo, R. T. (1993). A methodology for the systematic and quantitative study of cell contact guidance in oriented collagen gels – correlation of fibroblast orientation and gel birefringence. *J. Cell. Sci.* 105, 317–331.
- Harjanto, D., and Zaman, M. H. (2010). Computational study of proteolysis-driven single cell migration in a three-dimensional matrix. *Ann. Biomed. Eng.* 38, 1815–1825. doi:10.1007/s10439-010-9970-0
- Helmlinger, G., Netti, P. A., Lichtenberg, H. C., Melder, R. J., and Jain, R. K. (1997). Solid stress inhibits the growth of multicellular tumorspheroids. *Nat. Biotechnol.* 15, 778–783. doi:10.1038/nbt0897-778

- Hogg, N. A. S., Harrison, C. J., and Tickle, C. (1983). Lumen formation in the developing mouse mammary-gland. *J. Embryol. Exp. Morphol.* 73, 39–57.
- Huang, S., and Ingber, D. E. (2005). Cell tension, matrix mechanics, and cancer development. *Cancer Cell* 8, 175–176. doi:10.1016/j.ccr.2005.08.009
- Jonas, O., Mierke, C. T., and Kas, J. A. (2011). Invasive cancer cell lines exhibit biomechanical properties that are distinct from their noninvasive counterparts. *Soft Matter* 7, 11488–11495. doi:10.1039/c1sm05532a
- Kam, Y., Rejniak, K. A., and Anderson, A. R. A. (2012). Cellular modeling of cancer invasion: integration of in silico and in vitro approaches. *J. Cell. Physiol.* 227, 431–438. doi:10.1002/jcp.22766
- Katira, P., Zaman, M. H., and Bonnez, R. T. (2012). How changes in cell mechanical properties induce cancerous behaviour. *Phys. Rev. Lett.* 108:028103. doi:10.1103/PhysRevLett.108.028103
- Kaupilla, S., Stenback, F., Risteli, J., Jukkola, A., and Risteli, L. (1998). Aberrant type I and type III collagen gene expression in human breast cancer in vivo. *J. Pathol.* 186, 262–268. doi:10.1002/(SICI)1096-9896(1998110)186:3<262::AID-PATH191>3.0.CO;2-3
- Kim, Y., and Othmer, H. G. (2013). A hybrid model of tumor-stromal interactions in breast cancer. *Bull. Math. Biol.* doi:10.1007/s11538-012-9787-0. [Epub ahead of print].
- Klein, E. A., Yin, L. Q., Kothapalli, D., Castagnino, P., Byfield, F. J., Xu, T. N., et al. (2009). Cell-cycle control by physiological matrix elasticity and in vivo tissue stiffening. *Curr. Biol.* 19, 1511–1518. doi:10.1016/j.cub.2009.07.069
- Kraning-Rush, C. M., Califano, J. P., and Reinhart-King, C. A. (2012). Cellular traction stresses increase with increasing metastatic potential. *PLoS ONE* 7:e32572. doi:10.1371/journal.pone.0032572
- Kumar, S., and Weaver, V. (2009). Mechanics, malignancy, and metastasis: the force journey of a tumor cell. *Cancer Metastasis Rev.* 28, 113–127. doi:10.1007/s10555-008-9173-4
- Lautenschlager, F., Paschke, S., Schinkinger, S., Bruel, A., Beil, M., and Guck, J. (2009). The regulatory role of cell mechanics for migration of differentiating myeloid cells. *Proc. Natl. Acad. Sci. U.S.A.* 106, 15696–15701. doi:10.1073/pnas.0811261106
- Lekka, M., Laidler, P., Ignacak, J., Labedz, M., Lekki, J., Struszczyk, H., et al. (2001). The effect of chitosan on stiffness and glycolytic activity of human bladder cells. *Biochim. Biophys. Acta* 1540, 127–136. doi:10.1016/S0167-4889(01)00125-2
- Levental, K. R., Yu, H. M., Kass, L., Lakins, J. N., Egeblad, M., Erler, J. T., et al. (2009). Matrix crosslinking forces tumor progression by enhancing integrin signaling. *Cell* 139, 891–906. doi:10.1016/j.cell.2009.10.027
- Lopez, J. I., Mouw, J. K., and Weaver, V. M. (2008). Biomechanical regulation of cell orientation and fate. *Oncogene* 27, 6981–6993. doi:10.1038/ncr.2008.348
- Macklin, P., and Lowengrub, J. (2007). Nonlinear simulation of the effect of microenvironment on tumor growth. *J. Theor. Biol.* 245, 677–704. doi:10.1016/j.jtbi.2006.12.004
- Macklin, P., and Lowengrub, J. S. (2008). A new ghost cell/level set method for moving boundary problems: application to tumor growth. *J. Sci. Comput.* 35, 266–299. doi:10.1007/s10915-008-9190-z
- Macklin, P., McDougall, S., Anderson, A. R. A., Chaplain, M. A. J., Cristini, V., and Lowengrub, J. (2009). Multiscale modelling and nonlinear simulation of vascular tumour growth. *J. Math. Biol.* 58, 765–798. doi:10.1007/s00285-008-0216-9
- Mammoto, A., and Ingber, D. E. (2009). Cytoskeletal control of growth and cell fate switching. *Curr. Opin. Cell Biol.* 21, 864–870. doi:10.1016/j.cub.2009.08.001
- Montel, F., Delarue, M., Elgeti, J., Vignjevic, D., Cappello, G., and Prost, J. (2012). Isotropic stress reduces cell proliferation in tumor spheroids. *New J. Phys.* 14:055008. doi:10.1088/1367-2630/14/5/055008
- Moreo, P., Garcia-Aznar, J. M., and Doblaré, M. (2008). Modeling mechanosensing and its effect on the migration and proliferation of adherent cells. *Acta Biomater.* 4, 613–621. doi:10.1016/j.actbio.2007.10.014
- Nelson, C. M., and Gleghorn, J. P. (2012). Sculpting organs: mechanical regulation of tissue development. *Annu. Rev. Biomed. Eng.* 14, 129–154. doi:10.1146/annurev-bioeng-071811-150043
- Painter, K. J. (2009). Modelling cell migration strategies in the extracellular matrix. *J. Math. Biol.* 58, 511–543. doi:10.1007/s00285-008-0217-8
- Paredes, J., Albergaria, A., Oliveira, J. T., Jeronimo, C., Milanezi, F., and Schmitt, F. C. (2005). P-cadherin overexpression is an indicator of clinical outcome in invasive breast carcinomas and is associated with CDH3 promoter hypomethylation. *Clin. Cancer Res.* 11, 5869–5877. doi:10.1158/1078-0432.CCR-05-0059
- Park, S., Koch, D., Cardenas, R., Kas, J., and Shih, C. K. (2005). Cell motility and local viscoelasticity of fibroblasts. *Biophys. J.* 89, 4330–4342. doi:10.1529/biophysj.104.053462
- Paszek, M. J., Zahir, N., Johnson, K. R., Lakins, J. N., Rozenberg, G. I., Gefen, A., et al. (2005). Tensional homeostasis and the malignant phenotype. *Cancer Cell* 8, 241–254. doi:10.1016/j.ccr.2005.08.010
- Peyton, S. R., Ghajar, C. M., Khatiwala, C. B., and Putnam, A. J. (2007). The emergence of ECM mechanics and cytoskeletal tension as important regulators of cell function. *Cell Biochem. Biophys.* 47, 300–320. doi:10.1007/s12013-007-0004-y
- Plodinec, M., Loparic, M., Monnier, C. A., Obermann, E. C., Zanetti-Dallenbach, R., Oertle, P., et al. (2012). The nanomechanical signature of breast cancer. *Nat. Nanotechnol.* 7, 757–765. doi:10.1038/nnano.2012.167
- Ramis-Conde, L., Chaplain, M. A. J., and Anderson, A. R. A. (2008a). Mathematical modelling of cancer cell invasion of tissue. *Math. Comput. Model.* 47, 533–545. doi:10.1016/j.mcm.2007.02.034
- Ramis-Conde, L., Drasdo, D., Anderson, A. R. A., and Chaplain, M. A. J. (2008b). Modeling the influence of the E-cadherin-beta-catenin pathway in cancer cell invasion: a multiscale approach. *Biophys. J.* 95, 155–165. doi:10.1529/biophysj.107.114678
- Rejniak, K. A., and McCawley, L. J. (2010). Current trends in mathematical modeling of tumor-microenvironment interactions: a survey of tools and applications. *Exp. Biol. Med.* 235, 411–423. doi:10.1258/ebm.2009.009230
- Rejniak, K. A., Wang, S. Z. E., Bryce, N. S., Chang, H., Parvin, B., Jourquin, J., et al. (2010). Linking changes in epithelial morphogenesis to cancer mutations using computational modeling. *PLoS Comput. Biol.* 6:e1000900. doi:10.1371/journal.pcbi.1000900
- Remmerbach, T. W., Wottawah, F., Dietrich, J., Lincoln, B., Wittekind, C., and Guck, J. (2009). Oral cancer diagnosis by mechanical phenotyping. *Cancer Res.* 69, 1728–1732. doi:10.1158/0008-5472.CAN-08-4073
- Ribeiro, A. S., Albergaria, A., Sousa, B., Correia, A. L., Bracke, M., Seruca, R., et al. (2010a). Extracellular cleavage and shedding of P-cadherin: a mechanism underlying the invasive behaviour of breast cancer cells. *Oncogene* 29, 392–402. doi:10.1038/ncr.2009.338
- Ribeiro, A. S., Carreto, L. C., Albergaria, A., Sousa, B., Ricardo, S., Milanezi, F., et al. (2010b). Co-expression of E- and P-cadherin in breast cancer: role as an invasion suppressor or as an invasion promoter? *EJC Suppl.* 8, 131–132.
- Rizki, A., Weaver, V. M., Lee, S. Y., Rozenberg, G. I., Chin, K., Myers, C. A., et al. (2008). A human breast cell model of preinvasive to invasive transition. *Cancer Res.* 68, 1378–1387. doi:10.1158/0008-5472.CAN-07-2225
- Rubenstein, B. M., and Kaufman, L. J. (2008). The role of extracellular matrix in glioma invasion: a cellular Potts model approach. *Biophys. J.* 95, 5661–5680. doi:10.1529/biophysj.108.140624
- Sanga, S., Frieboes, H. B., Zheng, X. M., Gatenby, R., Bearer, E. L., and Cristini, V. (2007). Predictive oncology: a review of multidisciplinary, multiscale in silico modeling linking phenotype, morphology and growth. *Neuroimage* 37, S120–S134. doi:10.1016/j.neuroimage.2007.05.043
- Scianna, M., and Preziosi, L. (2013). Modeling the influence of nucleus elasticity on cell invasion in fiber networks and microchannels. *J. Theor. Biol.* 317, 394–406. doi:10.1016/j.jtbi.2012.11.003
- Stein, A. M., Vader, D. A., Weitz, D. A., and Sander, L. M. (2011). The micro-mechanics of three-dimensional collagen-I gels. *Complexity* 16, 22–28. doi:10.1002/cplx.20332
- Stolarska, M. A., Kim, Y., and Othmer, H. G. (2009). Multiscale models of cell and tissue dynamics. *Philos. Trans. A Math. Phys. Eng. Sci.* 367, 3525–3553. doi:10.1098/rsta.2009.0095
- Suresh, S. (2007). Biomechanics and biophysics of cancer cells. *Acta Mater.* 55, 3989–4014. doi:10.1016/j.actamat.2007.04.022
- Swaminathan, V., Myhre, K., O'Brien, E. T., Berchuck, A., Blobe, G. C., and Superfine, R. (2011). Mechanical

- stiffness grades metastatic potential in patient tumor cells and in cancer cell lines. *Cancer Res.* 71, 5075–5080. doi:10.1158/0008-5472.CAN-11-0247
- Swanton, C., Burrell, R. A., and Futreal, P. A. (2011). Breast cancer genome heterogeneity: a challenge to personalised medicine? *Breast Cancer Res.* 13, 104–105. doi:10.1186/bcr2807
- Torquato, S. (2011). Toward an Ising model of cancer and beyond. *Phys. Biol.* 8, 015017. doi:10.1088/1478-3975/8/1/015017
- Trucu, D., Lin, P., Chaplain, M. A. J., and Wang, Y. (2013). A multiscale moving boundary model arising in cancer invasion. *Multiscale Model. Simul.* 11, 309–335. doi:10.1137/110839011
- Ulrich, T. A., Pardo, E. M. D., and Kumar, S. (2009). The mechanical rigidity of the extracellular matrix regulates the structure, motility, and proliferation of glioma cells. *Cancer Res.* 69, 4167–4174. doi:10.1158/0008-5472.CAN-08-4859
- Vader, D., Kabla, A., Weitz, D., and Mahadevan, L. (2009). Strain-induced alignment in collagen gels. *PLoS ONE* 4:e5902. doi:10.1371/journal.pone.0005902
- Van Marck, V., Stove, C., Van Den Bossche, K., Stove, V., Paredes, J., Haeghen, Y. V., et al. (2005). P-cadherin promotes cell-cell adhesion and counteracts invasion in human melanoma. *Cancer Res.* 65, 8774–8783. doi:10.1158/0008-5472.CAN-04-4414
- Vijayagopal, P., Figueroa, J. E., and Levine, E. A. (1998). Altered composition and increased endothelial cell proliferative activity of proteoglycans isolated from breast carcinoma. *J. Surg. Oncol.* 68, 250–254. doi:10.1002/(SICI)1096-9098(199808)68:4<250::AID-JSO9>3.3.CO;2-9
- Visvader, J. E. (2011). Cells of origin in cancer. *Nature* 469, 314–322. doi:10.1038/nature09781
- West-Foyle, H., and Robinson, D. N. (2012). Cytokinesis mechanics and mechanosensing. *Cytoskeleton (Hoboken)* 69, 700–709. doi:10.1002/cm.21045
- Wolf, K., Wu, Y. I., Liu, Y., Geiger, J., Tam, E., Overall, C., et al. (2007). Multi-step pericellular proteolysis controls the transition from individual to collective cancer cell invasion. *Nat. Cell Biol.* 9, 893–U839. doi:10.1038/ncb1616
- Yang, C. M., Chien, C. S., Yao, C. C., Hsiao, L. D., Huang, Y. C., and Wu, C. B. (2004). Mechanical strain induces collagenase-3 (MMP-13) expression in MC3T3-E1 osteoblastic cells. *J. Biol. Chem.* 279, 22158–22165. doi:10.1074/jbc.M401343200
- Zaman, M. H. (2006). Multiscale modeling of tumor cell migration. *Phys. Biol.* 851, 117–122.
- Zaman, M. H., Matsudaira, P., and Lauffenburger, D. A. (2007). Understanding effects of matrix protease and matrix organization on directional persistence and translational speed in three-dimensional cell migration. *Ann. Biomed. Eng.* 35, 91–100. doi:10.1007/s10439-006-9205-6
- Zaman, M. H., Trapani, L. M., Siemeski, A., MacKellar, D., Gong, H., Kamm, R. D., et al. (2006). Migration of tumor cells in 3D matrices is governed by matrix stiffness along with cell-matrix adhesion and proteolysis. *Proc. Natl. Acad. Sci. U.S.A.* 103, 13897–13897. doi:10.1073/pnas.0604460103
- Zhang, Y. H., Nojima, S., Nakayama, H., Jin, Y. L., and Enza, H. (2003). Characteristics of normal stromal components and their correlation with cancer occurrence in human prostate. *Oncol. Rep.* 10, 207–211.

Conflict of Interest Statement: The authors declare that the research was conducted in the absence of any commercial or financial relationships that could be construed as a potential conflict of interest.

Received: 07 February 2013; paper pending published: 18 March 2013; accepted: 21 May 2013; published online: 11 June 2013.

Citation: Katira P, Bonnecaze RT and Zaman MH (2013) Modeling the mechanics of cancer: effect of changes in cellular and extra-cellular mechanical properties. *Front. Oncol.* 3:145. doi: 10.3389/fonc.2013.00145

This article was submitted to *Frontiers in Molecular and Cellular Oncology*, a specialty of *Frontiers in Oncology*.

Copyright © 2013 Katira, Bonnecaze and Zaman. This is an open-access article distributed under the terms of the Creative Commons Attribution License, which permits use, distribution and reproduction in other forums, provided the original authors and source are credited and subject to any copyright notices concerning any third-party graphics etc.



Computational and experimental models of cancer cell response to fluid shear stress

Michael J. Mitchell and Michael R. King*

Department of Biomedical Engineering, Cornell University, Ithaca, NY, USA

Edited by:

Katarzyna A. Rejniak, H. Lee Moffitt Cancer Center & Research Institute, USA

Reviewed by:

Christian Stock, University of Muenster, Germany
Owen McCarty, Oregon Health and Science University, USA

***Correspondence:**

Michael R. King, Department of Biomedical Engineering, Cornell University, 205 Weill Hall, Ithaca, NY 14853, USA.
e-mail: mike.king@cornell.edu

It has become evident that mechanical forces play a key role in cancer metastasis, a complex series of steps that is responsible for the majority of cancer-related deaths. One such force is fluid shear stress, exerted on circulating tumor cells by blood flow in the vascular microenvironment, and also on tumor cells exposed to slow interstitial flows in the tumor microenvironment. Computational and experimental models have the potential to elucidate metastatic behavior of cells exposed to such forces. Here, we review the fluid-generated forces that tumor cells are exposed to in the vascular and tumor microenvironments, and discuss recent computational and experimental models that have revealed mechanotransduction phenomena that may play a role in the metastatic process.

Keywords: cancer metastasis, circulating tumor cells, mechanotransduction, shear stress, blood, interstitial flow

INTRODUCTION

To initiate the metastatic spread of cancer through the bloodstream, tumor cells must transit through microenvironments of dramatically varying physical forces. Cancer cells must be able to migrate through the stroma, intravasate through the endothelium into blood or lymphatic vessels, flow within the vessels and subsequently extravasate through the endothelium, and migrate and colonize in tissue at a secondary site (Chambers et al., 2002; Steeg, 2006; Chaffer and Weinberg, 2011). In soft tissues, cancer cells are exposed to mechanical forces due to fluid shear stress, hydrostatic pressure, and tension and compression forces (Butcher et al., 2009; DuFort et al., 2011). During intravasation and extravasation, cells undergo dramatic elastic deformations to transmigrate through endothelial cell–cell junctions (Tseng et al., 2004; Wirtz et al., 2011). Once in the circulation, tumor cells must be able to withstand immunological stress, blood cell collisions, and hemodynamic shear forces, while also utilizing flow to adhere to the endothelial wall and subsequently extravasate to form a secondary tumor (Hughes and King, 2011). Across all of these steps, a deeper understanding is needed of how biophysical forces contribute to biochemical changes in cancer cells, which can reveal novel strategies in the treatment of metastasis.

Fluid shear stress is one of the prominent forces that cells are exposed to, and its effects on blood cells, endothelial cells, smooth muscle cells (SMCs), and others have been extensively studied (Moazzam et al., 1997; Civelek et al., 2002; Li et al., 2005). However, much less is known about fluid shear stress effects on tumor cells. Cancer cells experience two main types of fluid shear stress: stresses generated by blood flow in the vascular microenvironment, and those generated by interstitial flows in the tumor microenvironment (Michor et al., 2011; Swartz and Lund, 2012). Stresses generated by interstitial and blood flows could contribute to the metastatic process by enhancing tumor

cell invasion and circulating tumor cell (CTC) adhesion to blood vessels, respectively. However, it is difficult to predict tumor cell behavior to such forces; it is difficult to experimentally measure such flows in the tumor microenvironment (Shieh and Swartz, 2011), and there is a general lack of data on force-dependent CTC receptor–ligand interactions with the endothelium (Cheung et al., 2011). Sophisticated experimental techniques coupled with computational modeling are needed to predict cell behavior upon exposure to varying complex physical forces.

In this review, we provide examples of both experimental and computational methods to model and predict how cancer cells respond to fluid shear forces. We begin by describing the fluid shear forces that cancer cells are exposed to in both the tumor and vascular microenvironments, generated mainly by blood and interstitial flows. An overview is provided on computational modeling to estimate the forces exerted on cells in blood and tissues, along with simulations to predict cell behavior under such flows. We then describe recent cancer cell mechanotransduction phenomena upon exposure to fluid shear stress, such as altering cancer cell resistance to fluid shear stress, sensitivity to apoptosis-inducing ligands, and invasive and migratory potential. We conclude with current computational models that aim to integrate fluid shear forces with chemical signaling, such as the effect of the glycocalyx on transmitting physical forces and inducing mechanotransduction in cancer cells, as well as the integration of signal transduction networks into adhesive dynamics (AD) simulations to predict cell adhesion in the microvasculature.

FLUID SHEAR STRESS EXPOSURE IN THE TUMOR MICROENVIRONMENT

Cancer cells in the tumor microenvironment are exposed to multiple physical forces including fluid shear stress, hydrostatic pressure, tension, and compression, which have been treated in detail

previously (Butcher et al., 2009; Wirtz et al., 2011; Swartz and Lund, 2012). Here, cancer cell exposure to physical forces generated by interstitial flows will be discussed briefly.

Interstitial flow is the slow movement of fluid around cells and through the pores of the extracellular matrix (ECM) that comprise the interstitium (**Figure 1A**). One of the main functions of interstitial flow is lymphatic drainage, which returns plasma from leaky capillaries back to the bloodstream. Drainage occurs due to Starling's forces, which are osmotic and hydrostatic pressure gradients between blood vessels, interstitium, and the lymphatics (Schmid-Schonbein, 1990). The composition of interstitial fluid can vary depending on the location in the body, but in soft tissues is generally similar to the blood plasma that leaks from capillaries, and contains approximately 40% of the protein concentration of plasma (Swartz and Fleury, 2007). The velocities of interstitial flows are believed to range from 0.1 to $1.0 \mu\text{m s}^{-1}$ in normal tissues (Chary and Jain, 1989; Dafni et al., 2002). Cell surface shear stresses are believed to be on the order of 0.1 dyn cm^{-2} (Pedersen et al., 2007; Tarbell and Shi, 2012).

Interstitial flows can be elevated significantly in the tumor microenvironment, and play a crucial role in tumor progression. Chary and Jain (1989) utilized fluorescence recovery after photobleaching (FRAP) to measure interstitial fluid velocities of bovine serum albumin in normal and neoplastic tissues. Harrell et al. utilized live imaging of tumor-bearing mice to measure downstream lymph flow via injection of fluorescent nanoparticles. Measurements were performed in both normal and neoplastic tissues; all tumor-bearing mice in the study showed increases in lymph flow, compared to control mice without tumors (Harrell et al., 2007).

Elevated interstitial flows in the tumor microenvironment are likely due to increased tumor interstitial fluid pressure (IFP). Boucher and Jain (1992) implanted colon adenocarcinoma cells into mice, tracked the development of the tumor vasculature using intravital microscopy, and measured IFP using micropipettes and a servo-null system. IFP measurements increased significantly as the vasculature developed, demonstrating that tumor interstitial

hypertension is associated with tumor angiogenesis (Boucher et al., 1996). IFP is elevated in a uniform manner throughout tumors, and drops significantly at the tumor periphery (Boucher et al., 1990). Thus, IFP gradients facilitate fluid flow outward from tumors, presenting a mass transport barrier for the delivery of chemotherapeutics (Netti et al., 1995; Lunt et al., 2008).

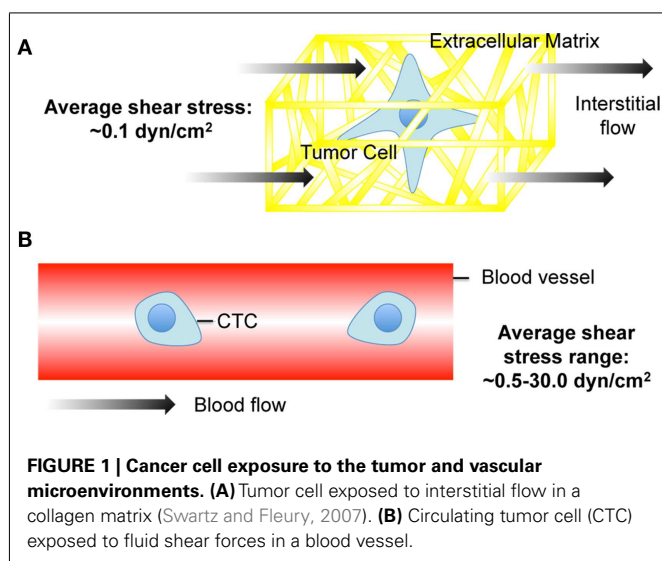
Increased IFP also effects tumor biology, as it applies increased physical force to the ECM and alters interstitial flows that the tumor and surrounding cells are exposed to. Nearby lymphatic vessels respond to elevated interstitial flow by upregulating chemokine CCL21 expression, along with cell adhesion molecules E-selectin and ICAM-1 (Miteva et al., 2010). Secretion of CCL21 directs tumor cells toward lymphatic vessels (Shields et al., 2006), while ICAM-1 and E-selectin upregulation enhances cell transmigration into lymphatic vessels (Johnson et al., 2006; Miteva et al., 2010). Lymph nodes can also be affected, as increased interstitial flows aid in lymph node architecture remodeling to colonize tumor cells, as well as protect the tumor from an immune response (Shieh and Swartz, 2011).

Fibroblasts, which deposit, turn over, and remodel ECM to maintain connective tissue homeostasis, can aid in tumor progression due to elevated interstitial flows. Elevated interstitial flows can upregulate transforming growth factor beta-1 (TGF- β_1) expression (Ng et al., 2005; Ng and Swartz, 2006; Wipff et al., 2007; Ahamed et al., 2008), which can induce a tumor-associated fibroblast phenotype characterized by enhanced contractility and increased secretion of cytokines, angiogenic growth factors, and matrix metalloproteinase (MMPs) (Hinz et al., 2002; De Wever et al., 2004a,b; Orimo and Weinberg, 2006). Recently, Shieh et al. (2011) demonstrated that interstitial flows can enhance tumor cell invasion when cocultured with dermal fibroblasts in a 3D collagen matrix. Fibroblast invasion was enhanced due to increased expression of TGF- β (Chaffer and Weinberg, 2011) and MMPs, while it appeared that tumor cell invasion was enhanced due to fibroblast-dependent remodeling of the ECM (Shieh et al., 2011).

FLUID SHEAR STRESS EXPOSURE IN VASCULAR MICROENVIRONMENT

To enter the vascular microenvironment, cancer cells penetrate surrounding tissue and enter nearby blood and lymphatic vessels in a process called intravasation. The underlying mechanisms that govern intravasation are not well understood; it is still in question whether intravasation is an active or passive process (Bockhorn et al., 2007), and whether tumor cells enter the circulation via endothelial cell-cell junctions or directly through endothelial cells themselves (Khuon et al., 2010). Regardless of their mechanism of entry, cancer cells are exposed to a new set of conditions once in the vascular microenvironment, including immunological stress, collisions with blood cells, and hemodynamic shear forces, all of which can affect their survival and proliferation.

Cancer cells are primarily exposed to erythrocytes, leukocytes, and platelets upon entering the bloodstream, as studies have shown that the concentration of cancer cells in the blood of patients is on the order of one in a million leukocytes (Maheswaran and Haber, 2010), or one in a billion blood cells (Yu et al., 2011). Exposure to such cells can lead to immunological stresses and blood cell collisions that can affect cancer cell viability (Wirtz et al., 2011),



although there is evidence that the association of platelets with cancer cells in the bloodstream can promote tumor metastasis (McCarty et al., 2000; Gay and Felding-Habermann, 2011).

Cancer cells are also exposed to hemodynamic shear forces in the bloodstream (**Figure 1B**), which range from 0.5 to 4.0 dyn cm⁻² in the venous circulation and 4.0–30.0 dyn cm⁻² in arterial circulation (Turitto, 1982). Shear rates can range from approximately 160 s⁻¹ in veins to 900 s⁻¹ in arteries. Such shear stresses and rates can affect cancer cell viability and thus the chances of metastasis. For example, B16 melanoma cell exposure to fluid shear stress in a cone-and-plate viscometer at shear rates greater than 300 s⁻¹ induced a significant loss of cell viability (Brooks, 1984).

In contrast, fluid shear stress is an essential component of cancer metastasis, as it is critical for cancer cell adhesion to the endothelial cell wall and subsequent extravasation into tissues. A variety of cancer cell lines are known to express sialylated carbohydrate ligands, which adhesively interact with selectin proteins on the inflamed microvasculature (Gout et al., 2008; Köhler et al., 2010; Läubli and Borsig, 2010). Thus, cancer cells are believed to undergo an adhesion cascade similar to leukocytes, which consists of a sequence of steps involving tethering, rolling, and firm adhesion to the endothelium (Chambers et al., 1995; Coussens and Werb, 2002). Multiple studies have documented that a variety of tumor cell lines bind to E-selectin proteins under physiological shear stresses of the post-capillary venules (Giavazzi et al., 1993; Barthel et al., 2009).

Much less is known about fluid shear stresses that cancer cells could be exposed to in lymphatic vessels. Lymphatic vessels have been stained with fluorescein isothiocyanate (FITC)-labeled macromolecules to measure lymphatic flow in single lymphatic capillaries of humans *in vivo* using intravital capillary microscopy (Fischer et al., 1996). The recorded median linear velocity in lymphatic capillaries was 9.7 μm s⁻¹, and shear stresses in lymph node sinuses have been estimated to be 10-fold lower than hematogenous shear stresses (Resto et al., 2008). Despite the dramatic decrease in shear stress levels, parallel plate flow chamber studies have shown that human head and neck squamous carcinoma cells can bind to lymphocyte L-selectin at lymphatic shear stress levels of 0.07–0.08 dyn cm⁻² (Resto et al., 2008).

COMPUTATIONAL METHODS TO MODEL CELL EXPOSURE TO INTERSTITIAL FLOWS

Interstitial flow mechanics were initially described by French hydraulics engineer Henry Darcy, who studied the flow of water through sand beds as a means of providing filtered drinking water to his city. During his studies, he developed the formula known as Darcy's law:

$$\bar{u} = \frac{-K \nabla P}{\mu},$$

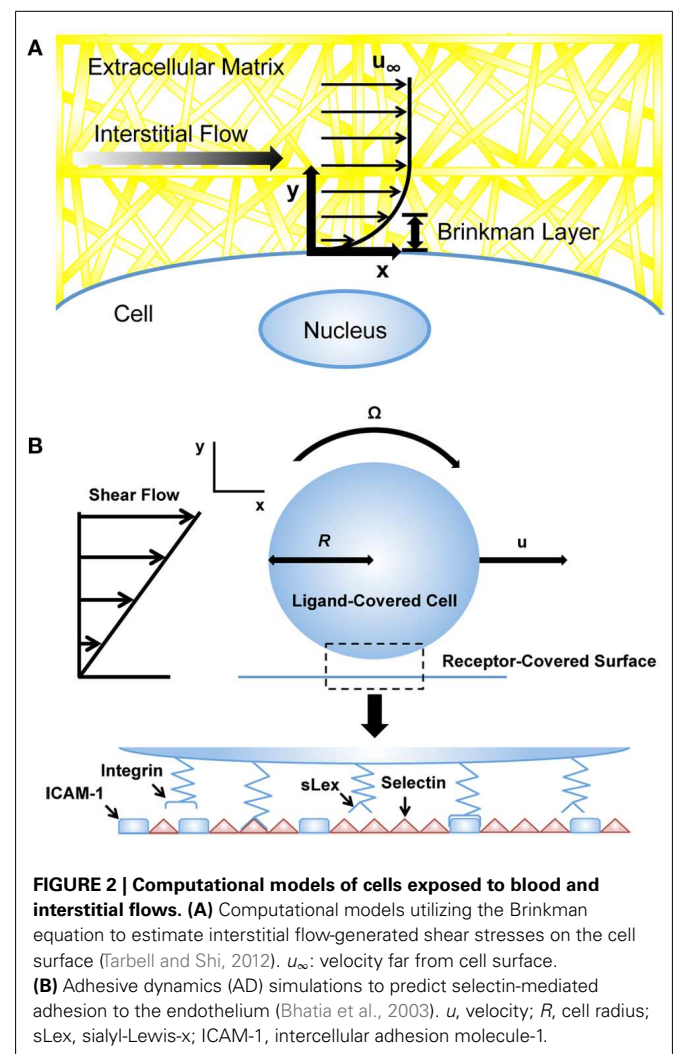
where K is the permeability of the medium, ∇P is the pressure gradient vector, μ is the viscosity of the fluid, and \bar{u} is the averaged velocity through the bulk. Darcy's law works well when the average velocity or mass flow rate needs to be determined, but is first order with respect to velocity. To account for interstitial

flows between boundaries, Brinkman developed a second order term, taking into account no-slip boundary conditions adjacent to bounding walls (**Figure 2A**; Brinkman, 1949). The Brinkman equation is described as:

$$\nabla P = -\frac{\mu}{K} \bar{u} + \mu \nabla^2 \bar{u}.$$

Permeability measurements have been performed for a variety of tissues *in vitro*, *in vivo*, and *ex vivo*, including muscle (Rasheid Zakaria et al., 1997), dermis (Bert and Reed, 1995), cartilage (Levick, 1987), tumors (Netti et al., 2000; McGuire et al., 2006), and fibrin and collagen gels (Diamond, 1999; Ng and Swartz, 2003), making the Darcy and Brinkman equations useful for both experimental measurements of interstitial flows and computational models of cells exposed to such flows.

Initial models of interstitial flows exerted on cells were developed for tissues including smooth muscle, cartilage, and bone (Kwan et al., 1984; Grodzinsky et al., 2000; Hellmich and Ulm, 2005). For example, Wang and Tarbell (1995) modeled the tunica media of an artery as a periodic array of cylindrical, impermeable SMCs embedded in a matrix consisting of collagen and



proteoglycans, and used Brinkman's theory to model interstitial flow across the tissue. The model was able to estimate the effective hydraulic permeability of the tissue and shear stresses exerted on SMCs, which were estimated to be on the order of 1.0 dyn cm^{-2} despite exposure to low interstitial flows (Wang and Tarbell, 1995). In an early model describing the mechanics of interstitial-lymphatic transport, Swartz et al. developed a theoretical and experimental model demonstrating how interstitial flow is dependent on hydraulic conductivity, elasticity, and lymphatic conductance. They then utilized this model to examine fluid balance in normal and chronically swollen (edematous conditions) mouse tails, in which they found that remodeling of the matrix dampened and eventually stagnated fluid movement in the case of edema (Swartz et al., 1999).

COMPUTATIONAL METHODS TO MODEL CELL BEHAVIOR IN THE CIRCULATION

A variety of computational methods have been developed to model cell behavior in the vascular microenvironment, including adhesive dynamics (AD), which has been utilized to simulate cell adhesion to the endothelial cell surface under flow (Hammer and Lauffenburger, 1987; Hammer and Apte, 1992). The motivation of such simulations is to predict how adhesiveness quantitatively depends on factors such as shear rate and viscosity, which can reveal adhesion phenomena that might not necessarily follow intuition. AD is a mechanically rigorous cell adhesion simulation that models individual molecular bonds as compliant springs. In the simulation, the cell can be modeled as a rigid spherical particle covered with a random distribution of adhesion molecules (Figure 2B). The endothelial cell wall can be modeled as a surface covered with counter-receptor molecules of random distribution. Bonds randomly form between adhesion molecules of the cell and counter-receptors on the wall; these bonds can then break contingent on the appropriate kinetics, which depend on the instantaneous force loading on the spring endpoints. The rates of bond formation and rupture can be calculated using the Bell model for kinetics of single biomolecular bond failure (Bell, 1978; Bell et al., 1984):

$$k_r = k_r^0 \exp\left(\frac{r_0 F}{k_b T}\right)$$

where k_r is the rate of dissociation, k_r^0 is the unstressed off-rate, F is the force on the bond, r_0 is the reactive compliance, T is the temperature, and k_b is the Boltzmann constant. The rate of bond formation follows from the Boltzmann distribution of affinity, while also incorporating the effects of relative motion between the cell and surface (King et al., 2005). To solve the algorithm, unbound receptors in the defined contact area are first tested for formation against the probability:

$$P_f = 1 - \exp(-k_f \Delta t)$$

where P_f is the probability of bond formation, and t is time. Next, bound receptors are tested for breakage against the probability:

$$P_r = 1 - \exp(-k_r \Delta t)$$

where P_r is the probability of bond rupture. External forces and torques on the cell are then summed, and a mobility calculation determines the motion of the cell. Cell and bond positions are updated based on the kinematics of cell motion. Torques exerted by fluid flow and hydrodynamic forces cause the adherent cell to slowly roll forward on a reactive surface. The motion of fluid is governed by the Stokes equation:

$$\mu \nabla^2 u = \nabla P, \quad \nabla \cdot u = 0,$$

where u is the velocity, μ is the viscosity of the fluid, and P is the pressure. No-slip boundary conditions are applied at the cell surface and the planar wall.

While AD has not yet been used to model cancer cell adhesion, many simulations have been performed using leukocytes, which can be a close parallel to a CTC that has undergone the epithelial-mesenchymal transition (EMT). Chang et al. (2000) utilized AD to develop a state diagram for leukocyte adhesion under flow. In the diagram, observed adhesive behaviors (rolling, firm adhesion, or no adhesion) were plotted at given dissociation rates and bond interaction lengths, which spanned several orders of magnitude. Caputo and Hammer (2005) incorporated deformable microvilli with clustered adhesion molecules onto the surface of the simulated leukocyte, and found that the deformability of the microvilli can affect the cell's ability to roll on a surface. King and Hammer (2001a,b) modeled the effect of cell-cell hydrodynamic interactions on the dynamics of leukocyte adhesion using Multi-particle AD (MAD), which revealed a mechanism for secondary hydrodynamic recruitment of leukocytes to the blood vessel wall, independent of leukocyte-leukocyte contact interactions.

Critical parameters of AD simulations are the kinetics of selectin-carbohydrate bonds, as force-dependent dissociation rates dictate the rolling adhesion of leukocytes. Numerous studies have investigated the kinetics for leukocyte selectin ligands using experimental techniques such as flow chamber tethering experiments, atomic force microscopy, and dynamic force spectroscopy (Smith et al., 1999). However, such kinetics for newly identified selectin ligands expressed by metastatic tumor cells, which appear distinct from those found on the surface of leukocytes (Thomas et al., 2008; Shirure et al., 2012), have not yet been well characterized. Future experimental studies measuring bond dissociation kinetics for selectins and CTC selectin ligands will enable the development of more predictive computational models of cancer cell adhesion to microvasculature.

CURRENT EXPERIMENTAL MODELS OF CANCER CELL MECHANOTRANSDUCTION

FLUID SHEAR STRESS ALTERS CANCER CELL RESPONSE TO APOPTOSIS-INDUCING LIGANDS

The targeting and treatment of CTCs within the circulation is currently being investigated as an approach to prevent their metastatic spread. For example, microfluidic devices coated with E-selectin conjugated liposomal doxorubicin have been shown to capture cancer cells from flow, deliver doxorubicin into the cell, and induce cell death (Mitchell et al., 2012a,b). Similarly, microfluidic devices immobilized with E-selectin and tumor necrosis factor (TNF)-related apoptosis-inducing ligand (TRAIL) have been shown to

capture and kill cancer cells (Rana et al., 2009) while exerting minimal toxic effects on human leukocytes (Rana et al., 2012). However, little is known about how fluid shear stress exposure can affect cancer cell response to drug treatments.

Our recent study examined how colorectal adenocarcinoma COLO 205 and prostate adenocarcinoma PC-3 cancer cell exposure to physiologically relevant fluid shear stresses in a cone-and-plate viscometer altered their response to TRAIL (Figure 3; Mitchell and King, 2013). Experiments were devised in such a way that fluid shear stress alone had negligible effects on cancer cell death. Cancer cells were treated with both TRAIL, which can bind to death receptors DR4 and DR5 on the cancer cell surface to initiate apoptosis (Ashkenazi, 2002), and doxorubicin, which induces cell death via inhibition of topoisomerase II and DNA intercalation (Young et al., 1981; Osheroff et al., 1994). Interestingly, treatment of both COLO 205 and PC-3 cancer cell lines with TRAIL followed by exposure to 2.0 dyn cm⁻² of fluid shear stress significantly increased the number of apoptotic cells, compared to TRAIL-treated cancer cells exposed to static conditions. The sensitization effect was both fluid shear stress dose- and time-dependent, as the number of apoptotic cells increased over a range of shear stress magnitudes (0.05–2.0 dyn cm⁻²) and shear stress exposure times (1–120 min). However, such sensitization was not evident in doxorubicin treatment, as the percentage of apoptotic cells remained nearly identical in doxorubicin-treated samples exposed to either fluid shear stress or static conditions. The results indicated that such sensitization could be receptor-mediated apoptosis specific.

It is possible that death receptors on the cancer cell surface can sense and respond to fluid shear forces. The idea of circulating

cells expressing mechanosensitive receptors has recently been investigated in leukocytes (Makino et al., 2006; Mitchell and King, 2012), where it is believed that G-protein coupled receptors can sense fluid shear stress and alter neutrophil adhesion to the microvasculature. However, little is known about the effects of fluid shear stress on CTC surface receptors. Insight into the mechanistic basis of such processes could reveal new strategies for treating cancer cells in the circulation, and reducing the likelihood of metastasis.

CANCER CELL RESISTANCE TO FLUID SHEAR STRESS

Recently, a microfluidic protocol was developed to assess cancer cell resistance to fluid shear stress (Barnes et al., 2012). In the protocol, dilute cancer cell suspensions were drawn up into a syringe, which was then loaded into an automatic syringe pump (Figure 4A). Cancer cell suspensions were exposed to brief, millisecond pulses of high fluid shear stress as they were expelled from the syringe pump, and subsequently analyzed for cell viability using bioluminescent imaging. The maximum fluid shear stress that cancer cells were briefly exposed to in this experiment reached 6400 dyn cm⁻². Note that CTCs are momentarily exposed to shear stresses as high as 3000 dyn cm⁻² at vessel bifurcations, in the heart, and near the walls of large blood vessels (Strony et al., 1993; Malek et al., 1999). While cancer cell viability decreased after repeated millisecond pulse exposures to high fluid shear stress, the study revealed that cancer cells of epithelial origin were surprisingly resistant to fluid shear stress, in comparison to non-transformed epithelial cells. Resistance to fluid shear stress was dependent on several oncogenes, as *myc*- and *ras*-transformed cell lines showed an increase in fluid shear stress resistance. The

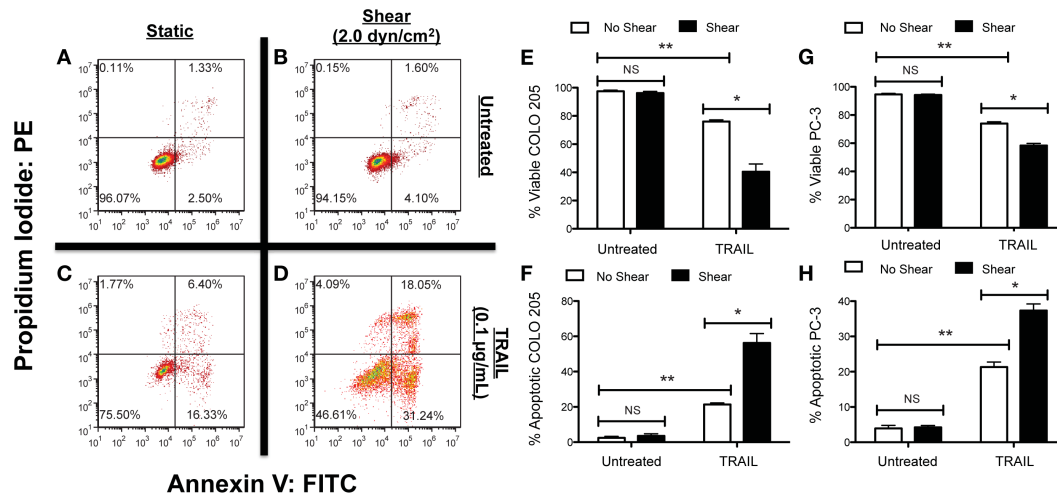


FIGURE 3 | Fluid shear stress sensitizes cancer cells to the apoptosis-inducing ligand TRAIL. Colorectal adenocarcinoma COLO 205 cells exposed to non-shear conditions (A) and fluid shear stress (B), respectively. COLO 205 cells treated with TRAIL and then exposed to non-shear conditions (C) and fluid shear stress (D). Lower left-hand and right-hand quadrants of each flow cytometry figure represent viable cells and cells in early stages of apoptosis, respectively. Upper left-hand and right-hand quadrants represent cells

undergoing necrosis and late stage apoptosis, respectively. Percentage of viable (E) and apoptotic (F) COLO 205 cells after treatment with TRAIL followed by exposure to non-shear or shear conditions ($n=3$). Percentage of viable (G) and apoptotic (H) PC-3 cells treated under the same conditions ($n=3$). PE, phycoerythrin; FITC, fluorescein isothiocyanate. Error bars represent 95% confidence intervals. * $P < 0.05$. ** $P < 0.01$. NS, non-significant. Figure reprinted with permission from Mitchell and King (2012).

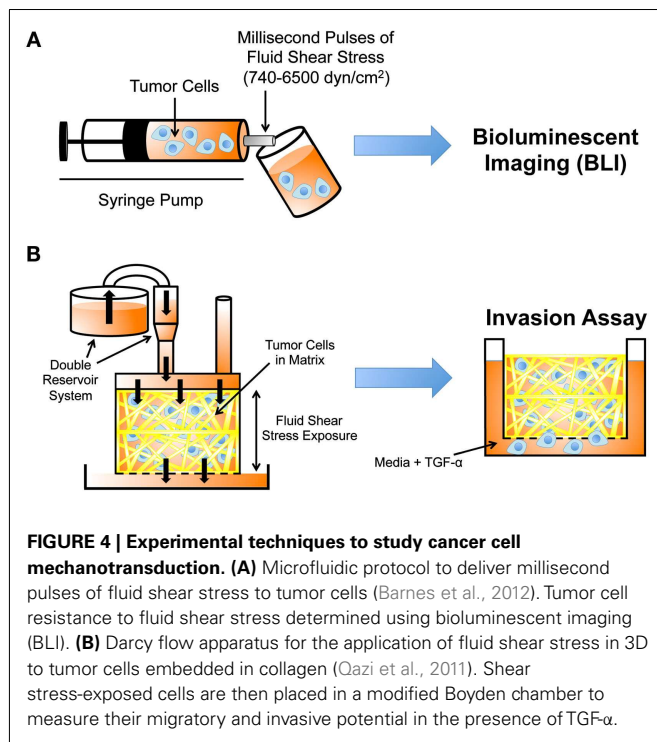


FIGURE 4 | Experimental techniques to study cancer cell mechanotransduction. (A) Microfluidic protocol to deliver millisecond pulses of fluid shear stress to tumor cells (Barnes et al., 2012). Tumor cell resistance to fluid shear stress determined using bioluminescent imaging (BLI). **(B)** Darcy flow apparatus for the application of fluid shear stress in 3D to tumor cells embedded in collagen (Qazi et al., 2011). Shear stress-exposed cells are then placed in a modified Boyden chamber to measure their migratory and invasive potential in the presence of TGF- α .

resistance response required extracellular calcium and actin polymerization, as the absence of calcium or treatment with EGTA, cytochalasin D, or ROCK inhibitor Y27632 all reduced cancer cell viability upon fluid shear stress exposure. In particular, extracellular calcium is important for cellular repair mechanisms based on an extracellular calcium-dependent membrane resealing process (Terasaki et al., 1997).

FLUID SHEAR STRESS REGULATES CANCER CELL INVASIVE POTENTIAL

Prior work has shown that the chemokine gradients generated by interstitial flows can enhance tumor cell migration (Shields et al., 2007), however it is not well understood whether fluid shear stress can regulate intrinsic properties of cancer cells, thus altering their invasive potential. Recent work by Qazi et al. (2011) detailed a Darcy flow apparatus for the application of fluid shear stress to a 3D collagen gel embedded with glioma cells, coupled with a modified Boyden chamber invasion assay. In the apparatus, a double reservoir system applied hydrostatic pressure, which drove media throughout the 3D collagen gel and exerted shear stress on the glioma cells (Figure 4B). Cancer cells were exposed to fluid shear stresses ranging from 0.1 to 0.6 dyn cm⁻². The media filtrate from the gel was collected in a separate reservoir, and the media collected was used to calculate flow rates, velocities, and shear stresses. Collagen gels were removed at the end of the flow period, and placed within modified Boyden chambers containing TGF- α to initiate invasion assays.

Fluid shear stress significantly reduced U87 and CNS-1 glioma cell migration by as much as 92% and 58% respectively, when compared to controls. Migration suppression was not due to flow-induced chemokine gradients, however, as cells were exposed to fluid shear stress followed by exposure to TGF- α in static

Boyden chambers. Invasion was dependent on matrix metalloproteinases (MMPs), as MMP-1 and MMP-2 gene expression was significantly downregulated in cancer cells upon exposure to 0.55 dyn cm⁻² fluid shear stress. Previous studies have shown that fluid shear stress can affect MMP expression and activity in non-tumor cell types such as fibroblasts, chondrocytes, and SMCs (Yokota et al., 2003; Garanich et al., 2007; Shi and Tarbell, 2011), however this was one of first studies revealing that fluid shear stress-induced mechanotransduction is involved in interstitial flow-induced cancer cell motility.

INTERSTITIAL FLOW INDUCES TUMOR CELL FOCAL ADHESION KINASE ACTIVATION

A recent study investigated two competing mechanisms which can alter tumor cell migration upon exposure to interstitial flow: an autologous chemotaxis-based mechanism which distributes autocrine chemokine via convection to create a chemokine gradient, and a mechanism whereby interstitial flow activates focal adhesion kinase (FAK) and modulates forces critical for tumor cell migration (Fincham and Frame, 1998; Sieg et al., 1998). Polacheck et al. (2011) developed a microfluidic cell culture system to investigate the effects of interstitial flow on the directional bias and dynamics of tumor cell migration in a 3D matrix. Utilizing two channels separated by a region in which tumor cells were suspended in a 3D collagen gel, a pressure gradient was applied across the gel to generate consistent interstitial flow velocities ranging from 0.3 to 3.0 $\mu\text{m s}^{-1}$, representative of a range of values measured *in vivo* (Dafni et al., 2002; Heldin et al., 2004). Confocal reflective microscopy was used to track cell migration under flow, and it was found that interstitial flow and cell seeding density can both influence the direction of tumor cell migration.

Upon exposure to interstitial flow at low seeding densities, MDA-MB-321 metastatic breast cancer cells migrated in the downstream direction, or “with the flow.” However, cancer cells exposed to interstitial flow at high seeding densities migrated upstream, or “against the flow.” Treatment with CCR7 blocking antibodies, to block the binding of secreted ligand CCL21 needed to initiate autologous chemotaxis, caused cells to shift their migration directionality and migrated upstream upon exposure to flow. Cells that migrated in the opposite direction of flow displayed increased phosphorylation at Tyr-397 in FAK, which plays a role in Src kinase activation and focal adhesion formation (Li et al., 1997; Jalali et al., 1998). Upon blockage of Src kinase activity, upstream tumor cell migration decreased and displayed random cell migration.

CURRENT ADVANCES IN MODELING MECHANOTRANSDUCTION PHENOMENA

MODELING GLYCOCALYX EFFECTS ON INTERSTITIAL FLUID SHEAR STRESS TRANSMISSION TO CANCER CELLS

The glycocalyx is a layer of proteoglycans and glycoproteins that covers eukaryotic cells, which can serve as a mechanosensor of fluid shear stress in endothelial cells and SMCs (Yao et al., 2007; Shi et al., 2011). Tumor cells also possess a glycocalyx (Krähling et al., 2009), however its effects as a mechanosensor have not been previously investigated. It has been hypothesized that fluid shear stress generated by interstitial flows is too weak to induce mechanotransduction.

Tarbell and Shi (2012) recently developed a computational model to estimate the interstitial flow-generated fluid and solid stresses on the surface of a glycocalyx-covered cell embedded in ECM (**Figure 5A**). Previously estimated parameters such as the Darcy permeability of the ECM, tumor cell glycocalyx thickness, and interstitial fluid flow velocity were incorporated into the model to calculate the fluid and solid stresses on the cell surface. Brinkman equations were used to describe interstitial fluid flow through pores of both the ECM and glycocalyx. A previously described model (Secomb et al., 2001) was used to calculate mechanical equilibrium of forces in the direction of flow to calculate the solid stresses transmitted via the glycocalyx. While fluid stresses exerted on the tumor cell surface were estimated to be quite low (less than 0.1 dyn cm^{-2}), the solid stresses transmitted to the cell via the glycocalyx were predicted to be over 5.0 dyn cm^{-2} , a magnitude which is known to activate endothelial cells (Malek et al., 1999). Future models could incorporate mechanical effects along with chemical signaling pathways to better predict cancer cell mechanotransduction in tissues.

INTEGRATING SIGNAL TRANSDUCTION NETWORKS INTO ADHESIVE DYNAMICS SIMULATIONS

Recently, signal transduction models were incorporated into AD simulations to couple signaling pathways with cell adhesion. In the model, leukocytes were assigned a random spatial distribution of integrin lymphocyte function-associated antigen-1 (LFA-1), in

addition to selectin ligands such as PSGL-1. The reactive surfaces were covered with selectin molecules and intracellular adhesion molecule-1 (ICAM-1), which binds to active LFA-1 and mediates firm arrest. Krasik et al. (2006) integrated the mitogen-activated protein kinase (MAPK) signal transduction pathway as a modular Hill function within the AD framework to model neutrophil arrest with deterministic activation. Selectin ligation triggered the MAPK cascade in this model, which can cause inactive LFA-1 to become activated, enabling binding to ICAM-1 and subsequent neutrophil arrest. This model has since incorporated a stochastic signal transduction model, utilizing a Monte Carlo simulation within the microvilli of model neutrophils (Krasik et al., 2008).

Caputo et al. generated an AD simulation with an integrated signal transduction network that incorporates selectin, integrin, and chemokine interactions between the neutrophil and the substrate. A random distribution of the G-protein coupled receptor CXCR1 and chemokine interleukin-8 (IL-8) were displayed on the leukocyte and the reactive surfaces, respectively (**Figure 5B,C**). CXCR1 can interact with IL-8, which initiates a signaling cascade leading to LFA-1 activation on the cell (Caputo and Hammer, 2009). Beste et al. (2012) developed a model of T-lymphocyte arrest by combining AD with a kinetic model for chemokine-triggered inside-out integrin activation. The model incorporated signaling data measured in experiments to simulate the time scale for T-lymphocyte arrest, and provided a predictive simulation for understanding chemokine control of T-lymphocyte recruitment.

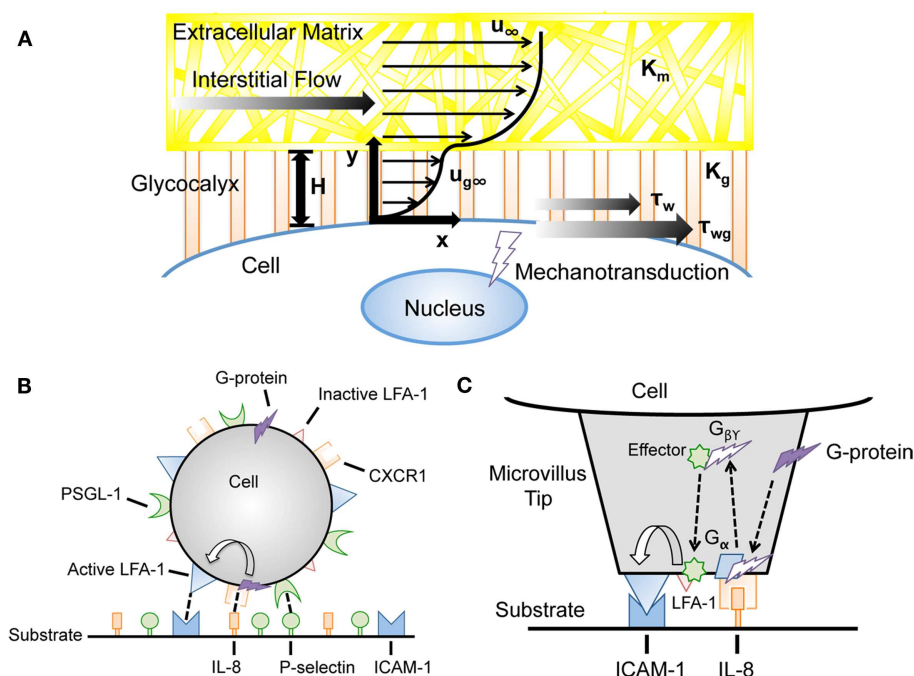


FIGURE 5 | Advances in computational modeling reveal mechanotransduction phenomena. (A) Interstitial flow models incorporating the force-transducing cell glycocalyx to determine interstitial flow contributions to fluid shear stress-dependent mechanotransduction (Tarbell and Shi, 2012). u_∞ , velocity far from cell surface; K_m , matrix Darcy permeability; K_g , glycocalyx Darcy

permeability; H , glycocalyx layer thickness; u_{g0} , velocity profile in glycocalyx; τ_w , surface fluid stress; τ_{wg} , surface solid stress.

(B,C) Incorporation of cell signaling networks to predict flow-mediated cell adhesion in the presence of chemoattractants (Caputo and Hammer, 2009). IL-8, interleukin-8; PSGL-1, P-selectin glycoprotein ligand-1; LFA-1, lymphocyte function-associated antigen-1.

The integration of signal transduction networks into AD simulations could prove particularly useful for the study of cancer metastasis, as molecular defects could be implemented within the signaling cascade to predict its effects on CTC adhesion to the endothelium.

COMPUTATIONAL MODELS OF INTEGRIN–LIGAND INTERACTIONS AT THE CELL–ECM INTERFACE

A model based on the AD simulation was developed to both chemically and mechanically model integrin dynamics at the cell–ECM interface (Paszek et al., 2009). Paszek et al. developed the model to determine whether the cell glycocalyx and the chemical and physical parameters of the ECM can control the formation of integrin clusters, which act as mechanical anchors and can regulate cell survival, motility, differentiation, and morphogenesis (Hynes, 2002; Miranti and Brugge, 2002; Berrier and Yamada, 2007). Integrin–ligand bonds were modeled as individual Hookean springs, and the Bell model was utilized to calculate kinetic rates of bond formation and rupture, which are distance-dependent (Bell, 1978; Bell et al., 1984). In addition, the model included a lattice spring model (LSM) of the cell–ECM interface, consisting of a lattice of interconnecting nodes and springs to calculate the stress–strain behavior of the interface (Ostojia-Starzewski et al., 1996). Model parameters including the glycocalyx, membrane, and bond spring constants, on- and off-rates, and receptor and ligand density were estimated based on experimental measurements.

Integrin clustering began as a fast process, as simulations showed that new integrin bond formation events were more likely to occur near existing integrin bonds where the separation distance between integrins and ligands was reduced. However, bond rearrangements due to bond breakage and reformation were found to slow down the integrin clustering process over time. Glycocalyx thickness also affected integrin clusters, with larger, denser clusters forming with increased glycocalyx thickness. The interplay between integrin–ligand affinity and cell–ECM repulsion due to the glycocalyx also affected clustering; high affinity interactions coupled with thinner glycocalyx resulted in bound integrin receptors with minimal clustering. A thicker glycocalyx relative to integrin bond length, along with an adequate receptor–ligand affinity, resulted in both integrin binding and clustering. Integrin clustering increased due to increases in the ratio of glycocalyx stiffness to membrane stiffness, as it increased the minimal matrix ligand density. Integrin clustering was shown to be sensitive to ECM stiffness; compliant substrates could not promote cooperative binding,

while integrin clustering increased with increasing substrate stiffness above 2000 Pa. While the computational model only incorporates basic biology, a combination of the mechanical model with molecular interactions revealed cell adhesion behavior observed in experiments (Cluzel et al., 2005; Paszek et al., 2009). Future models should focus on the incorporation of applied fluid shear forces, along with integrin–cytoskeleton interactions, to predict how adhesions on the cancer cell surface can sense and respond to the tumor microenvironment.

CONCLUSION

Fluid shear stresses generated by blood and interstitial flows alter cancer cell behavior in the vascular and tumor microenvironments, respectively, and contribute to the progression of cancer metastasis. Interstitial flow-generated forces elevate tumor IFP, and create challenges to chemotherapeutic delivery to the tumor interior. Such forces also induce phenotypic changes of cells in the surrounding microenvironment, which enhance tumor cell migration and invasion. Shear flows in the circulation affect tumor cell viability while also playing a role in CTC adhesion to the endothelium, a crucial step for subsequent tumor cell extravasation and metastasis. Recent experimental studies have revealed that fluid shear stress can modulate intrinsic characteristics of cells, in addition to the extrinsic roles of fluid flow that have been previously documented. Cancer cell mechanotransduction observed in recent experiments, including tumor cell resistance to shear stress, regulation of migration and invasion, and sensitivity to chemotherapeutics, have potentially wide ranging implications for metastasis. Recent computational models have incorporated mechanical fluid forces with chemical signaling networks, along with mechanotransducing components on the cancer cell surface, such as the glycocalyx. Future approaches utilizing computational models of fluid shear stress effects on intrinsic tumor cell signaling networks, coupled with *in vitro* and *in vivo* experimental validation, may better predict cell behavior in such dynamic microenvironments, and potentially provide novel approaches for the prevention of metastasis.

ACKNOWLEDGMENTS

The work described was supported by the Cornell Center on the Microenvironment and Metastasis through Award Number U54CA143876 from the National Cancer Institute. The content is solely the responsibility of the authors and does not necessarily represent the official views of the National Cancer Institute or the National Institutes of Health.

REFERENCES

- Ahamed, J., Burg, N., Yoshinaga, K., Janczak, C. A., Rifkin, D. B., and Collier, B. S. (2008). In vitro and in vivo evidence for shear-induced activation of latent transforming growth factor- β 1. *Blood* 112, 3650–3660.
- Ashkenazi, A. (2002). Targeting death and decoy receptors of the tumour-necrosis factor superfamily. *Nat. Rev. Cancer* 2, 420–430.
- Barnes, J. M., Nauseef, J. T., and Henry, M. D. (2012). Resistance to fluid shear stress is a conserved biophysical property of malignant cells. *PLoS ONE* 7:e50973. doi:10.1371/journal.pone.0050973
- Barthel, S. R., Wiese, G. K., Cho, J., Opperman, M. J., Hays, D. L., Siddiqui, J., et al. (2009). Alpha 1,3 fucosyltransferases are master regulators of prostate cancer cell trafficking. *Proc. Natl. Acad. Sci. U. S. A.* 106, 19491–19496.
- Bell, G. I. (1978). Models for the specific adhesion of cells to cells. *Science* 200, 618–627.
- Bell, G. I., Dembo, M., and Bongrand, P. (1984). Cell adhesion. Competition between nonspecific repulsion and specific bonding. *Biophys. J.* 45, 1051–1064.
- Berrier, A. L., and Yamada, K. M. (2007). Cell–matrix adhesion. *J. Cell. Physiol.* 213, 565–573.
- Bert, J. L., and Reed, R. K. (1995). Flow conductivity of rat dermis is determined by hydration. *Biorheology* 32, 17–27.
- Beste, M. T., Lee, D., King, M. R., Koretzky, G. A., and Hammer, D. A. (2012). An integrated stochastic model of “inside-out” integrin activation and selective T-lymphocyte recruitment. *Langmuir* 28, 2225–2237.
- Bhatia, S. K., King, M. R., and Hammer, D. A. (2003). The state diagram for cell adhesion mediated by two receptors. *Biophys. J.* 84, 2671–2690.
- Bockhorn, M., Jain, R. K., and Munn, L. L. (2007). Active versus passive mechanisms in metastasis: do cancer cells crawl into vessels, or

- are they pushed? *Lancet Oncol.* 8, 444–448.
- Boucher, Y., Baxter, L. T., and Jain, R. K. (1990). Interstitial pressure gradients in tissue-isolated and subcutaneous tumors: implications for therapy. *Cancer Res.* 50, 4478–4484.
- Boucher, Y., and Jain, R. K. (1992). Microvascular pressure is the principal driving force for interstitial hypertension in solid tumors: implications for vascular collapse. *Cancer Res.* 52, 5110–5114.
- Boucher, Y., Leunig, M., and Jain, R. K. (1996). Tumor angiogenesis and interstitial hypertension. *Cancer Res.* 56, 4264–4266.
- Brinkman, H. C. (1949). A calculation of the viscous force exerted by a flowing fluid on a dense swarm of particles. *Appl. Sci. Res.* 1, 27–34.
- Brooks, D. E. (1984). The biorheology of tumor cells. *Biorheology* 21, 85–91.
- Butcher, D. T., Alliston, T., and Weaver, V. M. (2009). A tense situation: forcing tumour progression. *Nat. Rev. Cancer* 9, 108–122.
- Caputo, K. E., and Hammer, D. A. (2005). Effect of microvillus deformability on leukocyte adhesion explored using adhesive dynamics simulations. *Biophys. J.* 89, 187–200.
- Caputo, K. E., and Hammer, D. A. (2009). Adhesive dynamics simulation of G-protein-mediated chemokine-activated neutrophil adhesion. *Biophys. J.* 96, 2989–3004.
- Chaffer, C. L., and Weinberg, R. A. (2011). A perspective on cancer cell metastasis. *Science* 331, 1559–1564.
- Chambers, A. F., Groom, A. C., and MacDonald, I. C. (2002). Dissemination and growth of cancer cells in metastatic sites. *Nat. Rev. Cancer* 2, 563–572.
- Chambers, A. F., MacDonald, I. C., Schmidt, E. E., Koop, S., Morris, V. L., Khokha, R., et al. (1995). Steps in tumor metastasis: new concepts from intravital microscopy. *Cancer Metastasis Rev.* 14, 279–301.
- Chang, K. C., Tees, D. F., and Hammer, D. A. (2000). The state diagram for cell adhesion under flow: leukocyte rolling and firm adhesion. *Proc. Natl. Acad. Sci. U.S.A.* 97, 11262–11267.
- Chary, S. R., and Jain, R. K. (1989). Direct measurement of interstitial convection and diffusion of albumin in normal and neoplastic tissues by fluorescence photobleaching. *Proc. Natl. Acad. Sci. U.S.A.* 86, 5385–5389.
- Cheung, L. S.-L., Raman, P. S., Balzer, E. M., Wirtz, D., and Konstantopoulos, K. (2011). Biophysics of selectin-ligand interactions in inflammation and cancer. *Phys. Biol.* 8, 015013.
- Civelek, M., Ainslie, K., Garanich, J. S., and Tarbell, J. M. (2002). Smooth muscle cells contract in response to fluid flow via a Ca²⁺-independent signaling mechanism. *J. Appl. Physiol.* 93, 1907–1917.
- Cluzel, C., Saltel, F., Lussi, J., Paulhe, F., Imhof, B. A., and Wehrle-Haller, B. (2005). The mechanisms and dynamics of $\alpha\beta 3$ integrin clustering in living cells. *J. Cell Biol.* 171, 383–392.
- Coussens, L. M., and Werb, Z. (2002). Inflammation and cancer. *Nature* 420, 860–867.
- Dafni, H., Israely, T., Bhujwalla, Z. M., Benjamin, L. E., and Neeman, M. (2002). Overexpression of vascular endothelial growth factor 165 drives peritumor interstitial convection and induces lymphatic drain. *Cancer Res.* 62, 6731–6739.
- De Wever, O., Nguyen, Q. D., Van Hoorde, L., Bracke, M., Bruyneel, E., Gespach, C., et al. (2004a). Tenascin-C and SF/HGF produced by myofibroblasts in vitro provide convergent pro-invasive signals to human colon cancer cells through RhoA and Rac. *FASEB J.* 18, 1016–1018.
- De Wever, O., Westbroek, W., Verloes, A., Bloemen, N., Bracke, M., Gespach, C., et al. (2004b). Critical role of N-cadherin in myofibroblast invasion and migration in vitro stimulated by colon-cancer-cell-derived TGF- β or wounding. *J. Cell Sci.* 117, 4691–4703.
- Diamond, S. L. (1999). Engineering design of optimal strategies for blood clot dissolution. *Annu. Rev. Biomed. Eng.* 1, 427–462.
- DuFort, C. C., Paszek, M. J., and Weaver, V. M. (2011). Balancing forces: architectural control of mechanotransduction. *Nat. Rev. Mol. Cell Biol.* 12, 308–319.
- Fincham, V. J., and Frame, M. C. (1998). The catalytic activity of Src is dispensable for translocation to focal adhesions but controls the turnover of these structures during cell motility. *EMBO J.* 17, 81–92.
- Fischer, M., Franzeck, U. K., Herrig, I., Costanzo, U., Wen, S., Schiesser, M., et al. (1996). Flow velocity of single lymphatic capillaries in human skin. *Am. J. Physiol. Heart Circ. Physiol.* 270, H358–H363.
- Garanich, J. S., Mathura, R. A., Shi, Z. D., and Tarbell, J. M. (2007). Effects of fluid shear stress on adventitial fibroblast migration: implications for flow-mediated mechanisms of arterIALIZATION and intimal hyperplasia. *Am. J. Physiol. Heart Circ. Physiol.* 292, H3128–H3135.
- Gay, L. J., and Felding-Habermann, B. (2011). Contribution of platelets to tumour metastasis. *Nat. Rev. Cancer* 11, 23–134.
- Giavazzi, R., Foppolo, M., Dossi, R., and Remuzzi, A. (1993). Rolling and adhesion of human tumor cells on vascular endothelium under physiological flow conditions. *J. Clin. Invest.* 92, 3038–3044.
- Gout, S., Tremblay, P., and Huot, J. (2008). Selectins and selectin ligands in extravasation of cancer cells and organ selectivity of metastasis. *Clin. Exp. Metastasis* 25, 335–344.
- Grodzinsky, A. J., Levenston, M. E., Jin, M., and Frank, E. H. (2000). Cartilage tissue remodeling in response to mechanical forces. *Annu. Rev. Biomed. Eng.* 2, 691–713.
- Hammer, D. A., and Apte, S. M. (1992). Simulation of cell rolling and adhesion on surfaces in shear flow: general results and analysis of selectin-mediated neutrophil adhesion. *Biophys. J.* 63, 35–57.
- Hammer, D. A., and Lauffenburger, D. A. (1987). A dynamical model for receptor-mediated cell adhesion to surfaces. *Biophys. J.* 52, 475–487.
- Harrell, M. I., Iritani, B. M., and Rud-dell, A. (2007). Tumor-induced sentinel lymph node lymphangiogenesis and increased lymph flow precede melanoma metastasis. *Am. J. Pathol.* 170, 774–786.
- Heldin, C.-H., Rubin, K., Pietras, K., and Ostman, A. (2004). High interstitial fluid pressure – an obstacle in cancer therapy. *Nat. Rev. Cancer* 4, 806–813.
- Helmlich, C., and Ulm, F.-J. (2005). Drained and undrained poroelastic properties of healthy and pathological bone: a poro-micromechanical investigation. *Transport Porous Med.* 58, 243–268.
- Hinz, B., Gabbiani, G., and Chaponnier, C. (2002). The NH₂-terminal peptide of α -smooth muscle actin inhibits force generation by the myofibroblast in vitro and in vivo. *J. Cell Biol.* 157, 657–663.
- Hughes, A. D., and King, M. R. (2011). Nanobiotechnology for the capture and manipulation of circulating tumor cells. *Wiley Interdiscip. Rev. Nanomed. Nanobiotechnol.* 4, 291–309.
- Hynes, R. O. (2002). Integrins: bidirectional, allosteric signaling machines. *Cell* 110, 673–687.
- Jalali, S., Li, Y. S., Sotoudeh, M., Yuan, S., Li, S., Chien, S., et al. (1998). Shear stress activates p60src-Ras-MAPK signaling pathways in vascular endothelial cells. *Arterioscler. Thromb. Vasc. Biol.* 18, 227–234.
- Johnson, L. A., Clasper, S., Holt, A. P., Lalor, P. F., Baban, D., and Jackson, D. G. (2006). An inflammation-induced mechanism for leukocyte transmigration across lymphatic vessel endothelium. *J. Exp. Med.* 203, 2763–2777.
- Khuon, S., Liang, L., Dettman, R. W., Sporn, P. H., Wysolmerski, R. B., and Chew, T. L. (2010). Myosin light chain kinase mediates transcellular intravasation of breast cancer cells through the underlying endothelial cells: a three-dimensional FRET study. *J. Cell Sci.* 123, 431–440.
- King, M. R., and Hammer, D. A. (2001a). Multiparticle adhesive dynamics: hydrodynamic recruitment of rolling leukocytes. *Proc. Natl. Acad. Sci. U.S.A.* 98, 14919–14924.
- King, M. R., and Hammer, D. A. (2001b). Multiparticle adhesive dynamics. Interactions between stably rolling cells. *Biophys. J.* 81, 799–813.
- King, M. R., Sumagin, R., Green, C. E., and Simon, S. I. (2005). Rolling dynamics of a neutrophil with redistributed L-selectin. *Math. Biosci.* 194, 71–79.
- Köhler, S., Ullrich, S., Richter, U., and Schumacher, U. (2010). E-/P-selectins and colon carcinoma metastasis: first in vivo evidence for their crucial role in a clinically relevant model of spontaneous metastasis formation in the lung. *Br. J. Cancer* 102, 602–609.
- Krähling, H., Mally, S., Eble, J. A., Noël, J., Schwab, A., and Stock, C. (2009). The glycocalyx maintains a cell surface pH nanoenvironment crucial for integrin-mediated migration of human melanoma cells. *Pflügers Arch.* 458, 1069–1083.
- Krasik, E. F., Caputo, K. E., and Hammer, D. A. (2008). Adhesive dynamics simulation of neutrophil arrest with stochastic activation. *Biophys. J.* 95, 1716–1728.
- Krasik, E. F., Yee, K. L., and Hammer, D. A. (2006). Adhesive dynamics simulation of neutrophil arrest with deterministic activation. *Biophys. J.* 91, 1145–1155.
- Kwan, M. K., Lai, W. M., and Mow, V. C. (1984). Fundamentals of fluid transport through cartilage in compression. *Ann. Biomed. Eng.* 12, 537–558.
- Läubli, H., and Borsig, L. (2010). Selectins promote tumor metastasis. *Semin. Cancer Biol.* 20, 169–177.
- Levick, J. R. (1987). Flow through interstitium and other fibrous matrices. *Q. J. Exp. Physiol.* 72, 409–437.
- Li, S., Kim, M., Hu, Y. L., Jalali, S., Schlaepfer, D. D., Hunter, T., et al. (1997). Fluid shear stress activation

- of focal adhesion kinase. Linking to mitogen-activated protein kinases. *J. Biol. Chem.* 272, 30455–30462.
- Li, Y.-S. J., Haga, J. H., and Chien, S. (2005). Molecular basis of the effects of shear stress on vascular endothelial cells. *J. Biomech.* 38, 1949–1971.
- Lunt, S. J., Fyles, A., Hill, R. P., and Milosevic, M. (2008). Interstitial fluid pressure in tumors: therapeutic barrier and biomarker of angiogenesis. *Future Oncol.* 4, 793–802.
- Maheswaran, S., and Haber, D. A. (2010). Circulating tumor cells: a window into cancer biology and metastasis. *Curr. Opin. Genet. Dev.* 20, 96–99.
- Makino, A., Prossnitz, E., Bune-mann, M., Wang, J., Yao, W., and Schmid-Schonbein, G. (2006). G protein-coupled receptors serve as mechanosensors for fluid shear stress in neutrophils. *Am. J. Physiol. Cell Physiol.* 290, C1633–C1639.
- Malek, A. M., Alper, S. L., and Izumo, S. (1999). Hemodynamic shear stress and its role in atherosclerosis. *JAMA* 282, 2035–2042.
- McCarty, O., Mousa, S., Bray, P., and Konstantopoulos, K. (2000). Immobilized platelets support human colon carcinoma cell tethering, rolling, and firm adhesion under dynamic flow conditions. *Blood* 96, 1789–1797.
- McGuire, S., Zaharoff, D., and Yuan, F. (2006). Nonlinear dependence of hydraulic conductivity on tissue deformation during intratumoral infusion. *Ann. Biomed. Eng.* 34, 1173–1181.
- Michor, F., Liphardt, J., Ferrari, M., and Widom, J. (2011). What does physics have to do with cancer? *Nat. Rev. Cancer* 11, 657–670.
- Miranti, C. K., and Brugge, J. S. (2002). Sensing the environment: a historical perspective on integrin signal transduction. *Nat. Cell Biol.* 4, E83–E90.
- Mitchell, M. J., Chen, C. S., Ponmudi, V., Hughes, A. D., and King, M. R. (2012a). E-selectin liposomal and nanotube-targeted delivery of doxorubicin to circulating tumor cells. *J. Control. Release* 160, 609–617.
- Mitchell, M. J., Castellanos, C. A., and King, M. R. (2012b). Nanostructured surfaces to target and kill circulating tumor cells while repelling leukocytes. *J. Nanomater.* 2012, 1–10.
- Mitchell, M. J., and King, M. R. (2013). Fluid shear stress sensitizes cancer cells to receptor-mediated apoptosis via trimeric death receptors. *New J. Phys.* 15, 015008.
- Mitchell, M. J., and King, M. R. (2012). Shear-induced resistance to neutrophil activation via the formyl peptide receptor. *Biophys. J.* 102, 1804–1814.
- Miteva, D. O., Rutkowski, J. M., Dixon, J. B., Kilarski, W., Shields, J. D., and Swartz, M. A. (2010). Transmural flow modulates cell and fluid transport functions of lymphatic endothelium. *Circ. Res.* 106, 920–931.
- Moazzam, F., DeLano, F., Zweifach, B., and Schmid-Schonbein, G. (1997). The leukocyte response to fluid stress. *Proc. Natl. Acad. Sci. U.S.A.* 94, 5338–5343.
- Netti, P. A., Baxter, L. T., Boucher, Y., Skalak, R., and Jain, R. K. (1995). Time-dependent behavior of interstitial fluid pressure in solid tumors: implications for drug delivery. *Cancer Res.* 55, 5451–5458.
- Netti, P. A., Berk, D. A., Swartz, M. A., Grodzinsky, A. J., and Jain, R. K. (2000). Role of extracellular matrix assembly in interstitial transport in solid tumors. *Cancer Res.* 60, 2497–2503.
- Ng, C. P., Hinz, B., and Swartz, M. A. (2005). Interstitial fluid flow induces myofibroblast differentiation and collagen alignment in vitro. *J. Cell. Sci.* 118(Pt 20), 4731–4739.
- Ng, C. P., and Swartz, M. A. (2003). Fibroblast alignment under interstitial fluid flow using a novel 3-D tissue culture model. *Am. J. Physiol. Heart Circ. Physiol.* 284, H1771–H1777.
- Ng, C. P., and Swartz, M. A. (2006). Mechanisms of interstitial flow-induced remodeling of fibroblast-collagen cultures. *Ann. Biomed. Eng.* 34, 446–454.
- Orimo, A., and Weinberg, R. A. (2006). Stromal fibroblasts in cancer: a novel tumor-promoting cell type. *Cell Cycle* 5, 1597–1601.
- Osheroff, N., Corbett, A. H., and Robinson, M. J. (1994). Mechanism of action of topoisomerase II-targeted antineoplastic drugs. *Adv. Pharmacol.* 29, 105–126.
- Ostojia-Starzewski, M., Sheng, P. Y., and Alzebedeh, K. (1996). Spring network models in elasticity and fracture of composites and polycrystals. *Comput. Mater. Sci.* 7, 82–93.
- Paszek, M. J., Boettiger, D., Weaver, V. M., and Hammer, D. A. (2009). Integrin clustering is driven by mechanical resistance from the glycocalyx and the substrate. *PLoS Comput. Biol.* 5:e1000604. doi:10.1371/journal.pcbi.1000604
- Pedersen, J. A., Boschetti, F., and Swartz, M. A. (2007). Effects of extracellular fiber architecture on cell membrane shear stress in a 3D fibrous matrix. *J. Biomech.* 40, 1484–1492.
- Polacheck, W. J., Charest, J. L., and Kamm, R. D. (2011). Interstitial flow influences direction of tumor cell migration through competing mechanisms. *Proc. Natl. Acad. Sci. U.S.A.* 108, 11115–11120.
- Qazi, H., Shi, Z. D., and Tarbell, J. M. (2011). Fluid shear stress regulates the invasive potential of glioma cells via modulation of migratory activity and matrix metalloproteinase expression. *PLoS ONE* 6:e20348. doi:10.1371/journal.pone.0020348
- Rana, K., Liesveld, J. L., and King, M. R. (2009). Delivery of apoptotic signal to rolling cancer cells: a novel biomimetic technique using immobilized TRAIL and E-selectin. *Biotechnol. Bioeng.* 102, 1692–1702.
- Rana, K., Reinhart-King, C. A., and King, M. R. (2012). Inducing apoptosis in rolling cancer cells: a combined therapy with aspirin and immobilized TRAIL and E-selectin. *Mol. Pharm.* 9, 120702162958000.
- Rasheid Zakaria, E. L., Lofthouse, J., and Flessner, M. F. (1997). In vivo hydraulic conductivity of muscle: effects of hydrostatic pressure. *Am. J. Physiol.* 273(Pt 2), H2774–H2782.
- Resto, V. A., Burdick, M. M., Dagia, N. M., McCammon, S. D., Fennwald, S. M., and Sackstein, R. (2008). L-selectin-mediated lymphocyte-cancer cell interactions under low fluid shear conditions. *J. Biol. Chem.* 283, 15816–15824.
- Schmid-Schonbein, G. W. (1990). Microlymphatics and lymph flow. *Physiol. Rev.* 70, 987–1028.
- Secomb, T. W., Hsu, R., and Pries, A. R. (2001). Effect of the endothelial surface layer on transmission of fluid shear stress to endothelial cells. *Biorheology* 38, 143–150.
- Shi, Z. D., and Tarbell, J. M. (2011). Fluid flow mechanotransduction in vascular smooth muscle cells and fibroblasts. *Ann. Biomed. Eng.* 39, 1608–1619.
- Shi, Z. D., Wang, H., and Tarbell, J. M. (2011). Heparan sulfate proteoglycans mediate interstitial flow mechanotransduction regulating MMP-13 expression and cell motility via FAK-ERK in 3D collagen. *PLoS ONE* 6:e15956. doi:10.1371/journal.pone.0015956
- Shieh, A. C., Rozansky, H. A., Hinz, B., and Swartz, M. A. (2011). Tumor cell invasion is promoted by interstitial flow-induced matrix priming by stromal fibroblasts. *Cancer Res.* 71, 790–800.
- Shieh, A. C., and Swartz, M. A. (2011). Regulation of tumor invasion by interstitial fluid flow. *Phys. Biol.* 8, 015012.
- Shields, J. D., Emmett, M. S., Dunn, D. B. A., Joory, K. D., Sage, L. M., Rigby, H., et al. (2006). Chemokine-mediated migration of melanoma cells towards lymphatics – a mechanism contributing to metastasis. *Oncogene* 26, 2997–3005.
- Shields, J. D., Fleury, M. E., Yong, C., Tomei, A. A., Randolph, G. J., and Swartz, M. A. (2007). Autologous chemotaxis as a mechanism of tumor cell homing to lymphatics via interstitial flow and autocrine CCR7 signaling. *Cancer Cell* 11, 526–538.
- Shirure, V. S., Reynolds, N. M., and Burdick, M. M. (2012). Mac-2 binding protein is a novel E-selectin ligand expressed by breast cancer cells. *PLoS ONE* 7:e44529. doi:10.1371/journal.pone.0044529
- Sieg, D. J., Ilic, D., Jones, K. C., Damsky, C. H., Hunter, T., and Schlaepfer, D. D. (1998). Pyk2 and Src-family protein-tyrosine kinases compensate for the loss of FAK in fibronectin-stimulated signaling events but Pyk2 does not fully function to enhance FAK-cell migration. *EMBO J.* 17, 5933–5947.
- Smith, M. J., Berg, E. L., and Lawrence, M. B. (1999). A direct comparison of selectin-mediated transient, adhesive events using high temporal resolution. *Biophys. J.* 77, 3371–3383.
- Steeg, P. S. (2006). Tumor metastasis: mechanistic insights and clinical challenges. *Nat. Med.* 12, 895–904.
- Strony, J., Beaudoin, A., Brands, D., and Adelman, B. (1993). Analysis of shear stress and hemodynamic factors in a model of coronary artery stenosis and thrombosis. *Am. J. Physiol.* 265(Pt 2), H1787–H1796.
- Swartz, M. A., and Fleury, M. E. (2007). Interstitial flow and its effects in soft tissues. *Annu. Rev. Biomed. Eng.* 9, 229–256.
- Swartz, M. A., Kaipainen, A., Netti, P. A., Brekken, C., Boucher, Y., Grodzinsky, A. J., et al. (1999). Mechanics of interstitial-lymphatic fluid transport: theoretical foundation and experimental validation. *J. Biomech.* 32, 1297–1307.
- Swartz, M. A., and Lund, A. W. (2012). Lymphatic and interstitial flow in the tumour microenvironment: linking mechanobiology with immunity. *Nat. Rev. Cancer* 12, 210–219.

- Tarbell, J. M., and Shi, Z. D. (2012). Effect of the glycocalyx layer on transmission of interstitial flow shear stress to embedded cells. *Bio-mech. Model. Mechanobiol.* 12, 111–121.
- Terasaki, M., Miyake, K., and McNeil, P. L. (1997). Large plasma membrane disruptions are rapidly resealed by Ca²⁺-dependent vesicle-vesicle fusion events. *J. Cell Biol.* 139, 63–74.
- Thomas, S. N., Zhu, F., Schnaar, R. L., Alves, C. S., and Konstantopoulos, K. (2008). Carcinoembryonic antigen and CD44 variant isoforms cooperate to mediate colon carcinoma cell adhesion to E- and L-selectin in shear flow. *J. Biol. Chem.* 283, 15647–15655.
- Tseng, Y., Lee, J. S. H., Kole, T. P., Jiang, L., and Wirtz, D. (2004). Micro-organization and visco-elasticity of the interphase nucleus revealed by particle nanotracking. *J. Cell. Sci.* 117(Pt 10), 2159–2167.
- Turitto, V. T. (1982). Blood viscosity, mass transport, and thrombogenesis. *Prog. Hemost. Thromb.* 6, 139–177.
- Wang, D. M., and Tarbell, J. M. (1995). Modeling interstitial flow in an artery wall allows estimation of wall shear stress on smooth muscle cells. *J. Biomech. Eng.* 117, 358–363.
- Wipff, P.-J., Rifkin, D. B., Meister, J.-J., and Hinz, B. (2007). Myofibroblast contraction activates latent TGF- β 1 from the extracellular matrix. *J. Cell Biol.* 179, 1311–1323.
- Wirtz, D., Konstantopoulos, K., and Searson, P. C. (2011). The physics of cancer: the role of physical interactions and mechanical forces in metastasis. *Nat. Rev. Cancer* 11, 512–522.
- Yao, Y., Rabodzey, A., and Dewey, C. F. (2007). Glycocalyx modulates the motility and proliferative response of vascular endothelium to fluid shear stress. *Am. J. Physiol. Heart Circ. Physiol.* 293, H1023–H1030.
- Yokota, H., Goldring, M. B., and Sun, H. B. (2003). CITED2-mediated regulation of MMP-1 and MMP-13 in human chondrocytes under flow shear. *J. Biol. Chem.* 278, 47275–47280.
- Young, R. C., Ozols, R. F., and Myers, C. E. (1981). The anthracycline anti-neoplastic drugs. *N. Engl. J. Med.* 305, 139–153.
- Yu, M., Stott, S., Toner, M., Maheswaran, S., and Haber, D. A. (2011). Circulating tumor cells: approaches to isolation and characterization. *J. Cell Biol.* 192, 373–382.
- Conflict of Interest Statement:** The authors declare that the research was conducted in the absence of any commercial or financial relationships that could be construed as a potential conflict of interest.

Received: 15 January 2013; paper pending published: 07 February 2013; accepted: 18 February 2013; published online: 05 March 2013.

Citation: Mitchell MJ and King MR (2013) Computational and experimental models of cancer cell response to fluid shear stress. *Front. Oncol.* 3:44. doi: 10.3389/fonc.2013.00044

This article was submitted to *Frontiers in Molecular and Cellular Oncology*, a specialty of *Frontiers in Oncology*.

Copyright © 2013 Mitchell and King. This is an open-access article distributed under the terms of the Creative Commons Attribution License, which permits use, distribution and reproduction in other forums, provided the original authors and source are credited and subject to any copyright notices concerning any third-party graphics etc.



Mathematical modeling of cancer invasion: the role of membrane-bound matrix metalloproteinases

Niall E. Deakin* and Mark A. J. Chaplain

Division of Mathematics, University of Dundee, Dundee, UK

Edited by:

Katarzyna Anna Rejniak, H. Lee
Moffitt Cancer Center and Research
Institute, USA

Reviewed by:

Ami Radunskaya, Pomona College,
The Claremont Colleges, USA
Amina Eladdadi, The College of Saint
Rose, USA

*Correspondence:

Niall E. Deakin, Division of
Mathematics, University of Dundee,
Dundee DD1 4HN, Scotland, UK.
e-mail: niall@maths.dundee.ac.uk

One of the hallmarks of cancer growth and metastatic spread is the process of local invasion of the surrounding tissue. Cancer cells achieve protease-dependent invasion by the secretion of enzymes involved in proteolysis. These overly expressed proteolytic enzymes then proceed to degrade the host tissue allowing the cancer cells to disseminate throughout the microenvironment by active migration and interaction with components of the extracellular matrix (ECM) such as collagen. In this paper we develop a mathematical model of cancer invasion which consider the role of matrix metalloproteinases (MMPs). Specifically our model will focus on two distinct types of MMP, i.e., soluble, diffusible MMPs (e.g., MMP-2) and membrane-bound MMPs (e.g., MT1-MMP), and the roles each of these plays in cancer invasion. The implications of MMP-2 activation by MMP-14 and the tissue inhibitor of metalloproteinases-2 are considered alongside the effect the architecture of the matrix may have when applied to a model of cancer invasion. Elements of the ECM architecture investigated include pore size of the matrix, since in some highly dense collagen structures such as breast tissue, the cancer cells are unable to physically fit through a porous region, and the crosslinking of collagen fibers. In this scenario, cancer cells rely on membrane-bound MMPs to forge a path through which degradation by other MMPs and movement of cancer cells becomes possible.

Keywords: cancer invasion, mathematical model, metalloproteinases, membrane-bound MMPs, extracellular matrix

INTRODUCTION

For metastasis to occur, cancer cells must exhibit invasion through a variety of structured media such as the highly dense collagen constitution of some peritumoral stroma (Hanahan and Weinberg, 2000, 2011). This can occur by the secretion of enzymes that are capable of degrading components of the ECM or by the adoption of an amoeboid phenotype that allows cancer cells to travel through the medium in a protease-independent manner (Friedl and Wolf, 2003; Sahai, 2005).

Mathematical modeling of solid-tumor growth dates back to the works of Thomlinson and Gray (1955) and Burton (1966), where oxygen was modeled as a nutrient diffusing from the outer edge (boundary) of a tumor inwards to investigate its role in necrosis. Mathematical modeling has continued to develop to investigate a number of topics in cancer progression and invasion, including models taking into account: oxygen/nutrient driven dynamics, the immune response, the acidity of the environment, force-based pressure, the microenvironment in general, and protease-dependent invasion using the techniques of partial differential equations for densities of cells, individual-based models including cellular automaton models and multi-scale models as outlined in the review papers of Araujo and McElwain (2004), Rejniak and McCawley (2010), and Lowengrub et al. (2010) and the references therein.

In this paper, we focus on a continuum, deterministic approach to protease-dependent invasion where matrix degrading enzymes cleave collagen fibrils and other ECM components rather than

protease-independent invasion where mechanical forces physically displace matrix fibrils and cancer cells adopt an amoeboid-like shape (epithelial-mesenchymal transition). The microenvironment of the tumor plays a significant role in cancer progression with matrix metalloproteinases acting as regulators, allowing obstacles to be overcome (Rowe and Weiss, 2009; Kessenbrock et al., 2010).

Matrix metalloproteinases (MMPs) are one mechanism by which cancer cells have the ability to invade. These proteolytic enzymes are a family of 23 enzymes in humans which have the capacity to degrade virtually all components of the surrounding tissue (Kleiner and Stetler-Stevenson, 1999). This in turn facilitates cancer growth and spread by virtue of the available space left in the absence of the degraded ECM as well as by other proteins that are released by the degraded tissue encouraging the cancer growth (Werb, 1997; López-Otín and Overall, 2002). Haptotaxis is a process of directed cell migration whereby cells move in response to gradients of adhesion sites naturally present in the ECM.

MMPs are zinc-dependent endopeptidases whose main function is in the regular turnover of the ECM (Nagase and Woessner, 1999). This process is exploited in cancer growth and invasion where various MMPs are over expressed. The expression of MMPs faces control at the level of transcription but can also face inhibition when moving from the proMMP state to an active MMP as well as inhibition when it exists in its active state.

The family of MMPs can exhibit both pro- and anti-invasive characteristics (Nöel et al., 2012) but in this paper we focus on the

pro-invasive MMPs of MMP-2, MMP-9, and MT1-MMP. MMP-2 and MMP-9 are secreted in their inactive zymogen forms of proMMP-2 and proMMP-9 whereas the fully active MT1-MMP is expressed on the cell surface after being activated internally. The activation process by which the various MMPs develop into their fully active form differs between them. This interplay between the enzymes is emphasized by the coexpression of proMMP-2, MT1-MMP, MMP-2, and TIMP2 in a variety of tissues (Kinoh et al., 1996). While MT1-MMP was initially thought to have activity limited to activating MMP-2, it has since been found to also have a direct role in tissue degradation (d'Ortho et al., 1997).

The main constituent of the stroma is the structural, cross-linked type I collagen. MT1-MMP exhibits strong type I collagenolytic capabilities and weak gelatinolytic capabilities. Conversely, MMP-2 exhibits weak type I collagenolytic capabilities and strong gelatinolytic capabilities (Tam et al., 2004) where it is unable to degrade cross-linked collagen type I and type IV but is able to degrade the uncross-linked variants (Zhang et al., 2013). MMP-2 can, however, critically degrade type IV collagen, the main component of the basement membrane and an extracellular barrier. As MT1-MMP is bound to cancer cells, its region of proteolytic activity is more restricted than that of the freely diffusive proteolytic enzyme MMP-2. This means that tissue degradation in advance of the cancer cells is the result of the soluble MMPs. While MT1-MMP activity is restricted in range, it has an advantage in its capability of overcoming environments of higher collagen density such as exists in some peritumoral stroma. Sabeh et al. (2009) have shown that when cancer cells are faced with structural barriers created in reconstituted gels by covalently cross-linked fibrils of type I collagen, or that exist in the stromal environment of the mammary gland, invasion is dependent on MT1-MMP-mediated proteolysis.

Other mathematical models that have examined the activation of MMP-2 by MT1-MMP include Karagiannis and Popel (2004), Donzé et al. (2011), and Hoshino et al. (2012). Karagiannis and Popel (2004) developed a set of non-spatial ordinary differential equations of this activation system and examined the interplay between the activation system of MMP-2 and ectodomain shedding of MT1-MMP. They found that in the absence of TIMP2, ectodomain shedding of MT1-MMP dominated dynamics but that introducing TIMP2 would encourage MMP-2 activation and protect MT1-MMP from shedding. They later developed their model to examine proteolysis during the migration of a tip endothelial cell as is relevant in angiogenesis (Karagiannis and Popel, 2006). Donzé et al. (2011) performed global robustness and sensitivity of the model and explored the possibility of oscillatory dynamics in the system. Hoshino et al. (2012) developed their extensive model of all possible interactions of enzymes using A-Cell (Ichikawa, 2001). They provide experimental validation alongside their computational model used to investigate the significance of turnover of MT1-MMP for proteolysis at invadopodia. In this paper, we apply a reduced form of the activation system of MMP-2 to our model of cancer cell invasion where tissue degradation is mediated by either MT1-MMP or MMP-2.

The architecture of the ECM plays a pivotal role when considering cancer cell invasion. Li et al. (2008) and Sabeh et al. (2009) have made attempts to create *in vitro* environments that better represent

those found *in vivo* by embedding multicellular spheroids of HT-1080 fibrosarcoma cells within gels of cross-linked native type I collagen. Both studies found that MT1-MMP silencing blocks virtually all collagenolytic and invasive activity. In this paper, we provide an approach that considers what effect the architecture of the ECM, such as pore size of tissue and proportion of ECM made up of cross-linked collagen, may have when applied to a model of cancer invasion. We are able to consider a heterogeneous ECM and incorporate haptotaxis as occurring only in response to ECM gradients created by the release of enzymes such as MMPs.

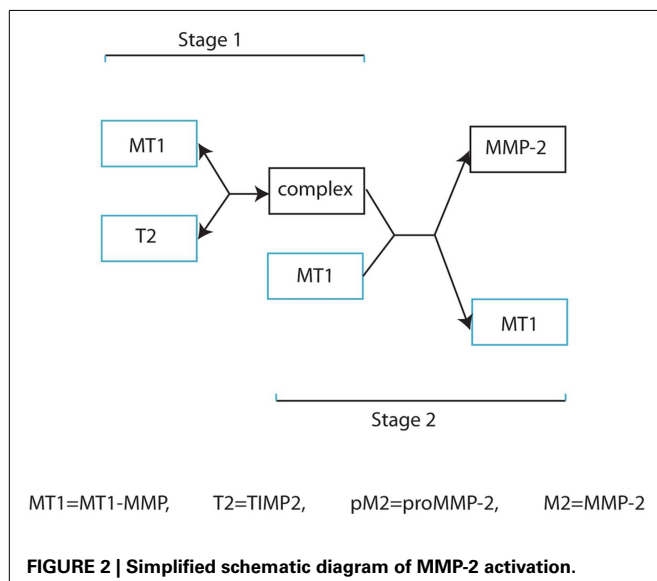
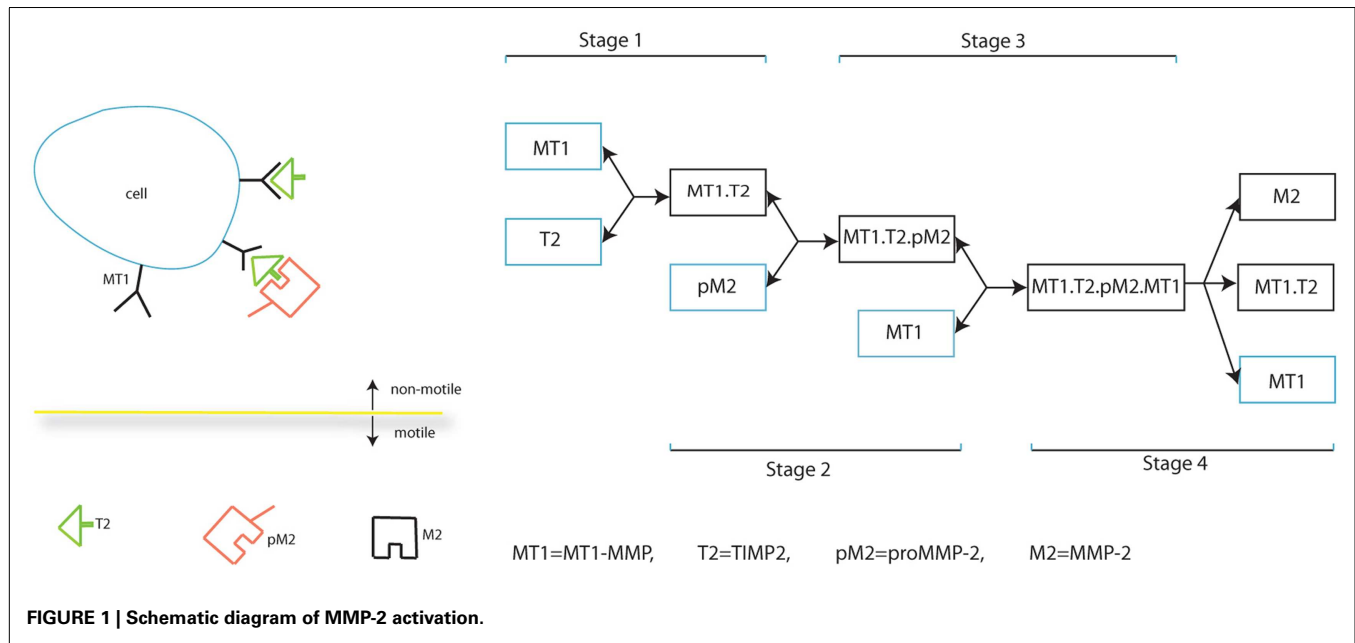
In this paper therefore, we develop a mathematical model of cancer invasion which consider the role of matrix metalloproteinases (MMPs). Specifically our model will focus on two distinct types of MMP, i.e., soluble, diffusible MMPs (e.g., MMP-2), and membrane-bound MMPs (e.g., MT1-MMP), and the roles each of these plays in cancer invasion. Our model will also consider the influence of the structure of the matrix on cancer cell invasion and to achieve this (using a continuum PDE model) we will introduce the concept of a “matrix suitability modifier.”

MATERIALS AND METHODS

In this section, we present our mathematical model which describes the interplay between MMPs in cancer invasion, specifically MT1-MMP activation of MMP-2, the balance between TIMP2 inhibition of both MT1-MMP and MMP-2, and the dual role of TIMP2 as inhibitor of species and activator of MMP-2. The full process of MMP-2 activation is shown in **Figure 1**. The species/complexes in a blue box are produced while those in the black box are simply formed. Whether a species/complex is free to move, without considering lateral diffusion on a cell and the relative movement of a cell, is also indicated.

Our invasion model is based on a simplified form of MMP-2 activation as outlined in **Figure 2**, and involves considering stages 2, 3, and 4 of **Figure 1** as a single process. This retains the key details of whether a complex is stationary or not in relation to cell movement and is a significant factor considering the relative speed of binding of the freely diffusive TIMP2 to a complex bound to the cell. However, we feel that this simplification of the process is appropriate in capturing the dynamics of the two functional forms by which invasion is facilitated. A basic model is presented in the Supplementary Material to clarify the difference between these two functional forms of invasion mediated by the highly localized tissue degradation by MT1-MMP and the more extensive tissue degradation by the diffusible MMP-2.

In our model we denote by $c(\mathbf{x}, t)$ the cancer cell density, $v(\mathbf{x}, t)$ the ECM density, $m_s(\mathbf{x}, t)$ the MMP-2 concentration, and by $m_t(\mathbf{x}, t)$ the MT1-MMP concentration. In addition, we let $T(\mathbf{x}, t)$ denote the TIMP2 concentration, $f(\mathbf{x}, t)$ the concentration of the complex of MT1-MMP:TIMP2 (with an assumed proMMP-2 attached) and $s(\mathbf{x}, t)$ the “matrix suitability modifier.” The matrix suitability modifier acts as an environmental factor by reducing the level of a cell population that can physically move through the matrix – as an extension of the volume-filling principles – by taking into account the pore size of the collagen substrate along with reducing the amount of matrix that is considered available to be degraded. In this model, we consider a matrix environment with a neutral effect on these processes to have a matrix suitability modifier value



of 1, which results in the standard dynamics expected from such a model. A matrix environment containing difficult regions of ECM for cancer cells to invade will be represented by a matrix suitability modifier with a value $0 \leq s < 1$, with values toward zero describing an environment that is more difficult for cancer cells to navigate through, as well as a reduction in ECM that is available to be degraded. We also impose the condition that $s + v \geq 1$, otherwise instead of limiting movement and tissue degradation, movement would be encouraged in the opposite direction and the ECM degradation term would cause the density of ECM to increase.

As both MT1-MMP and the intermediate complex are bound to cancer cells, they experience movement in the same direction as the cancer cells and with a magnitude determined by the concentration of enzymes at that location. We consider both

MMP-2 and MT1-MMP to undergo natural decay. We include collagen-induced MT1-MMP expression in our model through a function $\alpha_{mt}c(1 + v)$ (Zigrino et al., 2001). This may take into account observations showing that collagen-dense mouse mammary tissues result in cancer cells with a more invasive phenotype Provenzano et al. (2008). We also include volume-filling of the form $(1 - c - v)$ to represent the competition for space between the cancer cells and ECM. This is applied both to the haptotactic response of cancer cells to ECM gradients and to the growth rates for both the cancer cell and ECM populations. Finally, we have an ECM remodeling rate of $\mu_v(1 - c - v)$ (cf. Gerisch and Chaplain (2008)). The full model is therefore given as:

$$\frac{\partial c}{\partial t} = \nabla \cdot (D_c \nabla c - \chi c (s - 1 + v) (1 - c - v) \nabla v) + \mu_c c (1 - c - v), \quad (1)$$

$$\frac{\partial v}{\partial t} = -\delta (s - 1 + v) (m_s + m_t) + \mu_v (1 - c - v), \quad (2)$$

$$\frac{\partial m_s}{\partial t} = \nabla \cdot (D_{m_s} \nabla m_s) - \phi_{31} T m_s + \phi_{32} m_t f - \beta_{m_s} m_s, \quad (3)$$

$$\frac{\partial m_t}{\partial t} = m_t \nabla \cdot (D_c \nabla c - \chi c (s - 1 + v) (1 - c - v) \nabla v) - \phi_{41} T m_t + \phi_{42} - \beta_{m_t} m_t + \alpha_{mt} c (1 + v), \quad (4)$$

$$\frac{\partial T}{\partial t} = \nabla \cdot (D_T \nabla T) - \phi_{51} T m_s - \phi_{52} T m_t + \phi_{53} f + \alpha_T c, \quad (5)$$

$$\frac{\partial f}{\partial t} = f \nabla \cdot (D_c \nabla c - \chi c (s - 1 + v) (1 - c - v) \nabla v) + \phi_{61} T m_t - \phi_{62} f m_t - \phi_{63} f, \quad (6)$$

$$\frac{\partial s}{\partial t} = \delta_s m_t (1 - s). \quad (7)$$

In all computational simulations, we apply zero-flux boundary conditions to equations (1), (3–6). The initial conditions

imposed depend on the precise invasion scenario we are considering. In our the first invasion scenario (cf. **Figure 3**) we have a cluster of cancer cells in the center of a homogeneous ECM with a small amount of activated enzymes already

released, i.e., $c(0) = e^{\left(\frac{-(x^2+y^2)}{0.02}\right)}$, $v(0)=1-c(0)v(0) = 1-c(0)$, $m_s(0)=m_s(0)=T(0)=f(0)=c(0)m_s(0) = m_t(0) = T(0) = f(0) = c(0)$. The initial condition for the matrix suitability modifier s is best seen in **Figure 3C**. The initial conditions used for c , v , s in the second invasion scenario are best seen from the plots in **Figures 7A–C**, and also in this case $m_s(0)=m_t(0)=T(0)=f(0)=c(0)$.

PARAMETER ESTIMATION

We non-dimensionalize the model using the reference variables $\tau = 10^4$ s and $L = 0.1$ cm. While the reference enzyme concentration can be difficult to obtain, we take it be 1 nM with concentrations throughout the considered timeframe to be within the range 0–25 nM. Tutton et al. (2003) find pre-operative MMP-2 levels in plasma of colorectal cancer patients of 568.9 ng/ml = 7.89 nM while Butler et al. (1998) and English et al. (2001) performed experiments with enzyme concentrations of order 100 nM. The parameters β_{ms} , β_{mt} , α_{mt} , and α_T were therefore chosen so that the concentrations of active MT1-MMP and MMP-2 are in the range 0–25 nM. The baseline parameter set presented in **Table 1** is used for all computational simulations of the model unless otherwise specified.

RESULTS

In this section we present the computational simulation results of our invasion model equations (1–7) in a 2-dimensional domain

(all parameter values are from the baseline set). The first scenario we consider is one in which the tissue is considered to have neutral effects on invasion in the top half of the domain by having a matrix suitability modifier $s = 1$, with the lower half of the domain having moderate characteristics limiting invasion by having the matrix suitability modifier of $s = \frac{1}{2}$, as shown in **Figure 3C**. The value of $s = \frac{1}{2}$ may represent a region that contains a tissue where (i) half the constituent parts of the ECM are cross-linked collagen, (ii) half the considered ECM has a pore size below a threshold α that blocks invasion, (iii) more than half the considered ECM has a pore size in the range $\alpha-\beta$ that slows invasion, or (iv) some combination of the factors presented in (i–iii) that has the equivalent effect. As can be seen from the plots in **Figure 3** we observe an asymmetric invasion by the cancer cells, with a reduced invasion in the lower half of the domain (cf. **Figure 3D**) and also a reduced degradation of ECM in the lower half of the domain (cf. **Figure 3E**).

Figures 4 and **5** show the corresponding evolution of the various enzyme concentrations using the baseline parameter set. The plots in **Figures 4F** and **5F** show that any free TIMP2 that is produced or released from a complex is quickly bound to either free MT1-MMP or MMP-2. The plots in **Figures 4D** and **5D** show that while MMP-2 can freely diffuse throughout the environment, its profile is affected by the source term coming from the asymmetric cancer cell invasion dynamics. The plots in **Figures 4E** and **5E** show how the degradative effect of MT1-MMP is limited by its dependence on transport by the cancer cells. This is demonstrated by a reduced invasive profile in the bottom half of each plot.

In **Figure 6** we examine an invasive scenario where the effects of the suitability of the matrix play little or no role. This is achieved by increasing the parameter δ_s to a value of 10 (all other parameters

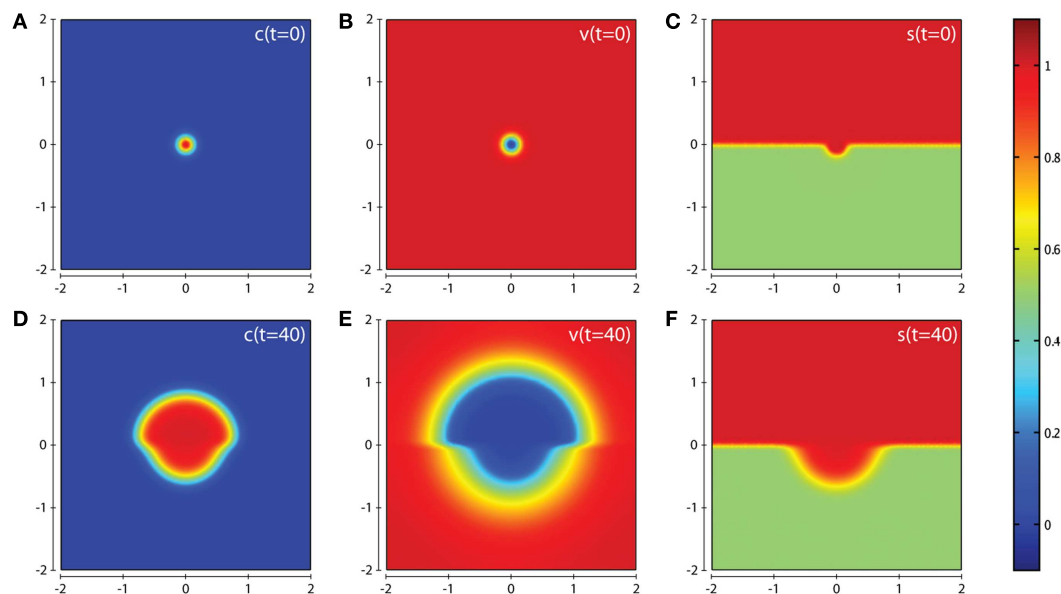


FIGURE 3 | Plots showing the simulation results obtained in a two-dimensional domain where asymmetric invasion of the ECM is achieved by the cancer cells. We use the matrix suitability modifier s to represent a medium with neutral abilities in the upper half of the region ($s = 1$; red) and with a reduced, moderate, suitability for invasion in the

lower half ($s = 0.5$; green). Plots **(A–C)** show the initial values of the cancer cell and ECM densities as well as the initial layout of the matrix suitability modifier with **(D–F)** showing their resultant profiles at $t = 40$ (corresponding to ~ 4.6 days). Simulations are performed using the baseline parameter set.

Table 1 | Baseline parameter set for the model.

	Non-dimensional form	Original	Unit	Reference
D_c	3.5×10^{-4}			Anderson et al. (2000)
χ	5×10^{-3}			Anderson et al. (2000)
μ_c	0.3			Anderson et al. (2000)
δ	1			Anderson et al. (2000)
μ_v	0.2			Anderson et al. (2000)
D_{ms}	1.29×10^2	1.29×10^8	cm^2s^{-1}	Collier et al. (2011)
ϕ_{31}	5	5×10^5	$\text{M}^{-1}\text{s}^{-1}$	Estimated
ϕ_{32}	0.195	1.95×10^4	$\text{M}^{-1}\text{s}^{-1}$	Estimated
β_{ms}	0.1 D	1×10^{-5}	s^{-1}	Estimated
α_{mt}	5	5×10^{-4}	s^{-1}	Estimated
ϕ_{41}	27.4	2.74×10^6	$\text{M}^{-1}\text{s}^{-1}$	Toth et al. (2000)
ϕ_{42}	2	2×10^{-4}	s^{-1}	Toth et al. (2000)
β_{mt}	0.1	1×10^{-5}	s^{-1}	Estimated
D_T	1.29×10^2	1.29×10^8	cm^2s^{-1}	Collier et al. (2011)
α_T	4	4×10^{-4}	s^{-1}	Estimated
ϕ_{51}	5	5×10^5	$\text{M}^{-1}\text{s}^{-1}$	Estimated
ϕ_{52}	27.4	2.74×10^6	$\text{M}^{-1}\text{s}^{-1}$	Toth et al. (2000)
ϕ_{53}	2	2×10^{-4}	s^{-1}	Toth et al. (2000)
ϕ_{61}	27.4	2.74×10^6	$\text{M}^{-1}\text{s}^{-1}$	Toth et al. (2000)
ϕ_{62}	0.195	1.95×10^4	$\text{M}^{-1}\text{s}^{-1}$	Estimated
ϕ_{63}	2	2×10^{-4}	s^{-1}	Toth et al. (2000)
δ_s	0.025			Estimated

kept at baseline values and using the same initial conditions as in **Figures 3** and **4**). This scenario represents a region of tissue that is difficult to invade and degrade by MMP-2 alone in the lower half of the domain, but one that is rapidly remodeled when in range of MT1-MMP to a condition that is considered to have a neutral effect on invasion. Under these conditions, it can be seen from the plot in **Figure 6D** that the cancer cells invade in a symmetric manner (unlike the scenario in **Figure 3D**). However, we can also see from the plot in **Figure 6E** that there is a reduced degradation of ECM due to MMP-2 in the lower half of the domain compared with the upper half. This shows the significance of the rate that MT1-MMP is able to remodel the ECM in the spatial layout of the tumor. The corresponding plots of the concentrations MMP-2, MT1-MMP, the intermediary complex f , and TIMP2 at $t = 20$ and $t = 40$ are given in Figures S2 and S3 of the Supplementary Material.

In **Figure 7**, we present the computational simulation results of cancer cell invasion in a more heterogeneous environment such as would be expected in certain *in vitro* experiments (and also *in vivo*). For this scenario, we used the baseline parameter set, except for the parameter δ_s which is reduced by a factor of ten to a value of 0.0025. The plots in **Figures 7D–F** show that the cancer cells take a longer time to invade the less suitable regions of ECM resulting in a heterogeneous invasion pattern. In **Figure 7F**, we can see that there are regions of higher cancer cell density (small red zones) in advance of regions of lower cancer cell density (small green zones) but without having broken off from the main mass entirely. The corresponding plots of the concentrations of MMP-2 and MT1-MMP at $t = 10, 50, 100$ are given in Figure S4 of the Supplementary Material. The effect of varying the parameter δ_s can be seen by comparing the results in **Figure 7** with Figure S5

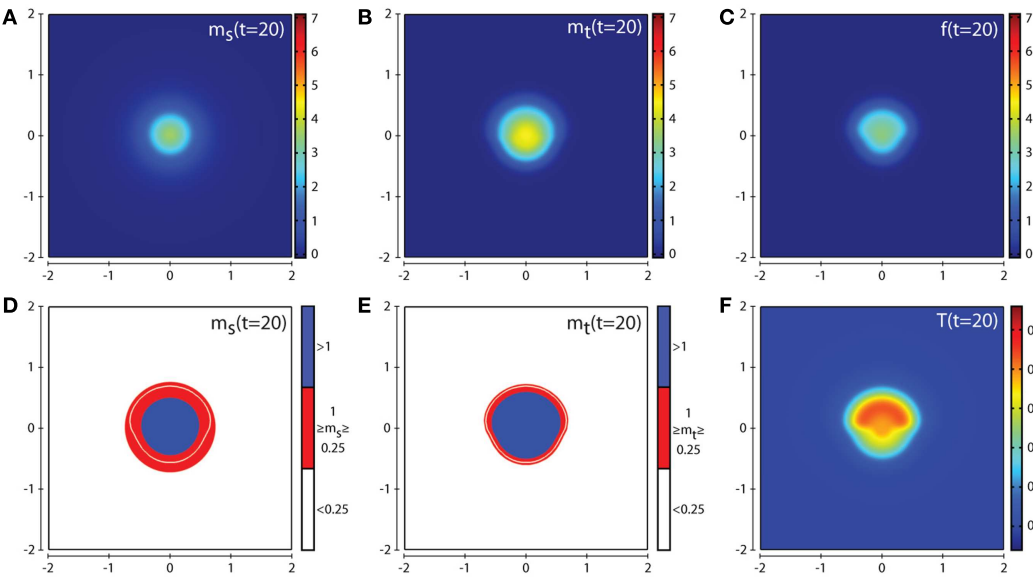


FIGURE 4 | Plots showing the simulation results obtained in a two-dimensional domain where asymmetric invasion of the ECM is achieved by the cancer cells. The concentrations of MMP-2, MT1-MMP, the intermediary complex f , and TIMP2 at $t = 20$ (corresponding to ~ 2.3 days) are shown in plots (A–C,F) respectively. Plots (D,E) show the

MMP-2 and MT1-MMP concentrations at $t = 20$ with appropriate thresholds near the invasive front of the cancer cell invasion. The white contour line shows the cancer cell density at level 0.01 chosen to represent the maximum extent of invasion. Simulations are performed using the baseline parameter set.

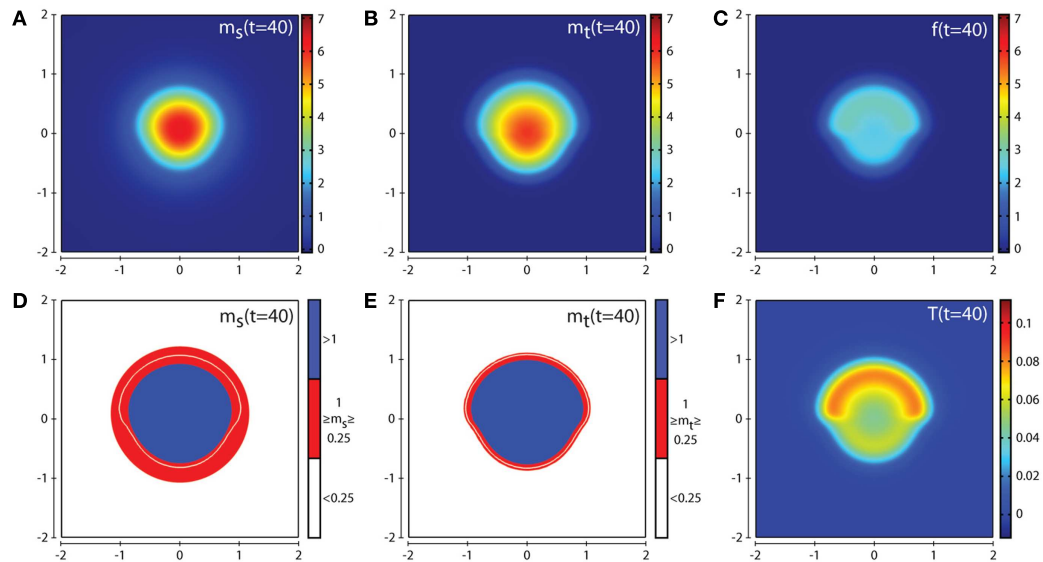


FIGURE 5 | Plots showing the simulation results obtained in a two-dimensional domain where asymmetric invasion of the ECM is achieved by the cancer cells. The concentrations of MMP-2, MT1-MMP, the intermediary complex f , and TIMP2 at $t = 40$ (corresponding to ~ 4.6 days) are shown in plots (A–C,F) respectively. Plots (D,E) show the

MMP-2 and MT1-MMP concentrations at $t = 40$ with appropriate thresholds near the invasive front of the cancer cell invasion. The white contour line shows the cancer cell density at level 0.01 chosen to represent the maximum extent of invasion. Simulations are performed using the baseline parameter set.

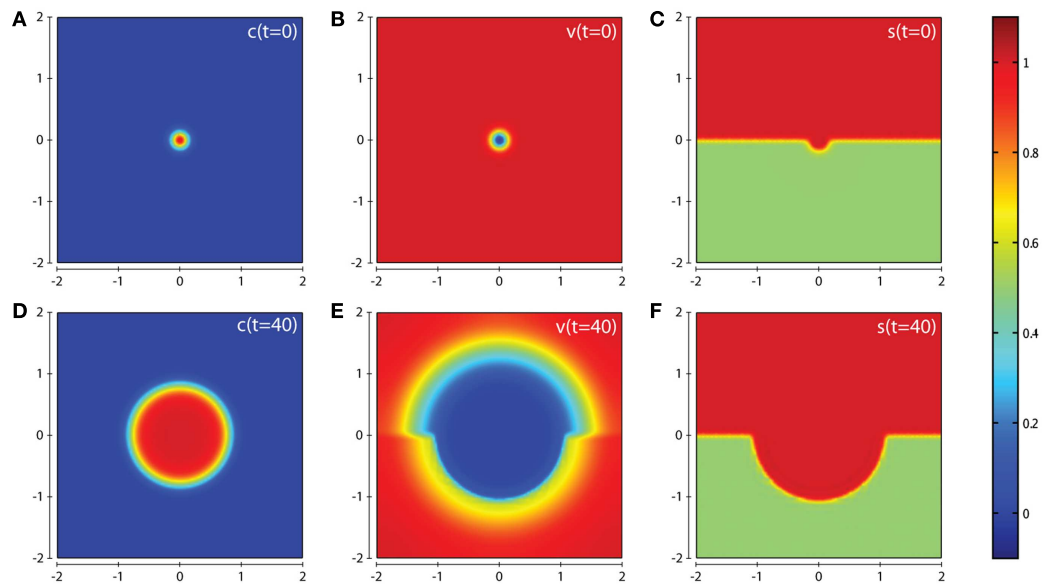


FIGURE 6 | Plots showing the simulation results obtained in a two-dimensional domain where the suitability modifier s represents a medium with neutral abilities in the upper half of the region ($s = 1$; red) and a reduced, moderate, suitability for invasion in the lower half ($s = 0.5$; green). We consider a scenario where the suitability modifier is rapidly brought back to a neutral state by performing simulations using the

baseline parameter set with the exception of $\delta_s = 10$. Plots (A–C) show the initial values of the cancer cell and ECM densities as well as the initial layout of the matrix suitability modifier with plots (D–F) showing their resultant profiles at $t = 40$ (corresponding to ~ 4.6 days). As can be seen, in this case there is an almost symmetric invasion pattern. This shows the influence of the parameter δ_s on invasion.

in the Supplementary Material, where we have used the default parameter set but we do not observe any regions of high cancer cell density in advance of regions of lower cancer cell density.

DISCUSSION

In this paper we have presented a mathematical model for cancer invasion of tissue, focusing on the roles of soluble and

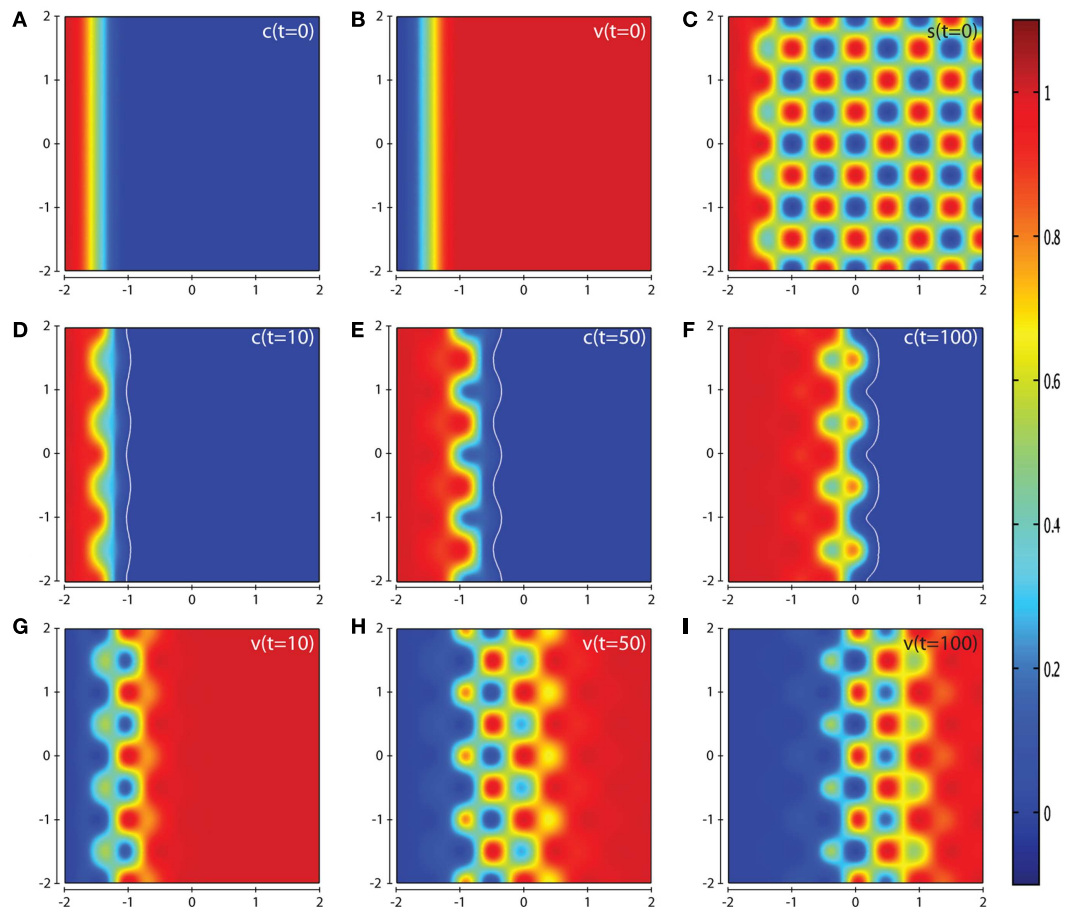


FIGURE 7 | Plots showing the simulation results obtained in a two-dimensional domain with a spatially complex matrix suitability modifier s to more accurately depict the observations of certain *in vivo* experiments. Plots (A–C) show the initial values of the cancer cell and ECM densities as well as the initial structure of the matrix suitability modifier. Plots (D–F) show the resultant profiles of cancer cell density at $t = 10, 50$, and 100 (corresponding to $\sim 1.15, 5.75$, and 11.5 days, respectively). The white contour

line shows the cancer cell density at level 0.01 chosen to represent the maximum extent of invasion. Plots (G–I) show the resultant profiles of ECM density at $t = 10, 50$, and 100 . The simulations were performed using the baseline parameter set with the exception of the parameter $\delta_s = 0.0025$. The plots show a highly heterogeneous invasion pattern at the invasive front, once again highlighting the role of the matrix suitability modifier s and the parameter δ_s .

bound MMPs. Additionally we introduced the concept of “matrix suitability,” governed by the variable s in our model. By considering the suitability of the matrix as a factor affecting ECM degradation and the movement of enzymes and cancer cells, we were able to generate heterogeneity in the ECM caused solely by matrix degradation. This meant we were able to focus on the effects of these gradients explicitly caused by matrix degradation rather than ECM density gradients due to intrinsic tissue heterogeneity. The computational simulation results showed that the matrix suitability modifier and its regulation played an important role in determining the precise pattern of invasion. As has been observed in the experimental data of Sabeh et al. (2009) and Li et al. (2008), we have shown that the architecture of the tissue can negatively impact invasion under circumstances of pore size being below an optimal level or in environments of cross-linked collagen type I and IV, with both of these conditions requiring tissue remodeling specifically by MT1-MMP. In addition to this, invasion is reduced where TIMP2 is overly produced. To investigate the matrix suitability

modifier from a biological perspective, experiments would need to be carried out to obtain the initial layout of the suitability modifier as well as the parameter δ_s . The first step in doing this would be to find out the effects of different tissue pore size on cancer cell migration to establish what range of pore sizes would be considered a neutral modifier, what range of pore sizes allow migration at reduced levels, and what range of pore sizes completely block migration. This could be done by using the approaches of Nyström et al. (2005) and Martins et al. (2009) where they performed *in vitro* experiments using a collagen:matrigel assay to investigate the invasiveness of cancer cells to establish a quantitative “invasive index” in organotypic cultures. Once there is quantitative data for these effects, obtaining data on the structure of the tissue through effective imaging techniques such as those described in Wolf et al. (2009) would allow one to generate realistic initial conditions of the matrix suitability modifier. An estimate of the parameter δ_s could then be obtained by validating the model against experiments similar to those found in Sabeh et al. (2009) or

Li et al. (2008), who performed *in vitro* experiments using a cross-linked native type I collagen assay to investigate the importance of MT1-MMP in cancer invasion.

Future work in developing the model will involve a parameter sensitivity analysis for the system. However, one observation that we have already noticed is that by increasing the production of TIMP2 to 10 times its original value (i.e., $\alpha_T = 40$) greatly reduces matrix degradation over the time interval considered and the cancer cell population increases by only 56% from its initial value (see Figure S7 in the Supplementary Material). This is due to an abundance of TIMP2 molecules binding to MT1-MMP molecules before free MT1-MMP are able to take part in activating MMP-2, as described in stage 2 of Figure 2. These observations are in line with the observed biological results of Strongin et al. (1995), Sabeh et al. (2009). We also note that for low levels of TIMP2 production, activation of MMP-2 is reduced while the concentration of active MT1-MMP is increased and the total level of ECM degradation is reduced.

We will also consider a more detailed activation system for MMP-2. While we reduced the full activation system of MMP-2 (shown in Figure 1) to the simpler system used in the model (shown in Figure 2), it is not clear if the activation system of Figure 1 captures the full range of dynamics involved in this process. Another component of the activation system which could be considered is an intermediate form of MMP-2 occurring between the proMMP-2 and fully active MMP-2. In our model, there is no intermediate form of MMP-2, since we assume proMMP-2 is in abundance and always present in the MT1-MMP:TIMP2 complex. To consider any complementary effects

of further activation systems of MMP-2 on cancer cell invasion, they must first be established. Lafleur et al. (2003) have proposed that proMMP-2 binds to a different cell receptor than is modeled in our current model of the MT1-MMP:TIMP2 complex. The proMMP-2 is processed into an intermediate form of MMP-2 before binding to the MT1-MMP:TIMP2 complex and auto-catalyzing into active MMP-2. Investigations into further activation systems by focusing on each stage of Figure 1 may be helped by the work of Nishida et al. (2008) who showed that an artificial receptor for proMMP-2 was able to take the place of the MT1-MMP:TIMP2 complex in binding proMMP-2 to the cell surface without inhibiting active MT1-MMP or MMP-2. In order to gain the full benefit of such modeling efforts (at the cell and receptor scale), we will also require to adapt the current model to take into account novel multi-scale modeling approaches, some of which have already been formulated specifically to investigate cancer invasion [cf. Trucu et al. (2013)].

ACKNOWLEDGMENTS

The authors gratefully acknowledge the support of the ERC Advanced Investigator Grant 227619, “M5CGS – From mutations to metastases: multiscale mathematical modeling of cancer growth and spread.”

SUPPLEMENTARY MATERIAL

The Supplementary Material for this article can be found online at http://www.frontiersin.org/Molecular_and_Cellular_Oncology/10.3389/fonc.2013.00070/abstract

REFERENCES

- Anderson, A. R. A., Chaplain, M. A. J., Newman, E. L., Steele, R. J. C., and Thompson, A. M. (2000). Mathematical modelling of tumour invasion and metastasis. *Comput. Math. Methods Med.* 2, 129–154.
- Araujo, R. P., and McElwain, D. L. S. (2004). A history of the study of solid tumour growth: the contribution of mathematical modelling. *Bull. Math. Biol.* 66, 1039–1091.
- Burton, A. C. (1966). Rate of growth of solid tumours as a problem of diffusion. *Growth* 30, 157–176.
- Butler, G. S., Butler, M. J., Atkinson, S. J., Will, H., Tamura, T., Schade van Westrum, S., et al. (1998). The TIMP2 membrane type 1 metalloproteinase “receptor” regulates the concentration and efficient activation of progelatinase A: a kinetic study. *J. Biol. Chem.* 273, 871–880.
- Collier, I. E., Legant, W., Marmer, B., Lubman, O., Saffarian, S., Wakatsuki, T., et al. (2011). Diffusion of MMPs on the surface of collagen fibrils: the mobile cell surface-collagen substratum interface. *PLoS ONE* 6:e24029. doi:10.1371/journal.pone.0024029
- Donzé, A., Fanchon, E., Gattepaille, L. M., Maler, O., and Tracqui, P. (2011). Robustness analysis and behavior discrimination in enzymatic reaction networks. *PLoS ONE* 6:e24246. doi:10.1371/journal.pone.0024246
- d’Ortho, M. P., Will, H., Atkinson, S., Butler, G., Messent, A., Gavrilovic, J., et al. (1997). Membrane-type matrix metalloproteinases 1 and 2 exhibit broad-spectrum proteolytic capacities comparable to many matrix metalloproteinases. *Eur. J. Biochem.* 250, 751.
- English, W. R., Holtz, B., Vogt, G., Knauer, V., and Murphy, G. (2001). Characterization of the role of the “MT-loop”: an eight-amino acid insertion specific to progelatinase A (MMP2) activating membrane-type matrix metalloproteinases. *J. Biol. Chem.* 276, 42018–42026.
- Friedl, P., and Wolf, K. (2003). Proteolytic and non-proteolytic migration of tumour cells and leucocytes. *Biochem. Soc. Symp.* 70, 277–285.
- Gerisch, A., and Chaplain, M. A. (2008). Mathematical modelling of cancer cell invasion of tissue: local and non-local models and the effect of adhesion. *J. Theor. Biol.* 250, 684–704.
- Hanahan, D., and Weinberg, R. A. (2000). The hallmarks of cancer. *Cell* 100, 57–70.
- Hanahan, D., and Weinberg, R. A. (2011). Hallmarks of cancer: the next generation. *Cell* 144, 646–674.
- Hoshino, D., Koshikawa, N., Suzuki, T., Quaranta, V., Weaver, A. M., Seiki, M., et al. (2012). Establishment and validation of computational model for MT1-MMP dependent ECM degradation and intervention strategies. *PLoS Comput. Biol.* 8:e1002479. doi:10.1371/journal.pcbi.1002479
- Ichikawa, K. (2001). A-Cell: graphical user interface for the construction of biochemical reaction models. *Bioinformatics* 17, 483–484.
- Karagiannis, E. D., and Popel, A. S. (2004). A theoretical model of type I collagen proteolysis by matrix metalloproteinase (MMP) 2 and membrane type 1 MMP in the presence of tissue inhibitor of metalloproteinase 2. *J. Biol. Chem.* 279, 39105–39114.
- Karagiannis, E. D., and Popel, A. S. (2006). Distinct modes of collagen type I proteolysis by matrix metalloproteinase (MMP) 2 and membrane type I MMP during the migration of a tip endothelial cell: insights from a computational model. *J. Theor. Biol.* 238, 124–145.
- Kessenbrock, K., Plaks, V., and Werb, Z. (2010). Matrix metalloproteinases: regulators of the tumor microenvironment. *Cell* 141, 52–67.
- Kinoh, H., Sato, H., Tsunozuka, Y., Takino, T., Kawashima, A., Okada, Y., et al. (1996). MT-MMP, the cell surface activator of proMMP-2 (pro-gelatinase A), is expressed with its substrate in mouse tissue during embryogenesis. *J. Cell. Sci.* 109, 953–959.
- Kleiner, D. E., and Stetler-Stevenson, W. G. (1999). Matrix metalloproteinases and metastasis. *Cancer Chemother. Pharmacol.* 43(Suppl.), 42–51.
- Lafleur, M. A., Tester, A. M., and Thompson, E. W. (2003). Selective involvement of TIMP-2 in the second activation cleavage of pro-MMP-2: refinement of the pro-MMP-2 activation mechanism. *FEBS Lett.* 553, 457–463.
- Li, X. Y., Ota, I., Yana, I., Sabeh, F., and Weiss, S. J. (2008). Molecular dissection of the structural machinery underlying the tissue-invasive activity of membrane type-1 matrix metalloproteinase. *Mol. Biol. Cell* 19, 3221–3233.

- López-Otín, C., and Overall, C. M. (2002). Protease degradomics: a new challenge for proteomics. *Nat. Rev. Mol. Cell Biol.* 3, 509–519.
- Lowengrub, J. S., Friboes, H. B., Jin, F., Chuang, Y. L., Li, X., Macklin, P., et al. (2010). Nonlinear modelling of cancer: bridging the gap between cells and tumours. *Nonlinearity* 23, R1–R9.
- Martins, V. L., Vyas, J. J., Chen, M., Purdie, K., Mein, C. A., South, A. P., et al. (2009). Increased invasive behaviour in cutaneous squamous cell carcinoma with loss of basement-membrane type VII collagen. *J. Cell. Sci.* 122(Pt 11), 1788–1799.
- Nagase, H., and Woessner, J. F. (1999). Matrix metalloproteinases. *J. Biol. Chem.* 274, 21491–21494.
- Nishida, Y., Miyamori, H., Thompson, E. W., Takino, T., Endo, Y., and Sato, H. (2008). Activation of matrix metalloproteinase-2 (MMP-2) by membrane type 1 matrix metalloproteinase through an artificial receptor for proMMP-2 generates active MMP-2. *Cancer Res.* 68, 9096–9104.
- Nöel, A., Gutiérrez-Fernández, A., Sounni, N. E., Behrendt, N., Maquoi, E., Lund, I. K., et al. (2012). New and paradoxical roles of matrix metalloproteinases in the tumor microenvironment. *Front. Pharmacol.* 3:140. doi:10.3389/fphar.2012.00140
- Nyström, M. L., Thomas, G. J., Stone, M., Mackenzie, I. C., Hart, I. R., and Marshall, J. F. (2005). Development of a quantitative method to analyse tumour cell invasion in organotypic culture. *J. Pathol.* 205, 468–475.
- Provenzano, P. P., Inman, D. R., Eliceiri, K. W., Knittel, J. G., Yan, L., Rueden, C. T., et al. (2008). Collagen density promotes mammary tumor initiation and progression. *BMC Med.* 6:11. doi:10.1186/1741-7015-6-11
- Rejniak, K. A., and McCawley, L. J. (2010). Current trends in mathematical modeling of tumor-microenvironment interactions: a survey of tools and applications. *Exp. Biol. Med. (Maywood)* 235, 411–423.
- Rowe, R. G., and Weiss, S. J. (2009). Navigating ECM barriers at the invasive front: the cancer cell-stroma interface. *Annu. Rev. Cell Dev. Biol.* 25, 567–595.
- Sabeh, F., Shimizu-Hirota, R., and Weiss, S. J. (2009). Protease-dependent versus -independent cancer cell invasion programs: three-dimensional amoeboid movement revisited. *J. Cell Biol.* 185, 11–19.
- Sahai, E. (2005). Mechanisms of cancer cell invasion. *Curr. Opin. Genet. Dev.* 15, 87–96.
- Strongin, A. Y., Collier, I., Bannikov, G., Marmer, B. L., Grant, G. A., and Goldberg, G. I. (1995). Mechanism of cell surface activation of 72-kDa type IV collagenase. *J. Biol. Chem.* 270, 5331–5338.
- Tam, E. M., Moore, T. R., Butler, G. S., and Overall, C. M. (2004). Characterization of the distinct collagen binding, helicase and cleavage mechanisms of matrix metalloproteinase 2 and 14 (gelatinase A and MT1-MMP): the differential roles of the MMP hemopexin c domains and the MMP-2 fibronectin type II modules in collagen triple helicase activities. *J. Biol. Chem.* 279, 43336–43344.
- Thomlinson, R. H., and Gray, L. H. (1955). The histological structure of some human lung cancers and the possible implications for radiotherapy. *Br. J. Cancer* 9, 539–549.
- Toth, M., Bernardo, M. M., Gervasi, D. C., Soloway, P. D., Wang, Z., Bigg, H. F., et al. (2000). Tissue inhibitor of metalloproteinase (TIMP)-2 acts synergistically with synthetic matrix metalloproteinase (MMP) inhibitors but not with TIMP-4 to enhance the (Membrane type 1)-MMP-dependent activation of pro-MMP-2. *J. Biol. Chem.* 275, 41415–41423.
- Trucu, D., Lin, P., Chaplain, M., and Wang, Y. (2013). A multiscale moving boundary model arising in cancer invasion. *Multiscale Model. Simul.* 11, 309–335.
- Tutton, M. G., George, M. L., Eccles, S. A., Burton, S., Swift, R. I., and Abulafi, A. M. (2003). Use of plasma MMP-2 and MMP-9 levels as a surrogate for tumour expression in colorectal cancer patients. *Int. J. Cancer* 107, 541–550.
- Werb, Z. (1997). ECM and cell surface proteolysis: regulating cellular ecology. *Cell* 91, 439–442.
- Wolf, K., Alexander, S., Schacht, V., Coussens, L. M., von Andrian, U. H., van Rheenen, J., et al. (2009). Collagen-based cell migration models in vitro and in vivo. *Semin. Cell Dev. Biol.* 20, 931–941.
- Zhang, Y., Mao, X., Schwend, T., Littlechild, S., and Conrad, G. W. (2013). Resistance of corneal RFUVA-cross-linked collagens and small leucine-rich proteoglycans to degradation by matrix metalloproteinases. *Invest. Ophthalmol. Vis. Sci.* 54, 1014–1025.
- Zigrino, P., Drescher, C., and Mauch, C. (2001). Collagen-induced proMMP-2 activation by MT1-MMP in human dermal fibroblasts and the possible role of alpha2beta1 integrins. *Eur. J. Cell Biol.* 80, 68–77.

Conflict of Interest Statement: The authors declare that the research was conducted in the absence of any commercial or financial relationships that could be construed as a potential conflict of interest.

Received: 06 December 2012; accepted: 18 March 2013; published online: 03 April 2013.

Citation: Deakin NE and Chaplain MAJ (2013) Mathematical modeling of cancer invasion: the role of membrane-bound matrix metalloproteinases. *Front. Oncol.* 3:70. doi: 10.3389/fonc.2013.00070
This article was submitted to *Frontiers in Molecular and Cellular Oncology*, a specialty of *Frontiers in Oncology*. Copyright © 2013 Deakin and Chaplain. This is an open-access article distributed under the terms of the Creative Commons Attribution License, which permits use, distribution and reproduction in other forums, provided the original authors and source are credited and subject to any copyright notices concerning any third-party graphics etc.



Properties of tumor spheroid growth exhibited by simple mathematical models

Dorothy I. Wallace* and Xinyue Guo

Department of Mathematics, Dartmouth College, Hanover, NH, USA

Edited by:

Heiko Enderling, Tufts University
School of Medicine, USA

Reviewed by:

Philip Gerlee, University of
Gothenburg, Sweden
Mark Chaplain, University of Dundee,
UK
Cory Howk, Western Carolina
University, USA

*Correspondence:

Dorothy I. Wallace, Department of
Mathematics, HB 6188, Dartmouth
College, Hanover, NH 03768, USA.
e-mail: dwallace@math.
dartmouth.edu

Solid tumors, whether *in vitro* or *in vivo*, are not an undifferentiated mass of cells. They include necrotic regions, regions of cells that are in a quiescent state (either slowly growing or not growing at all), and regions where cells proliferate rapidly. The decision of a cell to become quiescent or proliferating is thought to depend on both nutrient and oxygen availability and on the presence of tumor necrosis factor, a substance produced by necrotic cells that somehow inhibits the further growth of the tumor. Several different models have been suggested for the basic growth rate of *in vitro* tumor spheroids, and several different mechanisms are possible by which tumor necrosis factor might halt growth. The models predict the trajectory of growth for a virtual tumor, including proportions of the various components during its time evolution. In this paper we look at a range of hypotheses about basic rates tumor growth and the role of tumor necrotic factor, and determine what possible tumor growth patterns follow from each of twenty-five reasonable models. Proliferating, quiescent and necrotic cells are included, along with tumor necrosis factor as a potential inhibitor of growth in the proliferating pool and two way exchange between the quiescent and proliferating pools. We show that a range of observed qualitative properties of *in vitro* tumor spheroids at equilibrium are exhibited by one particular simple mathematical model, and discuss implications of this model for tumor growth.

Keywords: tumor spheroid, mathematical oncology, mathematical biology, tumor models, necrosis, quiescence, tumor simulation

1. INTRODUCTION

Tumor spheroids cultured *in vitro* play an important role in cancer research. Various authors have pointed out that spheroids are a better representation of many types of *in vivo* tumors than monolayer culture, and less expensive than *in vivo* studies, as described by Santini et al. (2000) and Hirschhaeuser et al. (2010).

Spheroid growth is observed to cease spontaneously, with a characteristic long term anatomy and a variety of terminal volumes for any given cell line. At the earliest stage the spheroid may be an undifferentiated mass of proliferating tumor cells. At an intermediate stage the proliferating cells form a shell around the outside of the spheroid and the inner core will consist of live cells that are not actively dividing, which we will refer to as “quiescent.” These have been observed in tumor spheroids via imaging techniques (Sherar et al., 1987) and through isolation and staining (Preisler et al., 1977; Bauer et al., 1982). At later stages the inner core of the spheroid will be necrotic tissue, surrounded by a shell of quiescent cells, and an outermost layer of live, proliferating cells (Folkman and Hochberg, 1973; Sherar et al., 1987). Proliferating cells are the target of most cancer therapies. The quiescent cell population has been implicated as a population resistant to some of these therapies, playing an important role in tumor regrowth (Potmesil and Goldfeder, 1980; Kallman et al., 1982).

Numerous models for tumor spheroids, quiescence, and necrosis, are in the literature, and these exhibit the observed phenomena to greater or lesser degree. Models range from extremely complex

to simple with an enormous range in between. Simple models only attempt to match total tumor size (Marusic et al., 1994; Demidenko, 2006). These find a reasonably good match with logistic and Gompertz equations, which postulate a known bound on spheroid size.

The necrotic core is a feature of all but the simplest models. Tumor necrosis factor has been implicated as the cause of the eventual cessation of growth in spheroids (Freyer, 1988). Greenspan (1972) is possibly the earliest such model, employing numerous simplifying assumptions to arrive at differential equations that can be solved explicitly. Menchon and Condat (2008, 2009) come to the conclusion, based on mathematical models, that some inhibitory factor is necessary for growth cessation in spheroids. This has been a general observation for mathematical models that do not include an *a priori* known bound for the size of the spheroid in the governing equations, as is the case for logistic or Gompertz models.

Some models take diffusion of nutrients into account, producing the characteristic distribution of proliferating, quiescent and necrotic cells, relying on a variation of the diffusion equation and parameters for a variety of nutrients (Venkatasubramanian et al., 2006). An early example is by Gyllenberg and Webb (1990), whose model includes both quiescence and necrosis to arrive at a growth trajectory that resembles the observed Gompertz curve, but which drives the proliferating cell population to zero. To this scenario, some authors add cellular motion (Stein et al., 2007), a consideration of the forces that determine the shape of the tumor mass

(Frieboes et al., 2006), and mechanisms for the onset of necrosis (Menchon and Condat, 2008). Others achieve the similar structure through a combination of models at different level of structure (Jiang et al., 2005).

A series of models by Adam (1986, 1987a,b) dating back to the 1980s uses one dimensional diffusion with nutrient source and a time independent source of unspecified mitotic inhibitor responding to a switch. The continuously growing necrotic core observed in experiment suggests that the production of mitotic inhibitor is neither time independent nor switched discontinuously. Adam notes in his third paper that the necrotic core would have to be taken into account in future models, such as those presented in this paper, in order to match the observations in Folkman et al. (Folkman and Hochberg, 1973; Adam, 1987b). The more sophisticated treatment in Maggelakis and Adam (1990) yields the observed Gompertz curve but does this paper does not give information about the composition of the tumor at equilibrium. A similar series of models by McElwain and coauthors (McElwain and Ponzo, 1977; McElwain, 1978; McElwain and Morris, 1978) consider the diffusion process in a spheroid in detail.

The advantage of complex models is that they produce a range of outcomes, some of which are similar to observed growth patterns. The disadvantage is that they require knowledge of many specific parameters, some of which are hard to obtain. The models we consider in this paper are similar to the one developed by Landry et al. (1982), which over a limited time agreed with data from Folkman and Hochberg (1973) but did not include a quiescent component and did not have the bounded growth characteristic of tumor spheroids. They are also similar to one proposed by Piantadosi (1985), which includes all three components and places a bound on the reproducing subpopulation. These are some of the older, simpler models in the literature. They do not attempt to explain shape, only quantities of various cell types. They were developed before an understanding of the potential role of tumor necrosis factor, and deserved to be revisited with that role in mind. None of these examples includes the return of quiescent cells to the proliferating pool.

The goal of this paper is to find the simplest possible system of ordinary differential equations that produces the qualitative results observed in Folkman and Hochberg (1973), Sherar et al. (1987), and Freyer (1988), starting from the assumption that proliferating, quiescent and necrotic layers exist. As part of this search, we will rule out a large collection of simple models that, although conceptually reasonable, do not produce results consistent with these three papers. Simple, as interpreted here, means a system of ordinary differential equations that has approximately as many parameters as there are measured quantities. In these equations, diffusion is assumed to be uniform in the proliferating compartment and sufficient to produce growth. The movement of nutrient is not modeled, except as a variation between compartments. The image of a spheroid at equilibrium from the Folkman and Hochberg paper shows a very thin shell of proliferating cells, hardly enough to make the effects of diffusion prominent. Similarly, tumor necrosis factor inhibiting growth

of proliferating cells is assumed to reach those cells uniformly. Although clearly a simplification in some respects, such models are desirable as they allow an approximate fit to measured data with the correct range of qualitative behaviors, without requiring knowledge of quantities that are not easily measured and with few enough parameters that the range of possible answers is small.

These papers describe four quantities at moments in time: the tumor size in Folkman and Hochberg (1973) and Freyer (1988), and the amounts of proliferating, quiescent and necrotic cells in Sherar et al. (1987). The basic qualitative results are summarized in the following list.

1. Spheroids, no matter what the initial conditions may be, eventually develop three layers of proliferating, quiescent and necrotic cells (Sherar et al., 1987).
2. Growth of spheroids eventually stops. (Folkman and Hochberg, 1973).
3. When the growth stops, there remains a thin layer of actively proliferating cells at the boundary (Folkman and Hochberg, 1973).
4. The final size of the spheroids is correlated with thickness of the proliferating shell (Freyer, 1988).
5. The final size of the spheroids is correlated with the size at which necrosis begins (Freyer, 1988).
6. The more spheroids in a flask, the smaller the average size when growth ends (Folkman and Hochberg, 1973).

1.1. DEVELOPMENT OF MODELS

The models developed for this study track the dynamics of a three part tumor spheroid growing *in vitro*. The quantities tracked are

1. Proliferating cells, which after time form a concentric shell at the exterior of the spheroid, as observed in numerous imaging studies, including those of Freyer (1988), Folkman and Hochberg (1973), and Sherar et al. (1987). These are exposed to the nutrient solution. They may become quiescent or they may die and be shed from the spheroid. In early stage spheroids the proliferating cells may constitute the entire spheroid and grow at an intrinsic rate. A fraction of proliferating cells may also be shed into the surrounding medium.
2. Quiescent cells, which form a secondary, and usually thicker, shell inside the outer layer of proliferating cells. These arise as proliferating cells pass to a quiescent state. They may return to a proliferating state or experience cell death due to necrosis.
3. Necrotic cells, which form the core of the spheroid. These can be absent in small spheroids or constitute the majority of the spheroid mass in older cultures. They arise as quiescent cells die. Necrotic cells may also undergo dissolution and be removed from the system entirely.
4. Total spheroid size.

The basic system of three non-linear ordinary differential equations coming from items 1 to 3 above is shown in full generality below, with explanations of the individual terms following. Note

that 25 variations result from our considerations, each labeled with a number from 1 to 5 and a letter from A to E.

$$\frac{dP}{dt} = G(P) - b_{P,Q}P + c_{Q,P}Q - F(P, Q, N) - dP \quad (1)$$

$$\frac{dQ}{dt} = b_{P,Q}P - c_{Q,P}Q - e_{Q,N}Q + H(P, Q, N) \quad (2)$$

$$\frac{dN}{dt} = e_{Q,N}Q - mN \quad (3)$$

1.1.1. Growth of proliferating cells, $G(P)$

Growth of tumor spheroids is observed to cease. Thus there is some limiting factor on the growth of P . However, there is debate about the nature of this factor. A limit can be imposed directly by using logistic or Gompertzian growth for P , both of which have similar qualitative properties. However the access of proliferating cells to nutrient is likely to be dependent on the surface area of the spheroid, with any limitation to growth due to other factors such as tumor necrosis. Models 3, 4, and 5 below have different versions of this hypothesis. Yet another alternative is to assume simple exponential growth of P . We look at five variations of the function $G(P)$. All models include a death rate of proliferating cells, dP , that are assumed to be shed into surrounding medium and lost from the model.

1. Model 1 uses a logistic term to limit the growth of P : $G(P) = aP(1 - P)$. We could have used a Gompertzian model with similar qualitative results.
2. Model 2 assumes exponential growth: $G(P) = aP$, as in Piantadosi (1985).
3. Model 3 assumes that growth is proportional to the surface area of the spheroid: $G(P) = a(P + Q + N)^{2/3}$.
4. Model 4 assumes that growth is jointly proportional to both surface area and volume of P : $G(P) = aP(P + Q + N)^{2/3}$.
5. Model 5 uses the surface area of the spheroid as the limiting factor in a logistic growth term: $G(P) = aP(1 - P(P + Q + N)^{-2/3})$.

1.1.2. Transition from proliferating to quiescent, $b_{P,Q}P$, $c_{Q,P}Q$ and quiescent to necrotic, $e_{Q,N}Q$

Tumor spheroids exhibit a layer of quiescent cells (Sherar et al., 1987) which are thought to arise as proliferating cells lose access to nutrients. Similarly, quiescent cells die after sufficient lack of nutrient. In addition, it is known that quiescent cells may become proliferating cells again (Potmesil and Goldfeder, 1980), and so a return loop is included in the model, with a proportion of Q returning to the proliferating pool. These terms remain the same across all the models studied here. In *in vivo* tumors, the location of quiescent cells (and also necrotic cells) would depend on the geometry of this access, including the location of blood vessels, and the growth of these classes of cells is difficult to measure. For simplicity we use linear terms to describe this transition. There are two justifications for this. First, if we assume that passage to the quiescent state is a result of the limits of diffusion of nutrients, then as P approaches a limiting thickness the amount of proliferating cells transitioning to quiescent is proportional to the surface of the inside of the proliferating shell. Near the

limiting thickness surface area is approximately proportional to volume of P . Second, whatever rule governs the transition from P to Q may be expressed as a Taylor series in P whose leading term must be the linear one. For both of these reasons, a good first approximation to this process is linear dependence on P given by $b_{P,Q}P$. Similar arguments may be made for the other terms, $c_{Q,P}Q$ and $e_{Q,N}Q$. Thus we assume that constant proportion of P becomes Q , and a constant proportion of Q dies to become N .

1.1.3. The effect of tumor necrosis factor, $F(P, Q, N)$ and $H(P, Q, N)$

Extract of necrotic tumors is known to reduce the growth of tumor spheroids (Freyer, 1988), but the mechanism is unclear. It is possible that as quiescent cells become necrotic they release a substance that slows growth of proliferating cells. It is possible that the necrotic cells themselves continue to release such a substance. Finally, it is possible that some substance increases the rate at which proliferating cells become quiescent, and perhaps this is enough to stop growth. We have looked at all of these hypotheses, and summarized them in five cases.

- (A) Model A assumes that the proliferation of P is slowed when proliferating cells come in contact with substances released as quiescent cells die. F is thus proportional to both P and the rate of necrosis, cQ , so that $F(P, Q, N) = fQP$. This term can be interpreted as slower growth or as death and shedding of P cells; mathematically it makes no difference. The interesting feature of this model is that the growth reducing effect of necrosis is determined by the size of Q and thus is bounded in models where Q approaches equilibrium. In this model no extra rate of quiescence is assumed, so $H(P, Q, N) = 0$.
- (B) Model B only assumes that the passage of cells from proliferating to quiescent is increased in proportion to the number of proliferating cells. In this model, $F(P, Q, N) = 0$ and $H(P, Q, N) = hP$, so there is effectively no tumor necrosis factor that depends on Q or N .
- (C) Model C includes features of both Model A and Model B, so $F(P, Q, N) = fQP$ and $H(P, Q, N) = hP$.
- (D) Model D assumes that the proliferation of P is slowed when proliferating cells come in contact with substances released by all cells in the necrotic pool. F is thus proportional to both P and N , so that $F(P, Q, N) = fNP$. This term can be interpreted as slower growth or as death and shedding of P cells; mathematically it makes no difference. However, in models where P and Q do not go to zero, N can get arbitrarily large, unlike in models A and C. This model includes increased passage of proliferating cells to the quiescent pool, so $H(P, Q, N) = hP$.
- (E) Model E assumes only that the proliferation of P is slowed when proliferating cells come in contact with substances released by all cells in the necrotic pool, so $F(P, Q, N) = fNP$ and $H(P, Q, N) = 0$.

1.1.4. Dissolution of necrotic cells, mN

A cell that is dead long enough may dissolve and its contents be removed from the system. Indeed, this may be the very source of

substances that retard growth. For our initial numerical experiments, m was taken to be zero. In the results section we discuss the various growth patterns that result from these experiments, a few of which have good properties of the P and Q compartments, but which have constantly increasing values for N . This is reasonable because the system is live and dynamic, so there is always some death taking place. Taking m to be any positive constant allows N to reach equilibrium in these cases. Unless otherwise stated, however, we take $m = 0$.

1.1.5. Constants

Default constants for all runs are $a = 0.01$, $b_{PQ} = 0.01$, $c_{Q,P} = 0.005$, $d = 0.002$, $e_{Q,N} = 0.002$, $f = 0.01$, $h = 0.001$, $m = 0$. These constants always give tumors that grow, at least initially. Clearly, for each of these models we could choose sufficiently slow growth (or fast death) so that the tumor size decreases, but this is the less interesting case. Note that the constants were chosen for the purposes of comparing models and do not represent any particular cell line or data set. The constants chosen for these runs may all be scaled to a different time frame. A more realistic growth parameter, a , would be about 70 times larger than the one we chose here if the time unit is 1 day. Scaling all constants together results in faster growth but keeps equilibrium values the same. Data on how the volumes or cell counts of the P , Q , and N pools change over time for a particular type of spheroid is not available, so it is not possible to infer the constants in the model with any certainty. The results in this paper concern qualitative observations that depend on equilibrium values only, and therefore do not depend strongly on the exact constants chosen, as long as the system arrives at equilibrium.

2. MATERIALS AND METHODS

All twenty-five models were run with default settings using Matlab ODE 45 solver to compare qualitative outcomes. Subsequent comparisons and graphs for all figures in this paper were run on BGDEM software developed by Brian Reed. Adobe Photoshop was used to format all graphs for publication.

The twenty-five models under consideration fall into three broad groups when $m = 0$:

1. Models where P and Q approach a non-zero equilibrium: 1A, 1B, 1C, 2A, 2C, 3A, 3C, 3D, 3E, 5A, 5C. These models exhibit the basic qualitative behaviors of P and Q described in the literature.
2. Models in which P and Q approach zero: 1D, 1E, 2D, 2E, 4A, 4B, 4C, 4D, 4E, 5D, 5E. In these models total tumor growth stops as this occurs, as the growth of N stops. Introducing a small value for m does not change this behavior. It is possible that other behaviors would appear if m were large enough, but those behaviors would then depend on a parameter for which there is, as yet, no estimate.
3. Models in which P and Q grow without bound: 2B, 3B, 5B.

These results are summarized in **Table 1**, where * denotes a non-zero equilibrium, 0 denotes cases where P and Q approach zero, and u denotes unbounded growth.

A typical run from each of the first two categories is shown in **Figure 1**.

Table 1 | Summary of model behaviors for all cases.

	1	2	3	4	5
A	*	*	*	0	*
B	*	u	u	0	u
C	*	*	*	0	*
D	0	0	*	0	0
E	0	0	*	0	0

* denotes a non-zero equilibrium, 0 denotes cases where P and Q approach zero, and u denotes unsounded growth.

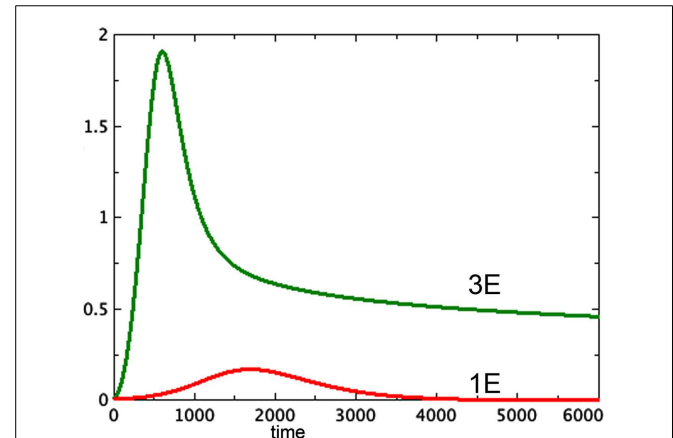


FIGURE 1 | Proliferating pools from models 3E and 1E compared.

$a = 0.01$, $b_{PQ} = 0.01$, $c_{Q,P} = 0.005$, $d = 0.002$, $e_{Q,N} = 0.002$, $f = 0.01$, $h = 0$, $P_0 = 0.01$, $Q_0 = 0$, $N_0 = 0$.

2.1. SOME COMMENTS ON THE EQUATIONS

The equation for Q' is a simple linear relationship between P and Q . Thus, if P reaches an equilibrium, so will Q in corresponding proportion, for all twenty-five models. Similarly, for all models N' is positive if $m = 0$, and will continue to increase as long as Q (and therefore P) is positive. Models for which P and Q go to non-zero equilibrium will thus still have N increasing. However this is a problem that can be easily solved by taking m to be any positive number, forcing N to an equilibrium. For models in which tumor growth depends on N (Models D and E), this has the effect of creating a non-zero equilibrium in cases that would otherwise have P and Q going to zero.

Model 3E, which we examine further in this paper, has non-zero equilibrium points given by the following equations.

$$Q = \frac{b}{c + e}P \quad (4)$$

$$N = \frac{e}{m}Q \quad (5)$$

$$0 = wX^4 - vX - u \quad (6)$$

Here $X = P^{1/3}$, $u = a(1 + \alpha + \beta)^{2/3}$, $v = (-b + c\beta - d)$, $w = f\alpha$, $\alpha = \frac{eb}{m(c+e)}$, $\beta = \frac{b}{(c+e)}$. The derivative of the right hand side of equation (6) has at most one real root, thus equation (6) has at most two real roots. By DesCartes' rule of signs (for positive parameters w, v, u) equation (6) has at most one real root. Thus, the non-zero equilibrium, if it exists, is unique.

3. RESULTS

3.1. MODEL B

These are the models in which necrotic factor plays no role. Of these, only 1B, which has logistic growth, reaches a non-zero equilibrium for P and Q , and that equilibrium is independent of initial conditions. The same would hold if we replace the logistic term with a Gompertz equation. The criticism of this model is conceptual. If there is a limit to growth, what is causing it? The limits of diffusion explain uniform spheroids of proliferating cells, but not actual spheroids, which grow to have a necrotic core that does not require nutrient. The thin shell of proliferating cells is within the range of diffusion, and should therefore not be limited in growth. As the spheroid grows, the surface with its thin layer of proliferating cells resembles a plate culture, which is known to grow in an unlimited fashion.

In model 4B, P and Q go to zero. This gives a spheroid of limited size, but it is dead. Models 2B, 3B, and 5B display unlimited growth.

3.2. MODELS A AND C

Models 1A, 1C, 2A, 2C, 3A, 3C, 5A, and 5C all show P and Q going to a non-zero equilibrium. This equilibrium may be calculated directly from the equations and does not depend on N , which continues to grow in these models. Thus, adding extra necrotic factor to these models (by increasing the initial quantity of N , for example) will have no effect on the eventual size of the proliferating and quiescent pools. It would be difficult to duplicate the results in Freyer (1988), which display a dependence of spheroid size on various factors related to the quantity N , using these models.

3.3. MODELS 3D AND 3E

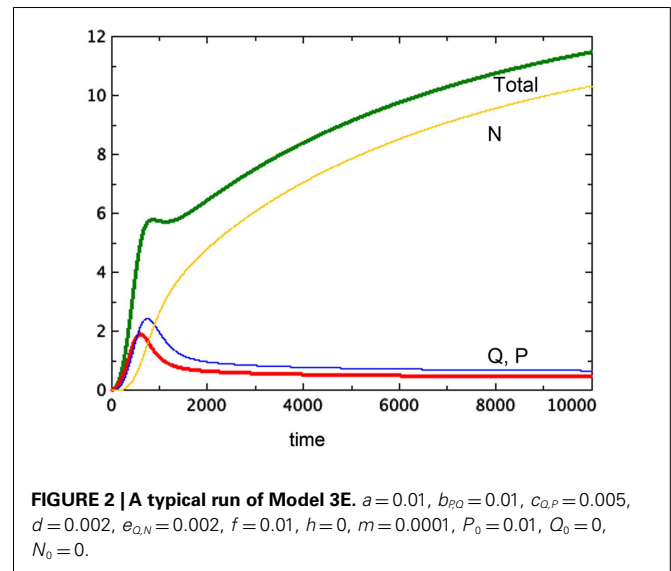
These models represent the best fit with qualitative observations. The growth term reflects the assumption that diffusion is the driving supplier of nutrients. The only difference between these two models is the rate at which proliferating cells become quiescent. In both of these, P and Q stabilize as N continues to grow, but the equilibrium values of P and Q cannot be deduced from the equations, which depend on N . By adjusting the value of m to be positive, we can arrange for N to arrive at any equilibrium value (depending on the equilibrium value of Q).

The hypothesis of growth that is dependent on surface area (Model 3) gives the best representation of experimental data among the various models tested. Model 3E will always include a non-trivial equilibrium for quiescent cells, as observed in Sherar et al. (1987). Furthermore, this model only arrives at equilibrium in the presence of a tumor necrotic factor that depends on the actual quantity of necrosis that has occurred (Models D and E). Finally, the extra feature of faster passage of proliferating cells to quiescent does not play an important role here, with the caveat that only a very simple form of this extra feature was tested. **Figure 2** shows a typical run of Model 3E.

3.4. A CLOSER LOOK AT EXPERIMENTAL RESULTS

We notice the following phenomena in Model 3E, which mirror the results of Folkman and Hochberg (1973):

1. **Figure 2** shows a typical run of Model 3E, displaying the proliferating pool and the total spheroid size. In early stages of

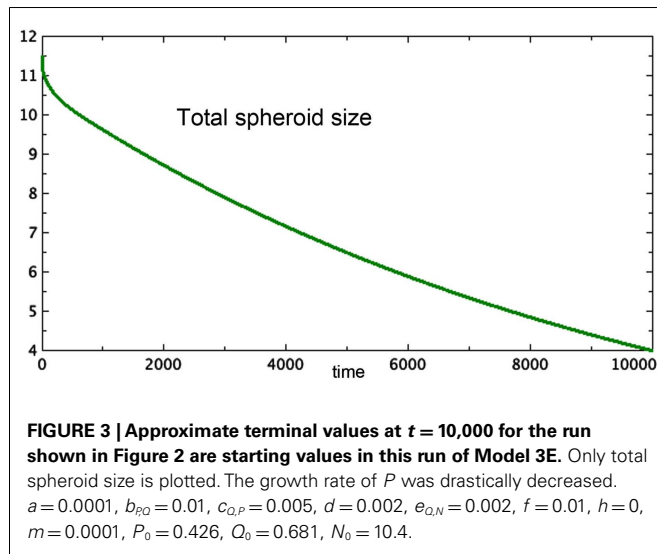


growth, the proliferating pool is a large fraction of the spheroid, while at equilibrium the proportion of the tumor accounted for by proliferating cells is much smaller. This phenomenon was observed by Folkman and Hochberg (1973), with proliferating cells being as much as 60% of the spheroid volume in early stages and dropping to 14% at equilibrium.

2. The data displayed in that same paper show a distinctive early overshoot of both the total volume and the proliferating pool, followed by a slight drop as the spheroid approaches equilibrium. That overshoot is also present in **Figure 2** of this paper, Model 3E.
3. **Figure 3** shows a late stage version of the 3E spheroid, in which the growth rate of proliferating cells is reduced drastically. Note that the growth term for this model is proportional to surface area, whereas the removal of P is linear. The two processes are not symmetric. The spheroid volume is seen to drop in a linear fashion. This was observed *in vitro* by Folkman and Hochberg when dormant spheroids were exposed continuously to a substance that prevented mitosis.

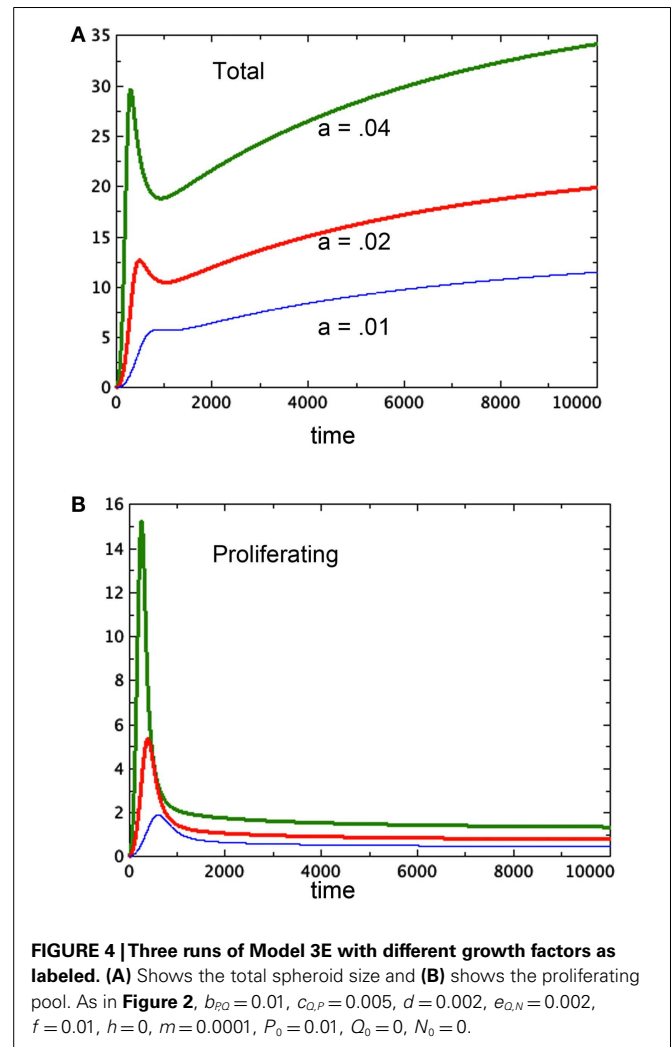
We now turn to the experiments done by Freyer (1988), in which a variety of cell lines were cultured as spheroids in flasks. Several features of this experiment are particularly important from the modeling standpoint. First, cell lines were cultured separately. Second, flasks were renewed with added nutrient and by removing excess spheroids to ensure a steady supply of nutrient to each spheroid. Third, multiple spheroids of varying sizes were in each flask. Freyer observes that the only parameter of the spheroids that he measured which was positively correlated with saturation size was the thickness of the viable cell rim. From the point of view of our models, this is the statement that the equilibrium values of P and total spheroid size at equilibrium were positively correlated. We show one scenario that results in the correlation observed by Freyer.

Freyer proposes that the variation in final size could be the result of variation in parameters associated to cell growth or decay. We can model this as a variation in the growth parameter a .



In **Figures 4A,B** we compare three runs of revised model 3E at $a = 0.04, 0.02, 0.01$ respectively. The figure shows that the equilibrium values of both the spheroid size and the size of the proliferating pool are positively correlated. Further, one can compare the equilibrium values of the proliferating pool with the equilibrium values of the spheroid size raised to the $2/3$ power, which correlates with surface area of the tumor. This ratio increases with tumor size in the example shown, indicating a thicker rim of proliferating cells in larger tumors, as observed in experiment. For the runs pictured, the ratios are 0.11, 0.096, and 0.067 respectively from the largest to the smallest spheroid. We can also deduce this result from equation (6) for the equilibrium values. The parameter a scales the constant u in that equation, lowering the graph of the quartic and raising the value of the positive root. However, Freyer also reports that the basic growth rates of the cell lines (either in spheroids or monoculture) did not correlate with final spheroid size. However, there could be an interplay of parameters at work to mask such a correlation. Altering other parameters may give a similar result. The model offered here at least shows the possibility of a positive correlation between final size and thickness of the proliferating cell layer.

A second observation of Freyer is that spheroid equilibrium size is correlated with the size of the spheroid at the onset of necrosis. His paper shows data in which the spheroid size at the onset of necrosis is estimated from data and the eventual spheroid size is inferred by fitting data to a Gompertz curve. This observation is thus more of an expectation based on models than an actual pair of measurements. Nonetheless, we ask whether Model 3E in this paper can support this expectation. In continuous models such as this one, there is an instantaneous start of necrosis, although the quantity may be quite small. If one spheroid exhibits the start of necrosis at a larger size than another, it could be due to different rates of transition from the quiescent to the necrotic pool, described by parameter e in our model. The moment at which necrosis becomes visible in the spheroid would be earlier for the model with the higher value of e . In **Figure 5**, we see the growth of two versions of Model 3E with different values of the parameter e .

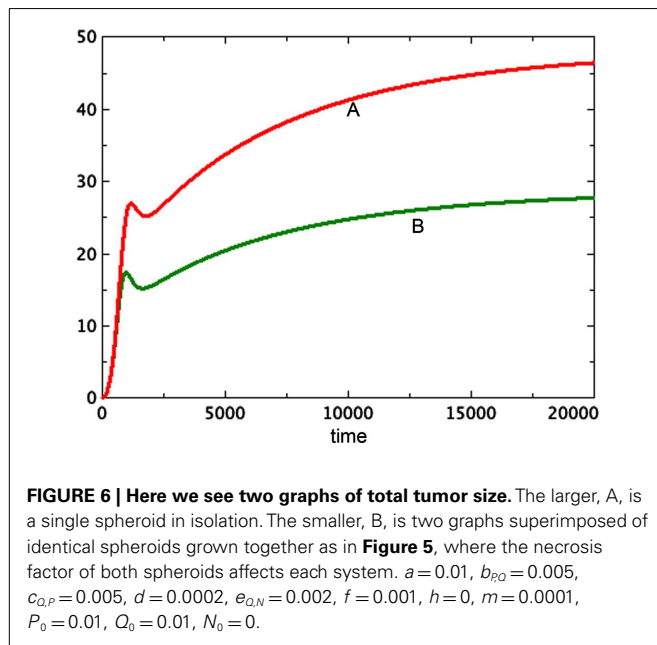
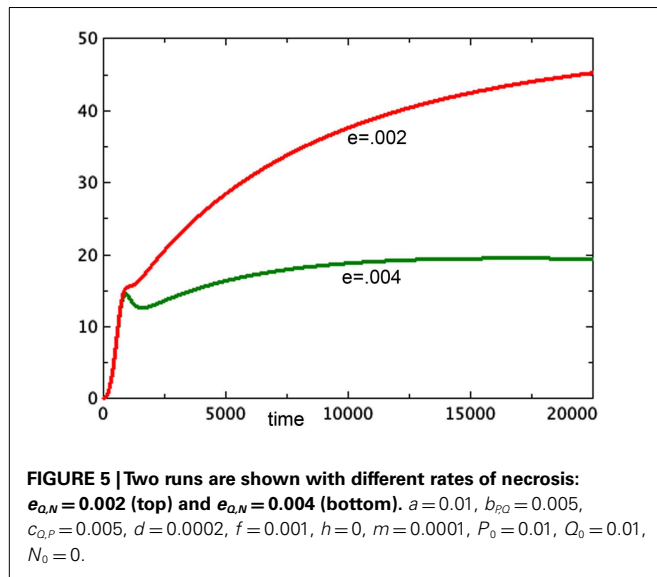


This difference does indeed produce spheroids of different sizes. The spheroid that has the higher rate of necrosis is the smaller one, consistent with Freyer's observations.

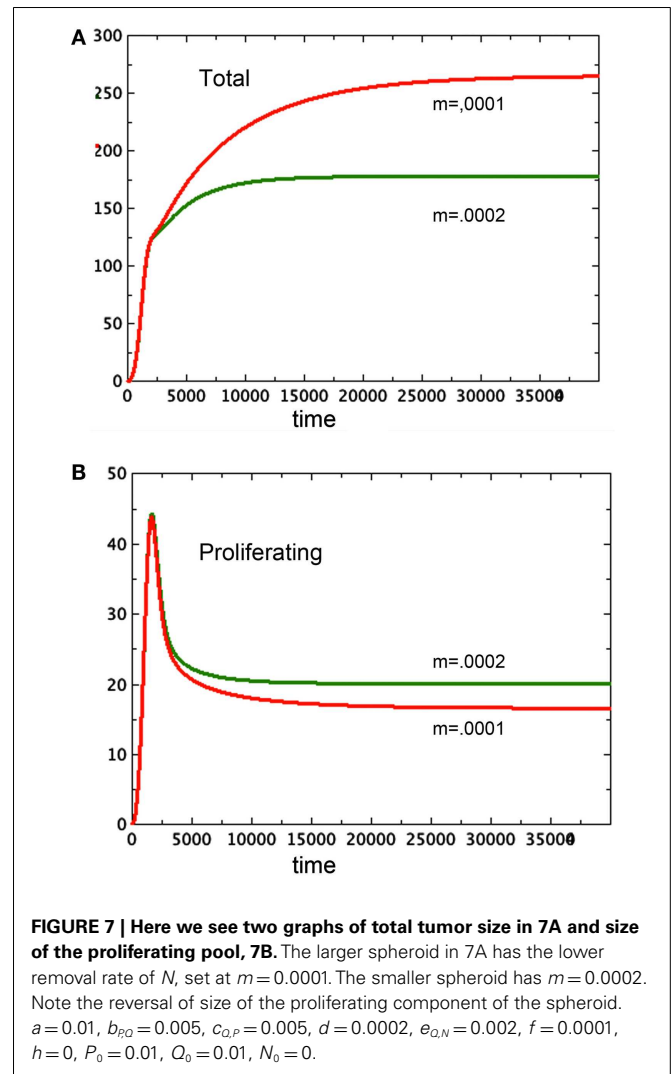
The possibility that tumor necrosis factor affects not only the spheroid producing it, but also others in the same flask, also helps explain the observation (Folkman and Hochberg, 1973) that the average size of spheroids in a flask was inversely proportional to the number of spheroids in the flask. In **Figure 6** we see the comparison of two systems: one represents a system with two identical spheroids. However, the necrosis factor used was the sum of the necrosis of both spheroids. That is, both spheroids suffer the effect of all of the toxin in the combined system. These two grow identically and reach a terminal size of approximately 27 units at $t = 20,000$. A third spheroid is grown in isolation, with the same initial conditions. It gets much larger, reaching about 45 units at $t = 20,000$. Thus neighboring spheroids limit each others' growth, creating the result observed by Folkman and Hochberg (1973).

4. DISCUSSION

We have shown that a simple model with compartments representing proliferating, quiescent and necrotic cells, can explain a



variety of observations on the growth and development of tumor spheroids *in vitro*. The successful model includes a growth term proportional to surface area, and a death term for proliferating cells that depends on the amount of tumor necrosis present. It also includes linear transitions between the proliferating and quiescent pools, and between the quiescent and necrotic pools. It includes a linear term for dissolution of necrotic cells as well. With these few ingredients we have a system that produces spheroids that eventually develop three layers of proliferating, quiescent and necrotic cells. Growth of these spheroids eventually stops. When the growth stops, there remains a thin layer of actively proliferating cells at the boundary. Under some assumptions about what might create spheroids of different sizes, we see that the final size of the spheroids is correlated with thickness of the proliferating shell.



Under the assumption of differing rates of necrosis we see spheroids of different terminal sizes, corresponding to a later appearance of visible necrosis. Under the hypothesis that multiple spheroids in the same flask share tumor necrosis factor with each other, we have a model in which the more spheroids are in a flask, the smaller the average size when growth ends. In short, the model we have selected fits a variety of qualitative observations about tumor spheroid growth.

Although more complex than the Gompertz model, the model presented here is not so complex that it becomes computationally unfeasible to match it to the development of a given tumor spheroid. It would be useful to modelers to have some data sets that track P , Q , and N over time for several cell lines. A model such as the one presented here will only be of practical use if it is tuned to a specific type of cell. The potential then exists for building more realistic models of *in vivo* tumors that are based on parameters solidly gained from the simpler *in vitro* spheroid.

Tumor spheroids are supposed to be a reasonable proxy for tumors *in vivo* before the onset of angiogenesis. However, existing models of angiogenesis do not take tumor necrosis factor

into account, even though it affects the growth of the proliferating cells. Using a model such as the one developed here as the basis for a more complex one that includes angiogenesis has the potential to illuminate one function of circulation currently left out of these models: the ability of blood flow to remove toxins. **Figure 7** elucidates this observation. Here we see two spheroid models that are identical except for one small change: N , along with the toxin it represents, is being removed from one of them at a steady rate of $0.0001N$ in one of them and $0.0002N$ in the other. The spheroid with the greater clearance rate of necrosis has a smaller total size, but it has a greater quantity of proliferating tissue. This observation adds to the complexity of angiogenesis.

One purpose of this study is eventually to develop a simple model incorporating both necrosis and angiogenesis. With data on the time development of both plate and spheroid cultures of a given cell type one, could easily find best fit parameters for model 3E as well as a few of the others. A model that is a good approximation of spheroid behavior may be extended by coupling it with a simple model of angiogenesis, as in Hahnfeldt et al. (1999), Komorova and Mironov (2005), or with a version of a more complex model as in Stamper et al. (2007) that has been reduced via a sensitivity analysis (as in Wallace and Winsor, 2012) to a simpler situation. One would do this by extending the spheroid model in two ways. First, the growth term would be replaced by an expression approximating contact area between proliferating cells and nutrient supply. Second, the clearance of necrosis factor would

become a function of contact between necrotic tissue and blood supply. Numerous papers have explored the nature of the contact regions between tumor and nutrient through the development of the geometry of both tumor and vasculature (as in Sansone et al., 2001), competition among cell types (as in Scalerandi et al., 2001), and other features. A simple model, however, might approximate the situation through mutual dependence of blood supply, volumes of the three quantities discussed here, and a fixed or evolving fractal dimension of contact. A model with few parameters may then be fitted to data sets for various cell lines to give a crude characterization of growth properties for cell types that goes beyond the basic growth rate determined from plate culture.

Hirschhaeuser et al. (2010) survey the uses of *in vitro* spheroids to study the interaction of tumors with their microenvironment, including various therapies. They point out the potential role of spheroids in selecting the most promising interventions at an early, and less expensive, stage of research. Mathematical models of spheroids that extend the simple model presented in this paper to include therapies or other interactions would be useful for selecting optimal delivery protocols to be tested *in vivo* as therapeutic interventions. Models *in silico* allow quick exploration of the result of variations in timing and dosage of therapies. Studies of cancer therapies *in vivo* could be doubly informed by *in vitro* spheroid studies that suggest which therapies work and why, combined with *in silico* models suggesting best strategies for delivery.

REFERENCES

- Adam, J. A. (1986). A simplified mathematical model of tumor growth. *Math. Biosci.* 81, 229–244.
- Adam, J. A. (1987a). A mathematical model of tumor growth 2. Effects of geometry and spatial nonuniformity on stability. *Math. Biosci.* 86, 183–211.
- Adam, J. A. (1987b). A mathematical model of tumor growth 3. Comparison with experiment. *Math. Biosci.* 86, 213–227.
- Bauer, K. D., Keng, P. C., and Sutherland, R. M. (1982). Isolation of quiescent cells from multicellular tumor spheroids using centrifugal elutriation. *Cancer Res.* 42, 72–78.
- Demidenko, E. (2006). The assessment of tumour response to treatment. *Appl. Stat.* 55, 365–377.
- Folkman, J., and Hochberg, M. (1973). Self-regulation of growth in three dimensions. *J. Exp. Med.* 138, 745–753.
- Freyer, J. P. (1988). Role of necrosis in regulating the growth saturation of multicellular spheroids. *Cancer Res.* 48, 2432–2439.
- Frieboes, H. B., Zheng, X., Sun, C.-H., Tromberg, B., Gatenby, R., and Cristini, V. (2006). An integrated computational/experimental model of tumor invasion. *Cancer Res.* 66, 1597–1604.
- Greenspan, H. P. (1972). Models for growth of a solid tumor by diffusion. *Stud. Appl. Math.* 51, 317–340.
- Gyllenberg, M., and Webb, G. F. (1990). A nonlinear structured population model of tumor growth with quiescence. *J. Math. Biol.* 28, 671–694.
- Hahnfeldt, P., Panigrahy, D., Folkman, J., and Hlatky, L. (1999). Tumor development under angiogenic signaling: a dynamical theory of tumor growth, treatment response, and postvascular dormancy. *Cancer Res.* 59, 4770–4775.
- Hirschhaeuser, F., Menneb, H., Dittfeld, C., West, J., Mueller-Klieser, W., and Kunz-Schughart, L. A. (2010). Multicellular tumor spheroids: an underestimated tool is catching up again. *J. Biotechnol.* 148, 315.
- Jiang, Y., Pjesivac-Grbovic, J., Cantrell, C., and Freyer, J. P. (2005). A multiscale model for avascular tumor growth. *Biophys. J.* 89, 3884–3894.
- Kallman, R. F., Combs, C. A., Franko, A. J., Furlong, B. M., Kelley, S. D., Kemper, H. L., et al. (1982). "Evidence for the recruitment of noncycling clonogenic tumor cells," in *Radiation Biology in Cancer Research, Proceedings of the 32nd Annual Symposium on Fundamental Cancer Research*, M. D. Anderson Hospital and Tumor Institute, eds H. R. Withers and R. Meyn (New York: Raven Press) 397–414.
- Komorova, N. L., and Mironov, V. (2005). On the role of endothelial progenitor cells in tumor neovascularization. *J. Theor. Biol.* 235, 338–349.
- Landry, J., Freyer, J. P., and Sutherland, R. M. (1982). A model for the growth of multicellular spheroids. *Cell Tissue Kinet.* 15, 585–594.
- Maggelakis, S. A., and Adam, J. A. (1990). Mathematical model of prevascular growth of a spherical carcinoma. *Math. Comput. Model.* 13, 23–28.
- Marusic, M., Bajzert, Z., Freyer, J. P., and Vuk-Pavlovic, S. (1994). Analysis of growth of multicellular tumour spheroids by mathematical models. *Cell Prolif.* 21, 13–94.
- McElwain, D. L. S. (1978). Re-examination of oxygen diffusion in a spherical cell with Michaelis-Menten oxygen uptake kinetics. *J. Theor. Biol.* 71, 255–263.
- McElwain, D. L. S., and Morris, L. E. (1978). Apoptosis as a volume loss mechanism in mathematical models of solid tumor growth. *Math. Biosci.* 39, 147–157.
- McElwain, D. L. S., and Ponzo, P. J. (1977). Model for growth of a solid tumor with nonuniform oxygen-consumption. *Math. Biosci.* 35, 267–279.
- Menchon, S. A., and Condat, C. A. (2008). Cancer growth: predictions of a realistic model. *Phys. Rev. E Stat. Nonlin. Soft Matter Phys.* 78, 022901.
- Menchon, S. A., and Condat, C. A. (2009). Modeling tumor cell shedding. *Eur. Biophys. J.* 38, 479–485.
- Piantadosi, S. (1985). A model of growth with first-order birth and death rates. *Comput. Biomed. Res.* 18, 220–232.
- Potmesil, M., and Goldfeder, A. (1980). Cell kinetics of irradiated experimental tumors: cell transition from the nonproliferating to the proliferating pool. *Cell Tissue Kinet.* 15, 563–570.
- Preisler, H., Walczak, I., Renick, J., and Rustum, Y. M. (1977). Separation of leukemic cells into proliferative and quiescent subpopulations by centrifugal elutriation. *Cancer Res.* 37, 3876–3880.
- Sansone, B. C., Scalerandi, M., and Condat, C. A. (2001). Emergence of taxis and synergy in angiogenesis. *Phys. Rev. Lett.* 87, 128102.
- Santini, M. T., Rainaldi, G., and Indovina, P. L. (2000). Apoptosis, cell adhesion and the extracellular matrix in the three-dimensional growth of multicellular tumor spheroids. *Crit. Rev. Oncol. Hematol.* 36, 75–87.

- Scalerandi, M., Sansone, B. C., and Condat, C. A. (2001). Diffusion with evolving sources and competing sinks: development of angiogenesis. *Phys. Rev. E Stat. Nonlin. Soft Matter Phys.* 65, 011902.
- Sherar, M. D., Noss, N. B., and Foster, F. S. (1987). Ultrasound backscatter microscopy images the internal structure of living tumour spheroids. *Nature* 330, 493–495.
- Stamper, I. J., Byrne, H. M., Owen, M. R., and Maini, P. K. (2007). Modelling the role of angiogenesis and vasculogenesis in solid tumour growth. *Bull. Math. Biol.* 69, 2737–2772.
- Stein, A. M., Demuth, T., Mobley, D., Berens, M., and Sander, L. M. (2007). A mathematical model of glioblastoma tumor spheroid invasion in a three-dimensional in vitro experiment. *Biophys. J.* 92, 356–365.
- Venkatasubramanian, R., Henson, M. A., and Forbes, N. S. (2006). Incorporating energy metabolism into a growth model of multicellular tumor spheroids. *J. Theor. Biol.* 242, 440–453.
- Wallace, D. I., and Winsor, P. (2012). “Sensitive dependence on the threshold for TAF signaling in solid tumors,” in *Proceedings of International Symposium on Mathematical and Computational Biology, BIOMAT 2011*, ed. R. Mondaini (Singapore: World Scientific Publishing), 264–278.
- Conflict of Interest Statement:** The authors declare that the research was conducted in the absence of any commercial or financial relationships that could be construed as a potential conflict of interest.
- Received: 04 October 2012; accepted: 27 February 2013; published online: 15 March 2013.*
- Citation: Wallace DI and Guo X (2013) Properties of tumor spheroid growth exhibited by simple mathematical models. Front. Oncol. 3:51. doi: 10.3389/fonc.2013.00051*
- This article was submitted to Frontiers in Molecular and Cellular Oncology, a specialty of Frontiers in Oncology. Copyright © 2013 Wallace and Guo. This is an open-access article distributed under the terms of the Creative Commons Attribution License, which permits use, distribution and reproduction in other forums, provided the original authors and source are credited and subject to any copyright notices concerning any third-party graphics etc.*



The need for integrative computational oncology: an illustrated example through MMP-mediated tissue degradation

Shannon M. Mumenthaler¹, Gianluca D'Antonio², Luigi Preziosi² and Paul Macklin^{1,3*}

¹ Center for Applied Molecular Medicine, Keck School of Medicine, University of Southern California, Los Angeles, CA, USA

² Dipartimento di Scienze Matematiche, Politecnico di Torino, Torino, Italia

³ Department of Biomedical Engineering, Viterbi School of Engineering, University of Southern California, Los Angeles, CA, USA

Edited by:

Katarzyna Anna Rejniak, H. Lee
Moffitt Cancer Center & Research
Institute, USA

Reviewed by:

Agnès Noël, University of Liege,
Belgium
Georgios Lolas, National Technical
University of Athens, Greece

*Correspondence:

Paul Macklin, Center for Applied
Molecular Medicine, Keck School of
Medicine, University of Southern
California, 2250 Alcazar Street, Suite
242, Los Angeles, CA 90033, USA
e-mail: paul.macklin@usc.edu

Physical oncology is a growing force in cancer research, and it is enhanced by integrative computational oncology: the fusion of novel experiments with mathematical and computational modeling. Computational models must be assessed with accurate numerical methods on correctly scaled tissues to avoid numerical artifacts that can cloud analysis. Simulation-driven analyses can only be validated by careful experiments. In this perspectives piece, we evaluate a current, widespread model of matrix metalloproteinase-driven tissue degradation during cancer invasion to illustrate that integrative computational oncology may not realize its fullest potential if either of these critical steps is neglected.

Keywords: matrix metalloproteinase, tissue degradation, integrative modeling, cancer, computational oncology

INTRODUCTION

Physical oncology – the study of the physical biology of cancer, the development of new physical measurement platforms, and the use of mathematical and computational modeling to understand complex cancer systems – has emerged as an important force in cancer research (1). Key to this approach is integrative computational oncology: multidisciplinary teams of biologists, oncologists, physicists, engineers, and mathematicians working together to generate novel platforms, where modeling informs experiments, and experiments drive modeling. Mathematical modeling can describe and simplify complex systems, facilitating analysis. Accurate simulations assist the analysis of these systems, yielding observations that drive biological hypotheses. Experimental biology is necessary for validating and refining these hypotheses and advancing our understanding of cancer. This special issue discusses successful examples of applying integrative modeling to cancer-related questions. However, neglecting any of these key ingredients can be detrimental and may blind teams to subtle modeling flaws, potentially resulting in misleading model assessment, incorrect biological conclusions, or unverifiable predictions.

In this perspectives piece, we will look at a widely used mathematical model of tissue degradation by matrix metalloproteinases (MMPs) in order to illustrate (1) the need for evaluation of mathematical models by proper numerical techniques, applied to biologically relevant space and time scales, and (2) that even with proper numerical analysis, only experiments can truly validate mathematical model predictions and help choose among plausible explanations of model findings.

MMP-MEDIATED TISSUE DEGRADATION

Progression from *in situ* carcinoma – where growth is constrained to a local site by a fully intact basement membrane (BM) – to invasive carcinoma requires disruption of the BM and penetration into the surrounding stroma. Once in the stroma, invading cancer cells often degrade and remodel the extracellular matrix (ECM) and later break through BM to enter blood vessels – a key step in metastasis. A quantitative understanding of proteolytic degradation of tissue is necessary in predicting (and disrupting!) cancer invasion and metastasis. It is currently unclear whether tissue degradation is primarily due to MMPs secreted by cancer cells or by stromal cells in response to tumor signaling. Quantitative modeling could help narrow down the possibilities to the most plausible models of stromal invasion, which can then be experimentally tested and validated.

Extracellular matrix is a 3-D cross-linked network of proteins and polysaccharides that provides structural support to cells; BM is a specialized form of ECM, although thinner (50–100 nm) and more dense (2, 3). ECM (including BM) can be degraded by MMPs secreted by tumor, stromal, and immune cells (4–6). MMPs are secreted in an inactive form that must be cleaved into an active form, and are further regulated by inhibitors of metalloproteinases. MMPs may be soluble and diffuse through tissue (e.g., MMP9), or membrane-bound (e.g., MT-MMP1) (6).

The most widely used tissue degradation models focus on soluble MMPs using reaction-diffusion equations [e.g., (7–9)], neglect inhibitors and promoters, and assume the MMP is immediately active. If E is the ECM density (or volume fraction) and M is the

MMP concentration (both dimensionless), then

$$\frac{\partial M}{\partial t} = \nabla \cdot (D \nabla M) + s(\mathbf{X}, t) - r_M E M - d_M M \quad (1)$$

$$\frac{\partial E}{\partial t} = -r_E E M. \quad (2)$$

D is the diffusion constant, s is the source (tumor or other cells), r_M and r_E are reaction rates, and d_M is the MMP decay rate. These standard reaction-diffusion equations are typically solved with finite differences on a Cartesian mesh [e.g., (7–9)]. The most clinically oriented BM degradation model we know of simulated BM as denser ECM on the same ECM computational mesh (10).

FUNCTIONAL FORMS AND PARAMETER VALUES

For this discussion, we assume $D = D_0 (1 - E)$ for a constant D_0 . We set $D_0 = 8 \times 10^{-9} \text{ cm}^2/\text{s}$ (11), $r_M = r_E = 1/200 \text{ s}^{-1}$ (11), and $d_M = 5 \times 10^{-5} \text{ s}^{-1}$ (12). This gives an (ECM-dependent) reaction-diffusion length scale L of $\sqrt{D_0(1-E)/(r_M E + d_M)} \sim 10 \mu\text{m}$ (“ \sim ” denotes “on the order of”) for $0 \leq E \leq 0.90$. This matches our biophysical expectations: MMPs are relatively large macromolecules diffusing through a tortuous ECM structure, so the length scale should be significantly smaller than for oxygen (typically $\sim 100 \mu\text{m}$). We initially set the $E = 0.85$.

MODEL EVALUATION REQUIRES GOOD NUMERICAL TECHNIQUES

Accurate numerical solution (and hence proper evaluation) of the model and its $\sim 10 \mu\text{m}$ length scale requires an $\sim 1 \mu\text{m}$ mesh size. To date, most published work has used small diffusion constants on relatively large 10–20 μm meshes [e.g., (7, 8)]. We solve Eqs 1 and 2 on a 1 μm mesh with standard centered finite differences, using the ghost fluid method to implement boundary conditions wherever the computational stencil intersects the BM (zero flux, or Neumann condition) or a cell boundary (constant, or Dirichlet condition for secreting cells; Neumann condition for non-secreting cells) (13–15). We describe the BM position as in D’Antonio et al. (16). Tumor cell sizes are set to the values in Macklin et al. (17).

CURRENT MODELS PREDICT RAPID “TUNNELING” THROUGH ECM

We simulated MMP secretion by stromal cells, as one might expect in response to tumor-secreted pro-inflammatory signals. To simplify the analysis, we set $M = 1$ on the stromal cells and positioned them at a fixed 10 μm from the BM (Figure 1: top left).

In the simulations, MMPs etch out a “hole” in the ECM whose edge expands outward at $\sim 1 \mu\text{m}$ per minute. See Figure 1 for the ECM distribution at 15, 25, and 40 min. This is consistent with an order of magnitude estimate using a Fisher–Kolmogorov-type traveling wave front speed:

$$v = 2L(E) r_M(E) \sim 2\sqrt{D_0(1-E)Er_M}$$

gives speeds of $0\text{--}3.75 \mu\text{m}/\text{min} \sim 1 \mu\text{m}/\text{min}$ for $0 \leq E \leq 0.90$, where $L(E)$ is as above and $r_M(E) = r_M E$.

A 1 $\mu\text{m}/\text{min}$ expansion rate of the degraded region is comparable to experimentally measured motile tumor cell velocities [e.g., $58.56 \pm 1.62 \mu\text{m}/\text{h}$ for neuN cells in (7)]. The predicted expansion

speed is quantitatively consistent with localized ECM degradation “keeping pace” with motile cells as they “tunnel” through the ECM. The simple ECM-MMP model (with sufficient numerical resolution) can produce biologically reasonable results on small time and spatial scales.

However, if extrapolated over long times, this model predicts that a 10 cm diameter of tissue could be degraded in about a month! This outpaces typical tumor expansion rates by over an order of magnitude: brain tumors (among the fastest growing tumors) typically expand at 80–100 $\mu\text{m}/\text{day}$ (18), requiring at least 500 days to infiltrate a 10 cm tissue. The simple MMP model would therefore predict an ever-widening gap between the advancing tumor front and the edge of the degraded tissue, contradicting typical observations that MMP activity is localized near the boundary of an advancing tumor.

This widely used model, once simulated accurately, does not adequately describe MMP-mediated tissue degradation around growing tumors. Neglected factors (e.g., activators and inhibitors) may be needed to confine proteolytic activity near tumor boundaries; similar approaches have been used to model urokinase-type plasminogen activators in tissue degradation (19). Alternatively, non-diffusing membrane-bound MMPs may be more relevant. New imaging technologies that dynamically capture ECM degradation could help select among possible alternative models (20, 21). Recent integrative experimental-computational work showed the critical role of MT-MMP activity during cancer cell invasion, finding that MT1-MMP turnover could be a potent anti-invasion therapeutic target (22). Ultimately, only carefully planned and executed experiments can help choose between these and other possible explanations.

ASSESSING DEGRADATION OF THE BASEMENT MEMBRANE

A 100 nm BM cannot be properly resolved on a 1 μm mesh. Solving (1)–(2) by finite differences (with correct physical dimensions) requires a prohibitive 10 nm computational mesh. Some have investigated this problem by solving on non-physiological basement membranes [e.g., one cellular automaton mesh point, or 10 μm thick (10)], making it difficult to evaluate the models.

Let us instead analyze a simplified problem to estimate the time scale to degrade a BM. Consider a small piece of BM of cross-sectional area A , volume fraction F , and thickness $T(t)$. The total amount of matrix $E(t)$ in the BM section is $AF T(t)$. If BM is degraded as in (2), then $dE/dt = -r_E M(t) E(t)$. If M is constant, then the time t_B required to degrade the BM to some threshold breaking amount E_B is given by

$$t_B = -1n(E(0)/E_B)/r_B M.$$

If $r_E = 1/200 \text{ s}^{-1}$ and $M = 1$, then a 100 nm section of BM is reduced to 10 nm thick [$E_B/E(0) = 0.1$] in under 8 min, and to 1 nm thick ($E_B/E(0) = 0.01$) in about 15 min.

This suggests several possibilities. (1) The cell “decision” of when to secrete MMPs is the limiting factor to penetrating the BM, rather than the proteolytic process itself. (2) Additional, non-modeled promoters/inhibitors are rate limiting. Only follow-up experiments can help determine the most plausible explanation, but rapid penetration of the BM by “willing” cells seems consistent with Boyden transwell migration assays (23) and known rapid

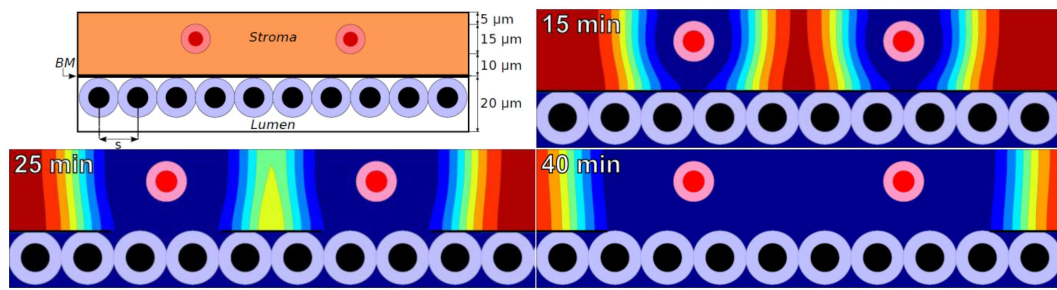


FIGURE 1 | Top left: initial configuration of epithelium (white lumen and tumor cells), a 100 nm basement membrane, stroma (orange), and stromal cells (red) that secrete MMPs. **Remaining plots:** ECM volume fraction [ranging from

blue (0%) to red (85%)] at 15, 25, and 40 min using a widespread ECM-MMP model with a biophysically reasonable reaction-diffusion length scale ($\sim 10 \mu\text{m}$) and degradation rate ($\sim 0.1\text{--}1 \text{ min}^{-1}$).

(\sim minutes) transmigration of leukocytes through endothelial and epithelial layers and associated membranes (24, 25).

CLOSING THOUGHTS

Accurate models are needed to simplify, analyze, and assess complex phenomena observed in cancer biology. In order to truly assess a model's underlying assumptions, evaluate its predictive value, and study its potential clinical utility, one must use proper numerical methods, reasonable geometries, and experimental validation. As illustrated by the tissue degradation model above, neglecting any of these key factors can lead to inaccurate dynamics, and may potentially cause a team to prematurely accept biological hypotheses. Dynamic feedback between experimental and computational biology systems is necessary to

drive and improve model development and refinement while ensuring that any resulting integrative platform is clinically relevant.

ACKNOWLEDGMENTS

Paul Macklin and Shannon M. Mumenthaler thank the USC Center for Applied Molecular Medicine for generous computational resources, and the National Institutes of Health for the Physical Sciences Oncology Center grant 5U54CA143907 for Multiscale Complex Systems Transdisciplinary Analysis of Response to Therapy (MC-START). Paul Macklin thanks the USC James H. Zumberge Research and Innovation Fund (2012 Large Interdisciplinary Award) for support via the Consortium for Integrative Computational Oncology.

REFERENCES

- Agus DB, Michor F. The sciences converge to fight cancer. *Nat Phys* (2012) **8**:773–4. doi:10.1038/nphys2464
- Leblond CP, Inoue S. Structure, composition, and assembly of basement membrane. *Am J Anat* (1989) **185**:367–90. doi:10.1002/aja.1001850403
- Liddington RC. Mapping out the basement membrane. *Nat Struct Mol Biol* (2001) **8**:573–4. doi:10.1038/89590
- Coussens LM, Werb Z. Matrix metalloproteinases and the development of cancer. *Chem Biol* (1996) **3**:895–904. doi:10.1016/S1074-5521(96)90178-7
- Egeblad M, Werb Z. New functions for the matrix metalloproteinases in cancer progression. *Nat Rev Cancer* (2002) **2**:161–74. doi:10.1038/nrc745
- Kessenbrock K, Plaks V, Werb Z. Matrix metalloproteinases: regulators of the tumor microenvironment. *Cell* (2010) **141**:52–67. doi:10.1016/j.cell.2010.03.015
- Anderson AR, Hassanein M, Branch KM, Lu J, Lobdell NA, Maier J, et al. Microenvironmental independence associated with tumor progression. *Cancer Res* (2009) **69**:8797–806. doi:10.1158/0008-5472.CAN-09-0437
- Macklin P, McDougall SR, Anderson ARA, Chaplain MAJ, Cristini V, Lowengrub JS. Multiscale modelling and nonlinear simulation of vascular tumour growth. *J Math Biol* (2009) **58**:765–98. doi:10.1007/s00285-008-0216-9
- Martin NK, Gaffney EA, Gatenby RA, Maini PK. Tumour-stromal interactions in acid-mediated invasion: a mathematical model. *J Theor Biol* (2010) **267**:461–70. doi:10.1016/j.jtbi.2010.08.028
- Basanta D, Strand DW, Lukner RB, Franco OE, Cliffl DE, Ayala GE, et al. The role of transforming growth factor-beta-mediated tumor-stroma interactions in prostate cancer progression: an integrative approach. *Cancer Res* (2009) **69**:7111–20. doi:10.1158/0008-5472.CAN-08-3957
- Saffarian S, Collier IE, Marmer BL, Elson EL, Goldberg G. Interstitial collagenase is a Brownian ratchet driven by proteolysis of collagen. *Science* (2004) **306**:108–11. doi:10.1126/science.1099179
- Kim Y, Friedman A. Interaction of tumor with its micro-environment: a mathematical model. *Bull Math Biol* (2010) **72**:1029–68. doi:10.1007/s11538-009-9481-z
- Macklin P, Lowengrub JS. Evolving interfaces via gradients of geometry-dependent interior Poisson problems: application to tumor growth. *J Comput Phys* (2005) **203**:191–220. doi:10.1016/j.jcp.2004.08.010
- Macklin P, Lowengrub JS. Nonlinear simulation of the effect of microenvironment on tumor growth. *J Theor Biol* (2007) **245**:677–704. doi:10.1016/j.jtbi.2006.12.004
- Macklin P, Lowengrub JS. A new ghost cell/level set method for moving boundary problems: application to tumor growth. *J Sci Comput* (2008) **35**:266–99. doi:10.1007/s10915-008-9190-z
- D'Antonio G, Macklin P, Preziosi L. An agent-based model for elasto-plastic mechanical interactions between cells, basement membrane and extracellular matrix. *Math Biosci Eng* (2013) **10**:75–101. doi:10.3934/mbe.2013.10.75
- Macklin P, Edgerton ME, Thompson AM, Cristini V. Patient-calibrated agent-based modelling of ductal carcinoma in situ (DCIS): from microscopic measurements to macroscopic predictions of clinical progression. *J Theor Biol* (2012) **301**:122–40. doi:10.1016/j.jtbi.2012.02.002
- Massey SC, Assanah MC, Lopez KA, Canoll P, Swanson KR. Glial progenitor cell recruitment drives aggressive glioma growth: mathematical and experimental modelling. *J R Soc Interface* (2012) **9**:1757–66. doi:10.1098/rsif.2012.0030
- Chaplain MAJ, Lolas G. Mathematical modelling of cancer cell invasion of tissue: the role of the urokinase plasminogen activation system. *Math Models Methods Appl Sci* (2005) **15**:1685–734. doi:10.1142/S0218202505000947
- Littlepage LE, Sternlicht MD, Rougier N, Phillips J, Gallo E, Yu Y, et al. Matrix metalloproteinases contribute distinct roles in neuroendocrine prostate carcinogenesis, metastasis, and angiogenesis progression. *Cancer Res* (2010) **70**:2224–34. doi:10.1158/0008-5472.CAN-09-3515

21. Scherer RL, VanSaun MN, McIntyre JO, Matrisian LM. Optical imaging of matrix metalloproteinase-7 activity in vivo using a proteolytic nanobeacon. *Mol Imaging* (2008) 7:118–31.
22. Hoshino D, Koshikawa N, Suzuki T, Quaranta V, Weaver AM, Seiki M, et al. Establishment and validation of computational model for MT1-MMP dependent ECM degradation and intervention strategies. *PLoS Comput Biol* (2012) 8:e1002479. doi:10.1371/journal.pcbi.1002479
23. Albini A, Iwamoto Y, Kleinman HK, Martin GR, Aaronson SA, Kozlowski JM, et al. A rapid in vitro assay for quantitating the invasive potential of tumor cells. *Cancer Res* (1987) 47:3239–45.
24. Ginzberg HH, Cherapanov V, Dong Q, Cantin A, McCulloch CA, Shannon PT, et al. Neutrophil-mediated epithelial injury during transmigration: role of elastase. *Am J Physiol Gastrointest Liver Physiol* (2001) 281:G705–17.
25. Shaw SK, Bamba PS, Perkins BN, Luscinskas FW. Real-time imaging of vascular endothelial-cadherin during leukocyte transmigration across endothelium. *J Immunol* (2001) 167:2323–30.

Conflict of Interest Statement: The authors declare that the research was conducted in the absence of any commercial or financial relationships that could be construed as a potential conflict of interest.

Received: 15 February 2013; accepted: 11 July 2013; published online: 26 July 2013.
Citation: Mumenthaler SM, D'Antonio G, Preziosi L and Macklin P (2013) The need for integrative computational oncology: an illustrated example

through MMP-mediated tissue degradation. *Front. Oncol.* 3:194. doi: 10.3389/fonc.2013.00194
This article was submitted to *Frontiers in Molecular and Cellular Oncology*, a specialty of *Frontiers in Oncology*. Copyright © 2013 Mumenthaler, D'Antonio, Preziosi and Macklin. This is an open-access article distributed under the terms of the Creative Commons Attribution License, which permits use, distribution and reproduction in other forums, provided the original authors and source are credited and subject to any copyright notices concerning any third-party graphics etc.



Stem cell control, oscillations, and tissue regeneration in spatial and non-spatial models

Ignacio A. Rodriguez-Brenes^{1*}, Dominik Wodarz^{1,2} and Natalia L. Komarova¹

¹ Department of Mathematics, University of California Irvine, Irvine, CA, USA

² Department of Ecology and Evolutionary Biology, University of California Irvine, Irvine, CA, USA

Edited by:

Heiko Enderling, Tufts University
School of Medicine, USA

Reviewed by:

Anna Marciniak-Czochra, University of
Heidelberg, Germany
Trachette Jackson, University of
Michigan, USA

*Correspondence:

Ignacio A. Rodriguez-Brenes,
Department of Mathematics,
University of California, 265 Steinhaus
Hall, Irvine, CA 9269, USA.
e-mail: iarodrig@uci.edu

Normal human tissue is organized into cell lineages, in which the highly differentiated mature cells that perform tissue functions are the end product of an orderly tissue-specific sequence of divisions that start with stem cells or progenitor cells. Tissue homeostasis and effective regeneration after injuries requires tight regulation of these cell lineages and feedback loops play a fundamental role in this regard. In particular, signals secreted from differentiated cells that inhibit stem cell division and stem cell self-renewal are important in establishing control. In this article we study in detail the cell dynamics that arise from this control mechanism. These dynamics are fundamental to our understanding of cancer, given that tumor initiation requires an escape from tissue regulation. Knowledge on the processes of cellular control can provide insights into the pathways that lead to deregulation and consequently cancer development.

Keywords: tissue regeneration, cell lineage control, tissue stability, mathematical models, cancer

INTRODUCTION

There is growing evidence that a subset of cancer cells possesses characteristics typically associated with stem cells (Reya et al., 2001; Wang et al., 2010). These so called cancer stem cells share with normal stem cells the capability to give rise to all cell types of a given lineage (Bonnet and Dick, 1997; Passegué et al., 2003). Like normal stem cells, they also have a large proliferative potential being the only cancer cells capable of repopulating a tumor and initiating metastasis (Al-Hajj et al., 2003; Clevers, 2011). In light of these findings it is crucial to understand how stem cells are regulated as part of a cell lineage in normal tissue.

In normal tissues, cell lineages are highly regulated to promote the rapid regeneration after an injury and to maintain tissue homeostasis under normal conditions. In particular when it comes to the regulation of stem cells two types of feedbacks have been proposed: long-range and short-range (Arino and Kimmel, 1986). The long-range feedbacks should respond to the loss of mature cells during an injury, while the short-range feedbacks would act in an autocrine fashion in stem cells (Andersen and Mackey, 2001; Bernard et al., 2003). In this article we focus on long-range feedback acting through signals emitted by differentiated cells that inhibit stem cell division and self-replication. This type of regulation has been biologically observed in numerous tissues including muscle, liver, bone, and the nervous and hematopoietic systems (McPherron et al., 1997; Daluiski et al., 2001; Yamasaki et al., 2003; Elgjo and Reichelt, 2004; Tzeng et al., 2011), and has led to the development of a significant number of mathematical models (see e.g., Ganguly and Puri, 2006; Lander et al., 2009; Marciniak-Czochra et al., 2009; Chou et al., 2010; Bocharov et al., 2011; Zhang et al., 2012).

Tumor initiation requires an escape from the control mechanisms just described and indeed, there is significant experimental evidence to support this assertion (Lim et al., 2000; Massagué,

2000; Woodford-Richens et al., 2001; Piccirillo et al., 2006; Lee et al., 2008). This underscores the importance of tissue regulation for cancer biology. In the next sections we will analyze the cell dynamics resulting from this regulatory mechanism, first in the context of general feedback functions and then using Hill equations in spatial and non-spatial settings.

Our work adds to a growing body of modeling literature that studies cell lineage dynamics and regulation. Conceptual issues for the study of stem cells are identified in Loeffler and Roeder (2002). Discrete and continuous models relevant to carcinogenesis, and particularly colon cancer, include (Tomlinson and Bodmer, 1995; Yatabe et al., 2001; Agur et al., 2002; Hardy and Stark, 2002; d'Onofrio and Tomlinson, 2007; Johnston et al., 2007; Boman et al., 2008). There are also numerous stem cell models in the context of the hematopoietic system (see e.g., Colijn and Mackey, 2005; Michor et al., 2005; Adimy et al., 2006; Glauche et al., 2007; Ashkenazi et al., 2008). In this paper we combine elements of stochastic and deterministic modeling and consider both mass action and spatial systems. The models identify parameters important for tissue stability and growth and offer a useful tool to study both healthy and cancerous hierarchical populations.

The stability and dynamics of multistage cell lineage models is an active topic of research. In Nakata et al. (2012), the authors systematically analyze the stability of a two and three compartment model where the regulation of proliferation rates is modeled using Hill functions equation (9). A similar model where feedback regulation acts instead on the probability of self-renewal is studied in Lo et al. (2009); here the stability analysis is performed first using a general feedback function for a two compartment model, and then using the feedback function equation (9) for a three compartment model. In Stiehl and Marciniak-Czochra (2011) the authors characterize the structure of stationary solutions of a n -compartment model with feedback on the self-renewal probability of cells. The

characterization is performed for a general form of the regulation function and for the special case that uses the functional form in equation (9).

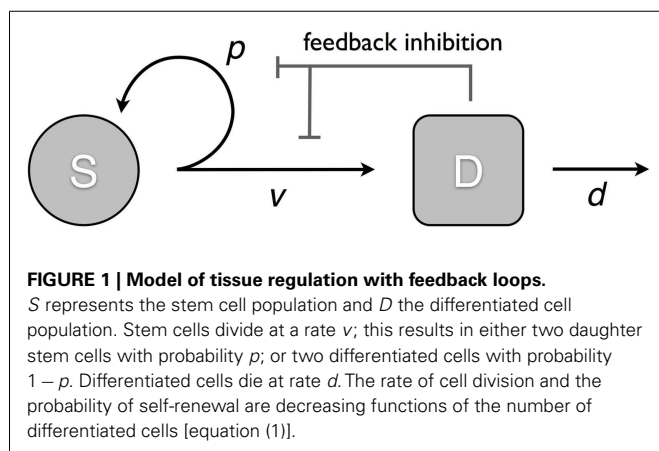
In this article we study the cell dynamics of a two compartment model, which includes feedback regulation in both the division rate and the self-renewal probability of cells. According to the model feedback on the self-renewal probability of stem cells is by itself sufficient to establish control. However if feedback on the division rate is not present, the recovery after an injury may lead to significant damped oscillations in the path back to equilibrium, which can result in the stochastic extinction of the cell population. Moreover, this oscillatory behavior is more pronounced when the stem cell load represents only a small fraction of the entire cell population. If this is the case, oscillations may still be avoided, but it comes at the price of slowing down the speed at which the system is able to recover after an injury. Spatial interactions and the addition of feedback inhibition on the cell division rate reduce the amplitude of oscillations and contributes to the robustness of the system. Feedback inhibition on the division rate also increases the speed of tissue regeneration promoting altogether faster and more stable recoveries from perturbed states.

RESULTS

CELLULAR CONTROL

We consider a model that takes into account two cell populations: stem cells, S , which have unlimited reproductive potential, and differentiated cells D , that eventually die out (this includes all cell populations with limited reproductive potential, such as transit cells). Stem cells divide at a rate v ; this results in either two daughter stem cells with probability p or two differentiated cells with probability $1 - p$. Differentiated cells die at rate d . The system is controlled through two negative feedback loops. Differentiated cells secrete factors that: (1) inhibit stem cell division, and (2) suppress self-renewal in stem cells (Figure 1). Hence, the self-renewal probability and division rate ($p(D)$ and $v(D)$) are strictly decreasing functions of the number of differentiated cells D . The ordinary differential equation (ode) model is given by:

$$\begin{aligned}\dot{S} &= (2p(D) - 1) v(D) S \\ \dot{D} &= 2(1 - p(D)) v(D) S - dD\end{aligned}\quad (1)$$



In addition to the symmetric stem cell divisions explicitly modeled in equation (1) asymmetric division in stem cells is also well documented (Clevers, 2005; Simons and Clevers, 2011). The extent to which these types of divisions occur in different tissues has important biological consequences and is the subject of considerable research efforts (Wu et al., 2007; Neumüller and Knoblich, 2009). However with regards to model (1), it is shown in Rodriguez-Brenes et al. (2011) (Supplementary Information) that the explicit introduction of asymmetric stem cell divisions leads to an equivalent mathematical formulation and does not alter any of the results.

From the expression for \dot{S} , we note that $p(0) > 0.5$ is a necessary condition to avoid the system from always going to the trivial steady solution $(S, D) = (0, 0)$. Also only feedback on the self-renewal probability p – unlike the feedback on v – is able to change the signs of \dot{S} or \dot{D} , which suggests that by itself feedback inhibition on p is sufficient to maintain control. We are interested in finding out how this negative regulation affects the cell population at homeostasis and during recovery after an injury. We begin by looking at the steady states \hat{S} and \hat{D} and \hat{D} which are defined by the following equations:

$$p(\hat{D}) = 1/2 \quad \& \quad \hat{S} = d/v(\hat{D}) \hat{D} \quad (2)$$

Hence, we find that the equilibrium number of differentiated cells \hat{D} depends only on the self-renewal probability $p(D)$. The equilibrium fraction of stem cells $\hat{S}/(\hat{S} + \hat{D})$ depends only on the ratio $d/v(\hat{D})$. In order to understand better the recovery of the system after a perturbation we look at the eigenvalues of the Jacobian matrix evaluated at (\hat{S}, \hat{D}) :

$$J = \begin{bmatrix} 0 & 2dp'(\hat{D}) \hat{D} \\ v(\hat{D}) & -d(2p'(\hat{D}) \hat{D} + 1) \end{bmatrix} \quad (3)$$

Let us write $b = (2p'(\hat{D}) \hat{D} + 1)$ and $\hat{v} = v(\hat{D})$. Then the eigenvalues are given by:

$$\lambda_{1,2} = \frac{-db \pm \sqrt{d^2 b^2 + 4d(b-1)\hat{v}}}{2} \quad (4)$$

The model described by equation (1) is an autonomous system of ordinary differential equations; therefore in a vicinity of the steady state point (\hat{S}, \hat{D}) the behavior of the system can be inferred by looking at the eigenvalues of the Jacobian. If we want the equilibrium values to be asymptotically stable, then the real part of the eigenvalues must be negative, which occurs if and only if $b > 0$. Conversely if $b < 0$, the equilibrium is unstable. If $b = 0$ (purely imaginary eigenvalues), the behavior of the system can not be inferred from equation (1) for general functions $v(D)$ and $p(D)$. In this case a Hopf bifurcation might be possible. However the bifurcation analysis would depend on the specific choice of the regulation functions.

The sign of the discriminant in equation (4) gives us further information into how the trajectories approach the steady state value. If the discriminant is negative then oscillations are expected as the cell population approaches equilibrium. Let us see how this

observation relates to the equilibrium fraction of stem cells in the population. As we noted earlier this fraction is entirely determined by the ratio $\epsilon \equiv d/\hat{v}$. If we want to avoid oscillations then dividing the discriminant by $d\hat{v}$ we find that the following inequality must hold:

$$\epsilon b^2 + 4b - 4 \geq 0 \quad (5)$$

Since $b = 1 + 2p'(\hat{D})\hat{D}$ we have $b < 1$ and if a stable steady exists we then have $0 < b < 1$. Hence the inequality in equation (5) implies that:

$$b \geq \frac{-2 + 2\sqrt{1 + \epsilon}}{\epsilon} \quad (6)$$

Stem cells typically represent a small fraction of the entire cell population which in terms of the ratio ϵ equals $\epsilon/(1 + \epsilon)$. As ϵ approaches zero we find:

$$\lim_{\epsilon \rightarrow 0} \frac{-2 + 2\sqrt{1 + \epsilon}}{\epsilon} = 1 \quad (7)$$

Given the inequality found in equation (6) and the fact that $b < 1$ we find that as the equilibrium fraction of stem cells approaches zero, b approaches one. For the eigenvalues we then have:

$$\lim_{b \rightarrow 1^-} \frac{-db \pm \sqrt{d^2 b^2 + 4d(b-1)\hat{v}}}{2} = -d, 0 \quad (8)$$

However, if the absolute value of one of the eigenvalues is very small, then the overall dynamics of the system is characterized by rapid approach to a slow manifold, followed by a very slow approach toward equilibrium. Hence, we find a trade-off between requiring a small equilibrium fraction of stem cells while avoiding oscillations and the speed at which the system is able to recover from a perturbation.

The study of oscillations is an important part of feedback regulation. Damped oscillations have been observed in healthy hematopoiesis (Marciniak-Czochra and Stiehl, 2012). Amongst pathologies periodic oscillations are a characteristic feature of cyclical neutropenia (Bernard et al., 2003). Oscillatory behavior has also been identified in chronic and acute myeloid leukemia (Andersen and Mackey, 2001; Colijn and Mackey, 2005; Adimy et al., 2006). Moreover it was shown in Nakata et al. (2012) that in a three compartment model with feedback on the cell division rate, the destabilization of the positive equilibrium can lead to oscillations with a constant amplitude.

Going back to the requirements ($b > 0$) that guarantee the existence of a stable non-trivial steady state we note that they are independent of feedback inhibition on the division rate. Moreover for a fixed equilibrium division rate \hat{v} the steady state population sizes are independent on the actual function $v(D)$. The role of feedback on the division rate in the system lies instead in increasing the speed at which the system recovers from a perturbation and reducing the amplitude of oscillations if they happen to occur. This result is consistent with numerical simulations performed in

Marciniak-Czochra et al. (2009), where it was observed that for short-time dynamics the coexistence of both regulatory mechanisms improves the efficiency of hematopoietic regeneration. Intuitively, oscillations occur when the number of differentiated cells is at equilibrium but the number of stem cell is not. If for example $S > \hat{S}$ and $D = \hat{D}$, then while the number of stem cells decreases toward its equilibrium value, the number of differentiated cells would grow. However, if there is feedback on the division rate, the difference between the rate of differentiated cell production and depletion $2(1 - p(D))v(D)S - dD$ would be smaller than in the absence of feedback $(2(1 - p(D))\hat{v}S - dD)$ and thus the maximum number of differentiated cells reached before the growth is reversed will not be as high. In the next sections we will present some numerical examples.

FEEDBACK INHIBITION USING HILL EQUATIONS

In this section we use Hill functions to model feedback inhibition equation (9):

$$p(D) = p_0 / (1 + gD^m), \quad v(D) = v_0 / (1 + hD^n) \quad (9)$$

Hill functions are widely used to describe ligand-receptor interactions (Alon, 2007), which makes them natural choices to model the actions of secreted feedback factors. Moreover they have been previously used to model the specific phenomena of cellular control for cell lineages in various tissues (Lander et al., 2009; Marciniak-Czochra et al., 2009; Chou et al., 2010; Bocharov et al., 2011; Zhang et al., 2012).

From expression equation (9) first note that the maximum self-renewal probability p_0 must satisfy $0.5 < p_0 \leq 1$. The value of b (defined in the previous section) in this case equals $1/(2p_0)$. Hence the condition $b > 0$, which is necessary and sufficient to guarantee the existence of a stable steady state, is always satisfied.

Let us look now at the issue of oscillations near the steady state in relation to the equilibrium fraction of stem cells. In this case the discriminant of the eigenvalues equals:

$$\Delta = \left(\frac{d}{2p_0}\right)^2 - 4v_0d \left(1 - \frac{1}{2p_0}\right) \quad (10)$$

If we once again call $\epsilon \equiv d/\hat{v}$, then the condition $\Delta \geq 0$ can be rewritten as:

$$\epsilon > 8p_0(2p_0 - 1) \quad (11)$$

If we require for example that the equilibrium fraction of stem cells is less than 10%, then (< 0.111). Substituting this value into the previous equation we find that $-0.0134 < p_0 < 0.5134$ and given that $p_0 > 0.5$ we have:

$$0.5 < p_0 < 0.5134 \quad (12)$$

Hence, in a vicinity of the steady state, non-oscillatory trajectories that result in less than 10% of stem cells at homeostasis require that p_0 lies within the small interval $[0.5, 0.5134]$ (see **Figure 2B**). These findings suggest that the maximum self-renewal probability is very close to 0.5.

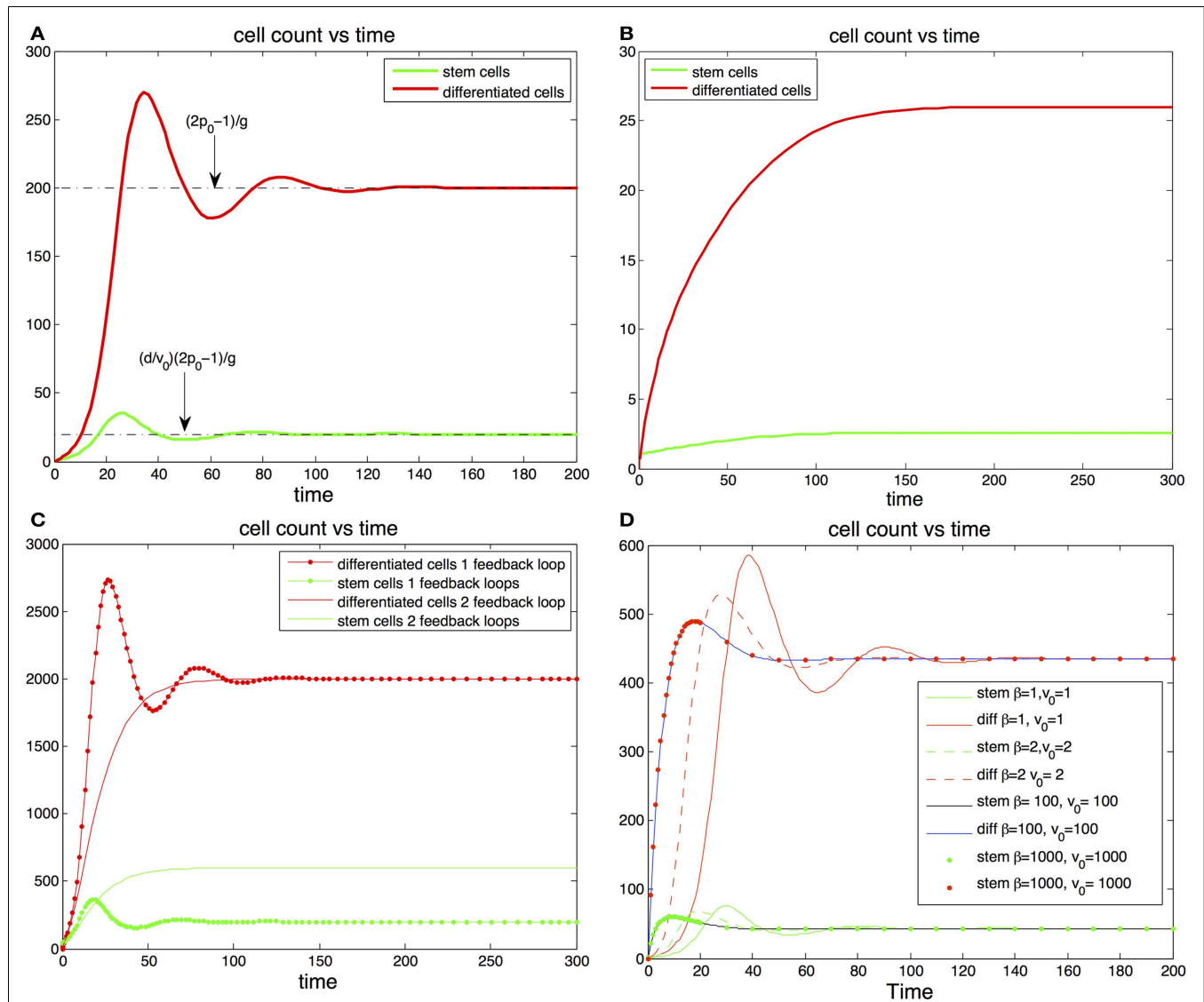


FIGURE 2 | (A,B) Cell population with one feedback loop. **(A)** The trajectories oscillate toward steady state values (dotted line). Parameters, $p_0 = 0.6$, $d = 0.1$, $g = 0.001$, $S(0) = 1$, $D(0) = 0$. **(B)** If there is only one feedback loop the maximum self-renewal probability must be very close to 0.5 to ensure that the trajectories approach the steady states monotonically. In this subfigure d and g are the same as in **(A)** but $p_0 = 0.513$. **(C,D)** cell population with two feedback loops. **(C)** The steady state number of differentiated cells depends only p_0 and g and is

independent of feedback on the division rates. The steady state number of stem cells increases when the number of feedback loops increase from one to two. The addition of feedback in the division rate dampens or altogether eliminates the oscillations. **(D)** Fitting fixed steady state values of stem cells and differentiated cells values with different levels of feedback inhibition in the division rate. The stronger the feedback signal in the division rate the smoother the transition the equilibrium transition to equilibrium.

Interestingly a small value of p_0 may have advantageous effects in the protection against cancer. Indeed the absence of feedback on differentiation leads to uncontrolled cell growth (Rodríguez-Brenes et al., 2011). Thus, having a small maximum self-renewal probability would result in a slower tumor growth rate in the event that feedback inhibition is lost. However, as we mentioned earlier this comes at the cost of reducing the speed of regeneration. In **Figures 2A,B** we track the trajectory of a cell population that has feedback on stem cell differentiation only (i.e., constant $v(D)$). In **Figure 2B** the fraction of stem cells is less than 10% and

the maximum self-renewal probability is kept small ($p_0 = 0.513$). Note how the system is able to recover from a severe perturbation ($D(0) = 0$) without presenting oscillations.

In **Figures 2C,D** we show results with feedback inhibition in both the self-renewal probability and the division rate of stem cells. As we discussed in the previous section, the addition of feedback on the division rate provides for smoother recoveries after a perturbation. Let us call $\beta(D) = 1 + hD^m$, then $v(D) = v_0/\beta(D)$ and $\beta(D)$ controls the strength of the inhibition signal. Clearly we can get a specific target division rate at equilibrium \hat{v} with different

combinations of the pair $(\nu_0, \beta(D))$; the larger the magnitude of these quantities, the stronger the feedback in the division rate will be. In **Figure 2D** we plot different trajectories for the same target number of cells with different combinations of the pair (β, ν_0) . Adding feedback inhibition on the division rate significantly dampens the magnitude of the oscillations and increases the speed at which the trajectories reach the steady states. The stronger the feedback signal the stronger the effect. Thus, even if feedback on the division rate is unnecessary to establish control, it promotes a faster and more stable recoveries in the system.

ROBUSTNESS

One of the negative consequences of oscillations may be the loss of the stem cell population which would result in the eventual extinction of the tissue. In this section we explore sufficient conditions that guarantee the survival of a population that starts at a critical level. In the ode model when a stable equilibrium exists it is easy to prove that zero is a repellent fix point. Hence the zero state cannot be reached from positive initial conditions. In practice this means that the stem cell population cannot hit zero as a result of a perturbation. Therefore to study extinction in the deterministic system we decide that extinction occurs when the number of stem cells falls below one (in the next section we present a stochastic formulation where complete extinction occurs). More precisely, we want to answer the following question: given a set value \hat{D} and the initial critical conditions $S(0) = 1$ and $D(0) = 0$, can we find a parameter region that guarantees the survival of the population? From the eigenvalue analysis we found that in a vicinity of the steady state, the magnitude of the oscillations is determined by the discriminant in equation (10) and everything being equal, a greater value of p_0 produces stronger oscillations. With this idea in mind we assume that given a choice of parameters ν_0, d, β that guarantee survival for a large upper bound self-renewal probability $p_0 = 0.9$ and $g = (2p_0 - 1)/\hat{D}$, then the same set of parameters guarantees survival for any other pair p_0, g , that satisfies $(2p_0 - 1)/g = \hat{D}$ and $p_0 < 0.9$. Furthermore, the addition of the feedback on the replication rate increases the value of \hat{S} and appears to dampen oscillations. Hence, we assume that any set of parameters that guarantee survival of the population with only one feedback loop should also guarantee survival when the two feedback loops are in place.

The previous considerations reduce our search to pairs (d, ν_0) that guarantee survival, given the initial conditions ($p_0 = 0.9, g = 0.8/\hat{D}, \beta = 1$). Finally we note that the amplitude of the oscillations depends on the ratio d/ν_0 and not on the actual magnitude of d and ν_0 so we only need to test different values for this ratio. Since this ratio is closely related to the percentage of stem cells by the equality $\hat{S} = d/\nu_0 \hat{D}$, then the results can be presented in terms of the steady state percentage of stem cells (**Figure 3D**).

The analysis performed here indicates that in the ode model there are ample parameter regimes that guarantee the survival of the population while maintaining a small stem cell load. In general the greater \hat{D} is the smaller the equilibrium fraction of stem cells may be to guarantee survival. Moreover in this analysis the system was required to rebound from very extreme initial conditions ($S(0) = 1$). In practice most injuries that are able to heal would rarely include populations that are reduced

to a single cell. Furthermore, as we found earlier the addition of feedback in the division rate and the reduction of the maximum self-renewal probability p_0 further increase the stability of the system.

STOCHASTIC MODEL

We are also interested in studying the effects of stochastic fluctuations in the model. With this aim in we implement the following algorithm using Gillespie's Method (Gillespie, 1977).

Algorithm:

Assume that at time t , the system is described by the pair $(S(t), D(t))$, and r_1, r_2 , and r_3 are random numbers uniformly distributed in $[0, 1]$.

1. Set $p(t) = p_0/(1 + gD)$ and $v(t) = \nu_0/(1 + hD)$.
2. Compute $a = v(t)S(t) + dD(t)$.
3. Set the new time $t' = t - 1/a \cdot \log(r_1)$.
4. If $a \cdot r_2 < dD(t)$, the next event is cell death of a differentiated cell, hence make $D(t') = D(t) - 1$.
5. If $a \cdot r_2 > dD(t)$, the next event is stem cell division. If $r_3 < p(t)$ the cell divides into two stem cells, hence make $S(t') = S(t) + 1$. If $r_3 > p(t)$ the cell divided into two differentiated cells, hence make $S(t') = S(t) - 1$ and $D(t') = D(t) + 2$.

In **Figures 3A,B** we plot two stochastic simulations with only one feedback loop together with the corresponding ode formulations. Note that in **Figure 3B** the simulation ends with the extinction of the cell population, even though the ode model does not go extinct. In general the extinction of the cell population is a more likely event when the steady state number of stem cells is small, given that random deviations from the mean can bring the number of stem cells to zero. The addition of a second feedback loop (**Figure 3C**) increases the stability and reduces the variance in the number of cells. A realization of the algorithm is a random walk that represents the distribution of the master equation, and which captures the stochastic fluctuations typically observed in systems with a small number of agents. As the number of cells increases, the fluctuations in the number of cells decrease and the thus the stochastic realizations increasingly resemble the corresponding trajectories produced by the ode (Gillespie, 1977).

There are two more things worthy of being noted. First the occurrence of random fluctuations makes the stochastic model even more sensitive to oscillations. Second in a stochastic setting an injury that severely depletes the number of cells is not guaranteed to be able to rebound and there may be a significant chance of extinction. These observations suggest that the control mechanism considered so far is not well suited for systems that rely on a critically small number of stem cells, such as the colon lining which may rely on as little as four stem cells per crypt (Marshman et al., 2002). Instead it is better suited to deal with systems with a large number of cells such as blood (Shizuru et al., 2005). Moreover the use of mass action equations assumes a well mixed system, which is a reasonable assumption for non-solid tissues. In the next section we will discuss the effects of adding spatial interactions to the model.

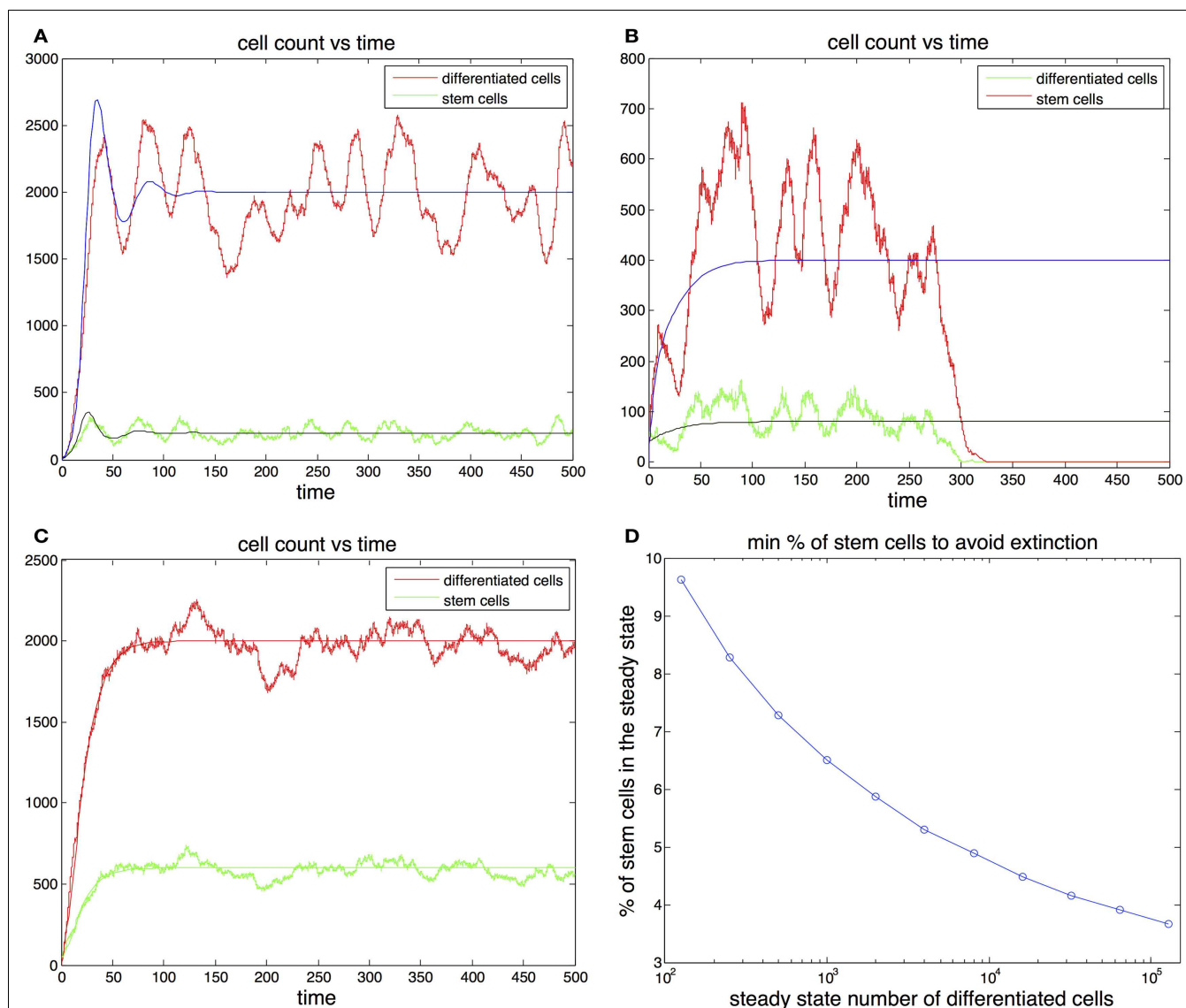


FIGURE 3 | (A,B) Cell population with one feedback loop. The stochastic simulation is shown in red for differentiated cells and green for stem cells. The ode is shown in blue for differentiated cells and black for stem cells. Parameters in **(A)** $p_0 = 0.6$, $d = 0.1$, $g = 0.0001$, $h = 0$, $S(0) = 10$, $D(0) = 0$. Parameters in **(B)** $p_0 = 0.52$, $d = 0.2$, $g = 0.0001$, $h = 0$, $S(0) = 40$, $D(0) = 0$. **(C)** Cell population with two feedback loops. Feedback in the division rate dampens oscillations. Parameters are the same as in **(A)** with the exception $h = 0.001$. **(D)** Sufficient conditions for

the survival of the population in the ode model. Let us call the curve in the graph $y(\bar{D})$. Then for any set of parameters that satisfy $(2p^0 - 1)/g = \bar{D}$, $p^0 \in (0.5, 0.9)$ and the steady state fraction of stem cells $f \geq y(\bar{D})$, the initial conditions $S(0) = 1$, $D(0) = 0$ guarantee the survival of the population. For example, for all $\bar{D} \geq 10^3$ if $p_0 \leq 0.9$ and the steady state fraction of stem cells $f \geq 0.064$ survival is guaranteed for any level of feedback on the division rate. (These conditions are sufficient but not necessary.)

SPATIAL MODEL

The spatial effects

In this section we consider cell dynamics in three dimensions. We assume that cells are restricted to a three-dimensional rectangular lattice of $n_I \times n_J \times n_K$ points. A lattice point can host at most one cell at any time. The position of each cell can be determined by its coordinates in the lattice (i, j, k) , $i = 1, \dots, n_I$, $j = 1, \dots, n_J$, and $k = 1, \dots, n_K$. Following the rules of the previous sections, stem cells divide either into two stem cells or two differentiated cells. For a cell to divide, there must be a free lattice

point adjacent to it. If the cell divides, then one offspring remains in the position occupied by the parent cell and the other occupies a position adjacent to the cell. There are cases in which a cell that is able to divide has more than one free adjacent lattice point that may be occupied by one of its two offspring. In this case we choose the site randomly, with each adjacent free lattice point having the same probability of hosting one of the two daughter cells. The events are chosen using the stochastic simulation algorithm (described above) modified to take into account the spatial rules. A graphical representation of the spatial

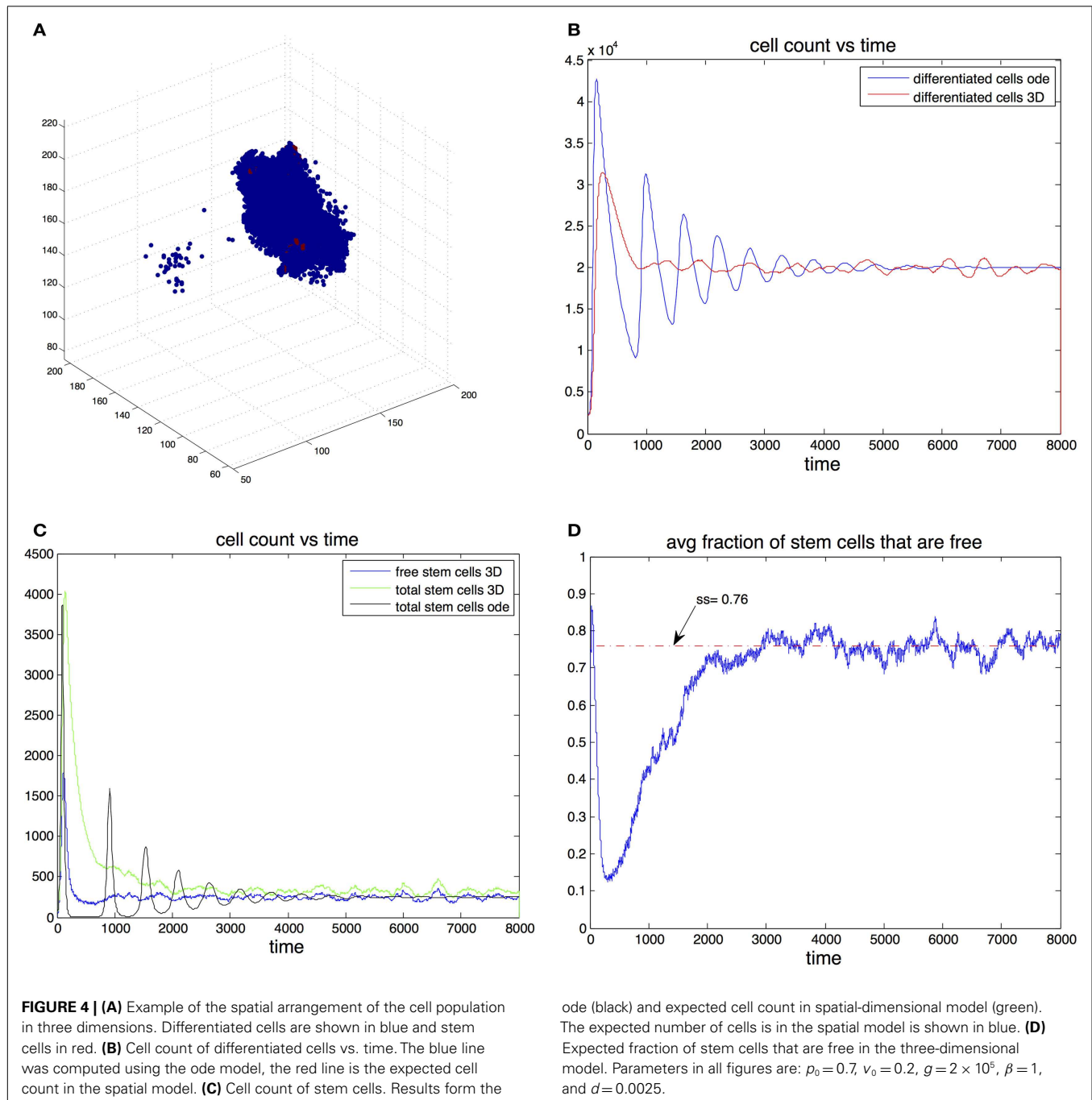
arrangement of the three-dimensional cell population is given in **Figure 4A**.

We found that adding space to the system results in smoother transitions from perturbed to equilibrium configurations. Compared to the non-spatial system, if oscillations are observed, the amplitudes are significantly reduced, which in turn results in much fewer instances that end with the stochastic extinction of the cell population. This behavior is exemplified by **Figures 4B,C**. Here we picked parameter regime ($p_0 = 0.7$, $v_0 = 0.2$, $g = 2 \times 10^{-5}$, $\beta = 1$, $d = 0.0025$) that produces oscillations in the non-spatial model. The initial conditions are $(S(0), D(0)) = 0.1(\hat{S}, \hat{D})$, where (\hat{S}, \hat{D})

are the steady state values from the ode model. With this initial conditions the number of stem cells in the ode model falls below one, which in practice means that the population goes extinct. Furthermore we performed 100 independent simulations using the stochastic non-spatial model and every one of them resulted in the extinction of the cell population. In contrast not one of 30 simulations using the spatial model resulted in extinction.

In the non-spatial model the steady state fraction of stem cells is:

$$\frac{\hat{S}}{\hat{S} + \hat{D}} = \frac{d\beta/v_0}{d\beta/v_0 + 1} \quad (13)$$



In the spatial model this quantity gives the steady state percentage of free stem cells – cells that have free space in an adjacent position in the grid and are thus able to divide. This means that for a given set of parameters, the equilibrium number of stem cells in the spatial model is greater than the equilibrium number in the non-spatial model. For example in **Figure 4C** the steady state fraction of stem cells in the ode model was approximately 0.0123 (as predicted by the formulas). In the three-dimensional model the expected steady state fraction of cells was approximately 0.0165, an increase of about 32% from the deterministic model's prediction.

The mechanism by which the spatial model is able to achieve a greater stability can be inferred by looking at **Figures 4C,D**. At the start of the simulation the number of differentiated cells is only 10% of the steady state value. Therefore the probability of differentiation is small and stem cells have a high probability of dividing into two stem cells. Once the number of differentiated cells is above \hat{D} , differentiation becomes the more likely event and in the ode model one sees a steep reduction in the number of stem cells that leads to extinction. In the spatial model however, the rapid growth phase of stem cells means the fraction of free cells is reduced as most stem cells are trapped by other stem cells. Only these free stem cells are able to divide, slowing down the speed at which stem cells are depleted. It is important to note that the spatial effects in this model act locally by reducing the space available for cell division, their strength thus depends on the degree of the graph. As the graph degree increases the spatial effects become weaker until eventually the mass action dynamics are fully recovered.

In a spatial setting the stem cell niche concept (Morrison et al., 1997; Simons and Clevers, 2011) might also play a role in promoting stability. If the amount of space in the niche were limited, this would place a cap in the maximum number of stem cells, which could in turn decrease the overshooting of the stem cell number observed during oscillations. Exactly how the explicit modeling of these microenvironments might affect the performance of the regulatory mechanisms investigated here should be the subject of future research.

DISCUSSION

In this article we studied the cell dynamics that arise from feedback inhibition in the self-renewal probability of stem cells and their division rate. We found that by itself feedback on the probability of self-renewal is sufficient to establish control and uniquely determines the equilibrium number of differentiated cells. The equilibrium fraction of stem cells on the other hand depends solely on the ratio of the death rate and the rate of stem cell division.

In the process of recovering after an injury this control mechanism may produce oscillations in the number of cells, a behavior that may be dangerous and of no obvious biological value. Near equilibrium oscillations are more likely to occur when the steady state fraction of stem cells is small. If this is the case, avoiding oscillations is still always possible, but it comes at the price of reducing the speed at which the cell populations recover from a perturbation. If feedback inhibition follows a Hill equation, avoiding oscillations while maintaining a small stem cell load requires that the maximum self-renewal probability be only slightly larger

than one-half. Feedback inhibition on the stem cell division rate does not affect the steady state values of either stem cells or differentiated cells, but it reduces the amplitude of oscillations if they happen to occur. Furthermore it can increase the speed of recovery after an injury, altogether promoting faster and more stable recoveries of the cell population.

On occasions, extreme oscillations may result in the extinction of the entire population. However, we find that there are ample parameter regimes in which this doesn't occur, even while the system is recovering from severe initial conditions. We found that the larger the equilibrium number of differentiated cells, the smaller the equilibrium fraction of stem cells may be while still avoiding extinction. Due to fluctuations, in a stochastic setting the danger of extinction through oscillations is greater. This suggests that the mass action model is only well suited as a quantitative tool for tissues where the steady state number of stem cells is not critically small.

We also explored how spatial interactions affect the cell dynamics in a stochastic setting. We found that spatial effects greatly reduce oscillations and the chances of random extinction, providing smoother transitions from a perturbed state to equilibrium. This increase in stability is achieved by reducing the number of stem cells that are capable of division at a given time. When recovering from an injury the rapid expansion of the stem cell population traps some of the stem cells, making them incapable of cell division. Hence, when the steady state number of differentiated cells is reached, a significant fraction of stem cells cannot divide. This reduces any possible further increase in the number of differentiated cells causing the magnitude of any oscillation to decrease as well.

The models of hierarchical cell populations studied here are relevant to both healthy and cancerous tissues. In Rodriguez-Brenes et al. (2011) we showed how cancer could develop from healthy hierarchical tissues by a unique sequence of phenotypic transitions, which gradually lead to a complete escape from regulation in stem-cell-driven tumors. Moreover, we compared the resulting tumor growth patterns with existing tumor growth data and saw that in many instances, the regulatory mechanisms of healthy tissues continue to operate to a degree in tumors. This underlines the importance to cancer biology of studying the principles of tissue regulation. Another example of the relation between tissue regulation and the process of carcinogenesis is found in Stiehl and Marciniak-Czochra (2012).

One important result for the cancerous transformation found in Rodriguez-Brenes et al. (2011) is that the negative feedback loops controlling the differentiation decisions must be the first to be inactivated. The breakage of the division control loops must happen at a later stage of carcinogenesis. Here we reevaluate this finding from a different perspective. In order to achieve the deregulation of divisions and rapid growth, cancerous cells must first acquire a mutation deactivating the differentiation control. Otherwise, the tissue may become unstable and enter stochastic fluctuations preventing steady growth. Therefore, a one-step transformation from healthy tissue to a tissue with no division control mechanism is highly unlikely. This can be viewed as a protection mechanism that organs put in the way of cancerous transformations, making the transition to cancer more difficult

and statistically delaying the onset of cancer (for related ideas, see also (Komarova and Cheng, 2006)).

The optimization task for healthy hierarchical tissues is to provide stable maintenance and a quick and reliable recovery from injuries. Over time, tissues have evolved (at least partially) to reach these objectives. In contrast, therapeutic approaches often pursue the opposite tasks: the destabilization of cancerous tissue,

increasing the chance of stochastic extinction (say, after a course of chemotherapy or surgery) and the slowing down of tumor growth. Our models show what parameters (and to what degree) are responsible for stability and growth. Understanding how various parameters contribute to cell population growth and stability can lead to novel ideas for cancer treatments, where one could target factors leading to growth retardation or destabilization.

REFERENCES

- Adimy, M., Crauste, F., and Ruan, S. (2006). Modelling hematopoiesis mediated by growth factors with applications to periodic hematological diseases. *Bull. Math. Biol.* 68, 2321–2351.
- Agur, Z., Daniel, Y., and Ginosar, Y. (2002). The universal properties of stem cells as pinpointed by a simple discrete model. *J. Math. Biol.* 44, 79–86.
- Al-Hajj, M., Wicha, M. S., Benito-Hernandez, A., Morrison, S. J., and Clarke, M. F. (2003). Prospective identification of tumorigenic breast cancer cells. *Proc. Natl. Acad. Sci. U.S.A.* 100, 3983–3988.
- Alon, U. (2007). “An Introduction to Systems Biology: Design Principles of Biological Circuits,” in *Volume 10 of Chapman and Hall/CRC Mathematical and Computational Biology Series*, eds A. M. Etheridge, L. J. Gross, S. Lenhart, P. K. Maini, S. Ranganathan, et al. (Boca Raton, FL: Chapman and Hall/CRC), 301.
- Andersen, L. K., and Mackey, M. C. (2001). Resonance in periodic chemotherapy: a case study of acute myelogenous leukemia. *J. Theor. Biol.* 209, 113–130.
- Arino, O., and Kimmel, M. (1986). Stability analysis of models of cell production systems. *Math. Model.* 7, 1269–1300.
- Ashkenazi, R., Gentry, S. N., and Jackson, T. L. (2008). Pathways to tumorigenesis – modeling mutation acquisition in stem cells and their progeny. *Neoplasia* 10, 1170–1182.
- Bernard, S., Bélair, J., and Mackey, M. C. (2003). Oscillations in cyclical neutropenia: new evidence based on mathematical modeling. *J. Theor. Biol.* 223, 283–298.
- Bocharov, G., Quil, J., Luzyanina, T., Alon, H., Chiglintsev, E., Cheresnev, V., et al. (2011). Feedback regulation of proliferation vs. differentiation rates explains the dependence of CD4 T-cell expansion on precursor number. *Proc. Natl. Acad. Sci. U.S.A.* 108, 3318–3323.
- Boman, B. M., Fields, J. Z., Cavanaugh, K. L., Guetter, A., and Runquist, O. A. (2008). How dysregulated colonic crypt dynamics cause stem cell overpopulation and initiate colon cancer. *Cancer Res.* 68, 3304–3313.
- Bonnet, D., and Dick, J. E. (1997). Human acute myeloid leukemia is organized as a hierarchy that originates from a primitive hematopoietic cell. *Nat. Med.* 3, 730–737.
- Chou, C.-S., Lo, W.-C., Gokoffski, K. K., Zhang, Y.-T., Wan, F. Y. M., Lander, A. D., et al. (2010). Spatial dynamics of multistage cell lineages in tissue stratification. *Biophys. J.* 99, 3145–3154.
- Clevers, H. (2005). Stem cells, asymmetric division and cancer. *Nat. Genet.* 37, 1027–1028.
- Clevers, H. (2011). The cancer stem cell: premises, promises and challenges. *Nat. Med.* 17, 313–319.
- Colijn, C., and Mackey, M. C. (2005). A mathematical model of hematopoiesis – I. Periodic chronic myelogenous leukemia. *J. Theor. Biol.* 237, 117–132.
- Daluiski, A., Engstrand, T., Bahamonde, M. E., Gamer, L. W., Agius, E., Stevenson, S. L., et al. (2001). Bone morphogenetic protein-3 is a negative regulator of bone density. *Nat. Genet.* 27, 84–88.
- d’Onofrio, A., and Tomlinson, I. P. (2007). A nonlinear mathematical model of cell turnover, differentiation and tumorigenesis in the intestinal crypt. *J. Theor. Biol.* 244, 367–374.
- Elgjo, K., and Reichelt, K. L. (2004). Chalcones: from aqueous extracts to oligopeptides. *Cell Cycle* 3, 1208–1211.
- Ganguly, R., and Puri, I. (2006). Mathematical model for the cancer stem cell hypothesis. *Cell Prolif.* 39, 3–14.
- Gillespie, D. T. (1977). Exact stochastic simulation of coupled chemical reactions. *J. Phys. Chem.* 81, 2340–2361.
- Glauche, I., Cross, M., Loeffler, M., and Roeder, I. (2007). Lineage specification of hematopoietic stem cells: mathematical modeling and biological implications. *Stem Cells* 25, 1791–1799.
- Hardy, K., and Stark, J. (2002). Mathematical models of the balance between apoptosis and proliferation. *Apoptosis* 7, 373–381.
- Johnston, M. D., Edwards, C. M., Bodmer, W. F., Maini, P. K., and Chapman, S. J. (2007). Mathematical modeling of cell population dynamics in the colonic crypt and in colorectal cancer. *Proc. Natl. Acad. Sci. U.S.A.* 104, 4008–4013.
- Komarova, N., and Cheng, P. (2006). Epithelial tissue architecture protects against cancer. *Math. Biosci.* 200, 90–117.
- Lander, A. D., Gokoffski, K. K., Wan, F. Y. M., Nie, Q., and Calof, A. L. (2009). Cell lineages and the logic of proliferative control. *PLoS Biol.* 7:e15. doi:10.1371/journal.pbio.1000015
- Lee, J., Son, M. J., Woolard, K., Donin, N. M., Li, A., Cheng, C. H., et al. (2008). Epigenetic-mediated dysfunction of the bone morphogenetic protein pathway inhibits differentiation of glioblastoma-initiating cells. *Cancer Cell* 13, 69–80.
- Lim, D. A., Tramontin, A. D., Trevejo, J. M., Herrera, D. G., García-Verdugo, J. M., and Alvarez-Buylla, A. (2000). Noggin antagonizes BMP signaling to create a niche for adult neurogenesis. *Neuron* 28, 713–726.
- Lo, W.-C., Chou, C.-S., Gokoffski, K. K., Wan, F. Y.-M., Lander, A. D., Calof, A. L., et al. (2009). Feedback regulation in multistage cell lineages. *Math. Biosci. Eng.* 6, 59–82.
- Loeffler, M., and Roeder, I. (2002). Tissue stem cells: definition, plasticity, heterogeneity, self-organization and models – a conceptual approach. *Cells Tissues Organs (Print)* 171, 8–26.
- Marciniak-Czochra, A., and Stiehl, T. (2012). “Mathematical models of hematopoietic reconstitution after stem cell transplantation,” in *Model Based Parameter Estimation: Theory and Applications*, eds H. G. Bock, T. H. Carraro, W. Jäger, S. Körkel, R. Rannacher, and J. P. Schlöder (New York: Springer), 191–207.
- Marciniak-Czochra, A., Stiehl, T., Ho, A. D., Jäger, W., and Wagner, W. (2009). Modeling of asymmetric cell division in hematopoietic stem cells: regulation of self-renewal is essential for efficient repopulation. *Stem Cells Dev.* 18, 377–385.
- Marshman, E., Booth, C., and Potten, C. (2002). The intestinal epithelial stem cell. *Bioessays* 24, 91–98.
- Massagué, J. (2000). TGF- β in cancer. *Cell* 103, 295–309.
- McPherron, A. C., Lawler, A. M., and Lee, S. J. (1997). Regulation of skeletal muscle mass in mice by a new TGF- β superfamily member. *Nature* 387, 83–90.
- Michor, F., Hughes, T. P., Iwasa, Y., Branford, S., Shah, N. P., Sawyers, C. L., et al. (2005). Dynamics of chronic myeloid leukaemia. *Nature* 435, 1267–1270.
- Morrison, S., Shah, M. N., and Anderson, D. (1997). Regulatory mechanisms in stem cell biology. *Cell* 88, 287–298.
- Nakata, Y., Getto, P., Marciniak-Czochra, A., and Alarcón, T. (2012). Stability analysis of multi-compartment models for cell production systems. *J. Biol. Dyn.* 6(Suppl. 1), 2–18.
- Neumüller, R. A., and Knoblich, J. A. (2009). Dividing cellular asymmetry: asymmetric cell division and its implications for stem cells and cancer. *Genes Dev.* 23, 2675–2699.
- Passegué, E., Jamieson, C. H. M., Ailles, L. E., and Weissman, I. L. (2003). Normal and leukemic hematopoiesis: are leukemias a stem cell disorder or a reacquisition of stem cell characteristics? *Proc. Natl. Acad. Sci. U.S.A.* 100(Suppl. 1), 11842–11849.
- Piccirillo, S. G. M., Reynolds, B. A., Zanetti, N., Lamorte, G., Binda, E., Broggi, G., et al. (2006). Bone morphogenetic proteins inhibit the tumorigenic potential of human brain tumour-initiating cells. *Nature* 444, 761–765.
- Reya, T., Morrison, S., Clarke, M., and Weissman, I. (2001). Stem cells, cancer, and cancer stem cells. *Nature* 414, 105–111.
- Rodríguez-Brenes, I. A., Komarova, N. L., and Wodarz, D. (2011). Evolutionary dynamics of feedback escape and the development of stem-cell-driven cancers. *Proc. Natl. Acad. Sci. U.S.A.* 108, 18983–18988.
- Shizuru, J. A., Negrin, R. S., and Weissman, I. L. (2005). Hematopoietic stem and progenitor cells: clinical and preclinical regeneration of the hematolymphoid system. *Annu. Rev. Med.* 56, 509–538.

- Simons, B. D., and Clevers, H. (2011). Strategies for homeostatic stem cell self-renewal in adult tissues. *Cell* 145, 851–862.
- Stiehl, T., and Marciniak-Czochra, A. (2011). Characterization of stem cells using mathematical models of multistage cell lineages. *Math. Comput. Model.* 53, 1505–1517.
- Stiehl, T., and Marciniak-Czochra, A. (2012). Mathematical modeling of leukemogenesis and cancer stem cell dynamics. *Math. Model. Nat. Phenom.* 7, 166–202.
- Tomlinson, I. P., and Bodmer, W. F. (1995). Failure of programmed cell death and differentiation as causes of tumors: some simple mathematical models. *Proc. Natl. Acad. Sci. U.S.A.* 92, 11130–11134.
- Tzeng, Y.-S., Li, H., Kang, Y.-L., Chen, W.-C., Cheng, W.-C., and Lai, D.-M. (2011). Loss of CXCL12/SDF-1 in adult mice decreases the quiescent state of hematopoietic stem/progenitor cells and alters the pattern of hematopoietic regeneration after myelosuppression. *Blood* 117, 429–439.
- Wang, R., Chadalavada, K., Wilshire, J., Kowalik, U., Hovinga, K. E., Geber, A., et al. (2010). Glioblastoma stem-like cells give rise to tumour endothelium. *Nature* 468, 829–833.
- Woodford-Richens, K. L., Rowan, A. J., Gorman, P., Halford, S., Bicknell, D. C., Wasan, H. S., et al. (2001). SMAD4 mutations in colorectal cancer probably occur before chromosomal instability, but after divergence of the microsatellite instability pathway. *Proc. Natl. Acad. Sci. U.S.A.* 98, 9719–9723.
- Wu, M., Kwon, H. Y., Rattis, F., Blum, J., Zhao, C., Ashkenazi, R., et al. (2007). Imaging hematopoietic precursor division in real time. *Cell Stem Cell* 1, 541–554.
- Yamasaki, K., Toriu, N., Hanakawa, Y., Shirakata, Y., Sayama, K., Takayanagi, A., et al. (2003). Keratinocyte growth inhibition by high-dose epidermal growth factor is mediated by transforming growth factor beta autoinduction: a negative feedback mechanism for keratinocyte growth. *J. Invest. Dermatol.* 120, 1030–1037.
- Yatabe, Y., Tavaré, S., and Shibata, D. (2001). Investigating stem cells in human colon by using methylation patterns. *Proc. Natl. Acad. Sci. U.S.A.* 98, 10839–10844.
- Zhang, L., Lander, A. D., and Nie, Q. (2012). A reaction-diffusion mechanism influences cell lineage progression as a basis for formation, regeneration, and stability of intestinal crypts. *BMC Syst. Biol.* 6:93. doi:10.1186/1752-0509-6-93
- could be construed as a potential conflict of interest.

Received: 05 December 2012; paper pending published: 05 January 2013; accepted: 29 March 2013; published online: 15 April 2013.

Citation: Rodriguez-Brenes IA, Wodarz D and Komarova NL (2013) Stem cell control, oscillations, and tissue regeneration in spatial and non-spatial models. *Front. Oncol.* 3:82. doi: 10.3389/fonc.2013.00082

This article was submitted to *Frontiers in Molecular and Cellular Oncology*, a specialty of *Frontiers in Oncology*.

Copyright © 2013 Rodriguez-Brenes, Wodarz and Komarova. This is an open-access article distributed under the terms of the Creative Commons Attribution License, which permits use, distribution and reproduction in other forums, provided the original authors and source are credited and subject to any copyright notices concerning any third-party graphics etc.

Conflict of Interest Statement: The authors declare that the research was conducted in the absence of any commercial or financial relationships that



Cancer stem cells: a minor cancer subpopulation that redefines global cancer features

Heiko Enderling, Lynn Hlatky and Philip Hahnfeldt *

Center of Cancer Systems Biology, St. Elizabeth's Medical Center, Tufts University School of Medicine, Boston, MA, USA

Edited by:

Katarzyna A. Rejniak, H. Lee Moffitt
Cancer Center & Research Institute,
USA

Reviewed by:

Alberto D'Onofrio, European Institute
of Oncology, Italy
Andrea Sottoriva, USC Keck School of
Medicine, USA

*Correspondence:

Philip Hahnfeldt, Center of Cancer
Systems Biology, St. Elizabeth's
Medical Center, Tufts University
School of Medicine, 736 Cambridge
Street, CBR-115, Boston, MA 02135,
USA.
e-mail: philip.hahnfeldt@tufts.edu

In recent years cancer stem cells (CSCs) have been hypothesized to comprise only a minor subpopulation in solid tumors that drives tumor initiation, progression, and metastasis; the so-called “cancer stem cell hypothesis.” While a seemingly trivial statement about numbers, much is put at stake. If true, the conclusions of many studies of cancer cell populations could be challenged, as the bulk assay methods upon which they depend have, by and large, taken for granted the notion that a “typical” cell of the population possesses the attributes of a cell capable of perpetuating the cancer, i.e., a CSC. In support of the CSC hypothesis, populations enriched for so-called “tumor-initiating” cells have demonstrated a corresponding increase in tumorigenicity as measured by dilution assay, although estimates have varied widely as to what the fractional contribution of tumor-initiating cells is in any given population. Some have taken this variability to suggest the CSC fraction may be nearly 100% after all, countering the CSC hypothesis, and that there are simply assay-dependent error rates in our ability to “reconfirm” CSC status at the cell level. To explore this controversy more quantitatively, we developed a simple cellular automaton model of CSC-driven tumor growth dynamics. Assuming CSC and non-stem cancer cells (CC) subpopulations coexist to some degree, we evaluated the impact of an environmentally dependent CSC symmetric division probability and a CC proliferation capacity on tumor progression and morphology. Our model predicts, as expected, that the frequency of CSC divisions that are symmetric highly influences the frequency of CSCs in the population, but goes on to predict the two frequencies can be widely divergent, and that spatial constraints will tend to increase the CSC fraction over time. Further, tumor progression times show a marked dependence on both the frequency of CSC divisions that are symmetric and on the proliferation capacities of CC. Together, these findings can explain, within the CSC hypothesis, the widely varying measures of stem cell fractions observed. In particular, although the CSC fraction is influenced by the (environmentally modifiable) CSC symmetric division probability, with the former converging to unity as the latter nears 100%, the CSC fraction becomes quite small even for symmetric division probabilities modestly lower than 100%. In the latter case, the tumor exhibits a clustered morphology and the CSC fraction steadily increases with time; more so on both counts when the death rate of CCs is higher. Such variations in CSC fraction and morphology are not only consistent with the CSC hypothesis, but lend support to it as one expected byproduct of the dynamical interactions that are predicted to take place among a relatively small CSC population, its CC counterpart, and the host compartment over time.

Keywords: mathematical model, cellular automaton, cancer stem cell, symmetric division, invasion, morphology

INTRODUCTION

Normal tissues undergo constant turnover, with cells dying due to age, injury, or shedding, and being replaced by new healthy cells. Homeostasis is accomplished by a potent subpopulation of stem cells. In recent years, a potent subpopulation of stemlike cells has also been proposed to exist as a minority population in cancers. First in leukemia and later in solid tumors, distinct cell populations were isolated that were either capable or not capable of initiating and sustaining, and re-initiating tumor growth (Furth and Kahn, 1937; Al-Hajj et al., 2003; Singh et al., 2003; Visvader and Lindeman, 2008; Vlashi et al., 2009). The picture to emerge – that of

a potent cancer stem cell (CSC) that initiates and progresses the tumor, with the bulk of the growing tumor being composed of replication-limited cancer cells (CCs) – stands in marked contrast to the long-established paradigm that cancer cells typically are long-lived, escape cell death, and have limitless replicative potential (Hanahan and Weinberg, 2000, 2011), and argues against one recent study (Quintana et al., 2008), which has been interpreted to suggest we may simply be “under-assaying” the preponderant stem cell population (Baker, 2008). Summing up this alternative paradigm is the CSC hypothesis, perhaps better described as a cancer “non-stem cell” hypothesis, which posits that in fact only a

few cells in the tumor population exhibit the immortal, stemlike trait. Confusion sometimes accompanying the CSC terminology regards the cell of origin of the disease. While the term “CSC” clearly suggests these cells possess stemlike qualities, this should not be taken to suggest they originate from normal stem cells. Indeed, the literature is split on the matter of origin (Haeno et al., 2009; Rahman et al., 2009; Shibata and Shen, 2013), with debates occurring occasionally even within the same tumor type, as in the case in glioblastoma (Stiles and Rowitch, 2008; Hambardzumyan et al., 2011).

Populations enriched for stemness can be isolated using different surface markers. The number of cells from such enriched populations that is necessary to form tumors gives an indication of the fraction of cells that are CSCs in the primary tumor. We calculated these ratios from data reported in the literature (Visvader and Lindeman, 2008) (Table 1), and found these tend to support numerous other reports that CSCs are indeed a rare population within a tumor (Reya et al., 2001; Pardal et al., 2003). In addition to identification of CSCs through surface proteins *in vitro* and *in vivo* mouse xenograft transplantation assays, novel approaches emerge that trace tumor hierarchy and help estimate CSC kinetics and frequency in spontaneous tumors or orthotropic models. One approach to monitor the division kinetics of stem and progenitor cells in normal epithelial tissues, skin papilloma, and invasive squamous cell carcinoma during unperturbed growth emerged from clonal analysis using genetic lineage tracing in mice (Driessens et al., 2012). Gao et al. (2013) used an integrated experimental and cellular Potts model approach to simulate glioblastoma population growth and response to irradiation, which identified the (a)symmetric division kinetics of glioblastoma stem cells necessary to reproduce the observed ratio of 2–3% of such cells.

Table 1 | Cancer stem cells in solid tumors.

Tumor type	Cells expressing CSC marker (%)	Minimal number of cells expressing marker for tumor formation	Calculated cancer stem cell ratio
Breast	11–35	200	1.1×10^{-3}
	ND	2000	
	3–10	500	
Brain	19–29	100	3.3×10^{-4}
	6–21	100	
Colon	1.8–25	200	5.4×10^{-4}
	0.7–6	3000	
	0.03–38	200	
Head and neck	0.1–42	5000	4.2×10^{-5}
Pancreas	0.2–0.8	100	3.5×10^{-5}
	1–3	500	
Lung	0.32–22	10,000	1.1×10^{-4}
Liver	0.03–6	5000	6×10^{-6}

Adapted from Visvader and Lindeman (2008).

Another integrated approach of single-molecule genomic data, spatial agent-based modeling, and statistical inference was recently introduced to derive tumor ancestral trees in patient-specific colorectal cancer samples that lead to the observation of a CSC fraction of 0.5–4% (Sottoriva et al., 2013).

One mechanism responsible for establishing the CSC fraction within a tumor is the relative frequency with which CSCs either create another CSC (by symmetric division) or a non-CSCs (by asymmetric division) (Caussinus and Hirth, 2007; Dingli et al., 2007b). Mechanisms known to directly affect the symmetric division probability, in turn, include availability of certain host growth factors such as EGF, and growth-factor-rich niches, which can skew division modes in favor of symmetric production of CSC up to 85% (Lathia et al., 2011). Another mechanism responsible for the observed CSC fraction in tumors is factor-independent, and may be traced to the aggregate population-level action of cell proliferation, migration, and apoptosis; a process we have previously described as “self-metastatic” growth (Norton, 2005; Enderling et al., 2009b). Underlying this notion, each CSC can only form a cluster of limited size (Prehn, 1991), until such time as it can opportunistically migrate out of its current cluster to seed a new cluster nearby.

To show how these influences comprising the CSC hypothesis can give rise to realistic tumor growth dynamics and morphologies, we used an agent-based cellular automaton model of tumor population dynamics that considers the kinetics and interactions of CSC and CCs. Consistent with observation, we show that host-dependent variations in (a)symmetric CSC division ratios can yield tumors with substantially different CSC pool sizes and overall tumor morphologies. Furthermore, we show, by virtue of the properties of CSCs and their progeny, that the CSC fraction in a tumor grows over time, regardless of how quickly the tumor as a whole grows. As will be argued, these findings can explain the large variation in CSC fractions within and among tumors reported throughout the literature (Reya et al., 2001; Visvader and Lindeman, 2008), and offer a new paradigm for cancer development within the CSC hypothesis.

MATERIALS AND METHODS

We use an agent-based cellular automaton model to describe the behavior of individual tumor cells dependent on intrinsic mechanisms of proliferation, migration, and cell death. By tracking the fate of multiple cells over time we simulated the emergence of interacting tumor cell populations that compete for the same environment (see Deutsch and Dormann, 2005 for an overview of similar approaches). Such theoretical frameworks are increasingly utilized to investigate different aspects of the CSC hypothesis (Deasy et al., 2003; Dingli and Michor, 2006; Ganguly and Puri, 2006; Ashkenazi et al., 2007; Bankhead et al., 2007; Dingli et al., 2007b; Michor, 2008; Piotrowska et al., 2008; Galle et al., 2009; Glauche et al., 2009; Johnston et al., 2010; Sottoriva et al., 2010). Ganguly and Puri (2006) developed a compartment model of normal stem cells, early and late progenitors, and mature cells in the neural lineage as well as their abnormal counterparts. Through numerical simulation of physiologic homeostasis in their deterministic ordinary differential equation model, the authors

explored the impact of mutations in the stem cell and early progenitor populations. As stem cells have a larger proliferation potential, they found that mutations in stem cells lead to a larger tumor population growth rate. Considering normal and abnormal stem and differentiated cell populations of the hematopoietic system, Dingli and Michor (2006) showed in a simple ordinary differential equation model that successful therapy must eradicate the CSCs. Therapy that targets mature CCs or partially induces differentiation of stem cells is unable to provide tumor control. Recent mathematical investigations into the fraction of CSCs in solid tumors either assumed a fixed proportion of these cells and explored the cell kinetic parameters in a hierarchical ordinary differential equation model that lead to proportional stability in the cancer lineage (Molina-Peña and Álvarez, 2012), or simulate the exponential phase of tumor growth and observe a constant minor proportion of CSCs in an ordinary differential equation model (Johnston et al., 2010) or in a cellular automaton approach (Morton et al., 2011). Recently, Hillen et al. (2013) used reaction-birth processes and developed a mean-field integro-differential equation system to describe spatio-temporal tumor growth under the CSC hypothesis. Analyzing the simplified ordinary differential equation system of their model, the authors were able to show that tumor growth accelerates with increased cell death and that the tumor population monotonically evolves to a pure CSC state. Using a partial differential equation approach to simulate the spatio-temporal dynamics of cell lineage in solid tumors, Youssefpour et al. (2012) were able to observe complex patterning with CSCs being predominantly located in individual clusters at the outer rim of the total population in response to a variety of cellular feedback mechanisms and oxygen tension. Similar to our agent-based model investigations into CSC-driven solid tumor growth (Enderling et al., 2009a,b), Sottoriva et al. (2010) recently developed a hybrid cellular automaton model to study tumor morphology and phenotypical heterogeneity in the classical cancer model where all cells can be considered CSCs, and in the CSC model with populations heterogeneous for proliferation potential. In addition to increasing invasiveness with decreased CSC fraction, the model revealed a constant CSC fraction during exponential growth phases. While Sottoriva and co-workers assumed intratumoral proliferation through pushing adjacent cells toward the tumor periphery, we set out to explore tumor growth dynamics and morphology evolution when proliferation is restricted to the tumor outer rim as a result of competition for space in the tumor interior (Brú et al., 2003; Drasdo and Höhme, 2005; Galle et al., 2009). We will explore global cancer features in an agent-based model as a function of environmentally modulated CSC symmetric division rates as well as the proliferative potential of the CC population, and discuss evolution of the tumor population and CSC fraction during local tissue invasion.

A detailed description of the agent-based model assumptions and biological motivation can be found elsewhere (Enderling et al., 2009a,b; Enderling and Hahnfeldt, 2011). To summarize, at time $t = 0$, we initiate a single cell in the center of our computational lattice (domain) of $10 \text{ mm} \times 10 \text{ mm}$, subdivided into 1000×1000 equal-sized lattice points of $(10 \mu\text{m})^2$ that can hold at the most one cell at any time. By simulating (a)symmetric cell proliferation, migration, and cell death kinetics at discrete time intervals Δt , a

population of cancer cells emerges, which we track until it reaches 100,000 cells. In this procedure, we assume CCs are able to proliferate a certain number of times, ρ_{\max} , before inevitable cell death and ultimate removal from the simulation. For CSCs, we assume $\rho_{\max} = \infty$. CSCs divide symmetrically with fixed probability p_s , and asymmetrically with probability $1 - p_s$. Cells need to mature through the cell cycle before division can occur, which takes a cell-type-dependent time τ . With available adjacent space, a cell can migrate with rate μ . Otherwise, the cell is forced into quiescence until space becomes available. With probability α , CCs undergo spontaneous cell death and vacate the space they occupy. CSCs are assumed to be immortal ($\alpha = 0$). A flowchart of the simulation process and decisions at the cell level is shown in Figure 1.

RESULTS

SYMMETRIC STEM CELL DIVISION PROBABILITY p_s AND TUMOR GROWTH

Tumor growth is simulated and analyzed for various stem cell division probabilities $p_s = (0.1, 0.25, 0.5, 0.75, 0.99)$ and various progeny proliferation capacities $\rho_{\max} = (10, 15, 20)$, which are in line with reported progeny division potentials for different tissues (Bernard et al., 2003; Ashkenazi et al., 2007). As previously shown, tumors in which CCs have high values of ρ_{\max} grow significantly slower than tumors with CCs with limited proliferation capacity (low ρ_{\max}) (Enderling et al., 2009a). With proliferation being dependent on available space, tumor growth is restricted to cells on the outer rim of cell clusters, which is frequently observed *in vitro* and *in vivo* (Brú et al., 2003; Drasdo and Höhme, 2005; Galle et al., 2009). CSCs become “trapped” in the tumor core and are forced into quiescence until space becomes available again – either after adjacent CCs have migrated away or died. These kinetics have been shown to be inversely dependent on CC proliferation capacity and death rate (Enderling and Hahnfeldt, 2011; Morton et al., 2011).

We now relate the effect of symmetric CSC division probability p_s on tumor growth. A high symmetric CSC division probability ($p_s = 0.99$; i.e., 99%) is found to yield tumors with a very large CSC population (93%). Tumors of 100,000 cells are formed within 49 days regardless of the CC proliferation capacity. Lower symmetric stem cell division probabilities of $p_s = 75\%$ and $p_s = 50\%$ result in both a smaller stem cell compartment (15.5 and 5.4%, respectively) and more progeny CCs that act to encapsulate and slow the expansion of the available CSCs, prolonging tumor growth to 56 and 72 days, respectively, for $\rho_{\max} = 10$, and 56(63) and 226(586) days for $\rho_{\max} = 15(20)$ (Figure 2). CSC fractions are reduced further to 1.8 and 0.5% for $p_s = 25\%$ and 10% , respectively. In the latter case, tumor growth takes as long as 3351(1451 and 282) days for $\rho_{\max} = 20(15 \text{ and } 10)$, respectively.

The intrinsic and/or extrinsic mechanisms that regulate (a)symmetric CSC division are not yet understood, but modeling predicts that if the symmetric division probability is even modestly less than 100% – which it must be given the observed cell fate heterogeneity within a tumor – the CSC compartment rapidly becomes a minor subpopulation within tumors (Figure 2) and remains that way at least for a long while.

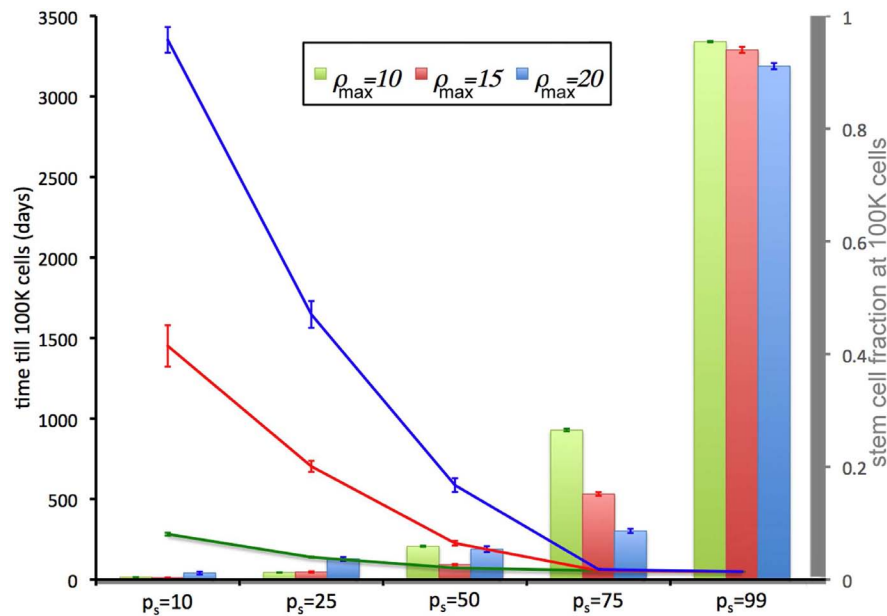


FIGURE 2 | Tumor development time and stem cell fractions depend on progeny proliferation capacity ρ_{\max} and stem cell symmetric division probability p_s . The time until the tumor reaches 100,000 cells (lines) decreases with increasing p_s . For small p_s ($p_s = 10\%$, 25%), the stem cell fraction (columns) increases with increasing progeny

proliferation capacity ρ , but for larger p_s the trend reverses. For $p_s = 50\%$ there is a *U*-shape dependence on ρ_{\max} . For $p_s \leq 75\%$, the stem cell fraction is substantially less than the symmetric division probability p_s . For $p_s = 50\%$, the average stem cell fraction in a 100,000-cell tumor is less than 5% for each ρ_{\max} .

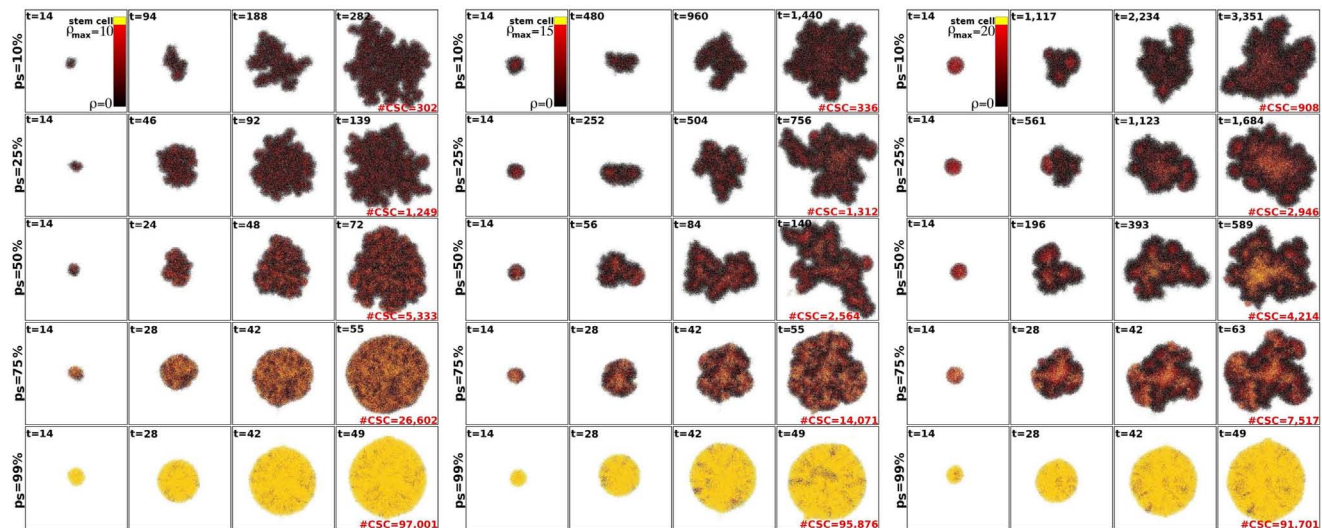


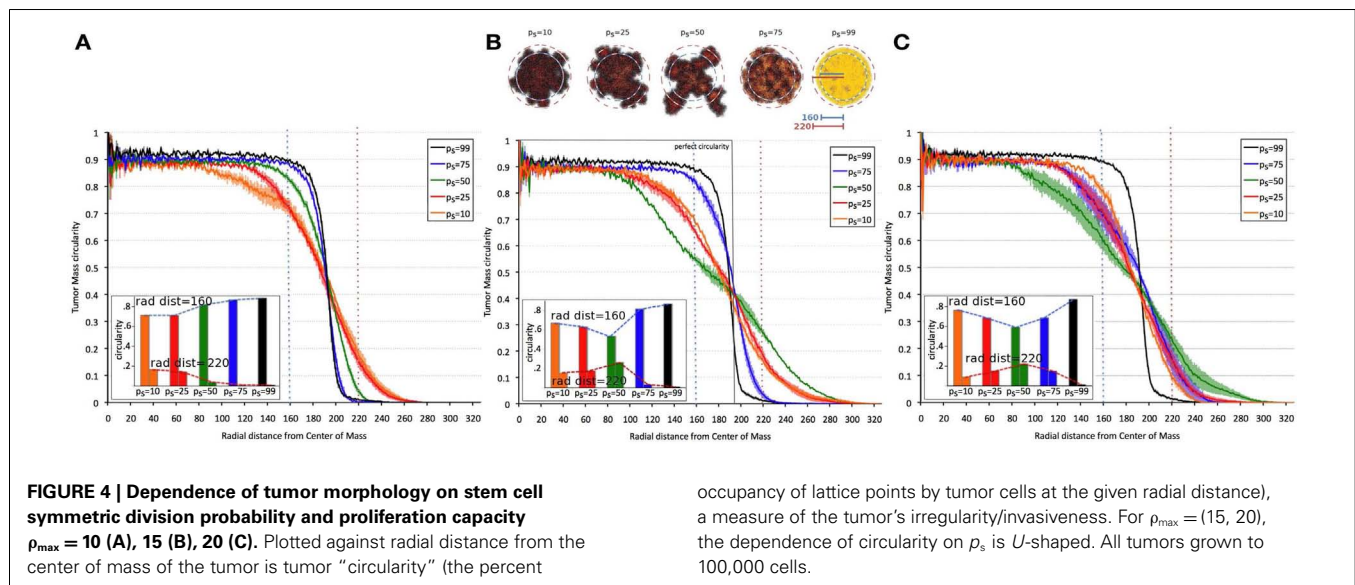
FIGURE 3 | Representative tumor morphologies for symmetric division probabilities $p_s = 10, 25, 50, 75$, and 99% (rows), and for $\rho_{\max} = 10, 15$, and 20 (panels left to right). All tumors grown to 100,000 cells.

cell fractions. Of note, in tumors with larger progeny proliferation capacities [$\rho_{\max} = (15, 20)$] there is a non-linear, *U*-shaped dependence of tumor compactness on stem cell fraction. Smaller and larger symmetric stem cell division probabilities p_s yield a more compact tumor morphology, whereas a symmetric division probability of $p_s = 50\%$ features the most invasive morphology

with the smallest dense core and the most widespread proliferative and motile regions.

STEM CELL FRACTION AS A FUNCTION OF TIME

Beyond the dependence of tumor growth dynamics on cell kinetic parameters, environmental constraints may also modulate tumor



progression and architecture. Tumors growing *in vivo* compete with the environment not only for oxygen and nutrients (which are not very limiting in the early phases of tumor growth), but also for space to grow and proliferate. Different host tissues, such as epithelial membranes or dense muscle structures (Figure 5) retard tumor progression. Single cells will eventually be able to infiltrate the tissue and thus form a path for local invasion. We introduce a “host tissue” in our computational domain by discretizing a hematoxylin-eosin (H&E)-stained tissue sample of a murine Lewis lung carcinoma – mouse muscle tissue interface. For the purpose of our study, we did not model anatomically precise cell structures but limited the tissue structure to average local cell densities (Figure 5). We introduce a single CSC in the top right corner of the domain and simulate tumor growth with either $p_s = 100\%$, representing a pure CSC tumor, or $p_s = 10\%$. Tumors consisting solely of stem cells quickly populate the empty space representative of tissue with low density, and with a reduced growth rate into the dense muscle structure and less dense tissue areas beyond. Heterogeneous tumor populations ($p_s = 10\%$) populate the less dense tissue via formation of self-metastases, as previously described (Enderling et al., 2009b), and the denser structures with a further reduced growth rate. Snapshots of the spatial distribution of 13,000 tumor cells for both tumors ($p_s = 100$ and 10%) reveal no difference in morphology (Figure 5). The circular and self-metastatic tumor morphologies evident in the respective tumors without host constraints (c.f., Figure 3) are no longer present. Instead, *in vivo* tumor morphology is dictated by host tissue architecture. What is seen, however, is a significant difference in tumor growth and growth rate history. While stem cell tumors fill the available space and form a mass of 13,000 cells within about 100 days, the heterogeneous tumor takes 20 times longer (72 months) to reach a comparable size and morphology (Figure 5). In the presented sample simulation, the empty space to the right of the muscle tissue is populated by the heterogeneous tumor within 12 months, but the invasion of the muscle structure takes significantly longer (another 60 months), during which time the overall CSC fraction goes from

60/9500 (0.6%) to 2050/13,000 (15.8%). Simulation snapshots at different time points clarify the heterogeneous tumor growth dynamics and stem cell fraction evolution (Figure 5). When the tumor population reaches the dense muscle structure, single cells try to invade the narrow gaps between muscle cells. As more than 99% of the tumor is comprised of CCs at the time invasion commences, the infiltrating and invading cells can only form small clusters of cells that eventually die out, blocking invasion routes, and inhibiting tumor invasion. Only the eventual opportunistic infiltration of a CSC results in successful metastatic seeding of these interstices within the muscle architecture. Figure 5 shows how these spaces fill with microscopic cancer nodules that over time disappear again, awaiting the chance entry of a stem cell. The necessity of rare CSCs, which are predominantly migration- and proliferation-inhibited by their own progeny as well as by host tissue, to infiltrate and invade host tissue structures can, at least in part, explain the frequently observed poor efficiency of metastatization (Luzzi et al., 1998; Wyckoff et al., 2000; Dingli et al., 2007a). As remarked, the overall CSC frequency increases over time as dying CCs get opportunistically replaced by CSCs. Such a time-dependent tumor stem cell fraction offers one plausible explanation for the wide spread of stem cell fractions reported in the literature even for tumors of the same tissue of origin (Quintana et al., 2008; Visvader and Lindeman, 2008) (c.f., Table 1). These results are amplified when the CC death rate is higher. With competition for space being a pivotal tumor-inhibiting factor, the introduction of a 10-fold higher spontaneous death rate α in CCs results in accelerated tumor growth and host tissue invasion, along with a more rapid increase in CSC number and percentage within the tumor (Figure 6).

DISCUSSION

The existence of a minor subpopulation of CSCs within a tumor that drives tumor initiation, growth, and progression is an attractive hypothesis to explain primary tumor dynamics and transplantation experiments. The existence of a minor fraction

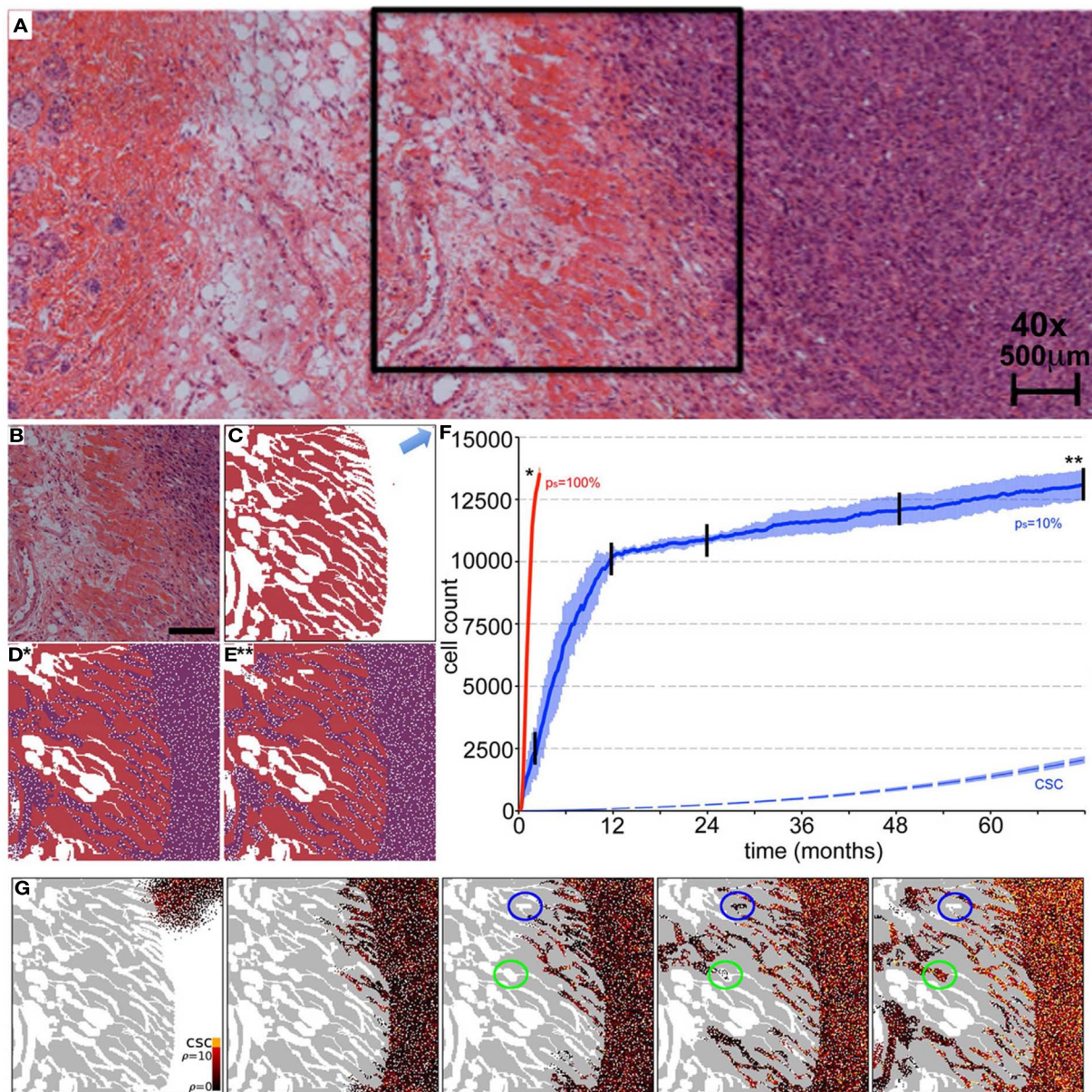


FIGURE 5 | Representative simulations of tumor growth from a single cancer stem cell and invasion of adjacent muscle and fat tissue. (A) H&E staining of an LLC tumor – host tissue interface. **(B)** Close-up of the marked region in **(A)** of the tumor outside and invading the muscle/fat tissue. Scale bar = 500 μm . **(C)** Initial condition for the computer model. Domain is initialized using an image mask of the muscle tissue identified in **(B)**. A single cancer stem cell is placed in the top right corner (arrow). **(D,E)** *In vivo* tumor morphology is dictated by host tissue architecture regardless of intrinsic tumor kinetics. **(D)** Cancer cells (purple) in a pure stem cell tumor ($p_s = 100\%$) have proliferated within the space and invaded the muscle. The simulation snapshot correlates to the time point marked by * in **(F)**. **(E)** Same as Case **(D)** but for the heterogeneous tumor ($p_s = 10\%$). The simulation snapshot correlates to the time point marked by ** in **(F)**. **(F)** Number of tumor cells over time for symmetric stem cell division probabilities $p_s = 100\%$ (red line) and $p_s = 10\%$ (blue plot). The simulation is run until both tumors reach a comparable size of 15,000 cells. The tumor composed purely of stem cells reaches this size after 100 days, whereas

the heterogeneous tumor ($p_s = 10\%$) takes more than 72 months. In the latter case, the area outside the muscle is completely occupied after 12 months, harboring 60 cancer stem cells (dashed blue plot). By time 72 months, the number of cancer stem cells outside the muscle has increased to 2050. Shown are the averages and standard deviations of 10 independent simulations **(G)** Representative simulation snapshots of different time points of tumor growth and invasion in a tumor with $p_s = 10\%$. The time points are marked in **(F)** with black vertical lines. The space adjacent to the muscle is quickly occupied, whereas the invasion of the muscle architecture takes a long time. Stem cells must invade to seed new cells in the less dense tissue within and beyond the muscles, but their invasion is inhibited by their non-stem offspring with limited proliferation capacity. Non-stem microtumors cannot be sustained and disappear over time (blue circles). Microtumors seeded by a stem cell manifest and become very stemmy (green circles). The stem cell pool in the tumor adjacent to the muscle increases steadily over time as non-stem daughter cells die off over time ($\alpha = 1\%$).

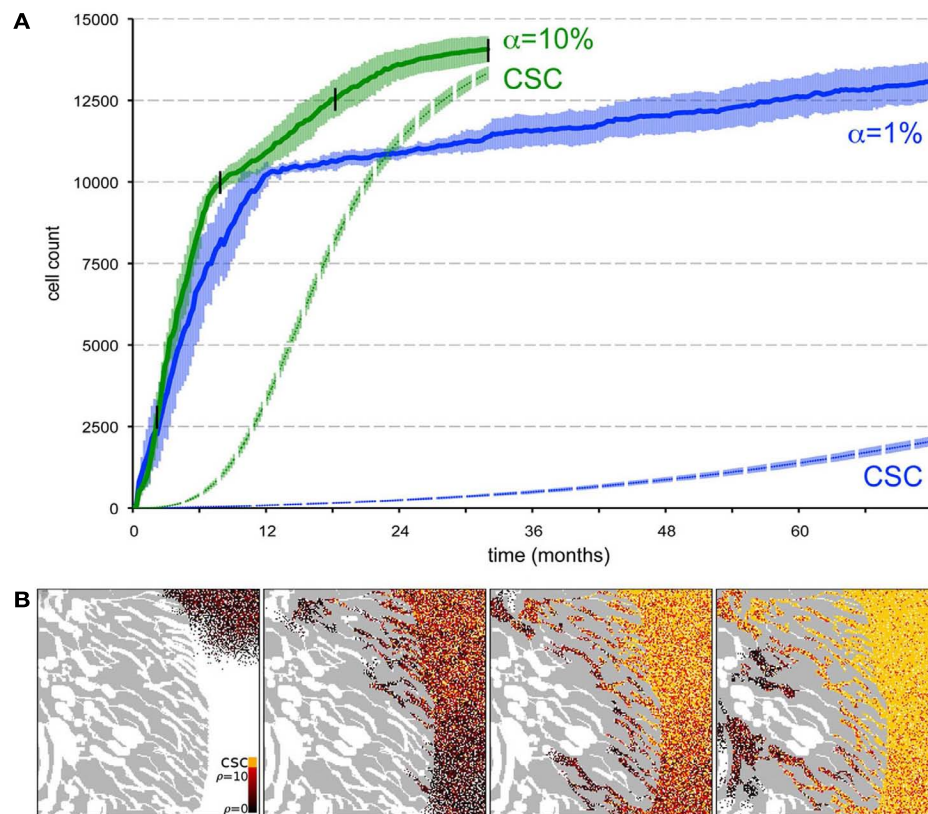


FIGURE 6 | Spontaneous cell death yields a higher stem cell fraction within the tumor and promotes tumor progression. (A) Comparison of tumor growth curves for tumors with spontaneous cell death rates $\alpha = 1\%$ (blue plot) and $\alpha = 10\%$ (green plot). Other parameters $p_s = 10\%$ and $p_{\max} = 10$. The dashed plots show the number of cancer stem in the tumor population adjacent to the muscle for both tumors. Shown are the

averages and standard deviations of 10 independent simulations. **(B)** Snapshots of different time points of tumor growth and invasion in a tumor with $\alpha = 10\%$. The time points are marked in **(A)** with black vertical lines. The stem cell pool in the tumor adjacent to the muscle increases rapidly over time as non-stem daughter cells die off quickly compared to $\alpha = 1\%$ in **Figure 5G**.

of CSCs in leukemia has long been appreciated (Furth and Kahn, 1937), but over the last 10 years or so, CSC-like populations have also been reported in solid tumors of, for example, the breast, brain, prostate, and colon (Al-Hajj et al., 2003; Singh et al., 2003; Cammareri et al., 2008; Hurt et al., 2008). The reported frequencies with which these cells occur in a tumor varies by many orders of magnitude; dependent, for example, on the chosen experimental setup and purification methods (Quintana et al., 2008; Visvader and Lindeman, 2008). Furthermore, the size of the CSC pool can be modulated by availability of certain host growth factors like EGF (Lathia et al., 2011), Sonic hedgehog (Takezaki et al., 2011), Wnt (Vermeulen et al., 2010), or Notch (Wang et al., 2009), supporting the idea of a CSC niche (He et al., 2009; Borovski et al., 2011). Here we present a cellular automaton model of tumor growth and invasion of heterogeneous cancer populations comprised of CSCs and their progeny. Simulations of the model reveal multiple indications on the fraction of CSCs in solid tumors: (i) intrinsic stem cell symmetric division probabilities results in tumors with different stem cell ratios and morphologies, (ii) CSCs are intrinsically a minor subpopulation within a tumor, and (iii) the stem cell ratio within a tumor is variable over time with intratumoral and

environmental competition for limited resources – space in the case of muscle invasion – selecting for and thus enriching in CSC fraction. In fact, competition such as for space and the resulting selection for CSCs has recently been shown to yield a pure CSC population over time (Hillen et al., 2013).

The frequency of symmetric division events in CSCs has previously been identified as a pivotal determinant of stem cell proportion experimentally (Cicalese et al., 2009) as well as in a variety of theoretical approaches including differential equations (Johnston et al., 2010), agent-based approaches (Enderling et al., 2009a), and hybrid models (Sottoriva et al., 2010).

CC proliferation capacity and the space- and time-dependent evolution of the CSC fraction in solid tumors offers a novel augmentation to the ongoing discussion about the frequencies at which CSCs are observed (Pardal et al., 2003; Quintana et al., 2008; Visvader and Lindeman, 2008). Furthermore, the CSC fraction, as determined by host environmental factors that control the symmetric division probability, determines whether the tumor exhibits an invasive or compact morphology, although the relationship is non-monotonic. Intrinsic tumor growth can be described as conglomerates of self-metastases (Enderling et al.,

2009b, 2010), but over time a solid tumor core forms with more or less invasive boundary clustering. While lower and higher stem cell fractions yield more compact morphologies, intermediate fractions result in the most invasive tumor morphologies. These results augment findings of a monotonic increase of invasiveness with decreased stem cell fraction (Sottoriva et al., 2010). When additional host spatial constraints are imposed on the growing tumor, intrinsic morphological features disappear. Conceivably, the indistinguishable pathological morphologies that result could, in a clinical setting based on empirical observations, lead to the recommendation of comparable treatment protocols. However, due to their different CSC fractions, morphologically comparable tumors could in fact demonstrate response patterns ranging from complete regression [for low CSC content (Enderling et al., 2009c)] to resistance and accelerated re-growth (Gao et al., 2013).

Herein we limited our study to early avascular tumor growth where the total population is sufficiently small such that oxygen diffusion and tension can be neglected and global tumor growth dynamics be derived from different intrinsic CC kinetics. Simulations of larger tumor volumes will require physiological extension of the model to include nutrient delivery (Anderson

and Chaplain, 1998; Ribba et al., 2004; Frieboes et al., 2007; Macklin et al., 2009) and vascular carrying capacities (Folkman, 1971; Folkman and Hochberg, 1973; Hahnfeldt et al., 1999). Furthermore, a translation from the cellular level model to a tissue-level continuous description might be more feasible to augment our understanding of the dynamics of larger populations (Hillen et al., 2013). For computational convenience we also limited this study to two spatial dimensions, but emphasize that extension to three spatial dimensions is algorithmically straightforward (Enderling et al., 2009b), with no qualitative change to be expected in the results here reported.

However, one transcendent feature expected to survive model simplifications is the possibility of widely varying stem cell compositions, highly dependent on host structural and biochemical context. This finding needs to be taken into account in both the clinical and research arenas, where heretofore, the threat has been presumed to come from the tumor bulk as a whole, not from a limited subpopulation within it.

ACKNOWLEDGMENTS

The work was supported by the National Cancer Institute under Award Number U54CA149233 (to Lynn Hlatky).

REFERENCES

- Al-Hajj, M., Wicha, M. S., Benito-Hernandez, A., Morrison, S. J., and Clarke, M. F. (2003). Prospective identification of tumorigenic breast cancer cells. *Proc. Natl. Acad. Sci. U.S.A.* 100, 3983–3988.
- Anderson, A. R. (2005). A hybrid mathematical model of solid tumour invasion: the importance of cell adhesion. *Math. Med. Biol.* 22, 163–186.
- Anderson, A. R., and Chaplain, M. A. (1998). Continuous and discrete mathematical models of tumor-induced angiogenesis. *Bull. Math. Biol.* 60, 857–899.
- Anderson, A. R., Weaver, A. M., Cummings, P. T., and Quaranta, V. (2006). Tumor morphology and phenotypic evolution driven by selective pressure from the microenvironment. *Cell* 127, 905–915.
- Ashkenazi, R., Jackson, T. L., Dontu, G., and Wicha, M. S. (2007). Breast cancer stem cells—research opportunities utilizing mathematical modeling. *Stem Cell Rev.* 3, 176–182.
- Baker, M. (2008). Melanoma in mice casts doubt on scarcity of cancer stem cells. *Nature* 456, 553.
- Bankhead, A. III, Magnuson, N. S., and Heckendorn, R. B. (2007). Cellular automaton simulation examining progenitor hierarchy structure effects on mammary ductal carcinoma in situ. *J. Theor. Biol.* 246, 491–498.
- Bernard, S., Bélair, J., and Mackey, M. C. (2003). Oscillations in cyclical neutropenia: new evidence based on mathematical modeling. *J. Theor. Biol.* 223, 283–298.
- Borowski, T., de Sousa E Melo, F., Vermeulen, L., and Medema, J. P. (2011). Cancer stem cell niche: the place to be. *Cancer Res.* 71, 634–639.
- Brú, A., Albertos, S., Luis Subiza, J., García-Asenjo, J. L., and Brú, I. (2003). The universal dynamics of tumor growth. *Biophys. J.* 85, 2948–2961.
- Cammareri, P., Lombardo, Y., Francipane, M. G., Bonventre, S., Todaro, M., and Stassi, G. (2008). Isolation and culture of colon cancer stem cells. *Methods Cell Biol.* 86, 311–324.
- Caussinus, E., and Hirth, F. (2007). Asymmetric stem cell division in development and cancer. *Prog. Mol. Subcell. Biol.* 45, 205–225.
- Cicalese, A., Bonizzi, G., Pasi, C. E., Faretta, M., Ronzoni, S., Giulini, B., et al. (2009). The tumor suppressor p53 regulates polarity of self-renewing divisions in mammary stem cells. *Cell* 138, 1083–1095.
- Deasy, B. M., Jankowski, R. J., Payne, T. R., Cao, B., Goff, J. P., Greenberger, J., et al. (2003). Modeling stem cell population growth: incorporating terms for proliferative heterogeneity. *Stem Cells* 21, 536–545.
- Deutsch, A., and Dormann, S. (2005). “Cellular automaton modeling of biological pattern formation: characterization, applications, and analysis,” in *Modeling and Simulation in Science, Engineering and Technology*, eds A. Deutsch and S. Dormann (Boston: Birkhäuser), 59–104.
- Dingli, D., and Michor, F. (2006). Successful therapy must eradicate cancer stem cells. *Stem Cells* 24, 2603–2610.
- Dingli, D., Michor, F., Antal, T., and Pacheco, J. M. (2007a). The emergence of tumor metastases. *Cancer Biol. Ther.* 6, 383–390.
- Dingli, D., Traulsen, A., and Michor, F. (2007b). (A)symmetric ion and cancer. *PLoS Comput. Biol.* 3:e53. doi:10.1371/journal.pcbi.0030053
- Drasdo, D., and Höhme, S. (2005). A single-cell-based model of tumor growth in vitro: monolayers and spheroids. *Phys. Biol.* 2, 133–147.
- Driessens, G., Beck, B., Caauwe, A., Simons, B. D., and Blanpain, C. (2012). Defining the mode of tumour growth by clonal analysis. *Nature* 488, 527–530.
- Enderling, H., Anderson, A. R., Chaplain, M. A., Beheshti, A., Hlatky, L., and Hahnfeldt, P. (2009a). Paradoxical dependencies of tumor dormancy and progression on basic cell kinetics. *Cancer Res.* 69, 8814–8821.
- Enderling, H., Hlatky, L., and Hahnfeldt, P. (2009b). Migration rules: tumours are conglomerates of self-metastases. *Br. J. Cancer* 100, 1917–1925.
- Enderling, H., Park, D., Hlatky, L., and Hahnfeldt, P. (2009c). The importance of spatial distribution of stemness and proliferation state in determining tumor radioresponse. *Math. Model. Nat. Phenom.* 4, 117–133.
- Enderling, H., and Hahnfeldt, P. (2011). Cancer stem cells in solid tumors: is “evading apoptosis” a hallmark of cancer? *Prog. Biophys. Mol. Biol.* 106, 391–399.
- Enderling, H., Hlatky, L., and Hahnfeldt, P. (2010). Tumor morphological evolution: directed migration and gain and loss of the self-metastatic phenotype. *Biol. Direct* 5, 23.
- Folkman, J. (1971). Tumor angiogenesis: therapeutic implications. *N. Engl. J. Med.* 285, 1182–1186.
- Folkman, J., and Hochberg, M. (1973). Self-regulation of growth in three dimensions. *J. Exp. Med.* 138, 745–753.
- Frieboes, H. B., Lowengrub, J. S., Wise, S., Zheng, X., Macklin, P., Bearer, E. L., et al. (2007). Computer simulation of glioma growth and morphology. *Neuroimage* 37(Suppl. 1), S59–S70.
- Furth, J., and Kahn, M. C. (1937). The transmission of leukemia of mice with a single cell. *Am. J. Cancer* 31, 276–282.
- Galle, J., Hoffmann, M., and Aust, G. (2009). From single cells to tissue architecture—a bottom-up approach to modelling the spatio-temporal organisation of complex multicellular systems. *J. Math. Biol.* 58, 261–283.
- Ganguly, R., and Puri, I. K. (2006). Mathematical model for the cancer stem cell hypothesis. *Cell Prolif.* 39, 3–14.
- Gao, X., McDonald, J. T., Hlatky, L., and Enderling, H. (2013). Acute and fractionated irradiation differentially modulate glioma stem

- cell division kinetics. *Cancer Res.* 73, 1481–1490.
- Glauche, I., Moore, K., Thielecke, L., Horn, K., Loeffler, M., and Roeder, I. (2009). Stem cell proliferation and quiescence two sides of the same coin. *PLoS Comput. Biol.* 5:e1000447. doi:10.1371/journal.pcbi.1000447
- Haeno, H., Levine, R. L., Gilliland, D. G., and Michor, F. (2009). A progenitor cell origin of myeloid malignancies. *Proc. Natl. Acad. Sci. U.S.A.* 106, 16616–16621.
- Hahnfeldt, P., Panigrahy, D., Folkman, J., and Hlatky, L. (1999). Tumor development under angiogenic signaling: a dynamical theory of tumor growth, treatment response, and postvascular dormancy. *Cancer Res.* 59, 4770–4775.
- Hambardzumyan, D., Cheng, Y.-K., Haeno, H., Holland, E. C., and Michor, F. (2011). The probable cell of origin of NF1- and PDGF-driven glioblastomas. *PLoS ONE* 6:e24454. doi:10.1371/journal.pone.0024454
- Hanahan, D., and Weinberg, R. A. (2000). The hallmarks of cancer. *Cell* 100, 57–70.
- Hanahan, D., and Weinberg, R. A. (2011). Hallmarks of cancer: the next generation. *Cell* 144, 646–674.
- Hatzikirou, H., Brusch, L., Schaller, C., Simon, M., and Deutsch, A. (2010). Prediction of traveling front behavior in a lattice-gas cellular automaton model for tumor invasion. *Comput. Math. Appl.* 59, 2326–2339.
- He, S., Nakada, D., and Morrison, S. J. (2009). Mechanisms of stem cell self-renewal. *Annu. Rev. Cell Dev. Biol.* 25, 377–406.
- Hillen, T., Enderling, H., and Hahnfeldt, P. (2013). The tumor growth paradox and immune system-mediated selection for cancer stem cells. *Bull. Math. Biol.* 75, 161–184.
- Hurt, E. M., Kawasaki, B. T., Klarman, G. J., Thomas, S. B., and Farrar, W. L. (2008). CD44+ CD24 (-) prostate cells are early cancer progenitor/stem cells that provide a model for patients with poor prognosis. *Br. J. Cancer* 98, 756–765.
- Johnston, M. D., Maini, P. K., Jonathan Chapman, S., Edwards, C. M., and Bodmer, W. F. (2010). On the proportion of cancer stem cells in a tumour. *J. Theor. Biol.* 266, 708–711.
- Lathia, J. D., Hitomi, M., Gallagher, J., Gadani, S. P., Adkins, J., Vasanji, A., et al. (2011). Distribution of CD133 reveals glioma stem cells self-renew through symmetric and asymmetric cell divisions. *Cell Death Dis.* 2, e200.
- Luzzi, K. J., MacDonald, I. C., Schmidt, E. E., Kerkvliet, N., Morris, V. L., Chambers, A. F., et al. (1998). Multistep nature of metastatic inefficiency: dormancy of solitary cells after successful extravasation and limited survival of early micrometastases. *Am. J. Pathol.* 153, 865–873.
- Macklin, P., McDougall, S., Anderson, A. R., Chaplain, M. A., Cristini, V., and Lowengrub, J. (2009). Multiscale modelling and nonlinear simulation of vascular tumour growth. *J. Math. Biol.* 58, 765–798.
- Michor, F. (2008). Mathematical models of cancer stem cells. *J. Clin. Oncol.* 26, 2854–2861.
- Molina-Peña, R., and Álvarez, M. M. (2012). A simple mathematical model based on the cancer stem cell hypothesis suggests kinetic commonalities in solid tumor growth. *PLoS ONE* 7:e26233. doi:10.1371/journal.pone.0026233
- Morton, C. I., Hlatky, L., Hahnfeldt, P., and Enderling, H. (2011). Non-stem cancer cell kinetics modulate solid tumor progression. *Theor. Biol. Med. Model.* 8, 48.
- Norton, L. (2005). Conceptual and practical implications of breast tissue geometry: toward a more effective, less toxic therapy. *Oncologist* 10, 370–381.
- Pardal, R., Clarke, M. F., and Morrison, S. J. (2003). Applying the principles of stem-cell biology to cancer. *Nat. Rev. Cancer* 3, 895–902.
- Piotrowska, M. J., Enderling, H., van der Heiden, U., and Mackey, M. C. (2008). “Mathematical modeling of stem cells related to cancer,” in *Cancer and Stem Cells*, eds T. Dittmar and K. S. Zaenker (New York: Nova Science Publishers, Inc.).
- Prehn, R. T. (1991). The inhibition of tumor growth by tumor mass. *Cancer Res.* 51, 2–4.
- Quintana, E., Shackleton, M., Sabel, M. S., Fullen, D. R., Johnson, T. M., and Morrison, S. J. (2008). Efficient tumour formation by single human melanoma cells. *Nature* 456, 593–598.
- Rahman, R., Heath, R., and Grundy, R. (2009). Cellular immortality in brain tumours: an integration of the cancer stem cell paradigm. *Biochim. Biophys. Acta* 1792, 280–288.
- Reya, T., Morrison, S. J., Clarke, M. F., and Weissman, I. L. (2001). Stem cells, cancer, and cancer stem cells. *Nature* 414, 105–111.
- Ribba, B., Alarcón, T., Marron, K., Maini, P. K., and Agur, Z. (2004). “The use of hybrid cellular automaton models for improving cancer therapy,” in *Proceedings, Cellular Automata: 6th International Conference on Cellular Automata for Research and Industry, ACRI, 2004, Lecture Notes in Computer Science 3305*, eds P. M. A. Soot, B. Chopard, and A. G. Hoekstra (Berlin: Springer-Verlag), 444–453.
- Shibata, M., and Shen, M. M. (2013). The roots of cancer: stem cells and the basis for tumor heterogeneity. *Bioessays* 35, 253–260.
- Singh, S. K., Clarke, I. D., Terasaki, M., Bonn, V. E., Hawkins, C., Squire, J., et al. (2003). Identification of a cancer stem cell in human brain tumors. *Cancer Res.* 63, 5821–5828.
- Sottoriva, A., Spiteri, I., Shibata, D., Curtis, C., and Tavaré, S. (2013). Single-molecule genomic data delineate patient-specific tumor profiles and cancer stem cell organization. *Cancer Res.* 73, 41–49.
- Sottoriva, A., Verhoeff, J. J., Borovski, T., McWeeney, S. K., Naumov, L., Medema, J. P., et al. (2010). Cancer stem cell tumor model reveals invasive morphology and increased phenotypical heterogeneity. *Cancer Res.* 70, 46–56.
- Stiles, C. D., and Rowitch, D. H. (2008). Glioma stem cells: a midterm exam. *Neuron* 58, 832–846.
- Takezaki, T., Hide, T., Takanaga, H., Nakamura, H., Kuratsu, J., and Kondo, T. (2011). Essential role of the Hedgehog signaling pathway in human glioma-initiating cells. *Cancer Sci.* 102, 1306–1312.
- Vermeulen, L., de Sousa, E., Melo, F., van der Heijden, M., Cameron, K., de Jong, J. H., et al. (2010). Wnt activity defines colon cancer stem cells and is regulated by the microenvironment. *Nat. Cell Biol.* 12, 468–476.
- Visvader, J. E., and Lindeman, G. J. (2008). Cancer stem cells in solid tumours: accumulating evidence and unresolved questions. *Nat. Rev. Cancer* 8, 755–768.
- Vlashi, E., Kim, K., Lagadec, C., Donna, L. D., McDonald, J. T., Eghbali, M., et al. (2009). In vivo imaging, tracking, and targeting of cancer stem cells. *J. Natl. Cancer Inst.* 101, 350–359.
- Wang, Z., Li, Y., Banerjee, S., and Sarkar, F. H. (2009). Emerging role of Notch in stem cells and cancer. *Cancer Lett.* 279, 8–12.
- Wyckoff, J. B., Jones, J. G., Condeelis, J. S., and Segall, J. E. (2000). A critical step in metastasis: in vivo analysis of intravasation at the primary tumor. *Cancer Res.* 60, 2504–2511.
- Youssefpour, H., Li, X., Lander, A. D., and Lowengrub, J. S. (2012). Multispecies model of cell lineages and feedback control in solid tumors. *J. Theor. Biol.* 304, 39–59.

Conflict of Interest Statement: The authors declare that the research was conducted in the absence of any commercial or financial relationships that could be construed as a potential conflict of interest.

Received: 15 January 2013; accepted: 24 March 2013; published online: 15 April 2013.

Citation: Enderling H, Hlatky L and Hahnfeldt P (2013) Cancer stem cells: a minor cancer subpopulation that redefines global cancer features. *Front. Oncol.* 3:76. doi: 10.3389/fonc.2013.00076

This article was submitted to *Frontiers in Molecular and Cellular Oncology*, a specialty of *Frontiers in Oncology*. Copyright © 2013 Enderling, Hlatky and Hahnfeldt. This is an open-access article distributed under the terms of the Creative Commons Attribution License, which permits use, distribution and reproduction in other forums, provided the original authors and source are credited and subject to any copyright notices concerning any third-party graphics etc.



Mathematical optimization of the combination of radiation and differentiation therapies for cancer

Jeff W. N. Bachman and Thomas Hillen*

Department of Mathematical and Statistical Sciences, Centre for Mathematical Biology, University of Alberta, Edmonton, AB, Canada

Edited by:

Katarzyna A. Rejniak, H. Lee Moffitt
Cancer Center and Research Institute,
USA

Reviewed by:

John D. Nagy, Arizona State
University, USA
Marek Kimmel, Rice University, USA

*Correspondence:

Thomas Hillen, Department of
Mathematical and Statistical
Sciences, Centre for Mathematical
Biology, University of Alberta, 632
Central Academic Building,
Edmonton, AB T6G 2G1, Canada.
e-mail: thillen@ualberta.ca

Cancer stem cells (CSC) are considered to be a major driver of cancer progression and successful therapies must control CSCs. However, CSC are often less sensitive to treatment and they might survive radiation and/or chemotherapies. In this paper we combine radiation treatment with differentiation therapy. During differentiation therapy, a differentiation promoting agent is supplied (e.g., TGF- β) such that CSCs differentiate and become more radiosensitive. Then radiation can be used to control them. We consider three types of cancer: head and neck cancer, brain cancers (primary tumors and metastatic brain cancers), and breast cancer; and we use mathematical modeling to show that combination therapy of the above type can have a large beneficial effect for the patient; increasing treatment success and reducing side effects.

Keywords: cancer stem cells, tumor stem cells, radiation treatment, differentiation therapy, combination therapy, cancer modeling

1. INTRODUCTION

Cancer stem cells (CSC) have been identified in many cancer types as the driving force behind cancer growth and progression (Dick, 2003; Singh et al., 2003; Sell, 2004; Todaro et al., 2007; Maitland and Colling, 2008. Dingli and Michor (2006) attested as title of their 2006 paper that “Successful therapy must eradicate cancer stem cells.” This is hard to do, since CSC can be found at any location in the tumor (Youssefpour et al., 2012) and they are difficult to identify *in vivo* (Kummermehr, 2001). Furthermore, cancer stem cells are less sensitive to radiation or other cell killing agents (Kim and Tannock, 2005; Pajonk et al., 2010). One method to sensitize cancer stem cells is to use differentiation promoting growth factors that force CSCs to differentiate and become more sensitive to radiation. Possible differentiation promoters, which are discussed in the literature, are members of the TGF- β superfamily (Transforming growth factor – β ; see Lander et al., 2009; Watabe and Miyazono, 2009; Meulmeester and Ten Dijke, 2011). TGF- β is known to increase stem cell differentiation, but it also affects other characteristics of growing tumors such as invasion and immune evasion. Here we focus on the differentiation stimulating properties of TGF- β . Other examples of differentiation therapy agents include ATRA-therapy (all-trans-retinoic acid) for acute promyelocytic leukemia (Sell, 2004) and a combination of INF- β (interferon-beta) and MEZ (mezerein) for treatment of melanoma (Leszczyniecka et al., 2001). Many more agents are currently investigated for their differentiation promoting activities (Leszczyniecka et al., 2001).

The mathematical modeling of cancer progression and treatment has a long history and individual treatments as well as combination therapies have been studied. A comprehensive review is given in Swierniak et al. (2009).

Our modeling and analysis of differentiation therapy and the combination with radiation therapy was motivated through a

detailed computational model of Youssefpour et al. (2012). The model of Youssefpour et al. (2012) consist of a coupled system of partial differential equations for CSC, transient amplifying cells (TAC), differentiated cancer cells (DC), growth factors and growth inhibiting factors, and differentiation promoters. In addition, the model is spatially explicit and physical properties related to pressure and force balances are included. This model was developed over a series of publications (see Wise et al., 2008 and references therein).

Youssefpour et al. (2012) combine the detailed cancer model with differentiation therapy and with radiation therapy. They find that an appropriate combination of differentiation therapy and radiation therapy can control the cancer in situations where each individual treatment would fail. Their treatment terms are generic terms for differentiation and radiation treatments and they have not been modeled for a specific cancer type. The goal of this paper is to challenge Youssefpour’s findings for the specific cases of head and neck cancer, brain cancers, and breast cancer. We adapt the model of Youssefpour et al. (2012) to be able to include realistic growth and death rates, realistic differentiation therapies, realistic radiation therapy schedules, and appropriate tissue dependent radio-sensitivities. We sacrifice, however, the spatial structure of the model and we study the well mixed, spatially homogeneous situation. We argue that if the effect of combination therapy can be clearly demonstrated on a simpler model, then this mechanism will be part of a more complicated model as well. We find that for average parameters of brain cancers and for breast cancer we can confirm the finding of Youssefpour et al. (2012) in that, combination therapy can control a tumor, where each individual method would fail. For head and neck cancer, we find that differentiation therapy can drastically reduce the amount of radiation that is needed to control the tumor.

2. MATERIALS AND METHODS

We use mathematical modeling and numerical simulations to predict the outcome of these therapies. Our mathematical model is based on a model for cancer stem cells that was derived in Hillen et al. (2013). It describes the interplay of cancer stem cells $U(t)$ and non-stem cancer cells $V(t)$. To describe radiation therapy we use the well-established linear quadratic model (see Fowler, 1989) with realistic standard treatments (five treatments per week, week-ends off) and with tissue specific radiosensitivity parameters α and β (see Fowler, 1989). The parameterization of differentiation therapy is more difficult, since differentiation promoters are hard to quantify. Here we use the model and parameters of Youssefpour et al. (2012).

2.1. THE MATHEMATICAL MODEL

We begin with the spatially homogeneous, cancer stem cell model developed by Hillen et al. (2013). By spatial homogeneity, we mean that cell density, cell growth, and the distribution of chemicals are homogeneous throughout the tumor region.

$$\dot{U}(t) = \delta m_U k(P(t)) U(t) \quad (1)$$

$$\begin{aligned} \dot{V}(t) = & (1 - \delta) m_U k(P(t)) U(t) \\ & + m_V k(P(t)) V(t) - a_V V(t) \end{aligned} \quad (2)$$

where $U(t)$ is the volume fraction of cancer stem cells (CSCs) with respect to the total domain of interest, which contains both tumor and host cells. Similarly, $V(t)$ is the volume fraction of non-stem tumor cells (TCs) with respect to the total domain of interest. The total volume fraction of the tumor is represented by $P(t)$, that is, $P(t) = U(t) + V(t)$. The parameter δ is the probability that a CSC will give rise to another CSC, when it divides. Thus, $1 - \delta$ is the probability that a CSC will give rise to one CSC and one TC, when it divides. It is assumed that the parent CSC remains (Sell, 2004). The growth rates of the CSCs and TCs are given by m_U and m_V , respectively. The apoptosis rate of the TCs is represented by a_V ; we assume that CSCs do not undergo apoptosis since they have unlimited replicative potential. Cell growth and differentiation are tempered by $k(P(t))$, which is essentially a volume constraint. Hillen et al. (2013) assume that $k(P)$ is monotonically decreasing in P and piecewise differentiable, and they set $k(P) > 0$ for $P \in [0, P^*)$ and $k(P) = 0$ for all $P \geq P^*$, for some $P^* > 0$. For the purposes of this paper, we adopt the version of $k(P)$ used by Hillen et al. (2013) and assume normalization of $P^* = 1$ limiting P to a maximum volume fraction of one, and $k(0) = 1$. For simulations we use:

$$k(P) = \max \{1 - P^4, 0\} \quad (3)$$

To match the notation used by Youssefpour et al. (2012) we set $\delta = 2p - 1$. It follows that $1 - \delta = 2(1 - p)$. In this case, p is the probability that a CSC gives rise to two CSCs, rather than two TCs, when it divides. That is, p is the probability that a CSC renews itself, and $1 - p$ is the probability that a CSC differentiates. While this model of CSC division ignores asymmetric division, it is equivalent to the model in equations (1) and (2), as shown in

the Appendix of Hillen et al. (2013). The resulting model is given in equations (4) and (5).

$$\dot{U}(t) = (2p - 1) m_U k(P(t)) U(t) \quad (4)$$

$$\begin{aligned} \dot{V}(t) = & 2(1 - p) m_U k(P(t)) U(t) \\ & + m_V k(P(t)) V(t) - a_V V(t) \end{aligned} \quad (5)$$

2.2. BEHAVIOR OF THE UNTREATED TUMOR MODEL

As noted in Hillen et al. (2013), if there are no CSCs, the TC population is governed by the equation

$$\dot{V}(t) = m_V k(V(t)) V(t) - a_V V(t)$$

and since k is assumed to be decreasing, the TC population is fated to die out if $m_V k(0) < a_V$. Further, if we assume that k is strictly decreasing, then the TC population dies out if

$$m_V k(0) \leq a_V \quad (6)$$

since either $V = 0$ and the TCs are already extinct, or $V > 0$ and so $k(V) < k(0)$ and $m_V k(V) < a_V$ for all $V > 0$.

The steady states of the model defined in (1, 2) are discussed in detail in Hillen et al. (2013), where it is assumed that the growth rates m_U and m_V are both one and that the TC apoptosis rate a_V is greater than zero. Here, we give the main results, which also apply to the model as stated in (1, 2) or equivalently in (4, 5). We note that in the untreated tumor, we assume $\delta \in (0, 1)$, that is $p \in (0.5, 1)$, such that $(2p - 1) > 0$. The steady states of the system are

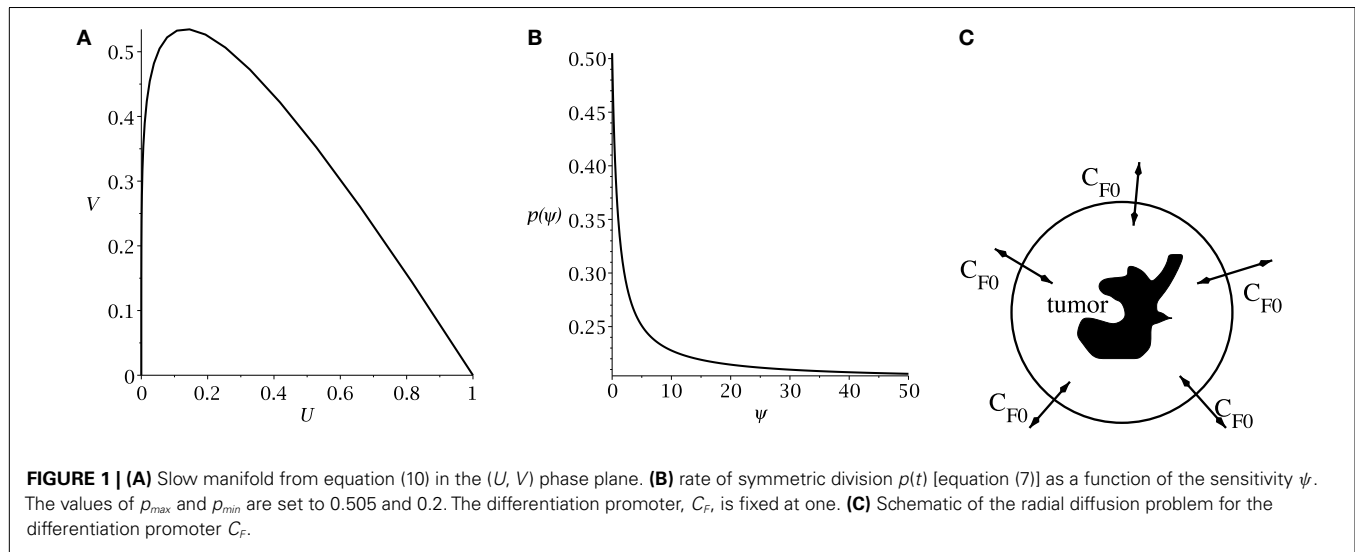
$$\begin{aligned} X_0 = (0, 0), \quad X_V = (0, V_0), \quad X_U = (1, 0), \\ \text{with } k(V_0) = \frac{a_V}{m_V}. \end{aligned}$$

The origin, X_0 , has eigenvalues $\lambda_1 = (2p - 1) m_U k(0) > 0$ and $\lambda_2 = m_V k(0) - a_V$. Thus, X_0 is an unstable steady state. The TC only steady state, X_V , occurs where V_0 solves $m_V k(V_0) = a_V$ and has eigenvalues $\lambda_1 = (2p - 1) m_U k'(V_0) > 0$ and $\lambda_2 = m_V k'(V_0) V_0$. Thus, X_V is also unstable. The linearization for the pure CSC steady state, X_U , has negative trace, $m_U k'(1) - a_V$, and positive determinant, $-a_V(2p - 1) m_U k'(1)$, thus both eigenvalues are negative, and X_U is a stable steady state. Hillen et al. (2013) have shown that X_U is globally asymptotically stable in the biologically relevant region where $U \in [0, 1]$, $V \geq 0$, and $U + V \leq 1$.

Hillen et al. (2013) derive the slow manifold of the system defined by (1, 2), where they take $m_U = m_V = 1$. The slow manifold is a subset of the phase space $((U, V)$ -plane) which describes the long time dynamics of the system. As shown in Hillen et al. (2013), solutions very quickly converge to the slow manifold, and then they slowly follow this manifold getting closer to the attractor at $(1, 0)$. This same slow manifold applies to the system defined by equations (4) and (5). We simply restore m_U and m_V and set $\delta = 2p - 1$, as described above, giving the slow manifold (see Figure 1A):

$$M := \{(U, V) : (a_V - m_V k(P)) V = m_U k(P) U, P = U + V\}$$

The main result of Hillen et al. (2013) is the existence of the *Tumor Growth Paradox*. They show that a tumor with larger death



rate a_V grows quicker on the slow manifold. As a consequence, tumors with larger death rate outgrow tumors with lower death rate. The reason is that increased TC death can liberate CSC which were surrounded by TC, and it can allow CSC to replicate and produce more CSCs. As a result, the tumor becomes bigger. See Hillen et al. (2013) for the detailed argumentation using geometric singular perturbation analysis of the system.

2.3. MODELING OF DIFFERENTIATION THERAPY

Following Youssefpour et al. (2012), we model differentiation therapy through a simple relationship between the average level of the differentiation promoter, which we denote C_F , and the probability of CSC self-renewal, p . Unlike the model of Youssefpour et al. (2012) our model does not include a self-renewal promoter; thus, we use the relationship set forth by Youssefpour et al. (2012) but we omit the self-renewal promoting factor:

$$p(t) = p_{min} + (p_{max} - p_{min}) \left(\frac{1}{1 + \psi C_F(t)} \right) \quad (7)$$

where p_{max} is the maximum probability of self-renewal, and p_{min} is the minimum probability of self-renewal. The value of p_{max} is attained if no differentiation promoter C_F is present, while p_{min} is attained for $C_F \rightarrow \infty$. Youssefpour et al. (2012) choose $p_{max} = 1$ and $p_{min} = 0.2$ in their therapy simulations. Unlike Youssefpour and coworkers, we do not model the production of differentiation promoters by tumor cells. Thus, C_F solely represents the level of differentiation promoter prescribed during differentiation therapy. To address this lack of endogenous differentiation promoters, we choose $p_{max} = 0.505$, which is equivalent to setting $\delta = 0.01$, as was done by Hillen et al. (2013). Following Youssefpour et al. (2012) we choose $p_{min} = 0.2$. The parameter ψ models the sensitivity of the CSCs to the differentiation promoter. The dependence of $p(t)$ on the sensitivity ψ is shown in Figure 1B. Other possible effects of differentiation therapy, such as effects on growth rates, are ignored, as they are by Youssefpour et al. (2012).

To model the average level of differentiation promoter within the spatially homogeneous tumor as a function of time, $C_F(t)$,

we assume that the tumor resides in a spherical region of tissue and that the differentiation promoter enters this area through the boundary. The ODE system [equations (4) and (5)] gives the mean tumor behavior in this spherical tissue region. Growth promoter that enters the region from the boundary will diffuse very quickly and attain a steady state distribution over this region. To compute this value of $C_F(t)$ we solve the problem of diffusion over a sphere of radius R and average the solution over the volume of the sphere. A schematic is given in Figure 1C. We use a lower case letter to describe the radial symmetric solution $c_F(r, t)$ of the following boundary value problem

$$\frac{\partial c_F}{\partial t} = \omega \left(\frac{\partial}{\partial r} \left(\frac{\partial c_F}{\partial r} \right) + \frac{2}{r} \frac{\partial c_F}{\partial r} \right)$$

$$c_F(R, t) = C_{F0}(t).$$

Here ω is the effective diffusivity of the differentiation promoter. We set $\omega = 10^{-7} \text{ cm}^2/\text{s}$ throughout our simulations. Before differentiation therapy begins, $C_{F0}(t)$ is zero. When differentiation therapy begins, the boundary condition on the sphere is set to $C_{F0}(t) = 1$ and the promoter diffuses into the sphere. When differentiation therapy ends, the boundary condition is simply set to zero and the promoter diffuses out of the sphere. We then set

$$C_F(t) = \frac{3}{R^3} \int_0^R c_F(r, t) r^2 dr.$$

2.4. MODELING OF RADIATION THERAPY

To model external beam fractionated radiotherapy, we apply the broadly used linear quadratic (LQ) model. The surviving fraction of cells, $S(d)$, after a single fraction of d grays (Gy) of radiation, is given by

$$S(d) = \exp(-\alpha d - \beta d^2) \quad (8)$$

where α may be interpreted as lethal damage due to a single track of radiation, and β may be interpreted as lethal damage due to

the misrepair of DNA damage produced by two separate tracks of radiation (Sachs et al., 2001). As a simple approximation of the radiation resistance of CSCs, we assume that they are better able to repair DNA double strand breaks such that the quadratic interaction term β is zero for CSC. We further assume that there is no interaction between DNA damage produced by separate fractions of radiation, owing to the relatively large time between fractions, typically 1 day, when compared to typical DNA repair times on the order of 1 h (O'Rourke et al., 2009).

Rather than incorporate an appropriate form of the LQ model into the system of ODEs [equations (4) and (5)], we simply apply equation (8) to the CSC volume fraction, U , and to the TC volume fraction, V , at scheduled times during the simulation, using α and β values appropriate for each cell type. For example, if a fraction is scheduled to be delivered at the beginning of the two-hundredth day of the simulation, the simulation is stopped at this time, the LQ model is applied to U and V , using their respective parameter values, and the simulation is continued at 200 days plus the fraction duration, using the surviving fractions given by equation (8) as the new initial conditions. We assume fraction durations of 10 min throughout our simulations.

2.5. TUMOR CONTROL PROBABILITY

We use tumor control probability (TCP) to model the probability that the cells remaining after treatment will die out. To reflect the fact that we must eliminate all CSCs for treatment success (Dingli and Michor, 2006), and the fact that TCs are doomed to die out in the absence of CSCs, we calculate TCP based on the number of CSCs remaining after treatment, using the Poisson TCP formula (see Gong et al., 2013 for Poisson TCP and other TCP models).

$$TCP = \exp(-N_U) \approx \exp\left(-U \frac{4}{3} \pi R^3 \rho\right) \quad (9)$$

where N_U stands for the number of CSCs; R is the radius of the spherical region of interest in cm, as described in the section on differentiation therapy; and ρ is the density of cells in the region of interest, which we assume to be 10^9 cells per cm^3 , a typical cell density for tumors (for example, see Joiner et al., 2009). The closer TCP is to one, the greater the probability that all CSCs die out and the tumor is controlled.

2.6. NUMERICAL SIMULATIONS

For all numerical simulations of the tumor model [equations (4) and (5)] we assume the mitosis rates of the CSCs and TCs are equal. That is, $m_U = m_V$. Further, following Youssefpour et al. (2012), we assume the apoptosis and mitosis rates of the TCs are equal: $a_V = m_V$. These assumptions imply that the TC populations dies out if $k(0) \leq 1$, which is equation (6) for this case. When combined with our earlier assumptions regarding $k(P)$ and with our chosen form for $k(P)$ [equation (3)], we see that in our model TCs are always doomed to die out in the absence of CSCs. Our assumptions regarding the mitosis rates and TC apoptosis rate also simplify the form of the slow manifold to

$$M := \{(U, V) : (1 - k(P)) V = k(P) U, P = U + V\} \quad (10)$$

for all simulations.

Whenever we apply radiation therapy, we assume no difference in the ability of CSCs and TCs to withstand lethal single track damage. Thus, we use the same α value for both cell types. As mentioned previously, we set $\beta = 0$ for CSCs to simulate perfect repair of two-track non-lethal damage.

All numerical simulations are carried out in Maple™, using the dsolve ODE solver employing the rkf45 numerical method. For every simulation, the initial conditions are $(U_0, V_0) = (0.1, 0.1)$, and therapy begins on the two-hundredth day. These settings allow the tumor system to hit the slow manifold, M , before treatment begins, in each of our simulations.

To prevent negative volume fractions during numerical simulation, we introduce a simple cutoff function

$$G(x) = \begin{cases} 1, & x > \lambda \\ 0, & x \leq \lambda \end{cases} \quad (11)$$

where λ is chosen to allow the TCP to approach one before the cutoff is imposed. The system we use for numerical simulation, incorporating the cutoff function is

$$\begin{aligned} \dot{U}(t) &= (2p - 1)mk(P(t))U(t)G(U(t)) \\ \dot{V}(t) &= 2(1 - p)mk(P(t))U(t)G(U(t)) \\ &\quad + mk(P(t))V(t)G(V(t)) - mV(t)G(V(t)) \end{aligned}$$

where $m = m_U = m_V = a_V$.

As a measure of treatment success, we calculate the TCP [equation (9)] using the value of U obtained at the end of treatment, which is defined as the latter of: (a) the completion of the final radiation fraction, and (b) the point in time when $p(t)$ reaches 0.5, after differentiation therapy has ended. This second point (b), accounts for the effect of lingering differentiation promoter, after the promoter is no longer being applied.

3. RESULTS

We summarize the chosen parameter values in Table 1 and we give relevant references and explanations in the following subsections.

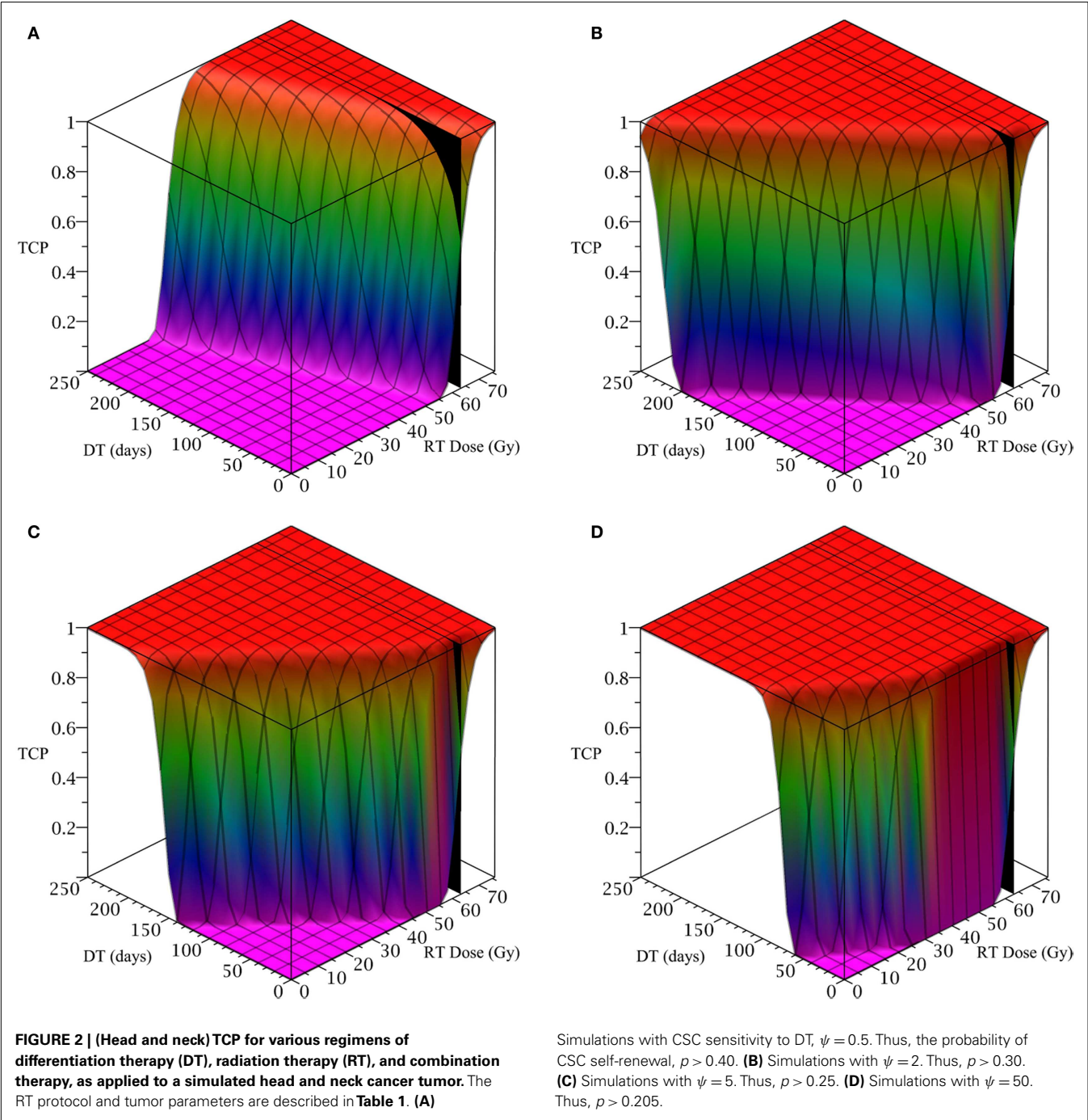
3.1. HEAD AND NECK CANCER TUMOR SIMULATIONS

To simulate head and neck tumor, we choose the following parameter values for the LQ model: an α/β ratio of 10 Gy and an α value of 0.35 Gy^{-1} (Fowler, 2010). We set the mitosis rates of the TCs and CSCs to $\ln 2/3 \text{ day}^{-1}$, using a cell doubling time of 3 days as per Fowler (2010). We note that this is an estimate of cell doubling time for cells undergoing cytotoxic treatment, which tend to have shorter doubling times than untreated cells (Fowler, 2010). For the radius of the domain of interest, R , we choose 1.5 cm. All simulations of radiation therapy use fraction sizes of 2.53 Gy, delivered once per day, on weekdays only. We used one of the optimized head and neck radiation schedules recommended by Fowler as a constraint on radiotherapy, which is 25 fractions of 2.53 Gy each, for a total of 63.25 Gy delivered over 32 days (Fowler, 2010). This schedule is optimized to satisfy a late tissue constraint of 70 Gy EQD_{3/2} and an acute mucosal constraint of 51 Gy EQD_{10/2} while delivering the maximum possible BED to the tumor, given the chosen fraction size and weekday only schedule (Fowler, 2010). We indicate the position of this schedule in Figure 2 using a black

Table 1 | Summary of model parameters for the three cancers studied here.

Cancer	α/β [Gy]	α [Gy ⁻¹]	β [Gy ⁻²]	m [day ⁻¹]	R [cm]	d [Gy]	Max D [Gy]
Head and neck	10	0.35	0.035	ln 2/3	1.5	2.53	63.25
Brain cancer	12	0.3	0.025	ln 2/3.9	1.9	3.8	57.5
Breast	2.88	0.08	0.0027	ln 2/8.2	0.25	2.26	65.54

All radiation treatment schedules are standard treatments, with one fraction each week day and weekends off. Further references and explanations are given in the text below.



plane at 63.25 Gy, which we take as our constraint on radiation therapy.

The only parameter not yet specified is the sensitivity ψ toward the differentiation promoter and we have no experimental data available. In **Figure 2**, we show four simulations of the tumor control probability for four different sensitivities $\psi = 0.5, 2, 5, 50$ which covers a wide range of possible values. The x -axis denotes the duration of the differentiation treatment and the y -axis denotes the total radiation dose. The black plane indicates the maximum tolerable radiation dose in this particular treatment. The colored plane is the tumor control probability (TCP). We see in all four Figures that the TCP is 0 near the origin and it rises sharply to values close to one as both treatment modalities are increased. In **Figure 2B** for example, we see that radiation alone reaches a TCP of about 60% for the maximum dose. In combination with differentiation therapy of 50 days, we observe treatment success already at total dose of 40 Gray. This effect is more pronounced for higher sensitivity parameter ψ . Notice that the curve for 0 DT days is the same in all four figures.

A good quantitative measurement for efficiency of a treatment is the TCP = 50% value. To illustrate how the treatment regimens change for a fixed TCP, we list a few treatment regimens that result in a 50% TCP in **Table 2**. We see that for large enough sensitivity ψ , the total radiation dose can be drastically reduced if differentiation therapy is applied.

3.2. BRAIN CANCER SIMULATIONS

To simulate a brain cancer, we use an average α/β ratio of 12 Gy and α value of 0.3 Gy^{-1} , as estimated by Yuan et al. (2008) for brain cancers (primary tumors as well as brain metastatic cancers). This gives a β value of 0.025 Gy^{-2} . For the radius of the domain of interest, R , we use 1.9 cm, which is roughly the radius of a sphere of volume 28.8 cm^3 , the volume of a brain metastatic cancer arising from non-small-cell lung cancer, reported in the same paper (Yuan et al., 2008). For the CSC and TC growth rates, we use

In $2/3.9 \text{ day}^{-1}$, where 3.9 is an estimate of the mean potential doubling time of brain metastatic cancer originating from various primary cancers, as measured by flow cytometry (Struikmans et al., 1997). All simulations involving radiation use a fraction size of 3.8 Gy, delivered once per day on weekdays only. This fraction size is listed by Yuan et al. (2008) as part of a hypofractionated stereotactic radiotherapy regimen involving 15 fractions, and it approaches the radiation tolerance for normal brain tissue. We take the total dose of 57.5 Gy listed by Yuan et al. (2008) as our constraint on radiation therapy, which appears as a black plane in **Figure 3**.

The results as documented in **Figure 3** are very similar to those for the head and neck cancer. One difference is that without any differentiation therapy, the cancer cannot be controlled by radiation alone. At least not within the given parameter values. In **Table 3** we list some TCP 50% values for this case.

3.3. BREAST CANCER TUMOR SIMULATIONS

To simulate the treatment of a small breast tumor, perhaps remaining after the resection of a large tumor, we choose $R = 0.25 \text{ cm}$. The CSC and TC growth rates are set to $\ln 2/8.2 \text{ day}^{-1}$, where 8.2 is the median potential doubling time of human breast tumors measured by Rew et al. (1992) using flow cytometry. Plausible parameter values for the LQ model [equation (8)] are taken from Qi et al. (2011): $\alpha/\beta = 2.88 \text{ Gy}$ and $\alpha = 0.08 \text{ Gy}^{-1}$. We use a fraction size of 2.26 Gy, delivered once per day on weekdays only. Our radiation constraint, indicated by a black plane in **Figure 4**, is 65.54 Gy, which corresponds to 29 fractions, the maximum number of fractions that satisfy the late tissue constraint of 70 Gy EQD_{3/2} and the acute mucosal constraint of 51 Gy EQD_{10/2} given in Fowler (2010).

Since the breast tumor in this example is late responding (low α/β -ratio), it is very difficult to control the cancer with radiation alone. The maximum tolerable dose of 65.54 Gy is reached much earlier than the TCP shows any growth. Using radiation in combination with differentiation therapy gives some hope that the cancer can be eradicated. Provided, however, that the CSC cells are sensitive enough to the differentiation promoter. In **Table 4** we list a few TCP 50% values.

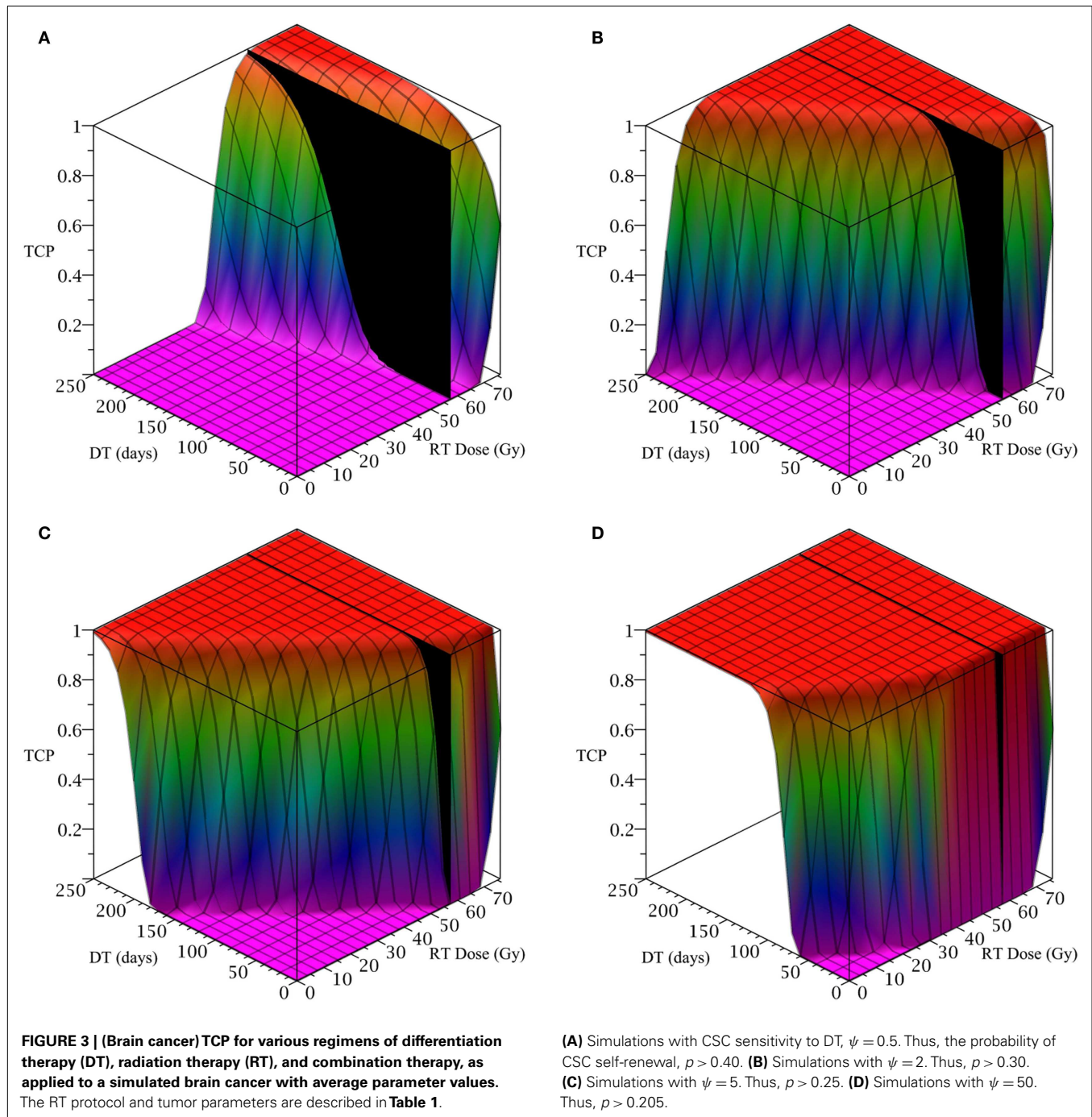
4. DISCUSSION

Current treatment modalities of cancer include surgery, radiation, chemotherapy, immuno-therapies, hormone therapies, and differentiation therapies. All of these methods have distinct advantages and limitations and clinicians often combine various methods to obtain the best results. In fact, in most cases a surgical removal or a radiation treatment is followed by chemotherapy. However, if chemotherapy is based on a single cytotoxic agent then the sensitive part of the tumor is killed but the resistant cell population persists; leading to chemo-resistance (Swierniak et al., 2009). The sensitivity to ionizing radiation can also vary in a tumor, where quiescent cells, or stem cells are less radiosensitive than cells that are actively proliferating (Kim and Tannock, 2005; Pajonk et al., 2010). Differentiation therapy describes the attempt to force stem cells into differentiation to increase their sensitivity to treatment agents (Lesczyniecka et al., 2001; Sell, 2004). This idea is conceptually intriguing and it is our

Table 2 | A selection of head and neck cancer tumor treatment parameters resulting in TCP \approx 0.5.

DT sensitivity, ψ	DT duration (days)	Total radiation (Gy)	TCP
N/A	0	63.25	0.581
0.5	9	60.72	0.498
	29	58.19	0.506
2	18	53.13	0.492
	35	48.07	0.490
5	20	45.54	0.508
	39	37.95	0.486
50	4	35.42	0.498
	36	15.18	0.505

*These are selected from simulations using the model parameters in **Table 1** where differentiation therapy is varied in increments of a single day, from 0 to 60 days, and radiation therapy in increments of a single fraction, from 0 to 75.9 Gy total radiation. The TCP without differentiation therapy is given as a point of reference.*



attempt in this paper to quantify the possible benefit for three specific cases: head and neck cancer, brain cancers, and breast cancer.

Our results are based on a mathematical model for the dynamics of cancer stem cells (CSC) and non-stem cancer cells (TC). The model is derived from previous models of Youssefpour et al. (2012) and Hillen et al. (2013) and it includes control through differentiation therapy and radiation treatment. The benefit of a given treatment is computed using the (Poissonian) tumor control probability (TCP).

We found very good references to most of the model parameters such as growth rates, doubling times, tumor volumes, and radiation sensitivities (see **Table 1**). However, we were not able to find good measurements for the sensitivity parameter ψ . Differentiation therapy alone has been used successfully in several cases. For example, about 70% of acute promyelocytic leukemia can be controlled by ATRA-therapy (all-trans-retinoic acid, Sell, 2004). Melanoma can be treated with the differentiation promoter cocktail of interferon- β and mezerein (Leszczyniecka et al., 2001); and Lander et al. (2009) and Youssefpour et al. (2012) suggest the use of

the differentiation promoter TGF- β . However, to our knowledge, the effect of these promoters has never been quantified. Hence we reside to explore a wide range of possible sensitivities ψ .

In each case we found a clear advantage of combination therapy, where differentiation therapy drastically reduces the total radiation dose. We are able to confirm the findings of Youssefpour et al. (2012) for the cases of head and neck cancer, brain cancers,

and breast cancer data. For future studies it is important to get estimates for the sensitivity ψ and we hope that research groups around the world might be able to identify this in the future.

It should be noted that the above model is over-simplistic to fully model a growing tumor. For the brain-tumor, for example, the spatial extent of the tumor is a dominating problem for treatment. The knowledge of an optimal combination therapy schedule is only useful if the overall treatment volume is known. It is the focus of ongoing research to identify a suitable treatment volume (see Konukoglu et al., 2010; Painter and Hillen, 2013). In addition, the immune response will be an important player in each of the tumors mentioned above. As discussed by Hanahan and Weinberg (2011), the immune system can be both, tumor promoting and

Table 3 | A selection of brain cancer treatment parameters resulting in TCP \approx 0.5.

DT sensitivity, ψ	DT duration (days)	Total radiation (Gy)	TCP
N/A	0	76.0*	0.602
0.5	17	72.2*	0.501
	50	68.4*	0.504
2	19	64.6*	0.504
	46	57.0	0.502
5	17	57.0	0.518
	35	49.4	0.500
50	3	41.8	0.500
	47	11.4	0.503

These are selected from simulations using the model parameters in **Table 1** where differentiation therapy is varied in increments of a single day, from 0 to 60 days, and radiation therapy in increments of a single fraction, from 0 to 76 Gy total radiation. The TCP without differentiation therapy is given as a point of reference.

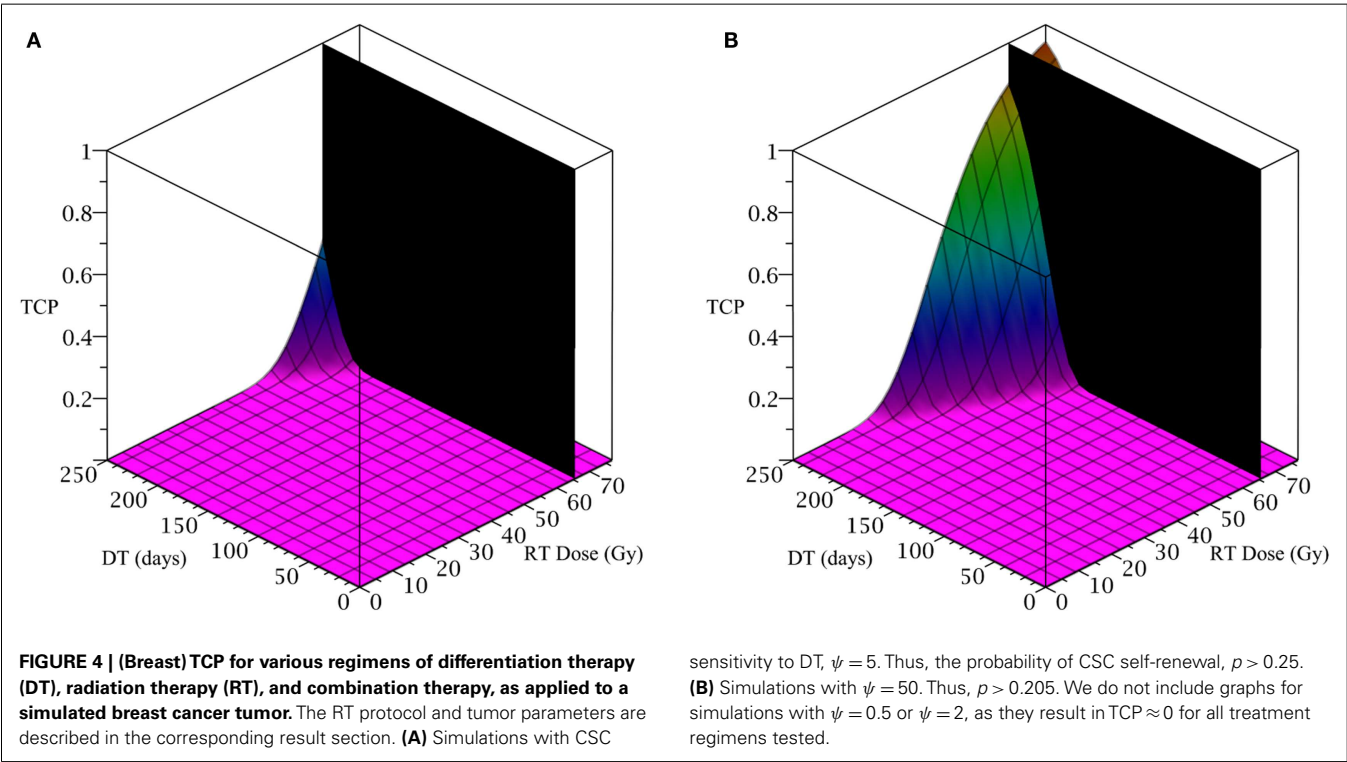
*Violates radiation constraint of 57.5 Gy.

Table 4 | A selection of breast cancer tumor treatment parameters resulting in TCP \approx 0.5.

DT sensitivity, ψ	DT duration (days)	Total radiation (Gy)	TCP
5	238	76.84*	0.499
	247	72.32*	0.505
50	204	74.58*	0.503
	222	63.28	0.500

These are selected from simulations using the model parameters in **Table 1** where differentiation therapy is varied in increments of a single day, from 180 to 250 days, and radiation therapy in increments of a single fraction, from 0 to 76.84 Gy total radiation. We use a minimum of 180 days of differentiation therapy, as the TCP remains near 0 until this level of DT is applied (see **Figure 4**).

*Violates radiation constraint of 65.54 Gy.



tumor inhibiting and the complex interactions are not fully understood. When we face all these additional difficulties, it appears as an advantage to have a simple sub-model, such as (4, 5), which clearly and consistently shows the benefit of combination therapy for a wide range of parameters and a selection of different tumors. This suggests that a combination of differentiation therapy and radiation therapy should be considered as a serious alternative.

REFERENCES

- Dick, J. (2003). Breast cancer stem cells revealed. *Proc. Natl. Acad. Sci. U.S.A.* 100, 3547–3549.
- Dingli, D., and Michor, F. (2006). Successful therapy must eradicate cancer stem cells. *Stem Cells* 24, 2603–2610.
- Fowler, J. (1989). The linear quadratic formula and progress in fractionated radiotherapy. *Br. J. Radiol.* 62, 679–694.
- Fowler, J. F. (2010). 21 Years of biologically effective dose. *Br. J. Radiol.* 83, 554–568.
- Gong, J., Dos Santos, M. M., Finlay, C., and Hillen, T. (2013). Are more complicated tumor control probability models better? *Math. Med. Biol.* 30, 1–19.
- Hanahan, D., and Weinberg, R. (2011). Hallmarks of cancer: the next generation. *Cell* 144, 646–674.
- Hillen, T., Enderling, H., and Hahnfeldt, P. (2013). The tumor growth paradox and immune system-mediated selection for cancer stem cells. *Bull. Math. Biol.* 75, 161–184.
- Joiner, M., Van der Kogel, A., and Steel, G. G. (2009). *Basic Clinical Radiobiology*, 4th Edn. London: Hodder Arnold.
- Kim, J., and Tannock, I. (2005). Repopulation of cancer cells during therapy: an important cause of treatment failure. *Nat. Rev. Cancer* 5, 516–525.
- Konukoglu, E., Clatz, O., Bondia, P., Delignette, H., and Ayache, N. (2010). Extrapolation glioma invasion margin in brain magnetic resonance images: suggesting new irradiation margins. *Med. Image Anal.* 14, 111–125.
- Kummermehr, J. (2001). Tumor stem cells – the evidence and the ambiguity. *Acta Oncol. (Madr.)* 40, 981–988.
- Lander, A., Gokoffski, K., Wan, F., Nie, Q., and Calof, A. (2009). Cell lineages and the logic of proliferation control. *PLoS Biol.* 7:e15. doi:10.1371/journal.pbio.1000015
- Leszczyniecka, M., Roberts, T., Dent, P., Grant, S., and Fisher, P. B. (2001). Differentiation therapy of human cancer: basic science and clinical applications. *Pharmacol. Ther.* 90, 105–156.
- Maitland, N., and Colling, T. (2008). Prostate cancer stem cells: a new target for therapy. *J. Clin. Oncol.* 26, 2862–2870.
- Meulmeester, E., and Ten Dijke, P. (2011). The dynamic roles of TGF-beta in cancer. *J. Pathol.* 223, 205–218.
- O'Rourke, S. F. C., McAneney, H., and Hillen, T. (2009). Linear quadratic and tumor control probability modelling in external beam radiotherapy. *J. Math. Biol.* 58, 799–817.
- Painter, K., and Hillen, T. (2013). Mathematical modelling of glioma growth: the use of diffusion tensor imaging DTI data to predict the anisotropic pathways of cancer invasion. *J. Theor. Biol.* 323, 25–39.
- Pajonk, E., Vlashi, E., and McBride, W. (2010). Radiation resistance of cancer stem cells: the 4 R's of radiobiology revisited. *Stem Cells* 24, 639–648.
- Qi, X. S., White, J., and Li, X. A. (2011). Is α/β for breast cancer really low? *Radiother. Oncol.* 100, 282–288.
- Rew, D. A., Campbell, I. D., Taylor, I., and Wilson, G. D. (1992). Proliferation indices of invasive breast carcinomas after in vivo 5-bromo-2'-deoxyuridine labelling: a flow cytometric study of 75 tumours. *Br. J. Surg.* 79, 335–339.
- Sachs, R. K., Hlatky, L. R., and Hahnfeldt, P. (2001). Simple ODE models of tumor growth and anti-angiogenic or radiation treatment. *Math. Comput. Model.* 33, 1297–1305.
- Sell, S. (2004). Stem cell origin of cancer and differentiation therapy. *Crit. Rev. Oncol. Hematol.* 51, 1–28.
- Singh, S., Clarke, I. D., Terasaki, M., Bonn, V. E., Hawkins, C., Squire, J., et al. (2003). Identification of a cancer stem cell in human brain tumors. *Cancer Res.* 63, 5821–5828.
- Struikmans, H., Rutgers, D. H., Jansen, G. H., Tulleken, C. A. F., van der Tweel, I., and Battermann, J. J. (1997). S-phase fraction, 5-bromo-2'-deoxy-uridine labelling index, duration of S-phase, potential doubling time, and DNA index in benign and malignant brain tumors. *Radiat. Oncol. Investig.* 5, 170–179.
- Swierniak, A., Kimmel, M., and Smieja, J. (2009). Mathematical modelling as a tool for planning anticancer therapy. *Eur. J. Pharmacol.* 625, 108–121.
- Todaro, M., Alea, M. P., Di Stefano, A. B., Cammareri, P., Vermeulen, L., Iovino, F., et al. (2007). Colon cancer stem cells dictate tumor growth and resist cell death by production of interleukin-4. *Cell Stem Cell* 1, 389–402.
- Watabe, T., and Miyazono, J. (2009). Roles of TGF-beta family signaling in stem cell renewal and differentiation. *Cell Res.* 19, 103–115.
- Wise, S., Lowengrub, J., Frieboes, H., and Cristini, V. (2008). Three-dimensional multispecies nonlinear tumor growth – I. Model and numerical method. *J. Theor. Biol.* 253, 524–543.
- Youssefpour, H., Li, X., Lander, A., and Lowengrub, J. (2012). Multispecies model of cell lineages and feedback control in solid tumors. *J. Theor. Biol.* 304, 39–59.
- Yuan, J., Wang, J. Z., Lo, S., Grecula, J. C., Ammirati, M., Montebello, J. F., et al. (2008). Hypofractionation regimens for stereotactic radiotherapy for large brain tumors. *Int. J. Radiat. Oncol. Biol. Phys.* 72, 390–397.

Conflict of Interest Statement: The authors declare that the research was conducted in the absence of any commercial or financial relationships that could be construed as a potential conflict of interest.

Received: 12 December 2012; accepted: 28 February 2013; published online: 18 March 2013.

Citation: Bachman JWN and Hillen T (2013) Mathematical optimization of the combination of radiation and differentiation therapies for cancer. *Front. Oncol.* 3:52. doi: 10.3389/fonc.2013.00052

This article was submitted to *Frontiers in Molecular and Cellular Oncology*, a specialty of *Frontiers in Oncology*.

Copyright © 2013 Bachman and Hillen. This is an open-access article distributed under the terms of the Creative Commons Attribution License, which permits use, distribution and reproduction in other forums, provided the original authors and source are credited and subject to any copyright notices concerning any third-party graphics etc.



Cellular Potts modeling of tumor growth, tumor invasion, and tumor evolution

András Szabó^{1,2,3*} and Roeland M. H. Merks^{1,2,3,4*}

¹ Biomodeling and Biosystems Analysis, Life Sciences Group, Centrum Wiskunde and Informatica, Amsterdam, Netherlands

² Netherlands Consortium for Systems Biology, Amsterdam, Netherlands

³ Netherlands Institute for Systems Biology, Amsterdam, Netherlands

⁴ Mathematical Institute, Leiden University, Leiden, Amsterdam, Netherlands

Edited by:

Katarzyna Anna Rejniak, H. Lee
Moffitt Cancer Center and Research
Institute, USA

Reviewed by:

Katarzyna Anna Rejniak, H. Lee
Moffitt Cancer Center and Research
Institute, USA
Luigi Preziosi, Politecnico di Torino,
Italy

*Correspondence:

András Szabó and Roeland M. H.
Merks, Life Sciences Group, Centrum
Wiskunde and Informatica, Science
Park 123, 1098 XG Amsterdam,
Netherlands.
e-mail: andras.szabo@cwil.nl;
merks@cwil.nl

Despite a growing wealth of available molecular data, the growth of tumors, invasion of tumors into healthy tissue, and response of tumors to therapies are still poorly understood. Although genetic mutations are in general the first step in the development of a cancer, for the mutated cell to persist in a tissue, it must compete against the other, healthy or diseased cells, for example by becoming more motile, adhesive, or multiplying faster. Thus, the cellular phenotype determines the success of a cancer cell in competition with its neighbors, irrespective of the genetic mutations or physiological alterations that gave rise to the altered phenotype. What phenotypes can make a cell “successful” in an environment of healthy and cancerous cells, and how? A widely used tool for getting more insight into that question is cell-based modeling. Cell-based models constitute a class of computational, agent-based models that mimic biophysical and molecular interactions between cells. One of the most widely used cell-based modeling formalisms is the cellular Potts model (CPM), a lattice-based, multi particle cell-based modeling approach. The CPM has become a popular and accessible method for modeling mechanisms of multicellular processes including cell sorting, gastrulation, or angiogenesis. The CPM accounts for biophysical cellular properties, including cell proliferation, cell motility, and cell adhesion, which play a key role in cancer. Multiscale models are constructed by extending the agents with intracellular processes including metabolism, growth, and signaling. Here we review the use of the CPM for modeling tumor growth, tumor invasion, and tumor progression. We argue that the accessibility and flexibility of the CPM, and its accurate, yet coarse-grained and computationally efficient representation of cell and tissue biophysics, make the CPM the method of choice for modeling cellular processes in tumor development.

Keywords: cellular Potts model, cell-based modeling, tumor growth model, evolutionary tumor model, tumor metastasis model, multiscale modeling, tumor invasion model

1. INTRODUCTION

The development of a tumor is initiated as the genomes of individual cells in an organism become destabilized. Such genetic instability usually kills cells, but in rare cases it modifies the properties of the cell in a way that allows it to proliferate and form a tumor. These biological capabilities are known as the “hallmarks of cancer” (Hanahan and Weinberg, 2000, 2011), which include: (1) self-sufficiency in proliferative signaling, (2) evasion of growth suppressors, (3) the ability to resist apoptotic signals from the environment, (4) limitless replicative potential, (5) secretion of pro-angiogenic signals, (6) invasion and metastasis, (7) reprogramming metabolism (e.g., the Warburg effect), (8) evasion of the immune system, and (9) recruitment of healthy cells to create a “tumor microenvironment.” Experimental and computational studies of cancer typically focus on the molecular peculiarities of tumor tissues relative to healthy tissues. The main reasons for this genetic focus are that (a) genetic changes of the cells are main cause for acquisition of tumor cell capabilities, (b) molecular information is readily accessible using high-throughput techniques,

including next generation sequencing, and (c) the molecular level is the main target for pharmacological agents (Uren et al., 2008; Shah et al., 2009; Pleasance et al., 2010; Pugh et al., 2012). Such tumor sequencing studies help identify the key genes involved in cancers, and sequencing information is helpful in classifying tumors (Thomas et al., 2007).

The molecular data used in these studies is typically averaged over the whole-tumor mass, so regional differences within the tumor or between metastases get lost. Nevertheless, genetic heterogeneity of tumors is an inevitable consequence of the genetic instability of tumor cells (Marusyk et al., 2012), and further intratumor heterogeneity may arise from epigenetic differences between cells, driven by transcriptional noise or signaling from the microenvironment. To test for heterogeneity, Yachida et al. (2010) sequenced samples of different regions of a pancreatic tumor and of its metastases. They indeed found genetic differences between the metastases, which they could trace back to corresponding regional differences within the primary tumor. Gerlinger et al. (2012) report similar regional differences within renal carcinomas.

Thus, these studies have identified significant degrees of intra-tumor heterogeneity that whole-tumor sequencing studies will underestimate. These findings underline the importance of spatial structure within tumors and thus will have direct implication for understanding tumor development.

A better understanding of the causes and consequences of tumor heterogeneity is key to developing improved treatment strategies. In a heterogeneous tumor, a single pharmaceutical agent may target cells differently. As a result, treatments may select for resistant variants, potentially leading to a tumor relapse (Marusyk et al., 2012). Intratumor competition of tumor cells for resources including nutrients, oxygen, or growth space may set off a process of somatic evolution responsible for tumor progression (Anderson et al., 2006). Like in any evolutionary process, the success of a tumor cell clone during such intratumor competition will depend only indirectly on the cell's genome, *via* the cellular phenotype and the cell's environment, which consists of the other tumor cells, the extracellular matrix, and the healthy tissue. What matters for the cell's survival and reproduction in the tumor, is its ability to respond to biophysical and molecular cues in the microenvironment, and face challenges in the microenvironment more efficiently than its competitors. Such cues and challenges include mechanical stiffness of the surrounding tissue, physical pressure due to growth, nutrient or growth factor gradients and availability, or accessibility to the immune system. Thus, to understand the effects of intratumor heterogeneity, apart from genetic studies, biophysical studies of cell behavior are crucial. The key to understanding cancer is not to collect more data, hoping that "the (data) would somehow arrange themselves in a compelling and true solution" (Dobzhansky paraphrased in Gatenby, 2012); we need to find "cancer's first principles" instead, and "use data to support or refute a postulated theoretical framework" (Gatenby, 2012).

In this paper we review attempts to develop such theoretical frameworks for collective cell behavior during tumor development. Mathematical descriptions of tumor growth and development range from continuum-level descriptions of gene-regulatory networks or tumor cell populations, to detailed, spatial models of individual and collective cell behavior. The scale of the biological phenomenon of interest, and the scale at which we can collect data or control the behavior of the system motivates the level of description of choice. Space-free models focus, e.g., on the dynamics of the gene or metabolic regulatory networks of individual cells (Vazquez et al., 2010; Frezza et al., 2011), or they describe the relative growth of tumor cells and healthy cells using population-dynamics approaches (Gatenby and Vincent, 2003; Stamper et al., 2007; Basanta et al., 2012).

Here we focus on cell-based models (Merks and Glazier, 2005), a class of modeling formalisms that predicts collective cell behavior from coarse-grained, phenomenological descriptions of the behavior of the cells. The *input* to a cell-based model is a dynamical description of the active behavior and biophysics of cells and of the properties of extracellular materials, a description that often simplifies the underlying genetic networks to the minimal level of complexity required for explaining the cell's responses to extracellular signals. The *output* of a cell-based model is the collective cell behavior that emerges non-intuitively from the interactions

between the cells in the model. In this way, cell-based models help unravel how tissue-level phenomena, e.g., tumor growth, metastasis, tumor evolution, follow from the – ultimately genetically regulated – behavior of single cells. A range of cell-based modeling techniques is available. The least detailed cell-based models describe the position and volume of individual cells. Such single-particle approaches include cellular automata (CA, see for example: Alarcón et al., 2003; Anderson et al., 2006; Hatzikirou et al., 2008; Enderling et al., 2009; Sottoriva et al., 2010; Owen et al., 2011), which represent cells as points on a lattice. Off-lattice single-particle approaches describe cells as points or spheroids in continuous space; applications in tumor growth include the studies of Drasdo et al. (1995), Drasdo and Höhme (2003), Gevertz and Torquato (2006), Kim et al. (2007), Van Leeuwen et al. (2009), Macklin et al. (2012), or Kim and Othmer (2013). Single-particle cell-based models are well suited for describing the emergence of spatial and clonal structure in growing tumors, but they are less suitable to answer more detailed, biomechanical questions on how the tissue changes due to cancer cell growth. Such morphological changes can result from local cell rearrangements through cell shape change or intercalation (Keller and Davidson, 2004). For answering such questions, we need to describe the individual cells in more detail and include their shape, elasticity, polarity, etc. Multi-particle cell-based models make this possible by using a collection of particles to represent the cell. Off-lattice, multi-particle methods either describe cells by their boundaries (Brodland et al., 2007; Farhadifar et al., 2007; Rejniak, 2007; Merks et al., 2011) or as collections of connected particles (Newman, 2005; Sandersius et al., 2011b). For broad reviews of single-particle and multi-particle cell-based models of tumor development, see, e.g., Rejniak and Anderson (2011) and Hatzikirou et al. (2005). Here we will review computational models of tumor growth based on a multi-particle, lattice-based cell-based model: the cellular Potts model (Graner and Glazier, 1992; Glazier and Graner, 1993).

2. A MULTI-PARTICLE, CELL-BASED METHOD ON THE LATTICE: THE CELLULAR POTTS MODEL

In the cellular Potts model (CPM), cells are represented as spatially extended objects with explicit cell shapes. This makes it possible to define the cell neighborhood more precisely. The model describes amoeboid cell motion, cellular rearrangements, and pressure inside the tissue. The CPM was introduced by Graner and Glazier (Graner and Glazier, 1992; Glazier and Graner, 1993) for modeling cell sorting according to the differential adhesion hypothesis of Steinberg (1970), and was applied thereafter to various phenomena in vertebrate biological development, including convergent extension (Zajac et al., 2003), blood vessel network formation (Merks et al., 2006, 2008; Szabo et al., 2008), vascular sprouting (Bauer et al., 2007; Szabó and Czirók, 2010), ureteric bud branching in kidney development (Hirashima et al., 2009), and somitogenesis (Hester et al., 2011). Its proven utility in describing normal embryonic development, makes the CPM a natural choice for modeling pathological developmental mechanisms in cancer.

The CPM is defined on a regular, square or hexagonal lattice, with a spin $\sigma(\vec{x}) \in \mathbb{Z}^{+,0}$ defined on each lattice site \vec{x} . Biological cells are represented as domains on the lattice with identical spin $\sigma(\vec{x})$, where $\sigma \in \mathbb{N}$ can be seen as a cell identification number, and

$\sigma = 0$ typically identifies a medium or the extracellular matrix. Each cell and the medium is additionally marked with a label $\tau(\sigma) \in \mathbb{Z}^{+,0}$ to identify a biological cell type. The CPM describes amoeboid cell movement with a Metropolis algorithm, which iteratively attempts to copy the spin value $\sigma(\vec{x})$ of a randomly selected site \vec{x} into a randomly chosen adjacent lattice site \vec{x}' .

The spin-copy attempt is accepted with probability 1 if it would decrease the value of a globally defined Hamiltonian, H , or with Boltzmann probability if it would increase the value of H :

$$p(\sigma(\vec{x}) \rightarrow \vec{x}') = \begin{cases} 1 & , \text{ if } \Delta H(\sigma(\vec{x}) \rightarrow \vec{x}') < 0 \\ \exp[\Delta H(\sigma(\vec{x}) \rightarrow \vec{x}') / \mu(\sigma)] & , \text{ if } \Delta H(\sigma(\vec{x}) \rightarrow \vec{x}') \geq 0 \end{cases} \quad (1)$$

where $\Delta H(\sigma(\vec{x}) \rightarrow \vec{x}')$ is the change in the Hamiltonian due to the attempted copy, and $\mu(\sigma)$ parameterizes the intrinsic cell motility. The Hamiltonian approach acts to represent the balance of effective (both physical and phenomenological) forces acting on the cells, with the spatial gradient of the Hamiltonian proportional to the force acting on that location, $\vec{\nabla} H(\vec{x}) \propto \vec{F}(\vec{x})$.

In the originally proposed model the Hamiltonian function consists of a volume constraint term responsible for maintaining an approximately constant cell volume and a surface energy term responsible for cell-cell adhesion properties:

$$\begin{aligned} H &= H_v + H_a = \\ &= \sum_{\sigma} \lambda_v (V_{\sigma} - V_{\sigma}^T)^2 + \sum_{(\vec{x}, \vec{x}')} J(\tau(\sigma(\vec{x})), \tau(\sigma(\vec{x}')) (1 - \delta(\sigma(\vec{x})), \sigma(\vec{x}'))). \end{aligned} \quad (2)$$

Here, V_{σ} is the volume and V_{σ}^T is the target volume of the cell σ . $\sigma(\vec{x})$ denotes the cell number of the cell occupying position \vec{x} and $\tau(\sigma(\vec{x}))$ is its cell type. $J(\tau(\sigma(\vec{x})), \tau(\sigma(\vec{x}')))$ is the adhesion coefficient between cell types $\tau(\sigma(\vec{x}))$ and $\tau(\sigma(\vec{x}'))$, and $\delta(\sigma(\vec{x}), \sigma(\vec{x}'))$ is Kronecker's delta function with a value 1 if $\sigma(\vec{x}) = \sigma(\vec{x}')$ and 0 otherwise. The first summation runs over all cells and penalizes the deviation of the cell's volume from a prescribed target volume with a coefficient λ_v . The second term sums the adhesion energies (J) of all adjacent lattice site pairs (\vec{x}, \vec{x}') , with the Kronecker delta selecting lattice pairs at cell boundaries, where $\sigma(\vec{x}) \neq \sigma(\vec{x}')$. As $J(\tau(\sigma(\vec{x})), \tau(\sigma(\vec{x}')))$ is typically positive, cells tend to minimize their surface area with other cells or the medium, making the adhesion term equivalent to surface tension (Glazier and Graner, 1993). The Monte Carlo Step (MCS) is the usual time measure in the model. One MCS is defined as N elementary steps, or copy-attempts, where N is the number of lattice sites in the grid. This choice ensures that on average all sites are updated in every MCS, decoupling the system size and the number of copy-attempts needed to update the whole configuration.

The basic CPM has been extended with numerous cell behaviors relevant for tumor biology. To represent growth factors (Jiang et al., 2005), extracellular materials (Turner and Sherratt, 2002), nutrients (Jiang et al., 2005; Shirinifard et al., 2009), or other diffusing chemicals, the CPM often interacts with systems of partial-differential equations, which are typically solved numerically on a grid matching with that of the CPM. To model the cell's

response to the chemical fields, most studies assume that cells are more likely to extend (or retract) pseudopods along concentration gradients (Turner and Sherratt, 2002; Bauer et al., 2007; Rubenstein and Kaufman, 2008; Tripodi et al., 2010). To this end, an additional energy bias is incorporated in the Hamiltonian at the time of copying (Savill and Hogeweg, 1997):

$$\Delta H_{\chi}(\sigma(\vec{x}) \rightarrow \vec{x}') = \Delta H(\sigma(\vec{x}) \rightarrow \vec{x}') - \chi(c(\vec{x}) - c(\vec{x}')), \quad (3)$$

for the copying step $\sigma(\vec{x}) \rightarrow \vec{x}'$, where $c(\vec{x})$ represents the concentration at position \vec{x} , and χ is a scalar parameter setting the relative strength of the chemotactic motion in the Hamiltonian (equation (2)).

Cell growth and division are implemented in the model either by increasing the target volume V_{σ}^T (Stott et al., 1999; Shirinifard et al., 2009), or keeping it fixed while dividing the cell into two smaller daughter cells (Turner and Sherratt, 2002; Rubenstein and Kaufman, 2008). Cell division can be triggered when certain conditions are met, such as the cell reaches a certain size (Jiang et al., 2005), or volume-to-surface ratio (Stott et al., 1999), or can depend on the time since last division (Sottoriva et al., 2011), and so on. Further extensions make it possible to model, e.g., the effect of cell shape (Merks et al., 2006; Starck et al., 2007; Palm and Merks, 2013), anisotropic differential adhesion (Zajac et al., 2003), persistent cell motion (Szabó et al., 2010; Kabla, 2012). These behaviors can be made specific for the cell types $\tau(\sigma)$ included in the model, e.g., tumor, stromal, necrotic tumor cell, and cancer stem cells. The extracellular matrix can also be modeled in varying levels of detail. We will discuss these extensions in more detail as they occur in the tumor models reviewed below.

3. AVASCULAR TUMOR GROWTH

The outgrowth of primary, avascular tumors originating from a small, proliferative population of cells is a first step toward tumor development, and it forms a basis for more elaborate models of tumor development. Models of avascular tumors aim to reproduce the growth characteristics and spatial organization of avascular tumors from first principles, including cellular division rates, and local accessibility of nutrients. Laird (1964) showed that many avascular tumor growth curves are well characterized by Gompertz growth curves (Gompertz, 1825): an initial exponential growth phase, followed by a deceleration of the growth rate and a final, steady-state size of the tumor due to exhaustion of growth resources. The number of cells in the tumor, $N(t)$, at time t is given by the formula:

$$N(t) = N_0 \exp \left[\frac{A}{\alpha} (1 - e^{-\alpha t}) \right]. \quad (4)$$

Here N_0 is the initial number of cells in the tumor, α characterizes the deceleration of the growth rate, and A/α sets the maximum size of the tumor. Because of the limited supply of nutrients from the surrounding stroma via diffusion, avascular tumors *in vitro* follow Gompertz-like, saturated growth curves, while the diffusion depth of the nutrient stratifies the aggregate into a necrotic core, a quiescent layer, and a proliferative rim (Folkman and Hochberg, 1973).

3.1. MODELING GOMPERTZ GROWTH FROM FIRST PRINCIPLES

One of the first simulations that reproduced Gompertz growth from first principles using the CPM was reported by Stott et al. (1999). Their three-dimensional model represents stromal cells, proliferating tumor cells, quiescent tumor cells, and necrotic cells (Figure 1A). The model is based on the experimental observation that the volume of proliferating cells in an *in vitro* tumor is constant throughout growth (McElwain and Pettet, 1993). The thickness of this outer proliferative layer is denoted by D_q , and the first necrotic cells appear at approximately $4D_q$ distance from the outer surface of the aggregate (McElwain and Pettet, 1993). This property is used to reconstruct the nutrient levels within the aggregate: cells are assumed to change their “type” (proliferative, quiescent, necrotic) depending on nutrient availability. The level of nutrients at depth D_q is a constant N_q . Nutrient levels at other positions are assumed proportional to $R - d$, where R is the tumor radius and d is the distance from the tumor surface. The nutrient level determines the growth rate of proliferative cells in the model, as

$$G = \begin{cases} 0 & , \text{ if } 0 \leq N \leq N_q, \\ \frac{1}{2} \left(1 - \frac{N}{N_q}\right)^2 & , \text{ if } N_q \leq N \leq 3N_q, \\ 2 & , \text{ otherwise.} \end{cases} \quad (5)$$

Cell growth and cell necrosis are implemented by increasing or decreasing the target volumes, $dV^T/dt = G$, of the cells over time. Necrotic cells further from the interface decrease their target volume faster. Proliferating cells grow and divide when reaching a certain volume-to-surface ratio. Simulations of the model correctly reproduce the growth of avascular tumors: an exponential growth phase is followed by a linear phase, after which the tumor reaches a steady size. The final size of the aggregate is maintained by the balance of cell proliferation at the tumor edge, and the decay of necrotic cells at the center. In this state cells are gradually shifted from the outer rim toward the necrotic core. The model also reproduces the stratified, spatial organization of avascular tumors, with a proliferative rim, a quiescent layer, and a necrotic core. However, this is not unexpected, since the nutrient, that determines the cell types, is an explicit function of the distance from the tumor–stroma interface. This is a good approximation, if the nutrient diffuses uniformly from the stroma into the tumor.

A more complete model of tumor spheroids was presented by Jiang et al. (2005). They simulate the diffusion of nutrients, waste, growth factors, and inhibitory factors. They use a simplified, intracellular model of the cell cycle based on a Boolean network in each cell to determine if a cell is proliferative or quiescent. The secreted growth factors and inhibitory factors are assumed to regulate the progression through the cell cycle by altering the activation state of proteins within the Boolean network. A set of partial-differential equations describes the secretion, diffusion and uptake of the nutrients, waste products, growth factors, and inhibitory factors, as:

$$\frac{\partial c_i(\vec{x}, t)}{\partial t} = D_i \nabla^2 c_i(\vec{x}, t) + S_i(\tau(\sigma(\vec{x}))) - \epsilon_i c_i(\vec{x}, t), \quad (6)$$

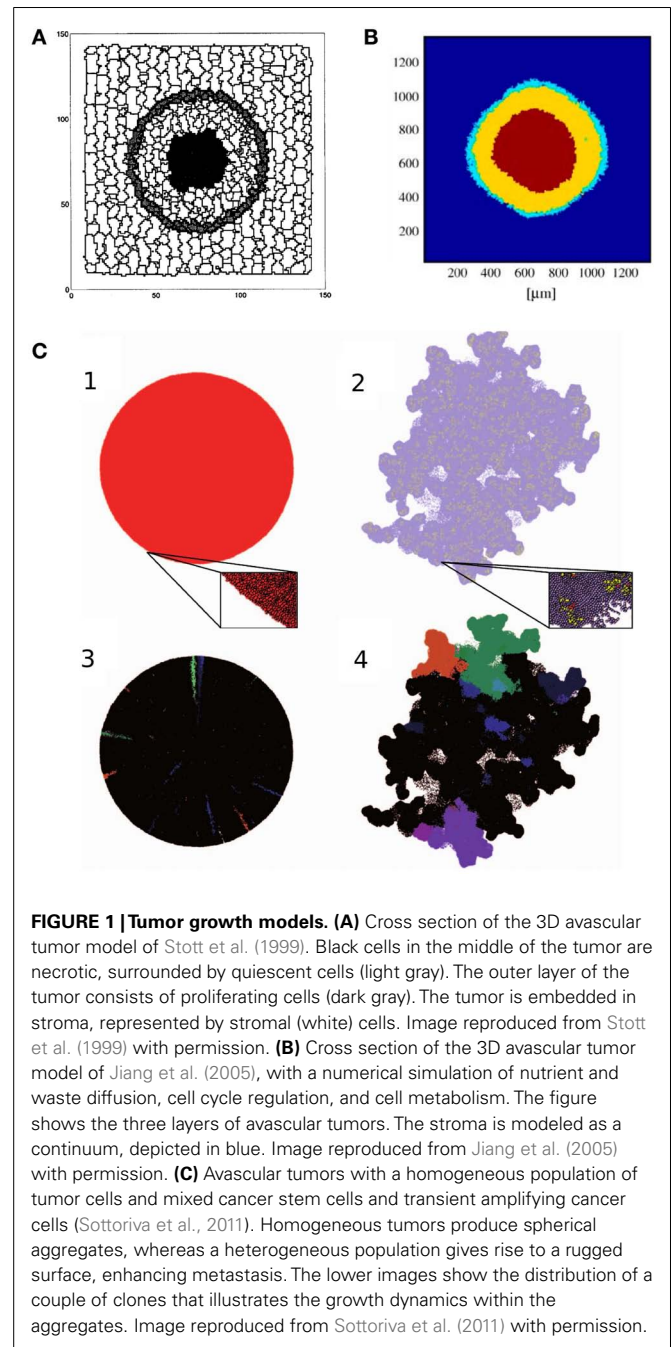


FIGURE 1 | Tumor growth models. (A) Cross section of the 3D avascular tumor model of Stott et al. (1999). Black cells in the middle of the tumor are necrotic, surrounded by quiescent cells (light gray). The outer layer of the tumor consists of proliferating cells (dark gray). The tumor is embedded in stroma, represented by stromal (white) cells. Image reproduced from Stott et al. (1999) with permission. **(B)** Cross section of the 3D avascular tumor model of Jiang et al. (2005), with a numerical simulation of nutrient and waste diffusion, cell cycle regulation, and cell metabolism. The figure shows the three layers of avascular tumors. The stroma is modeled as a continuum, depicted in blue. Image reproduced from Jiang et al. (2005) with permission. **(C)** Avascular tumors with a homogeneous population of tumor cells and mixed cancer stem cells and transient amplifying cancer cells (Sottoriva et al., 2011). Homogeneous tumors produce spherical aggregates, whereas a heterogeneous population gives rise to a rugged surface, enhancing metastasis. The lower images show the distribution of a couple of clones that illustrates the growth dynamics within the aggregates. Image reproduced from Sottoriva et al. (2011) with permission.

with c_i denoting the concentration of glucose, oxygen, metabolic waste, growth factors, or inhibitory factors. D_i is an effective diffusion coefficient, $S_i(\tau(\sigma(\vec{x})))$ is the source, and ϵ_i is the decay rate of the substances. As a boundary condition, the authors assume constant concentrations in the medium surrounding the tumor ($S_i(\text{medium}) = \text{const}_i$). Consumption and production at position \vec{x} depends on the cell type $\tau(\sigma(\vec{x}))$ occupying that position. Proliferative and quiescent cells produce waste, and consume nutrients and growth factors, while necrotic cells do not consume any substance. Necrotic and quiescent cells produce inhibitory factors. Cells metabolize nutrients through anaerobic glycolysis and

respiration, producing lactate as waste. They assumed that metabolic activity determines cell survival: cells turn necrotic if glucose concentrations drop below 0.06 mM, or at oxygen concentrations below 0.02 mM, or at lactate concentrations above 8 mM. Cell shedding is introduced in the model by allowing mitotic cells to detach from the aggregate at a constant rate at the tumor surface. These cells are then taken out from the simulation. With these assumptions, the proliferative rim, the quiescent layer, and necrotic core emerge in the model (**Figure 1B**).

Jiang et al. (2005) compare their simulation to the growth of *in vitro* aggregates of mouse mammary tumor cells cultured in suspension. They fitted a Gompertz model to both the experimental and simulated tumor growth curves, which yielded estimates for the initial cell doubling time (related to parameters α and A in equation (4)). The resulting estimate of the equilibrium number of tumor cells in the spheroids, $N_0 \exp(A/\alpha)$, differed at most by a factor of 2 between model and experiments.

The model of Jiang et al. (2005) also predicted the appearance of the spheroids' stratification. The combined width of the proliferative rim and the quiescent layer remains constant during growth, whereas the radius of the necrotic core increases linearly in time, which the simulation accurately reproduce. Based on these results the authors propose that the size of the necrotic core is governed by the accumulation of wastes and depletion of nutrients, and is independent of the cell cycle. Interestingly, the inclusion of a simplified model of the cell cycle accurately reproduced cell phase distributions in tumor spheroids, and the growth arrest characteristic of avascular tumors. Since the authors reproduced growth dynamics without any mechanically restricting extracellular microenvironment, they conclude that such biophysical constraints are not necessarily crucial for the growth arrest of the observed tumor aggregates.

3.2. ANISOTROPIC TUMOR GROWTH: THE CANCER STEM CELL HYPOTHESIS

A higher level of heterogeneity within tumors was suggested by the cancer stem cell hypothesis (Reya et al., 2001). The hypothesis assumes that only a small fraction of tumor cells, the cancer stem cells (CSC), are capable of unlimited reproduction, while the main tumor mass consists of cells with only limited replication potential. It is still not clear where the CSCs originate from: they could be transformed stem cells, or cancerous cells that acquire self-renewal properties (Visvader and Lindeman, 2008). In this view, tumors are inherently heterogeneous with respect to proliferation potential. The hypothesis is still debated, but supportive evidence is accumulating: Visvader and Lindeman (2008) list several experimental attempts to isolate CSCs from solid tumors, by propagating and passaging cells. These studies aimed at identifying cell-surface markers for CSC properties, with candidates including CD44, CD133, and ESA.

Sottoriva et al. (2011) explored the effect of CSCs on tumor development using the CPM. Two cell types are represented in their model: CSCs, that are allowed to divide indefinitely, and differentiated cells, that divide only a limited number of times. CSCs divide either symmetrically to give rise to two CSCs, or asymmetrically to produce a CSC and a differentiated cell. Cells are killed at random with a constant rate. Confirming their previous

result from a cellular automata model (Sottoriva et al., 2010), Sottoriva et al. (2011) show that the presence (or absence) of CSCs affect tumor morphology in their CPM. Tumors in which all cells have infinite reproductive potential grow into a spherical shape. In comparison, tumors in which only CSCs can reproduce indefinitely, tend to assume a more irregular shape (**Figure 1C**): in these populations the whole tumor is made up of a collection of small, spherical tumors, each originating from one CSC. In this view, the tumor is an aggregate of self-metastases (Enderling et al., 2009). The authors argue that the emergent irregular surface of the whole aggregate is reminiscent of invasive tumor growth.

To explore if and how the presence of a CSC population within a tumor aggregate affects the emergence of treatment resistance, Sottoriva et al. (2011) implemented a simple model of evolutionary dynamics: the division rate of model cells is set by an abstract, arbitrary fitness function, which is proposed to depend on an inheritable and mutating methylation pattern on the DNA of the individual cells. Tumor therapy is implemented by killing a percentage of cells at a specific time, that results in new growth space around the survivors, lowering the selection pressure within the aggregate, and leading to a second expansion. They observe that with CSCs, tumors are able to develop a larger variety of methylation patterns after regrowth. During regrowth the total number of mutations in tumors with CSCs is higher than in tumors without CSCs: in the former case a small number of CSCs will recreate the whole population through a large number of divisions per CSC, leading to accumulation of mutations. In tumors without CSCs all cells contribute to repopulation equally, with fewer divisions per cell, and therefore lower chance of mutation accumulations. Accumulated mutations can help tumor cells to escape local fitness maxima, leading to a faster evolution, and possibly giving rise to more resistant cells. These simulations indicate how seemingly effective treatments may induce a more resistant or invasive phenotype. Gao et al. (2013) show experimental evidence that *in vitro* glioblastoma cultures indeed increase their growth rate and the fraction of CSCs in the populations after irradiation with less than lethal dose. To quantitatively explore the reason behind growth acceleration, they present a CPM similar to the model of Sottoriva et al. (2011). They calibrate the probability of symmetric CSC divisions using CSC ratios in *in vitro* and *in vivo* glioblastoma populations. The resistance of CSCs to radio therapy is incorporated in the model, and calibrated using dose dependent survival measurements after acute irradiation. When comparing acute and fractionated irradiation response, the authors found that the relative increase in CSCs after fractionated treatment cannot be explained solely by radioresistance of CSCs. These model simulations suggest that repeated exposure to radiation might increase the symmetric division rate of CSCs, and/or increase the division rate of CSCs. These effects remain to be tested experimentally.

3.3. TRANSITION BETWEEN HOMEOSTASIS AND UNCONTROLLED GROWTH

A key issue in cancer, not considered by the above models, is tissue homeostasis (Anderson et al., 2011). In fact, explaining dynamical homeostasis of a tissue in which cells are continuously renewed in a balanced way, may be a far more challenging problem than modeling uncontrolled growth. Initiation of tumor growth then

amounts to the loss of tissue homeostasis. Although not specially targeted at modeling cancer, an abstract model by Tripodi et al. (2010) makes a first step in this direction. They argue that metabolic exchange is one of the main regulators of tissue renewal and robustness of developmental patterns. They implemented a growing heterogeneous population of cells that are interdependent on one another for metabolic purposes. To do so, they extended the CPM with a set of rules regulating the cell's ability to secrete and consume diffusing nutrients from their environment, and move toward (or away from) nutrients and other chemicals. The nutrients that the cells consume are metabolized to an internal energy used for maintenance, division, or chemotactic movement. The relative rates of these budget terms are determined by a set of parameters, and are the same for all cells within one simulation. Different cell types in the model produce different nutrients that can be used by one other cell type, creating a cross-feeding system. Cells can also change types during the simulation. Two main budget parameters control the behavior of the population: the rate of maintenance, and the rate of nutrient consumption. A system with high consumption and low maintenance rates generates a proliferative population similar to cancer, whereas lower consumption and higher maintenance rate yields a population in dynamic homeostasis. Whether the uncontrolled growth of the high consumption, low maintenance metabolic phenotype predicted by the model of Tripodi relates to the reprogramming of cellular energy metabolism in cancer as seen in the Warburg effect (Levine and Puzio-Kuter, 2010), will be an interesting topic of future theoretical and experimental research.

4. VASCULAR TUMOR GROWTH

To enable their sustained growth, tumors must attract new blood vessels and remodel the vasculature in a process called angiogenesis. The blood vessels provide nutrients and oxygen to the tumor and remove waste from the vicinity of tumors. Several authors have looked at the interaction between growing tumors and the vasculature. In this section we will review a cellular Potts model studying the growth dynamics of vascular tumors. Models focusing on the mechanisms of angiogenesis (for example: Manoussaki et al., 1996; Gamba et al., 2003; Merks et al., 2006, 2008; Szabo et al., 2007, 2008; Bauer et al., 2009; Daub and Merks, 2013; Palm and Merks, 2013) are reviewed elsewhere (for example, Chaplain et al., 2006; Jiang et al., 2012; Peirce et al., 2012; Bentley et al., 2013).

Shirinifard et al. (2009) studied the interaction of tumor growth and the vasculature. The blood vessels, modeled as a network of elastically connected endothelial cells, provide oxygen to the tumor at a constant rate. Oxygen is considered as the only nutrient that restricts tumor growth, assuming that other nutrients are either depleted at the same locations as the oxygen, or are not limiting. Tumor cells in the model are considered either normal, hypoxic or necrotic, depending on their metabolic state, determined by oxygen levels in their microenvironment. The growth rate of normal and hypoxic tumor cells thus depends on the oxygen levels:

$$\frac{dV^T}{dt} = \frac{G_m O(\vec{R})}{G_k + O(\vec{R})}. \quad (7)$$

Here V^T is the cell's target volume, $O(\vec{R})$ represents the oxygen levels at the cell's center of mass (\vec{R}) and parameters G_m and G_k define the dynamics of growth. Once the cells reach doubling volume, they divide. Hypoxic cells secrete VEGF-A, which attracts endothelial cells through chemotaxis, and induces their growth. Necrotic cells decrease their volume at a constant rate until they completely disappear.

The authors identified distinct phases of tumor growth with tumors capable and incapable of inducing blood vessel growth. In both cases, tumors grow exponentially in the initial regime until the development of hypoxic areas (Figure 2A). After that, the growth rates of angiogenic tumors and non-angiogenic tumors start to diverge. In non-angiogenic tumors, necrotic cells appear shortly after hypoxic cells, creating the three layers typical of avascular tumors. Cells protrude from the spherical tumor towards the vessels due to oxygen inhomogeneities, resulting in vessel rupture and more access to oxygen. The tumor continues to grow slowly along the existing vasculature, producing a cylindrical aggregate (Figure 2B). In angiogenic tumors, hypoxic cells secrete VEGF-A, and activate angiogenesis. Neovascular cells form a peri-tumor network, but do not penetrate the tumor itself. The spherical angiogenic tumor gradually assumes a cylindrical shape, similar to the avascular tumor. Due to the intense neovascularization at the tumor surface, however, cells have sufficient oxygen supply, so they do not follow the preexisting vasculature. This allows the tumor to grow from cylindrical shape into a broader sheet, a paddle-like structure (Figure 2C).

One intriguing behavior arising from the model is the effect of random cell motility within the tumor. Increased motility results in more mixing, therefore it allows more cells to access higher oxygen concentrations at the tumor surface. As oxygen concentration is linked to cell growth, variations in cell size will be smaller with increased motility. However, since the inhomogeneity in cell growth drives the transition from spherical to cylindrical shape, increased cell motility results in a less invasive tumor. This contra-intuitive mechanism is a good example of how computer simulations can help in elucidating mechanisms of cancer. The model neglects blood flow, interstitial pressure, the extracellular matrix, nutrients, and a large part of cell signaling. Despite these simplifications, Shirinifard et al. (2009) claim that the initial avascular tumor growth stages in the model are reminiscent to the first and second stages of gliomas.

5. TUMOR-STROMA INTERACTIONS

We will next review models investigating another general structure in the stroma besides the vasculature: the extracellular matrix (ECM). This heterogeneous spatial network provides mechanical scaffold for the tissues. In order to grow out of the aggregate and invade the host, tumor cells have to be able to migrate through the ECM. For this reason, cells develop the ability to remodel the surrounding ECM (Friedl and Wolf, 2008). ECM representation in models vary. Some authors model the ECM surrounding the tumor as a homogeneous substance, assuming that the size of ECM components is significantly smaller than the cell size. Others argue that structures within the matrix, such as collagen fibers, reach and typically exceed the size of the cells, therefore they represent the ECM as a heterogeneous substance. Studies in the

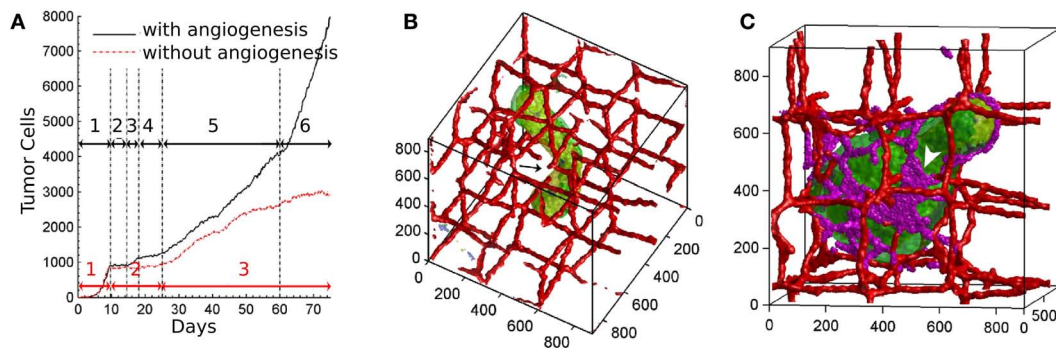


FIGURE 2 | Vascular tumor growth of Shirinifard et al. (2009).

(A) Number of normal proliferative tumor cells in the non-angiogenic (red curve) and angiogenic (black curve) model, showing different stages of development. Black arrows: (1) the exponential growth phase of the spherical tumor; (2) no growth; (3) the linear-spherical phase; (4) slow growth; (5) the linear-cylindrical phase; (6) the linear-sheet phase. Red

Arrows: (1) the exponential growth phase of the spherical tumor; (2) slow growth; (3) cylindrical growth phase. **(B)** Cylindrical shaped non-angiogenic tumor. Tumor cells are shown in green, the vasculature is red. **(C)** Paddle-shaped angiogenic tumor. Neovascular endothelial cells are shown in purple. Images reproduced from Shirinifard et al. (2009) with permission.

following sections consider the interface between the tumor and the stroma.

5.1. INVASIVENESS AND HAPTOTAXIS

Cells have been described to move toward higher concentrations of ECM, a property termed haptotaxis. This behavior might naturally play a role in tumor invasion, therefore it has been in the focus of more computational studies.

Turner and Sherratt (2002) reproduce invasion in streams, also known as “fingering,” eventually resulting in an advancing front that separates from the main tumor mass (**Figure 3A**). In this model the system is filled with ECM initially, and it is assumed to be exponentially degraded in the vicinity of cells. Cells divide with a division probability increasing with time and with increasing cell-ECM contact. This assumption is based on the observation that cells divide more often if they have more contact with the ECM (Huang and Ingber, 1999).

In this model, the tumor front invades deeper into the ECM if the cells have higher haptotactic sensitivity, or if they secrete proteolytic enzymes at a higher rate. Interestingly, increasing both the haptotactic sensitivity and the secretion rate of the proteolytic enzymes simultaneously leads to more effective invasion than invasion driven by either of these mechanisms alone. Counterintuitively, the model suggests that an increase in cell proliferation results in a slower invasion. The reason for this behavior is found in the mechanism of invasion: cells at the invasion front detach from the main tumor body. As the haptotactic effect is highest at the very edge of the front, the back of the front and the main tumor mass is exposed to a smaller haptotactic gradient. Due to cell-cell adhesion, these cells pull the invading front back and thus slow the invasion. Cell proliferation creates an increasing tumor mass and keeps the cells at the front connected for a longer time. In a follow-up paper, Turner et al. (2004) extended their model to explore possible effects of tamoxifen treatment on tumor invasion. This more detailed model explicitly describes the secretion and diffusion of proteolytic enzymes and TGF- β . Tamoxifen increases TGF- β secretion

in tumors, resulting in reduced cell proliferation rates and higher apoptosis rates. Based on experimental observations (Koli and Arteaga, 1996; Nakata et al., 2002), increase in TGF- β expression increases haptotaxis index of cells in the model. Turner and co-workers find that TGF- β treatment can increase invasiveness: although high levels of TGF- β decrease the tumor cell population, the interface morphology becomes more irregular, reminiscent of more invasive tumors. By inducing apoptosis inside the tumor, TGF- β dilutes the aggregate, making it easier for cells to separate from the main tumor and invade the ECM. This behavior is further enhanced by the increase in haptotactic response due to TGF- β .

The model framework of Turner and colleagues has been extended by Scianna and Preziosi (2012), to include intracellular regulation of cell motility, based on extracellular growth factor concentrations. In accord with the findings of Turner and Sherratt (2002), Scianna and Preziosi (2012) point out that therapies aiming at increasing cell-cell adhesion between tumor cells, or loosening adhesions between tumor cells and the ECM, lead to a more compact tumor aggregate, that is easier to remove surgically. Inhibiting the matrix degrading ability of tumor cells, or inhibiting their ability to haptotax also resulted in less disperse invasion fronts in the model of Scianna and Preziosi (2012). These results were obtained by simulating invasion of a homogeneous environment. Givero et al. (2010) showed that these hold in a more realistic environment as well. They simulated *in vitro* ovarian cancer transmigration essays, where single tumor cells or a group of tumor cells invade a connected layer of mesothelial cells. They show that depending on the cohesion of the tumor cells, invasion occurs at multiple or single loci. In both their *in vitro* experiments and model simulations, Givero and colleagues show that individual cells can penetrate, or intercalate, the monolayer without damaging it. A group of tumor cells, however, disrupts the monolayer as they invade. Using their model, they demonstrate that the mode of invasion – group or individual – depends on the relative adhesion between tumor cells and tumor cells and the mesothelial cells.

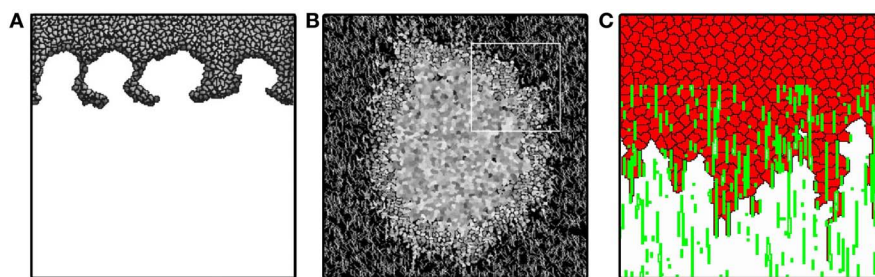


FIGURE 3 | Tumor invasion with homogeneous and heterogeneous ECM.

(A) Invasion front of tumor penetrating the stroma via “viscous fingers.” Image reproduced from Turner and Sherratt (2002) with permission. **(B)** Avascular tumor model of Rubenstein and Kaufman (2008), exploring invasion along

ECM fibers. Image reproduced from Rubenstein and Kaufman (2008) with permission. **(C)** Invasion front of persistently moving cancer cells penetrate in “fingers” along ECM fibers describe penetration dynamics even without cell division. Image produced based on the model of Szabó et al. (2012).

5.2. INVASIVENESS AND NUTRIENT SUPPLY

In the previous section we described studies of tumor invasion due to cell-ECM interactions. Popławski et al. (2009) show how invasion fronts can be affected by nutrient availability. They show that tumor starvation (low nutrient flux) promotes tumor invasion, and cell–stroma adhesion (surface tension) defines the width of invading clusters of cells. Following Turner and co-workers, Popławski et al. (2009) assumed that tumor cells secrete matrix degrading enzymes. In their model matrix digestion releases a nutrient or growth factor required for cell growth. Cell growth is an increasing function of available substrate, and cells divide when reaching doubling size. Cell death is not considered in the model. Tumor metabolism efficiency is implicitly included in the model by controlling substrate uptake and cell growth rate independently.

The authors find that if nutrient supply is abundant, e.g., if the substrate consumption is relatively low, the tumor assumes a dense and spherical morphology. In this case cell-matrix surface tension (or cell-cell adhesion strength) does not affect tumor morphology. If the nutrient becomes more limiting, the tumor assumes a lobed, branched shape, and becomes sensitive to the cell-matrix surface tension parameter: lower surface tension allows for more rugged tumor surface. As the substrate cannot reach deep areas inside the tumor, growth slows down closer to the tumor center, resulting in deep grooves, in a mechanism related to the classic diffusion-limited aggregation model (Witten and Sander, 1981). This effect is counteracted by the surface tension which smoothens regions of high positive curvature. Therefore the substrate penetration length (set by substrate consumption) and the capillary length (set by surface tension) together define the surface morphology. The results of Popławski et al. (2009) suggest that depriving nutrients from tumors might increase their invasive potential. Thus they suggest that anti-angiogenic tumor therapies, which aim to reduce the nutrient supply of tumors, might actually induce invasive, metastatic tumor phenotypes.

5.3. HETEROGENEOUS EXTRACELLULAR MATRIX AND CELL MIGRATION

Although the scale of the extracellular matrix building blocks are negligible when compared with the size of the cell, the matrix can still contain structures comparable to or even larger than a

cell. These not only include inhomogeneities in matrix density, but also anisotropic structures such as collagen filaments. Rubenstein and Kaufman (2008) explore avascular tumor growth using a model including both a homogeneous and a filamentous extracellular matrix component, representing diffusible matrix proteins and collagen fibers (**Figure 3B**). Based on the angiogenesis model of Bauer et al. (2007), the ECM is represented as a special frozen cell type that is not allowed to move. Cells are allowed to occupy ECM sites, but when they leave the site, the ECM is restored. Cells strongly adhere to filamentous ECM, and also require this contact for cell division.

Cells in the model of Rubenstein and Kaufman (2008) consume a non-diffusing nutrient and produce waste, producing stratified avascular tumor growth. Cell division is controlled by explicit contact with the ECM: if a cell has reached a target surface area and is in contact with a collagen fiber or matrix, it divides. This results in a proliferating rim around the tumor. Due to a large difference in cell-cell and cell-matrix adhesion, cells are shed at the rim, even in the absence of collagen fibers (similar to the model of Jiang et al., 2005). Cells elongate and invade along fibers in the vicinity of the tumor surface, producing a growth similar to a Gompertz growth. Due to the depletion of nutrients and constant proliferation at the edge, however, the tumor diameter does not stabilize, as expected in a Gompertzian growth. In their two-dimensional *in vitro* experiments Rubenstein and Kaufman observed that tumor cells spread fastest at intermediate collagen concentrations, an effect that their computational model reproduces. Their simulations suggest that this behavior is only valid for shorter collagen fibers, where the density of collagen has to be high in order to form long, contiguous fibers. As collagen density increases and the network is interconnected, cells invade along the fibers. At sufficiently high densities cells overpopulate the immediate neighborhood of the tumor, thus preventing it from faster expansion. One can view this behavior as cells getting stuck at the border of the tumor. Another interesting insight is that fiber anisotropy might direct the invasion when the connected fiber length is significantly larger than the cell size. When cells are allowed to change the structure of the fibrous matrix by degrading it, invasion distance decreases and cells become more rounded. When cells deposit collagen matrix, their invasion becomes slower, much like in the case of high collagen density simulations. Allowing full remodeling of the

ECM, however, results in more invasive tumors than with only degradation or only deposition.

The proposed invasion mechanism is driven by haptotaxis and proliferation at the invading front. Although this model qualitatively reproduces growth curves comparable with experimental observations, it does not account for invasion without cell proliferation. Szabó et al. (2012) show experimentally, that tumor cell lines are able to invade collagen gels *in vitro* even if their proliferation was inhibited. The authors reproduce the fingered invasion morphology and invasion speeds using a model similar to Rubenstein and Kaufman (2008). The model does not account for cell proliferation, nutrients, or waste, but cells are moving in a persistent manner (see below) in a fibrous, aligned matrix environment (Figure 3C). The model results suggest that persistent cell motion may also play a role in invasion, besides proliferation and haptotaxis.

In order to efficiently invade the microenvironment, cells might acquire the ability to move persistently. Motion persistence can result from gradients of nutrients, ECM, growth factors, or pressure, but persistent cell motion might also be intrinsic to cells, as described by *in vitro* studies of Stokes et al. (1991) and Selmeczi et al. (2005). In a cellular Potts model focusing on persistent cell motility, Kabla (2012) explores the necessary conditions for inducing a stream of cells in a heterogeneous cell population. Kabla represents both tumor tissue and the stroma as a densely packed epithelium, with tumor cells having a higher motility and persistence than healthy cells. Persistent motion is modeled using an internal direction of movement in cells (\vec{P}_i), that biases the probability of cell extensions and retractions through the Hamiltonian, as:

$$\Delta H(\sigma(\vec{x}) \rightarrow \vec{x}') = \Delta H_0(\sigma(\vec{x}) \rightarrow \vec{x}') + \lambda_p \sum_{i \in \{\sigma(\vec{x}), \sigma(\vec{x}')\}} \frac{\vec{P}_i}{|\vec{P}_i|} \frac{\Delta \vec{r}}{|\Delta \vec{r}|}. \quad (8)$$

Here $\Delta \vec{r}$ represents the vector pointing from site \vec{x} to site \vec{x}' . The direction of cell motion, \vec{P}_i , is the average cell displacement of the cell in the previous k timesteps and λ_p sets the relative strength of the polarity bias in the Hamiltonian (equation (2)). A similar implementation of persistent motion has been experimentally validated earlier by Szabó et al. (2010), where the direction of cell motion is evolving in time as:

$$\Delta \vec{P}_i = -\frac{1}{k} \vec{P}_i + \Delta \vec{R}_i, \quad (9)$$

where $\Delta \vec{R}_i$ is the displacement of the cell centroid in the whole timestep (MCS). In Kabla's model, tumor cells invade the healthy tissue in streams collectively, with motility and persistence values that would not allow individual cells to metastasize. In contrast to angiogenesis, where the presence of a small, specialized tip cell population is essential for sprouting, Kabla shows that tip cells are not essential in tumor invasion.

Scianna et al. (2013) further studied the invasion of porous ECM in 2D and 3D configurations. They sub-divided each cell into a nucleus and a cytosol region, which enables them to describe the invasion of dense matrices more realistically and to reproduce

experimentally measured cell migration behaviors. Movement of the simulated cells is maximal in intermediate pore sizes, when the cells are still able to move through them. They show that an increased average alignment of the ECM fibers directs cell motion into a more linear pattern, which results in an increased migration persistence. Furthermore, they show that cell migration is only affected by matrix degrading enzyme production in high density matrices.

6. DISCUSSION

In this review we presented an overview on tumor models using the cellular Potts model. The models resolve cell shape, which allows us to model behavior at the cell level, and give a fair representation of the cellular microenvironment. The reviewed models demonstrate how the CPM can be applied to model tumor growth, the spatial structure of tumors, the effect of tumor heterogeneity on tumor development, the implications of angiogenesis, and how the invasion of tumor cells depends on nutrient availability or the extracellular matrix. Furthermore, the models described above explain cell shedding at the tumor edge, tumor surface morphology, or the counterintuitive effect of tumor treatment on heterogeneous tumors. To better understand the properties of the CPM, it is useful to compare it with other, similar models. Such a comparison is given by Andasari and colleagues, who studied how cell-cell adhesion and metastasis is influenced by cell signaling in epithelial tumors. They directly compared their results obtained using a CPM (Andasari and Chaplain, 2012) with results from a cell-center model (Andasari et al., 2011). While in the cell-center model the malignant cells leave the epithelium in a wave, spreading radially outwards from an initial cell, in the CPM this radial pattern becomes more stochastic and irregular. This example shows how the intrinsic stochasticity of the CPM affects the system on the multicellular scale.

Despite its advantages, the CPM also has its disadvantages. The dynamics of the model represents a constraint to the simulated cells: the maximum speed of cells in the model is limited to the size of the lattice neighborhood per MCS. A related mechanical constraint is the limited speed of compression waves: if one side of a floating 3D aggregate is pushed, the aggregate will deform instead of translating as a whole unit. This is a result of the over-damped nature of the model, and might present complications when modeling *in vitro* tumor invasion from an aggregate (for a more detailed discussion, see Szabó et al., 2012). Furthermore, model dynamics is non-local due to the volume constraint term, which complicates mean-field analyses (Voss-Böhme, 2012) and computational parallelization (Chen et al., 2007) of the model. Some of these disadvantages, e.g., grid effects, are resolved by other multi-particle cell-based models. Probably the closest model framework to the CPM is the subcellular element model (ScEM), introduced by Newman (2005). Cells in the ScEM are represented by elements (analogous to a lattice site in the CPM) that interact with other elements in the same cell and other cells. Instead of copying, the elements of the ScEM are allowed to move in continuous space. Similar to the CPM, the interaction between elements determines the dynamics of the cell, making it a flexible system. The ScEM is a promising framework with studies focusing on phenomena from single cell rheology (Sandersius and Newman, 2008)

to multicellular epithelial tissue behavior (Newman, 2008; Sandersius et al., 2011a) and invasion (Sandersius et al., 2011b). Another example of a well developed, off-lattice model is the immersed boundary framework (IBCell), introduced by Rejniak (2007). The model has been applied to tumor modeling (Anderson et al., 2009), together with two other cellular automata-like approaches (the hybrid discrete continuum model, and evolutionary hybrid cellular automata model), to show the counterintuitive connection between nutrient availability and tumor surface fingering, similar to Popławski et al. (2009). The model represents cells with boundary points that are connected elastically (similar to models for plant cells, see for example: Merks et al., 2011). The advantage of the model compared with the CPM is its ability to explicitly represent the physical connections between cells, which makes it a strong model for 2D simulations. Extending the IBCell to 3D, however, is not straight-forward and would require high technical skills.

Although these off-lattice models solve some of the problems inherent to a lattice-based approach, an advantage of the CPM is its direct extensibility to three-dimensions, and the availability of community-driven open source implementations, e.g., *CompuCell3D*¹ and Tissue Simulation Toolkit². The packages provide a straight-forward set of tools for constructing cell-based models without the need to spend significant time on model development. *CompuCell3D* is easily extended with new cell behaviors, subcellular compartments, and extracellular materials. The framework can be configured to include diffusing substances (such as growth factors, or nutrients). More recent extensions make it possible to include extracellular matrix materials in the CPM. The level of

detail at which the ECM is described depends on the particular problem that the model addresses, ranging from the ECM as an extracellular, homogeneous field, to a fibrous matrix represented with a special CPM “cell.” Cell behavior, such as chemotaxis, cell elongation, cell proliferation and growth, or persistent motility can all be readily implemented as modules in the framework. In its original application the smallest scales of a CPM model were the pseudopods and the single cells. More recently the CPM has been extended with additional subcellular structures, including intracellular compartments, epithelial junctions, and focal adhesions, many of which are now made available as modules for *CompuCell3D* (Swat et al., 2012). These subcellular extensions have been applied to modeling cell organelles (Scianna et al., 2013), and mechanically connected tissues, such as epithelia (for example, Shirinifard et al., 2012). Another useful extension is the possibility to run ODE models of regulatory networks inside each of the cells of a CPM. To this end, *CompuCell3D* has recently been integrated with the SBML-compliant regulatory network modeling tool Systems Biology Workbench (SBW), see, e.g., Hester et al., 2011. This development opens the door to multiscale models of tumor development, in which existing, SBML-compliant models of signaling, genetic regulation, and metabolism of tumor cells can be studied in a more detailed, realistic multicellular context.

ACKNOWLEDGMENTS

The authors would like to thank the constructive comments of the reviewers. This work was cofinanced by the Netherlands Consortium for Systems Biology (NCSB), which is part of the Netherlands Genomics Initiative/Netherlands Organisation for Scientific Research. The investigations were in part supported by the Division for Earth and Life Sciences (ALW) with financial aid from the Netherlands Organization for Scientific Research (NWO).

REFERENCES

- Alarcón, T., Byrne, H. M., and Maini, P. K. (2003). A cellular automaton model for tumour growth in inhomogeneous environment. *J. Theor. Biol.* 225, 257–274.
- Andasari, V., and Chaplain, M. A. J. (2012). Intracellular modelling of cell-matrix adhesion during cancer cell invasion. *Math. Model. Nat. Phenom.* 7, 29–48.
- Andasari, V., Gerisch, A., Lolas, G., South, A. P., and Chaplain, M. A. J. (2011). Mathematical modeling of cancer cell invasion of tissue: biological insight from mathematical analysis and computational simulation. *J. Math. Biol.* 63, 141–171.
- Anderson, A. R. A., Basanta, D., Gerlee, P., and Rejniak, K. A. (2011). “Evolution, regulation, and disruption of homeostasis, and its role in carcinogenesis,” in *Multiscale Cancer Modeling*, eds T. S. Deisboeck and G. S. Stamatakis (Boca Raton: Taylor & Francis), 1–30.
- Anderson, A. R. A., Rejniak, K. A., Gerlee, P., and Quaranta, V. (2009). Microenvironment driven invasion: a multiscale multimodel investigation. *J. Math. Biol.* 58, 579–624.
- Anderson, A. R. A., Weaver, A. M., Cummings, P. T., and Quaranta, V. (2006). Tumor morphology and phenotypic evolution driven by selective pressure from the microenvironment. *Cell* 127, 905–915.
- Basanta, D., Gatenby, R. A., and Anderson, A. R. A. (2012). Exploiting evolution to treat drug resistance: combination therapy and the double bind. *Mol. Pharm.* 9, 914–921.
- Bauer, A. L., Jackson, T. L., and Jiang, Y. (2007). A cell-based model exhibiting branching and anastomosis during tumor-induced angiogenesis. *Biophys. J.* 92, 3105–3121.
- Bauer, A. L., Jackson, T. L., and Jiang, Y. (2009). Topography of extracellular matrix mediates vascular morphogenesis and migration speeds in angiogenesis. *PLoS Comput. Biol.* 5:e1000445. doi:10.1371/journal.pcbi.1000445
- Bentley, K., Jones, M., and Cruys, B. (2013). Predicting the future: towards symbiotic computational and experimental angiogenesis research. *Exp. Cell Res.* doi:10.1016/j.yexcr.2013.02.001
- Brodland, G. W., Viens, D., and Veldhuis, J. H. (2007). A new cell-based FE model for the mechanics of embryonic epithelia. *Comput. Methods Biomech. Biomed. Eng.* 10, 121–128.
- Chaplain, M. A. J., McDougall, S. R., and Anderson, A. R. A. (2006). Mathematical modeling of tumor-induced angiogenesis. *Annu. Rev. Biomed. Eng.* 8, 233–257.
- Chen, N., Glazier, J. A., Izaguirre, J. A., and Alber, M. S. (2007). A parallel implementation of the cellular Potts Model for simulation of cell-based morphogenesis. *Comput. Phys. Commun.* 176, 670–681.
- Daub, J. T., and Merks, R. M. H. (2013). A cell-based model of extracellular-matrix-guided endothelial cell migration during angiogenesis. *Bull. Math. Biol.* doi:10.1007/s11538-013-9826-5
- Drasdo, D., and Höhme, S. (2003). Individual-based approaches to birth and death in avascular tumors. *Math. Comput. Model.* 37, 1163–1175.
- Drasdo, D., Kree, R., and McCaskill, J. S. (1995). Monte Carlo approach to tissue-cell populations. *Phys. Rev. E* 52, 6635–6657.
- Enderling, H., Anderson, A. R. A., Chaplain, M. A. J., Beheshti, A., Hlatky, L., and Hahnfeldt, P. (2009). Paradoxical dependencies of tumor dormancy and progression on basic cell kinetics. *Cancer Res.* 69, 8814–8821.
- Farhadifar, R., Röper, J.-C., Aigouy, B., Eaton, S., and Jülicher, F. (2007). The influence of cell mechanics, cell-cell interactions, and proliferation on epithelial packing. *Curr. Biol.* 17, 2095–2104.
- Folkman, J., and Hochberg, M. (1973). Self-regulation of growth in three dimensions. *J. Exp. Med.* 138, 745–753.
- Frezza, C., Zheng, L., Folger, O., Rajagopalan, K. N., MacKenzie, E. D., Jerby, L., et al. (2011). Haem oxygenase is synthetically lethal with the tumour suppressor fumarate hydratase. *Nature* 477, 225–228.

- Friedl, P., and Wolf, K. (2008). Tube travel: the role of proteases in individual and collective cancer cell invasion. *Cancer Res.* 68, 7247–7249.
- Gamba, A., Ambrosi, D., Coniglio, A., de Candia, A., Di Talia, S., Giraudo, E., et al. (2003). Percolation, morphogenesis, and burgers dynamics in blood vessels formation. *Phys. Rev. Lett.* 90, 118101.
- Gao, X., McDonald, J. T., Hlatky, L., and Enderling, H. (2013). Acute and fractionated irradiation differentially modulate glioma stem cell division kinetics. *Cancer Res.* 73, 1481–1490.
- Gatenby, R. (2012). Perspective: finding cancer's first principles. *Nature* 491, S55.
- Gatenby, R. A., and Vincent, T. L. (2003). An evolutionary model of carcinogenesis. *Cancer Res.* 63, 6212–6220.
- Gerlinger, M., Rowan, A. J., Horswell, S., Larkin, J., Endesfelder, D., Gronroos, E., et al. (2012). Intratumor heterogeneity and branched evolution revealed by multiregion sequencing. *N. Engl. J. Med.* 366, 883–892.
- Gevertz, J. L., and Torquato, S. (2006). Modeling the effects of vasculature evolution on early brain tumor growth. *J. Theor. Biol.* 243, 517–531.
- Giverson, C., Scianina, M., Preziosi, L., Lo Buono, N., and Funaro, A. (2010). Individual cell-based model for in vitro mesothelial invasion of ovarian cancer. *Math. Model. Nat. Phenom.* 5, 203–223.
- Glazier, J. A., and Graner, F. (1993). Simulation of the differential adhesion driven rearrangement of biological cells. *Phys. Rev. E* 47, 2128–2154.
- Gompertz, B. (1825). On the nature of the function expressive of the law of human mortality, and on a new mode of determining the value of life contingencies. *Philos. Trans. R. Soc. Lond.* 115, 513–583.
- Graner, F., and Glazier, J. A. (1992). Simulation of biological cell sorting using a two-dimensional extended Potts model. *Phys. Rev. Lett.* 69, 2013–2016.
- Hanahan, D., and Weinberg, R. A. (2000). The hallmarks of cancer. *Cell* 100, 57–70.
- Hanahan, D., and Weinberg, R. A. (2011). Hallmarks of cancer: the next generation. *Cell* 144, 646–674.
- Hatzikirou, H., Breier, G., and Deutsch, A. (2008). "Cellular automaton models of tumor invasion," in *Encyclopedia of Complexity and Systems Science*, Chap. 417, ed. R. A. Meyers (Heidelberg: Springer), 1–18.
- Hatzikirou, H., Deutsch, A., Schaller, C., Simon, M., and Swanson, K. (2005). Mathematical modelling of glioblastoma tumour development: a review. *Math. Models Methods Appl. Sci.* 15, 1779–1794.
- Hester, S. D., Belmonte, J. M., Gens, J. S., Clendenon, S. G., and Glazier, J. A. (2011). A multi-cell, multi-scale model of vertebrate segmentation and somite formation. *PLoS Comput. Biol.* 7:e1002155. doi:10.1371/journal.pcbi.1002155
- Hirashima, T., Iwasa, Y., and Morishita, Y. (2009). Dynamic modeling of branching morphogenesis of ureteric bud in early kidney development. *J. Theor. Biol.* 259, 58–66.
- Huang, S., and Ingber, D. E. (1999). The structural and mechanical complexity of cell-growth control. *Nat. Cell Biol.* 1, E131–E138.
- Jiang, Y., Bauer, A. L., and Jackson, T. L. (2012). "Cell-based models of tumor angiogenesis," in *Modeling Tumor Vasculature: Molecular, Cellular, and Tissue Level Aspects and Implications*, ed. T. L. Jackson (New York: Springer), 135–150.
- Jiang, Y., Pjesivac-Grbovic, J., Cantrell, C., and Freyer, J. P. (2005). A multiscale model for avascular tumor growth. *Biophys. J.* 89, 3884–3894.
- Kabla, A. J. (2012). Collective cell migration: leadership, invasion and segregation. *J. R. Soc. Interface* 9, 3268–3278.
- Keller, R., and Davidson, L. (2004). "Cell crawling, cell behaviour and biomechanics during convergence and extension," in *Cell Motility: From Molecules to Organisms*, Chap. 18, eds A. Ridley, M. Peckham, and P. Clark (Chichester: John Wiley & Sons, Ltd), 277–297.
- Kim, Y., and Othmer, H. G. (2013). A hybrid model of tumor-stromal interactions in breast cancer. *Bull. Math. Biol.* doi:10.1007/s11538-012-9787-01-47
- Kim, Y., Stolarska, M. A., and Othmer, H. G. (2007). A hybrid model for tumor spheroid growth in vitro i: theoretical development and early results. *Math. Models Methods Appl. Sci.* 17, 1773–1798.
- Koli, K. M., and Arteaga, C. L. (1996). Complex role of tumor cell transforming growth factor (TGF)- β s on breast carcinoma progression. *J. Mammary Gland Biol. Neoplasia* 1, 373–380.
- Laird, A. K. (1964). Dynamics of tumor growth. *Br. J. Cancer* 18, 490–502.
- Levine, A. J., and Puzio-Kuter, A. M. (2010). The control of the metabolic switch in cancers by oncogenes and tumor suppressor genes. *Science* 330, 1340–1344.
- Macklin, P., Edgerton, M. E., Thompson, A. M., and Cristini, V. (2012). Patient-calibrated agent-based modelling of ductal carcinoma in situ (dcis): from microscopic measurements to macroscopic predictions of clinical progression. *J. Theor. Biol.* 301, 122–140.
- Manoussaki, D., Lubkin, S. R., Vernon, R. B., and Murray, J. D. (1996). A mechanical model for the formation of vascular networks in vitro. *Acta Biotheor.* 44, 271–282.
- Marusyk, A., Almendro, V., and Polyak, K. (2012). Intra-tumour heterogeneity: a looking glass for cancer? *Nat. Rev. Cancer* 12, 323–334.
- McElwain, D. L. S., and Pettet, G. J. (1993). Cell migration in multi-cell spheroids: swimming against the tide. *Bull. Math. Biol.* 55, 655–674.
- Merks, R. M. H., and Glazier, J. A. (2005). A cell-centered approach to developmental biology. *Physica A* 352, 113–130.
- Merks, R. M. H., Brodsky, S. V., Goligorsky, M. S., Newman, S. A., and Glazier, J. A. (2006). Cell elongation is key to in silico replication of in vitro vasculogenesis and subsequent remodeling. *Dev. Biol.* 289, 44–54.
- Merks, R. M. H., Guravage, M., Inzé, D., and Beemster, G. T. S. (2011). VirtualLeaf: an open-source framework for cell-based modeling of plant tissue growth and development. *Plant Physiol.* 155, 656–666.
- Merks, R. M. H., Perryn, E. D., Shirinifard, A., and Glazier, J. A. (2008). Contact-inhibited chemotaxis in de novo and sprouting blood-vessel growth. *PLoS Comput. Biol.* 4:e1000163. doi:10.1371/journal.pcbi.1000163
- Nakata, D., Hamada, J. I., Ba, Y., Matsushita, K., Shibata, T., Hosokawa, M., et al. (2002). Enhancement of tumorigenic, metastatic and in vitro invasive capacity of rat mammary tumor cells by transforming growth factor- β . *Cancer Lett.* 175, 95–106.
- Newman, T. J. (2005). Modeling multicellular systems using subcellular elements. *Math. Biosci. Eng.* 2, 611–622.
- Newman, T. J. (2008). "Grid-free models of multicellular systems, with an application to large-scale vortices accompanying primitive streak formation," in *Multiscale Modeling of Developmental Systems, Current Topics in Developmental Biology*, Vol. 81, eds S. Schnell, P. K. Maini, S. A. Newman, and T. J. Newman (Amsterdam: Academic Press), 157–182.
- Owen, M. R., Stamper, I. J., Muthana, M., Richardson, G. W., Dobson, J., Lewis, C. E., et al. (2011). Mathematical modeling predicts synergistic antitumor effects of combining a macrophage-based, hypoxia-targeted gene therapy with chemotherapy. *Cancer Res.* 71, 2826–2837.
- Palm, M. M., and Merks, R. M. H. (2013). Vascular networks due to dynamically arrested crystalline ordering of elongated cells. *Phys. Rev. E* 87:012725. doi:10.1103/PhysRevE.87.012725
- Peirce, S. M., Mac Gabhann, F., and Bautch, V. L. (2012). Integration of experimental and computational approaches to sprouting angiogenesis. *Curr. Opin. Hematol.* 19, 184–191.
- Pleasant, E. D., Stephens, P. J., O'Meara, S., McBride, D. J., Meynert, A., Jones, D., et al. (2010). A small-cell lung cancer genome with complex signatures of tobacco exposure. *Nature* 463, 184–190.
- Poplawski, N. J., Agero, U., Gens, J. S., Swat, M., Glazier, J. A., and Anderson, A. R. A. (2009). Front instabilities and invasiveness of simulated avascular tumors. *Bull. Math. Biol.* 71, 1189–1227.
- Pugh, T. J., Weeraratne, S. D., Archer, T. C., Pomeranz Krummel, D. A., Auclair, D., Bochicchio, J., et al. (2012). Medulloblastoma exome sequencing uncovers subtype-specific somatic mutations. *Nature* 488, 106–110.
- Rejniak, K. A. (2007). An immersed boundary framework for modeling the growth of individual cells: an application to the early tumour development. *J. Theor. Biol.* 247, 186–204.
- Rejniak, K. A., and Anderson, A. R. A. (2011). Hybrid models of tumor growth. *Wiley Interdiscip. Rev. Syst. Biol. Med.* 3, 115–125.
- Reya, T., Morrison, S. J., Clarke, M. F., and Weissman, I. L. (2001). Stem cells, cancer, and cancer stem cells. *Nature* 414, 105–111.
- Rubenstein, B. M., and Kaufman, L. J. (2008). The role of extracellular matrix in glioma invasion: a cellular Potts model approach. *Biophys. J.* 95, 5661–5680.
- Sandersius, S. A., Chuai, M., Weijer, C. J., and Newman, T. J. (2011a). Correlating cell behavior with tissue topology in embryonic epithelia. *PLoS ONE* 6:e18081. doi:10.1371/journal.pone.0018081
- Sandersius, S. A., Weijer, C. J., and Newman, T. J. (2011b). Emergent cell and tissue dynamics from subcellular

- modeling of active biomechanical processes. *Phys. Biol.* 8:045007. doi:10.1088/1478-3975/8/4/045007
- Sandersius, S. A., and Newman, T. J. (2008). Modeling cell rheology with the subcellular element model. *Phys. Biol.* 5:015002. doi:10.1088/1478-3975/5/1/015002
- Savill, N. J., and Hogeweg, P. (1997). Modelling morphogenesis: from single cells to crawling slugs. *J. Theor. Biol.* 184, 229–235.
- Scianna, M., and Preziosi, L. (2012). A hybrid model describing different morphologies of tumor invasion fronts. *Math. Model. Nat. Phenom.* 7, 78–104.
- Scianna, M., Preziosi, L., and Wolf, K. (2013). A Cellular Potts Model simulating cell migration on and in matrix environments. *Math. Biosci. Eng.* 10, 235–261.
- Selmeczi, D., Mosler, S., Hagedorn, P. H., Larsen, N. B., and Flyvbjerg, H. (2005). Cell motility as persistent random motion: theories from experiments. *Biophys. J.* 89, 912–931.
- Shah, S. P., Morin, R. D., Khattri, J., Prentice, L., Pugh, T., Burleigh, A., et al. (2009). Mutational evolution in a lobular breast tumour profiled at single nucleotide resolution. *Nature* 461, 809–813.
- Shirinifard, A., Gens, J. S., Zaitlen, B. L., Poplawski, N. J., Swat, M., and Glazier, J. A. (2009). 3D multi-cell simulation of tumor growth and angiogenesis. *PLoS ONE* 4:e7190. doi:10.1371/journal.pone.0007190
- Shirinifard, A., Glazier, J. A., Swat, M., Gens, J. S., Family, F., Jiang, Y., et al. (2012). Adhesion failures determine the pattern of choroidal neovascularization in the eye: a computer simulation study. *PLoS Comput. Biol.* 8:e1002440. doi:10.1371/journal.pcbi.1002440
- Sottoriva, A., Verhoeff, J. J. C., Borovski, T., McWeeney, S. K., Naumov, L., Medema, J. P., et al. (2010). Cancer stem cell tumor model reveals invasive morphology and increased phenotypical heterogeneity. *Cancer Res.* 70, 46–56.
- Sottoriva, A., Vermeulen, L., and Tavaré, S. (2011). Modeling evolutionary dynamics of epigenetic mutations in hierarchically organized tumors. *PLoS Comput. Biol.* 7:e1001132. doi:10.1371/journal.pcbi.1001132
- Stamper, I. J., Byrne, H. M., Owen, M. R., and Maini, P. K. (2007). Modelling the role of angiogenesis and vasculogenesis in solid tumour growth. *Bull. Math. Biol.* 69, 2737–2772.
- Starruß, J., Bley, Th., Søgaard Andersen, L., and Deutsch, A. (2007). A new mechanism for collective migration in *Myxococcus xanthus*. *J. Stat. Phys.* 128, 269–286.
- Steinberg, M. S. (1970). Does differential adhesion govern self-assembly processes in histogenesis? Equilibrium configurations and the emergence of a hierarchy among populations of embryonic cells. *J. Exp. Zool.* 173, 395–433.
- Stokes, C. L., Lauffenburger, D. A., and Williams, S. K. (1991). Migration of individual microvessel endothelial cells: stochastic model and parameter measurement. *J. Cell. Sci.* 99, 419–430.
- Stott, E. L., Britton, N. F., Glazier, J. A., and Zajac, M. (1999). Stochastic simulation of benign avascular tumour growth using the Potts model. *Math. Comput. Model.* 30, 183–198.
- Swat, M. H., Thomas, G. L., Belmonte, J. M., Shirinifard, A., Hmeljak, D., and Glazier, J. A. (2012). “Multi-scale modeling of tissues using CompuCell3D,” in *Computational Methods in Cell Biology, Methods in Cell Biology*, Vol. 110, Chap. 13, eds A. R. Asthagiri and A. P. Arkin (London: Academic Press), 325–366.
- Szabó, A., and Czirók, A. (2010). The role of cell-cell adhesion in the formation of multicellular sprouts. *Math. Model. Nat. Phenom.* 5, 106–122.
- Szabó, A., Mehes, E., Kosa, E., and Czirók, A. (2008). Multicellular sprouting in vitro. *Biophys. J.* 95, 2702–2710.
- Szabó, A., Perryn, E. D., and Czirók, A. (2007). Network formation of tissue cells via preferential attraction to elongated structures. *Phys. Rev. Lett.* 98:038102. doi:10.1103/PhysRevLett.98.038102
- Szabó, A., Ünneper, R., Méhes, E., Tsal, W. O., Argraves, W. S., Cao, Y., et al. (2010). Collective cell motion in endothelial monolayers. *Phys. Biol.* 7:046007. doi:10.1088/1478-3975/7/4/046007
- Szabó, A., Varga, K., Garay, T., Hegedűs, B., and Czirók, A. (2012). Invasion from a cell aggregate – the roles of active cell motion and mechanical equilibrium. *Phys. Biol.* 9:016010. doi:10.1088/1478-3975/9/1/016010
- Thomas, R. K., Baker, A. C., DeBiasi, R. M., Winckler, W., LaFramboise, T., Lin, W. M., et al. (2007). High-throughput oncogene mutation profiling in human cancer. *Nat. Genet.* 39, 347–351.
- Tripodi, S., Ballet, P., and Rodin, V. (2010). “Computational energetic model of morphogenesis based on multi-agent cellular Potts model,” in *Advances in Computational Biology, Advances in Experimental Medicine and Biology*, Vol. 680, ed. H. R. Arabnia (New York: Springer), 685–692.
- Turner, S., and Sherratt, J. A. (2002). Intercellular adhesion and cancer invasion: a discrete simulation using the extended Potts model. *J. Theor. Biol.* 216, 85–100.
- Turner, S., Sherratt, J. A., and Cameron, D. (2004). Tamoxifen treatment failure in cancer and the nonlinear dynamics of TGFβ. *J. Theor. Biol.* 229, 101–111.
- Uren, A. G., Kool, J., Matentzoglou, K., de Ridder, J., Mattison, J., van Uiter, M., et al. (2008). Large-scale mutagenesis in p19ARF- and p53-deficient mice identifies cancer genes and their collaborative networks. *Cell* 133, 727–741.
- Van Leeuwen, I. M. M., Mirams, G. R., Walter, A., Fletcher, A., Murray, P., Osborne, J., et al. (2009). An integrative computational model for intestinal tissue renewal. *Cell Prolif.* 42, 617–636.
- Vazquez, A., Liu, J., Zhou, Y., and Oltvai, Z. N. (2010). Catabolic efficiency of aerobic glycolysis: the warburg effect revisited. *BMC Syst. Biol.* 4:58. doi:10.1186/1752-0509-4-58
- Visvader, J. E., and Lindeman, G. J. (2008). Cancer stem cells in solid tumours: accumulating evidence and unresolved questions. *Nat. Rev. Cancer* 8, 755–768.
- Voss-Böhme, A. (2012). Multi-scale modeling in morphogenesis: a critical analysis of the cellular Potts model. *PLoS ONE* 7:e42852. doi:10.1371/journal.pone.0042852
- Witten, T. A. Jr., and Sander, L. M. (1981). Diffusion-limited aggregation, a kinetic critical phenomenon. *Phys. Rev. Lett.* 47, 1400–1403.
- Yachida, S., Jones, S., Bozic, I., Antal, T., Leary, R., Fu, B., et al. (2010). Distant metastasis occurs late during the genetic evolution of pancreatic cancer. *Nature* 467, 1114–1117.
- Zajac, M., Jones, G. L., and Glazier, J. A. (2003). Simulating convergent extension by way of anisotropic differential adhesion. *J. Theor. Biol.* 222, 247–259.

Conflict of Interest Statement: The authors declare that the research was conducted in the absence of any commercial or financial relationships that could be construed as a potential conflict of interest.

Received: 21 December 2012; paper pending published: 22 February 2013; accepted: 02 April 2013; published online: 16 April 2013.

Citation: Szabó A and Merks RMH (2013) Cellular Potts modeling of tumor growth, tumor invasion, and tumor evolution. *Front. Oncol.* 3:87. doi: 10.3389/fonc.2013.00087

This article was submitted to *Frontiers in Molecular and Cellular Oncology*, a specialty of *Frontiers in Oncology*.

Copyright © 2013 Szabó and Merks. This is an open-access article distributed under the terms of the Creative Commons Attribution License, which permits use, distribution and reproduction in other forums, provided the original authors and source are credited and subject to any copyright notices concerning any third-party graphics etc.



Ovarian tumor attachment, invasion, and vascularization reflect unique microenvironments in the peritoneum: insights from xenograft and mathematical models

Mara P. Steinkamp^{1†}, Kimberly Kanigel Winner^{2†}, Suzy Davies³, Carolyn Muller³, Yong Zhang⁴, Robert M. Hoffman⁴, Abbas Shirinifard⁵, Melanie Moses^{2,6}, Yi Jiang^{7*} and Bridget S. Wilson^{1*}

¹ Department of Pathology, University of New Mexico, Albuquerque, NM, USA

² Department of Biology, University of New Mexico, Albuquerque, NM, USA

³ Department of OB/GYN, University of New Mexico, Albuquerque, NM, USA

⁴ AntiCancer Inc., and Department of Surgery, University of California San Diego, San Diego, CA, USA

⁵ Department of Physics, Institute of Biocomplexity, University of Indiana, Bloomington, IN, USA

⁶ Department of Computer Science, University of New Mexico, Albuquerque, NM, USA

⁷ Department of Mathematics and Statistics, Georgia State University, Atlanta, GA, USA

Edited by:

Katarzyna A. Rejniak, H. Lee Moffitt Cancer Center & Research Institute, USA

Reviewed by:

Frederique Gaits-iacovoni, INSERM U1048, France

Roeland M. Merks, Centrum Wiskunde & Informatica, Netherlands

*Correspondence:

Yi Jiang, Department of Mathematics and Statistics, Georgia State University, 750 COE, 7th floor, 30 Pryor Street, Atlanta, GA 30303, USA.
e-mail: yijiangl1@gmail.com;
Bridget S. Wilson, MSC08-4640, Cancer Research Facility, Room 201, University of New Mexico Health Sciences Center, Albuquerque, NM 87131-0001, USA.
e-mail: bwilson@salud.unm.edu

[†] Mara P. Steinkamp and Kimberly Kanigel Winner have contributed equally to this work.

Ovarian cancer relapse is often characterized by metastatic spread throughout the peritoneal cavity with tumors attached to multiple organs. In this study, interaction of ovarian cancer cells with the peritoneal tumor microenvironment was evaluated in a xenograft model based on intraperitoneal injection of fluorescent SKOV3.ip1 ovarian cancer cells. Intra-vital microscopy of mixed GFP-red fluorescent protein (RFP) cell populations injected into the peritoneum demonstrated that cancer cells aggregate and attach as mixed spheroids, emphasizing the importance of homotypic adhesion in tumor formation. Electron microscopy provided high resolution structural information about local attachment sites. Experimental measurements from the mouse model were used to build a three-dimensional cellular Potts ovarian tumor model (OvTM) that examines ovarian cancer cell attachment, chemotaxis, growth, and vascularization. OvTM simulations provide insight into the relative influence of cancer cell–cell adhesion, oxygen availability, and local architecture on tumor growth and morphology. Notably, tumors on the mesentery, omentum, or spleen readily invade the “open” architecture, while tumors attached to the gut encounter barriers that restrict invasion and instead rapidly expand into the peritoneal space. Simulations suggest that rapid neovascularization of SKOV3.ip1 tumors is triggered by constitutive release of angiogenic factors in the absence of hypoxia. This research highlights the importance of cellular adhesion and tumor microenvironment in the seeding of secondary ovarian tumors on diverse organs within the peritoneal cavity. Results of the OvTM simulations indicate that invasion is strongly influenced by features underlying the mesothelial lining at different sites, but is also affected by local production of chemotactic factors. The integrated *in vivo* mouse model and computer simulations provide a unique platform for evaluating targeted therapies for ovarian cancer relapse.

Keywords: ovarian cancer, tumor modeling, tumor microenvironment, metastasis, cellular Potts model, cell adhesion, angiogenesis, chemotaxis

INTRODUCTION

Ovarian cancer is often detected at a late stage of disease after the cancer has locally disseminated to the peritoneum. Visible tumors are surgically removed and residual microscopic disease is targeted with chemotherapy. However, 90% of patients who originally respond to treatment will relapse with chemotherapy-resistant disease (McGuire et al., 1996). Relapse is thought to occur because residual cancer cells aggregate in the peritoneal fluid and form microscopic tumor spheroids that are more resistant to chemotherapy (Shield et al., 2009). These spheroids can then adhere to the surface of organs in the peritoneum and seed new tumors, encouraged by chemokines and growth factors within the peritoneal fluid (Milliken et al., 2002; Bast et al., 2009).

A common feature of the peritoneal environment is the mesothelial lining that cancer cells must sequentially bind to (Strobel and Cannistra, 1999; Casey et al., 2001; Kenny et al., 2008) and penetrate (Burlison et al., 2006; Iwanicki et al., 2011) in order to adhere to underlying tissues. Recent *in vitro* studies suggest that this penetration step can occur within a few hours after spheroid attachment (Iwanicki et al., 2011). Nevertheless, unique features associated with different organs clearly influence progression in this disease. For example, ovarian cancer cells preferentially colonize the omentum, a fatty tissue that has pockets of resident immune cells referred to as “milky spots” and easily accessible blood vessels (Gerber et al., 2006; Khan et al., 2010; Nieman et al., 2011). Cancer cells also colonize other organs in the peritoneum,

with distinct growth rates and morphology depending on the site. It is reasonable to expect that these heterogeneous tumor populations will respond differently to treatment, motivating further investigation into the features of the microenvironment that govern these differences.

To establish a mouse model of ovarian cancer relapse, SKOV3.ip1 cells expressing fluorescent proteins [GFP, red fluorescent protein (RFP)] were injected into the peritoneum of nude mice and the resulting tumors growing on the omentum, intestine, mesentery, and spleen were imaged. Excised tumors were processed for both transmission and light microscopy, providing detailed information about the cellular environment and vascularization patterns.

The distinct features in tumor morphology at different sites led us to consider the potential contributions of local chemotactic factors, oxygenation and adhesion through mathematical modeling. In recent years, mathematical models have moved beyond the generic models of tumor growth and development (e.g., Jiang et al., 2005; Shirinifard et al., 2009; Morton et al., 2011; Giverso and Preziosi, 2012) and are now able to realistically model cancers, e.g., breast cancer (Chauviere et al., 2010; Macklin et al., 2012) and colon cancer (Dunn et al., 2012). Few have addressed the unique features of ovarian cancer. Arakelyan et al. (2005) modeled ovarian tumor growth response to the dynamics of vascular density and vessel size (Arakelyan et al., 2005). Giverso et al. (2010) developed a two-dimensional model of early ovarian tumor spheroid invasion through the mesothelium and underlying extracellular matrix (ECM) (Giverso et al., 2010).

In the present work, our focus is on understanding the distinct features of tumor morphology at different sites in ovarian cancer relapse in three dimensions. The cellular Potts model framework was chosen because of its previous successes in studying similar problems in tumor growth and angiogenesis (Jiang et al., 2005; Shirinifard et al., 2009). Our cell-based and geometrically realistic ovarian tumor model (OvTM), takes into account characteristics of the peritoneal microenvironment and provides insight into the earliest steps in spheroid attachment, invasion, and vascularization within the peritoneum. In particular, homotypic and heterotypic adhesion observed between SKOV3.ip1 xenograft cancer cells and the niche tissue structure are the starting point of OvTM. We applied the model to explore the roles of cell adhesion, cell migration and proliferation as influenced by the microenvironment at two sites and were able to reproduce experimental observations. The ultimate goal of our model is a realistic representation of spheroid growth, whose dimensions and morphology qualitatively resemble the tumors disseminated in different tissue niches in the peritoneal cavity in our mouse xenografts. Such a model can be further developed to include short-term drug delivery after debulking surgery, allowing the evaluation of local drug responsiveness.

MATERIALS AND METHODS

CELL CULTURE AND CELL LINES

SKOV3.ip1 parental cells and GFP-stable transfectants were kind gifts of Laurie Hudson and Angela Wandinger-Ness (UNM). This aggressive line was passaged through a nude mouse (Yu et al., 1993). Cells were maintained in RPMI-1640 medium supplemented with 5% heat-inactivated FBS, 1% L-glutamine,

1% sodium pyruvate, and 0.5% penicillin/streptomycin (Invitrogen, Grand Island, NY, USA). SKOV3.ip1-GFP cells were treated with 250 μ g/ml hygromycin to maintain GFP expression. To create RFP-expressing SKOV3.ip1 cells, parental cells were transfected with the pTagRFP-N vector (Axxora, San Diego, CA, USA) using Lipofectamine LTX reagent (Invitrogen). Stably fluorescent cells were selected with geneticin sulfate (Invitrogen) for 1 week. Transfectants were sorted for high fluorescence using a Beckman Coulter Legacy MoFlo cell sorter (UNM Flow Cytometry Core Facility).

INTRAPERITONEAL MOUSE MODEL OF OVARIAN CANCER RELAPSE

All mouse procedures were approved by the University of New Mexico Animal Care and Use Committee, in accordance with NIH guidelines for the Care and Use of Experimental Animals.

Nu/nu nude mice (NCI) or nude mice ubiquitously expressing RFP (Anticancer Inc., San Diego, CA, USA) (Yang et al., 2009) were engrafted by intraperitoneal injection with 100 μ l of a single cell suspension containing five million SKOV3.ip1 cells expressing GFP. Tumor adhesion and invasion was assessed at 4 days and 2 weeks post-injection. For low magnification assessment of total tumor burden, eight nude mice were imaged using a Pan-A-See-Ya Panoramic Imaging System (Lighttools, Inc., Encinitas, CA, USA) 2 or 3 weeks post-injection of SKOV3.ip1 GFP cells. For improved resolution images (up to 16 \times , single cell resolution), mice were imaged on the OV100 Olympus whole mouse imaging system (Olympus Corp., Tokyo, Japan) at AntiCancer, Inc., San Diego, CA, USA, as previously reported (Yamauchi et al., 2006).

Where described, sections of intestine and attached mesentery with tumors were excised (Fu and Hoffman, 1993) and fixed in zinc fixative for 30 min (Howdieshell et al., 2011). Samples were mounted on glass slides with ProLong Gold mounting media (Invitrogen). GFP fluorescence and brightfield images were collected on a Nikon TE2000 Microscope (UNM Microscopy Core Facility) using an Axiocam digital color camera and SlideBook Image Acquisition software.

CO-INJECTION EXPERIMENTS

SKOV3.ip1-GFP cells and SKOV3.ip1-RFP cells (2.5×10^6 each population) were harvested from culture by trypsinization and mixed together as a single cell suspension immediately before injecting a total of five million cells into the peritoneum of three nude mice. For consecutive injections, 2.5 million SKOV3.ip1-GFP cells were injected IP into three nude mice followed by injection of 2.5 million SKOV3.ip1-RFP cells a week later. The mice were sacrificed at the end of week 2 and tumors were imaged on the OV100.

HISTOLOGY AND IMMUNOFLOUORESCENCE

Mouse tumors were fixed in formalin or zinc fixative, embedded in paraffin, sectioned and hematoxylin/eosin (H&E) stained by TriCore (Albuquerque, NM, USA) or processed for immunofluorescence using anti-CD31 antibodies (BD Biosciences, San Jose, CA, USA). Images were acquired on a Zeiss AxioSkop or LSM500 confocal microscopes. The area of mesenteric tumors was determined by analysis of images from H&E-stained sections using ImageJ (Schneider et al., 2012). The cross-sectional tumor area corresponding to the hypoxic threshold was calculated to be

$<104,000 \mu\text{m}^2$ based on the diameter of the spheroid in **Figure 7B** ($364 \mu\text{m}$).

TRANSMISSION ELECTRON MICROSCOPY

Tissue was collected and fixed in 2% glutaraldehyde, post-fixed with osmium tetroxide, dehydrated in ascending alcohols, and embedded in Epon. Ultra-thin sections were stained and imaged on a Hitachi H600 transmission electron microscope (TEM). To identify SKOV3.ip1 cells present in tissue samples, their characteristic nuclear ultrastructure was determined from high magnification TEM images taken of SKOV3.ip1-GFP cells grown as 5,000 cell spheroids in a U-bottom Lipidure-coated 96-well plate (NOF America, Irvine, CA, USA) for 48 h.

THE OVARIAN TUMOR MODEL

We based our model on the following set of major assumptions that are inspired by the biology and empirical data.

1. The three-dimensional (3-D) tissues we model consist of ovarian tumor (SKOV3.ip1), mesothelial, adipocyte, endothelial, and smooth muscle cells, as well as ECM fibers and peritoneal fluid.
2. Adhesion strengths between various cell types are prescribed and remain constant, e.g., adhesion between SKOV3.ip1 cells is stronger than between SKOV3.ip1 and mesothelial cells.
3. The chemical environment consists of oxygen, tumor-secreted VEGF, adipocyte-secreted IL-8 (Nieman et al., 2011), and another unidentified growth factor (Growth Factor 2) secreted by blood vessels.
4. Both IL-8 and Growth Factor 2 are chemoattractants for tumor cells. VEGF is a chemoattractant for endothelial cells. Chemotaxis speed is proportional to the chemical gradient.
5. Cells consume oxygen supplied by the peritoneal fluid and blood vessels. When oxygen levels are below a threshold value (20 mm Hg), tumor cells become hypoxic and stop growing. They resume proliferation if oxygen rises above the threshold level.
6. Cells are required to approximately double in volume before dividing and their division times have a Gaussian distribution.
7. Ovarian tumor model does not represent the flow of peritoneal fluid (or ascites). Because the diffusion process for all chemicals considered in our study is much faster than the cellular processes under consideration, chemicals are well-mixed. Therefore, it is reasonable to omit convective delivery of chemicals in this model.
8. Cells can become immobilized if we impose shape constraints. Addition of a surface area constraint as well as a high volume constraint can make cells insensitive to changes in adhesion and to low chemotaxis constants. Adhesion parameter sensitivity analysis was therefore conducted without a surface area constraint on the cells. This constraint was added after adhesion optimization to produce cells that were more spheroidal, as they are seen *in vivo*.

The 3-D ovarian tumor growth and invasion model, OvTM, is based on the cellular Potts model framework using CompuCell3D (Cickovski et al., 2007; Swat et al., 2009). Ovarian cancer

cells growing in the peritoneum were simulated using parameters obtained from the mouse model and from published data. Parameters for the SKOV3.ip1 cells, endothelial cells, oxygen, growth factors, and measurements of mouse peritoneal tissue are shown in **Table 1**.

In the OvTM, five cell types are considered: ovarian tumor (SKOV3.ip1), mesothelial, adipocyte, endothelial, and smooth muscle. ECM fibers and peritoneal fluid are represented as special types. This cell-based model describes cell growth, division, death, and chemotactic migration within a 3-D tissue environment that mimics the specific organ site.

Cells are domains on a 3-D lattice. Each cell has an ID number, S , on each lattice site i of the cell domain, and an associated cell type τ . Cell-cell and cell-environment interactions are specified by an “effective energy”:

$$H = \sum_{i,j} J_{\tau}(S_i), \tau(S_j) [1 - \delta(S_i, S_j)] + \sum_S \lambda [V(S) - V^t(S)]^2 + \sum_i \mu C_i. \quad (1)$$

The parameter J describes the cell-type-dependent adhesion. Adhesion coefficients (J) for the cell types in each model are listed in **Tables 2** and **3**. The Kronecker delta function δ ensures no energy is within cells where ID numbers are the same, limiting adhesion to cell boundaries. A cell's volume V is elastically constrained to V^t , the target cell volume; V^t is constant for the tissue cells, but is set to increase linearly for proliferating cells. μ is the chemical potential describing the strength of chemotaxis, and C is the chemical concentration at the cell. This term applies to cancer and endothelial cells when their respective chemoattractant signals are above threshold activation values.

A modified Metropolis algorithm was used to simulate cell dynamics. A cell boundary lattice site is selected at random; the cell number, S , is copied to an unlike neighbor site S' (selected at random). This copying corresponds to the cell S protruding a unit volume into the neighboring cell S' . The difference between the effective energies before and after the protrusion event, E , determines if this copying event will be accepted. If the energy decreases, the protrusion is accepted; if it increases, the protrusion is accepted with a Boltzmann probability, $\exp(-E/T)$. The effective temperature, T , describes the amplitude of cytoskeletal fluctuation (Mombach et al., 1995). By such microscopic membrane protrusion and retraction, the cells perform biased random walks, and rearrange themselves, within the constraints of their volumes and chemical guidance.

Chemical dynamics

Chemical dynamics are evaluated through continuous diffusion equations and are considered well-mixed in the peritoneal fluid. Chemicals acting as chemoattractants to SKOV3.ip are: adipocyte-secreted IL-8 (Nieman et al., 2011), and an unidentified growth factor secreted from the vessel (Growth Factor 2). The chemoattractant for endothelial cells during angiogenesis is VEGF. A system of partial differential equations describes the chemical dynamics, including diffusion through tissues, growth factor decay, glucose and oxygen consumption, and cell-uptake of signal molecules.

Table 1 | OvTM parameters.

	Value	Units	Source
CHEMICAL FIELDS			
O ₂ concentration (blood and peritoneal fluid)	98.5	mm Hg	Shirasawa et al. (2003), Kizaka-Kondoh et al. (2009)
O ₂ diffusion (D_{O_2})	84,000	$\mu\text{m}^2/\text{min}$	MacDougall and McCabe (1967)
VEGF diffusion (D_V)	600	$\mu\text{m}^2/\text{min}$	Serini et al. (2003), Bauer et al. (2009)
VEGF decay (γ_V)	0.01083	/min	Serini et al. (2003), Bauer et al. (2009)
VEGF secretion: normoxic tumor cell (α_V)	3.82×10^{-7}	pg/min/cell	Huang et al. (2000)
Chemotactic Factor 2 diffusion (D_{C_2})	700	$\mu\text{m}^2/\text{min}$	e Serini et al. (2003), Bauer et al. (2009)
Chemotactic Factor 2 decay (κ_{C_2})	0.01083	/min	e Serini et al. (2003), Bauer et al. (2009)
Chemotactic Factor 2 secretion (α_{C_2})	1.8×10^{-4}	pg/min/cell	e Serini et al. (2003), Bauer et al. (2009)
IL-8 diffusion (D_{C_1})	15000	$\mu\text{m}^2/\text{min}$	Li Jeon et al. (2002)
IL-8 decay (equal to VEGF) (ρ_{C_1})	0.01083	/min	e as in Jain et al. (2008)
IL-8 secretion by visceral adipocyte (α_{C_1})	2.2×10^{-4}	pg/min/cell	Bruun et al. (2004)
IL-8 background concentration (peritoneal fluid)	1.732	pg/ml	Barcz et al. (2002)
METABOLIC PARAMETERS			
O ₂ consumption: proliferating cancer cell (ϵ)	4.93	fmoles/min/cell	Freyer and Sutherland (1985), Casciari et al. (1992)
O ₂ threshold for hypoxia and VEGF production	19	mm Hg	Höckel and Vaupel (2001), Evans et al. (2006), Shirinifard et al. (2009)
VEGF activation threshold for angiogenesis	0.0001	pg/cell volume	e
VEGF deactivation threshold for angiogenesis	0.00002	pg/cell volume	e
RATE PARAMETERS			
SKOV3.ip1 invasion speed	10	$\mu\text{m}/\text{h}$	e from Iwanicki et al. (2011)
Rate of ECM degradation	0.55	$\mu\text{m}^2/\text{min}$	Bauer et al. (2009)
SKOV3.ip1 cell cycle duration	25.5 ± 1	h	m
Vascular endothelial cell cycle duration	24 ± 1	h	Ausprunk and Folkman (1977), Levine et al. (2001), Bagley et al. (2003)
Cell volume after division	96 ± 17	%	e from m
MORPHOMETRIC PARAMETERS			
Cancer cell radius	3.50	μm	m
Average adipocyte cell radius	10.1	μm	m
ECM (extracellular matrix) thickness	2	μm	m
ECM collagen fiber radius	1	μm	m
ECM collagen fiber length	20	μm	e
Vascular endothelial cell diameter (initial size)	10	μm	Bauer et al. (2009)
Height of mesothelial cell on mesentery	0.44–2.5	μm	m, Khanna and Krediet (2009)
Average distance between adipocytes in the mesentery	0.2	μm	m

Values were obtained from direct measurement (indicated by “m”) of tissues and tumors or from previously published work. Where experimental values were not available, values were estimated for the model (indicated by “e”).

Table 2 | Combined tension and adhesion matrix for OvTM simulations of spheroid invasion, growth and angiogenesis.

	PF	VM	PTC	SE	VW	A	ECM	SM
PF	0	10	10	10	10	10	10	10
VM	10	0	20	20	10	20	0	10
PTC	10	20	0	0	0	3	3	0
SE	9.5	19.5	-0.5	1	0	13	5.5	2.5
VW	10	10	0	0	0	13	0	0
A	3.5	13.5	-3.5	6.5	6.5	13	1	0
ECM	9.5	-0.5	2.5	0.5	-0.5	0.5	1	0
SM	10	10	0	2.5	0	0	0	0

White boxes show adhesion coefficients between cell types (J_{ij}) and green boxes show adhesion coefficients between cells of the same type (J_{ii}). Gray boxes show the surface tension values between cell types. Surface tension is defined as $ST_{ij} = J_{ij} - (J_{ii} + J_{jj})/2$ (Glazier and Graner, 1993). Negative ST_{ij} signifies attraction, and positive ST_{ij} signifies repulsion. Surface tension = 0 for all ST_{ii} , but homotypic adhesion J_{ii} can still be strong. Maximum adhesion is 0. Mesenteric invasion models contain PF, peritoneal fluid; VM, visceral mesothelium; PTC, proliferating tumor cells; VW, vessel wall endothelial cells, A, adipocytes; ECM, extracellular matrix (ECM). Included in the spheroid growth model are: PTC, proliferating cancer cell; PF, peritoneal fluid, VM, visceral mesothelium, VW, vessel wall endothelial cells; ECM, extracellular matrix; SM, smooth muscle. Models with angiogenesis further include VW, vessel wall endothelial cells; SE, sprouting endothelial cells.

$$\frac{\partial C_1}{\partial t} = D_{C_1} \nabla^2 C_1 - \rho_{C_1} C_1 + \alpha_{C_1} \delta[\tau(S), \text{adipocyte}], \quad (2)$$

$$\frac{\partial C_2}{\partial t} = D_{C_2} \nabla^2 C_2 - \kappa_{C_2} C_2 + \alpha_{C_2} \delta[\tau(S), \text{vessel}], \quad (3)$$

$$\frac{\partial V}{\partial t} = D_V \nabla^2 V - \gamma_V V + \alpha_V \delta[\tau(S), \text{tumor}], \quad (4)$$

where C_1 is IL-8, C_2 is Growth Factor 2, and V is VEGF. These equations describe diffusion through tissue, decay, and production by source cells.

Oxygen is delivered by the vessel (see **Figure 7**) and diffuses from the peritoneal fluid. Its level is kept constant within the peritoneum. Diffusion of O_2 through tissue and its consumption by the cells is described as:

$$\frac{\delta O_2}{\delta t} = D_{O_2} \nabla^2 O_2 - \epsilon \delta[\tau(S), \text{tumor}] \quad (5)$$

Depending on the availability of oxygen in their surrounding environment, cancer cells have the potential to be proliferating, quiescent or necrotic. Although the capability for cancer cells to become hypoxic or necrotic was integrated into the model, the spheroids we simulated were too small in diameter to develop internal hypoxia under normal physiological conditions, and never became hypoxic or necrotic.

The secretion rates for IL-8, VEGF, and Chemotactic Factor 2 were taken from quantitative experiments (or estimated for Chemotactic Factor 2). Oxygen was kept constant at the simulation boundaries with the value corresponding to the steady-state oxygen level in the mouse peritoneal fluid (~ 98.5 mmHg). Background IL-8 was also kept constant at the z boundaries, defined

as normal to the mesothelium surface, with the value corresponding to its steady-state concentration in the peritoneal fluid. IL-8 concentration at the x and y boundaries was constant at levels diffusing from the adipocytes. Boundary values of VEGF and Chemotactic Factor 2 were set to steady-state at 0, as background values were unknown and the cells generated small, concentrated fields that reached approximately 0 at the distance of the simulation boundaries. For the diffusion rates of these four chemicals ($D > 15 \mu\text{m}^2/\text{min}$), CompuCell3D cannot generate boundary conditions for tissues or cell types, as the necessary solver requires extra solutions per time step that make running models intractably slow (e.g., $\sim 525,000$ extra solutions per time step are required in the case of oxygen, resulting in ~ 24 h simulation time/1 min experimental time simulated). All parameters are listed in **Table 1**.

The chemotaxis constant for SKOV3.ip1 cell response to IL-8 was increased until the cells were moving through the IL-8 gradient in mesenteric fat tissue at a rate we derived from the ovarian cancer spheroid experiments by Iwanicki et al. (2011). Chemotaxis by tumor cells to Chemotactic Factor 2 coming from the vessel was tuned to have the same order of magnitude of response as to IL-8 (order of magnitude (IL-8 concentration \times chemotaxis constant) = order of magnitude (Chemotactic Factor 2 concentration \times chemotaxis constant), where the chemotaxis constant = 1×10^{13}).

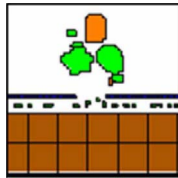
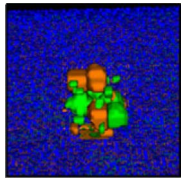
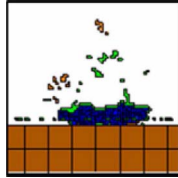
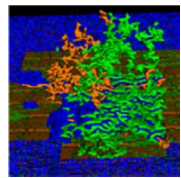
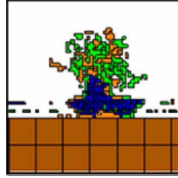
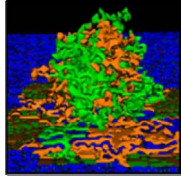
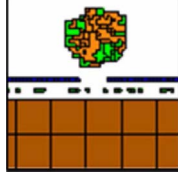
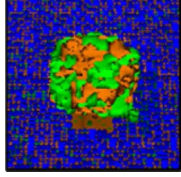
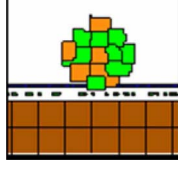
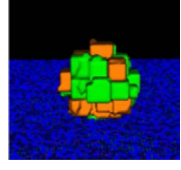
Cell reproduction

In OvTM, the cellular level model and the chemical environment model are integrated through the choice of a common time-scale. In the cellular Potts model, each Monte Carlo Step (MCS) corresponds to as many cellular protrusion events as the number of lattice sites in the simulation domain. We define one MCS to correspond to 1 min of real time. The chemical equations (Eqs 2, 3, and 4) are solved at the time step of 1 min, when the cell lattice configuration and states are assumed constant. The cells update their states according to their local chemical concentrations. The cell lattice is then updated for one MCS assuming chemicals stay constant. Such iterative feedback and update links the discrete cellular Potts model and the continuous chemical equations together. Each cell has its own division time and age clock. Division time for cells is set on a Gaussian distribution; SKOV3.ip1 cells divide between 24.5 and 26.5 h and endothelial cells divide between 23 and 25 h. A cell divides when two conditions are satisfied: (a) the cell's age is greater than or equal to its division time, and (b) the cell's volume is greater than or equal to its target volume, which increases linearly with the cell's age. When the cell (S) divides, it is halved into two daughter cells, S and S' .

Tissue microenvironments

The three OvTM model scenarios each represent several cubic millimeters of peritoneal space, about one third of which is tissue. (The invasion model is 7.6 mm^3 and contains 2.6 mm^3 of tissue.) The rest of the volume is filled with peritoneal fluid present in the mammalian peritoneal cavity. Cell shapes and sizes were determined by cell morphometry studies of normal mice, nude mice, and SKOV3.ip1 xenografts. Thickness of the adipose layer surrounding vessels of the mesentery was taken from the literature. Tissue rigidity in smooth muscle and adipocytes was estimated

Table 3 | Exploration of adhesion parameters in spheroids attached to the surface of the small intestine.

Parameters tested			Results	Spheroid images	
				2-D (tumor center)	3-D
Low homotypic adhesion and low heterotypic adhesion to non-tumor cells			By 24 h, tumor cells show reduced volume and the spheroid is no longer cohesive		
Cell type 1	Cell type 2	Adhesion 1 ⇔ 2			
PTC	PTC	20			
PTC	other	20			
other = PF, ECM, VM, and SM					
Low homotypic adhesion and high heterotypic adhesion			By 24 h, the spheroid has fragmented while the mesothelium has aggregated		
Cell type 1	Cell type 2	Adhesion 1 ⇔ 2			
PTC	PTC	20			
PTC	other	Tested 0, 1, 3, and 5			
High homotypic adhesion and high heterotypic adhesion			By 12 h, the spheroid has begun to disintegrate and the mesothelium has aggregated at the base of the spheroid		
Cell type 1	Cell type 2	Adhesion 1 ⇔ 2			
PTC	PTC	0			
PTC	other	0			
High homotypic adhesion and low heterotypic adhesion			At 24 h, a coherent spheroid with a similar appearance to the SKOV3.ip1 in vivo tumors can be seen. The mesothelium remains intact. However, cells are abnormally convoluted		
No surface area constraint					
Cell type 1	Cell type 2	Adhesion 1 ⇔ 2			
PTC	PTC	0			
PTC	other	Tested 10 and 20			
High homotypic adhesion and low heterotypic adhesion			This model most closely approximates the shape of SKOV3.ip1 spheroids and cells in vivo as shown at 12 h		
Additional surface area constraint					
Cell type 1	Cell type 2	Adhesion 1 ⇔ 2			
PTC	PTC	0			
PTC	other	See Table 2			

Abbreviations are the same as in **Table 2**.

based on cell junctions and spacing from EM images of mouse tissues. The depth of penetration of SKOV3.ip1 cells on both tissue types was based upon xenograft tumors in our microscopic images.

The tissue microenvironments we considered were the outer surface of the intestine (**Figures 2 and 7**) and the mesentery (**Figure 5**). A layer of mesothelium covers both surfaces. Both environments are initialized with a tumor spheroid of seven cells contacting the center of the contiguous mesothelial surface in the peritoneal cavity.

On the intestine, smooth muscle lies beneath the mesothelium, separated from it by a thin layer of ECM. Ovarian cancer cells can push aside the mesothelium and degrade ECM (Kenny et al., 2008; Sodek et al., 2008), but strong adhesion between the muscle cells

prevents further invasion. Scattered blood vessels lie just below the mesothelium. In our model, initiation of angiogenesis was triggered by a threshold VEGF level. When the local VEGF concentration exceeds a threshold, endothelial cells lining the blood vessels begin to proliferate and migrate, organizing into vascular sprouts.

Tumors on the omentum or mesentery can invade through the mesothelium and migrate through the loose matrix and adipocyte fields below. On the mesentery, ovarian cancer cells adhering to the mesothelium push past the mesothelial cells as chemotactic gradients originating from adipocytes and vasculature stimulate migration into the tissue.

Both models are initialized with a tumor spheroid of seven cells contacting the center of the contiguous mesothelial surface in the

peritoneal cavity. We assume ECM degradation rate by SKOV3.ip1 tip cells at the invading front is the same as the degradation rate by endothelial cells at the sprout tip (Bauer et al., 2009).

The process of angiogenesis is driven by endothelial cell chemotaxis toward VEGF, and by differential adhesive interactions between endothelial sprout cells and cancer cells. This simple model suggests that, to produce vasculature morphology similar to that in very small xenograft tumors, latent endothelial cells must become proliferating endothelial cells and initiate angiogenic behavior as soon as the spheroid comes within diffusion distance for low concentrations of VEGF of the vessel. Given VEGF production of 3.82×10^{-7} pg/min/SKOV3.ip1 cell, the threshold for the switch from latent to sprouting endothelial cells is set at 2.08×10^{-8} pg/cell volume, which initiates angiogenesis when the spheroid is about 5 μm from the vessel.

Exploration of adhesion parameters

To reproduce the morphology of *in vivo* SKOV3.ip1 xenografts on the intestine, we tested four combinations of homotypic and heterotypic adhesion parameters (Table 3). Only when tumors were parameterized to have high homotypic adhesion between cancer cells along with low heterotypic adhesion between cancer cells and components of the microenvironment (peritoneal fluid, ECM, visceral mesothelium, and smooth muscle cells) did cancer cells form rounded spheroids similar to those seen *in vivo*. A surface area constraint was also imposed on the cancer cells to maintain cell integrity. We ran at least five replica simulations for each parameter set, and observed no qualitative differences, within small variations, in our results.

RESULTS

SKOV3.ip1 OVARIAN CANCER CELLS ADHERE TO THE SURFACE OF NUMEROUS ORGANS IN THE PERITONEUM AND FORM LARGE TUMORS BY 2 WEEKS POST-INJECTION

To recapitulate the essential steps in ovarian cancer relapse from minimal residual disease in the peritoneum, five million SKOV3.ip1 human ovarian cancer cells expressing GFP were injected into the peritoneum of nude mice as a single cell suspension. Mice were euthanized after 2 weeks and mounted on the stage of an OV100 fluorescence imaging system. As shown in Figure 1A, macroscopic tumors developed on numerous organs in the peritoneum during this period. The main sites of attachment were the omentum (Figures 1A,B), the surface of the stomach (Figure 1C) and small intestine, the mesentery (Figure 1D) and the spleen (Figure 1E). Tumors also developed on the liver in half of the mice examined. The largest tumors grew from the omentum and expanded into the peritoneum, reaching volumes up to 200 mm^3 by 2 weeks. Even within this short time frame, the tumors are well vascularized with vessels penetrating and wrapping around the outside of the largest tumors. Many smaller tumors can be found attached to the mesentery, often visible to the naked eye, ranging in size from 0.4 mm^3 to 1 mm^3 .

STRONG HOMOTYPIC INTERACTIONS DRIVE SKOV3.ip1 AGGREGATION

It has been hypothesized that ovarian cancer cells aggregate and form spheroids when suspended in peritoneal fluid and that these spheroids then attach to the peritoneal surface and form large

tumors (Shield et al., 2009). To test this hypothesis and to assess the clonality of the tumors at distinct sites, a mixture of SKOV3.ip1-GFP and SKOV3.ip1-RFP cells were co-injected into nude mice as a single cell suspension. The resulting tumors were imaged 2 weeks later. Tumors on the omentum developed as well-mixed chimeras, with both green and red fluorescence throughout (Figures 2A,B). In higher magnification images, small areas with predominantly red fluorescence can be distinguished from areas with predominantly green fluorescence, but there are no large sections of tumor expressing a single fluorescent protein (Figure 2C). The majority of the observed mesenteric tumors ($92 \pm 2\%$ of 51 observed tumors) also have mixed green and red fluorescence, indicating that even these small tumors originated from a mixed spheroid (Figures 2D,E). The few small tumors consisting solely of GFP-positive or RFP-positive cells may represent rare instances where a single cell, or a small group of singly fluorescent cells, was able to adhere and grow (Figure 2E, arrow).

These data provided the first essential parameters for initialization of our OvTM mathematical model, since adhesion is a predominant feature of the cellular Potts framework (Graner and Glazier, 1992). Simulations were initiated with an adherent spheroid on the surface of the intestine. The spheroid subsequently pushes through the mesothelium. This process has been observed *in vitro*, where tumor spheroids cause retraction of the mesothelium using a myosin-mediated process (Iwanicki et al., 2011).

The *in silico* experiments using OvTM showed that only by assigning high homotypic adhesion strength to the cancer cells could the model reproduce spheroid cohesiveness and growth (Figure 2F). For details on how the adhesion parameters were optimized, see Section “Materials and Methods” (Table 3). Simulations in which cancer cells adhered more strongly to other cancer cells than to any other cell type, produced the most rounded tumor morphology that closely resembled the xenograft tumors. Adding a cellular surface area constraint maintained the integrity of the cells themselves. Since the model indicated that tumor cell homotypic adhesion is an essential feature governing dissemination and growth, this concept was further tested experimentally by sequentially introducing fluorescent cancer cells into the peritoneum (Figure 3). In this experiment, tumors were first established by injection of 2.5 million SKOV3.ip1-GFP cells. After a period of 1 week to permit engraftment of the green-fluorescent cells, an equal number of SKOV3.ip1-RFP cells were injected. Following another week, the relative distribution and burden of both green and red fluorescent tumor cells were evaluated. As expected, SKOV3.ip1-GFP tumors formed on the omentum, mesentery, and spleen. Notably, the majority of red fluorescent cells adhered to and enveloped the pre-existing GFP-positive tumors as can be seen on the omental tumors (Figure 3A) and on the spleen (Figure 3B), rather than forming tumors independently. Although some exclusively RFP-positive tumors were present on the mesentery (Figure 3C, arrows), 70% of the 24 RFP-positive tumors examined were also GFP-positive.

TUMOR CELLS MIGRATE THROUGH THE OPEN ARCHITECTURE OF THE MESENTERY IN RESPONSE TO CHEMOTACTIC SIGNALS

Our next goal was to identify specific features of the microenvironment that underlie differences in ovarian tumor morphology

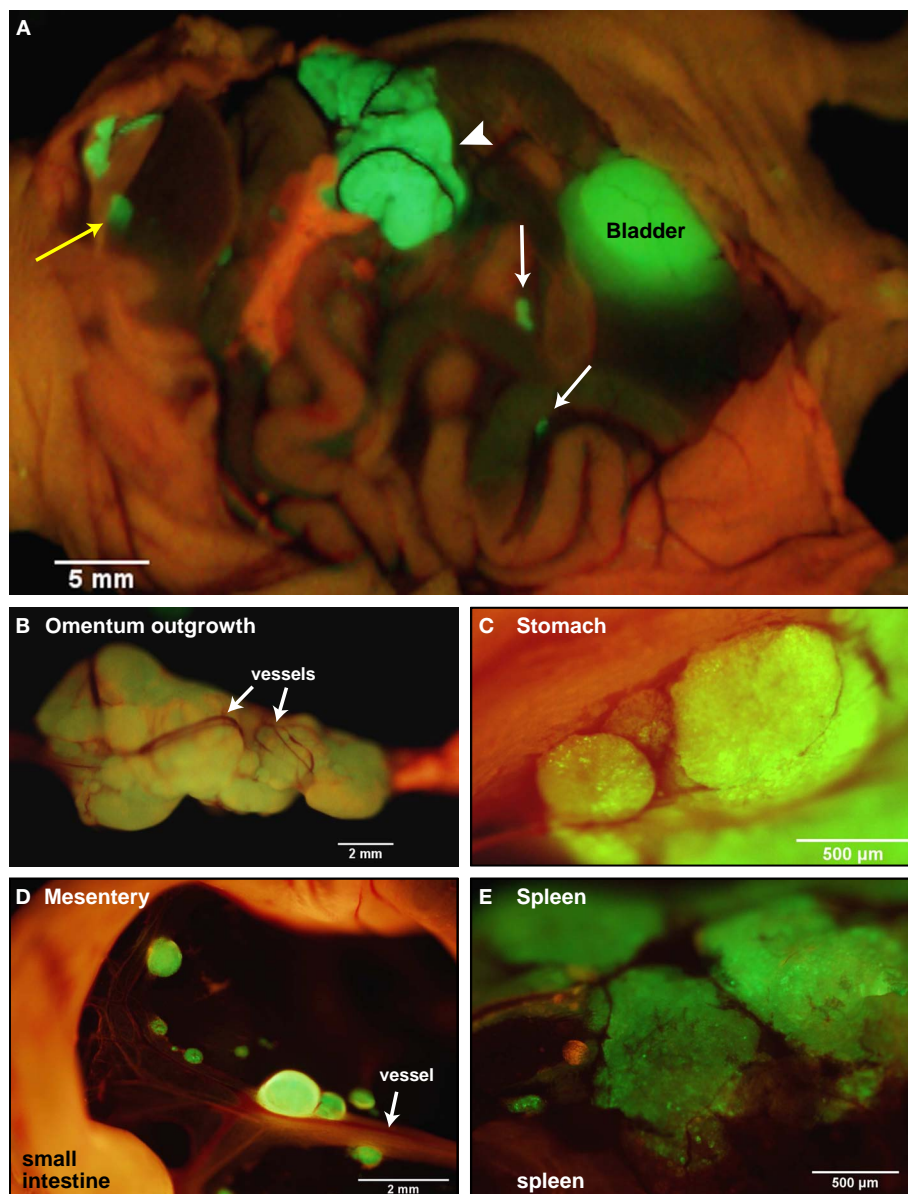


FIGURE 1 | SKOV3.ip1-GFP cells colonize the surface of many organs in the mouse peritoneum. (A) Image of SKOV3.ip1 tumors growing from the omentum (large central tumor, arrowhead), the intestine, attached mesentery (white arrows), and the liver (yellow arrow) of an RFP nude mouse. Tumors on the spleen are not visible in this image. **(B)** The largest tumors are attached to the omentum located

on the larger curvature of the stomach and are well vascularized. **(C)** Tumors attached to the stomach are spherical and non-invasive. **(D)** On the mesentery, small tumors are located adjacent to major blood vessels (arrow). **(E)** Small tumors growing on the spleen have a flatter, sponge-like morphology with less well defined borders between the tumor (green) and the normal tissue.

by examining the structure of external tissue layers facing the peritoneum. Both normal and tumor-associated tissues were extracted and prepared for TEM imaging. The micrograph in **Figure 4A** illustrates the open architecture of the normal mesentery, with loosely packed fat cells below the mesothelium. The mesothelial layer is remarkably thin in some areas, ranging from 0.4 to 2.5 μm in thickness. A second image (**Figure 4B**) shows a cross-section of mesentery excised from mice engrafted with SKOV3.ip1 human ovarian cancer cells. Labels mark the locations of probable tumor

cells, identified by the characteristic ultrastructure of their nuclei. The tumor cells are interior to the mesothelium and adjacent to a small blood vessel.

To understand how tumors are established in the mesentery, SKOV3.ip1-GFP cells were injected into the peritoneum and 4 days later segments of the mesentery were removed for whole mount imaging. As shown in **Figures 4C,D**, images from this early time point provide a window into the initial steps in the engraftment process. Small groups of fluorescent cancer cells were seen within

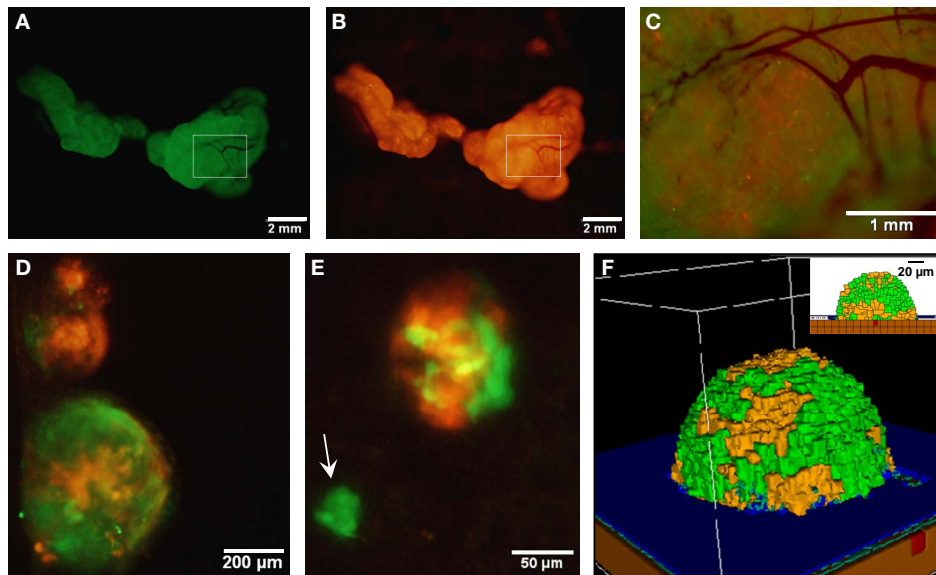


FIGURE 2 | Co-injected SKOV3.ip1-GFP and RFP cells yield chimeric tumors. Equal numbers of SKOV3.ip1-GFP and SKOV3.ip1-RFP cells were injected as a single-cell suspension into the peritoneum of nude mice. (A–C) Large tumors on the omentum are both GFP-positive (GFP-filter) (A) and RFP-positive (RFP-filter) (B). White boxes: magnified region shown in (C). (C) A 5X magnified composite image of the tumor from (A,B) showing a mixture of GFP- and RFP-positive cells. (D,E) Chimeric tumors on the mesentery have patches of green and red

fluorescence. A clonal tumor that is only GFP-positive can be seen (E), (arrow). (F) Endpoint of a mathematical simulation initialized with a mixed GFP/RFP spheroid of 56 cells attached to the mesothelial surface of the intestine. A $180 \times 180 \times 180 \mu\text{m}$ lattice (5.832 mm^3) is partitioned into layers of smooth muscle (brown), extracellular matrix fibers (teal), mesothelium (dark blue), and vessel (red) creating a 0.84 mm^3 tissue layer. Above the tissue is peritoneal fluid. The 3-D image shows a chimeric tumor (orange and green cells) after 7 days of growth.

the mesenteric adipose layer (Figure 4C) or beneath the adipose layer immediately adjacent to vessels (Figure 4D).

We next used OvTM to evaluate the conditions necessary for cancer cells to migrate to mesenteric vessels within this short time period. The cellular Potts model is particularly well suited for this type of modeling, since it specifically represents cell–cell interactions and cell movement, which is governed by local contacts and chemotactic gradients. The 3-D stochastic model was populated with heterogeneous cell types (cancer cells, adipocytes, endothelial cells, and mesothelium) and geometric features (shape, location, organization, and thickness of tissue layers) based on TEM images. Extracellular factors, such as chemokines and oxygen, are described by diffusion equations with sources and sinks. In each case, cancer cells push through the mesothelial layer and degrade the underlying ECM, as shown experimentally (Sodek et al., 2008). Simulations can then demonstrate the extent of tumor invasion in response to different chemotactic environments.

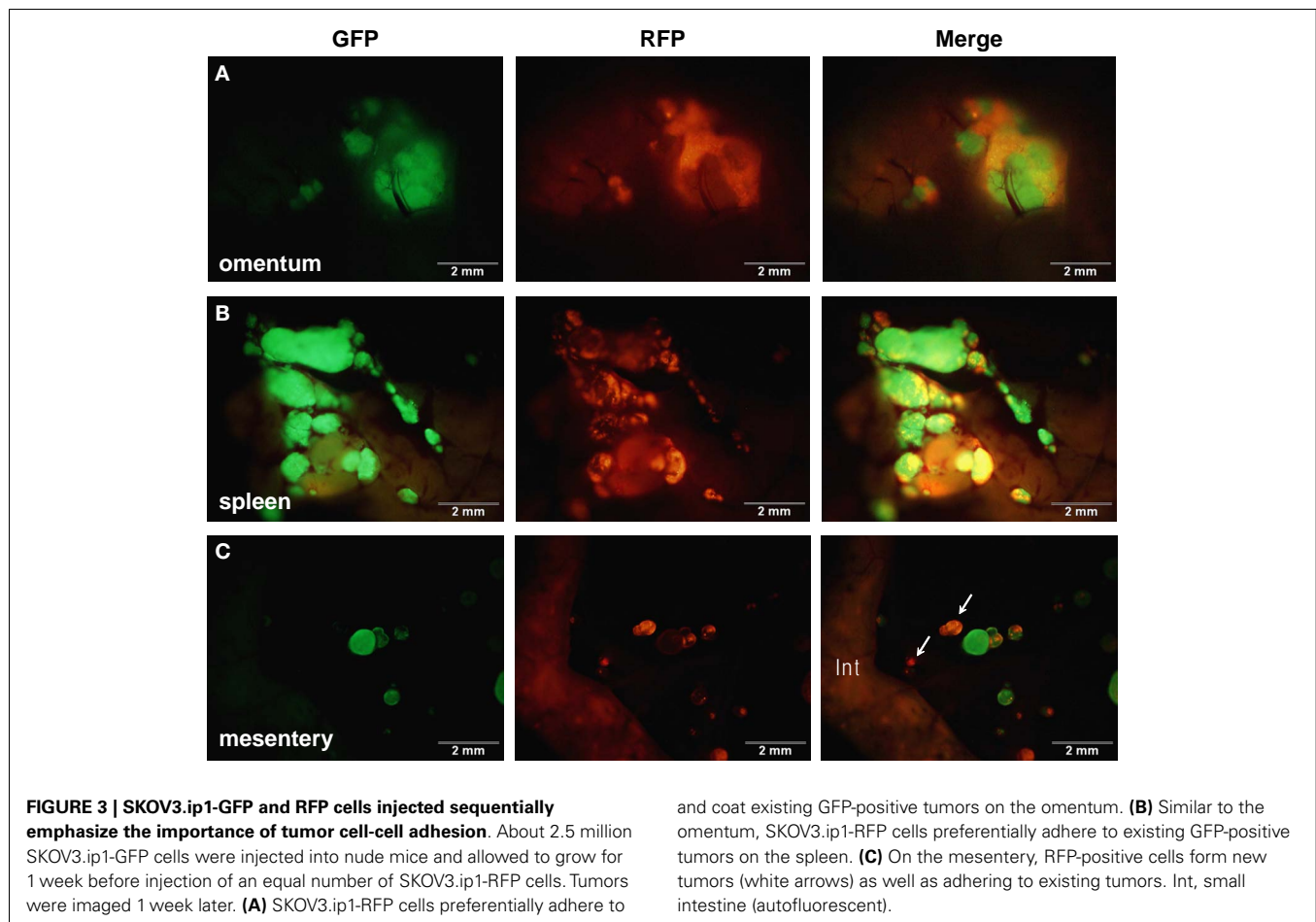
Figure 5 shows results from three scenarios that were considered in these simulations. Movies for representative simulations are provided in Supplementary Data (Movies S1–S3 in Supplementary Material). For each case, a spheroid of seven cancer cells was initially positioned on a 3-D geometrical model of the mesentery. Mesothelial cells form the boundary with the peritoneum; adipocytes are dispersed within the interior, and a single vessel transverses the tissue.

In the first scenario, there is no local production of chemotactic factors imposed. The spheroid is positioned such that it is in contact with the ECM. In the absence of chemotactic factors, the

spheroid dissolves the ECM and presses into the adipose tissue after 2 days (Figure 5A). This progression is too slow to explain cancer cell localization near mesenteric blood vessels in the mouse model.

SKOV3.ip1 cells have been shown to home toward chemokine-producing adipocytes and upregulate the IL-8 receptor (CXCR1) when co-cultured with adipocytes (Nieman et al., 2011). Therefore, in the second scenario, simulation parameters were modified such that all adipocytes within the mesentery secrete IL-8 at a rate of $2.2 \times 10^{-4} \text{ pg/min/cell}$ (Bruun et al., 2004), which diffuses at $1.5 \times 10^4 \mu\text{m}^2/\text{min}$ (Li Jeon et al., 2002). Cancer cells are then allowed to chemotax up the resulting IL-8 gradient. In our model, spheroid invasion of the ultra-thin mesothelium is rapid, occurring at a rate of $10 \mu\text{m/h}$ based upon the *in vitro* experiments of Iwanicki et al. (2011). The pseudo-colored image in Figure 5B shows the predicted distribution of IL-8 in the mesenteric tissue at steady state, illustrating the initial conditions experienced by the tumor spheroid. Simulated IL-8 concentrations within the peritoneum agree with those measured experimentally (Barcz et al., 2002). When IL-8 chemotaxis is included in the simulation, the spheroid moves past the mesentery barrier and pushes between adipocytes to settle near the center of the adipose layer where the IL-8 concentration is greatest (Figure 5D). This occurs within 500 min after initialization. In this case, rapid chemotaxis occurs, but the cancer cells do not localize near the vessel.

In the final case, both adipose and endothelial cells are assumed to produce chemotactic factors that attract cancer cells. We introduce a new chemotactic factor (Chemotactic Factor 2) that originates from the mesenteric vessel. Steady-state values represented



in the pseudo-colored profile in **Figure 5C** show that a significant gradient can be established by endothelial cell secretion of Chemotactic Factor 2 at a rate of 1.8×10^{-4} pg/min/cell, which is comparable to that of IL-8 secretion from the adipocytes, and assuming diffusion and decay rates similar to VEGF. When cells are arranged in this geometry, the presence of both chemotactic gradients causes spheroids to penetrate the mesothelial layer, move by chemotaxis through the loose adipose layer toward the vessel, and halt at the tightly adherent barrier of the vessel wall (**Figure 5E**). Together with the experimental data, these results support the conclusion that both adipocytes and endothelial cells are likely sources of chemokines that attract ovarian tumor cells.

SMALL SKOV3.ip1 TUMORS ATTACHED TO SURFACES OF THE STOMACH OR SMALL INTESTINE ARE NON-INVASIVE AND INITIATE ANGIOGENESIS

We next focused on explanations for the distinct morphology of tumors attached to the stomach or small intestine, which do not invade the tissue and instead grow outward into the peritoneal cavity (**Figure 6A**). We again sought insight from high resolution TEM images. As shown **Figure 6C** (mesentery) and **Figure 6D** (stomach), the outer mesothelial layer remains relatively thin over these organs (typically 0.5μ thick). The next layer is distinguished by dense collagen deposits. Prominent smooth muscle layers can

be seen in both the small intestine and stomach, where the muscle cells are closely opposed and connected by gap junctions (Friend and Gilula, 1972) (arrows, **Figure 6B**).

The morphology of a tumor attached to the outer rim of the lower intestine is seen at a lower magnification in **Figure 6E**, which shows a representative section from a formalin-fixed, paraffin block stained with H&E (hematoxylin and eosin). The smooth muscle of the small intestine remains intact at the tumor/tissue interface. Thus, tumors attached to the exterior of the gut are presented with a discrete barrier and adapt by growth into the available and flexible space between organs. The intestine has a capillary bed that provides oxygen to the mesothelium and contributes to the oxygenated peritoneal environment (**Figure 6F**). Because of the lack of a smooth muscle barrier, these vessels may provide a more accessible endothelial source for neoangiogenesis critical to tumor success.

Microscopic evaluations provide support for this hypothesis (**Figures 6B,E**). Fluorescence imaging shows the remarkable extent of tumor vascularization, even in young GFP-positive tumors attached to the intestinal wall at 2 weeks post-implantation (**Figure 6B**). A red arrowhead in **Figure 6E** points to a vessel visible within the tumor cross-section. This evidence led us to conduct simulations to explain the rapid onset of neovascularization in the absence of invasion.

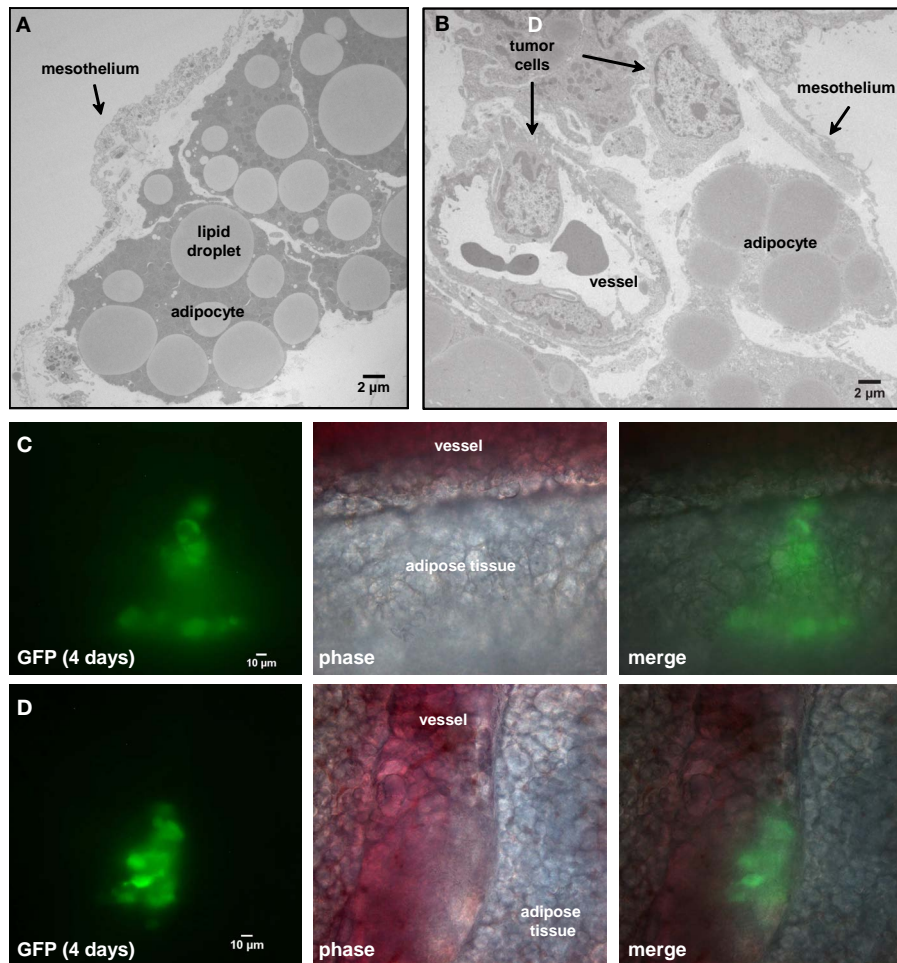


FIGURE 4 | Four days post-injection, tumor cells have invaded the mesentery and migrated through adipose tissue to approach mesenteric blood vessels. (A) Transmission electron micrograph of the edge of the mesentery from a nude mouse. The mesentery architecture is open with loosely connected adipose cells below the mesothelium. Adipocytes are identified by their large lipid droplets. **(B)** Transmission electron micrograph of

mesentery excised 4 days post-injection of SKOV3.ip1 cells. Arrows mark the locations of probable cancer cells. The cancer cells lie close to a blood vessel. **(C)** Cancer cells invading mesenteric adipose tissue adjacent to a vessel. On the right, GFP fluorescence of the cancer cells; middle, brightfield; left, composite image. **(D)** Cancer cells closely opposed to a mesenteric vessel. Panels are arranged as in **(C)**.

SKOV3.ip1 TUMOR SPHEROIDS ARE INITIALLY WELL OXYGENATED AND LIKELY INDUCE NEOVASCULARIZATION VIA CONSTITUTIVE SECRETION OF ANGIOGENIC FACTORS

For the *in silico* model of angiogenesis, micron-scale geometric parameters for the tissue surface architecture were again determined from TEM images. For the gut, adhesion between smooth muscle cells is set sufficiently high as to prevent spheroid penetration below the mesothelial and collagen layers. Under these constraints, simulations of tumor adhesion and growth result in the formation of spherical tumors that are consistent with the morphology of engrafted tumors on mouse intestine (compare **Figures 6A** and **7C**). Since these simulations incorporate published values for oxygen content in the peritoneal fluid and oxygen diffusion rate (MacDougall and McCabe, 1967; Kizaka-Kondoh et al., 2009), it is possible to calculate the distribution of oxygen in all locations during tumor growth. By coarse-graining the

model (1 voxel = 1 cell), we were able to determine the oxygen concentration gradients for large spheroids suspended in the peritoneal fluid. In spheroids of varying sizes, oxygen concentration decreased within the core. However, spheroids up to 336 μm in diameter (58,000 cells) approach the hypoxic threshold of 19 mm Hg of O₂ (Höckel and Vaupel, 2001), but are not yet hypoxic at their core (**Figure 7A**). Continued growth to 364 μm in diameter (74,000 cells) results in a hypoxic core with an oxygen concentration of 0.5 mm Hg (**Figure 7B**), leading to the prediction that the hypoxic threshold is reached when the spheroid is between these two sizes. Tumor sizes in mouse samples were compared based on the cross-sectional area of tumors in H&E-stained sections. Mesenteric tumor vascularization with respect to tumor area is shown as scatter dot plots in **Figure 7E**. Of the 76 tumors measured, all tumors above the predicted hypoxic threshold (red) were vascularized. However, 57% of small

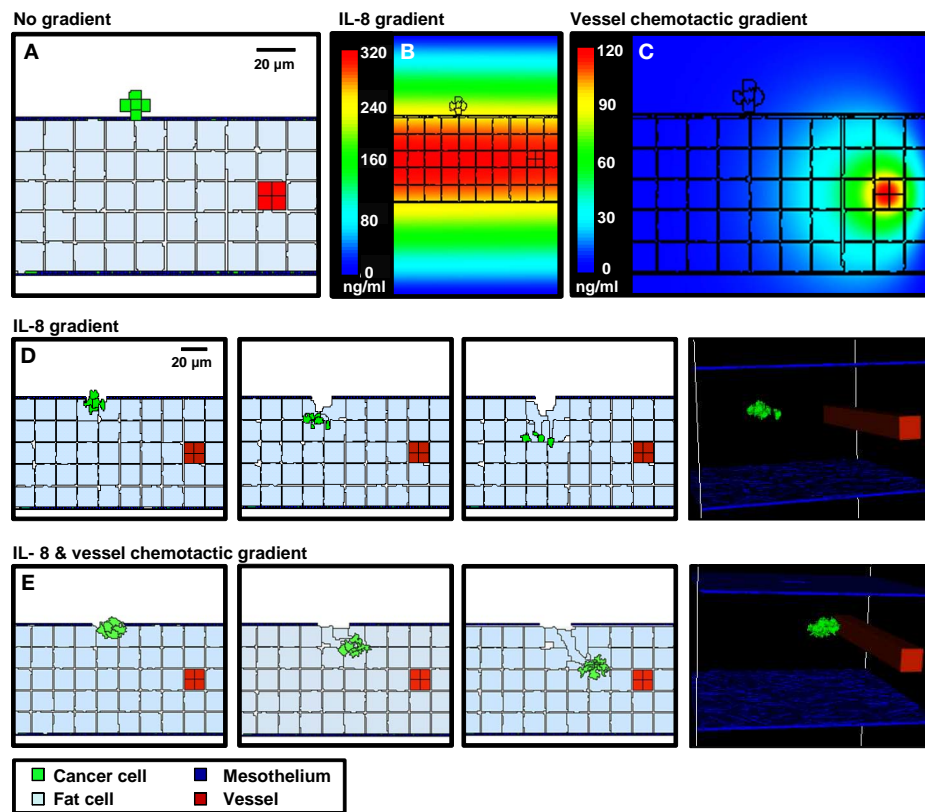


FIGURE 5 | 3-D simulations of cancer cell attachment and migration to the mesenteric vessel. (A) The initial configuration of the simulation has a seven-cell spheroid attached to the surface of the mesentery. To model this environment, a $170 \times 170 \times 263 \mu\text{m}$ lattice (7.6 mm^3) is partitioned into five layers of adipocytes (light blue) sandwiched between single layers of mesothelium (dark blue) and ECM (teal) creating a 2.6 mm^3 tissue layer surrounded by peritoneal fluid. A blood vessel on the right is represented by a solid rod (red). In the absence of chemotactic signals, the spheroid penetrates only the thin mesothelial layer at 1–2 min of simulation. **(B,C)** Steady-state

distributions of chemotactic factors tested in these simulations. The color scale represents variation in factor concentrations in ng/ml. **(B)** The IL-8 gradient created by secretion of IL-8 from adipocytes. **(C)** A chemotactic gradient based on secretion of a hypothetical chemotactic factor (Chemotactic Factor 2) from mesenteric vessels. **(D)** Sequences in the simulation where a chemotactic gradient based on IL-8 is originating from the adipocytes. The spheroid migrates toward the center of the adipose layer. **(E)** Sequences of a simulation where chemotactic signals originate from both the adipocytes and the vessel. The spheroid migrates through the adipose layer toward the vessel.

tumors with an area of $<104,000 \mu\text{m}^2$ (below the predicted hypoxic threshold) were also vascularized. These results suggest that angiogenesis is not solely hypoxia-driven in the SKOV3.ip1 model.

In the next series of simulations, we examined how angiogenesis might originate from these spheroids in the absence of hypoxic signaling. There is experimental evidence that SKOV3.ip1 cells constitutively express VEGF *in vivo* and *in vitro* even when maintained in well-oxygenated tissue culture conditions (Yoneda et al., 1998). Secretion of VEGF by the cancer cells was therefore incorporated into these simulations. Small spheroids attached to the gut penetrate the mesothelial layer, permitting VEGF secreted from cancer cells to initiate chemotactic gradients and attract endothelial cells that line blood vessels in the sub-mesothelial layer. The process of angiogenesis is driven by endothelial cell chemotaxis toward VEGF, and adhesive interactions between endothelial sprout cells and cancer cells. To produce vasculature visually similar to that in very small xenograft tumors, latent endothelial

cells must begin to proliferate and migrate as soon as the spheroid comes close enough to the vessel to allow diffusion of low concentrations of VEGF. Given spheroid VEGF production of $3.82 \times 10^{-7} \text{ pg/min/SKOV3.ip1 cell}$, the threshold for the switch from latent to sprouting endothelial cells was set at 2.08×10^{-8} , to initiate angiogenesis when the spheroid is $\sim 5 \mu\text{m}$ from the vessel.

Angiogenesis in the OvTM model follows validated methods that treat VEGF as diffusible molecules whose gradient, together with the biophysical environment, drives endothelial migration and proliferation, and eventually morphogenesis of vessel sprouts (Bauer et al., 2007; Shirinifard et al., 2009). Parameters and model assumptions are described in the Materials and Methods. Simulation results show that constitutive production of VEGF from even a small spheroid of SKOV3.ip1 cells should be capable of initiating vascular outgrowths that penetrate the spheroid within 12 h of attachment (**Figure 7D**; Movie S4 in Supplementary Material). Results of the computational model are consistent with our

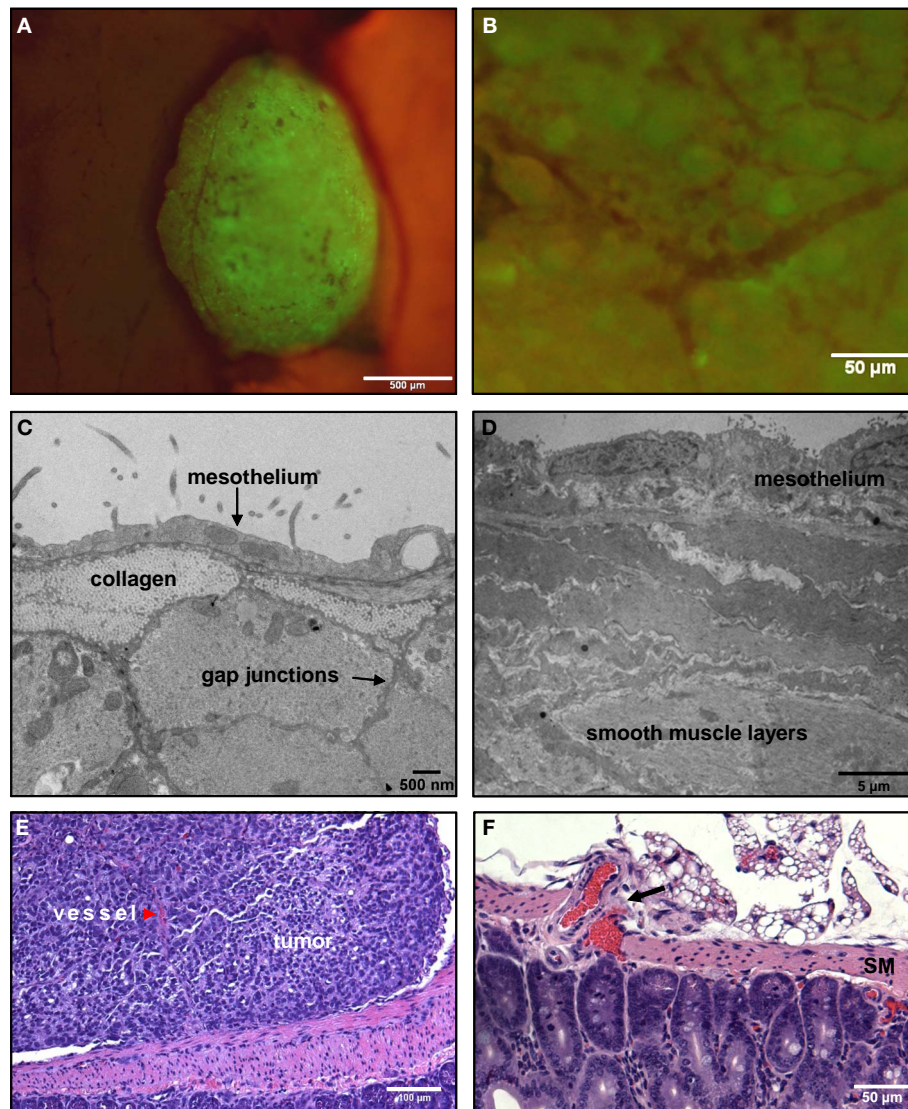


FIGURE 6 | Tumors that adhere to the walls of the small intestine are spherical and non-invasive. (A) An SKOV3.ip1-GFP tumor adhering to the wall of the small intestine 2 weeks post-injection in an RFP nude mouse. Shown is a composite GFP/RFP image. Small vessels are visible on the surface of the tumor. **(B)** Higher magnification image of the vascular tree infiltrating a green-fluorescent tumor on the intestine. **(C)** Transmission electron micrograph of the small intestine wall. Tissue was collected from a nude mouse 4 days post-injection with SKOV3.ip1-GFP

cells. The wall of the small intestine consists of a thin layer of mesothelium overlaying bundles of smooth muscle fibers. **(D)** TEM image of stomach ultrastructure, illustrating the distinct cellular layers. **(E)** An H&E-stained section of a tumor attached to the small intestine. There is a clear delineation between the intestine and the tumor. The tumor is vascularized (red arrowhead). **(F)** An H&E-stained section of the surface of a mouse intestine. Arrow points to vessels at the intestine-mesentery junction.

experimental observations that even very small tumors, comprised of less than 20,000 SKOV3.ip1 cells, are fully vascularized (**Figure 7F**). They are also consistent with 3-D images of tumor slices stained for confocal fluorescence imaging that show extensive tumor vascularization 3 weeks post-injection (**Figure 7G**). In this final image, an anti-CD31 antibody (red) marks endothelial cells, Hoechst (blue) stains the cell nuclei and an anti-GFP antibody (green) labels the GFP-positive cancer cells. A rotating 3-D view of this tumor section is found in Movie S5 in Supplementary Material.

DISCUSSION

In this work, we combine a murine xenograft model with a computational model, OvTM, to evaluate critical factors governing the dissemination and growth patterns of ovarian cancer in the peritoneum. These models best represent ovarian cancer relapse after debulking surgery, where disease progression initiates from microscopic residual disease in the peritoneal chamber.

In cellular Potts models, the variety of constraints placed on cells must be properly balanced to produce biologically reasonable cellular and tissue structure and movement. We quantitatively

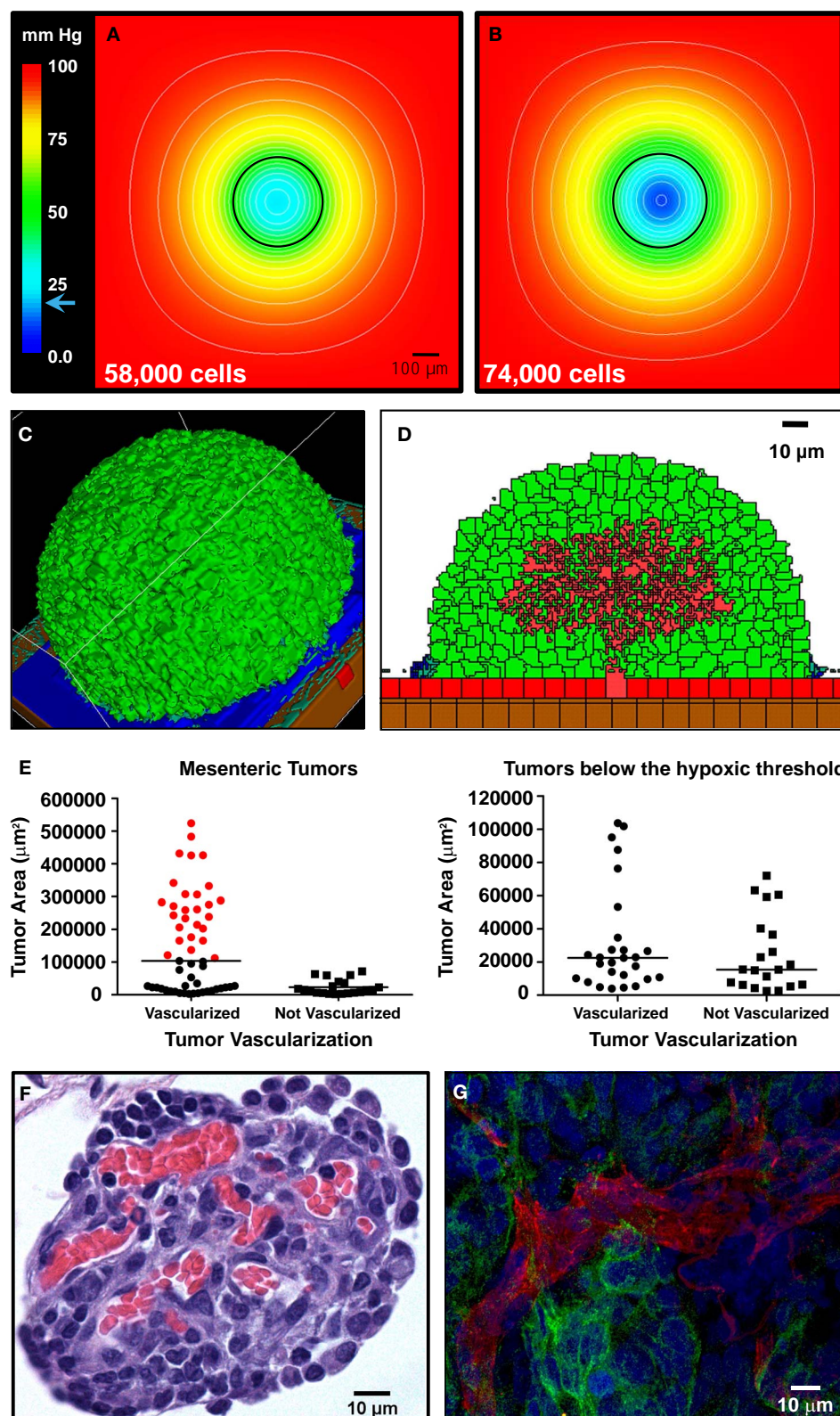


FIGURE 7 | Continued

FIGURE 7 | Vascularization of tumors is rapid and can be attributed to constitutive release of angiogenic factors by SKOV3.ip1 cells. (A,B)

Representations of the steady-state oxygen gradients from coarse-grained simulations of spheroids suspended in peritoneal fluid. The color scale indicates the range of oxygen concentrations in mm Hg. Black circles mark the perimeter of the spheroids. **(A)** The oxygen gradient through the middle of a spheroid 336 μm in diameter (58,000 cells). At this size, all cells are well oxygenated with an oxygen partial pressure above the hypoxic threshold of 19 mm Hg (indicated on the color scale as a blue arrow). The lowest oxygen concentration at the core of the spheroid is 21.6 mm Hg. **(B)** The oxygen gradient through the middle of a spheroid 364 μm in diameter (74,000 cells). By the time a spheroid has reached this size, the core is hypoxic (0.5 mm Hg). **(C,D)** OvTM simulations of angiogenesis in a tumor attached to the intestinal wall, assuming constitutive release of VEGF from cancer cells. **(C)** 3-D image of the simulation after 78 days when the tumor has grown to 6,400 cells. **(D)** 2-D slice through the middle of the tumor in **(D)** to show

vessel tree morphology. **(E)** Scatter dot plots of mesenteric tumor vascularization with respect to cross-sectional tumor area as determined from H&E-stained sections of mouse intestine and mesentery collected 3 weeks post-injection. Areas of all mesenteric tumors measured are plotted on the left. Tumors with areas above the predicted hypoxic threshold are in red. All non-vascularized tumors fall below the hypoxic threshold. The right plot shows the area and vascularization status of small tumors that fall below the hypoxic threshold. A majority of these small tumors (57%) are also vascularized. Lines indicate the median value. **(F)** Cross-sectional view of a small mesenteric tumor after H&E staining. Red blood cells (red) can be seen populating vessels within the tumor (blue). **(G)** Confocal image of ovarian tumor removed from the surface of the gut and labeled with anti-CD31 antibody (endothelial cell marker, red fluorescence) to distinguish tumor vasculature. An anti-GFP antibody with an FITC-labeled secondary antibody marks GFP-expressing cancer cells; Hoechst (blue fluorescence) labels the nuclei of all cells in the field of view.

modeled oxygenation in a simple spheroid to estimate at what diameter the tumor center would become hypoxic, for comparison with diameters of vascularized tumors observed in the mouse xenografts. Cancer cell homotypic and heterotypic adhesions on smooth muscle were then tuned to regenerate the spheroidal morphology of SKOV3.ip1 xenograft tumors on the small intestine or stomach (**Figure 6A**). To simulate the depth to which spheroids penetrate in soft tissue due to a chemotactic motive force, the underlying tissue structure was adjusted to represent a fatty section of the mesentery. In the simulations, tumors remain on the surface of smooth muscle, a tissue with many underlying tight junctions (**Figures 6C,D**), and invade soft tissues with space between cells, such as the mesentery (**Figure 4A**).

Finally, we simulated VEGF-driven angiogenic morphogenesis borrowing from previous methods using cellular Potts models for tumor-driven angiogenesis (Bauer et al., 2007, 2009; Shirinifard et al., 2009), in which endothelial cell chemotaxis toward soluble VEGF leads to angiogenic sprouting and branching. These models treated VEGF as a diffusible molecule whose gradient, together with the biophysical environment, drives endothelial migration and proliferation, and eventually morphogenesis of vessel sprouts. We did not include other angiogenesis dynamics from Bauer et al. (2009), which considered endothelial cell interactions with the ECM to further drive sprouting morphogenesis, nor does our model assess tumor growth as in Shirinifard et al. (2009), which modeled tumor growth in response to a growing network of surrounding vessels providing nutrients. Instead, angiogenesis was modeled as a simple morphogenetic process driven by chemotaxis and differential adhesion that penetrates a 3-D tumor. The sprouting vessel's base cell (or cells) has a semi-permanent elastic bond to the existing vessel, describing the labile adhesion interactions between them. Otherwise, differential adhesions between tumor and endothelial cells facilitate endothelial sprouting up the VEGF gradient.

The basic OvTM model and parameter set remain the same for all three groups of simulations (spheroids on muscle, spheroids invading mesenteric fat, and angiogenic sprouts in spheroids on muscle), except for the following: Between the cases of spheroid growth in different niches, the tissue surface is comprised of different cell types with their associated parameters. In angiogenesis simulations, the volume constraint for cancer cells was increased to

help prevent cell fragmentation during migration. Constraints on endothelial cells in the angiogenesis model (proliferating endothelial, non-proliferating endothelial, and permanent vessel) include elastic labile adhesion bonds between each type of vascular cell and its neighbors. The CC3D simulation code will be available upon request to the authors.

We show that, for the aggressive SKOV3.ip1 cell line, homotypic adhesion between cancer cells is a defining feature that favors the aggregation of cancer cells into small spheroids. The spheroid morphology may promote adhesion-mediated cell survival signals and allow cancer cells to evade anoikis, a cell death program usually triggered by loss of cell adhesion to the ECM (Kim et al., 2012). We speculate that these strong homotypic interactions may help to explain the typical clinical presentation where ovarian cancer is largely confined to the peritoneum and often accompanied by ascites. It is notable that others have shown spheroids are less susceptible to chemotherapeutic agents and may therefore contribute to relapse (Shield et al., 2009).

While some treatment regimens have focused on reducing metastatic spread through limiting cancer cell adhesion to the mesothelium (Sawada et al., 2012), we were interested in whether interactions between cancer cells might also be an important target. Using serial injections of green-fluorescent and red-fluorescent cells, we demonstrated that newly introduced cancer cells preferentially adhere to existing tumors. Strong cell-cell adhesion between cancer cells that stabilizes tumor clusters in the simulations could explain this observation. However, autocrine factors may also contribute to cancer cell homing, similar to the release of IL-6 and IL-8 from breast tumors that draws circulating tumor cells back to the primary tumor site (Kim et al., 2009). Although the mechanism is not well understood, therapies targeting ovarian cancer cell-cell homotypic adhesion may be worth consideration. In addition to limiting tumor mass, such drugs might be administered in combination with conventional chemotherapy to improve drug penetration.

Distinct niches within the peritoneal microenvironment also help to restrict cancer cells to the peritoneum and limit metastatic spread to other anatomical sites. Based upon the animal and mathematical models, colonization and growth is favored in loosely organized tissues. There are similarities between the open architectures of the mesentery and omentum, two organs that are

colonized by SKOV3.ip1 cells and share rich beds of adipose tissue known to secrete cytokines and growth factors attractive to cancer cells (Collins et al., 2009; Klopp et al., 2012). The adipocyte-rich omentum has a slightly thicker mesothelial layer than the mesentery, but has stomata or openings in the mesothelium above the milky spots that expose the underlying layers (Cui et al., 2002). The open architecture of these organs offers few barriers to cancer cells that undergo chemotaxis in response to local chemokine production. In contrast, even the aggressive SKOV3.ip1 cancer cell line is largely blocked by physical barriers such as the smooth muscle layers in the GI tract.

Our work is consistent with recent studies by Nieman et al. (2011), who showed that SKOV3.ip1 cells adhere to the omentum as early as 20 min post-injection and migrate in response to IL-8 and other chemotactic agents produced by adipocytes. In addition, we provide new evidence suggesting that SKOV3.ip1 cells migrate through the mesothelium and adipose tissue toward mesenteric vessels. Chemotaxis of cancer cells toward existing vessels has been observed in rodent models injected subcutaneously with mammary carcinoma cells (Li et al., 2000). Based on results from OvTM simulations, we propose that a chemotactic factor originating from the vessel may mediate this process. Although the identity of the factor is unknown, it is possible that vessels also produce an IL-8 gradient that attracts cancer cells, since activated vascular smooth muscle cells are capable of producing IL-8 (Wang et al., 1991). Growth factors secreted by perivascular tumor-associated macrophages, such as the epidermal growth factor (EGF), could also promote local survival and proliferation of tumors that take up residence near vessels (Lewis and Pollard, 2006).

Interestingly, rodent models that showed tumor migration to blood vessels also exhibited early angiogenesis in tumors consisting of fewer than 300 cells (Li et al., 2000). The constitutive expression of angiogenic factors by SKOV3.ip1 cells may be the single

most important feature contributing to the aggressive growth of this cancer cell line after engraftment. In preliminary data not shown, microarray studies showed that VEGF mRNA levels differ less than twofold in cultured SKOV3.ip1 cells versus *in vivo*. In OvTM simulations, this modest level of constitutive production is sufficient for even minute tumor spheroids to recruit endothelial cells from nearby vessels (Figure 7). This result is in contrast to the classical solid tumor situation, where angiogenesis is initiated only after the interior tumor cells become hypoxic and upregulate VEGF production (Shweiki et al., 1992; Pugh and Ratcliffe, 2003). In patients, however, it is important to note that the balance of constitutive and induced production of angiogenic factors by cancer cells may vary widely. Therefore, assessment of angiogenic factor transcriptional profiles or direct measurement of angiogenic factor levels in serum/cystic fluid may be critical to identify patients at risk for relapse, a concept that has also been proposed by others (Harlozinska et al., 2004; Li et al., 2004).

ACKNOWLEDGMENTS

Use of the UNM Electron Microscopy, Fluorescence Microscopy, and Flow Cytometry Shared Resource Centers at the UNM SOM and Cancer Center, and NIH support for these cores, is gratefully acknowledged. Angela Welford and Rachel Grattan collected the EM images for this work. The authors thank Dr. Glazier and other members of the CompuCell3D development team. Dr. Hoffman is the founder of AntiCancer Inc. This work was supported by NIH R01CA119232 (Wilson), NIH P50GM065794 (Wilson), and NIH R25CA153825 (Oliver).

SUPPLEMENTARY MATERIAL

The Supplementary Material for this article can be found online at http://www.frontiersin.org/Molecular_and_Cellular_Oncology/10.3389/fonc.2013.00097/abstract

REFERENCES

- Arakelyan, L., Merbl, Y., and Agur, Z. (2005). Vessel maturation effects on tumour growth: validation of a computer model in implanted human ovarian carcinoma spheroids. *Eur. J. Cancer* 41, 159–167.
- Ausprunk, D. H., and Folkman, J. (1977). Migration and proliferation of endothelial cells in preformed and newly formed blood vessels during tumor angiogenesis. *Microvasc. Res.* 14, 53–65.
- Bagley, R. G., Walter-Yohrling, J., Cao, X., Weber, W., Simons, B., Cook, B. P., et al. (2003). Endothelial precursor cells as a model of tumor endothelium. *Cancer Res.* 63, 5866–5873.
- Barcz, E., Skopinska Rózewska, E., Kaminski, P., Demkow, U., Bobrowska, K., and Marianowski, L. (2002). Angiogenic activity and IL-8 concentrations in peritoneal fluid and sera in endometriosis. *Int. J. Gynaecol. Obstet.* 79, 229–235.
- Bast, R. C., Hennessey, B., and Mills, G. B. (2009). The biology of ovarian cancer: new opportunities for translation. *Nat. Rev. Cancer* 9, 415–428.
- Bauer, A. L., Jackson, T. L., and Jiang, Y. (2007). A cell-based model exhibiting branching and anastomosis during tumor-induced angiogenesis. *Biophys. J.* 92, 3105–3121.
- Bauer, A. L., Jackson, T. L., and Jiang, Y. (2009). Topography of extracellular matrix mediates vascular morphogenesis and migration speeds in angiogenesis. *PLoS Comput. Biol.* 5:e1000445. doi:10.1371/journal.pcbi.1000445
- Bruun, J. M., Lihn, A. S., Madan, A. K., Pedersen, S. B., Schiøtt, K. M., Fain, J. N., et al. (2004). Higher production of IL-8 in visceral vs. subcutaneous adipose tissue. Implication of nonadipose cells in adipose tissue. *Am. J. Physiol. Endocrinol. Metab.* 286, E8–E13.
- Burleson, K. M., Boente, M. P., Pambuccian, S. E., and Skubitz, A. P. (2006). Disaggregation and invasion of ovarian carcinoma ascites spheroids. *J. Transl. Med.* 4, 6.
- Casciari, J. J., Sotirchos, S. V., and Sutherland, R. M. (1992). Variations in tumor cell growth rates and metabolism with oxygen concentration, glucose concentration, and extracellular pH. *J. Cell. Physiol.* 151, 386–394.
- Casey, R. C., Burleson, K. M., Skubitz, K. M., Pambuccian, S. E., Oegema, T. R. Jr., Ruff, L. E., et al. (2001). β 1-integrins regulate the formation and adhesion of ovarian carcinoma multicellular spheroids. *Am. J. Pathol.* 159, 2071–2080.
- Chauviere, A. H., Hatzikirou, H., Lowengrub, J. S., Frieboes, H. B., Thompson, A. M., and Cristini, V. (2010). Mathematical oncology: how are the mathematical and physical sciences contributing to the war on breast cancer? *Curr. Breast Cancer Rep.* 2, 121–129.
- Cickovski, T., Aras, K., Alber, M. S., Izaguirre, J. A., Swat, M., Glazier, J. A., et al. (2007). From genes to organisms via the cell a problem-solving environment for multicellular development. *Comput. Sci. Eng.* 9, 50–60.
- Collins, D., Hogan, A., O'shea, D., and Winter, D. (2009). The omentum: anatomical, metabolic, and surgical aspects. *J. Gastrointest. Surg.* 13, 1138–1146.
- Cui, L., Johkura, K., Liang, Y., Teng, R., Ogiwara, N., Okouchi, Y., et al. (2002). Biodefense function of omental milky spots through cell adhesion molecules and leukocyte proliferation. *Cell Tissue Res.* 310, 321–330.
- Dunn, S. J., Appleton, P. L., Nelson, S. A., Nathke, I. S., Gavaghan, D. J., and Osborne, J. M. (2012). A two-dimensional model of the colonic crypt accounting for the role of the basement membrane and pericryptal fibroblast sheath. *PLoS Comput. Biol.* 8:e1002515. doi:10.1371/journal.pcbi.1002515
- Evans, S. M., Schrlau, A. E., Chalian, A. A., Zhang, P., and Koch, C. J.

- (2006). Oxygen levels in normal and previously irradiated human skin as assessed by EF5 Binding. *J. Invest. Dermatol.* 126, 2596–2606.
- Freyer, J. P., and Sutherland, R. M. (1985). A reduction in the in situ rates of oxygen and glucose consumption of cells in EMT6/Ro spheroids during growth. *J. Cell. Physiol.* 124, 516–524.
- Friend, D. S., and Gilula, N. B. (1972). Variations in tight and gap junctions in mammalian tissues. *J. Cell Biol.* 53, 758–776.
- Fu, X., and Hoffman, R. M. (1993). Human ovarian carcinoma metastatic models constructed in nude mice by orthotopic transplantation of histologically-intact patient specimens. *Anticancer Res.* 13, 283–286.
- Gerber, S. A., Rybalko, V. Y., Bigelow, C. E., Lugade, A. A., Foster, T. H., Frelinger, J. G., et al. (2006). Preferential attachment of peritoneal tumor metastases to omental immune aggregates and possible role of a unique vascular microenvironment in metastatic survival and growth. *Am. J. Pathol.* 169, 1739–1752.
- Giverson, C., and Preziosi, L. (2012). Modelling the compression and reorganization of cell aggregates. *Math. Med. Biol.* 29, 181–204.
- Giverson, C., Scianna, M., Preziosi, L., Buono, N. L., and Funaro, A. (2010). Individual cell-based model for in vitro mesothelial invasion of ovarian cancer. *Math. Model. Nat. Phenom.* 5, 203–223.
- Glazier, J. A., and Graner, F. (1993). Simulation of the differential adhesion driven rearrangement of biological cells. *Phys. Rev. E Stat. Phys. Plasmas Fluids Relat. Interdiscip. Topics* 47, 2128–2154.
- Graner, F., and Glazier, J. A. (1992). Simulation of biological cell sorting using a two-dimensional extended Potts model. *Phys. Rev. Lett.* 69, 2013–2016.
- Harlozinska, A., Sedlacek, P., Kulpa, J., Grybos, M., Wojcik, E., Van Dalen, A., et al. (2004). Vascular endothelial growth factor (VEGF) concentration in sera and tumor effusions from patients with ovarian carcinoma. *Anticancer Res.* 24, 1149–1157.
- Höckel, M., and Vaupel, P. (2001). Tumor hypoxia: definitions and current clinical, biologic, and molecular aspects. *J. Natl. Cancer Inst.* 93, 266–276.
- Howdieshell, T. R., McGuire, L., Maestas, J., and McGuire, P. G. (2011). Pattern recognition receptor gene expression in ischemia-induced flap revascularization. *Surgery* 150, 418–428.
- Huang, S., Robinson, J. B., Deguzman, A., Bucana, C. D., and Fidler, I. J. (2000). Blockade of nuclear factor-kappaB signaling inhibits angiogenesis and tumorigenicity of human ovarian cancer cells by suppressing expression of vascular endothelial growth factor and interleukin 8. *Cancer Res.* 60, 5334–5339.
- Iwanicki, M. P., Davidowitz, R. A., Ng, M. R., Besser, A., Muranen, T., Merriitt, M., et al. (2011). Ovarian cancer spheroids use myosin-generated force to clear the mesothelium. *Cancer Discov.* 1, 144–157.
- Jain, H., Nör, J., and Jackson, T. (2008). Modeling the VEGF-Bcl-2-CXCL8 pathway in intratumoral angiogenesis. *Bull. Math. Biol.* 70, 89–117.
- Jiang, Y., Pjesivac-Grbovic, J., Cantrell, C., and Freyer, J. P. (2005). A multiscale model for avascular tumor growth. *Biophys. J.* 89, 3884–3894.
- Kenny, H. A., Kaur, S., Coussens, L. M., and Lengyel, E. (2008). The initial steps of ovarian cancer cell metastasis are mediated by MMP-2 cleavage of vitronectin and fibronectin. *J. Clin. Invest.* 118, 1367–1379.
- Khan, S., Funk, H., Thiolloy, S., Lotan, T., Hickson, J., Prins, G., et al. (2010). In vitro metastatic colonization of human ovarian cancer cells to the omentum. *Clin. Exp. Metastasis* 27, 185–196.
- Khanna, R., and Krediet, R. T. (eds) (2009). *Nolph and Gokal's Textbook of Peritoneal Dialysis*. New York: Springer.
- Kim, M.-Y., Oskarsson, T., Acharyya, S., Nguyen, D. X., Zhang, X. H. F., Norton, L., et al. (2009). Tumor self-seeding by circulating cancer cells. *Cell* 139, 1315–1326.
- Kim, Y.-N., Koo, K.-H., Sung, J. Y., Yun, U.-J., and Kim, H. (2012). Anoikis resistance: an essential prerequisite for tumor metastasis. *Int. J. Cell Biol.* 2012: 306879. doi:10.1155/2012/306879
- Kizaka-Kondoh, S., Itasaka, S., Zeng, L., Tanaka, S., Zhao, T., Takahashi, Y., et al. (2009). Selective killing of hypoxia-inducible factor-1-active cells improves survival in a mouse model of invasive and metastatic pancreatic cancer. *Clin. Cancer Res.* 15, 3433–3441.
- Klopp, A. H., Zhang, Y., Solley, T., Amaya-Manzanares, F., Marini, F., Andreeff, M., et al. (2012). Omental adipose tissue-derived stromal cells promote vascularization and growth of endometrial tumors. *Clin. Cancer Res.* 18, 771–782.
- Levine, H. A., Pamuk, S., Sleeman, B. D., and Nilsen-Hamilton, M. (2001). Mathematical modeling of capillary formation and development in tumor angiogenesis: penetration into the stroma. *Bull. Math. Biol.* 63, 801–863.
- Lewis, C. E., and Pollard, J. W. (2006). Distinct role of macrophages in different tumor microenvironments. *Cancer Res.* 66, 605–612.
- Li, C.-Y., Shan, S., Huang, Q., Braun, R. D., Lanzen, J., Hu, K., et al. (2000). Initial stages of tumor cell-induced angiogenesis: evaluation via skin window chambers in rodent models. *J. Natl. Cancer Inst.* 92, 143–147.
- Li, L., Wang, L., Zhang, W., Tang, B., Zhang, J., Song, H., et al. (2004). Correlation of serum VEGF levels with clinical stage, therapy efficacy, tumor metastasis and patient survival in ovarian cancer. *Anticancer Res.* 24, 1973–1979.
- Li Jeon, N., Baskaran, H., Dertinger, S. K. W., Whitesides, G. M., Van De Water, L., and Toner, M. (2002). Neutrophil chemotaxis in linear and complex gradients of interleukin-8 formed in a micro-fabricated device. *Nat. Biotech.* 20, 826–830.
- MacDougall, J. D. B., and McCabe, M. (1967). Diffusion coefficient of oxygen through tissues. *Nature* 215, 1173–1174.
- Macklin, P., Edgerton, M. E., Thompson, A. M., and Cristini, V. (2012). Patient-calibrated agent-based modelling of ductal carcinoma in situ (DCIS): from microscopic measurements to macroscopic predictions of clinical progression. *J. Theor. Biol.* 301, 122–140.
- McGuire, W. P., Hoskins, W. J., Brady, M. F., Kucera, P. R., Partridge, E. E., Look, K. Y., et al. (1996). Cyclophosphamide and cisplatin compared with paclitaxel and cisplatin in patients with stage III and stage IV ovarian cancer. *N. Engl. J. Med.* 334, 1–6.
- Milliken, D., Scotton, C., Raju, S., Balkwill, F., and Wilson, J. (2002). Analysis of chemokines and chemokine receptor expression in ovarian cancer ascites. *Clin. Cancer Res.* 8, 1108–1114.
- Mombach, J. C., Glazier, J. A., Raphael, R. C., and Zajac, M. (1995). Quantitative comparison between differential adhesion models and cell sorting in the presence and absence of fluctuations. *Phys. Rev. Lett.* 75, 2244–2247.
- Morton, C. I., Hlatky, L., Hahnfeldt, P., and Enderling, H. (2011). Non-stem cancer cell kinetics modulate solid tumor progression. *Theor. Biol. Med. Model.* 8, 48.
- Nieman, K. M., Kenny, H. A., Penicka, C. V., Ladanyi, A., Buell-Gutbrod, R., Zillhardt, M. R., et al. (2011). Adipocytes promote ovarian cancer metastasis and provide energy for rapid tumor growth. *Nat. Med.* 17, 1498–1503.
- Pugh, C. W., and Ratcliffe, P. J. (2003). Regulation of angiogenesis by hypoxia: role of the HIF system. *Nat. Med.* 9, 677–684.
- Sawada, K., Ohyagi-Hara, C., Kimura, T., and Morishige, K.-I. (2012). Integrin inhibitors as a therapeutic agent for ovarian cancer. *J. Oncol.* 2012: 915140. doi:10.1155/2012/915140
- Schneider, C. A., Rasband, W. S., and Eliceiri, K. W. (2012). NIH Image to ImageJ: 25 years of image analysis. *Nat. Methods* 9, 671–675.
- Serini, G., Ambrosi, D., Giraudo, E., Gamba, A., Preziosi, L., and Busolin, F. (2003). Modeling the early stages of vascular network assembly. *EMBO J.* 22, 1771–1779.
- Shield, K., Ackland, M. L., Ahmed, N., and Rice, G. E. (2009). Multicellular spheroids in ovarian cancer metastases: biology and pathology. *Gynecol. Oncol.* 113, 143–148.
- Shirasawa, T., Izumizaki, M., Suzuki, Y.-I., Ishihara, A., Shimizu, T., Tamaki, M., et al. (2003). Oxygen affinity of hemoglobin regulates O₂ consumption, metabolism, and physical activity. *J. Biol. Chem.* 278, 5035–5043.
- Shirinifard, A., Gens, J. S., Zaitlen, B. L., Poplawski, N. J., Swat, M., and Glazier, J. A. (2009). 3D multi-cell simulation of tumor growth and angiogenesis. *PLoS ONE* 4:e7190. doi:10.1371/journal.pone.0007190
- Shweiki, D., Itin, A., Soffer, D., and Keshet, E. (1992). Vascular endothelial growth factor induced by hypoxia may mediate hypoxia-initiated angiogenesis. *Nature* 359, 843–845.
- Sodek, K. L., Brown, T. J., and Ringuette, M. J. (2008). Collagen I but not Matrigel matrices provide an MMP-dependent barrier to ovarian cancer cell penetration. *BMC Cancer* 8:223. doi:10.1186/1471-2407-8-223
- Strobel, T., and Cannistra, S. A. (1999). β 1-Integrins partly mediate binding of ovarian cancer cells to peritoneal mesothelium *in vitro*. *Gynecol. Oncol.* 73, 362–367.

- Swat, M. H., Hester, S. D., Balter, A. I., Heiland, R. W., Zaitlen, B. L., and Glazier, J. A. (2009). Multicell simulations of development and disease using the CompuCell3D simulation environment. *Methods Mol. Biol.* 500, 361–428.
- Wang, J. M., Sica, A., Peri, G., Walter, S., Padura, I. M., Libby, P., et al. (1991). Expression of monocyte chemotactic protein and interleukin-8 by cytokine-activated human vascular smooth muscle cells. *Arterioscler. Thromb.* 11, 1166–1174.
- Yamauchi, K., Yang, M., Jiang, P., Xu, M., Yamamoto, N., Tsuchiya, H., et al. (2006). Development of real-time subcellular dynamic multicolor imaging of cancer-cell trafficking in live mice with a variable-magnification whole-mouse imaging system. *Cancer Res.* 66, 4208–4214.
- Yang, M., Reynoso, J., Bouvet, M., and Hoffman, R. M. (2009). A transgenic red fluorescent protein-expressing nude mouse for color-coded imaging of the tumor microenvironment. *J. Cell. Biochem.* 106, 279–284.
- Yoneda, J., Kuniyasu, H., Crispens, M. A., Price, J. E., Bucana, C. D., and Fidler, I. J. (1998). Expression of angiogenesis-related genes and progression of human ovarian carcinomas in nude mice. *J. Natl. Cancer Inst.* 90, 447–454.
- Yu, D., Wolf, J. K., Scanlon, M., Price, J. E., and Hung, M. C. (1993). Enhanced c-erbB-2/neu expression in human ovarian cancer cells correlates with more severe malignancy that can be suppressed by E1A. *Cancer Res.* 53, 891–898.
- Conflict of Interest Statement:** The authors declare that the research was conducted in the absence of any commercial or financial relationships that could be construed as a potential conflict of interest.
- Received: 20 December 2012; accepted: 09 April 2013; published online: 17 May 2013.*
- Citation: Steinkamp MP, Winner KK, Davies S, Muller C, Zhang Y, Hoffman RM, Shirinifard A, Moses M, Jiang Y and Wilson BS (2013) Ovarian tumor attachment, invasion, and vascularization reflect unique microenvironments in the peritoneum: insights from xenograft and mathematical models. Front. Oncol. 3:97. doi: 10.3389/fonc.2013.00097*
- This article was submitted to Frontiers in Molecular and Cellular Oncology, a specialty of Frontiers in Oncology. Copyright © 2013 Steinkamp, Winner, Davies, Muller, Zhang, Hoffman, Shirinifard, Moses, Jiang and Wilson. This is an open-access article distributed under the terms of the Creative Commons Attribution License, which permits use, distribution and reproduction in other forums, provided the original authors and source are credited and subject to any copyright notices concerning any third-party graphics etc.*



Tumor evolution in space: the effects of competition colonization tradeoffs on tumor invasion dynamics

Paul A. Orlando^{1*}, Robert A. Gatenby² and Joel S. Brown³

¹ Biometry Research Group, Division of Cancer Prevention, National Cancer Institute, Rockville, MD, USA

² Department of Radiology, Moffitt Cancer Center, Tampa, FL, USA

³ Department of Biological Sciences, University of Illinois at Chicago, Chicago, IL, USA

Edited by:

Heiko Enderling, Tufts University
School of Medicine, USA

Reviewed by:

Yosef Cohen, University of
Minnesota, USA

Richard Durrett, Duke University, USA

*Correspondence:

Paul A. Orlando, Biometry Research
Group, Division of Cancer Prevention,
National Cancer Institute, 6130
Executive Blvd, Executive Plaza
North, Suite 3131, Rockville, MD
20892, USA.
e-mail: paul.orlando@nih.gov

We apply competition colonization tradeoff models to tumor growth and invasion dynamics to explore the hypothesis that varying selection forces will result in predictable phenotypic differences in cells at the tumor invasive front compared to those in the core. Spatially, ecologically, and evolutionarily explicit partial differential equation models of tumor growth confirm that spatial invasion produces selection pressure for motile phenotypes. The effects of the invasive phenotype on normal adjacent tissue determine the patterns of growth and phenotype distribution. If tumor cells do not destroy their environment, colonizer and competitive phenotypes coexist with the former localized at the invasion front and the latter, to the tumor interior. If tumors cells do destroy their environment, then cell motility is strongly selected resulting in accelerated invasion speed with time. Our results suggest that the widely observed genetic heterogeneity within cancers may not be the stochastic effect of random mutations. Rather, it may be the consequence of predictable variations in environmental selection forces and corresponding phenotypic adaptations.

Keywords: tumor invasion, spatial ecology, competition colonization tradeoff, partial differential equation model, spatial selection

INTRODUCTION

Competition-colonization tradeoffs underlie an important mechanism of coexistence in ecological communities with spatial variation of competitor abundances (Tilman, 1994). In these communities, some species excel at colonizing unoccupied space whereas others excel at competing within already occupied space. But, no species simultaneously excels at both. Ecologists have demonstrated competition colonization tradeoffs in a number of communities (e.g., birds: Rodríguez et al., 2007, ants: Stanton et al., 2002, plants: Turnbull et al., 2004). They can be important in structuring ecological communities (e.g., Turnbull et al., 1999; Cadotte et al., 2006).

Competition colonization tradeoffs may also play an important role in the ecological and evolutionary dynamics of population invasions and range expansions. Researchers have noted that selective pressures at an invasion front could be markedly different than selective pressures at the core of an invasion (e.g., Phillips, 2009; Burton et al., 2010). Evolutionary ecologists have shown that phenotypic change by natural selection occurs during species invasions and is critical for understanding invasion dynamics (e.g., Simmons and Thomas, 2004; Broennimann et al., 2007; Barrett et al., 2008).

A well-known example of eco-evolutionary dynamics is the invasion and spread of the cane toad (*Bufo marinus*) across northern Australia. Detailed examination of the spreading population demonstrates two divergent phenotypes based on selection for colonization along the invasion front (Phillips et al., 2006). The colonizing phenotype has longer legs, moves more often, and is found near the front of the invasion. Phillips (2009) has shown

that the phenotype at the invasion front tend to be *r*-selected, in that they reproduce sooner than toads in the core. Evidence suggests that a tradeoff for increased dispersal may be manifest in increased spinal stress and arthritis (Brown et al., 2007).

We highlight the notion that tumor invasion parallels the process of population invasion into novel habitats and subsequent range expansion. Accordingly, concepts and modeling from ecology and evolution can be applied to understand the ecological and evolutionary dynamics of tumors. While the modern paradigm of cancer biology sees cancer as arising because of cell level selection pressures, oncologists have largely neglected the role of ecology in determining these selection pressures and subsequent evolution (Gatenby, 2012). Integrating these viewpoints has the potential to further our understanding of the growth and invasion of tumors.

There is clear evidence of evolutionary processes within clinical cancers resulting in multiple genetically distinct clones (Yachida et al., 2010; Gerlinger et al., 2012). However, this is typically attributed to random mutations that result in an overall proliferative advantage rather than local adaptations to specific environmental selection forces. Selection in tumors could be markedly different at the tumor host interface than within the host. Moreover, there is evidence that suggests the presence of both colonization and competition phenotypes among cancer cells within a tumor. For example, invadopodia are actin rich invasive cell membrane protrusions that degrade the extracellular matrix (Weaver, 2006). Invadopodia have been observed in a wide range of cancers and appear to confer invasion potential. In contrast, the phenotypes of many cancer cells appear to promote the development

of a local tumor infrastructure. For example, vascular endothelial growth factor (VEGF) is a protein secreted by many tumor cells and promotes tumor vascularity and blood flow by inducing growth and movement of endothelial cells (Carmeliet and Jain, 2000; Goodsell, 2003). The former phenotype may arise due to selection pressures at the invasion front, and the latter may arise due to selection pressures within the interior of the tumor.

In this article we use partial differential equation (PDE) models that are spatially, ecologically, and evolutionarily explicit to explore the effects of competition colonization tradeoffs on the evolution of tumors. PDE models of population growth in space have a history in both the fields of ecology (e.g., Holmes et al., 1994) and tumor biology (e.g., Chaplain et al., 2006; Eikenberry et al., 2009). Our approach is novel in that we explicitly model a phenotypic distribution of the cancer cells (also, see Benichou et al., 2012; Bouin et al., 2012). In our model, cancer cells are distributed in physical space and phenotype space. As such our model may better reflect the ecological and evolutionary dynamics of tumor invasion by incorporating population dynamics and heritable phenotypic changes.

We use our models to investigate four important questions relevant to the eco-evolutionary dynamics of range expansions and tumor biology.

When does cell motility evolve? Models of range expansion show that motility can evolve, and this has been demonstrated in general population models and tumor specific models (e.g., Gerlee and Anderson, 2009; Aktipis et al., 2012). We use our models to reaffirm these results and to explore when and if cell motility evolves.

Does the type of movement matter? Previous work with spatial PDE models has demonstrated that spatial heterogeneity with temporal homogeneity selects against diffusive movement, but can select for directed adaptive movement (Dockery et al., 1998; Cantrell et al., 2006). However, there has not been an analysis comparing different movement types in models of range expansion. We use our models to compare the effects of different types of movement rules on the overall eco-evolutionary dynamics.

Does the evolution of cell motility result in phenotypic differentiation in space? The cane toads are clearly an example of phenotypic divergence in space. However, recent theoretical work by Shine et al. (2011) has shown that selection is not necessary for phenotypic divergence in a spatial context. Rather spatial assortment of phenotypes can simply be a consequence of the fact that faster moving phenotypes tend to move to the invasion front, and the slower moving phenotypes tend to stay in the core, and this facilitates assortive mating. Theoreticians have demonstrated the effect of spatial sorting in PDE models of range expansion (Benichou et al., 2012; Bouin et al., 2012). We use our models to ask if selection for motility results in phenotypic divergence in space. More specifically, we investigate whether a competition colonization tradeoff is required for this type of landscape scale coexistence.

Does invasion speed accelerate? The speed of the cane toad invasion has accelerated, by as much as five times in a half century (Phillips et al., 2006, 2007). Researchers attribute this acceleration to the evolution of a more specialized colonizer phenotype.

Individual toads have been shown to move longer distances per unit time in recent times as compared to historic records. Theory also predicts accelerated invasion speed with the evolution of dispersal (Travis and Dytham, 2002). Thus, we explore with our models whether the evolution of motility results in accelerated invasion speed.

MODEL DESCRIPTION

We develop two spatially and evolutionarily explicit PDE models to explore tumor invasion with a competition colonization tradeoff. The models contrast two extreme perspectives on tumor dynamics. In the first model, cancer cells invade the surrounding microenvironment and subsequently reach a carrying capacity. In the second model, cancer cells invade the surrounding microenvironment and subsequently destroy the environment, resulting in local extinction of the cancer cells. In both models, cancer cells are characterized by their phenotype and location in physical space. Thus, we include a phenotypic dimension (w), which describes a phenotypic distribution (Cohen, 2009) of cancer cells. To model a competition colonization tradeoff, we assume that increased w corresponds to increases in a cell's ability to move in physical space and decreases its ability to compete for resources. Numerical solutions to the models describe the time evolution of the phenotypic distribution of cells in space. Mutation and differential success of phenotypes results in ecological and evolutionary dynamics. Cell movement produces spatial ecological dynamics.

MODEL 1 – A HABITAT–CONTINUUM TUMOR MODEL

With the first model, we consider an ecological situation where cancer cells invade the surrounding environment and engineer the environment, such that it is a suitable habitat. This model is a phenomenological representation of angiogenesis and other types of environmental engineering by the cancer cells. We model a logistically growing population of cancer cells (c) in one-dimensional space (x), with phenotype (w). We consider two different versions of the model; one for the evolution of random movement and one for the evolution of directed movement. The corresponding PDEs are given by

$$\frac{\partial c(x, w, t)}{\partial t} = \lambda c \left(\frac{K(w) - T_c}{K(w)} \right) + \mu(w) \frac{(\partial^2 c)}{\partial x^2} - \frac{\partial}{\partial x} \left(\chi c \frac{\partial F}{\partial x} \right) + M(w). \quad (1)$$

$$\frac{\partial c(x, w, t)}{\partial t} = \lambda c \left(\frac{K(w) - T_c}{K(w)} \right) + \mu \frac{\partial^2 c}{\partial x^2} - \frac{\partial}{\partial x} \left(\chi(w) c \frac{\partial F}{\partial x} \right) + M(w). \quad (2)$$

The first term in the equations describes standard logistic population growth, with an intrinsic growth rate λ , and carrying capacity $K(w)$. T_c represents the total cell density at a spatial position x . T_c is calculated by integrating over the phenotypic dimension, giving $T_c = \int_0^1 c(x, w) dw$.

The second and third terms are derived by Fick's first and second laws of flux. The second term describes random movement in space, as characterized by a Laplacian operator scaled by the

cell motility coefficient μ . The third term describes directed cell movement in space via the spatial fitness gradient ($\partial F/\partial x$) and proportional to the tactic sensitivity coefficient χ . The tactic sensitivity coefficient scales the tendency of cells to move in response to a chemical gradient. Here, the fitness function is defined as the per capita growth rate of cells in the absence of cell movement or mutation:

$$F = \lambda \left(\frac{K(w) - T_c}{K(w)} \right).$$

Since the fitness term is density dependent, the cells “adaptively” move to areas with lower cell densities. The fourth and final term in the model describes mutation or movement in phenotype space (see below for description).

The competition colonization tradeoff enters the model through the carrying capacity $K(w)$ and the cell movement parameters. To explore the effect of the evolution of different cell movement rules on invasion dynamics, we model the evolution of cell movement in two different ways (Eqs 1 and 2). The phenotypic variable w either increases the cell motility coefficient μ , $\mu = \rho_{1w}$ Eq. (1), or increases the tactic sensitivity coefficient χ , $\chi = \rho_{1w}$ Eq. (2). Throughout, we refer to the former as random cell movement and the latter as directed cell movement. In both cases, increasing w necessarily decreases cell competitiveness by decreasing the carrying capacity of a specific phenotype,

$$K(w) = \kappa \exp(-\rho_2 w).$$

Following Cohen (2009), we use a discrete function (Eq. 3) to describe mutation with regard to a continuous phenotypic trait (w). The B function describes the per capita birth rate of a particular phenotype, with ε describing the mutational step size. As in Cohen (2009) we assume for simplicity that each phenotype has a constant per capita birth rate λ , such that the negative part of the per capita logistic growth equation represents death rates. This simplification then leads to Eq. 4. We use second order Taylor series approximations of the terms in Eq. 3 to convert the discrete equation into a continuous approximation. Equation 4 shows the second order Taylor series approximation to Eq. 3. We use Eq. 5 as the mutation term in the model.

$$M'(w) = \frac{1}{2} \eta [B(w + \varepsilon) c(w + \varepsilon) + B(w - \varepsilon) c(w - \varepsilon) - 2B(w) c(w)] \quad (3)$$

$$M'(w) = \frac{1}{2} \eta \lambda [c(w + \varepsilon) + c(w - \varepsilon) - 2c(w)] \quad (4)$$

$$M(w) = \frac{1}{2} \eta \lambda \varepsilon^2 \frac{\partial^2 c}{\partial w^2} \quad (5)$$

MODEL 2 – A HABITAT-DESTRUCTION TUMOR MODEL

Our second model considers an ecological scenario where cancer cells invade and subsequently destroy the microenvironment. This model represents tumors with a significant necrotic core. We use a modified version of the haptotaxis model introduced by Anderson

(2005). The system of PDEs is given by

$$\frac{\partial c(x, y, w, t)}{\partial t} = vZ(p)c - D(w)c + \mu \Delta_{x,y}c - \nabla_{x,y}(\chi(w)c \nabla_{x,y}m) + M(w) \quad (6)$$

$$\frac{\partial c(x, y, w, t)}{\partial t} = vZ(p)c - D(w)c + \mu \Delta_{x,y}c - \nabla_{x,y}(\chi(w, m)c \nabla_{x,y}p) + M(w) \quad (7)$$

$$\frac{\partial m(x, y, t)}{\partial t} = -\alpha m T_c \quad (8)$$

$$\frac{\partial p(x, y, t)}{\partial t} = \gamma m - \sigma p - Z(p)T_c + \omega \Delta_{x,y}p \quad (9)$$

This model includes, cancer cell density (c), extracellular matrix density (m), and oxygen concentration (p) as state variables. The model assumes that cancer cells use extracellular matrix macromolecules for movement, and in the process, degrade these molecules. Furthermore, the matrix molecules produce oxygen, which the cancer cells depend on for reproduction. Thus, as cancers cells invade the surrounding environment they leave a wake of habitat-destruction by degrading the extracellular matrix and their oxygen supply. We assume that oxygen uptake by the cancer cells is described by a saturating function $Z(p) = \psi p/(\theta + p)$, where ψ is the maximum uptake rate and θ is the half saturation concentration of oxygen. v is the conversion efficiency of consumed oxygen to new cancer cells. δ is the per capita death rate of cancer cells. As in the previous model, μ and χ represent the cell motility coefficient and the tactic sensitivity coefficient respectively. M represents mutation, which we modify slightly from before (see below). Equation 6 shows that the matrix macromolecules decline from an initial abundance. In Anderson's original model, the degradation of the matrix was mediated through a matrix degradation protein that the cancer cells produced. For simplicity, here we consider that the cancer cells directly degrade the matrix molecules. Empirically, this mechanism may be captured by invadopodia for instance. α Describes the per capita rate at which cancer cells contact and degrade matrix molecules. Finally, the rate of change of oxygen concentration is linearly dependent on matrix molecules, where γ is the per molecule production of oxygen (Eq. 9), and σ is the per capita degradation rate of oxygen. Oxygen also declines through consumption. ω is the diffusion coefficient for oxygen.

To explore the effects of the evolution of different cell movement rules on invasion dynamics, we model two different versions of the tradeoff. Since the cells use the matrix molecules for movement, we assume that the cell motility coefficient is small and that the main mechanism of cell movement is through haptotaxis or chemotaxis. In both versions, the cost of increased tactic sensitivity is mediated through increased per capita death rate of cancer cells. Thus, $D = \delta + \rho_{2w}$. Where δ is the minimum per capita death rate, and ρ_2 scales the effect of increased cell motility on cell death rate. In the haptotaxis version of the model Eq. (6), we assume that directed cell movement is in the direction of increasing matrix molecules, with a speed proportional to the haptotactic coefficient, which is a function of the cells phenotype. $\chi = \rho_{1w}$. In the chemotactic version of the

model Eq. (7), directed cell movement is in the direction of increasing oxygen concentration. The chemotactic sensitivity coefficient is a function of the density of matrix macromolecules and cell phenotype. $\chi = m\rho_{1w}$. This models a situation where cells move toward areas with higher oxygen concentrations, but depend on matrix macromolecules for movement. As with the first model, this second version considers adaptive movement of cells.

The mutation term in this model is slightly different than the last model, since we have a specific function that describes the birth rate of each phenotype. The birth rate, $B(w)$ is given by the first terms of Eqs 6 and 7, $B(w) = vZ(w)c(w)$, substituting this into Eq. 3 above, and performing the Taylor series approximation as described above, gives $M(w) = (1/2)\eta\epsilon^2\partial^2 B/\partial w^2$ for the mutation term in the model.

In the first model, we consider a spatial line of 10 mm. In the second model, we consider a spatial area of 10 mm \times 10 mm. We used Neumann (no flux) boundary conditions for both the spatial and the phenotypic boundaries.

NUMERICAL ANALYSIS

We analyzed both models through numerical simulations, for which we used the method of lines approach (Schiesser and Griffiths, 2009). We used upwind spatial finite differences for the tactic terms. Anderson's (2005) original model is particularly difficult to solve numerically. We confirmed the validity of our scheme, by solving Anderson's original model and comparing our results to those of Walker and Webb (2007) and Chertock and Kurganov (2008). We found our results to be in good agreement with those of others.

For the first model, we used two different initial conditions. For an initial condition of mostly the competitor phenotype, we used

$$c(x, w, 0) = 5 \max \{0, (0.3 - (x - 5)^2)\} * \exp(-100 * w).$$

For an initial condition with mostly colonizers, we used:

$$c(x, w, 0) = 5 \max \{0, (0.3 - (x - 5)^2)\} * \exp(-100 * (1 - w)).$$

Both initial conditions represent a small population of cancer cells in the center of the spatial domain.

We used the following parameters for first model:

$\lambda = 0.5$, $\kappa = 1e-5$, $\eta = 1e-3$, $\rho_2 = 1$. $\rho_1 = 1e-2$ and $\mu = 1e-5$ for the evolution of chemotactic sensitivity. $\chi = 1e-4$ and $\rho_1 = 1e-3$ for the evolution of cell motility.

For the second model, we used the following initial conditions for both versions of the model:

$$c(x, y, w, 0) = 500 \max \left\{ 0, \left(0.3 - (x - 5)^2 + (y - 5)^2 \right) \right\} \\ \times \exp(-100 * w). \\ m(x, y, 0) = 0.05 \cos((\pi x^2)/20) * \sin((\pi y^2)/20) + 0.1.$$

$p(x, y, 0) = 5m(x, y, 0)$. These initial conditions are similar to those of Walker and Webb (2007). They represent a small population of cancer cells in the center of the domain and a heterogeneous spatial distribution of ECM and oxygen.

We used the following parameters for the second model:

$\mu = 1e-5$, $\alpha = 1e-2$, $\sigma = 0.1$, $\gamma = 30$, $\omega = 5e-2$, $\eta = 1e-3$, $\delta = 0.2$, $\rho_1 = 0.1$, $\rho_2 = 5e-2$, $\theta = 0.5$, $v = 10$, $\psi = 0.1$.

To investigate selection for cell motility we compare three evolutionary situations with both models: (1) there is no cost to increased cell motility (no tradeoff, $\rho_2 = 0$), (2) there is a cost, but no benefit – variation in the phenotypic variable (w) does not correspond to increased cell motility (i.e., $\rho_1 = 0$), and (3) there is a cost to increased cell motility (tradeoff, $\rho_1 > 0$, $\rho_2 > 0$). The strongest selection for cell motility should occur when there is no cost. On the contrary, in the situation, where the phenotypic variable (w) does not correspond to increased cell motility, there is a cost, but no benefit. This situation is considered because mutation and selection create a phenotypic distribution. Thus, even if cell motility is selected against (i.e., $w = 0$ is optimum) there will still be an increase in the mean value of cell motility due to mutation. So this serves as a null case for comparison. When there is both a cost and a potential benefit, then the trait should increase in the population beyond when there is just a cost, but below the value when there is no cost.

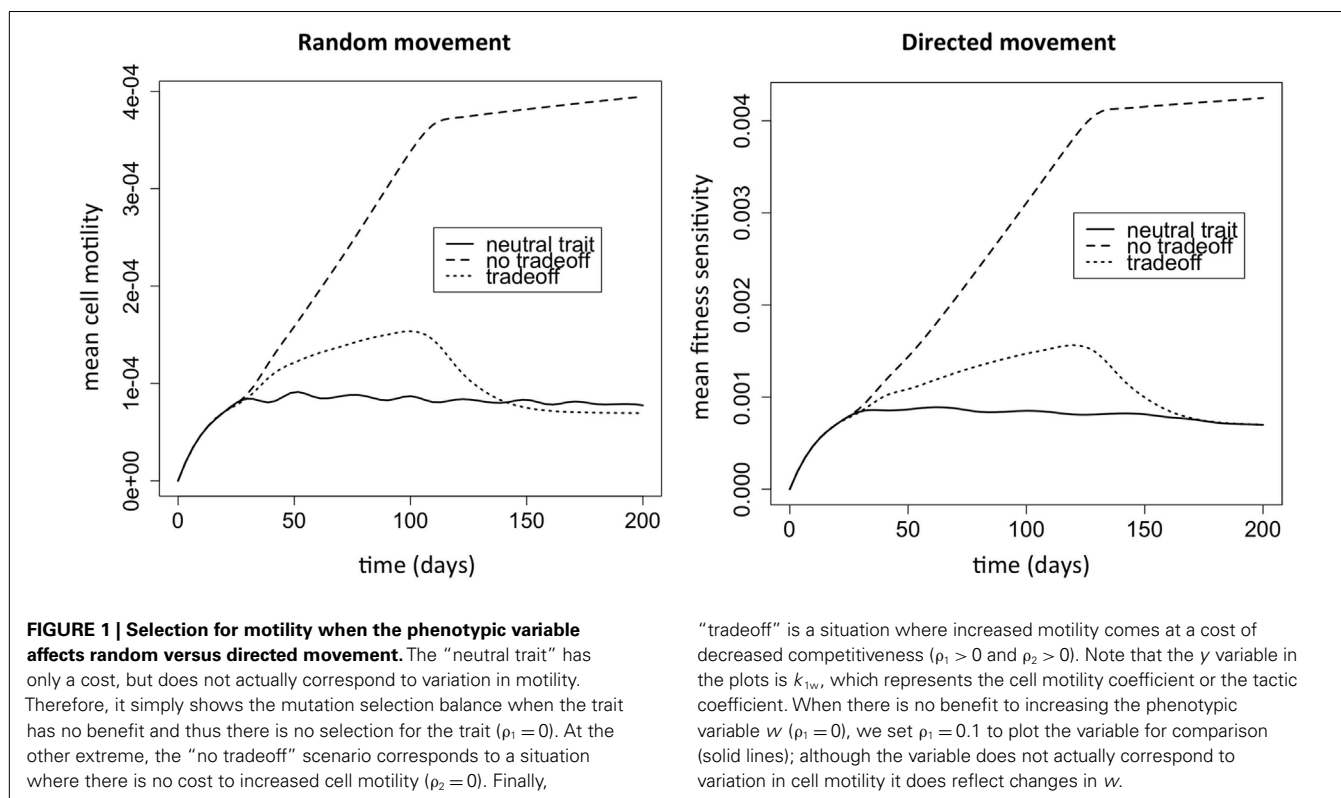
RESULTS

MODEL 1 – COMPETITION COLONIZATION TRADEOFFS IN A HABITAT-CONTINUUM TUMOR MODEL

We first investigate natural selection for cell motility. We do this by comparing the three evolutionary situations discussed above. The strongest selection pressure for cell motility should occur when there is no cost to increased cell motility. When there is only a cost and no benefit to the trait, then there should be selection against the trait. In this case, the fittest phenotype is the most competitive, and the distribution will simply reflect a mutational spread around this most fit phenotype. When there is a tradeoff, and motility is selected for, the mean trait value should intuitively lie somewhere between these extremes. **Figure 1** shows the dynamics of the mean evolutionary trait for the three scenarios. After around 30 days, sufficient phenotypic variation has accumulated and the population size has achieved a size that manifests a positive selection for motility. After close to 100 days, most of the space has been colonized, and there is selection against motility and in favor of competition instead.

Figure 2 shows the dynamics of the total cancer cell density in time and space. There are no major differences in the dynamics produced by the two different movement rules. However, there are large differences between the phenotypic initial conditions. When the majority of the population is initially composed of strong competitors, the population increases rapidly, and then begins to spread laterally. When the initial composition of the population is mostly motile cells, the population first spreads rapidly in space and then grows up to carrying capacity. The dynamics of our model are characterized by traveling waves of cancer cells in physical space (e.g., Murray, 2003).

Selection for motility should be occurring at the margins of the tumor, and thus this can potentially create phenotypic divergence in space. **Figure 3** shows snapshots of the distribution of cancer cells in physical space and in phenotype space. There is a clear pattern of phenotypic divergence in space, with the evolution of both



random and directed movement and with both initial conditions. This pattern still exists without a tradeoff ($k_1 = 0$). However, in the absence of a tradeoff the phenotypic differentiation in space is not as well defined. This is because motile phenotypes are not selected against in the core of the tumor.

Finally, we were interested in how the evolution of cell motility would affect invasion speed. To this end, **Figure 4** shows contours of cancer cell densities in space and time. The invasion speed is calculated as the slopes of the contour lines. The figure shows that in general, the evolution of cell motility produces linear invasion speeds over time. There are only slight non-linearities. As we have shown, mean cell motility is increasing over time due to natural selection. Invasion speed should increase with the cell motility and with the chemotactic coefficients. This is shown by the fact that the invasion speed is much quicker if the cell population is initially composed of highly motile cells (**Figures 4A,C**). However, the phenotypic distributions tend to obscure the effect of increasing cell motility on invasion speed. This occurs because once an area is crowded with cells; there is selection to invade adjacent un-crowded areas. As cells invade the adjacent areas, the fittest phenotype is the best competitor. Because of this, a wide range of phenotypes can coexist in space. **Figure 5** shows the normalized phenotypic distributions at 100 days. The distributions are wide and skewed toward the competitors. So even though mean motility increases over time, the variance obscures this signal for the population as a whole. Even when there is no tradeoff, and thus stronger selection for motility, invasion speeds remain relatively constant over time.

MODEL 2 – COMPETITION COLONIZATION TRADEOFFS IN A HABITAT-DESTRUCTION TUMOR MODEL

The second model is fundamentally different from the first in that there is no permanent niche for competitors in this model. Instead, the environment is consumed and destroyed as the cancer cells advance and spread. Therefore, selection for motility should be strong, since it is the only niche for the cells. **Figure 6** shows that there is selection for motility. The lines in the plot correspond to the same three evolutionary scenarios we considered with model 1. Given the parameters we chose, there is strong selection for motility. In this model, the cells do not reach a carrying capacity, and so there is not a strong reversal of selection once the space is filled.

As in the habitat–continuum model, the two different movement rules produce very similar tumor invasion dynamics. **Figure 7** shows snapshots in time of the tumor cell densities in two dimensional physical space. As the dynamics proceed, there is an expanding wavefront of cancer cells in physical space. Eventually, the cancer cells destroy the ECM and their oxygen supply. Thus, the model reaches an equilibrium with zero cancer cells, ECM, or oxygen.

In this model there is no clear spatial coexistence of phenotypes. Due to the ephemeral nature of oxygen following invasion into a new area, phenotypes that move less frequently or slower are less fit.

Figure 8 shows the contours of total cancer cell densities in time and space. In this plot, we fix the x dimension to the center of the domain. The thin distribution of cancer cell densities at any time show how the cancer cells spread into an area and subsequently

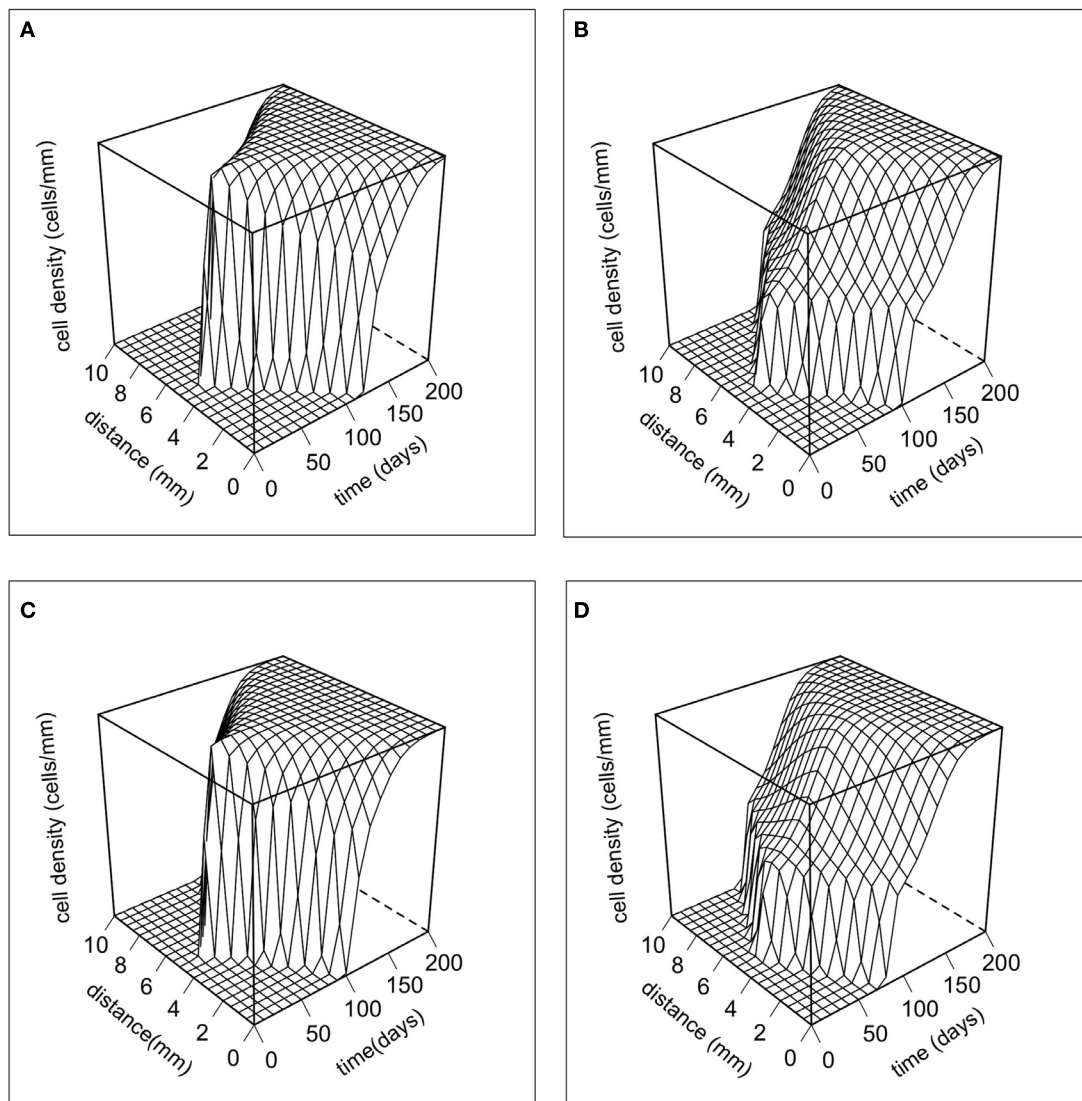


FIGURE 2 | The dynamics of the total cancer cell density in space and time. The total cancer cell density (T_c) at a particular spatial location is integrated over the phenotypic dimension. **(A)** Random cell movement with an initially competitive phenotypic distribution.

(B) Random cell movement with an initially motile phenotypic distribution. **(C)** Directed cell movement with an initially competitive phenotypic distribution. **(D)** Directed cell movement with an initially motile phenotypic distribution.

decline as the matrix molecules are degraded. The contours clearly show that there is an acceleration of invasion speed. This happens because there is stronger and more consistent selection for motility. Because of this, there are bigger fitness differences maintained between the phenotypes, and phenotypic variation is reduced. **Figure 9** shows the phenotypic distributions for the evolution of the two different movement types at $t = 100$ days. In this case, the phenotypic variance is much reduced compared to the results of the habitat–continuum model.

DISCUSSION

Competition colonization tradeoffs are commonly observed in ecological communities. Furthermore, during biological invasions the populations in the leading edge adapt to different selection

forces compared to those in the geographic core (e.g., Phillips et al., 2006). We address the influence of competition colonization tradeoffs on tumor invasion dynamics, since tumors dynamics in many ways parallel species invasions and range expansions into new habitats. We used two different models. The habitat–continuum tumor model sees the tumor as having a continuum from interior to edge habitats. Due to angiogenesis and other “ecological engineering,” regions of the tumor interior remain suitable habitat for the cancer cells. The habitat–destruction tumor model sees the cancer cells as “consuming” the environment. This creates a tumor with a necrotic interior and an expanding edge.

Both of our models clearly predict that evolution of cell motility. Furthermore, this evolution is mainly due to natural selection,

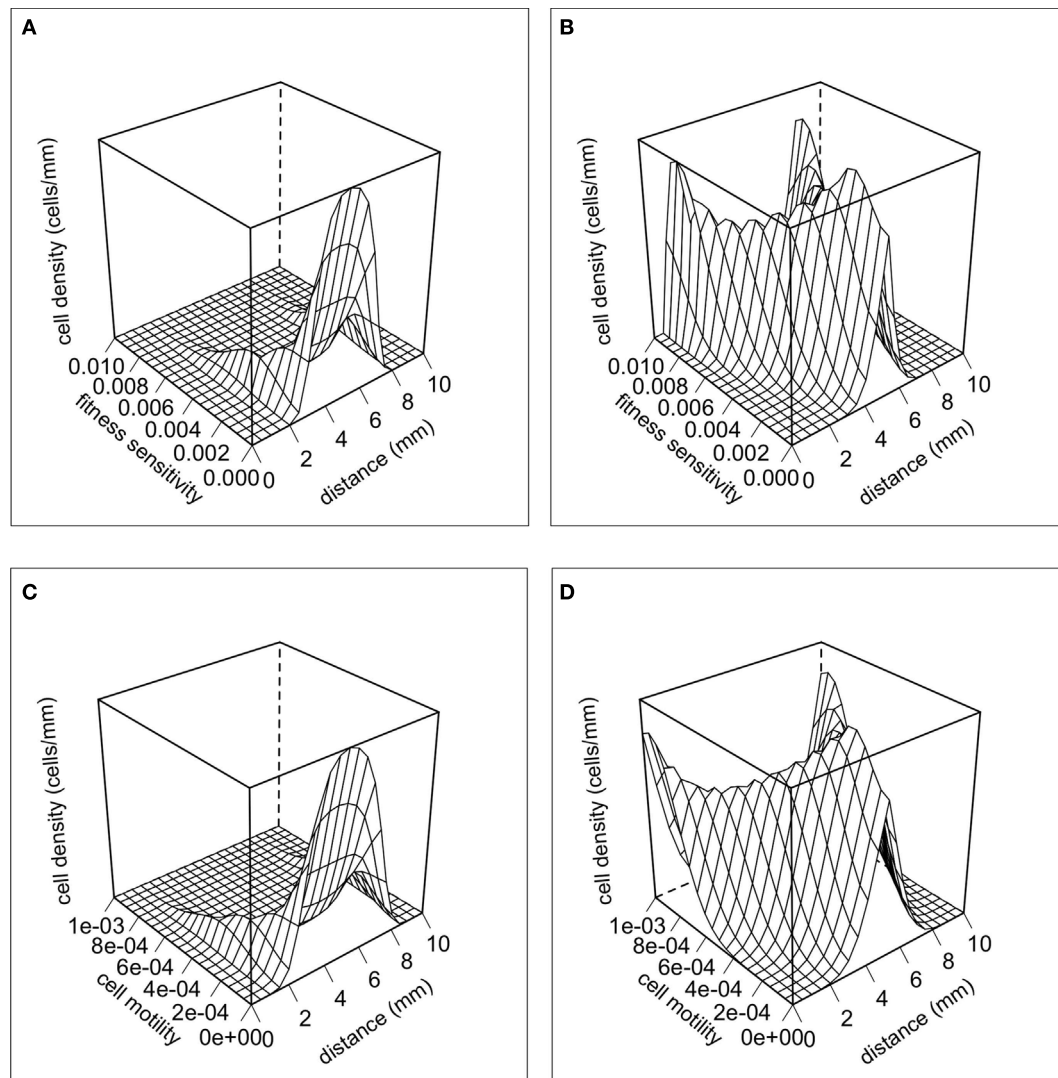


FIGURE 3 | The distributions of cells in physical space and phenotypic space at $t = 100$ days. (A) Random cell movement with an initially competitive phenotype distribution. **(B)** Random cell movement with an

initially motile phenotypic distribution. **(C)** Directed cell movement with an initially competitive phenotypic distribution. **(D)** Directed cell movement with an initially motile phenotypic distribution.

since the motile phenotypes increased in abundance relative to other phenotypes in the population. Many other researchers have shown that motility is selected for during population invasion into new habitats. For example, Aktipis et al. (2012) recently showed that cell motility evolves in response to local environmental degradation, and may be a co-adaptation or consequence of altered cell metabolism.

We also found that in general the evolution of different types of cell movement has almost no effect on the global dynamics of the invasion. The more adaptive movement will likely be evolutionarily favored, but we predict that this will have very little impact on the overall invasion dynamics. However, if evolution affects haptotaxis or chemotaxis, and the underlying spatial distribution of the molecules, which direct movement are sufficiently different, then it is plausible that the evolution of different movement rules

may produce drastically different invasion dynamics. In the tumor specific model we considered, oxygen is produced by the matrix macromolecules and as a consequence their spatial distributions are similar and thus haptotaxis and chemotaxis produce similar results.

We did find important differences between the habitat-continuum and the habitat-destruction models in terms of tumor invasion dynamics and phenotypic evolution. In the habitat-continuum tumor model, we found that the invasion speed was relatively linear over time. This occurred because there is relatively weak and ephemeral selection for cell movement at a particular location, which allows for the coexistence of many phenotypes and hence large diversity. The resulting variance in the phenotypic distribution obscures the signal of increasing cell movement. Our habitat-destruction tumor model on the other hand does

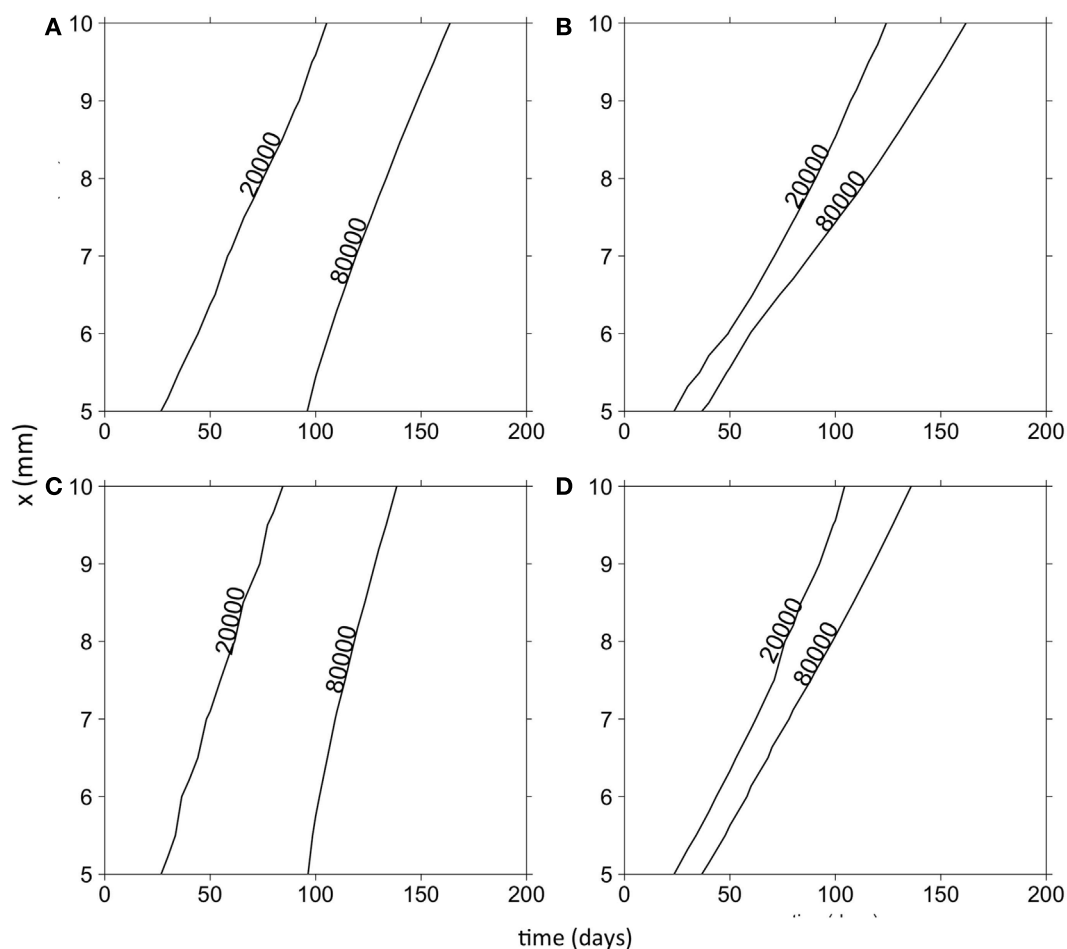


FIGURE 4 | Contour plots of the total cancer cell density in time and space. (A) Random cell movement with an initially competitive phenotypic distribution. **(B)** Random cell movement with an initially motile phenotypic

distribution. **(C)** Directed cell movement with an initially competitive phenotypic distribution. **(D)** Directed cell movement with an initially motile phenotypic distribution.

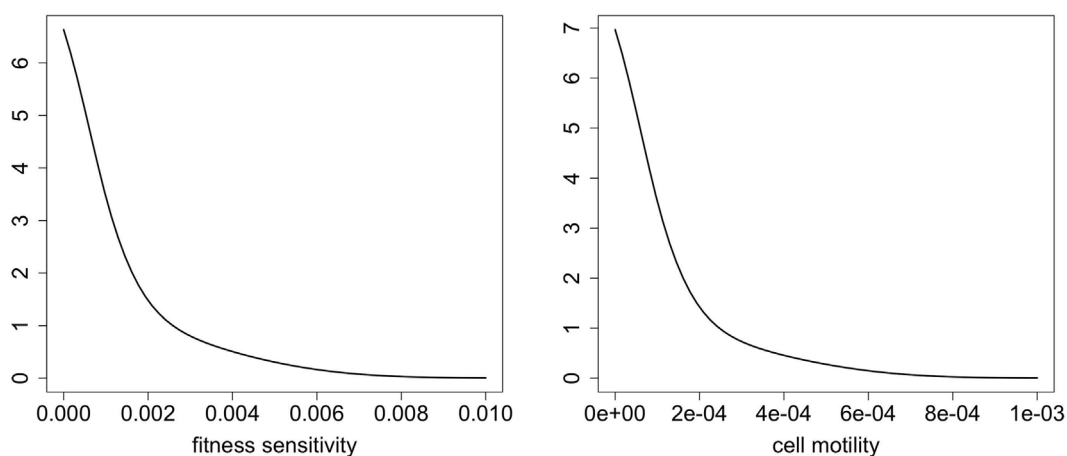


FIGURE 5 | Normalized phenotypic distributions for directed and random movement at $t = 100$ days. These distributions are integrated over space to include the entire spatial domain.

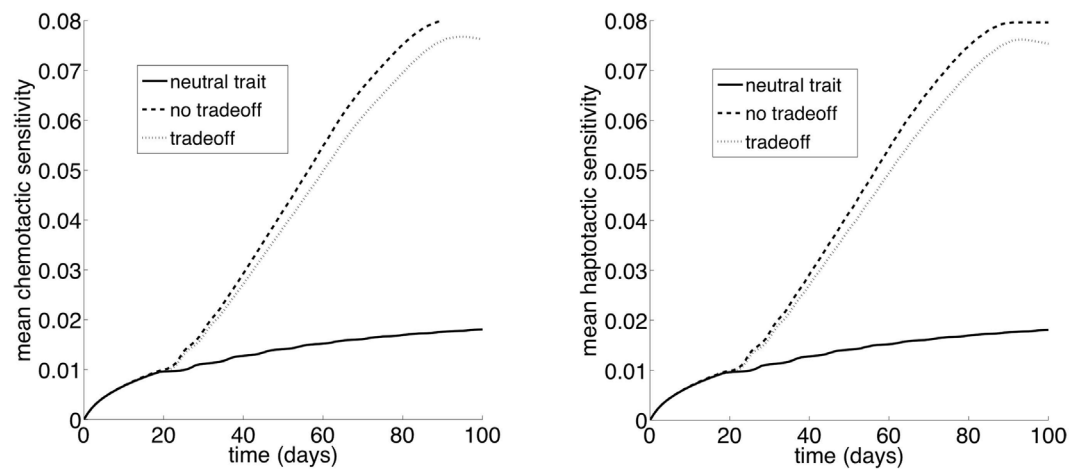


FIGURE 6 | Selection for motility when chemotactic versus haptotactic movement evolves. The “neutral trait” has only a cost, but does not actually correspond to variation in motility. Therefore, it simply shows the mutation selection balance when the trait has no benefit and thus there is no selection for the trait ($\rho_1 = 0$). At the other extreme, the “no tradeoff” scenario corresponds to a situation where there is no cost to increased cell motility ($\rho_2 = 0$). Finally, “tradeoff” is a situation where

increased motility comes at a cost of decreased competitiveness ($\rho_1 > 0$ and $\rho_2 > 0$). Note that the y variable in the plots is k_{1w} , which represents the cell motility coefficient or the tactic coefficient. When there is no benefit to increasing the phenotypic variable w ($\rho_1 = 0$), we set $\rho_1 = 0.1$ to plot the variable for comparison (solid lines); although the variable does not actually correspond to variation in cell motility it does reflect changes in w .

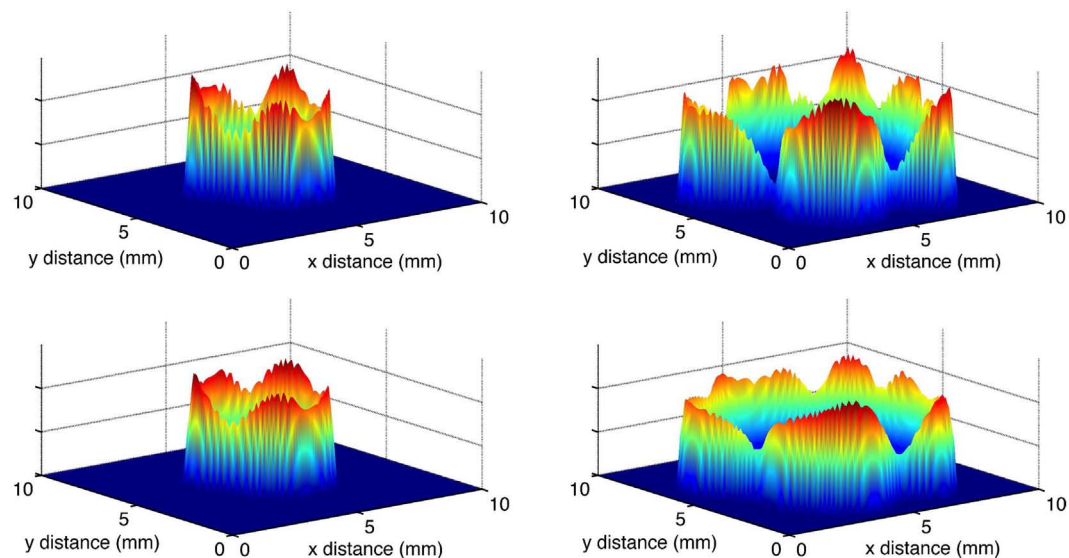


FIGURE 7 | Snapshots of the total normalized cancer cell density in two-dimensional physical space. The left and right panels show $t = 50$ and $t = 75$ days, respectively. The top and bottom panels show the evolution of chemotaxis and haptotaxis, respectively.

include strong selection for cell movement, which reduces phenotypic diversity and results in a strong directed increase in cell movement and invasion speed with time. Since, the environment is destroyed as cancer cells grow in a particular spatial location there is constant selection to invade the frontier, and this selection drives an accelerated invasion speed. Hence, we predict that in tumors with a narrow band of living cells and a large necrotic core invasion speed will accelerate with time.

As empirical research into tumor dynamics progresses, it will be important to determine, whether models with evolving cell motility provide better predictions of tumor growth than models without evolutionary changes. Data on tumor growth has been of low resolution and only very simple models have been fit to this data. For example, it appears that the best dynamic model we currently have to explain tumor dynamics is the power law model (Hart et al., 1998). Higher resolution data, for example data that

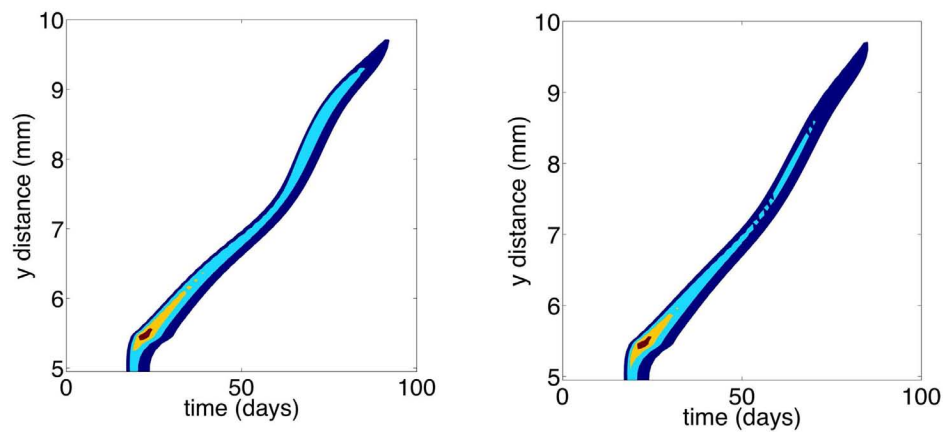


FIGURE 8 | Contour plots showing total cancer cell densities in space and time. Blue corresponds to lower cell densities and red corresponds to higher cell densities. The x dimension is fixed at 5 mm. The left and right panels show the evolution of chemotaxis and haptotaxis, respectively.

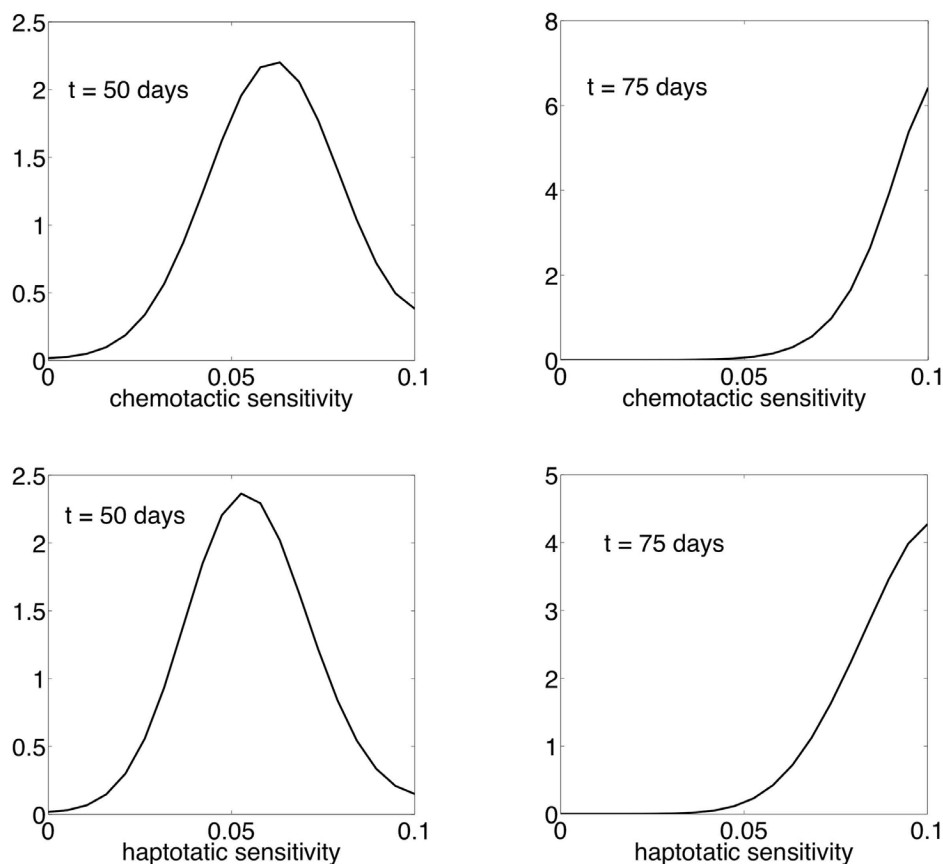


FIGURE 9 | Normalized phenotypic distributions for the evolution of chemotaxis and haptotaxis at $t = 50$ and $t = 75$ days. The evolution of chemotaxis and haptotaxis are shown in the top and bottom panels, respectively.

resolves cell densities in space, and more sophisticated predictive models will ultimately progress our understanding of the mechanisms that produce patterns of tumor growth and invasion (see McDaniel et al., 2012).

In our habitat-destruction model, the wake of habitat-destruction precludes a permanent niche for a competitive phenotype. As a result, there is no spatial coexistence of phenotypes. However, the habitat-continuum tumor model generates

the coexistence of the colonizer and competitor phenotypes. Furthermore, there is clear phenotypic differentiation in space. Part of this differentiation may be due to spatial sorting. Benichou et al. (2012) demonstrated the effect of spatial sorting in a very similar model. However, there is selection for movement in our model, and this creates an even stronger pattern of spatial differentiation. Furthermore, given the competition colonization tradeoff, the phenotypes are even more strictly localized in space than they otherwise would be. We predict that in tumors characterized by smaller regions of necrosis and successful angiogenesis, there will be two distinct phenotypic populations – motile and invasive cells at the tumor margin and angiogenic cells in the tumor interior.

While distinct genetic populations have been observed in tumors, there has been no attempt to determine a specific spatial distribution. We predict that spatial mapping of both clinical and experimental tumors should show invasive cellular features such as invadopodia to be most common in the tumor rim while cells expressing VEGF should be more common in tumor regions

deep to the edge. Interestingly, Grillon et al. (2011) recently examined spatial distribution of a few cell membrane proteins in C6 glioblastoma tumors growing in a rat brain. They found Na^+/H^+ exchanger (NHE-1) and lactate- H^+ cotransporter (MCT1) were upregulated at the tumor edge, while MCT4 and carbonic anhydrase (CAIX) were not upregulated at the tumor edge. A future research challenge in characterizing cancer cell phenotypes will be to differentiate phenotypic plasticity (changes that can occur within an individual cell) from heritable phenotypic changes (inter-generational changes).

In conclusion, we propose that understanding the role of ecology and evolutionary adaptations in tumors is necessary to fully understand tumor biology. The genetic evolution occurring within tumors is well documented, but the governing dynamics for that evolution should be strongly influenced by environmental selection forces. It is plausible that the competition colonization tradeoff that commonly influences spatial distributions of species and phenotypes in nature also influences intratumoral evolution.

REFERENCES

- Aktipis, C. A., Maley, C. C., and Pepper, J. W. (2012). Dispersal evolution in neoplasms: the role of dysregulated metabolism in the evolution of cell motility. *Cancer Prev. Res. (Phila.)* 5, 266–275.
- Anderson, A. R. (2005). A hybrid mathematical model of solid tumour invasion: the importance of cell adhesion. *Math. Med. Biol.* 22, 163–186.
- Barrett, S. C., Colautti, R. I., and Eckert, C. G. (2008). Plant reproductive systems and evolution during biological invasion. *Mol. Ecol.* 17, 373–383.
- Benichou, O., Calvez, V., Meunier, N., and Voituriez, R. (2012). Front acceleration by dynamic selection in Fisher population waves. *Phys. Rev. E Stat. Nonlin. Soft Matter Phys.* 86, 041908.
- Bouin, E., Calvez, V., Meunier, N., Mirrahimi, S., Perthame, B., Raoul, G., et al. (2012). Invasion fronts with variable motility: phenotype selection, spatial sorting and wave acceleration. *C. R. Acad. Sci. Paris Ser. I* 350, 761–766.
- Broennimann, O., Treier, U. A., Müller-Schärer, H., Thuiller, W., Peterson, A. T., and Guisan, A. (2007). Evidence of climatic niche shift during biological invasion. *Ecol. Lett.* 10, 701–709.
- Brown, G. P., Shilton, C., Phillips, B. L., and Shine, R. (2007). Invasion, stress, and spinal arthritis in cane toads. *Proc. Natl. Acad. Sci. U.S.A.* 104, 17698–17700.
- Burton, O. J., Phillips, B. L., and Travis, J. M. (2010). Trade-offs and the evolution of life-histories during range expansion. *Ecol. Lett.* 13, 1210–1220.
- Cadotte, M. W., Mai, D. V., Jantz, S., Collins, M. D., Keele, M., and Drake, J. A. (2006). On testing the competition-colonization trade-off in a multispecies assemblage. *Am. Nat.* 168, 704–709.
- Cantrell, R. S., Cosner, C., and Lou, Y. (2006). Movement toward better environments and the evolution of rapid diffusion. *Math. Biosci.* 204, 199–214.
- Carmeliet, P., and Jain, R. K. (2000). Angiogenesis in cancer and other diseases. *Nature* 404, 249–257.
- Chaplain, M. A., McDougall, S. R., and Anderson, A. R. A. (2006). Mathematical modeling of tumor-induced angiogenesis. *Annu. Rev. Biomed. Eng.* 8, 233–257.
- Chertock, A., and Kurganov, A. (2008). A second-order positivity preserving central-upwind scheme for chemotaxis and haptotaxis models. *Numer. Math.* 111, 169–205.
- Cohen, Y. (2009). Evolutionary distributions. *Evol. Ecol. Res.* 11, 611–635.
- Dockery, J., Hutson, V., Mischaikow, K., and Pernarowski, M. (1998). The evolution of slow dispersal rates: a reaction diffusion model. *J. Math. Biol.* 37, 61–83.
- Eikenberry, S. E., Sankar, T., Preul, M. C., Kostelich, E. J., Thalhauser, C. J., and Kuang, Y. (2009). Virtual glioblastoma: growth, migration and treatment in a three-dimensional mathematical model. *Cell Prolif.* 42, 511–528.
- Gatenby, R. (2012). Perspective: finding cancer's first principles. *Nature* 491, S55.
- Gerlee, P., and Anderson, A. R. A. (2009). Evolution of cell motility in an individual-based model of tumour growth. *J. Theor. Biol.* 259, 67–83.
- Gerlinger, M., Rowan, A. J., Horswell, S., Larkin, J., Endesfelder, D., Gronroos, E., et al. (2012). Intratumor heterogeneity and branched evolution revealed by multiregion sequencing. *N. Engl. J. Med.* 366, 883–892.
- Goodsell, D. S. (2003). The molecular perspective: VEGF and angiogenesis. *Stem Cells* 21, 118–119.
- Grillon, E., Farion, R., Fablet, K., De Waard, M., Tse, C. M., Donowitz, M., et al. (2011). The spatial organization of proton and lactate transport in a rat brain tumor. *PLoS ONE* 6:e17416. doi:10.1371/journal.pone.0017416
- Hart, D., Shochat, E., and Agur, Z. (1998). The growth law of primary breast cancer as inferred from mammography screening trials data. *Br. J. Cancer* 78, 382–387.
- Holmes, E. E., Lewis, M. A., Banks, J. E., and Veit, R. R. (1994). Partial differential equations in ecology: spatial interactions and population dynamics. *Ecology* 75, 17–29.
- McDaniel, K. J., Kostelich, E., Kuang, Y., Nagy, J. D., Preul, M., Moore, N. Z., et al. (2012). “Data assimilation in brain tumor models,” in *Mathematical Models and Methods in Biomedicine*, eds U. Ledzewicz, H. Schattler, A. Friedman, and E. Kashdan (Berlin: Springer), 233–262.
- Murray, J. D. (2003). *Mathematical Biology II: Spatial Models and Biomedical Applications*. New York: Springer.
- Phillips, B. L. (2009). The evolution of growth rates on an expanding range edge. *Biol. Lett.* 5, 802–804.
- Phillips, B. L., Brown, G. P., Greenlees, M., Webb, J. K., and Shine, R. (2007). Rapid expansion of the cane toad (*Bufo marinus*) invasion front in tropical Australia. *Austral. Ecol.* 32, 169–176.
- Phillips, B. L., Brown, G. P., Webb, J. K., and Shine, R. (2006). Invasion and the evolution of speed in toads. *Nature* 439, 803–803.
- Rodríguez, A., Jansson, G., Andrén, H., Rodríguez, A., Jansson, G., and Andrén, H. (2007). Composition of an avian guild in spatially structured habitats supports a competition-colonization trade-off. *Proc. Biol. Sci.* 274, 1403–1411.
- Schiesser, W. E., and Griffiths, G. W. (2009). *A Compendium of Partial Differential Equation Models*. Cambridge: Cambridge University Press.
- Shine, R., Brown, G. P., and Phillips, B. L. (2011). An evolutionary process that assembles phenotypes through space rather than through time. *Proc. Natl. Acad. Sci. U.S.A.* 108, 5708–5711.
- Simmons, A. D., and Thomas, C. D. (2004). Changes in dispersal during species' range expansions. *Am. Nat.* 164, 378–395.
- Stanton, M. L., Palmer, T. M., and Young, T. P. (2002). Competition-colonization trade-offs in a guild of African acacia-ants. *Ecol. Monogr.* 72, 347–363.
- Tilman, D. (1994). Competition and biodiversity in spatially structured habitats. *Ecology* 75, 2–16.

- Travis, J. M., and Dytham, C. (2002). Dispersal evolution during invasions. *Evol. Ecol. Res.* 4, 1119–1129.
- Turnbull, L. A., Coomes, D., Hector, A., and Rees, M. (2004). Seed mass and the competition/colonization trade-off: competitive interactions and spatial patterns in a guild of annual plants. *J. Ecol.* 92, 97–109.
- Turnbull, L. A., Rees, M., and Crawley, M. J. (1999). Seed mass and the competition/colonization trade-off: a sowing experiment. *J. Ecol.* 87, 899–912.
- Walker, C., and Webb, G. F. (2007). Global existence of classical solutions for a haptotaxis model. *SIAM J. Math. Anal.* 38, 1694–1713.
- Weaver, A. M. (2006). Invadopodia: specialized cell structures for cancer invasion. *Clin. Exp. Metastasis* 23, 97–105.
- Yachida, S., Jones, S., Bozic, I., Antal, T., Leary, R., Fu, B., et al. (2010). Distant metastasis occurs late during the genetic evolution of pancreatic cancer. *Nature* 467, 1114–1117.
- Conflict of Interest Statement:** The authors declare that the research was conducted in the absence of any commercial or financial relationships that could be construed as a potential conflict of interest.

Received: 21 December 2012; paper pending published: 28 January 2013; accepted: 20 February 2013; published online: 06 March 2013.

Citation: Orlando PA, Gatenby RA and Brown JS (2013) Tumor evolution in space: the effects of competition

colonization tradeoffs on tumor invasion dynamics. *Front. Oncol.* 3:45. doi: 10.3389/fonc.2013.00045

This article was submitted to *Frontiers in Molecular and Cellular Oncology*, a specialty of *Frontiers in Oncology*.

Copyright © 2013 Orlando, Gatenby and Brown. This is an open-access article distributed under the terms of the Creative Commons Attribution License, which permits use, distribution and reproduction in other forums, provided the original authors and source are credited and subject to any copyright notices concerning any third-party graphics etc.



From patient-specific mathematical neuro-oncology to precision medicine

A. L. Baldock^{1,2}, R. C. Rockne^{1,2,7}, A. D. Boone³, M. L. Neal^{3,4}, A. Hawkins-Daarud^{1,2}, D. M. Corwin^{1,2}, C. A. Bridge^{1,2}, L. A. Guyman^{1,2}, A. D. Trister⁵, M. M. Mrugala⁶, J. K. Rockhill⁵ and K. R. Swanson^{1,2,7*}

¹ Department of Neurological Surgery, Northwestern University, Chicago, IL, USA

² Brain Tumor Institute, Northwestern University, Chicago, IL, USA

³ Department of Pathology, University of Washington, Seattle, WA, USA

⁴ Department of Medical Education and Biomedical Informatics, University of Washington, Seattle, WA, USA

⁵ Department of Radiation Oncology, University of Washington, Seattle, WA, USA

⁶ Department of Neurology, University of Washington, Seattle, WA, USA

⁷ Department of Applied Mathematics, University of Washington, Seattle, WA, USA

Edited by:

Heiko Enderling, Tufts University School of Medicine, USA

Reviewed by:

Frank Kruyt, University Medical Center Groningen, Netherlands
Markus Rehm, Royal College of Surgeons in Ireland, Ireland

*Correspondence:

K. R. Swanson, Department of Neurological Surgery, Northwestern University Feinberg School of Medicine, 676 N Saint Clair Street, Suite 2210, Chicago, IL 60611, USA.
e-mail: kristin.swanson@northwestern.edu

Gliomas are notoriously aggressive, malignant brain tumors that have variable response to treatment. These patients often have poor prognosis, informed primarily by histopathology. Mathematical neuro-oncology (MNO) is a young and burgeoning field that leverages mathematical models to predict and quantify response to therapies. These mathematical models can form the basis of modern “precision medicine” approaches to tailor therapy in a patient-specific manner. Patient-specific models (PSMs) can be used to overcome imaging limitations, improve prognostic predictions, stratify patients, and assess treatment response *in silico*. The information gleaned from such models can aid in the construction and efficacy of clinical trials and treatment protocols, accelerating the pace of clinical research in the war on cancer. This review focuses on the growing translation of PSM to clinical neuro-oncology. It will also provide a forward-looking view on a new era of patient-specific MNO.

Keywords: glioma, mathematical modeling, patient-specific, clinical modeling, personalized medicine, individualized health care

THE CLINICAL CHALLENGE OF PATIENT-SPECIFIC PROGNOSIS AND TREATMENT RESPONSE

Gliomas are heterogeneous primary brain tumors that exhibit widely varying phenotypes even within the same histological grade (Louis et al., 2007). These tumors are characterized by proliferating and invading adjacent normal brain tissue, resulting in a significant clinical challenge and generally high morbidity and mortality. Despite advances in medical imaging technologies, surgery, radiation therapy, and chemotherapies over the last several decades, the standard of care for newly diagnosed malignant gliomas does not reflect individual differences (Stupp et al., 2007; Nishikawa, 2010). Prognosis for glioma patients has hardly changed in over 50 years of cancer research. The incorporation of patient-specific measures of prognosis and treatment response allows tailor therapies for each patient.

INVISIBLE, INHERENT, INVASION

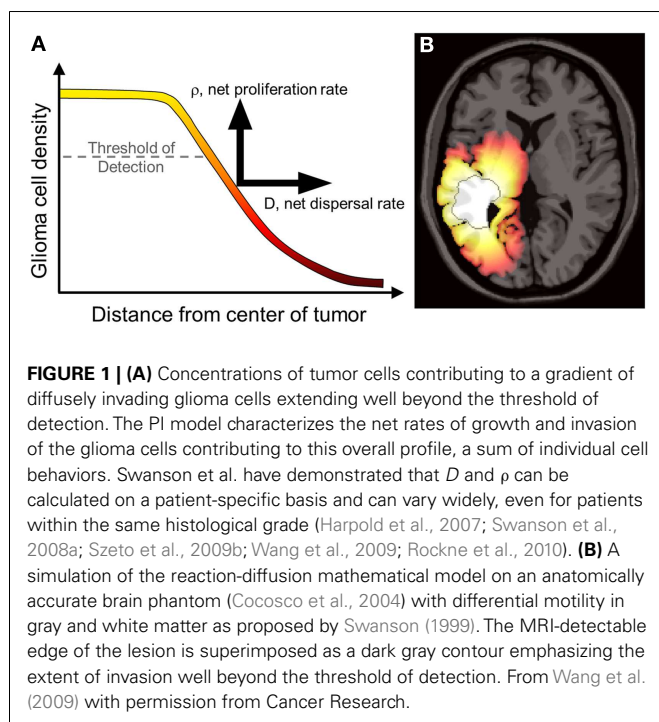
The most significant characteristic of gliomas of all grades is their diffuse invasion into the normal-appearing brain as seen in gross pathology and histological specimens. To reduce the morbidity of extensive biopsies, primary clinical assessment and staging of

gliomas relies on non-invasive radiographic imaging such as magnetic resonance imaging (MRI) and computed tomography (CT). However, neither of these imaging techniques quantifies the full extent of tumor invasion due to the inherent limits of detection, as illustrated in **Figure 1**. Furthermore, post-treatment surveillance for recurrence and progression is based on these same imaging technologies (Swanson, 1999; Harpold et al., 2007; Szeto et al., 2009b; Pallud et al., 2010). The inability to completely quantify the glioma cell population (invisibility) and diffuse extension into normal-appearing brain (invasion) along with wide heterogeneity between and within patients makes a personalized approach to treatment and measuring response difficult but necessary.

WHY USE MATHEMATICAL MODELING?

Currently, prognosis in glioma patients is based upon retrospective analyses of groups of patients with similar histopathological characteristics (Louis et al., 2007). This approach is unsatisfying because of the heterogeneity of disease phenotypes within each larger histological category as well as the lack of insight into treatment modalities that may most benefit an individual patient. Mathematical models are used to bridge this gap and have been used to illustrate individual differences in the dynamics of glioma growth and response to therapy in a research setting, with the potential for clinical translation on the horizon. To optimize individual treatment protocols, physicians and scientists require tools to evaluate the relative benefit obtained for each patient. The subset

Abbreviations: D, net rate of diffusion; FTB, fatal tumor burden; MM, mathematical modeling; MNO, mathematical neuro-oncology; MRI, magnetic resonance imaging; PSM, patient-specific modeling; ρ , net rate of proliferation; UVC, untreated virtual control.



of patients with the most aggressive tumors (and inherently worst prognosis) stand to benefit the most from the shift from one-size-fits-all treatment to a patient-specific approach, and models allow for the prospective identification of these patients.

Mathematical models already have a significant impact on clinical practice, as they are widely integrated into medical imaging technologies (e.g., Carson et al., 1998). Furthermore, mathematical models are found throughout the biological sciences, with one of the most common applications being population models for a single species (e.g., Murray, 2002). Yet it can be quite a leap for both the basic scientist and clinician to embrace the idea that a relatively simple mathematical model might shed light on such a complex disease process as malignant glioma. Some believe that gliomas are so biologically complex and heterogeneous that no model could provide insight into the inherent nature of disease. On the contrary, as clinical oncology strives to provide personalized management of cancer, mathematical models are playing a pivotal role in providing insight into disease growth, treatment response, and ultimately building the framework for precision medicine (Council, 2011).

PATIENT-SPECIFIC MATHEMATICAL NEURO-ONCOLOGY

The term Mathematical Oncology was coined in 2003 to reflect the burgeoning synergy between mathematical modeling techniques, cancer research, and clinical oncology (Gatenby and Maini, 2003). The term has been subsequently refined to Integrated Mathematical Oncology to emphasize the feedback that emerges through the integration of mathematics and oncology (Anderson and Quaranta, 2008). This review focuses on the patient-specific applications of Mathematical Neuro-Oncology (MNO) to provide predictive insight onto glioma prognosis and treatment response in individual patients. Although the field of neuro-oncology is

broad and encompasses many distinct neoplasms, to date, much of the literature has been devoted to the presentation of models and methodologies for estimating glioma growth from medical imaging and other clinical data.

In this paper, the focus is on models that will truly enable “precision medicine.” Thus the discussion below will revolve around only models the authors believe are patient-specific in nature and have in some way been subjected to validation tests. Specifically we have reviewed reaction-diffusion models such as those championed by Swanson, which take a macroscopic perspective of gliomas as a continuum of tumor cell concentration.

INDIVIDUAL TUMOR GROWTH KINETICS: A PREDICTABLE PATTERN

Gliomas of all histologic grades exhibit a constant velocity of the mean tumor radius if left untreated, resulting in predictable pattern of linear radial growth (Swanson and Alvord, 2002; Mandonnet et al., 2003, 2008; Pallud et al., 2006). Mandonnet et al. (2003) demonstrated this in 27 untreated low-grade gliomas (LGG) followed with serial routine MRI for up to 15 years. Despite the anatomic heterogeneity in tumor growth, the average radius of each glioma increased linearly with time, with rates ranging from 1 to 4 mm/year. Furthermore, the velocity of linear radial expansion was shown to predict time to malignant progression (Hlailhel et al., 2010) and is a significant predictor of survival (Pallud et al., 2006; Swanson et al., 2008a).

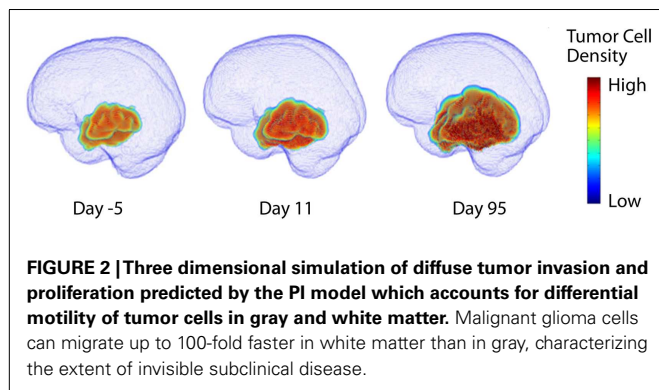
Constant linear radial growth is also seen in a rare example of an *untreated* high grade glioma known as glioblastoma multiforme (GBM). In this case a 75-year-old female presented to the emergency department with a complex partial seizure (CPS), prompting imaging that revealed a large tumor. She refused medical advice to undergo a biopsy to establish a diagnosis and subsequent treatment but allowed multiple imaging observations (Swanson and Alvord, 2002). The patient was found to have a GBM on autopsy, and the serial imaging revealed a consistent linear radial growth pattern.

THE PROLIFERATION-INVASION MODEL OF GLIOMA GROWTH

In the early 1990s, the research groups of Murray and Alvord developed a mathematical model to describe the diffuse infiltration and proliferation of glioma cells in the complex anatomy of the human brain (Figure 2). This model can be described in words as the rate of change of tumor cell density in time is equal to the net migration of tumor cells plus the net proliferation of tumor cells. Mathematically, the model is a partial differential equation with two parameters: net rates of migration (D , mm²/year) and proliferation (ρ , year⁻¹), both of which can be calculated on a patient-specific basis using routine clinical imaging prior to treatment.

$$\underbrace{\text{rate of change of tumor cell density over time}}_{\frac{\partial c}{\partial t}} = \underbrace{\text{net migration of tumor cells}}_{\nabla \cdot (D(x) \nabla c)} + \underbrace{\text{net proliferation of tumor cells}}_{\rho c \left(1 - \frac{c}{K}\right)}$$

This “proliferation-invasion” model (PI model) of glioma growth and infiltration is similar to Fisher’s equation which yields



the same predictable pattern of linear radial growth observed in low and high grade gliomas (Fisher, 1937). The velocity of growth predicted by this equation relates the velocity of radial growth to the square root of the product of net dispersal (D) and proliferation (ρ) parameters, $v = \sqrt{4D\rho}$. This relationship combined with an “invisibility index” (D/ρ) relating rates of invasion and proliferation provides two equations and two unknown parameters, tuning the PI model to patient-specific growth. The PI model can further incorporate differential motility of glioma cells through gray and white matter of the brain, providing predictions of diffuse tumor invasion through the regions of the brain that are specific to the patient’s tumor (Figure 2). This simple model has served as a foundation for patient-specific MNO and provided numerous insights into clinical behaviors such as survival outcome (Pallud et al., 2006; Swanson et al., 2008b; Wang et al., 2009; Rockne et al., 2010), hypoxia development (Szeto et al., 2009b), response to surgical resection (Swanson et al., 2008b), chemo- and radiation therapies (Rockne et al., 2010), biological aggressiveness (Szeto et al., 2009a; Ellingson et al., 2010b), and to date is the single most applied patient-specific clinical scale model for glioma growth and response to therapy. Extensions to this model include consideration of anisotropic growth in white matter tracts (Jbabdi et al., 2005). Mass effect and mechanical constraints of anatomical structures such as the skull, have been included to refine spatial agreement with patient scans (Clatz et al., 2005). Giatili and Stamatakis (2012) add adiabatic Neumann boundary conditions to more realistically model the boundary imposed by the skull. These efforts show room for further model development, but have yet to be applied to a patient population as large as that modeled by the PI model.

Advanced imaging techniques such as diffusion weighted MRI (DWI), MRI Spectroscopy, and Diffusion Tensor (DT) MRI have been used to suggest techniques for estimating patient-specific parameters D and ρ (Ellingson et al., 2010a; Konukoglu et al., 2010). Based on the assumption that the apparent diffusion coefficient (ADC), which measures magnitude of diffusion of water, is negatively proportional to tumor cell density, Ellingson et al. proposes that D and ρ of the PI model, modified such that proliferation is exponential and not saturated in a saturated environment can be estimated on a patient-specific basis using three ADC imaging time points. Ellingson et al. applied this methodology and found a stratification of D and ρ with histologic grading which

compares well with the previous estimates for high grade gliomas but differs significantly from the estimates for low-grade proliferation and invasion kinetics (Harpold et al., 2007). This difference may be explainable by the fact that the correlations between ADC and overall tissue cell density utilized by the Ellingson approach incorporates both normal and malignant cell densities while the PI model is only tracking the glioma cell density. Further exploiting opportunities provided by diffusion MRI, Konukoglu et al. (2010) uses DT-MRI to inform model predictions of separate diffusion rates in gray and white matter.

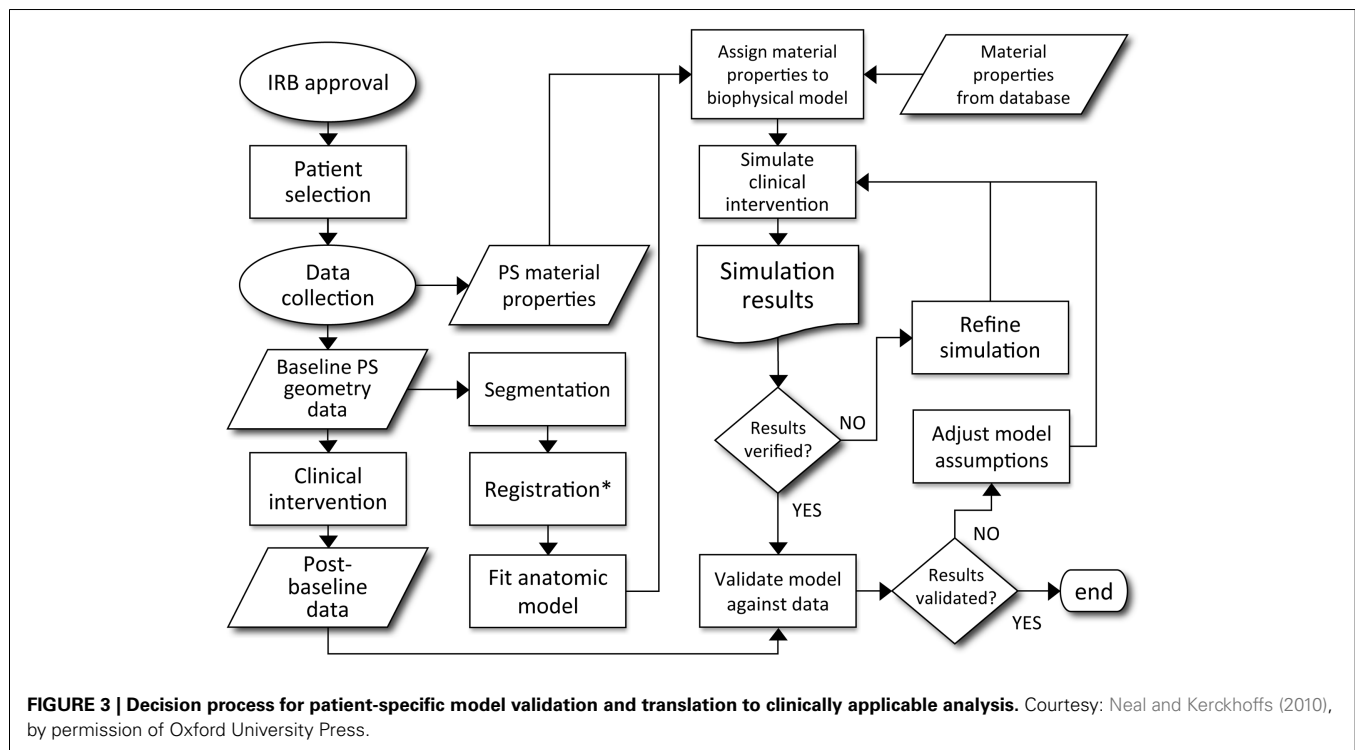
“GO OR GROW” HYPOTHESIS

Experimental data suggests that tumor states of proliferative and invasive capacity are mutually exclusive (Giese et al., 2003). The “go or grow” hypothesis has influenced mathematical models analyzing how the rates of switching between proliferative and migratory phenotypes affect macroscopic tumor growth (Gerlee and Nelander, 2012). Hatzikirou et al. (2012) used lattice-gas cellular automaton models to determine that the rapid recurrence of gliomas post-resection cannot be explained by mutation theory alone, but tumors modeled with “go or grow” behavior can recapitulate the observed macroscopic growth patterns. Such models can even suggest treatment strategies, such as tumor oxygenation which encourages cells to revert to a proliferative and less radio- and chemo-resistant state. As Giatili and Stamatakis (2012) points out, discrete agent and cell based models are better suited to answer questions of the biological constitution of tumors over space and time. Continuum models give better insight to spatial extent and concentration profile of the population of tumor cells. Hatzikirou et al. (2012) showed that although the glioma cell population is heterogeneous and composed of significant portions of cells in both proliferative and migratory states, the microscopic simulation scales up to a reaction-diffusion model on the macroscopic scale practically identical to the Fisher equation.

TURNING MATHEMATICAL PREDICTIONS INTO MATHEMATICAL NEURO-ONCOLOGY

In a review of computational models of brain tumors Juffer et al. (2008) bemoans a “severe limitation of current models is that they are in fact *not* patient-specific at all.” However, mathematical models come in many forms and with different purposes. Some models aim to provide qualitative understanding or intuition regarding the phenomena of interest, while others are intended to provide predictions for specific scenarios. The effective use of the latter type of models depends on many factors: defining the quantity of interest, choosing the appropriate model, acquiring data for calibration, and then successfully subjecting the model to validation tests. By definition, patient-specific biological models require calibration for each patient. This inherently leaves room for philosophical debate regarding sufficient validation tests for patient-specific biological models, however, a good example for predictions involving clinical intervention is provided in Figure 3 (Neal and Kerckhoffs, 2010). One should note that this entire type of process would need to be redone for each possible application of the model.

As might be inferred from Figure 3, the cause of the “limitation” Juffer et al. (2008) raise is due to the difficulty of the entire



process. The authors are only aware of work based on such an outline in the context of gliomas by the Swanson group (Swanson et al., 2002a, 2008b; Szeto et al., 2009b; Wang et al., 2009; Neal and Kerckhoffs, 2010; Rockne et al., 2010; Baldock et al., 2012a,b; Gu et al., 2012; Neal et al., 2012, 2013). But that is not to say that other efforts are not informative or useful. Indeed, many papers have been published (e.g., Zacharaki et al., 2009; Konukoglu et al., 2010), considering the formidable technical details involved in development and validation of a mathematical model that can be used to inform clinical decision making.

Additionally, models may be used for qualitative understanding of events. An example of such work is that by Bohman et al. (2010) where they investigated ontogeny and spatio-temporal evolution of gliomas. By looking at a set of 63 patient tumors, they determined that tumors abutting the ventricle in the sub ventricular zone (SVZ) are larger than those that do not (Figure 4). The simulation results then pointed to an explanation in that two tumors with identical growth rates, as defined by the continuum mathematical model, could display markedly different growth patterns due to the anatomy of the brain and ontogeny of the tumor. Thus, it is not necessary for a mathematical model to be patient-specific to produce clinically significant results.

PROGNOSIS OF INDIVIDUAL PATIENTS USING PRE-TREATMENT TUMOR GROWTH KINETICS

In a study of 32 newly diagnosed glioblastoma patients, Wang et al. (2009) used the PI model to find relationships between the Patient-specific model (PSM) parameters for glioma cell net dispersal (D), proliferation (ρ), and prognosis. As illustrated in Figure 1, patient-specific estimates D and ρ combine with the patient's MRI to yield a map of the diffuse gradient of glioma

cells that is expected to lie beyond thresholds visible to imaging (Figure 1). Wang et al. analyzed patient-specific tumor growth kinetics relative to the patients' actual survival and found that the model parameters (specifically, ρ and ρ/D) were significant predictors of prognosis in both univariate and multivariate analyses even when controlling for standard clinical prognostic parameters such as RTOG recursive partitioning analysis (RPA) classification.

Velocity of radial expansion on MRI and net proliferation rates were compared to RPA classification and it was found that patients with low velocity and proliferation lived longer than the median prognosis associated with each RPA class, and patients with high velocity and proliferation had shorter survival. A therapeutic response index (TRI) was also calculated for each patient. This is defined as the ratio between the patient's actual survival, and the time it takes for their untreated virtual control (UVC) tumor to reach fatal tumor burden (FTB) (Swanson, 2008; Wang et al., 2009). Patients with high rates of proliferation and velocity were found to have higher TRIs (Wang et al., 2009). This paper was perhaps the first in the literature for which a patient calibrated mathematical model for glioma growth generated prognostic parameters in a patient cohort.

QUANTIFYING TUMOR AGGRESSIVENESS IN INDIVIDUAL PATIENTS

Despite the predictable pattern of linear radial growth in gliomas, within histologic grade there may be great variability in response to treatment and overall prognosis (Bonavia et al., 2011). The hypothesis that more aggressive tumors are more hypoxic was tested using PI model metrics of biological aggressiveness. Szeto et al. (2009b) found there was a strong relationship between hypoxia and the ratio of PI model parameters for proliferation and

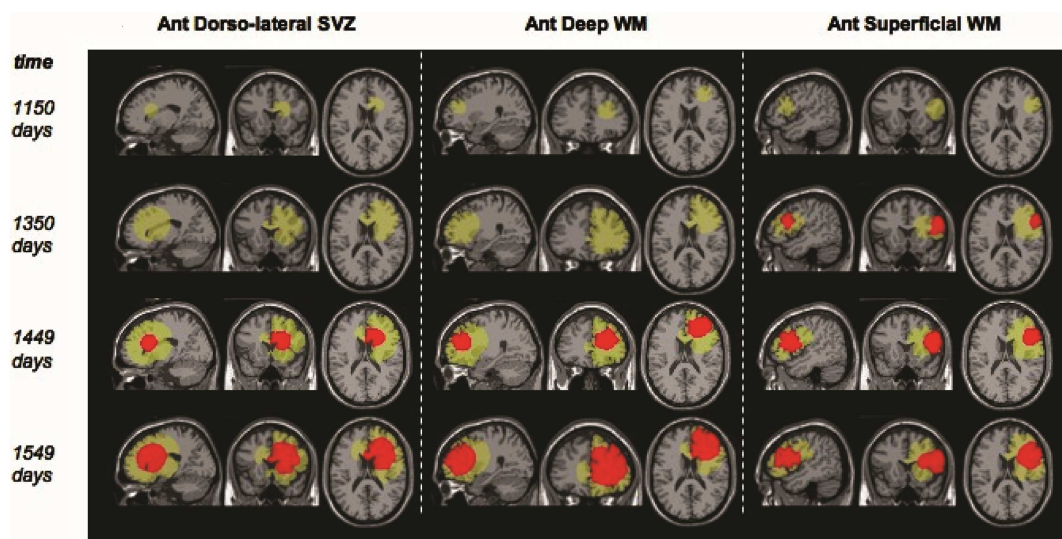


FIGURE 4 | “Example screenshots from glioma growth model simulations with varied points of origin. Images at four time points each for three simulated lesions provided in the sagittal, coronal, and axial planes for lesion start points at the anterior dorsolateral subventricular zone, anterior

deep white matter, and anterior superficial white matter. Green area reflects estimated T2-weighted image abnormality on magnetic resonance; red area reflects estimated T1-weighted image post-gadolinium abnormality.” Courtesy: Bohman et al. (2010).

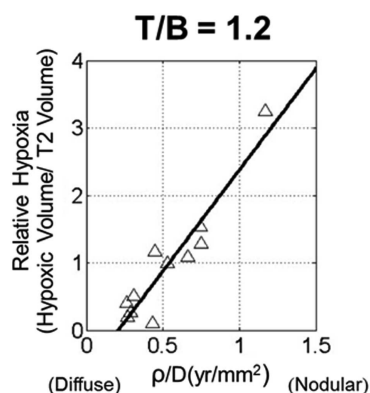


FIGURE 5 | Scatter plot of relative hypoxia (RH, the ratio of hypoxic volume to T2-weighted MRI volume) versus ρ/D for $n = 11$ glioblastoma patients. RH was determined over a variety of tissue to blood (T/B) tracer levels, ranging from 1.1 to 1.6 in increments of 0.1. A strong linear relationship between the variables is shown for all thresholds; correlations were statistically significant for all T/B levels considered. From Szeto et al. (2009b), with permission from Nature Publishing Group, Cancer Research.

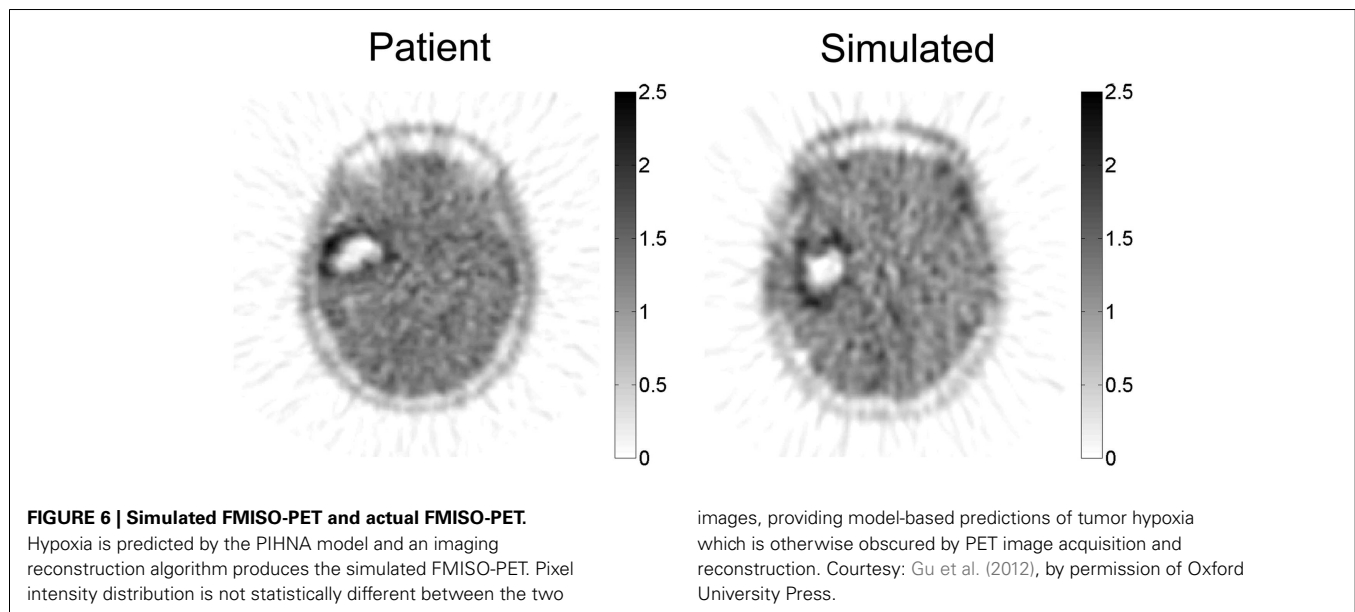
diffusion on 11 glioblastoma patients (Figure 5). Relative hypoxia (RH) was computed as the ratio of hypoxic volume obtained from pre-treatment ^{18}F -Fluoromisonidazole (FMISO) PET images to the region of hyper intensity on T2-weighted MRI. They found that a tumor with high proliferation relative to diffusion would be a relatively well demarcated lesion, while a low ratio would indicate a very diffuse tumor with more migratory capacity compared to the proliferation rate. A metric of tumor shape irregularity was also calculated and found to be negatively correlated with ρ/D .

This suggests that more irregularly shaped tumors are formed by cells with relatively high proliferation rates in highly hypoxic environments. These metrics yield patient-specific understanding and quantification of disease burden and relative biological aggressiveness and a tool in the MNO toolbox.

GOING BEYOND THE ROUTINE: ADVANCED IMAGING IN MATHEMATICAL MODELING

Extending the PI spatio-temporal model of glioma proliferation and invasion, Swanson's group (Swanson et al., 2011; Gu et al., 2012) incorporated neoangiogenesis—a defining hallmark of high grade glioma into the PI model. Briefly, this Proliferation-Invasion-Hypoxia-Necrosis-Angiogenesis (PIHNA) model includes invading normoxic glioma cells which become hypoxic when local resources are exhausted. This results in the local production of significant amounts of angiogenic factors that, in turn, stimulate an angiogenic response. If the angiogenic response is sufficiently robust, these hypoxic cells may revert to normoxia; however, if the angiogenic response is insufficient then necrosis may result. Patient-specific simulations of this type allow for the generation of spatio-temporal maps of normoxic cells, hypoxic cells, necrotic tissue, vascular volume fraction, and angiogenic factors.

The PIHNA model predicts a patient-specific spatial map of hypoxia, which can be compared with PET imaging with the hypoxia tracer ^{18}F -FMISO (Gu et al., 2012). Since there is significant image noise introduced from PET image acquisition and reconstruction, a combination of a pharmacokinetic model for the FMISO tracer kinetics and an image reconstruction algorithm for PET were applied to the patient-specific simulated hypoxic cell distribution to generate a patient-specific *in silico* PET image with striking similarity to the patient's actual image (Figure 6).



THE UNTREATED VIRTUAL CONTROL

To date, the most effective demonstration of the clinical utility of mathematical modeling has been in the context of UVC (**Figure 7**) (Swanson, 2008; Wang et al., 2009). The concept of an UVC is that a model that accurately describes the inherent, untreated disease behavior as a baseline for future comparisons for a specific patient. Deviations from the predicted “control” behavior can be assessed and used as a metric of response to therapy. Because gliomas have a simple, predictable pattern of untreated growth, the UVC approach is particularly simple to apply in this case.

TREATMENT RESPONSE AND OPTIMIZATION

Few treatment options exist for newly diagnosed glioma beyond surgery and chemoradiation following the landmark study which established standard of care for the disease (Stupp et al., 2007). Novel therapies are often reserved for the recurrent setting and have shown little benefit in prolonging survival. Due to the relative rarity of the disease, powering clinical studies can be challenging. Mathematical models quantifying response, sensitivity, and relative benefit of treatment (UVC) provide a novel and alternative means of stratifying patients for clinical studies.

DAYS GAINED SCORE AS A TREATMENT RESPONSE METRIC

The Days Gained score provides a measure of patient-specific treatment derived benefit in terms of treatment induced deflection in tumor growth from the UVC (Neal et al., 2013). This novel quantification stands in stark contrast to current metrics of response (e.g., Macdonald criteria, RANO, and RECIST) that do not account for the relative growth kinetics of individual tumors. One clear difference is that static imaging-based metrics allow a poor response for a slow growing tumor to be equated with a significant response from a fast growing tumor. Neal has shown that the Days Gained metric indeed performs better than these existing metrics in determining patients that will have a survival benefit from treatment. While these classic response criteria are actively being reconsidered in the context of gliomas (Wen et al.,

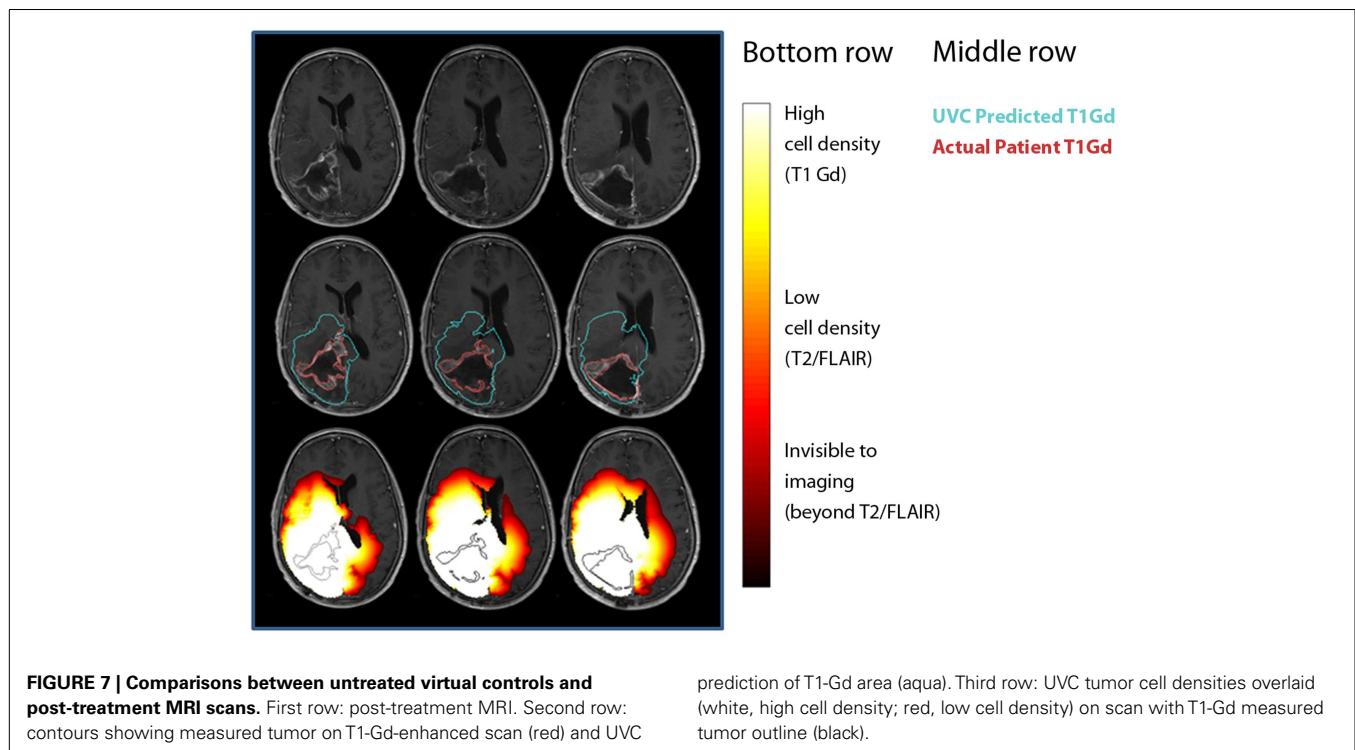
2010), the UVC PSM represents an opportunity to incorporate the implicit heterogeneity of glioma growth kinetics across patients into measures of treatment response.

SURGICAL RESECTION

Surgical resection is the first line response to clinical presentation and radiographic diagnosis of a malignant brain tumor. Although the survival benefit of subtotal (STR) versus gross total (GTR) removal of imageable tumor remains controversial, Swanson et al. (2008b) used mathematical modeling to simulate surgical resection using the PI model for 70 glioblastoma patients using contrast-enhanced T1-weighted MRI volume and radial velocity of tumor growth. The model was able to predict the survival curve for biopsy and subtotal resection groups (**Figure 8A**). Simulations were performed to represent 100 and 125% resections, the observed gross total resection survival curve was found to lie between these two virtual curves (**Figure 8B**). These results suggest that although GTR provides a survival benefit over patients receiving biopsies or subtotal resections, this is partially due to the preferential selection of patients with smaller tumors for gross total resection. This analysis, made possible with mathematical modeling, provides valuable insight into a controversial clinical debate.

QUANTIFYING AND PREDICTING RESPONSE TO RADIATION THERAPY

Beyond RECIST and Macdonald response criteria (Padhani and Ollivier, 2001; Galanis et al., 2006; Therasse et al., 2006), quantifying the *in vivo* biological effectiveness of radiotherapy in individual patients has remained elusive (Enderling et al., 2010). Rockne et al. (2009, 2010) incorporated the classic linear-quadratic model for radiation effectiveness (Bauman et al., 1999; Sachs et al., 2001) into the PI model to quantify the effectiveness of radiotherapy in individual glioma patients. The extended model (PIRT) uses radiation dose plans from the clinical treatment system and fractionation – e.g., 1.8 Gy fractions delivered to the T2 abnormality with a 2.5-cm margin. Nine glioblastoma patients with two MRIs



before the initiation of radiotherapy and at least one MR after the completion of radiation therapy were included in the study. The authors found a strong correlation between the net proliferation rate (ρ) of the glioma cells before the initiation of treatment and the radiation effectiveness (**Figure 9**). The predictive precision of this relationship was tested with a leave one out cross validation (LOOCV) analysis which revealed an average 2.4 mm difference between simulated and actual tumor volume post RT which given an average GBM radius of 2 cm represents a relative error of at most 15%. The error is substantially more resolved than the 25% categories presented in RECIST or Macdonald criteria (Padhani and Ollivier, 2001; Therasse et al., 2006). This approach has provided the first *in vivo* quantification of radiosensitivity in individual glioma patients as well as a predictive relationship between pre-treatment growth kinetics and response to therapy.

In silico models of tumor growth and response to radiotherapy allow for the investigation of factors affecting radiosensitivity and alternative treatment strategies that may be impractical in the clinic. Stamatakis et al. (2006) model studies the interdependent effects of oxygenation on radiosensitivity, angiogenesis, and clonogenic cell density on tumor growth. Lower oxygen enhancement ratio and lower clonogenic cell density were among the factors found to increase radiosensitivity, agreeing with clinical experience, although not directly compared with clinical data. Both Powathil et al. (2007) and Rockne et al. (2009) used a continuum reaction-diffusion model along with the classic linear-quadratic model for radiotherapy effect to investigate alternative fractionation strategies on a virtual tumor with fixed tumor growth kinetics and radio sensitivity. To date, neither model has incorporated the toxic effects of radiation on normal tissue. Holdsworth et al. (2012) builds upon these foundations by refining

intensity-modulated radiation therapy (IMRT) plans based on the criteria of maximizing cytotoxicity while minimizing normal tissue dose.

Swanson et al. (2008a) used the concept of a UVC to understand relative treatment response effects on individual survival time assuming a FTB (Concannon et al., 1960). Results of this investigation demonstrate that patient-specific rates of invasion and proliferation as estimated by a reaction-diffusion model can be calculated for individual patients and related to radio-resistance or radiosensitivity in individual patients and that the mathematical model can be used to determine radio efficacy by relating survival times predicted by the UVC to that observed in the patients, assuming a FTB. In this population, Swanson et al. were able to identify those patients that benefited significantly from radiotherapy by comparing model-predicted untreated survival time with actual (treated) survival time.

OPTIMIZING RADIATION THERAPY

In silico models of tumor growth and response to radiotherapy allow for the investigation of alternative treatment strategies that may be impractical in the clinic. Holdsworth et al. (2012) leveraged the patient-specific description of tumor growth and response in the PIRT model (Rockne et al., 2010) to generate biologically guided treatment plans. Using an adaptive, multiobjective evolutionary algorithm (MOEA), IMRT plans were optimized with respect to a variety of clinical objectives including maximizing normal tissue sparing and minimizing the tumor burden at various time points. By using the PIRT model-predicted tumor burden 12 weeks post-irradiation as an optimization objective for each week of simulated treatment, the MOEA computed radiotherapy plans that improved treatment gain by an average of 122.5 days

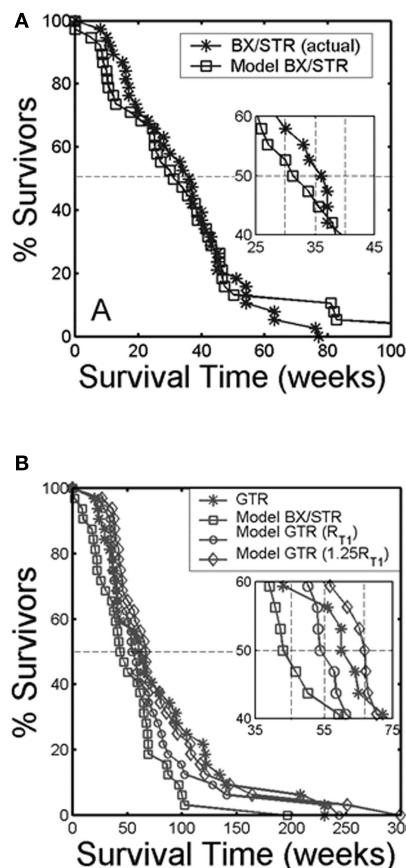


FIGURE 8 | (A) Survival curves for actual glioblastoma patients (asterisks) and virtual patients (squares) subjected to biopsy or subtotal resection (BX/STR, $N = 38$). Inset shows a close-up of the survival curves near the median survival times of 32.4 and 36.5 weeks. (B) Survival curves on a longer time scale following gross total resection (GTR, $N = 32$) in actual patients (asterisks) defined by the absence of residual tumor on post-operative enhanced CT. The virtual patients (matched to actual pre-operative T1-Gd volume and D/ρ ratio derived from the T1-Gd and T2 volumes) were subjected to no resection (BX/STR, squares), to resection of 100% of the T1-Gd volumes or radii, rT_1 (circles), and to resection of 125% of the T1-Gd volumes or radii, $1.25rT_1$ (diamonds). Inset shows a close-up of the survival curves near the median survival times of 44.9, 55, 62, and 66.9 weeks." Reprinted from Swanson et al. (2008b) with permission from Nature Publishing Group, British Journal of Cancer.

and reduced equivalent uniform dose (EUD) to normal tissue an average of 15.5 Gy for two example patients (Holdsworth et al., 2012).

PREDICTING PSEUDOPROGRESSION

Pseudoprogression is a puzzling clinical phenomenon defined by increased contrast enhancement on MRI within 100 days of radiation therapy that spontaneously improves with no subsequent change in treatment (Brandsma et al., 2008). It has been estimated that 20–47% of tumors exhibiting increased contrast enhancement on MRI within 12 weeks following chemoradiotherapy are not indicative of true progressive disease, but are a result of pseudoprogression (Brandsma et al., 2008; Clarke and Chang, 2009). This poses a significant clinical challenge as the

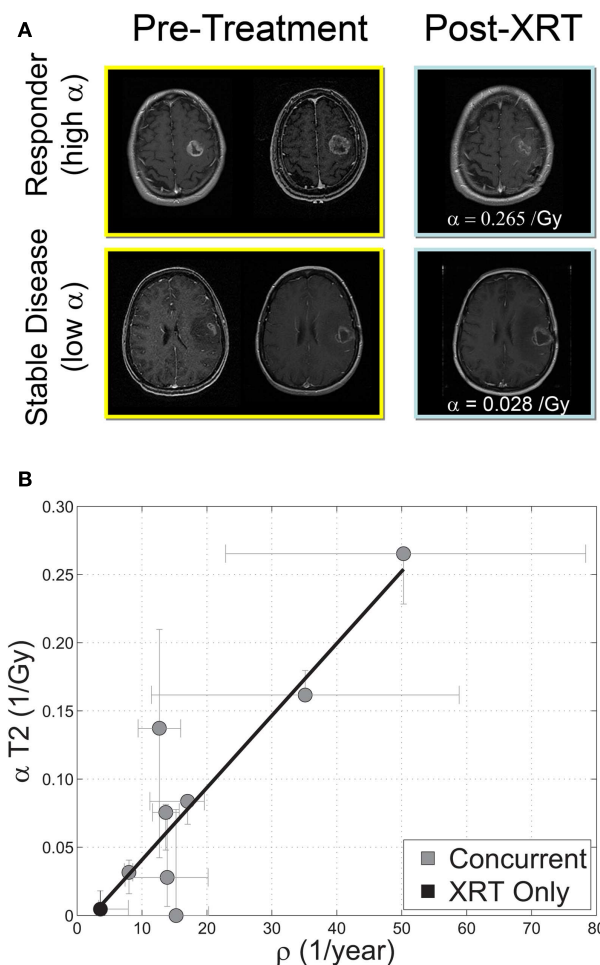


FIGURE 9 | (A) "Response to therapy is conventionally assessed by determining changes in gross tumor volume (GTV) on MRI prior to and after the administration of therapy. Post-contrast T1-weighted MRI images are shown for two glioblastoma patients that would typically be separated into generic groups: responder and stable disease. The radiation response parameter α gives an additional quantification of radiation response for each patient." (B) "Relationship between radiation response and tumor proliferation rate parameters α (Gy^{-1}) and ρ ($1/\text{year}$), respectively, with α calculated relative to changes in T2 GTV post therapy $r = 0.89$, $p < 0.05$, $N = 9$. Error bars on ρ are calculated by propagation of error in pre-treatment GTV as assessed by inter-observer variability of ± 1 mm in equivalent spherical radius. Error bars in α are computed by taking the maximum and minimum values of α in a leave one out cross validation (LOOCV) technique." Courtesy: Rockne et al. (2010), with permission from IOP Publishing Ltd.

current standard of care for recurrent glioma disease calls for immediate changes to chemotherapeutic regimens upon clinical assessment of tumor progression as indicated by increased contrast enhancement on MRI. In addition, recurrent glioma disease is often treated with a second surgical resection of the T1-weighted gadolinium enhanced region (Stupp et al., 2010). Although there is currently no understanding of the underlying biological mechanisms to understand and predict which patients will exhibit pseudoprogression, the Days Gained metric has been shown to discriminate pseudoprogression from true progression in individual

patients (Neal et al., 2013). Patients with pseudoprogression were found to have significantly higher Days Gained scores, connecting model-based metrics of response to clinical outcomes in individual patients.

SUMMARY

Gliomas present a unique clinical challenge. In addition to intra- and inter-tumoral heterogeneity, these lesions are defined by their diffuse invasion of otherwise normal-appearing brain tissue peripheral to the imageable abnormality. This diffuse growth limits the clinical utility of neuroimaging in interpreting treatment response. Current metrics of therapeutic response rely on observable changes to clinical imaging (Wen et al., 2010), ignoring the underlying growth dynamics of the tumor. Further, the current standard of care leaves few treatment options and may over-treat patients with slow growing tumors. Patient-specific mathematical modeling provides a novel means of developing UVCs for each patient's tumor and provides predictive insight into prognosis, treatment response, and optimal treatment design.

The future of patient-specific modeling and application depends on asking questions that mathematical models can realistically answer with data that can be obtained from patients either non-invasively or infrequently. PSM must be validated and incorporated into clinical trials to become broadly and directly applicable to patient care. Advantages of a patient-specific modeling approach include:

- o Identification of individualized tumor proliferation and invasion rates or other kinetic information about an individual patient's tumor (Swanson et al., 2002b; Mandonnet et al., 2003; Pallud et al., 2006; Harpold et al., 2007; Swanson, 2008; Szeto et al., 2009a,b; Wang et al., 2009; Boone et al., 2010; Rockne et al., 2010; Gu et al., 2012)
 - o Development of methods for quantifying and predicting response to therapy – alone and also with respect to UVCs provided by model predictions (Swanson et al., 2008a; Wang et al., 2009; Rockne et al., 2010)
 - o More informed treatment planning and response assessment tools that compare each patient's tumor growth against its own virtual control (Swanson et al., 2002a, 2008a,b; Harpold et al., 2007; Szeto et al., 2009b; Wang et al., 2009; Rockne et al., 2010; Gu et al., 2012)
- These advantages directly address a number of key unmet challenges in clinical neuro-oncology. In the coming years we anticipate a continued expansion of peer-reviewed journals dedicated to mathematical oncology, coordinated with increased funding for research in the area. Recently, Cancer Research has added a special section devoted exclusively to mathematical oncology, and the NIH has initiated special funding programs targeted at mathematical models through the Integrative Cancer Biology Program and Physical Sciences Oncology Center, among others. By producing individualized virtual tumors that predict disease progression in the absence of treatment, patient-specific modeling can contribute to the ongoing dialog regarding the design of appropriate response criteria (Wen et al., 2010), provide a means to perform virtual clinical trials to assess the likely benefit of novel neurotherapeutics, and move neuro-oncology toward individualized treatment plans optimized for maximum benefit.

ACKNOWLEDGMENTS

We wish to thank the James S. McDonnell foundation, the National Institutes of Health (R01NS060752, U54CA143970), the Brain Tumor Funders' Collaborative, the Academic Pathology Fund at the University of Washington and, *in memoriam*, Dr. Ellsworth C. Alvord Jr. for his unwavering mentorship and support.

REFERENCES

- Anderson, A. R., and Quaranta, V. (2008). Integrative mathematical oncology. *Nat. Rev. Cancer* 8, 227–234.
- Baldock, A. L., Anh, S., Rockne, R., Neal, M., Clark-Swanson, K., Sterin, G., et al. (2012a). Patient-specific invasiveness metric predicts benefit of resection in human gliomas. *Neuro-oncology* 14, 131–131.
- Baldock, A. L., Yagle, K., Anh, S., Born, D., Swanson, P., Rockne, R., et al. (2012b). Invasion and proliferation kinetics predict IDH-1 mutation in contrast-enhancing gliomas. *Neuro-oncology* 14, 131–131.
- Bauman, G. S., Fisher, B. J., McDonald, W., Amberger, V. R., Moore, E., and Del Maestro, R. F. (1999). Effects of radiation on a three-dimensional model of malignant glioma invasion. *Int. J. Dev. Neurosci.* 17, 643–651.
- Bohman, L. E., Swanson, K. R., Moore, J. L., Rockne, R., Mandigo, C., Hankinson, T., et al. (2010). Magnetic resonance imaging characteristics of glioblastoma multiforme: implications for understanding glioma ontogeny. *Neurosurgery* 67, 1319–1327; discussion 1318–1327.
- Bonavia, R., Inda, M.-D.-M., Cavenee, W. K., and Furnari, F. B. (2011). Heterogeneity maintenance in glioblastoma: a social network. *Cancer Res.* 71, 4055–4060.
- Boone, A. E., Rockne, R., Mrugala, M. M., and Swanson, K. R. (2010). Pre-treatment glioblastoma proliferation and invasion kinetics: a mechanism to predict pseudo progression. *Neuro-oncology* 12, 119.
- Brandsma, D., Stalpers, L., Taal, W., Sminia, P., and Van Den Bent, M. J. (2008). Clinical features, mechanisms, and management of pseudo-progression in malignant gliomas. *Lancet Oncol.* 9, 453–461.
- Carson, R., Daube-Witherspoon, M., and Herscovitch, P. (1998). *Quantitative Functional Brain Imaging with Positron Emission Tomography*. San Diego, CA: Academic Press.
- Clarke, J. L., and Chang, S. (2009). Pseudoprogression and pseudoresponse: challenges in brain tumor imaging. *Curr. Neurol. Neurosci. Rep.* 9, 241–246.
- Clatz, O., Sermesant, M., Bondiau, P. Y., Delingette, H., Warfield, S. K., Malandain, G., et al. (2005). Realistic simulation of the 3-D growth of brain tumors in MR images coupling diffusion with biomechanical deformation. *IEEE Trans. Med. Imaging* 24, 1334–1346.
- Cocosco, C. A., Zijdenbos, A. P., and Evans, A. C. (2004). A fully automatic and robust brain MRI tissue classification method (vol 7, pg 513, 2003). *Med. Image Anal.* 8, 93–94.
- Concannon, J. P., Kramer, S., and Berry, R. (1960). The extent of intracranial gliomata at autopsy and its relationship to techniques used in radiation therapy of brain tumors. *Am. J. Roentgenol. Radium Ther. Nucl. Med.* 84, 99–107.
- Council, N. R. (2011). *Toward Precision Medicine: Building a Knowledge Network for Biomedical Research and a New Taxonomy of Disease*. Washington: The National Academies Press.
- Ellingson, B. M., Laviollette, P. S., Rand, S. D., Malkin, M. G., Connelly, J. M., Mueller, W. M., et al. (2010a). Spatially quantifying microscopic tumor invasion and proliferation using a voxel-wise solution to a glioma growth model and serial diffusion MRI. *Magn. Reson. Med.* 65, 1131–1143.
- Ellingson, B. M., Malkin, M. G., Rand, S. D., Laviollette, P. S., Connelly, J. M., Mueller, W. M., et al. (2010b). Volumetric analysis of functional diffusion maps is a predictive imaging biomarker for cytotoxic and anti-angiogenic treatments in malignant gliomas. *J. Neurooncol.* 102, 95–103.
- Enderling, H., Chaplain, M. A. J., and Hahnfeldt, P. (2010). Quantitative modeling of tumor dynamics and radiotherapy. *Acta Biotheor.* 58, 341–353.
- Fisher, R. (1937). The wave of advance of advantageous genes. *Ann. Eugen.* 7, 353–369.
- Galanis, E., Buckner, J., Maurer, M., Sykora, R., Castillo, R., Ballman,

- K., et al. (2006). Validation of neuroradiologic response assessment in gliomas: measurement by RECIST, two-dimensional, computer-assisted tumor area, and computer-assisted tumor volume methods. *Neuro-oncology* 8, 156–165.
- Gatenby, R. A., and Maini, P. K. (2003). Mathematical oncology: cancer summed up. *Nature* 421, 321–321.
- Gerlee, P., and Nelander, S. (2012). The impact of phenotypic switching on glioblastoma growth and invasion. *PLoS Comput. Biol.* 8:e1002556. doi:10.1371/journal.pcbi.1002556
- Giatili, S. G., and Stamatakis, G. S. (2012). A detailed numerical treatment of the boundary conditions imposed by the skull on a diffusion-reaction model of glioma tumor growth. Clinical validation aspects. *Appl. Math. Comput.* 218, 8779–8799.
- Giese, A., Bjerkvig, R., Berens, M. E., and Westphal, M. (2003). Cost of migration: invasion of malignant gliomas and implications for treatment. *J. Clin. Oncol.* 21, 1624–1636.
- Gu, S., Chakraborty, G., Champley, K., Alessio, A. M., Claridge, J., Rockne, R., et al. (2012). Applying a patient-specific bio-mathematical model of glioma growth to develop virtual 18F-FMISO-PET images. *Math. Med. Biol.* 29, 31–48.
- Harpold, H., Alvord, E. J., and Swanson, K. (2007). The evolution of mathematical modeling of glioma proliferation and invasion. *J. Neuropathol. Exp. Neurol.* 66, 1–9.
- Hatzikirou, H., Basanta, D., Simon, M., Schaller, K., and Deutsch, A. (2012). “Go or Grow”: the key to the emergence of invasion in tumour progression? *Math. Med. Biol.* 29, 49–65.
- Hlaïhel, C., Guilloton, L., Guyotat, J., Streichenberger, N., Honnorat, J., and Cotton, F. (2010). Predictive value of multimodality MRI using conventional, perfusion, and spectroscopy MR in anaplastic transformation of low-grade oligodendrogliomas. *J. Neurooncol.* 97, 73–80.
- Holdsworth, C. H., Corwin, D., Stewart, R. D., Rockne, R. C., Trister, A. D., Swanson, K. R., et al. (2012). Adaptive IMRT using a multiobjective evolutionary algorithm integrated with a diffusion-invasion model of glioblastoma. *Phys. Med. Biol.* 57, 8271–8283.
- Jbabdi, S., Mandonnet, E., Duffau, H., Capelle, L., Swanson, K. R., Pelegriini-Issac, M., et al. (2005). Simulation of anisotropic growth of low-grade gliomas using diffusion tensor imaging. *Magn. Reson. Med.* 54, 616–624.
- Juffer, A. H., Marin, U., Niemitto, O., and Koivukangas, J. (2008). Computer modeling of brain tumor growth. *Mini Rev. Med. Chem.* 8, 1494–1506.
- Konukoglu, E., Clatz, O., Menze, B. H., Stieltjes, B., Weber, M. A., Mandonnet, E., et al. (2010). Image guided personalization of reaction-diffusion type tumor growth models using modified anisotropic eikonal equations. *IEEE Trans. Med. Imaging* 29, 77–95.
- Louis, D. N., Ohgaki, H., Wiestler, O. D., Cavenee, W. K., Burger, P. C., Juvet, A., et al. (2007). The 2007 WHO classification of tumours of the central nervous system. *Acta Neuropathol.* 114, 97–109.
- Mandonnet, E., Delattre, J., Tanguy, M., Swanson, K., Carpentier, A., Duffau, H., et al. (2003). Continuous growth of mean tumor diameter in a subset of grade II gliomas. *Ann. Neurol.* 53, 524–528.
- Mandonnet, E., Pallud, J., Clatz, O., Taillandier, L., Konukoglu, E., Duffau, H., et al. (2008). Computational modeling of the WHO grade II glioma dynamics: principles and applications to management paradigm. *Neurosurg. Rev.* 31, 263–268.
- Murray, J. (2002). *Mathematical Biology*. New York: Springer.
- Neal, M. L., and Kerckhoffs, R. (2010). Current progress in patient-specific modeling. *Brief. Bioinformatics* 11, 111–126.
- Neal, M. L., Trister, A. D., Ahn, S., Bridge, C., Lange, J., Baldock, A., et al. (2012). A response metric based on a minimal model of glioblastoma growth is prognostic for time to progression and overall survival. *Neuro-oncology* 14, 83–83.
- Neal, M. L., Trister, A. D., Cloke, T., Sodt, R., Ahn, S., Baldock, A. L., et al. (2013). Discriminating survival outcomes in patients with glioblastoma using a simulation-based, patient-specific response metric. *PLoS ONE* 8:e51951. doi:10.1371/journal.pone.0051951
- Nishikawa, R. (2010). Standard therapy for glioblastoma—a review of where we are. *Neurol. Med. Chir. (Tokyo)* 50, 713–719.
- Padhani, A., and Ollivier, L. (2001). The RECIST (Response Evaluation Criteria in Solid Tumors) criteria: implications for diagnostic radiologists. *Br. J. Radiol.* 74, 983–986.
- Pallud, J., Mandonnet, E., Duffau, H., Kujas, M., Guillemin, R., Galanaud, D., et al. (2006). Prognostic value of initial magnetic resonance imaging growth rates for World Health Organization grade II gliomas. *Ann. Neurol.* 60, 380–383.
- Pallud, J., Varlet, P., Devaux, B., Geha, S., Badoual, M., Deroulers, C., et al. (2010). Diffuse low-grade oligodendrogliomas extend beyond MRI-defined abnormalities. *Neurology* 74, 1724–1731.
- Powathil, G., Kohandel, M., Sivaloganathan, S., Oza, A., and Milosevic, M. (2007). Mathematical modeling of brain tumors: effects of radiotherapy and chemotherapy. *Phys. Med. Biol.* 52, 3291–3306.
- Rockne, R., Alvord, E. C., Rockhill, J. K., and Swanson, K. R. (2009). A mathematical model for brain tumor response to radiation therapy. *J. Math. Biol.* 58, 561–578.
- Rockne, R., Rockhill, J. K., Mrugala, M., Spence, A. M., Kalet, I., Hendrickson, K., et al. (2010). Predicting the efficacy of radiotherapy in individual glioblastoma patients *in vivo*: a mathematical modeling approach. *Phys. Med. Biol.* 55, 3271–3285.
- Sachs, R. K., Hlatky, L. R., and Hahnfeldt, P. (2001). Simple ODE models of tumor growth and anti-angiogenic or radiation treatment. *Math. Comput. Model.* 33, 1297–1305.
- Stamatakis, G. S., Antipas, V. P., Uzunoglu, N. K., and Dale, R. G. (2006). A four-dimensional computer simulation model of the *in vivo* response to radiotherapy of glioblastoma multiforme: studies on the effect of clonogenic cell density. *Br. J. Radiol.* 79, 389–400.
- Stupp, R., Hegi, M. E., Gilbert, M. R., and Chakravarti, A. (2007). Chemoradiotherapy in malignant glioma: standard of care and future directions. *J. Clin. Oncol.* 25, 4127–4136.
- Stupp, R., Tonn, J. C., Brada, M., Pentheroudakis, G., and Group, E. G. W. (2010). High-grade malignant glioma: ESMO clinical practice guidelines for diagnosis, treatment and follow-up. *Ann. Oncol.* 21(Suppl. 5), v190–v193.
- Swanson, K. (1999). *Mathematical Modeling of the Growth and Control of Tumors*. Seattle: University of Washington.
- Swanson, K., and Alvord, E. (2002). Serial imaging observations and postmortem examination of an untreated glioblastoma: a traveling wave of glioma growth and invasion. *Neuro-oncology* 4, 340.
- Swanson, K. R. (2008). Quantifying glioma cell growth and invasion *in vitro*. *Math. Comput. Model.* 47, 638–648.
- Swanson, K. R., Alvord, E. C., and Murray, J. D. (2002a). Quantifying efficacy of chemotherapy of brain tumors with homogeneous and heterogeneous drug delivery. *Acta Biotheor.* 50, 223–237.
- Swanson, K. R., Alvord, E. C., and Murray, J. D. (2002b). Virtual brain tumours (gliomas) enhance the reality of medical imaging and highlight inadequacies of current therapy. *Br. J. Cancer* 86, 14–18.
- Swanson, K. R., Harpold, H. L. P., Peacock, D. L., Rockne, R., Pennington, C., Kilbride, L., et al. (2008a). Velocity of radial expansion of contrast-enhancing gliomas and the effectiveness of radiotherapy in individual patients: a proof of principle. *Clin. Oncol.* 20, 301–308.
- Swanson, K. R., Rostomily, R. C., and Alvord, E. C. (2008b). A mathematical modelling tool for predicting survival of individual patients following resection of glioblastoma: a proof of principle. *Br. J. Cancer* 98, 113–119.
- Swanson, K. R., Rockne, R. C., Claridge, J., Chaplain, M. A., Alvord, E. C. Jr., and Anderson, A. R. A. (2011). Quantifying the role of angiogenesis in malignant progression of gliomas: *in silico* modeling integrates imaging and histology. *Cancer Res.* 71, 7366–7375.
- Szeto, M., Rockne, R., and Swanson, K. R. (2009a). Anatomic variation in quantitative measures of glioma aggressiveness. *International Conference on Mathematical Biology and Annual Meeting of the Society for Mathematical Biology*, Vancouver.
- Szeto, M. D., Chakraborty, G., Hadley, J., Rockne, R., Muzi, M., Alvord, E. C., et al. (2009b). Quantitative metrics of net proliferation and invasion link biological aggressiveness assessed by MRI with hypoxia assessed by FMISO-PET in newly diagnosed glioblastomas. *Cancer Res.* 69, 4502–4509.
- Therasse, P., Eisenhauer, E., and Verweij, J. (2006). RECIST revisited: a review of validation studies on tumour assessment. *Eur. J. Cancer* 42, 1031–1039.
- Wang, C. H., Rockhill, J. K., Mrugala, M., Peacock, D. L., Lai, A., Jusenius, K., et al. (2009). Prognostic significance of growth kinetics in newly diagnosed glioblastomas revealed by combining serial imaging with a novel bio-mathematical model. *Cancer Res.* 69, 9133–9140.
- Wen, P. Y., Macdonald, D. R., Reardon, D. A., Cloughesy, T. F., Sorensen, A. G., Galanis, E., et al. (2010). Updated

response assessment criteria for high-grade gliomas: response assessment in neuro-oncology working group. *J. Clin. Oncol.* 28, 1963–1972.

Zacharaki, E. I., Hoge, C. S., Shen, D. G., Biros, G., and Davatzikos, C. (2009). Non-diffeomorphic registration of brain tumor images by simulating tissue loss and tumor growth. *Neuroimage* 46, 762–774.

Conflict of Interest Statement: The authors declare that the research was conducted in the absence of any commercial or financial relationships that could be construed as a potential conflict of interest.

Received: 20 December 2012; paper pending published: 11 January 2013; accepted: 07 March 2013; published online: 02 April 2013.

Citation: Baldock AL, Rockne RC, Boone AD, Neal ML, Hawkins-Daarud A, Corwin DM, Bridge CA, Guyman LA, Trister AD, Mrugala MM, Rockhill JK and Swanson KR (2013) From patient-specific mathematical neuro-oncology to precision medicine. *Front. Oncol.* 3:62. doi:10.3389/fonc.2013.00062

This article was submitted to *Frontiers in Molecular and Cellular Oncology*, a specialty of *Frontiers in Oncology*.

Copyright © 2013 Baldock, Rockne, Boone, Neal, Hawkins-Daarud, Corwin, Bridge, Guyman, Trister, Mrugala, Rockhill and Swanson. This is an open-access article distributed under the terms of the Creative Commons Attribution License, which permits use, distribution and reproduction in other forums, provided the original authors and source are credited and subject to any copyright notices concerning any third-party graphics etc.



A model of dendritic cell therapy for melanoma

Lisette DePillis¹, Angela Gallegos² and Ami Radunskaya^{3*}

¹ Department of Mathematics, Harvey Mudd College, Claremont, CA, USA

² Department of Mathematics, Loyola Marymount University, Los Angeles, CA, USA

³ Department of Mathematics, Pomona College, Claremont Colleges, Claremont, CA, USA

Edited by:

Katarzyna Anna Rejniak, H. Lee
Moffitt Cancer Center and Research
Institute, USA

Reviewed by:

Yangjin Kim, University of Michigan,
USA

Kathleen Wilkie, Steward Research
and Specialty Projects Corporation,
USA

*Correspondence:

Ami Radunskaya, 610 North College
Avenue, Claremont, CA, USA.
e-mail: aradunskaya@pomona.edu

Dendritic cells are a promising immunotherapy tool for boosting an individual's antigen-specific immune response to cancer. We develop a mathematical model using differential and delay-differential equations to describe the interactions between dendritic cells, effector-immune cells, and tumor cells. We account for the trafficking of immune cells between lymph, blood, and tumor compartments. Our model reflects experimental results both for dendritic cell trafficking and for immune suppression of tumor growth in mice. In addition, *in silico* experiments suggest more effective immunotherapy treatment protocols can be achieved by modifying dose location and schedule. A sensitivity analysis of the model reveals which patient-specific parameters have the greatest impact on treatment efficacy.

Keywords: mathematical model, cancer, immunotherapy, melanoma, dendritic cell vaccine

1. INTRODUCTION

A promising immunotherapy approach to treating certain cancers involves the use of dendritic cells (DCs). DCs are part of the antigen-specific (adaptive) immune response and function as antigen-presenting cells. Immature DCs are derived in the bone marrow and reside in peripheral tissues. Upon encountering pathogen, DCs begin to mature, and travel to the lymphoid organs where they stimulate differentiation and maturation of cytotoxic T lymphocytes (CTLs). Some of these activated CTLs then travel to the infected tissue to form part of the adaptive immune response, while others become memory cells that are ready to mount a rapid response in case of a rechallenge by the pathogen.

Previous studies have established the efficacy of dendritic cell treatments for tumors in the murine system (DeMatos et al., 1998; Fields et al., 1998; Lee et al., 2007; Yamaguchi et al., 2007; Shinagawa et al., 2008). In these studies, DCs have been shown both to inhibit the growth of nascent tumors and to provide a memory response to previously encountered antigen. In the clinic, researchers have been able to extract immature dendritic cells from patients, culture them *ex vivo*, and load them with tumor antigens to create an individual-based vaccine that can boost a patient's response against their own cancerous cells (Pilon-Thomas et al., 2004; Taquet et al., 2008). The success of clinical trials of DC vaccines has resulted in the recent FDA approval of the first cancer vaccine for prostate cancer (Cheever, 2011). Despite promising clinical responses in vaccine trials, it remains difficult to predict which patients will actually respond to these vaccines and why (Trefzer et al., 2005; Boon et al., 2006). Mathematical models of DC therapy can provide insight into the mechanisms driving the kinetics of the immune response that may lead to these disparate patient responses.

Cell trafficking is an important aspect of the DC-mediated immune response. DCs must travel from the tumor to the peripheral lymph organs via the blood, and activated CTLs must travel from the lymph organs back to the tumor. Ludewig et al. (2004) have developed a model describing DC and CTL trafficking in

mice. The model includes activated and memory CTLs to capture both the immediate and long-term effect of DC injections. The DC trafficking model of Ludewig et al. was carefully calibrated using experimental data from murine studies.

In this paper we present an extension and modification of the model in Ludewig et al. (2004). Our extended model includes a tumor compartment to allow for analysis of various DC treatments and their effect on tumor growth, as well as the long-term behavior of the system. We find relevant model parameters using the data collected by Lee et al. (2007) describing tumor growth in response to varying levels of DC injections. We compare model simulations of various DC doses, injection sites, and dose times. We include a comparison to a prophylactic dosing schedule presented by Preynat-Seauve et al. (2007).

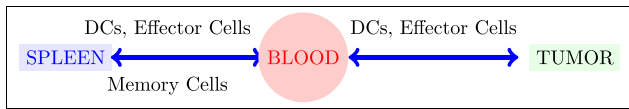
2. THE MODEL

The compartment model proposed by Ludewig et al. (2004) includes dendritic cells, activated CTLs, and memory CTLs. Our extended model includes tumor cells in addition to these immune cell populations. Adding a tumor compartment requires the determination of tumor-immune system parameters such as immune cell trafficking rates to and from the tumor, effector cell deactivation rates by tumor cells, effector cell death rates, intrinsic tumor growth rates, and tumor cell kill rates by effector cells. We note that this compartment model does not account for the geometry of the system. In particular, it does not explicitly incorporate the distance between the spleen and the tumor. However, in murine models, the transit times between compartments are small relative to the tumor growth time scale, so this simplification is reasonable. In this section we describe the processes included in the mathematical model.

2.1. MODEL DEFINITION

Our model consists of three compartments: the spleen, the blood, and the tumor. Dendritic cells and active effector cells can move between the blood and spleen compartments, and between the

blood and tumor compartments. We assume that memory effector cells can move between the spleen and the blood compartments. The system is not conservative: all types of cells are cleared through the blood, immune cells are created in response to the presence of tumor, and tumor cells grow according to a logistic growth law.



The nine state variables in our model are:

- D_{blood} , the number of dendritic cells in the blood compartment;
- D_{spleen} , the number of dendritic cells in the spleen compartment;
- E_{blood}^a , the number of activated CTLs in the blood compartment;
- E_{spleen}^a , the number of activated CTLs in the spleen compartment;
- E_{blood}^m , the number of memory CTLs in the blood compartment;
- E_{spleen}^m , the number of memory CTLs in the spleen compartment;
- E_{tumor}^a , the number of activated CTLs in the tumor compartment;
- T , the number of tumor cells;
- D_{tumor} , the number of dendritic cells in the tumor compartment, the tumor-infiltrating DCs.

We present the system of nine differential equations in groups representing the blood, spleen, and tumor compartments. The model parameters are described in detail in **Table A1** in Appendix.

2.1.1. Blood compartment

The equations describing DC and CTL flow in the blood are given by:

$$\frac{d}{dt} D_{blood} = -\mu_B D_{blood} + \mu_{TB} D_{tumor} + v_{blood}(t) \quad (1)$$

$$\frac{d}{dt} E_{blood}^a = \mu_{SB}(D_{spleen}) E_{spleen}^a - \mu_{BB} E_{blood}^a \quad (2)$$

$$\frac{d}{dt} E_{blood}^m = \mu_{SB}(D_{spleen}) E_{spleen}^m - \mu_{BB} E_{blood}^m \quad (3)$$

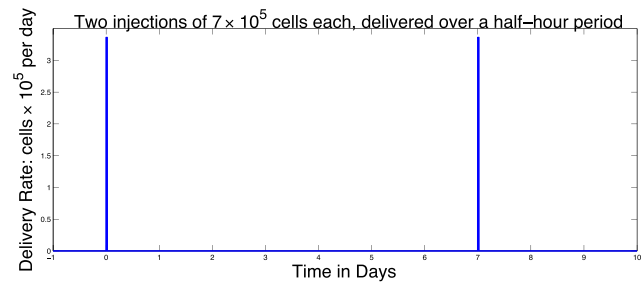
where, as holds throughout the model, the μ parameters represent flow rates between compartments. We include the “trapping” term from Ludewig et al. (2004) which describes the observed phenomenon of activated CTLs being held back in the spleen in the presence of DCs:

$$\mu_{SB}(D_{spleen}) = \mu_{SB}^* + \frac{\Delta\mu}{1 + \frac{D_{spleen}}{\theta_{shut}}},$$

$$\Delta\mu = \mu_{SB}^{Normal} - \mu_{SB}^*.$$

The function $v_{blood}(t)$ allows us to model injections of DCs into the blood. For example, two doses of 7×10^5 each given on Day 0 and Day 7 could be described by the function:

$$v_{blood}(t) = \begin{cases} \frac{7 \times 10^5}{1/48}, & t \in (0, 1/48) \cup (7, 7 + 1/48), \\ 0 & \text{otherwise.} \end{cases} \quad (4)$$



2.1.2. Spleen compartment

The differential equations for the spleen compartment describe interaction, death, and recruitment of DCs and CTL. The equations include one delay which represents the synaptic connection time: the contact time required between DCs and effector cells in the spleen before proliferation can begin. The other interactions we account for in the system do not involve a required contact time and thus are modeled without delay. The dynamics of the populations in the spleen are described by:

$$\frac{d}{dt} D_{spleen} = \text{Max } D \left(1 - e^{\left(\frac{-\mu_{BS} D_{blood}}{\text{Max } D} \right)} \right) - a_D D_{spleen} - b_{DE} E_{spleen}^a D_{spleen} \quad (5)$$

$$\begin{aligned} \frac{d}{dt} E_{spleen}^a = & \mu_{BSE} E_{blood}^a - \mu_{SB}(D_{spleen}) E_{spleen}^a + b_a D_{spleen} E_{spleen}^m \\ & + a_{EaS} (DC_{on} E_{naive} - E_{spleen}^a) - r_{am} E_{spleen}^a \\ & + b_p \frac{D_{spleen}(t - \tau_D) E_{spleen}^a(t - \tau_D)}{\theta_D + D_{spleen}(t - \tau_D)} \end{aligned} \quad (6)$$

$$\begin{aligned} \frac{d}{dt} E_{spleen}^m = & r_{am} E_{spleen}^a - (a_{Em} + b_a D_{spleen} + \mu_{SB}(D_{spleen})) E_{spleen}^m \\ & + \mu_{BSE} E_{blood}^m. \end{aligned} \quad (7)$$

Note that the term in equation (6),

$$DC_{on} = \begin{cases} 0 & \text{if } D_{spleen}(t) = 0 \\ 1 & \text{if } D_{spleen}(t) > 0. \end{cases}$$

indicates that we do not allow for new CTLs in the absence of DCs. Thus, the populations we model only exist due to the presence of tumor and mature DCs.

The first term in equation (5) reflects our assumption that there is a maximum rate at which mature DCs can enter the spleen. This is in agreement with observations that DCs cannot enter the spleen at an unlimited rate. Based on a range of values for the maximum rate we have set $\text{Max } D$ to 400 (cells per hour), reflecting the parameter fit obtained with the data from Lee et al. (2007) and Preynat-Seauve et al. (2007). As noted above, in equation (6) the final term introduces a delay, τ , into the system that reflects the synaptic connection time. Mathematically, this delay introduces more complexity into the system, especially regarding the stability analysis of the equilibria (see *Stability Analysis* below).

2.1.3. Tumor compartment

The tumor compartment contains activated effector CTLs, DCs, and tumor cells. The interactions of these populations within the

tumor are described by:

$$\frac{d}{dt} E_{tumor}^a = \mu_{BTE}(T) E_{blood}^a - a_{E_a T} E_{tumor}^a - c E_{tumor}^a T, \quad (8)$$

$$\frac{d}{dt} T = rT \left(1 - \frac{T}{k}\right) - \mathcal{D}T. \quad (9)$$

$$\frac{d}{dt} D_{tumor} = \frac{mT}{q+T} - (\mu_{TB} + a_D) D_{tumor} + v_{tumor}(t) \quad (10)$$

where

$$\mu_{BTE}(T) = \mu_{BB}(T/(\alpha + T)),$$

and

$$\mathcal{D} = d \frac{\left(\frac{E_{tumor}^a}{T}\right)^l}{s + \left(\frac{E_{tumor}^a}{T}\right)^l}. \quad (11)$$

The function $v_{tumor}(t)$ is similar to $v_{blood}(t)$ in the blood compartment, allowing us to inject DCs intratumorally in order to compare treatment protocols.

Note that in equation (9), tumor growth is fit to a logistic function as in previous models (de Pillis and Radunskaya, 2003; de Pillis et al., 2005, 2007, 2009; Cappuccio et al., 2006). The behavior of this particular model is robust to the choice of growth function, for example a Gompertz growth law gives similar results. However, we choose the logistic law since it provides a good fit to the experimental data we are using for model calibration (See **Figure 1**). Cytolysis of tumor cells by activated CTLs [equations (9) and (11)] is a ratio-dependent kill term introduced in de Pillis and Radunskaya (2003). Experimental results from Diefenbach et al. (2001) support ratio-dependent, antigen-specific killing, and the term has been employed to success in previous models (de Pillis and Radunskaya, 2003; de Pillis et al., 2005, 2007, 2009). The importance of

tumor-infiltrating dendritic cells has been demonstrated in several studies. See, for example, Preynat-Seauve et al. (2007). We allow DCs in the tumor to increase as a saturation-limited function of the size of the tumor population.

With this model we simulate a variety of treatment scenarios, including those investigated in Lee et al. (2007) and Preynat-Seauve et al. (2007). The model offers insight into how best to harness the tumor controlling potential of DCs.

3. RESULTS

3.1. PARAMETER DETERMINATION

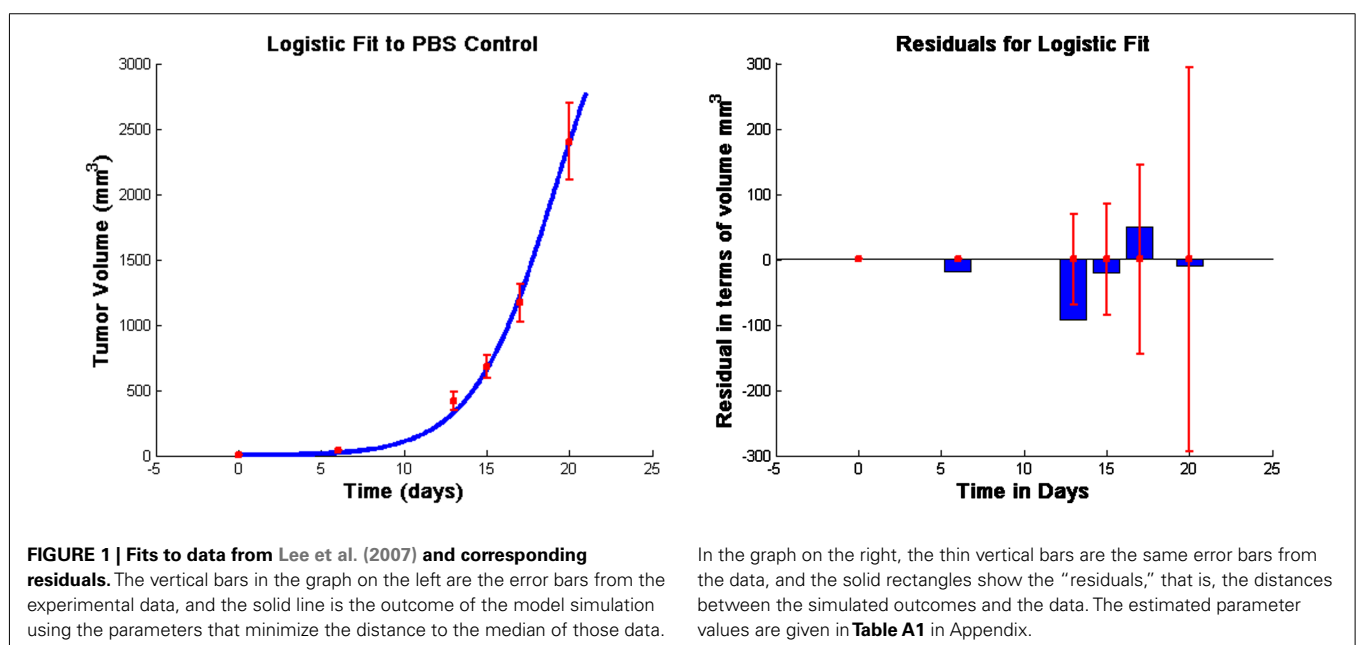
All unknown parameters were fit to data from Lee et al. (2007) using a Nelder–Mead least-squares algorithm. The data in Lee et al. (2007) were collected from C57BL/6 female mice who were subcutaneously inoculated with 5×10^5 B16F10 melanoma cells. We take this as day 0 for the purpose of fitting unknown parameters so that we may use 5×10^5 tumor cells as an initial condition. Injections of 1×10^5 , 7×10^5 , or 21×10^5 DCs were given at days 6, 8, and 10, following inoculation with tumor cells. Additionally, a control group was injected with PBS according to the same schedule (Lee et al., 2007). See **Figure 1**.

3.2. EQUILIBRIA AND STABILITY ANALYSIS

In order to determine the long-term behavior of the system, we find the equilibria and determine their stability.

3.2.1. Determination of the equilibria

The system has multiple equilibrium values, determined by setting equations (1–10) to zero. One solution to this system is the zero, or disease-free, equilibrium. To find the remaining non-zero equilibria, we first write all the state variables at equilibrium as functions of T , then search for the values of T that solve all equations simultaneously. We use asterisks to denote the value of the variables at equilibrium. Therefore, if there exists a non-zero value T^* that satisfies equation (9), we can use equation (8) to obtain



$$E_{tumor}^{a*} = \left\{ \frac{s(T^*)^l (k - T^*)}{T^* - k(1 - d/r)} \right\}^{1/l}. \quad (12)$$

The value for D_{tumor}^* can also be found in terms of T^* using equation (10):

$$D_{tumor}^* = \frac{mT^*}{q + T^*} \frac{1}{\mu_{TB} + a_D}, \quad (13)$$

where we have replaced DC_{death} with its assumed constant value a_D .

Given E_{tumor}^{a*} , we can use equation (8) to determine the equilibrium value of the active effector cells in the blood:

$$E_{blood}^{a*} = \frac{(a_{Ea}T + cT^*)(\alpha + T^*)}{\mu_{BB}T^*} E_{tumor}^{a*}. \quad (14)$$

We use equations (13) and (1) to obtain D_{blood}^* in terms of T^* :

$$D_{blood}^* = \frac{\mu_{TB}D_{tumor}^*}{\mu_B} = \frac{\mu_{TB}}{\mu_B} \left(\frac{1}{\mu_{TB} + a_D} \right) \frac{mT^*}{q + T^*}.$$

Equation (3) gives an expression for E_{blood}^{m*} in terms of E_{spleen}^{m*} ,

$$E_{blood}^{m*} = \frac{\mu_{SB}(D_{spleen})}{\mu_{BB}} E_{spleen}^{m*}.$$

Turning to the spleen compartment, we have:

$$E_{spleen}^{a*} = \frac{\mu_{BB}}{\mu_{SB}(D_{spleen})} E_{blood}^{a*}.$$

Using (14) and (12), this gives E_{spleen}^{a*} in terms of T^* . According to equation (5), knowing D_{blood}^* allows determination of D_{spleen}^* . Using equation (6) results in the following quadratic equation for D_{spleen}^* :

$$0 = -\theta_{shut}(\mu_{SB}^* + \Delta\mu) \mathcal{D}_{in} \{ \theta_{shut} \mu_{SB}^* a_D + \Delta\mu \theta_{shut} a_D + \theta_{shut} b_{DE} \mu_{BB} E_{blood}^{a*} - \mu_{SB}^* \mathcal{D}_{in} \} D_{spleen}^* + \{ \mu_{SB}^* a_D + b_{DE} E_{blood}^{a*} \mu_{BB} \} (D_{spleen}^*)^2, \quad (15)$$

where

$$\mathcal{D}_{in} = \text{Max } D \left\{ 1 - \exp \left(\frac{-\mu_{BS} D_{blood}}{\text{Max } D} \right) \right\}.$$

Solving this quadratic equation yields two different, relevant equilibrium values for D_{spleen}^* . From equation (7) we get a value for E_{spleen}^{m*} for each value of D_{spleen}^* :

$$E_{spleen}^{m*} = \frac{r_{am} E_{spleen}^{a*}}{a_{Em} + b_a D_{spleen}^* + \mu_{SB}(D_{spleen}^*) \{ 1 - \mu_{BSE} / \mu_{BB} \}}.$$

Finally, from equation (6), the roots of the following function, expressible in terms of one variable, T^* , yield equilibrium values for T^* .

$$Z(T^*) = \mu_{BSE} E_{blood}^{a*} - \mu_{SB}(D_{spleen}^*) E_{spleen}^{a*} + b_a D_{spleen}^* E_{spleen}^{m*} + a_{EaS} (DC_{on} E_{naive} - E_{spleen}^{a*}) - r_{am} E_{spleen}^{a*} + b_p \frac{D_{spleen}^* E_{spleen}^{a*}}{\theta_D + D_{spleen}^*}. \quad (16)$$

From equation (12), we see that as long as the values of T^* , and thus the roots of (16), lie between $k(1 - d/r)$ and k , a non-zero equilibrium state exists. Recall that d , r , and k are the parameters that represent the tumor cell kill, intrinsic growth rates, and tumor carrying capacity, respectively. The function $Z(T)$ is plotted in **Figure 2** for the parameter set given in **Table A1** in Appendix.

3.2.2. Stability of the equilibrium points

A stability analysis of the system of delay equations (1–10) can be carried out by analyzing the linear approximation to the system at an equilibrium point. Since the term $\mathcal{D}(T, E_{tumor}^{a*})$, given in equation (11), is not differentiable at $(0, 0)$, the system of DEs is not differentiable and, hence, has no linear approximation at the origin. Although we cannot use the linearization in this case, we do have numerical simulations that indicate that the tumor free equilibrium is initially unstable, but gains stability as the value of d , the immune strength parameter, is increased (see **Figure 9**). There is ongoing investigation of the analytical nature of the stability of the disease-free equilibrium.

At other equilibria, the linearization is given by two matrices of partial derivatives, J_0 and J_τ . To simplify the notation, we denote the nine state variables as x_1 through x_9 and the delayed state variables as $z_i(t) = x_i(t - \tau)$. If the rate of change of x_i is denoted by:

$$\frac{dx_i}{dt} = F_i(x_1, \dots, x_9, z_1, \dots, z_9)$$

then the entries of the Jacobians are:

$$J_0(i, j) = \frac{\partial F_i}{\partial x_j}, \quad J_\tau(i, j) = \frac{\partial F_i}{\partial z_j}$$

The formulas for the entries of J_0 and J_τ are given in Appendix B.

The eigenvalues of the derivative matrices at an equilibrium, \mathbf{E} can be determined by finding the roots of the characteristic polynomial $P(\lambda, \tau)$, where P is defined by:

$$P(\lambda, \tau) = \det(J_0(\mathbf{E}) + e^{-\lambda\tau} J_\tau(\mathbf{E}) - \lambda \mathbf{I})$$

For most systems of delay-differential equations, determining the roots of the characteristic polynomial is a non-trivial process. Given our equations and particular parameter set, there exist two positive equilibrium values of T^* (see **Figure 2**). However, only one of these values result in positive (biologically relevant) equilibrium

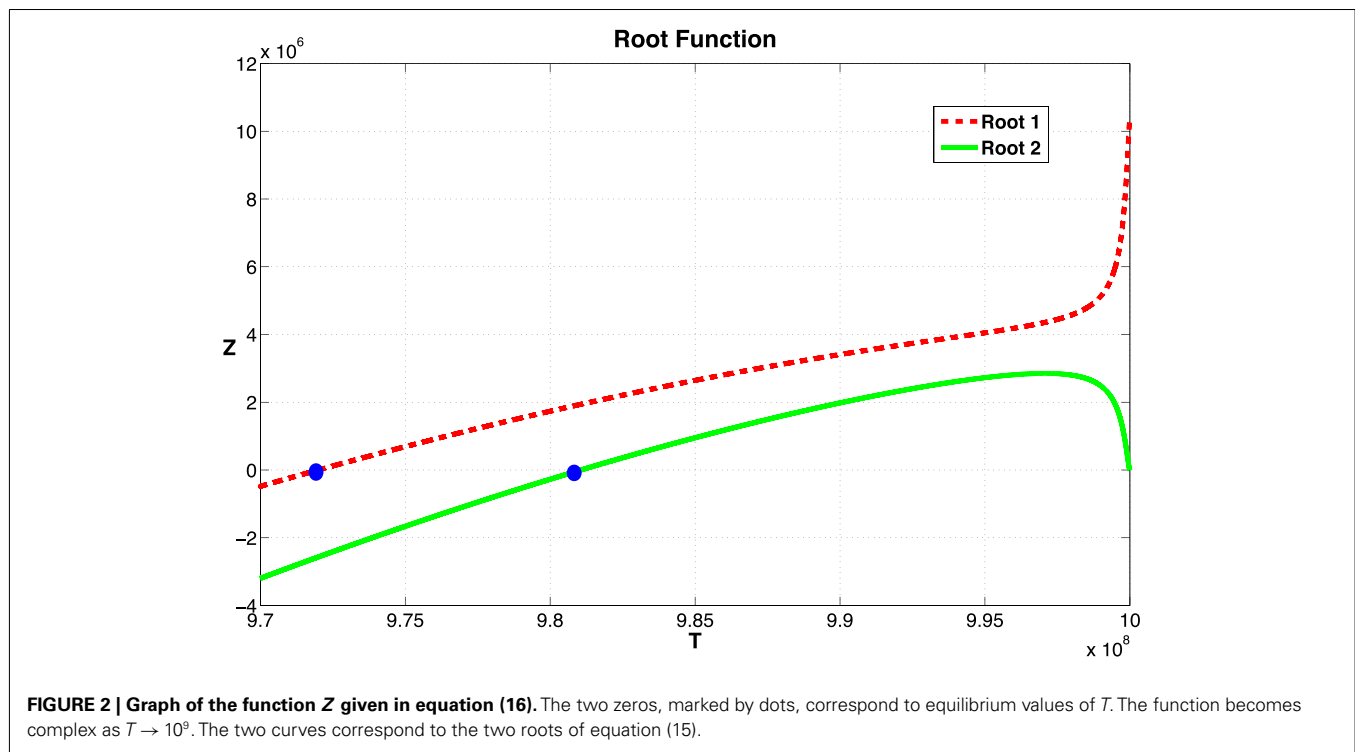


FIGURE 2 | Graph of the function Z given in equation (16). The two zeros, marked by dots, correspond to equilibrium values of T . The function becomes complex as $T \rightarrow 10^9$. The two curves correspond to the two roots of equation (15).

values for all other state variables (see Appendix B). For this biologically relevant equilibrium, in the non-delay (or $\tau = 0$) case, all eigenvalues of the derivative matrix J_0 have negative real part (see Appendix B). Because this is equivalent to the non-delay case, we know that when $\tau = 0$, the non-trivial equilibrium is stable. It is possible for an equilibrium to change stability as the delay increases from zero. In our case numerical simulations suggest that this equilibrium maintains its stability even for large values of the delay, τ (see Figure 3).

3.3. CALIBRATION AND VALIDATION OF DC EFFECT ON TUMOR GROWTH

In this section we discuss the validation of the model. Starting with parameter values estimated in Ludewig et al. (2004), we then calibrate DC and CTL dynamics against the data provided by the experiments in Lee et al. (2007). In the discussion section we present a number of numerical experiments in which we explore the difference between intravenous and intratumoral DC injections, as well as modifications of the dose timings with hypothetically improved treatment schedules.

Experiments carried out in Lee et al. (2007) give tumor growth data, both in the presence and absence of DC treatment. We fit our intrinsic tumor growth parameters to the PBS melanoma growth data provided by Lee et al. (2007). Since specific trafficking parameters to and from the tumor have not been measured, we used the tumor growth data provided to infer the parameter values needed for the tumor compartment DC and CTL dynamics.

In Lee et al. (2007), groups of three 6–8-week-old female C57BL/6 mice were challenged with 5×10^5 B16F10 melanoma cells on day 1, then treated with DC injections starting on days 6, 8, and 10. In separate experiments, DC doses of size 1×10^5 ,

7×10^5 , and 21×10^5 were administered. Lee et al. point out that the largest DC dose is most effective at slowing tumor growth. In fact, according to Lee et al., the largest dose regimen of 21×10^5 DCs injected three times provided up to 41% tumor growth suppression as compared to the control mice. Survival time for these mice was increased by approximately 60%. We note that, even with the most aggressive DC treatment attempted, tumor growth was not completely suppressed.

In Figure 4, left panel, we see the change in tumor volume over 20 days, and compare tumor growth with no DC treatment to growth with varying levels of DC treatment. Simulated DC doses are 1×10^5 , 7×10^5 , and 21×10^5 , reflecting the laboratory experiments of Lee et al. (2007). After a tumor challenge of 5×10^5 B16F10 melanoma cells on day 1, DC injections of the specified doses were then given intratumorally on days 6, 8, and 10. The simulation results fall well within the data ranges provided by Lee et al. (2007).

4. DISCUSSION

In Section 3 we validated and calibrated the model, and analyzed the long-term behavior of the system. We are now in a position to explore hypothetical treatment variations. In this section, we discuss the effects of varying treatment protocols, and possible implications for patients. In Section 4.1, we compare intratumoral DC injections to hypothetical intravenous DC injections. We will see that when injecting the smallest dose of DCs, hypothetical intravenous DC injections are more effective at suppressing tumor growth than are DCs injected directly into the tumor. However, intratumoral injections are more effective than intravenous injections when the highest DC dose is used. In Section 4.2, we explore the effect of modifying dose timings. We will see that fractionated

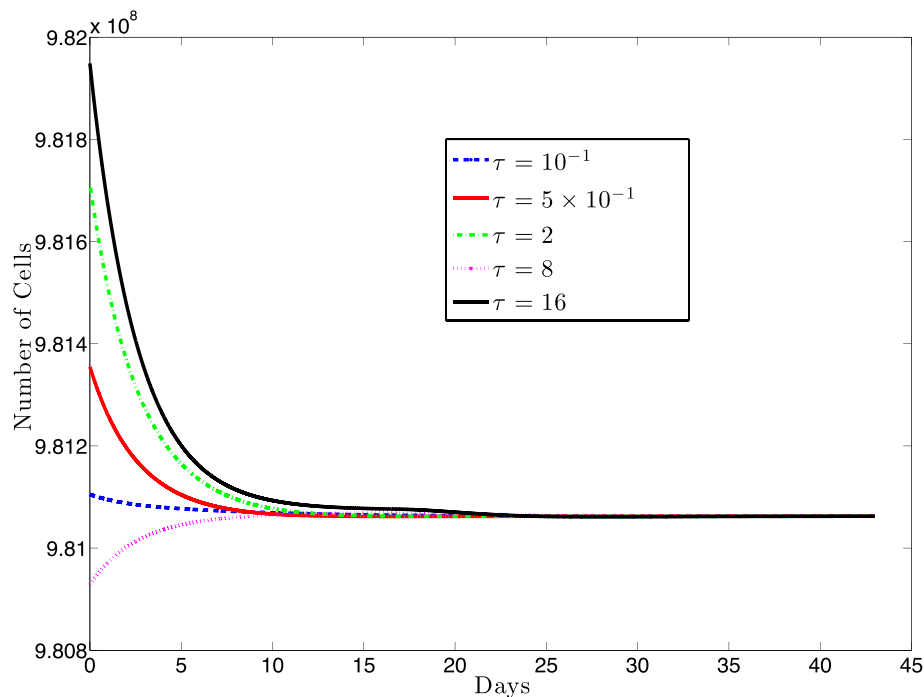


FIGURE 3 | This figure presents a sampling of several simulations for various values of the delay, τ and several different initial conditions (IC). The solid black line (topmost curve) shows a simulation with initial value 9.82×10^8 with $\tau = 16$. The other curves (from top to bottom) are the results of simulations using (τ, IC) pairs:

$(2, 9.817 \times 10^8)$, $(0.5, 9.835 \times 10^8)$, $(0.1, 9.811 \times 10^8)$, $(8, 9.8 \times 10^8)$. For each value of τ , we simulated several initial conditions ranging between 9.80×10^8 and 9.82×10^8 (other simulations not shown) and, in each case, the cell populations approached the same equilibrium value.

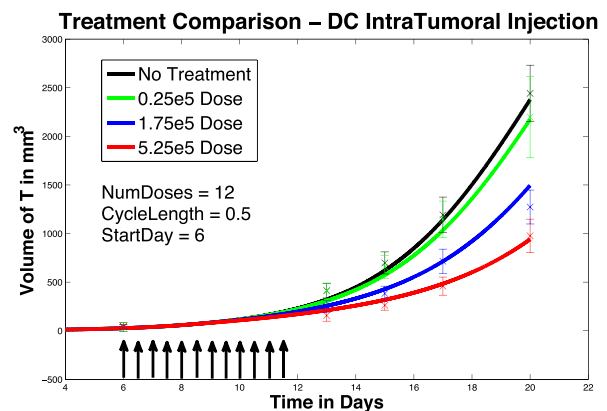
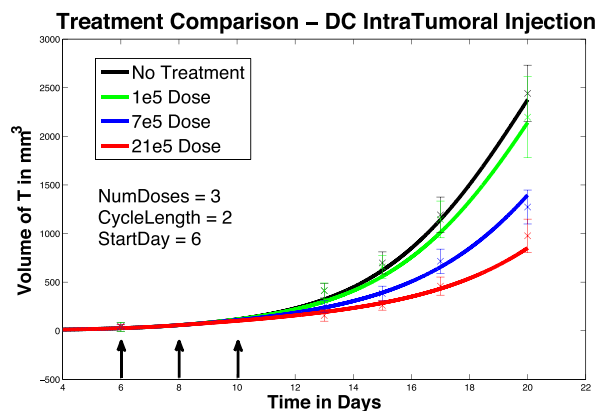


FIGURE 4 | Fractionated dosing comparison. Intratumoral injections. Compare original DC dosing schedule (left panel) to hypothetical fractionated dosing schedule (right panel).

doses that are administered intravenously delay tumor growth significantly. We will see that earlier treatment initiation also helps suppress tumor growth, but more so with intratumoral injections. Up to this point, we have found ways to slow tumor growth by varying dose timing and location, but have not been able to completely eliminate a tumor. In Section 4.3, we explore the effects of prophylactic DC dosing. We find that prophylactic DC dosing actually allows us to eliminate a tumor under the right circumstances.

We will see that as long as the CTL immune response is sufficiently strong, as reflected by the immune strength parameter d , a tumor that is introduced after DCs are injected can be completely suppressed.

4.1. INTRATUMORAL VERSUS INTRAVENOUS TREATMENT

We first compare the effect of treatment at two different injection sites. In the work of Preynat-Seauve et al. (2007) DC

trafficking resulting from different injection sites was compared. They observed that there is a “trapping effect” within the tumor: DCs injected intratumorally do not reach the lymph nodes in significant numbers, indicating that the DCs are “trapped” for a time within the tumor. Note that this trapping is a different phenomenon from the one described in Section 2.1 which referred to activated CTLs being held back in the spleen in the presence of DCs. Preynat-Seauve et al. observed that subcutaneous DC injections resulted in DCs getting to the lymph nodes in greater numbers. In our numerical experiments, we compare intratumoral DC injections (as was done in the Lee et al. (2007) experiments) to intravenous DC injections. We note that intravenous injections and subcutaneous injections are not equivalent, but both approaches do avoid the trapping effect of intratumoral injections.

In **Figure 5**, left panel, we see the effects on melanoma growth of hypothetical intravenous DC injections over a 20 day period. Simulated DC doses of size 1×10^5 , 7×10^5 , and 21×10^5 are administered. The no-treatment tumor growth case is also included for comparison. After a tumor challenge of 5×10^5 B16F10 melanoma cells on day 1, DC injections of the specified doses were then given on days 6, 8, and 10.

It is interesting to note that in these simulations, all three intravenous dose responses appear to be nearly equally effective. There is little difference between low-dose and high-dose intravenous injection outcomes, while there is a significant difference between low-dose and high-dose intratumoral injection outcomes. In addition, when we compare **Figure 5**, left panel, to **Figure 4**, left panel, we see that all three intravenous doses control the tumor growth about as effectively as the mid-sized 7×10^5 intratumoral dose (that is, the intravenous doses are all more effective than the lowest tumor dose, but less effective than the highest tumor dose). The reason for this result can be explained mathematically by the presence of the $MaxD$ term in the model, equation (5). This term limits the rate at which DCs can enter the spleen, which in turn limits how saturated with DCs the spleen can get. Consequently, this limited inflow rate works against any treatment that attempts to send DCs into the spleen too quickly. $MaxD$ term limits DC inflow into the spleen, the total number of DCs in the spleen over $MaxD$ limit. In

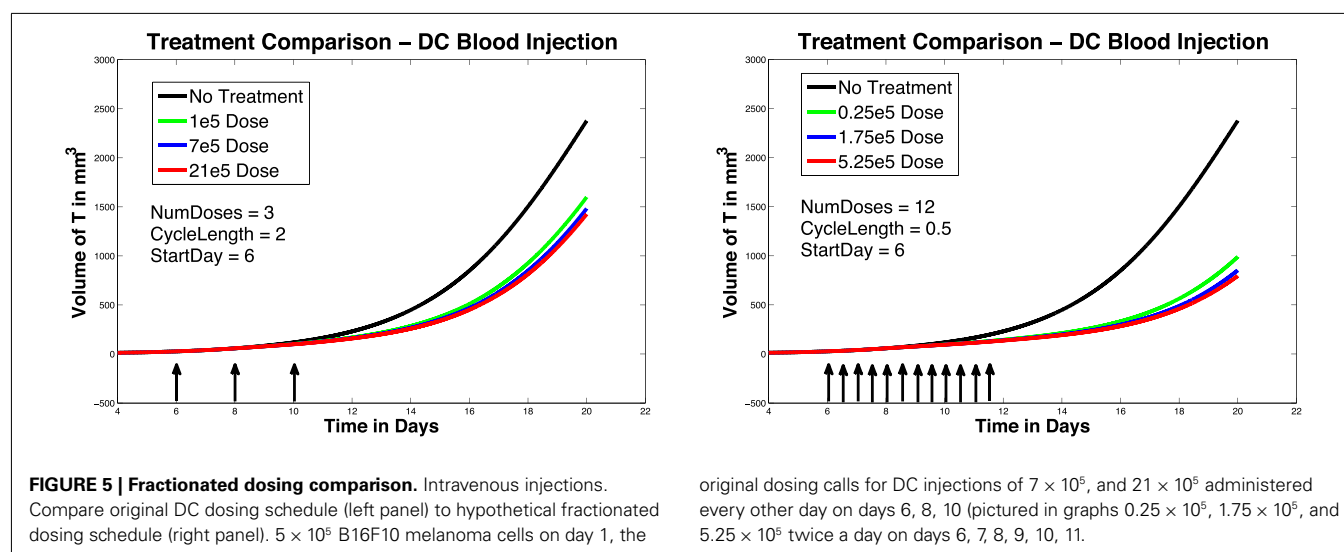
the case of the low-dose injections, the DCs injected intravenously all enter the spleen, since their entry rate is not limited by $MaxD$, while the low intratumoral dose suffers some DC loss from the tumor. This can explain why the low-dose intravenous injection is more effective than the low-dose intratumoral injection. However, in the high-dose injection cases, the number of DCs entering the spleen from the high-dose intravenous treatment is being limited by the $MaxD$ inflow ceiling. On the other hand, the high-dose intratumorally injected DCs enter the spleen more slowly, so even though there is still loss from the tumor, a greater total number of DCs remain in the spleen longer than in the case of the high-dose intravenous injection.

As discussed earlier, the model does not explicitly account for the distance between the spleen and the tumor. If we were to extend the model so that it could apply to human subjects, these distances could vary significantly between individuals. One possible model extension would incorporate the effect of transit times with a partial differential equation that includes a distance L along which cells diffuse and convect.

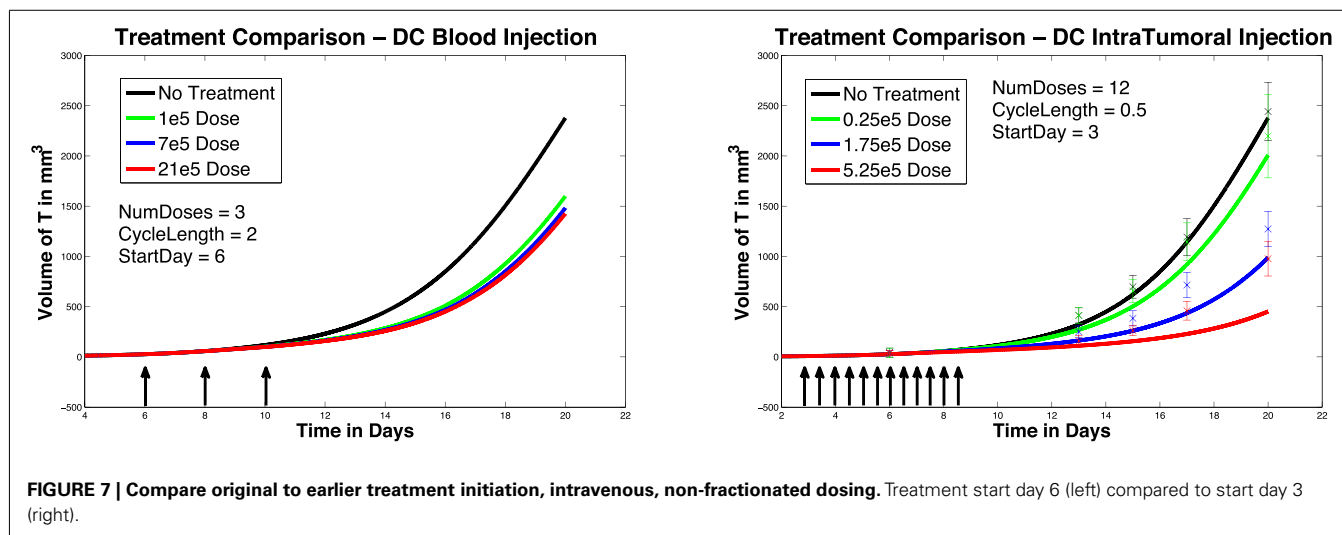
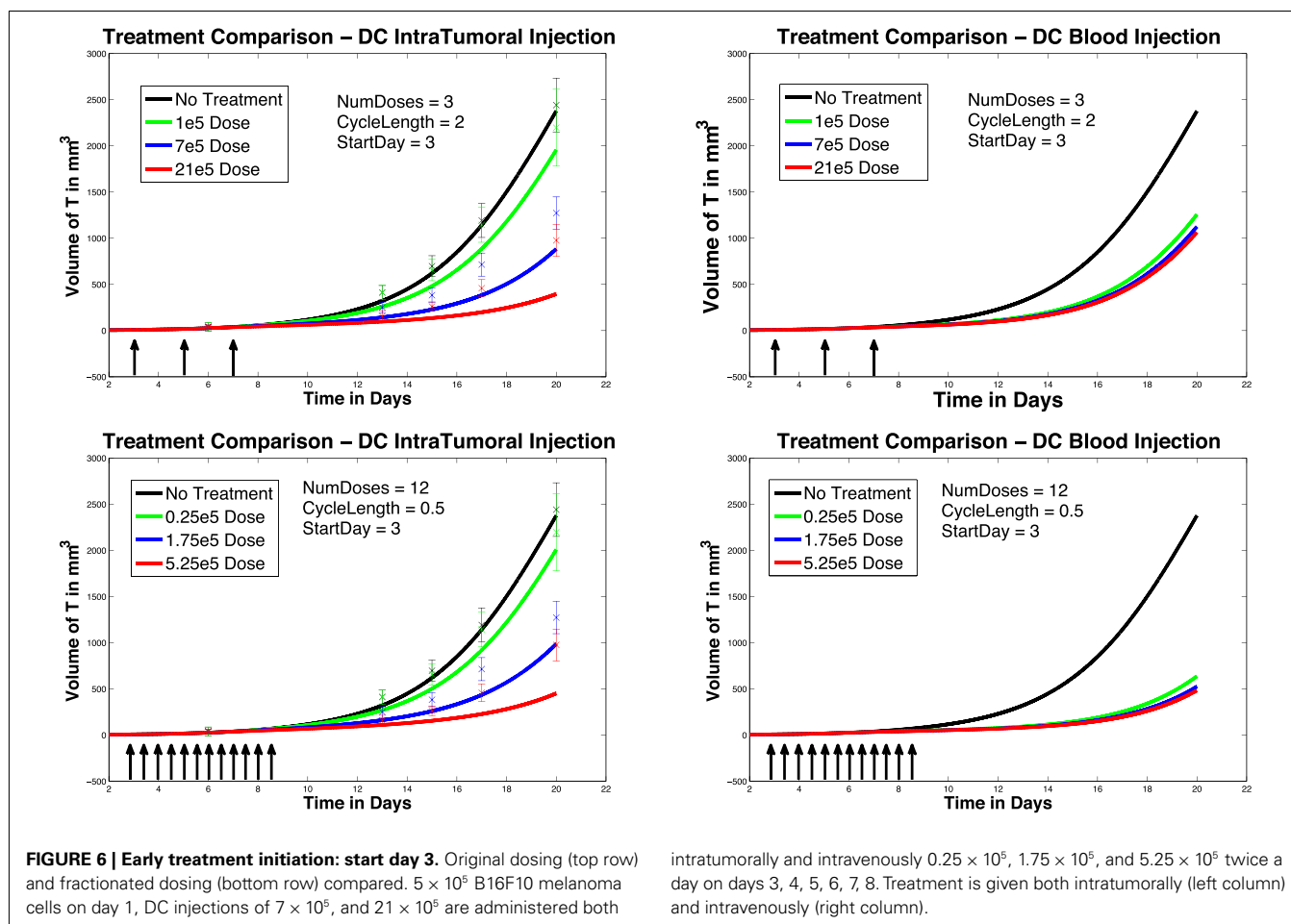
4.2. MODIFIED DOSING

In this section we explore the hypothetical effect of modifying dose timings. We first investigate the effect of administering the same total medication over a 20 day time frame, but with more frequent injections; that is, a *fractionated* dosing schedule. The original dosing schedule starts on day 6, and administers a total of three doses spaced apart by 2 days. The hypothetical fractionated dosing schedule we explore also starts on day 6, but administers doses twice a day at $1/4$ the original dose.

In **Figure 4**, we compare simulated melanoma growth in response to DCs administered according to the original protocol with a hypothetical fractionated dosing schedule. Injections are given intratumorally. The no-treatment tumor growth case is also included for comparison. After a tumor challenge of 5×10^5 B16F10 melanoma cells on day 1, the original dosing calls for DC injections of 1×10^5 , 7×10^5 , and 21×10^5 administered every other day on days 6, 8, 10. The hypothetical fractionated schedule administers doses of 0.25×10^5 , 1.75×10^5 , and



original dosing calls for DC injections of 7×10^5 , and 21×10^5 administered every other day on days 6, 8, 10 (pictured in graphs 0.25×10^5 , 1.75×10^5 , and 5.25×10^5 twice a day on days 6, 7, 8, 9, 10, 11.



5.25×10^5 twice a day on days 6, 7, 8, 9, 10, 11. The total DC treatment administered is the same in the original and fractionated dosing scenarios. It is clear that the fractionated schedule does not improve outcomes in the case of intratumoral injections.

In Figure 5, we again compare the original DC dosing schedule to a fractionated dosing schedule, but we now use intravenous injections. As before, after a tumor challenge of 5×10^5 B16F10 melanoma cells on day 1, the original treatment schedule calls for DCs of doses 1×10^5 , 7×10^5 , and 21×10^5 given every other day

on days 6, 8, 10. The hypothetical fractionated schedule administers doses of 0.25×10^5 , 1.75×10^5 , and 5.25×10^5 twice a day on days 6, 7, 8, 9, 10, 11. The total amount of DC administered is the same in both scenarios. The simulations highlight that although the fractionated schedule does not improve outcomes in the case of intratumoral injections, greater tumor control is observed when the fractionated treatment is administered intravenously. Although tumor growth is slowed with the intravenously dosed fractionated schedule, it is not completely controlled, and the tumor still eventually grows.

We next investigate the effect of starting the DC treatment regimen earlier than day 6. In this case, we compare fractionated DC doses both intratumorally and intravenously, but with treatment initiated on day 3 instead of day 6. The experimental outcomes are pictured in **Figure 6**. After a tumor challenge of 5×10^5 B16F10 melanoma cells on day 1, DC injections of 1×10^5 , 7×10^5 , and 21×10^5 are administered both intratumorally and intravenously on days 3, 5, 7 (pictured in graphs in the top row of **Figure 6**). The hypothetical fractionated schedule (pictured in the second row of **Figure 6**) administers doses of 0.25×10^5 , 1.75×10^5 , and 5.25×10^5 twice a day on days 3, 4, 5, 6, 7, 8. The

total DC treatment administered is the same in all scenarios. We see that in both the intratumoral and intravenous dosing cases, tumor growth is slowed when treatment starts on day 3. However, as before, fractionating the intratumoral doses does not have much effect (bottom left panel), but does slow tumor growth even further when administered intravenously (bottom right panel). Interestingly, the earlier start day has less effect when administered intravenously than it does when administered intratumorally, as can be seen in **Figure 7**. Here we compare non-fractionated intravenous dosing starting on day 6 (left panel) and on day 3 (right panel). Initial values and doses follow the original schedule. The result with fractionated dosing is similar, but is not pictured. We see that there is some improvement with the early start intravenous dosing, but the improvement is not as large as the improvement seen with the intratumoral doses started on day 3, as pictured in the left column of **Figure 6**.

4.3. PROPHYLACTIC VACCINATION

So far, we have been investigating the responses of our system to DC treatment *after* a tumor challenge. However, DC treatments have also been considered to have potential as prophylactic

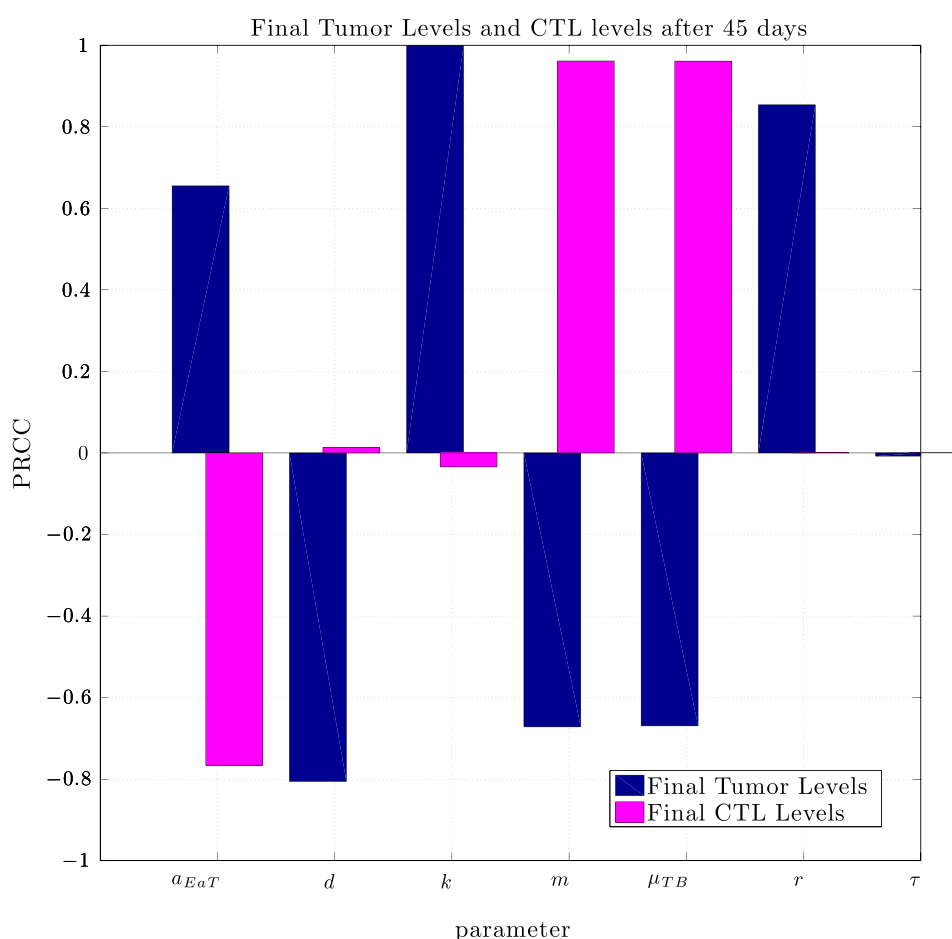


FIGURE 8 | Partially Ranked Correlation Coefficients (PRCC) for two outcomes: final tumor size, and final CTL levels. Parameters with negative PRCCs relative to final tumor levels are negatively correlated with tumor growth. Increasing such parameters would be beneficial to the patient. An increase in parameters with positive PRCCs relative to final tumor levels, or with negative PRCCs relative to final CTL levels could be harmful to the patient.

vaccines. For example, the work of Preynat-Seauve et al. (2007) details a variety of studies on tumor growth in mice inoculated with DC treatments *prior* to a tumor challenge. Although our model has not been constructed specifically to investigate preventative vaccination, we did see some interesting results when simulating such treatment. In one of the experiments from Preynat-Seauve et al. (2007), DC cells from tumors were cultivated and injected into B6C3F1 mice. Vaccination was performed twice, once weekly, with 10^5 tumor-infiltrating dendritic cells. The authors state that this number corresponds to the total number of CD11c+ cells recovered from a single 1 cm-diameter tumor. Two weeks after the last injection, mice were challenged with 2×10^5 melanoma cells (either K1735 or B16F10). According to the study, vaccinated mice were protected for 22 days, whereas naive mice succumbed to the tumor challenge.

Using the same parameter values we determined through fitting to the data in Lee et al. (2007), a simulation of pre-vaccination

with mature DCs showed no particular benefit. In order to determine the sensitivity of the system to a change in parameters we used the Latin Hypercube sampling method described in Blower and Dowlatabadi (1994) to compare simulations with 50,000 randomly generated parameter sets. The effect of a change in parameter values on tumor size and CTL levels after 45 days was quantified by calculating the partially ranked correlation coefficients for each parameter that showed a monotonic relationship to the outcomes. The results are shown in Figure 8.

The sensitivity analysis indicates that tumor levels are sensitive to the parameters d , m , and μ_{TB} . Since d , the fractional tumor kill rate by CTLs, has the potential to be manipulated through treatments (*c.f.* Chakraborty et al., 2003), we suggest that this parameter might play an important role in the vaccine's effectiveness. In subsequent simulations, when d was increased we observed a protective effect of prophylactic vaccination with DCs. In Figure 9 we see tumor growth both without and with DC vaccination with

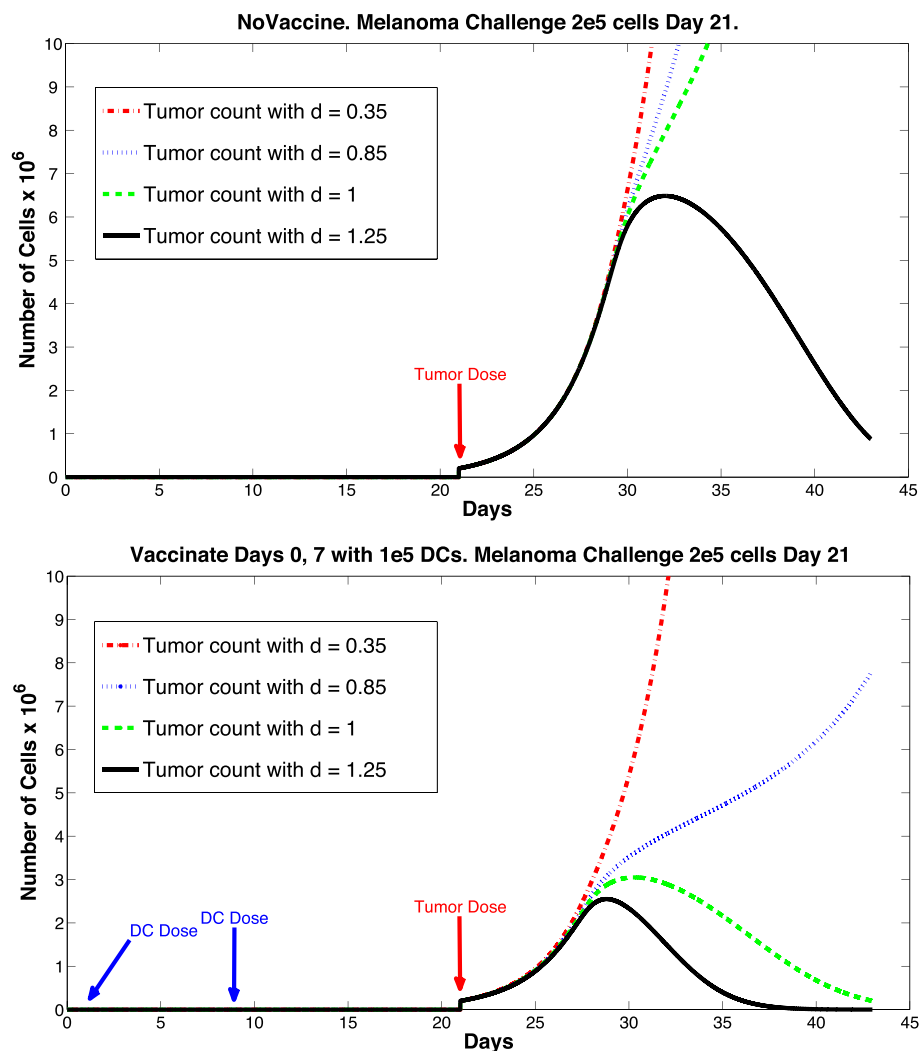


FIGURE 9 | Prophylactic vaccination and the effect of varying immune strength parameter d . Top panel, no vaccine. Bottom panel, vaccinate with DC treatments, days 0 and 7, 1×10^5 DCs per dose. Tumor challenge

on day 21, with 2×10^5 tumor cells. Dosing follows Preynat-Seauve et al. (2007) experiment. With $d = 1$, tumor is controlled as a result of vaccination.

$d = 0.35, 0.85, 1.0$, and 1.25 . The results for $d = 1$ are what interest us. When $d = 1.25$, the immune system is sufficiently effective to suppress tumor growth without treatment intervention. In contrast, when $d = 1$ or less, then without DC vaccination, the tumor grows rapidly. However, if the tumor challenge has been preceded by two doses of a DC vaccine, then even when $d = 1$, tumor growth is suppressed. We also extended the simulations out 165 days after the tumor challenge (not pictured). For $d \geq 1$, the tumor shrank to zero after vaccination and did not regrow. Numerically, this indicates that the zero tumor equilibrium is stable.

5. FUTURE DIRECTIONS

In this paper, we presented a model of Dendritic Cell trafficking and interaction with a tumor cell population. With this model, we achieved simulation outcomes that quantitatively match published data from studies on mice (Lee et al., 2007) that first were challenged with tumor and subsequently treated with DC therapy. We then used the model to test a wider variety of hypothetical

treatment scenarios. In addition, we examined the effects of prophylactic vaccination with DCs. The simulation results from the prophylactic vaccination scenarios that were discussed in the previous section are preliminary, but do show qualitative agreement with a different set of data from published laboratory experiments on mice (Preynat-Seauve et al., 2007).

In future work, we will investigate how to scale this model to reflect tumor growth and DC trafficking in humans. This will involve a careful examination of the effect of distances between the tumor site and the lymph organs. In addition, we will further investigate the effects of prophylactic vaccination. Our goal is to determine which parameters and model terms need tuning to achieve quantitative as well as qualitative outcomes that reflect the laboratory data.

ACKNOWLEDGMENTS

Ami Radunskey is partially supported by NSF grant DMS-1016136.

REFERENCES

- Blower, S. M., and Dowlatabadi, H. (1994). Sensitivity and uncertainty analysis of complex models of disease transmission: an HIV model, as an example. *Int. Stat. Rev.* 62, 229–243.
- Boon, T., Coulie, P. G., Van den Eynde, B. J., and van der Bruggen, P. (2006). Human T cell response against melanoma. *Annu. Rev. Immunol.* 24, 175–208.
- Cappuccio, A., Elishmereni, M., and Agur, Z. (2006). Cancer immunotherapy by interleukin-21: potential treatment strategies evaluated in a mathematical model. *Cancer Res.* 66, 7293–7300.
- Chakraborty, M., Abrams, S. I., Camphausen, K., Liu, K., Scott, T., Norman Coleman, C., et al. (2003). Irradiation of tumor cells up-regulates Fas and enhances CTL lytic activity and CTL adoptive immunotherapy. *J. Immunol.* 170, 6338–6347.
- Cheever, M. A. (2011). PROVENGE (sipuleucel-T) in prostate cancer: the first FDA-approved therapeutic cancer vaccine. *Clin. Cancer Res.* 17, 3520–3526.
- de Pillis, L. G., Fister, K. R., Gu, W., Collins, C., Daub, M., Gross, D., et al. (2009). Mathematical model creation for cancer chemotherapeutic. *Comput. Math. Methods Med.* 10, 165–184.
- de Pillis, L. G., Gu, W., and Radunskey, A. E. (2006). Mixed immunotherapy and chemotherapy of tumors: modeling, applications and biological interpretations. *J. Theor. Biol.* 238, 841–862.
- de Pillis, L. G., and Radunskey, A. (2003). “A mathematical model of immune response to tumor invasion,” in *Computational Fluid and Solid Mechanics 2003*, ed. K. J. Bathe (Elsevier Science Ltd), 1661–1668.
- de Pillis, L. G., Radunskey, A. E., and Wiseman, C. L. (2005). A validated mathematical model of cell-mediated immune response to tumor growth. *Cancer Res.* 65, 7950–7958.
- de Pillis, L. G., Radunskey, A. E., and Wiseman, C. L. (2007). Comment on: a validated mathematical model of cell-mediated immune response to tumor growth. *Cancer Res.* 67, 8420.
- DeMatos, P., Abdel-Wahab, Z., Vervaeke, C., Hester, D., and Seigler, H. (1998). Pulsing of dendritic cells with cell lysates from either B16 melanoma or MCA-106 fibrosarcoma yields equally effective vaccines against B16 tumors in mice. *J. Surg. Oncol.* 68, 79–91.
- Diefenbach, A., Jensen, E. R., Jamieson, A. M., and Raulet, D. H. (2001). Rael and H60 ligands of the NKG2D receptor stimulate tumour immunity. *Nature* 413, 165–171.
- Fields, R. C., Shimizu, K., and Mule, J. J. (1998). Murine dendritic cells pulsed with whole tumor lysates mediate potent antitumor immune responses in vitro and in vivo. *Proc. Natl. Acad. Sci. U.S.A.* 95, 9482–9487.
- Lee, T.-H., Cho, Y.-H., and Lee, M.-G. (2007). Larger numbers of immature dendritic cells augment an anti-tumor effect against established murine melanoma cells. *Biotechnol. Lett.* 29, 351–357.
- Ludewig, B. B., Krebs, P., Junt, T., Metters, H., Ford, N. J., Anderson, R. M., et al. (2004). Determining control parameters for dendritic cell-cytotoxic t lymphocyte interaction. *Eur. J. Immunol.* 34, 2407–2418.
- Pilon-Thomas, S., Verhaegen, M. E., and Mulé, J. J. (2004). Dendritic cell-based therapeutics for breast cancer. *Heart Dis.* 20, 65–71.
- Preynat-Seauve, O., Contassot, E., Schuler, P., French, L. E., and Huard, B. (2007). Melanoma-infiltrating dendritic cells induce protective antitumor responses mediated by t cells. *Melanoma Res.* 17, 169–176.
- Shinagawa, N., Yamazaki, K., Tamura, Y., Imai, A., Kikuchi, E., Yokouchi, H., et al. (2008). Immunotherapy with dendritic cells pulsed with tumor-derived gp96 against murine lung cancer is effective through immune response of CD8+ cytotoxic T lymphocytes and natural killer cells. *Cancer Immunol. Immunother.* 57, 165–174.
- Taquet, N., Roberts, L. K., Burkeholder, S., Phipps, P., Finholt, J., Walters, L., et al. (2008). Dendritic cell vaccine production facility: from design to operation. *Bioprocess. J.* 7, 28–33.
- Trefzer, U., Herberth, G., Wohlan, K., Milling, A., Thiemann, M., Sharav, T., et al. (2005). Tumour-dendritic hybrid cell vaccination for the treatment of patients with malignant melanoma: immunological effects and clinical results. *Vaccine* 23, 2367–2373.
- Yamaguchi, S., Tatsumi, T., Takehara, T., Sakamori, R., Uemura, A., Mizushima, T., et al. (2007). Immunotherapy of murine colon cancer using receptor tyrosine kinase epha2-derived peptide-pulsed dendritic cell vaccines. *Cancer* 110, 1469–1477.

Conflict of Interest Statement: The authors declare that the research was conducted in the absence of any commercial or financial relationships that could be construed as a potential conflict of interest.

Received: 03 December 2012; accepted: 02 March 2013; published online: 19 March 2013.

Citation: DePillis L, Gallegos A and Radunskey A (2013) A model of dendritic cell therapy for melanoma. *Front. Oncol.* 3:56. doi: 10.3389/fonc.2013.00056

This article was submitted to *Frontiers in Molecular and Cellular Oncology*, a specialty of *Frontiers in Oncology*.

Copyright © 2013 DePillis, Gallegos and Radunskey. This is an open-access article distributed under the terms of the Creative Commons Attribution License, which permits use, distribution and reproduction in other forums, provided the original authors and source are credited and subject to any copyright notices concerning any third-party graphics etc.

APPENDIX

A. PARAMETER VALUES

The parameters are described in **Table A1**. Refer to Ludewig et al. (2004) for justification and confidence intervals for the parameters measured in that study.

Table A1 | Parameter values.

Parameter name	Description	Value	Units	Reference
a_D	Natural death rate of DCs	0.2310	1/day	Ludewig et al. (2004)
a_{E_S}	Death rate of activated CTLs in spleen	0.1199	1/day	Ludewig et al. (2004)
a_{E_T}	Death rate of activated CTLs in tumor compartment	0.462	1/day	de Pillis et al. (2006)
a_{E_m}	Natural death rate of memory CTLs	0.01	1/day	Ludewig et al. (2004)
α	Component of μ_{BTE}	1	Cell	
$b_a = \tilde{b}_a / Q_{spleen}$	Per cell activation rate of memory CTLs by DCs	0.01	1/(cell · day)	
\tilde{b}_a	Activation rate of memory CTL concentration by DCs	1×10^{-3}	ml/(cell · day)	Ludewig et al. (2004)
$b_{DE} = \tilde{b}_{DE} / Q_{spleen}$	Per cell elimination rate of DCs by activated CTLs	1.3×10^{-6}	1/cell · day	
\tilde{b}_{DE}	Elimination rate of DCs by activated CTLs (per concentration)	1.3×10^{-7}	ml/cell/day	Ludewig et al. (2004)
b_p	Maximal expansion factor of activated CTL	85	1/day	Ludewig et al. (2004)
c	Rate at which activated CTLs are inactivated by tumor cells	9.42×10^{-12}	1/(cell · day)	de Pillis et al. (2006)
d	Maximum fractional tumor kill by CTLs	0.35	1/day	Fit to Lee et al. (2007)
E_{naive}	Number of naive CTL cells contributing to primary clonal expansion	370	Cells	Ludewig et al. (2004)
k	Carrying capacity of tumor	1.0×10^9	Cells	Fit to Lee et al. (2007)
l	Immune strength scaling exponent	$\frac{2}{3}$	Unitless	<i>Ad hoc</i> value
m	Maximum recruitment rate of DCs to tumor site	2.4388×10^4	Cells/day	Fit to Lee et al. (2007)
μ_B	Rate of DC emigration from blood. Note: $\mu_B = \mu_{BS} + 24(\mu_{BLi} + \mu_{BLu} + \mu_{BO})$, the sum of DC outflow to the spleen, liver, lung, and other parts of the body	27.072	1/day	Ludewig et al. (2004)
$\mu_{BB} = \tilde{\mu}_{BB} - \mu_{BL}$	Scaled and shifted elimination (clearance and extravasation) rate of CTL from blood	5.7	1/day	
$\tilde{\mu}_{BB}$	Total elimination rate of CTL from blood	5.8	1/day	Ludewig et al. (2004)
μ_{BL}	Transfer rate of DCs from the blood to the liver	0.1	1/day	Ludewig et al. (2004)
μ_{BS}	Transfer rate of DCs from blood to spleen	2.832	1/day	Ludewig et al. (2004)
$\mu_{BSE} = \tilde{\mu}_{BSE} Q_{spleen} / Q_{blood}$	Scaled transfer rate of activated CTLs from blood to spleen	7.33×10^{-4}	1/day	
$\tilde{\mu}_{BSE}$	Transfer rate of activated CTLs from blood to spleen	0.022	1/day	Ludewig et al. (2004)
$\mu_{BTE} = \mu_{BB} \frac{T}{\alpha + T}$	T-dependent rate at which effector cells enter the tumor compartment from the blood	Calculated	1/day	
μ_{LB}	Transfer rate of DCs from the liver to the blood	0.51	1/day	Ludewig et al. (2004)
μ_{SB}^{Normal}	Normal DC transfer rate from spleen to blood	0.512	1/day	Ludewig et al. (2004)
μ_{SB}^*	DC reduced transfer rate from spleen to blood	0.012	1/day	Ludewig et al. (2004)
μ_{TB}	Rate of transfer of DC from tumor to blood	0.0011	1/day	<i>Ad hoc</i> value

(Continued)

Table A1 | Continued

Parameter name	Description	Value	Units	Reference
q	Value of T necessary for half-maximal DC recruitment	100	Cells	Fit to Lee et al. (2007)
Q_{blood}	Murine blood volume	3	ml	Ludewig et al. (2004)
Q_{liver}	Murine liver volume	0.5	ml	Ludewig et al. (2004)
Q_{spleen}	Murine spleen volume	0.1	ml	Ludewig et al. (2004)
r	Tumor growth rate	0.3954	1/day	Fit to Lee et al. (2007)
r_{am}	Reversion rate of activated CTL to memory CTL	0.01	1/day	Ludewig et al. (2004)
s	Value of $(E_{tumor}^a/T)^I$ necessary for half-maximal activated CTL toxicity	1.4	Unitless	Fit to Lee et al. (2007)
τ_D	Duration of preprogramed CTL divisions	0.5	Days	Fit to Lee et al. (2007)
$\theta_D = \tilde{\theta}_D Q_{spleen}$	Scaled threshold in DC density in the spleen for half-maximal proliferation rate of CTL	212	Cell	
$\tilde{\theta}_D$	Threshold in DC density in the spleen for half-maximal proliferation rate of CTL	2.12×10^3	Cell/ml	Ludewig et al. (2004)
$\theta_{shut} = \tilde{\theta}_{shut} Q_{spleen}$	Scaled threshold in DC density in the spleen for half-maximal transfer rate from spleen to blood	1.3	Cells	Ludewig et al. (2004)
$\tilde{\theta}_{shut}$	Threshold in DC density in the spleen for half-maximal transfer rate from spleen to blood	13	Cells/ml	Ludewig et al. (2004)

B. STABILITY ANALYSIS: JACOBIANS

Recall that J_0 is the Jacobian for the non-delayed system, in other words, its entries are given by $J_0(i, j) = dF_i/dx_j$, and $J_\tau(i, j) = dF_i/dz_j$ is the Jacobian for the delayed system. For computational ease, we rename the state variables as follows:

$$\begin{aligned} D_{\text{blood}} &= x_1, & D_{\text{spleen}} &= x_2, & E_{\text{blood}}^a &= x_3, \\ E_{\text{spleen}}^a &= x_4, & E_{\text{blood}}^m &= x_5, & E_{\text{spleen}}^m &= x_6, \\ E_{\text{tumor}}^a &= x_7, & T &= x_8, & D_{\text{tumor}} &= x_9. \end{aligned}$$

There are only two delayed variables:

$$D_{\text{spleen}}(t - \tau) = z_2, \quad E_{\text{spleen}}^a(t - \tau) = z_4.$$

We perform the stability analysis without any treatment, i.e., $v_{\text{blood}} = v_{\text{tumor}} = 0$. The non-zero elements of J_0 are calculated to be:

$$\begin{aligned} J_0(1, 1) &= -\mu_B \\ J_0(1, 9) &= \mu_{TB} \\ J_0(2, 1) &= -\mu_{BS} e^{\left(\frac{-\mu_{BS} x_1}{\text{Max } D}\right)} \\ J_0(2, 2) &= -a_D - b_{DE} x_4 \\ J_0(2, 4) &= -b_{DE} x_2 \\ J_0(3, 2) &= \frac{-\Delta \mu}{\theta_{\text{shut}}} \frac{x_4}{(1 + x_2/\theta_{\text{shut}})^2} \\ J_0(3, 3) &= -\mu_{BB}, \\ J_0(3, 4) &= \mu_{SB}(D_{\text{spleen}}), \\ J_0(4, 2) &= \frac{-\Delta \mu}{\theta_{\text{shut}}} \frac{x_4}{(1 + x_2/\theta_{\text{shut}})^2} + b_a x_6 \\ J_0(4, 3) &= \mu_{BSE} \\ J_0(4, 4) &= -\mu_{SB}(D_{\text{spleen}}) - a_{E_a s} - r_{am} \\ J_0(4, 6) &= b_a x_2 \\ J_0(5, 2) &= \frac{-\Delta \mu}{\theta_{\text{shut}}} \frac{x_6}{(1 + x_2/\theta_{\text{shut}})^2} \\ J_0(5, 5) &= -\mu_{BB}, J_0(5, 6) = \mu_{SB}(D_{\text{spleen}}) \\ J_0(6, 2) &= -\left(b_a - \frac{\Delta \mu}{\theta_{\text{shut}}} \frac{1}{(1 + x_2/\theta_{\text{shut}})^2}\right) x_6 \\ J_0(6, 4) &= r_{am} \end{aligned}$$

$$J_0(6, 5) = \mu_{BSE}$$

$$J_0(6, 6) = -(a_{E_m} + b_a x_2 + \mu_{SB}(D_{\text{spleen}}))$$

$$J_0(7, 3) = \mu_{BTE}(T)$$

$$J_0(7, 7) = -a_{E_a} T - c x_8$$

$$J_0(7, 8) = \frac{\mu_{BB} \alpha}{(\alpha + x_8)^2} x_3 - c x_7$$

$$J_0(8, 7) = \frac{d s l (x_7/x_8)^{l-1}}{\left\{s + (x_7/x_8)^l\right\}^2}$$

$$J_0(8, 8) = r - \frac{2 r x_8}{k} - \frac{d s l (x_7/x_8)^l}{\left\{s + (x_7/x_8)^l\right\}^2} + \frac{d (x_7/x_8)^l}{s + (x_7/x_8)^l}$$

$$J_0(9, 8) = \frac{m q}{(q + x_8)^2}$$

$$J_0(9, 9) = -(\mu_{TB} + a_D)$$

where $\mu_{BTE}(T) = \mu_{BB} B \frac{T}{\alpha + T}$, and $\mu_{SB}(D_{\text{spleen}}) = \mu_{SB}^* + \frac{\Delta \mu}{1 + D_{\text{spleen}}/\theta_{\text{shut}}}$.

There are only two non-zero elements of J_τ :

$$J_\tau(5, 4) = b_p \frac{z_5 \theta_D}{(\theta_D + z_4)^2}, \quad J_\tau(5, 5) = \frac{b_p x_4}{\theta_D + z_4}.$$

As referenced in the text, there are two positive tumor equilibrium values, T^* :

$$T_1^* \approx 9.72 \times 10^8; \quad T_2^* \approx 9.81 \times 10^8.$$

However, the first one results in a non-biologically relevant equilibria as it corresponds to a negative equilibrium value for x_2, x_4, x_5 . For the non-delay case (i.e., $\tau = 0$), there are no J_τ elements. Thus we consider the eigenvalues of J_0 . At the positive (biologically relevant) equilibria, the eigenvalues of J_0 , as computed via MatLab to four decimal places, are

$$\vec{e} = [-27.0720, -11.1021, -0.6765, -0.4719, -0.3918, \\ -0.3092, -0.2321, -5.7000, -5.7000].$$

Each eigenvalue clearly satisfies $\mathcal{R}(\lambda) < 0$, indicating that, in the non-delay case, the biologically relevant equilibrium is stable.



The role of tumor tissue architecture in treatment penetration and efficacy: an integrative study

Katarzyna A. Rejniak^{1,2*}, Veronica Estrella³, Tingan Chen⁴, Allison S. Cohen³, Mark C. Lloyd^{4,5} and David L. Morse^{2,3,6}

¹ Integrated Mathematical Oncology, H. Lee Moffitt Cancer Center and Research Institute, Tampa, FL, USA

² Department of Oncologic Sciences, College of Medicine, University of South Florida, Tampa, FL, USA

³ Department of Cancer Imaging and Metabolism, H. Lee Moffitt Cancer Center and Research Institute, Tampa, FL, USA

⁴ Analytic Microscopy Core Facility, H. Lee Moffitt Cancer Center and Research Institute, Tampa, FL, USA

⁵ Department of Biological Sciences, University of Illinois at Chicago, Chicago, IL, USA

⁶ Department of Physics, College of Arts and Sciences, University of South Florida, Tampa, FL, USA

Edited by:

Heiko Enderling, Tufts University, USA

Reviewed by:

Luisa Lanfranccone, European Institute of Oncology, Italy

Yi Jiang, Los Alamos National Laboratory, USA

*Correspondence:

Katarzyna A. Rejniak, Integrated Mathematical Oncology, H. Lee Moffitt Cancer Center and Research Institute, 12902 Magnolia Drive, SRB-4 24000G, Tampa, FL 33612, USA.

e-mail: kasia.rejniak@moffitt.org

Despite the great progress that has been made in understanding cancer biology and the potential molecular targets for its treatment, the majority of drugs fail in the clinical trials. This may be attributed (at least in part) to the complexity of interstitial drug transport in the patient's body, which is hard to test experimentally. Similarly, recent advances in molecular imaging have led to the development of targeted biomarkers that can predict pharmacological responses to therapeutic interventions. However, both the drug and biomarker molecules need to access the tumor tissue and be taken up into individual cells in concentrations sufficient to exert the desired effect. To investigate the process of drug penetration at the mesoscopic level we developed a computational model of interstitial transport that incorporates the biophysical properties of the tumor tissue, including its architecture and interstitial fluid flow, as well as the properties of the agents. This model is based on the method of regularized Stokeslets to describe the fluid flow coupled with discrete diffusion-advection-reaction equations to model the dynamics of the drugs. Our results show that the tissue cellular porosity and density influence the depth of penetration in a non-linear way, with sparsely packed tissues being traveled through more slowly than the denser tissues. We demonstrate that irregularities in the cell spatial configurations result in the formation of interstitial corridors that are followed by agents leading to the emergence of tissue zones with less exposure to the drugs. We describe how the model can be integrated with *in vivo* experiments to test the extravasation and penetration of the targeted biomarkers through the tumor tissue. A better understanding of tissue- or compound-specific factors that limit the penetration through the tumors is important for non-invasive diagnoses, chemotherapy, the monitoring of treatment responses, and the detection of tumor recurrence.

Keywords: interstitial transport, tissue penetration, drug/biomarker efficacy, regularized Stokeslets Method, intravital fluorescence microscopy, mouse xenograft tumor model, tumor targeted agent, fluorescence molecular imaging

INTRODUCTION

Systemic chemotherapy is one of the main anticancer treatments used for most kinds of tumors that are clinically diagnosed. However, with a few exceptions, such as the treatment of chronic myeloid leukemia with *imatinib*, the drugs that have shown high promise for a cure in laboratory tests did not prove to be as successful in the clinical setting. In fact, only about 10% of the drugs that enter clinical trials are approved by the FDA (Peters, 2010), and the majority of potentially therapeutic compounds fail in Phase II of the clinical trials. This means that the drugs are not effective in treating the disease, even though they were potent in cell-culture assays and animal model systems (Peters, 2010). One of the reasons for the Phase II drug failures may be attributed to the fact that experimental models do not recreate the process of interstitial drug transport in the tissues in the same way that it occurs in the

patient's body. It is beyond question that even the most effective anticancer drug will not show high efficacy if it cannot reach all of the tumor cells in concentrations sufficient to exert a therapeutic effect. Moreover, it has been suggested (Minchinton and Tannock, 2006) that the poor penetration of the tumor tissue by drug particles may leave untreated certain cell populations capable of initiating tumor recurrence and/or resistance.

Recent advances in molecular imaging allow for the development of targeted imaging agents that are specific in binding to intracellular or extracellular targets (biomarkers). They can predict the pharmacological responses to therapeutic interventions and are being used during the diagnoses to determine the state of the disease and to plan (personalized) treatment. Imaging biomarkers that allow for the prediction and monitoring of patient responses to a given therapy are becoming an essential component

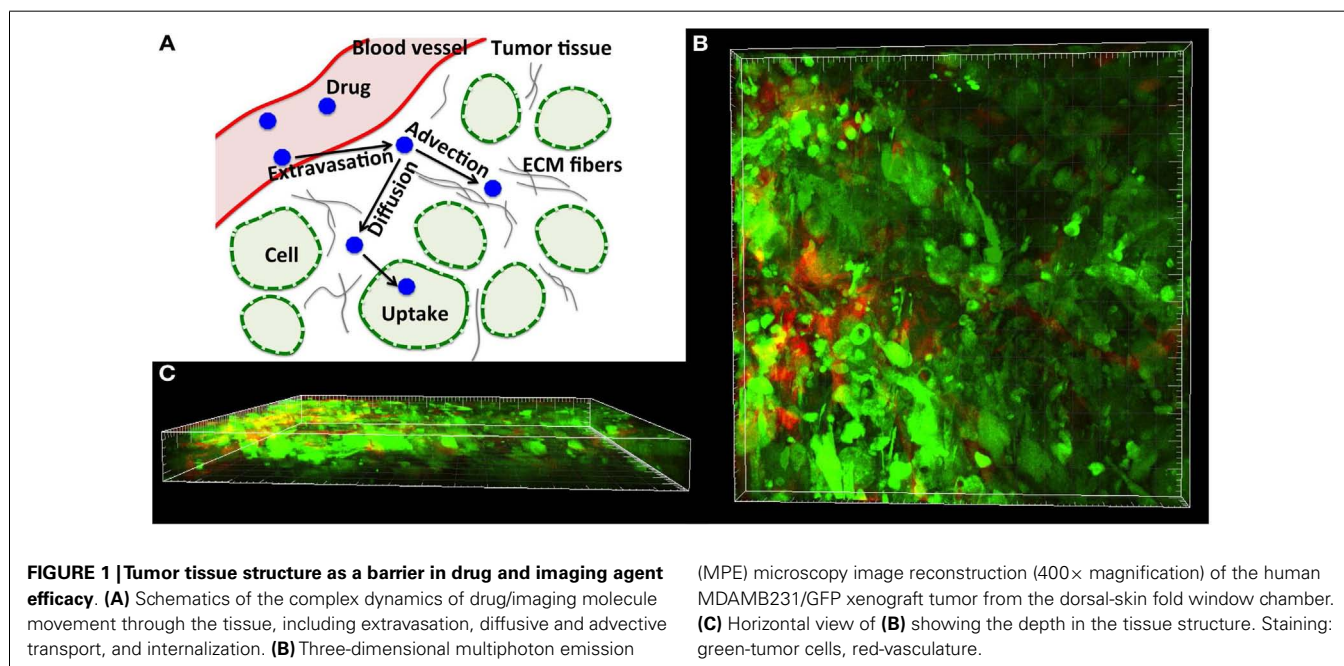
of drug development. Moreover, they can reduce the number of patients needed to test novel targeted therapeutic agents by identifying non-responders early-on. However, the transport of such biomarkers through the tumor tissue faces similar issues. In order to be a useful predictor, targeted imaging agents need to access the tumor tissue space and then be retained by individual cells through binding and uptake (Morse and Gillies, 2010).

Drug penetration refers to the movement of drug molecules from the bloodstream into the various tissues of the body (Minchinton and Tannock, 2006). After a drug is absorbed into the bloodstream, it rapidly circulates through the body; however, both the spatial and temporal distributions of the drug molecules may be different in different tissues types and the extent of the drug/biomarker particle penetration into the tissue depends on both the biochemical properties of the particles and biophysical properties of the tissues. For example, drugs that dissolve in water (water-soluble drugs) tend to stay in the bloodstream and in the fluid that surrounds the cells (interstitial fluid). Particles have different sizes and molecular weights and thus their penetration into the tumor tissue may depend on whether their transport through the interstitial space is dominated by their random motion (diffusion) or motion due to the fluid flow (advection) (Jain, 1987; Gade et al., 2009; Schmidt and Wittrup, 2009). The interstitial transport of drug molecules may also be affected by the tumor cellular structure (Grantab et al., 2006) and extracellular matrix (ECM) assembly (Netti et al., 2000). We are particularly interested in the cellular architecture of tumor tissue, which may be highly unorganized, irregular, and heterogeneous (Figure 1), and in the role that the size of the extracellular space between the cells plays in interstitial transport by both diffusion and interstitial fluid advection. We will investigate the complex interplay between these processes of extracellular transport and drug penetration.

Most *in silico* models applied to drug development use bio-statistics and bio-informatics methods to screen large numbers of therapeutic compounds. The pharmacokinetic (PK) properties of

the drugs are then determined by fitting the actual data to a theoretical compartmental model, followed by rigorous “goodness-of-fit” test statistics (Michelson et al., 2006). Although numerous computational methods have been developed for the *in silico* testing of various properties of drug particles (known under the acronym ADME-T: absorption, distribution, metabolism, excretion, and toxicity (Beresford et al., 2002; Boobis et al., 2002; Ekins and Rose, 2002; Kerns and Di, 2008; Huynh et al., 2009) they do not consider the spatial aspects of drug PKs and treat all organs as well-mixed compartments neglecting their natural heterogeneities. Thus, the poor penetration of the tumor tissue as a limiting factor for drug efficacy is not currently included in a typical ADME-T protocol.

Mathematical PK models that include tissue transport phenomena are usually defined as continuous mixture models with the tumor tissue being represented by a homogeneous material (Baxter and Jain, 1989; Jackson and Byrne, 2000; Zhao et al., 2007; Sinek et al., 2009; Shipley and Chapman, 2010). These models showed importance of the kinetics of the drug supply from the blood system, as well as its diffusive and advective transport, on the concentration profiles of biochemical compounds, and the significant impact of nutrient distribution on the drug’s therapeutic efficacy. However, they have not addressed the heterogeneity of the tumor cells, or the transport of individual drug/biomarker particles. These aspects will be incorporated in the mechanistic model described in this paper that is based on the fluid-structure interaction method of the regularized Stokeslets (Cortez, 2001). We take into account, explicitly, the cellular structure of the tumor tissue, and investigate how the tumor tissue composition influences the interstitial transport of chemical compounds. In particular, we analyze the relationship between the cellular porosity and/or cellular density of the tissue at the depth at which the drug/biomarker particles penetrate it. Our computational results are also compared to the experimental data showing the differences in the penetration and uptake of targeted imaging agents in tumors that express



the cell-surface receptor of interest (positive tumors) or not (negative tumors). This study will offer an insight into the potential mechanisms preventing the adequate delivery of anticancer drugs.

MATERIALS AND METHODS

THE MATHEMATICAL MODEL

We consider here a small (a few hundred of microns in length) two-dimensional patch of the tumor tissue (Ω) with explicitly defined tissue morphology composed of individual tumor cells ($\Gamma = \sum \Gamma_i$ where $i = 1, \dots, N_b$, and N_b is the number of cells) embedded in the ECM and surrounded by interstitial space filled with fluid ($\Omega \setminus \Gamma$, **Figure 2**). The reported experimental measurements of the interstitial fluid velocities are in the order of $0.1\text{--}2\ \mu\text{m/s}$ (Chary and Jain, 1989; Swartz and Fleury, 2007), thus the simulated time needed for drug particles to transverse the modeled tissue is in the order of a few minutes. Therefore, we treat all cells as stationary, i.e., we assume that during the simulation time the cells are immobile and will not grow, divide, or die (thus the cell shapes and positions are fixed). Moreover, since the characteristic cell-tissue length scale is in the order of $10\text{--}100\ \mu\text{m}$, the corresponding Reynolds number is small ($Re = \rho LV/\mu = 10^{-7}$ to 10^{-5} , where ρ is the fluid density, μ is the fluid viscosity, and L and V are the characteristic length and velocity scales, respectively). Hence, the fluid flow can be approximated by the Stokes equations:

$$\mu \Delta u(x) = \nabla p(x) - f(x), \quad (1)$$

$$\nabla \cdot u(x) = 0, \quad (2)$$

where p is the pressure, u is the fluid velocity, and $f = f_{\text{in}} + f_{\text{bnd}} + f_{\text{cell}}$, is the force applied to the domain edges ($\partial\Omega(f_{\text{in}}, f_{\text{bnd}})$), and cell boundaries ($\partial\Gamma(f_{\text{cell}})$) to create the physiologically relevant interstitial fluid flow and to keep the cells immobile. These equations are solved using the classical fluid-structure interaction method of the regularized Stokeslets (Cortez, 2001). In this method, each force f concentrated at a single point x_0 is smoothed over a small ball of radius ε using a cut-off function ϕ_ε , that is $f(x) = f_0 \phi_\varepsilon(x - x_0)$. The cut-off function needs to be radially symmetric, vary smoothly from its maximal value at the center to zero at the surface, and satisfy the condition: $\int \phi_\varepsilon(x) dx = 0$.

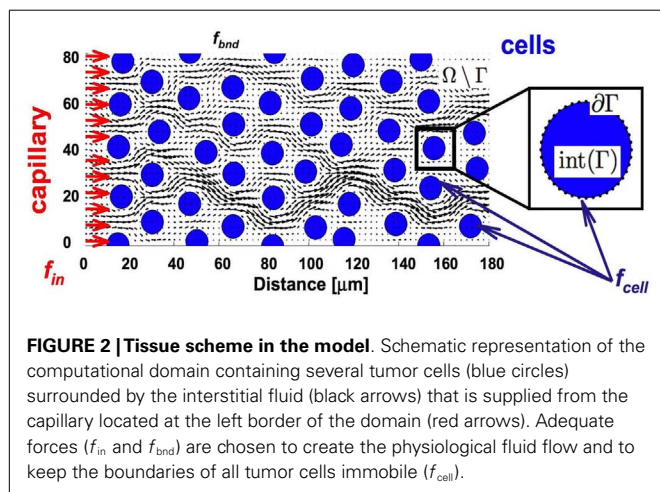


FIGURE 2 | Tissue scheme in the model. Schematic representation of the computational domain containing several tumor cells (blue circles) surrounded by the interstitial fluid (black arrows) that is supplied from the capillary located at the left border of the domain (red arrows). Adequate forces (f_{in} and f_{bnd}) are chosen to create the physiological fluid flow and to keep the boundaries of all tumor cells immobile (f_{cell}).

We follow (Tlupova and Cortez, 2009) and use the function $\phi_\varepsilon = \frac{2\varepsilon^4}{\pi(\|x\|^2 + \varepsilon^2)^3}$ for which the regularized Stokes equations have the exact solution. Other examples of suitable cut-off functions can be found in Cortez (2001) and Tlupova and Cortez (2009) together with their detailed derivation. Since the Stokes equations are linear, one may represent the fluid flow as a direct summation of the contributions from finitely many discrete forces f_k , which gives the following expression for the fluid velocity u that we will use in all our simulations (N is the number of forces):

$$u(x) = \sum_{k=1}^N \left\{ -\frac{1}{4\pi\mu} f_k \left(\ln(r^2 + \varepsilon^2) - \frac{2\varepsilon^2}{r^2 + \varepsilon^2} \right) + \frac{1}{4\pi\mu} \frac{1}{r^2 + \varepsilon^2} [f_k \cdot (x - x_k)] (x - x_k) \right\}, \quad (3)$$

where $r_k = \|x - x_k\|$. The regularization parameter ε has been chosen to be equal to the cell boundary point separation that is optimal for reducing the regularization error (Cortez et al., 2005; Tlupova and Cortez, 2009). In this model we assume that the fluid is supplied from the capillary located at the left boundary of the domain, and penetrates the interstitial space around the tumor cells ($\Omega \setminus \Gamma$) as shown in **Figure 2**.

The individual molecules (of the drug or imaging agents under consideration) are modeled as a collection of discrete particles y_p that enter the tissue via the transmural influx from a capillary (together with the interstitial fluid), and advance through the tissue by a combination of advective transport, with the fluid flow calculated using the regularized Stokeslets method, and diffusion modeled as Brownian motion with a diffusion coefficient D and a randomly chosen direction of movement ϖ . Particle movement (without cellular uptake) is confined to the extracellular space ($\Omega \setminus \Gamma$) only. The advective transport satisfies this condition since the fluid flow is zero at all cell boundaries. For the diffusive movement we ensure that the particles do not cross the cell membrane incidentally by maintaining their old positions whenever the randomly chosen direction of movement would push the particles into the intracellular space (Eq. 4, parameter α). The process of particle internalization by the cells is modeled separately by trapping the particle by the near-by cell boundary receptor if the particle comes close to the cell boundary (X_l within a small distance δ , Eq. 4). This is a very simplified way to model drug uptake, and results in 100% binding rate. However, molecular binding is usually not so efficient, and depends not only on the distance between the receptor and the ligand but also on the chemical or electrostatic forces between the two. The numerical procedure for updating the positions of the drug/imaging agent particles is given in Eq. 4,

$$y_p^{n+1} = \begin{cases} X_l, & \text{if } \|y_p^n - X_l\| \leq \delta \text{ \& } X_l \in \partial\Gamma, \\ y_p^n + \alpha \left(u(y_p^n) \Delta t + \sqrt{2D\Delta t} \varpi^n \right), & \text{otherwise} \end{cases}, \quad \delta \ll \varepsilon, \quad (4)$$

$$\text{and } \alpha = \begin{cases} 1, & y_p^n, y_p^{n+1} \in \Omega \setminus \Gamma, \\ 0, & y_p^n \in \Omega \setminus \Gamma, y_p^{n+1} \in \Gamma, \\ 0, & y_p^n \in \Gamma. \end{cases}$$

and the physical and computational parameters of the model are listed in **Table 1**.

The velocity in Eq. 3 can be used in two ways. First, for the given forces one can directly compute the induced velocity at any point in the domain. Second, since this equation is linear, one can use an iterative method, such as the generalized minimal residual method (*gmres*), to determine the forces that will result in the desired velocities at certain points in the domain (Cortez, 2001). Thus, our final computational algorithm can be summarized as follows: (1) use Eq. 3 to compute the forces (i) at the capillary which will result in the desired fluid and drug supply; (ii) on all cell boundaries to keep the cells immobile, and (iii) on the upper and lower edges of the computational domain to impose a zero flow there; (2) use Eq. 3 and the forces determined in (1) to compute the fluid velocities at all points representing the drug/imaging agent molecules; (3) use Eq. 4 to compute the new locations of all of the particles due to their advective transport at the local fluid velocity determined in (2), and their diffusive motion within the extracellular space. (4) Determine the cellular uptake of the particles, if the particles move close to the cell membrane receptors and the cells are capable of binding the particles. Repeat iteratively steps (2–4) to advance the particles through the tumor tissue.

INTRAVITAL IMAGING OF Dmt-Tic-Cy5 USING THE DORSAL WINDOW CHAMBER TUMOR XENOGRFT MODEL

A dorsal window chamber (DWC) xenograft tumor model was used to study the PKs of the tumor cell binding and uptake of the δ -opioid receptor (δ OR) targeted fluorescent agent Dmt-Tic-Cy5 (Josan et al., 2009). HCT116/ δ OR colon cancer cells engineered to express the δ OR on the cell-surface, or δ OR negative HCT116 parental cells were mixed with rat GFP expressing microvessels and aseptically inoculated within the exposed epidermis of the dorsal chamber. Following tumor cell implantation, a glass cover was placed in the chamber to cover the xenograft tumor. Ten days after cell implantation, mice were intravenously injected with 100 μ l of 5% 10,000 MW Cascade Blue Dextran (Invitrogen, CA, USA) in sterile H₂O to verify microvessel patency. Then, 45 nmol/kg of the δ OR specific Dmt-Tic-Cy5 probe was injected into the tail

vein. Confocal fluorescence microscopy images were continuously acquired for a period of time, during and after the injection of the probe, using an Olympus FV1000 (MPE) Multiphoton Laser Scanning Microscope (Lisa Muma Weitz Advanced Microscopy and Cell Imaging facility at USF) with 250 \times magnification and an acquisition rate of 3570 pixels/min. The presence of Dmt-Tic-Cy5 was measured by excitation with a 635 nm wavelength laser and the emitted light was detected using a 655–755 nm emission filter. All procedures were carried out in compliance with the Guide for the Care and Use of Laboratory Animal Resources (1996), National Research Council, and were approved by the Institutional Animal Care and Use Committee (IACUC) at the University of South Florida.

HISTOLOGICAL IMAGING OF HUMAN OVARIAN TUMOR

A sample of invasive ovarian tumor has been selected retrospectively from the Moffitt Cancer Registry database. A section of the formalin fixed and paraffin embedded (FFPE) tissue (4 μ m thick) has been stained with a hematoxylin and eosin stain (H&E). The whole slide was scanned using the Aperio™ (Vista, CA, USA) ScanScope XT with a 20 \times /0.8 NA objective lens at a rate of 3 min per slide via Basler tri-linear-array. All procedures were carried out in compliance with HIPAA regulations with patient consent and were approved by the Institutional Review Committee (IRB # Pro00003491) at the University of South Florida and the Moffitt Cancer Center Scientific Review Committee (SRC # 16511). The original H&E-stained histological image has been digitized using the ImageJ software (NIH, USA) and in house Matlab routines. The digitized version has been used for computational simulations using the model described in Section “The Mathematical Model.”

RESULTS

Experimental evidence (Gullino et al., 1965; Nugent and Jain, 1984; Jain, 1987; Netti et al., 2000; Levitt, 2003; Grantab et al., 2006) has shown that tissue histology, cell packing density, and the extent of the ECM, and the amount of interstitial water can vary significantly between cancers of various origins (breast, brain, ovary, and lung). For example, in tumors grown in rats the interstitial intertumoral space can vary from around 35% in certain carcinosarcomas and carcinomas, to around 65% in fibrocarcinomas and sarcomas (Jain, 1987). Our goal is to investigate how the structure and cellular composition of tumor tissues influences the interstitial transport of chemical compounds, such as drug or biomarker molecules. We will use a suit of idealized computational tissues with various morphological parameters (cellular size, tissue porosity) and different properties of drug particles (diffusion coefficient, cellular absorption) to run computational simulations and compare the depth and timing of the molecule distributions within the tissue. This systematic exploration allows us to determine the relative importance of the physical parameters of both the tissue and the drug required for effective interstitial transport. Finally, we will compare our simulation outcomes with experimental results from tumor cells grown in the DWC and treated with targeted imaging agents to determine their spatial and temporal penetration dynamics.

Table 1 | Model physical and computational parameters.

Parameter	Symbol	Value
Domain	Ω	210 \times 80 μ m
Tissue cellular porosity	ψ	40–90%
Tissue cellular density	ξ	2–6 Cells per column
Interstitial fluid input flow	u^{in}	(1, 0) μ m/s
Fluid viscosity	μ	2.5 \times 10 ³ μ g/(mm.s)
Regularization parameter	ϵ	0.5 μ m
Discretization parameter		0.5 μ m
Time step	Δt	0.1 s
Diffusion coefficient	D	2.5 \times 10 ^{−8} to 10 ^{−3} mm ² /s
Direction and distance of motion	ϖ	0–360° and [0, $\sqrt{(2D\Delta t)}$]
Uptake rate		100%
Binding distance	δ	0.5 ϵ

PERMEATION IN IDEALIZED TISSUES OF REGULAR ARCHITECTURE

We began our study by examining idealized computational tissues composed of identical regularly distributed circular cells. This allowed us to analyze the properties of the mechanistic model when tissue heterogeneity is ignored. Furthermore, we compared these results with cases where the regular tissue structure is perturbed. Since the interstitial transport takes place in the void space separating individual cells, the depth of tissue penetration depends on the relative volume of all voids, which we quantify as tissue cellular porosity, ψ . However, the particular pattern of the interstitial fluid flow for the fixed porosity value relies on the actual space between individual cells, and thus on the cell size and number (density) within the tissue. In the case of idealized tissues with regularly spaced circular cells we defined the tissue cellular density as the number of cells in each column, ξ . The subject of our investigation is the permeation time and penetration depth of the drug/biomarker particles transported by the interstitial fluid flow through a tissue with given morphological parameters (ψ, ξ).

Figure 3 shows a collection of tissue samples with regularly distributed cells for the three porosity values of $\psi = 40, 65$, and 90% , and the cellular densities of $\xi = 2, \dots, 6$ (the pattern of the interstitial fluid flow in each case is shown in blue).

We examined a total of 30 cases of regular cellular patterns in which the tissue's cellular porosity varied between 40 and 90%, and the tissue's cellular density varied between two and six cells. In each *in silico* tissue, all cells had identical radii determined in such a way to reach the desired values of both the cellular porosity of the tissue and its cellular density. Note that in each row in **Figure 3** the value of the tissue cellular porosity is fixed, and that for an increasing number of cells that occupy each column (cases ordered from left to right), the overall cellular density increases. However, it is not immediately clear how the tissue permeability, i.e., the extent of the interstitial fluid penetration of the tissue, is related to the tissue cellular structure. In fact, we will show that the less dense tissues may have lower permeation properties.

We first consider the advective transport only. In each case under consideration we computed the interstitial fluid field (**Figure 3**) that was a result of the steady fluid influx of the velocity $u^{\text{in}} = (1, 0) \mu\text{m/s}$ (Swartz and Fleury, 2007) along a capillary located at the left edge of the domain. Subsequently, we introduced identical numbers of drug particles ($N_p = 4800$) from uniformly spaced capillary fenestration, and traced the drug particles trajectories within the interstitial fluid flow during their transport. It is not known *a priori* whether all of the particles will be able to transverse the whole tissue patch, as there is the possibility that they may be carried with the flow to some tissue spots where the interstitial fluid velocity is very low or even zero (for example particles located near the cell boundaries). Therefore, to be able to compare the results across different tissue geometries we recorded the time (that we call the *permeation time*) when a certain fraction of the fastest drug particles (a quarter of all particles introduced to the system) reaches a prescribed distance from the capillary (we chose the distance of $120 \mu\text{m}$, which requires the particles to travel $2/3$ of the whole computational domain). The choice of both values, the distance at which the permeation time is measured and the fraction of particles to take into consideration are somewhat arbitrary, but our main goal is to compare the results between tissues of different properties using unified criteria. We do not expect the overall conclusions from our model simulations to be significantly different if we choose a different fraction of particles or a different distance from the capillary. The permeation time normalized by the minimal value across all 30 tissue samples is presented in **Figure 4A** as a surface plot. Here, the slowest permeation time for the tissue of $(\psi, \xi) = (40\%, 6)$ is more than twofold longer than the fastest permeation time for the tissue $(\psi, \xi) = (40\%, 2)$. **Figure 4B** shows a plot of the maximal distances reached by the drug particles at the fixed time equal to the minimal permeation time from **Figure 4A**. Seven particular tissue samples are shown in more detail (red points show final locations of drug particles at the permeation times from **Figure 4A**, gray points show locations of

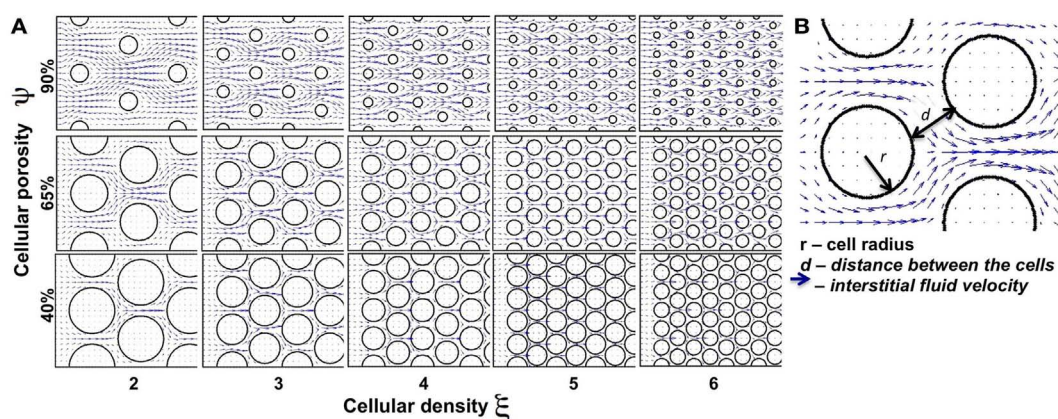


FIGURE 3 | Differences in the tissue's cellular structure.

(A) Collection of tissue samples with regularly distributed cells with various values of cellular porosity ψ (defined as a percentage of void spaces in the tissue; here $\psi = 40, 65, 90\%$) and cellular density ξ (determined by the number of cells in each column; here $\xi = 2, 3, \dots, 6$).

Tumor cells are represented by circles and the interstitial fluid velocity field initiated at the left edge of the domain is shown as blue arrows pointing in the direction of fluid flow. (B) The interstitial space is determined by the size (r) of the cells and distance (d) between the neighboring cells.

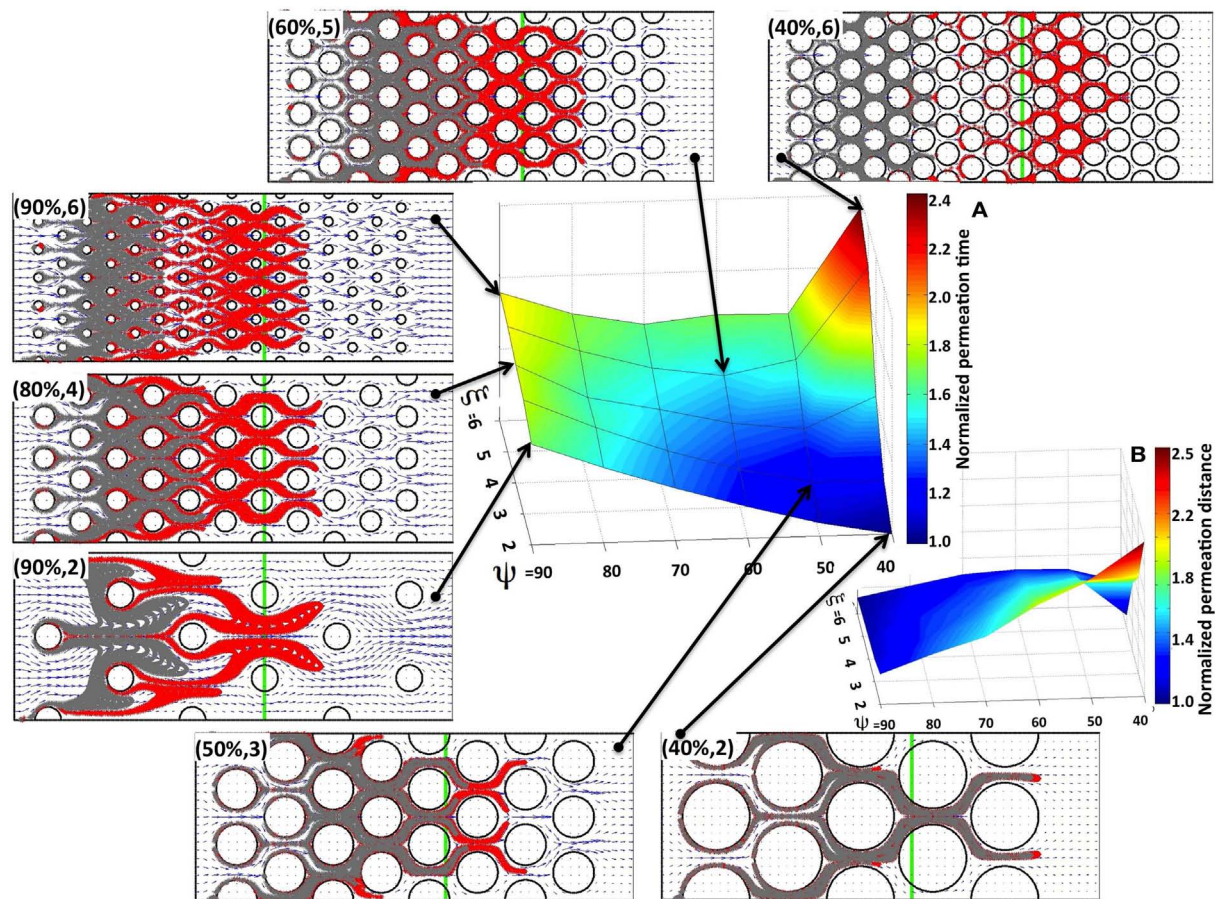


FIGURE 4 | Drug particle permeation times and depths for advective flow in regularly packed tumor tissues. Surfaces showing (A) the relative permeation time of drug particles (the time required for a quarter of the supplied drug particles to reach 2/3 of the computational domain length), and (B) the normalized depth of tissue penetration at a fixed time for tissues of varying cellular porosity and

cellular density (ψ , ξ). Seven specific tissue configurations of indicated cellular porosity and cellular density are shown in each case. The locations of drug particles at a fixed time from (B) are shown in gray, and their final positions at the permeation times from (A) are shown in red. The green vertical lines indicate the fixed distance at which the permeation time is recorded.

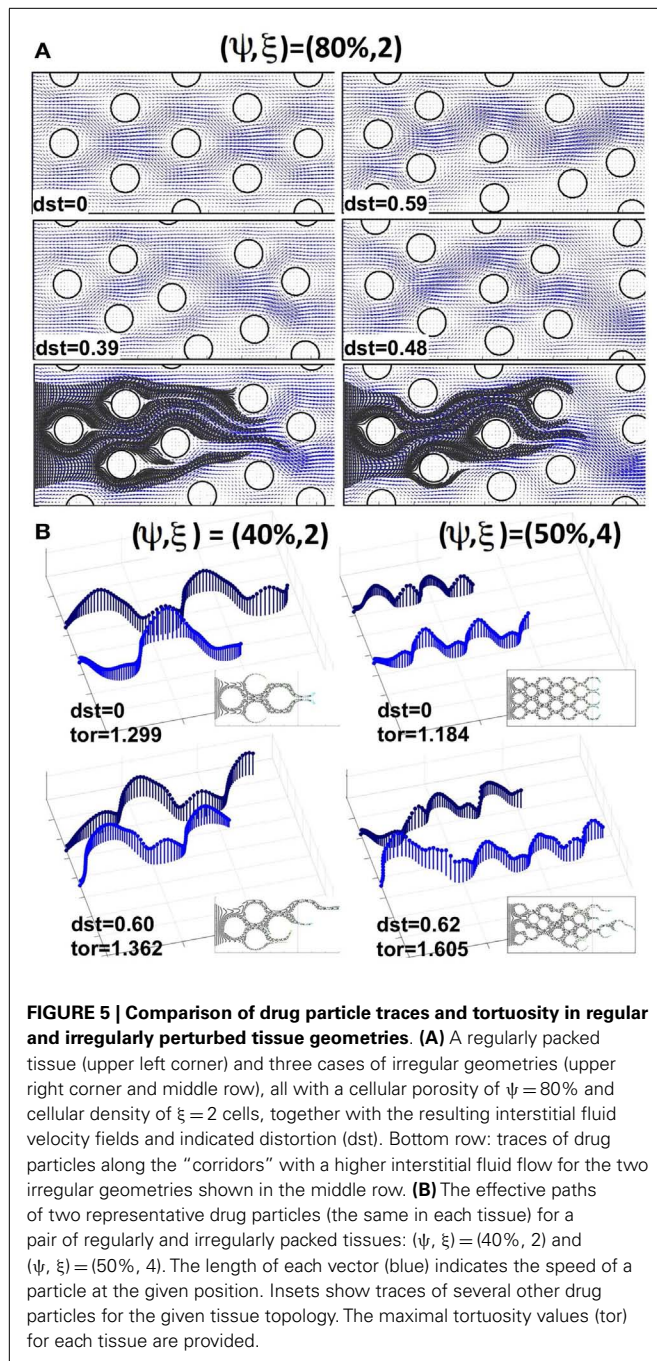
drug particles at the fixed time from **Figure 4B**). For the minimal permeation time (lower right inset) both the red and gray particles overlap.

As expected, for a given tissue cellular porosity the permeation time increases with increasing tissue cellular density as a result of the diminished space between neighboring cells (**Figure 4A**). However, for the cases when the cell column occupancy is small ($\xi = 2, 3, 4$) the tissues characterized by a lower cellular porosity, and thus with a smaller separation between neighboring cells, are traversed faster by the majority of the drug particles, and thus the corresponding permeation times are lower. The global minimum in permeation times occurs for the porosity $\psi = 40\%$ and cellular density $\xi = 2$. For higher cellular densities (i.e., larger numbers of cells occupying each column), the local minima in the permeation times occur at the middle-rank of a given tissue porosity, that is at $\psi = 60\%$. This is also confirmed in **Figure 4B**, where the larger traveled distances are observed in the cases of either low cellular porosity or low cellular density (right lower corner in **Figure 4B**). These results were obtained under the assumption

that the interstitial fluid influx u^{in} from the capillary is identical in all 30 *in silico* tissues considered here. As a consequence, the fluid velocity in denser tissues is higher, since the same amount of fluid is moving through a narrower space, and the drug molecule permeation time is faster.

PERMEATION IN IDEALIZED TISSUES OF IRREGULAR ARCHITECTURE

Now we consider cases in which the cells are non-uniformly distributed within the tissue. We examined tissue geometries obtained by shifting the locations of the tumor cells with respect to the regularly ordered tissues. **Figure 5A** shows a regularly (upper left corner) and three irregularly packed tissues (upper right corner and both pictures in the middle row), all with cellular porosities of $\psi = 80\%$ and cellular densities of $\xi = 2$ cells per column (the irregular tissue geometries were obtained from the regular ones by randomly shifting the cell centers around their initial positions without cell overlap). These tissue irregularities result in the asymmetrical flow of the interstitial fluid (fluid velocity fields on the same grid are shown in blue in **Figure 5A**), and in



the formation of interstitial “corridors” characterized by higher fluid flow. We quantify this distortion (on the scale of the whole tissue patch) by comparing the differences in the whole velocity fields between the irregularly and regularly packed tissues using the L_1 -norm, $dst = \|u_{reg} - u_{irreg}\|_1 / (N_x \times N_y)$, where $N_x \times N_y$ is the number of grid points upon which the fluid velocity field is evaluated (the distortion values for each tissue are shown in **Figure 5**). These emergent fluid corridors are followed by drug particles during their advective transport through the tumor interstitium (see **Figure 5A** bottom row).

The actual microscopic paths followed by the fluid flow carrying the drug particles can be geometrically complex. Thus, we use a quantitative metric of the drug particle path tortuosity in order to illustrate the differences between the individual routes of drug transport within the tissue. The path tortuosity τ is defined here as a ratio of the effective path length (L_e) to the shortest straight-line distance (L) between the initial and final positions of the moving particle, that is $\tau = L_e/L$. Note that the tortuosity of a straight line is 1, of a circular path is infinity, and that it has been estimated in Ramanujan et al. (2002) that the tortuosity of a well-packed system of cells is $\tau = \sqrt{2}$. Therefore, the determination of the mean and maximal tortuosity of individual drug particle paths can provide a better understanding of the void space complexity inside the tumor tissue and the patterns of the interstitial fluid flow. The average tortuosities under the advective flow taken over all 30 different regular and 150 irregular tissues considered in our simulations are similar ($\tau = 1.12 \pm 0.05$ and $\tau = 1.20 \pm 0.07$, respectively). However, for every irregularly packed tissue we have observed some drug particle paths of tortuosity above $\sqrt{2}$, and the average maximal tortuosity in these tissues is $\tau = 1.64 \pm 0.3$. Thus, the irregular tissue topology implies that some drug particles traverse across the tissues in a very complex way. **Figure 5B** shows the representative traces of the same drug particles for two pairs of tissues, one regularly and one irregularly packed. The case of minimal overall permeation $(\psi, \xi) = (40\%, 2)$ is shown in the left column, whereas the case of the highest average tissue tortuosity $(\psi, \xi) = (50\%, 4)$ is presented in the right column. The speed of each traced particle at every visited position inside the tissue is indicated by the length of the vertical vector. These values depend strongly on the cellular structure of the tissue, and oscillate around the cell perimeters. However, in the case of regular tissues these oscillations are periodic. Thus, when the particles are supplied through uniformly spaced capillary fenestration, they can cover the whole tissue width evenly. In contrast, in the irregular tissues the drug particles may travel across the width of the tissue by utilizing the fluid flow corridors, and even if the drug particles initial locations along the capillary were distinct, they may end up following the same path. Moreover, the speed of the drug particles in these cases is very non-homogeneous (as seen in **Figure 5B**, left lower image), and the tortuosities of many of the particles’ paths are above $\sqrt{2}$, in contrast to the regular cases. This causes a non-uniform exposure of the drug to the tumor cells. That is, some tissue regions are penetrated by large numbers of drug particles, whereas some tumor cells may not come in contact with sufficient concentrations of the drug particles to experience their therapeutic action. Such irregular interstitial flows also result in the faster transport of some drug particles (compare the lengths of each path shown in **Figure 5B**) and deeper penetration of the tissue when compared to the cases of regular cellular packing. Our simulations show that this phenomenon is more pronounced in tissues of higher cellular density. On average, across irregular tissues of the same cellular density and porosity, the permeation times are comparable to those in the regularly packed tissues (data not shown). However, for tissues in which there are multiple paths of high tortuosity, the permeation depth and time may be significantly higher.

PERMEATION UNDER A COMBINATION OF ADVECTIVE AND DIFFUSIVE TRANSPORTS

Drug and imaging particles, like metabolites and other molecules, are capable of random motion when suspended in a medium such as interstitial fluid. The extent and speed of this intrinsic, diffusion-type particle motility depend on the particle's molecular mass (Einstein relation). Here we consider a wide range of particle diffusion coefficients that cover both the small molecules of metabolites (such as oxygen or glucose), large nanoparticles (designed as carriers of therapeutic compounds), and all modalities in between (Nugent and Jain, 1984; Pluen et al., 2001; Avgoustiniatos et al., 2007; Schmidt and Wittrup, 2009). We tested six different values of particle diffusion coefficients in the range of 2.5×10^{-8} to $10^{-3} \text{ mm}^2/\text{s}$. As expected, we saw both transport phenomena: diffusion driven particle dispersal (for the Péclet numbers of 0.04–4), and advection-dominated particle relocation (for the Péclet numbers of 400–4000). The value of the Péclet number is a measure of the ratio between the advective displacement of the particles moved by the flow to the rate of the particle diffusion driven by an appropriate gradient ($Pe = L \times U/D$, where D is a diffusion coefficient, and L and U are the characteristic values of length and velocity, respectively used to determine the Reynolds number Re in The Mathematical Model section). We observed that for small Péclet numbers ($Pe = 0.04$ –4), the transport of particles was clearly diffusion-dominated in all considered tissues, for all values of tissue cellular density and porosity, and for both regularly and irregularly spaced cells. In all cases the entire interstitium was covered by drug particles (examples shown in Figure 6, left subspace). For the maximal Péclet number considered here ($Pe = 4000$), the transport was advection-driven, and all drug particles followed the high velocity corridors with minimal dispersion due to low diffusive properties (examples shown in Figure 6, right column). However for the values of the Péclet number of $Pe = 40$ and 400, the transport of the drug particles had different characteristics

depending on the tissue structure. In the case of $Pe = 40$, only the tissues of low cellular density ($\xi = 2$) showed dominant advective transport. For the tissues with higher cellular densities the drug particles only followed the fluid flow initially, and their diffusive capacities became finally predominant (examples shown in Figure 6). In the case of $Pe = 400$, only the tissues with a high cellular density ($\xi = 6$) showed diffusive characteristics. For all other tissues the transport was dominated by the interstitial fluid flow (Figure 6). Moreover, the average tortuosity of the drug particle traces for advection-dominated transport ($Pe = 4000$, all tissue samples) was equal to $\tau = 1.35$ which is similar to the average for the pure advection transport discussed above. In the cases of a small Péclet number, the average tortuosity is an order of magnitude larger: $\tau = 11.1$ (with the mean value of $\tau = 17.9, 10.7, 4.7$ for $Pe = 0.04, 0.4$, and 4, respectively).

COMPARISON WITH PERMEATION OF TARGETED IMAGING AGENTS

A direct comparison of our computational results with the drug distribution in tumor tissues is difficult. The *in vitro* experiments with either the 3D multicellular spheroids (Nederman et al., 1981; Walenta et al., 2002; Bryce et al., 2009) or multilayered tissue constructs (Kyle et al., 2004; Grantab et al., 2006; Modok et al., 2007; Al-Abd et al., 2008) do not reproduce the *in vivo* conditions faithfully (for example, the differences in interstitial pressure and interstitial fluid flow patterns are usually not captured). The effects of the drug actions on individual tumor cells in mouse models can be captured *ex vivo* by using the immunohistochemical staining of dead cells (Sun et al., 2012), or *in vivo* by using fluorescent drugs (Ozols et al., 1979; Lankelma et al., 1999; Primeau et al., 2005). However, intrinsically fluorescent drugs are scarce (doxorubicin, adriamycin); therefore, we will compare the results of our simulations to the penetration of fluorescent imaging agents targeted to bind to the specific cell membrane receptors expressed by some tumor cells.

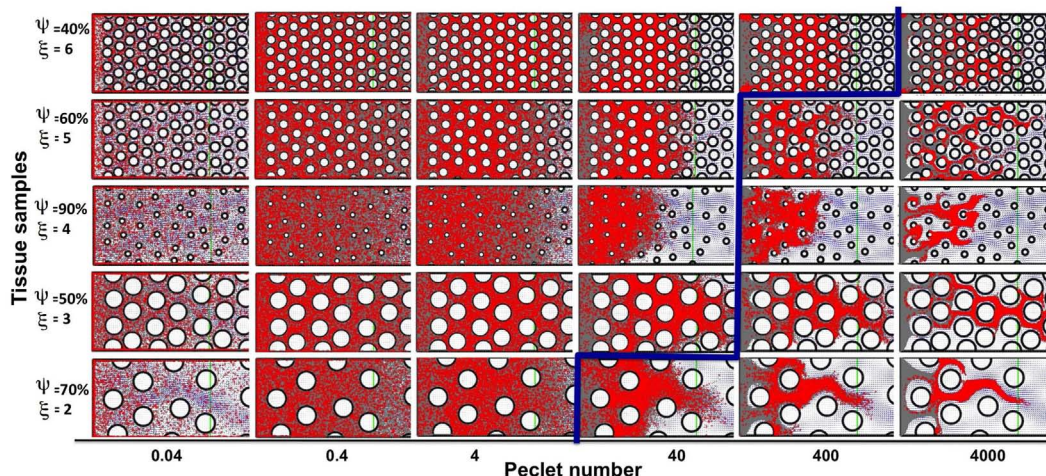


FIGURE 6 | Classification of particle traces for a combination of advective and diffusive transports. The model parameter space separated into diffusion (left-top) or advection (right-bottom) dominated particle transport (the separation shown in blue), shown for five representative tissue samples selected out of 30 considered in this study. For the small Péclet numbers

($Pe = 0.04$ –4) the transport is diffusion-dominated for all tissue topologies. For the maximal considered Péclet number ($Pe = 4000$) the transport is convection-driven for all tissue architectures. In the case of the medium Péclet numbers ($Pe = 40$ –400) the particle transport changes its characteristics depending on the tissue architecture.

Our experimental model of choice is the DWC that is surgically implanted on a mouse dorsal-skin flap and allows for monitoring the growth of xenograft tumors over time. When combined with a targeted fluorescent imaging agent (Dmt-Tic-Cy5) we can observe agent extravasation from the vascular system, its spread through the interstitial space, cellular uptake by tumor cells that express the target marker, and agent clearance from the tissue. Two different tumors were implanted, one that expresses and a second that does not express the targeted receptor. The tumors were imaged at different time-points following the administration of the agent (**Figure 7A**), and the fluorescence intensities of both tumor tissue types were recorded (**Figure 7B**). Clearly, the tumor expressing the targeted receptor ($\delta\text{OR}+$, **Figure 7A**, top row) showed the slow but steady accumulation of the fluorescent agent over the period of 24 h. For the tumor that did not express the targeted receptor ($\delta\text{OR}-$, **Figure 7A**, bottom row) the fluorescent agent was clearly visible in the mouse veins just after injection (**Figure 7A**, bottom row, left image); however, since it was not absorbed by the tumor cells, it cleared from the tumor tissue in about 10 min (**Figures 7A,B**, bottom row middle image). For simplicity, we called the latter case “untargeted,” since the imaging agent was not able to bind to the target cell membrane receptors.

The process of imaging agent molecule uptake via binding to cell membrane receptors was incorporated into our computational model by trapping these particles that come very close to the cell boundary points inside of the cell. The course of the time for a simulation of the targeted agent with cellular uptake is shown in **Figure 7D**. The top images show the individual particles inside of the cells (pink dots) and in the interstitial space (red dots). The bottom images show the corresponding fluorescent rendering that was created by dividing the whole computational domain into small square grids and counting the particles inside. The obtained particle concentration is presented as a heat map. **Figure 7E** shows the time sequence from a simulation without cellular uptake (untargeted). Both cases were run for the same tissue structure of cellular density $\xi = 5$, cellular porosity $\psi = 60\%$, and Péclet number $Pe = 40$.

In order to compare the simulated and experimental results we selected a small tissue section near the agent supply (vein) in the untargeted case and far from the vein in the targeted case. This is consistent with the way the experimental data was quantified. Again, following the experimental procedure, we counted all of the particles inside the selected reference window (indicated by blue rectangles in **Figures 7D,E**) and normalized the obtained counts by the maximal value from the whole time-course separately for each simulation. The quantification of the simulated results is shown in **Figure 7C**. Our results show a trend similar to the experimental data in the dynamics of both the targeted and untargeted agents. However, this comparison has only a qualitative value, because our computational model has not been tuned to the experimental setup, and certain model parameters (such as agent molecular binding or the level of intracellular agent saturation) have not been calibrated to match those in the experiments. Both the experimental and simulated data need to be analyzed further in order to compare the results quantitatively.

CONCLUSION AND DISCUSSION

In this paper we investigated how the structure and distribution of tumor cells influence the interstitial fluid flow and the delivery of chemical compounds, such as drug or imaging particles. We used a computational model based on the method of the regularized Stokeslets of Cortez (2001) that allows for modeling both the advective transport (with the interstitial flow due to the pressure differences between the vascular system and the tumor tissue), and the diffusive transport due to the Brownian motion of the particles. While the method of regularized Stokeslets has been used previously to model various swimming organisms (Flores et al., 2005; Cisneros et al., 2007) and biofilm dynamics (Cogan et al., 2005; Cogan, 2008, 2010), to our knowledge, it has not been applied in the studies of interstitial transport through the tumor tissues.

We focused in this paper on the interplay between both drug advective and diffusive modes of transport and the structure of the tissue, taking into account both the tissue cellular density and the extent of the interstitial space between the individual cells. The advective component of the interstitial penetration is especially important for the transport of particles characterized by larger molecular weights, such as certain drug molecules or imaging nanoparticles that usually have smaller diffusion coefficients. This is in contrast to small molecules, such as oxygen or glucose, which can move through the tissue solely by the diffusive process.

The results presented in this paper show that tumor cell distribution is characterized by tissue cellular porosity and its cellular density influences the depth of a drug's advective penetration in a non-linear manner, with sparsely packed tissues showing slower interstitial fluid flow and longer times of drug penetration when compared to more densely packed tissues. These results were obtained under the assumption that the fluid influx from the blood capillary is constant and the same in each case considered here, that is for each *in silico* tissue geometry. For simplicity, we directly imposed a specific fluid influx value on all our computational simulations. However, this parameter could be related to experimentally measurable quantities, such as the pressure differences between the capillary and the surrounding tissue or the tumor tissue. We also showed that irregularities in tissue composition and cell spatial configuration result in the emergence of tissue zones that have a lesser exposure to the drug molecules. This, in turn, may result in drug concentrations insufficient to provide therapeutic action. It has been suggested previously (Minchinton and Tannock, 2006) that the poor penetration of the tumor tissue by drug particles may leave some cell populations untreated and capable of initiating tumor regrowth or recurrence.

Our simulations also showed that tissues of higher irregular architecture were characterized by faster transport of some drug particles. Consequently, these particles were able to penetrate deeper into the tumor tissue and exert their therapeutic effects on a larger tissue area. Thus, we observed a certain dichotomy in our simulations. The advection-dominated drug particle transport in tissues of highly irregular architectures resulted in tissue regions of permanent low drug exposure even near the vascular system,

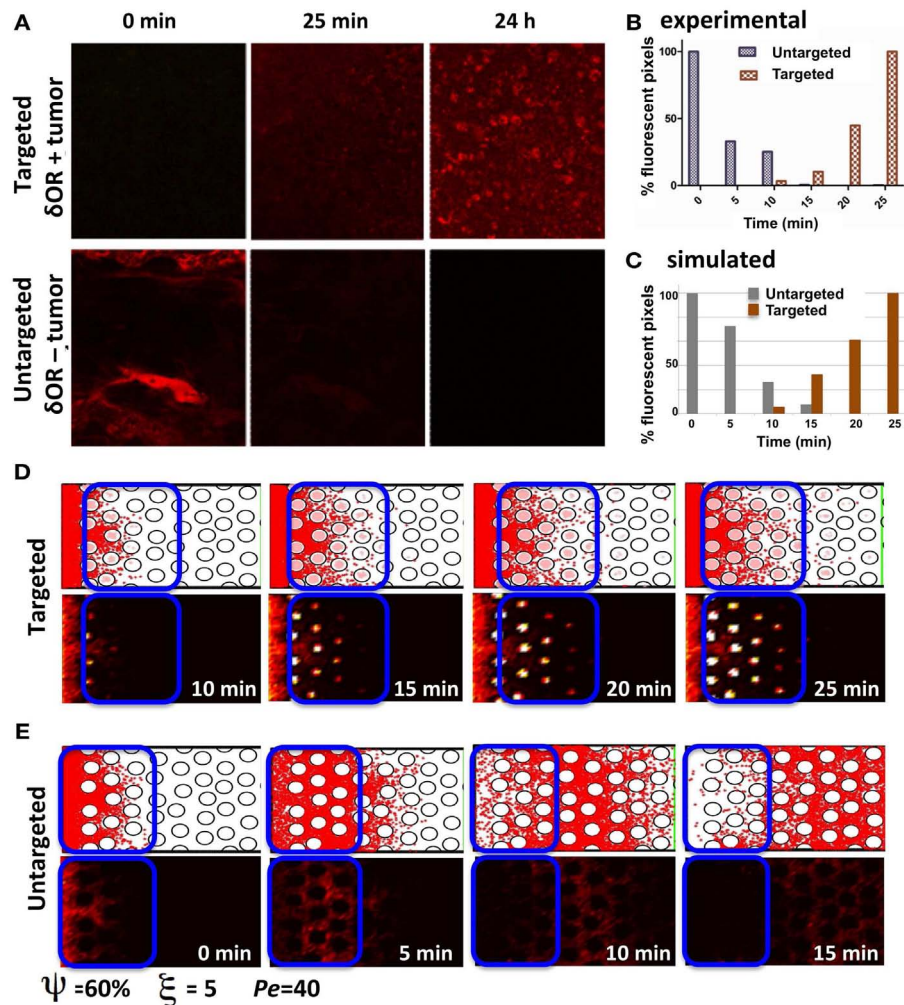


FIGURE 7 | Penetration of targeted and untargeted imaging agents: comparison of simulated and experimental data. (A) Confocal fluorescence microscopy images of target-expressing DWC tumors (top) and non-expressing tumors (bottom) at time-points immediately following the injection of the targeted fluorescent probe. **(B)** For both the targeted and untargeted tumors, the bar graph represents the percentage of pixels with fluorescence intensities above a threshold value higher than the low background signal over a 25 min time-course, with 100% being equal to largest number of pixels above the background in the time-course. **(C)** The

quantification of the simulated results from the section of the tissue indicated as a blue window in **(D, E)**. The simulated data has been normalized as in **(B)** for comparison. **(D)** The time sequence from a simulation with cellular uptake via receptor binding (targeted); the top images show individual particles, and the bottom images show the corresponding fluorescent rendering. **(E)** Time sequence from a simulation without cellular uptake (untargeted). Both simulations were run for the same tissue structure with a cellular density of $\xi = 5$, cellular porosity of $\psi = 60\%$, and Péclet number of $Pe = 40$.

and tissue regions far from the vascular system that were exposed to the drug action temporally. Thus drugs of higher diffusivity (smaller molecular size) were able to penetrate the tissue more uniformly, potentially bringing an effective treatment to all cells, but only near the vasculature. On the other hand, drugs of lower diffusivity were able to reach distant parts of the tissue. As a result, they could have an extended beneficial effect, but only if they can be absorbed quickly by the cells, or have a longer half-life time in order to allow for the drug accumulation to exert its lethal effects. These kinds of physico-chemical properties of individual molecules may be beneficial for the imaging agents that are not meant to kill the cells, thus small concentrations accumulated inside the cells may still fluorescently mark the tumor cells located farther

from the vasculature. However, in this case, the biomarkers need to bind to the specific membrane receptors quickly and have longer half-life times.

The research studies initiated in this paper are novel in the areas of computational drug design and bio-medical modeling. We proposed to investigate an important but overlooked area in testing anticancer drug efficacy: the effective penetration of tumor tissues by drug particles under various extrinsic conditions. Most research approaches addressing drug efficacy have concentrated on the molecular and genetic mechanisms of chemical compounds, whereas the role of the tumor microenvironment as a limiting factor in drug distribution has received much less attention. Moreover, the majority of *in silico* methods for assessing the

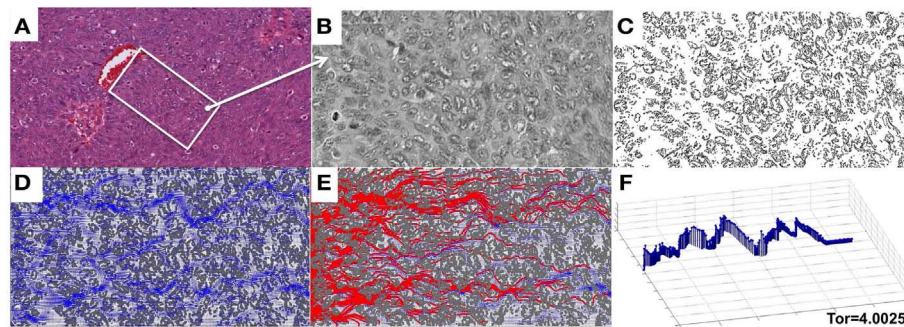


FIGURE 8 | Penetration of drug particles through a digitized ovarian tumor tissue. (A) An original H&E-stained histological image of ovarian tumor tissue with a centrally located vein. **(B)** A small patch of tissue selected from **(A)** and used for digitization. **(C)** A digitized version of the histological image

from **(B)** used for computational simulations. **(D)** The simulated interstitial fluid flow (blue). **(E)** The resulting traces of the simulated particles representing the drug or biomarker molecules. **(F)** The particle trace with maximal tortuosity of 4.0025.

ADME-T properties (absorption, distribution, metabolism, excretion, and toxicity) of pharmaceutical compounds do not consider the spatial aspects of drug pharmacokinetics and pharmacodynamics (PK/PD), but instead, treat the blood and all organs as well-mixed compartments neglecting their natural heterogeneity. It is interesting to note that the question of how the architecture of natural or fabricated obstacles influences the interstitial transport has been addressed in other scientific areas, including groundwater hydrology (Kang et al., 2010; Xie et al., 2011; Tsimpanogiannis and Lichtner, 2012), vortex dynamics in superconductors (Nori, 1996; Reinhardt et al., 1997; Silhanek et al., 2010), fuel conversion (Machado, 2012), and biofilm dynamics (Dillon and Fauci, 2000).

We focused in this study on analyzing the permeation properties of tissues characterized by different cellular architectures, but with identical circular cells. However, as can be seen in **Figure 1**, the realistic tumor tissues are far more complex. They are composed of cells that vary not only in their spatial configuration, but also in their size, shape, and receptor expression. In such highly irregular tissues the patterns of interstitial transport can be even more convoluted. To illustrate this, we applied our model to a digitized histological sample from human breast cancer tissue. **Figure 8** shows the original histological image of a small patch of tumor tissue, a digitized version of this image used for computational simulations, and the resulting fluid field and traces of the drug/biomarker particles. The maximal tortuosity is reported.

We also presented a qualitative comparison of the results from our model simulations with the data from the DWC experiments. However, in order to achieve the quantitative results, the model needs to be parameterized to reproduce the properties of a given tumor and the properties of a given drug or (un)targeted imaging agent. Fluorescently labeled probes, together with the DWC, form an ideal model for taking *in vivo* measurements at various time-points in the same animal. While certain measurements of these probes can be obtained *in vitro* (such as association and dissociation binding constants, mass and size, saturation levels, and cellular uptake), the fluorescent microscopy of DWC tumor xenografts enables observation of probe interactions within

a living tumor microenvironment. Mathematical modeling and analysis of these fluorescence image acquisitions allows for the estimation of the relative probe concentration in plasma and tumor tissue, rate of probe extravasation and penetration into the tumor, rate of cellular binding and internalization, and rate of vessel clearance. The tissue architecture can be determined from the *ex vivo* histological images as they are shown in **Figure 8**, and then used to fit the model parameters, i.e., interstitial velocity and probe effective diffusion. This can be done by performing multiple simulations with systematically varied parameters and then comparing the simulated results to intravital or *ex vivo* images.

The model presented here constitutes the basis for further extensions that will increase the model's realism by including several factors specific to either the drug/biomarker or the microenvironment. We plan to explicitly model drug particle size, mass, and electrical charge. Our oversimplified model of cellular uptake will be extended to incorporate the mechanisms of cellular efflux and influx, as well as the more elaborate models of molecular binding, including receptor-ligand reaction kinetics. Our future model extensions will also include models of different structures of the ECM, such as the extracellular fiber distribution and alignment. One of the important aspects of modeling anticancer drug actions is to integrate both cellular death and growth into the model, and to simulate much longer time regimes in order to test the tumor eradication or recurrence. The model could also be extended into the full three-dimensional space [the appropriate blob functions have been proposed previously (Cortez, 2001)]. The full version of this model will provide a tool for testing drug efficacy by independently varying the drug and tissue parameters over a wide range of values that are often difficult to replicate in laboratory experiments.

ACKNOWLEDGMENTS

We gratefully acknowledge the Comparative Medicine Department and Muma Weitz Advanced Microscopy and Cell Imaging facility at University of South Florida, and the Small Animal Imaging Laboratory, the Moffitt Cancer Registry, and Analytic Microscopy Core facility shared resources at the H. Lee

Moffitt Cancer Center & Research Institute. We would like to thank Dr. T. Torres for discussions in the initial phase of this project. The following grants were used to fund the experimental components of this study: NIH/NCI R01 CA097360 and

R01 CA123547 (David L. Morse). The computational work has been partially supported by the Miles for Moffitt Milestones Award, and partially by the Moffitt Support grant (Katarzyna A. Rejniak).

REFERENCES

- Al-Abd, A. M., Lee, J. H., Kim, S. Y., Kun, N., and Kuh, H. J. (2008). Novel application of multicellular layers culture for in situ evaluation of cytotoxicity and penetration of paclitaxel. *Cancer Sci.* 99, 423–431.
- Avgoustiniatos, E. S., Dionne, K. E., Wilson, D. F., Yarmush, M. L., and Colton, C. K. (2007). Measurements of the effective diffusion coefficient of oxygen in pancreatic islets. *Ind. Eng. Chem. Res.* 46, 6157–6163.
- Baxter, L. T., and Jain, R. K. (1989). Transport of fluid and macromolecules in tumors. I. Role of interstitial pressure and convection. *Microvasc. Res.* 37, 77–104.
- Beresford, A. P., Selick, H. E., and Tarbit, M. H. (2002). The emerging importance of predictive ADME simulations in drug discovery. *Drug Discov. Today* 7, 109–116.
- Boobis, A., Gundert-Remy, U., Kremers, P., MacHeras, P., and Pelkonen, O. (2002). In silico predictions of ADME and pharmacokinetics. *Eur. J. Pharm. Sci.* 17, 183–193.
- Bryce, N. S., Zhang, J. Z., Whan, R. M., Yamamoto, N., and Hambly, T. W. (2009). Accumulation of the anthraquinone and its platinum complexes in cancer cell spheroids: the effect of charge on drug distribution in solid tumour models. *Chem. Commun. (Camb.)* 19, 2673–2675.
- Chary, S. R., and Jain, R. K. (1989). Direct measurement of interstitial convection and diffusion of albumin in normal and neoplastic tissues by fluorescence photobleaching. *Proc. Natl. Acad. Sci. U.S.A.* 86, 5385–5389.
- Cisneros, L. H., Cortez, R., Dombrowski, C., Goldstein, R. E., and Kessler, J. O. (2007). Fluid dynamics of self-propelled microorganisms, from individuals to concentrated populations. *Exp. Fluids* 43, 737–753.
- Cogan, N. G. (2008). Two-fluid model of biofilm disinfection. *Bull. Math. Biol.* 70, 800–819.
- Cogan, N. G. (2010). An extension of the boundary integral method applied to periodic disinfection of a dynamic biofilm. *SIAM J. Appl. Math.* 70, 2281–2307.
- Cogan, N. G., Cortez, R., and Fauci, L. (2005). Modeling physiological resistance in bacterial biofilms. *Bull. Math. Biol.* 67, 831–853.
- Cortez, R. (2001). The method of regularized Stokeslets. *SIAM J. Sci. Comput.* 23, 1204–1225.
- Cortez, R., Fauci, L., and Medovikov, A. (2005). The method of regularized Stokeslets in three dimensions: analysis, validation, and application to helical swimming. *Phys. Fluids* 17, 031504.
- Dillon, R., and Fauci, L. (2000). A microscale model of bacterial and biofilm dynamics in porous media. *Biotechnol. Bioeng.* 68, 536–547.
- Ekins, S., and Rose, J. (2002). In silico ADME/Tox: the state of the art. *J. Mol. Graph. Model.* 20, 305–309.
- Flores, H., Lobaton, E., Mendez-Diez, S., Tlupova, S., and Cortez, R. (2005). A study of bacterial bundling. *Bull. Math. Biol.* 67, 137–168.
- Gade, T. P. F., Buchanan, I. M., Motley, M. W., Mazaheri, Y., Spees, W. M., and Koutcher, J. A. (2009). Imaging intratumoral convection: pressure-dependent enhancement in chemotherapeutic delivery to solid tumors. *Clin. Cancer Res.* 15, 247–255.
- Grantab, R., Sivananthan, S., and Tannock, I. F. (2006). The penetration of anticancer drugs through tumor tissue as a function of cellular adhesion and packing density of tumor cells. *Cancer Res.* 66, 1033–1039.
- Gullino, P. M., Grantham, F. H., and Smith, S. H. (1965). The interstitial water space of tumors. *Cancer Res.* 25, 727–731.
- Huynh, L., Masereeuw, R., Friedberg, T., Ingelman-Sundberg, M., and Manivet, P. (2009). In silico platform for xenobiotics ADME-T pharmacological properties modeling and prediction. Part I: beyond the reduction of animal model use. *Drug Discov. Today* 14, 401–405.
- Jackson, T. L., and Byrne, H. M. (2000). A mathematical model to study the effects of drug resistance and vasculature on the response of solid tumors to chemotherapy. *Math. Biosci.* 164, 17–38.
- Jain, R. K. (1987). Transport of molecules in the tumor interstitium: a review. *Cancer Res.* 47, 3039–3051.
- Josan, J., Morse, D. L., Xu, L., Trissal, M., Baggett, B., Davis, P., et al. (2009). Solid-phase synthetic strategy & bioevaluation of a labeled δ -opioid receptor ligand Dmt-Tic-Lys for in vivo imaging. *Org. Lett.* 11, 2479–2482.
- Kang, Q., Wang, M., Mukherjee, P. P., and Lichtner, P. C. (2010). Mesoscopic modeling of multiphysicochemical transport phenomena in porous media. *Adv. Mech. Eng.* 2010:11. doi:10.1155/2010/142879
- Kerns, E. H., and Di, L. (2008). *Drug-Like Properties: Concepts, Structure Design and Methods. From ADME to Toxicity Optimization*. London: Elsevier.
- Kyle, A. H., Huxham, L. A., Chiam, A. S. J., Sim, D. H., and Minchinton, A. I. (2004). Direct assessment of drug penetration into tissue using a novel application of three-dimensional cell culture. *Cancer Res.* 64, 6304–6309.
- Lankelma, J., Dekker, H., Luque, R. E., Luykx, S., Hoekman, K., van der Valk, P., et al. (1999). Doxorubicin gradients in human breast cancer. *Clin. Cancer Res.* 5, 1703–1707.
- Levitt, D. G. (2003). The pharmacokinetics of the interstitial space in humans. *BMC Clin. Pharmacol.* 3:3. doi:10.1186/1472-6904-3-3
- Machado, R. (2012). Numerical simulations of surface reaction in porous media with lattice Boltzmann. *Chem. Eng. Sci.* 69, 628–643.
- Michelson, S., Sehgal, A., and Friedrich, C. (2006). In silico prediction of clinical efficacy. *Curr. Opin. Biotechnol.* 17, 666–670.
- Minchinton, A. I., and Tannock, I. F. (2006). Drug penetration in solid tumours. *Nat. Rev. Cancer* 6, 583–592.
- Modok, S., Scott, R., Alderden, R. A., Hall, M. D., Mellor, H. R., Bohic, S., et al. (2007). Transport kinetics of four- and six-coordinate platinum compounds in the multicell layer tumour model. *Br. J. Cancer* 97, 194–200.
- Morse, D. L., and Gillies, R. J. (2010). Molecular imaging and targeted therapies. *Biochem. Pharmacol.* 80, 731–738.
- Nederman, T., Carlsson, J., and Malmqvist, M. (1981). Penetration of substances into tumor tissue – a methodological study on cellular spheroids. *In vitro* 17, 290–298.
- Netti, P. A., Berk, D. A., Swartz, M. A., Grodzinsky, A. J., and Jain, R. K. (2000). Role of extracellular matrix assembly in interstitial transport in solid tumors. *Cancer Res.* 60, 2497–2503.
- Nori, F. (1996). Intermittently flowing rivers of magnetic flux. *Science* 271, 1373–1374.
- Nugent, L. J., and Jain, R. K. (1984). Extravascular diffusion in normal and neoplastic tissues. *Cancer Res.* 44, 238–244.
- Ozols, R. F., Locker, G. Y., Doroshow, J. H., Grotzinger, K. R., Myers, C. E., and Young, R. C. (1979). Pharmacokinetics of Adriamycin and tissue penetration in murine ovarian cancer. *Cancer Res.* 39, 3209–3214.
- Petsco, G. A. (2010). When failure should be the option. *BMC Biol.* 8:61. doi:10.1186/1741-7007-8-61
- Pluen, A., Boucher, Y., Ramanujan, S., McKee, T. D., Gohongi, T., di Tomaso, E., et al. (2001). Role of tumor-host interactions in interstitial diffusion of macromolecules: cranial vs. subcutaneous tumors. *Proc. Natl. Acad. Sci. U.S.A.* 98, 4628–4633.
- Primeau, A. J., Rendon, A., Hedley, D., Lilge, L., and Tannock, I. F. (2005). The distribution of the anticancer drug doxorubicin in relation to blood vessels in solid tumors. *Clin. Cancer Res.* 11, 8782–8788.
- Ramanujan, S., Pluen, A., McKee, T. D., Brown, E. B., Boucher, Y., and Jain, R. K. (2002). Diffusion and convection in collagen gels: implications for transport in the tumor interstitium. *Biophys. J.* 83, 1650–1660.
- Reinhardt, C., Groth, J., Olson, C. J., Field, S. B., and Nori, F. (1997). Spatiotemporal dynamics and plastic flow of vortices in superconductors with periodic arrays of pinning sites. *Phys. Rev. B Condens. Matter* 54, 16108–16115.
- Schmidt, M. M., and Wittrup, K. D. (2009). A modeling analysis of the effects of molecular size and binding affinity on tumor targeting. *Mol. Cancer Ther.* 8, 2861–2871.
- Shipley, R. J., and Chapman, S. J. (2010). Multiscale modelling of fluid and drug transport in vascular tumours. *Bull. Math. Biol.* 72, 1464–1491.
- Silhanek, A. V., Kramer, R. G. B., Van de Vondel, J., Moshchalkov, V. V., Milosevic, M. V., Berdiyrov, G. R., et al. (2010). Freezing vortex rivers. *Physica C Supercond.* 470, 726–729.

- Sinek, J., Sanga, S., Zheng, X., Frieboes, H., Ferrari, M., and Cristini, V. (2009). Predicting drug pharmacokinetics and effect in vascularized tumors using computer simulation. *J. Math. Biol.* 58, 485–510.
- Sun, J. D., Liu, Q., Wang, J., Ahluwalia, D., Ferraro, D., Wang, Y., et al. (2012). Selective tumor hypoxia targeting by hypoxia-activated prodrug TH-302 inhibits tumor growth in preclinical models of cancer. *Clin. Cancer Res.* 18, 758–770.
- Swartz, M. A., and Fleury, M. E. (2007). Interstitial flow and its effects in soft tissues. *Annu. Rev. Biomed. Eng.* 9, 229–256.
- Tlupova, S., and Cortez, R. (2009). Boundary integral solutions of coupled Stokes and Darcy flows. *J. Comput. Phys.* 228, 158–179.
- Tsimpanogiannis, I. N., and Lichtner, P. C. (2012). Fluid displacement and solid formation in a porous medium using invasion percolation in a gradient with pore blocking. *Energy Fuels* 26, 3935–3950.
- Walenta, S., Schroeder, T., and Mueller-Klieser, W. (2002). Metabolic mapping with bioluminescence: basic and clinical relevance. *Biomol. Eng.* 18, 249–262.
- Xie, Y., Simmons, C. T., and Werner, A. D. (2011). Speed of free convective fingering in porous media. *Water Resour. Res.* 47, w11501.
- Zhao, J., Salmon, H., and Sarntinoranont, M. (2007). Effect of heterogeneous vasculature on interstitial transport within a solid tumor. *Microvasc. Res.* 3, 224–236.

Conflict of Interest Statement: The authors declare that the research was conducted in the absence of any commercial or financial relationships that could be construed as a potential conflict of interest.

Received: 18 December 2012; paper pending published: 04 February 2013; accepted: 22 April 2013; published online: 10 May 2013.

Citation: Rejniak KA, Estrella V, Chen T, Cohen AS, Lloyd MC and Morse DL (2013) The role of tumor tissue architecture in treatment penetration and efficacy: an integrative study. *Front. Oncol.* 3:111. doi: 10.3389/fonc.2013.00111
This article was submitted to *Frontiers in Molecular and Cellular Oncology*, a specialty of *Frontiers in Oncology*.
Copyright © 2013 Rejniak, Estrella, Chen, Cohen, Lloyd and Morse. This is an open-access article distributed under the terms of the Creative Commons Attribution License, which permits use, distribution and reproduction in other forums, provided the original authors and source are credited and subject to any copyright notices concerning any third-party graphics etc.



Regulation of cell proliferation and migration in glioblastoma: new therapeutic approach

Yangjin Kim*

Department of Mathematics, Konkuk University, Seoul, South Korea

Edited by:

Katarzyna A. Rejniak, H. Lee Moffitt
Cancer Center and Research Institute,
USA

Reviewed by:

Andrea Hawkins-Daarud, University of
Washington, USA
Xuefeng Gao, Center of Cancer
Systems Biology, USA

***Correspondence:**

Yangjin Kim, Department of
Mathematics, 120 Neungdong-ro,
Gwangjin-gu, Seoul, 143-701, South
Korea.
e-mail: ahyouhappy@konkuk.ac.kr

Glioblastoma is the most aggressive brain cancer with the poor survival rate. A microRNA, miR-451, and its downstream molecules, CAB39/LKB1/STRAD/AMPK, are known to play a critical role in regulating a biochemical balance between rapid proliferation and invasion in the presence of metabolic stress in microenvironment. We develop a novel multi-scale mathematical model where cell migration and proliferation are controlled through a core intracellular control system (miR-451-AMPK complex) in response to glucose availability and physical constraints in the microenvironment. Tumor cells are modeled individually and proliferation and migration of those cells are regulated by the intracellular dynamics and reaction-diffusion equations of concentrations of glucose, chemoattractant, extracellular matrix, and MMPs. The model predicts that invasion patterns and rapid growth of tumor cells after conventional surgery depend on biophysical properties of cells, dynamics of the core control system, and microenvironment as well as glucose injection methods. We developed a new type of therapeutic approach: effective injection of chemoattractant to bring invasive cells back to the surgical site after initial surgery, followed by glucose injection at the same location. The model suggests that a good combination of chemoattractant and glucose injection at appropriate time frames may lead to an effective therapeutic strategy of eradicating tumor cells.

Keywords: glioblastoma, cell migration and proliferation, miR-451, AMPK, cancer invasion and therapy

1. INTRODUCTION

Glioblastoma multiforme (GBM) is the most common and aggressive form of primary brain tumor with the median survival time of approximately 1 year from the time of diagnosis (Demuth and Berens, 2004; Styli et al., 2005; Jacobs et al., 2011). GBMs are characterized by rapid proliferation and aggressive invasion into surrounding normal brain tissue, which leads to inevitable recurrence after surgical resection of the primary tumor (Chintala et al., 1999). Surgery is the primary treatment method, generally followed by inefficient radiotherapy and chemotherapy. Innovative therapeutic approaches of targeting these invasive cells are needed in order to improve clinical outcome (Davis and McCarthy, 2001). Glioblastoma cells are encountered with many challenges such as hypoxia (lack of oxygen), acidity, and limited nutrient availability as tumor growth is proceeded. To keep up with rapid growth, tumor cells need to adapt to these biochemical changes in the harsh microenvironment (Godlewski et al., 2010a). In order to overcome these challenges and sustain their rapid growth, cancerous cells change their typical metabolism (oxidative phosphorylation and anaerobic glycolysis) to inefficient metabolic machinery [high levels of glucose uptake and lactate production; *Warburg Effect* (Warburg, 1956; Kim and Dang, 2006)].

The Krebs, or tricarboxylic acid (TCA) cycle is a main step for generating an energy source, ATP, in non-hypoxic normal cells. While this effective way of metabolism is used by differentiated cells, tumor cells favor a seemingly less effective way of metabolism, aerobic glycolysis (Heiden et al., 2009) due to production of lactic acid, and consumption of large amounts of glucose (Kim

and Dang, 2006). Adapting this aerobic glycolysis (Gatenby and Gillies, 2004), cancer cells appear to have an advantage of not having to rely on oxygen for energy source in hypoxic (hostile) microenvironment (Gatenby and Gillies, 2004; Kim and Dang, 2006). Better understanding of basic mechanism of glycolysis and intracellular dynamics may provide better clinical outcomes. For example, inhibition of glycolysis may prevent drug resistance (Xu et al., 2005). Cancer cells also adapt angiogenesis and migration as a way of ensuring an adequate glucose supply (Godlewski et al., 2010a). However, appropriate intracellular responses to glucose withdrawal are a crucial component of adaptation in order to survive periods of metabolic stress and maintain viability as a tumor grows (Jones and Thompson, 2009). The 5'-adenosine monophosphate activated protein kinase (AMPK) pathway is the major cellular sensor of energy availability (Hardie, 2007) and is activated in the presence of metabolic stress as a way of promoting glucose uptake and energy conservation (Hardie, 2007). Dysregulation of miRNAs, 22 nucleotide single-stranded non-coding RNAs (Bartel, 2009), has been associated with oncogenic activities and tumor suppressor (Esquela-Kerscher and Slack, 2006) in many cancer types, including glioblastoma where alterations in miRNA expression induces tumorigenesis (Godlewski et al., 2008; Lawler and Chiocca, 2009). For example, miR-21 promote glioma invasion by down-regulation of inhibitors of matrix metalloproteinase (MMP) (Gabriely et al., 2008). In a recent paper, Godlewski et al. (2010a) found that a particular microRNA, miR-451, determines glioma cell motility and proliferation by regulating its counterpart, AMPK signaling component (CAB39/LKB1/AMPK),

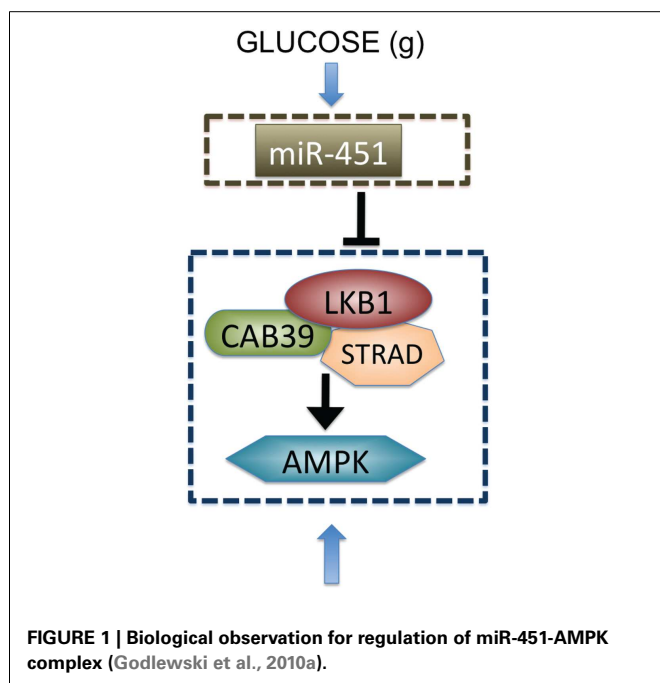
in response to various glucose levels. While normal glucose led to up-regulation of miR-451 expression and rapid cell proliferation, deprived glucose induced down-regulation of miR-451 and elevated cell migration. Godlewski et al. (2010a) also found mutual antagonism between miR-451 activity and AMPK complex levels, which was modeled using a mathematical model in Kim et al. (2011a). See **Figure 1**.

Invasion of glioma cells leads to treatment failure due to poor screening of invasive individual cells by the standard clinical device and difficulty in complete elimination of the migratory cells in typical brain surgery, causing tumor recurrence (Chintala et al., 1999). Many factors may contribute to glioma cell motility in the brain tissue. Extra cellular matrix (ECM) may stimulate glioma invasion in a process known as haptotaxis. Haptotactic process is suggested to be activated by pre-existing brain components and remodeling of the ECM via proteolysis (Chintala et al., 1999; Jaalinoja et al., 2000; Choe et al., 2002). Glioma cell's motility is also influenced by various chemoattractants, which include ligands of scatter factor/hepatocyte growth factor (SF/HGF) (Lamszus et al., 1998), the EGF family (Lund-Johansen et al., 1990), the TGF- β family (Platten et al., 2001), SDF-1 (Zhou et al., 2002), and certain lipids (Young and Brooklyn, 2007). We note that other authors studied the action of HGF or scatter factor on cell migration (Tamagnone and Comoglio, 1997; Luca et al., 1999; Stella and Comoglio, 1999; Trusolino and Comoglio, 2002; Scianna et al., 2009). Beside these factors, other cell types such as microglia can also provide indirect stimulation of cell migration by secreting matrix components and chemoattractants (Watters et al., 2005). Glioma cell migration may be regulated by specific substrates and structures in the brain as well. For instance, glioma cells are also known to follow preferred dispersion paths such as white matter tracts or the basal lamina of blood vessels. Invasion patterns of glioma cells in three-dimensional tumor spheroids were studied in Kim et al. (2009)

where the migration patterns exhibit a gradual shift from branching to dispersion and depend on three key parameters (cell-cell adhesion strength, haptotactic parameter, and chemotactic sensitivity). There are several publications based on a diffusion model (Swanson et al., 2003; Harpold et al., 2007).

Other authors investigated the transition between migration and proliferation using kinetic or diffusion models (Chauviere et al., 2010; Hatzikirou et al., 2010; Pham et al., 2012). A general review on hybrid models of tumor growth can be found in Rejniak and Anderson (2011). In the present paper, the detailed dynamics of a core control system (miR-451-AMPK) at each cell site is embedded in a hybrid model and is linked to extracellular glucose molecules which diffuse to brain tissue. In the hybrid model, tumor cells either migrate or proliferate in response to biochemical signals such as glucose and chemoattractants. Migratory cells are attracted to chemotactic source and secrete MMPs to degrade extracellular matrix (ECM). We show how the spatial migrating patterns of glioma cells can be controlled by the core system in the absence and presence of chemotactic source after initial surgery and explore how injection of glucose and chemoattractants could be manipulated for better therapeutic options. More importantly, we use the current model to test hypotheses on chemotaxis-glucose-driven therapy, i.e., eradicating "invisible" invasive cells after surgery. We propose that injection of chemoattractants after surgery followed by glucose injection at the tumor site would bring migratory glioma cells back to the surgical site and make them detectable by MRI, and the follow-up surgery may improve clinical outcomes by eradicating the remaining growing tumor cells.

In Section 2 we introduce a multi-scale mathematical model. In Section 3, we present the results from the hybrid model. Discussion and future work are provided in Section 4. Parameter estimation and non-dimensionalization of the model are given in Appendix.



2. MATERIALS AND METHODS

In this section, we introduce a multi-scale mathematical model of regulation of cell proliferation and migration in glioblastoma. We consider a brain tissue, $\Omega = [0, L]^2$, with glioblastoma tumor initially occupying a sphere $\Omega_c^0 = \{x: |x| < R_0, R_0 < L\}$, where R_0 is the initial radius of the tumor spheroid. A schematic of the hybrid model is shown in **Figure 2**. We first introduce the cell-mechanics part of the model.

2.1. THE CELL-MECHANICS

The mechanical behavior of individual cells is based on the models developed by Dallon and Othmer (2004) and Kim et al. (2007, 2011b). The forces on a cell in the model include (i) the dynamic drag forces from adhesive bonds with neighboring cells, (ii) the active forces \mathbf{T}_i exerted on the substrate or neighboring cells and the reaction force ($\mathbf{M}_{j,i}$), (iii) static friction force $\mathbf{S}_{j,i}$ for rigid attachment between cells or between a cell and the substrate. (See DO for a more detailed discussion of all forces involved.) The total force on the i th cell is then given by

$$\mathbf{F}_i = \sum_{j \in \mathcal{N}_i^a} \mathbf{M}_{j,i} + \sum_{j \in \mathcal{N}_i^a} \mathbf{T}_i + \sum_{j \in \mathcal{N}_i^d} \mu_{ij}(\mathbf{v}_j - \mathbf{v}_i) + \sum_{j \in \mathcal{N}_i^s} \mathbf{S}_{j,i} \quad (1)$$

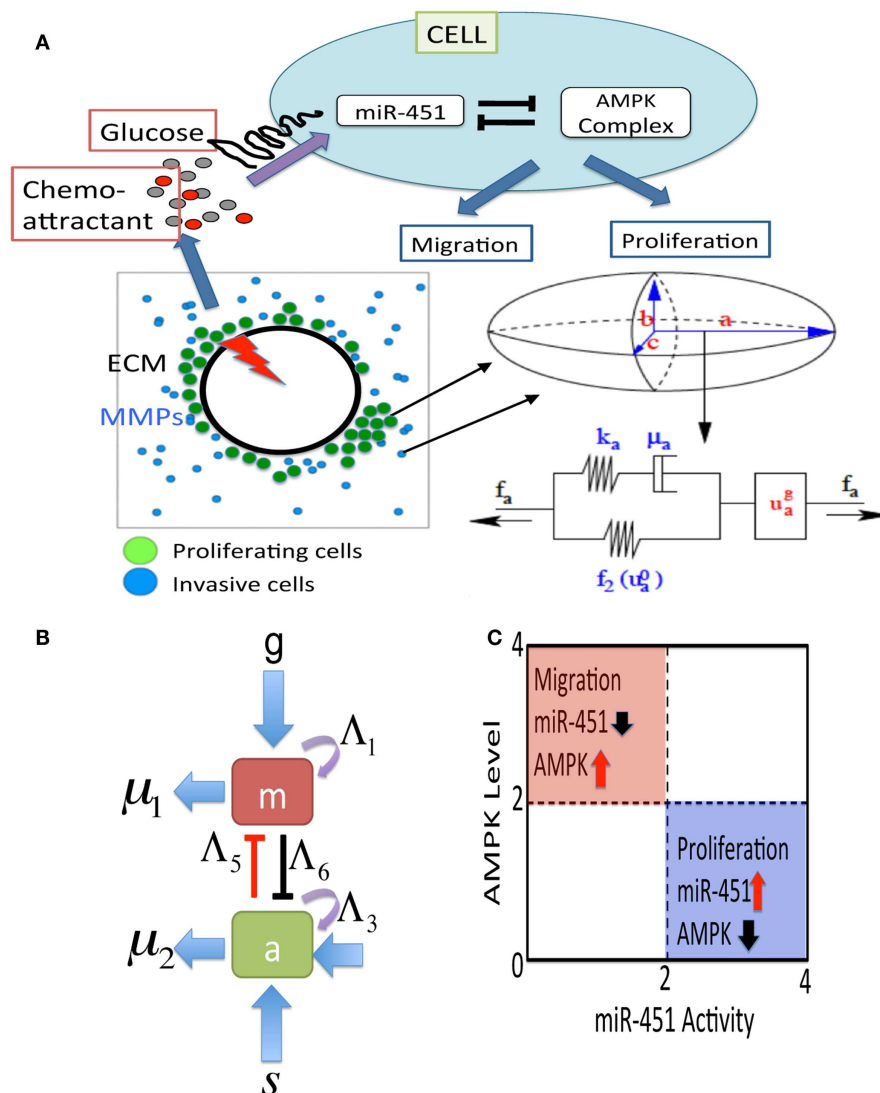


FIGURE 2 | (A) A schematic of the hybrid model for therapeutic approaches. (Top) Simplified model of the core control system (miR-451 and AMPK complex) in response to various glucose levels at a tumor cell site. The core system determines the cell fate, either proliferation or migration. Chemoattractants in the brain tissue determine the migration direction of the cell. (Bottom, Left) Model domain: some migratory cancer cells (blue) near the tumor core site are activated to become a proliferative one (green) via miR-451-AMPK regulation in response to glucose injection levels (red thunder) at the center of the tumor site.

(Bottom, right) changes in the length of the a -axis of a cell (the ellipsoid) under a given force (f_a ; arrow) consist of the passive change in the first component (a Maxwell element in parallel with a non-linear spring) and the change due to the growth (u_g^a). The growth component depends on the levels of miR-451 and AMPK complex, and the force (f_a). The mechanical and growth elements are the same along all axes.

(B) miR-451 activity and levels of its target complex (CAB39/LKB1/AMPK) were represented by “ m ” and “ a ,” respectively. **(C)** The migratory and proliferative regions based on miR-451 activity and AMPK levels.

where \mathcal{N}_i^a denotes the neighbors of i , including the substrate, upon which it can exert traction, \mathcal{N}_i^d is the set of “cells” (which includes substrate and extracellular matrix) that interact with i via a frictional force, and \mathcal{N}_i^s denotes the set of cells that statically bind to cell i . These force balance equations allow us to calculate all forces involved and track down locations of all cells in addition to biophysical response of the cells.

There are two different kinds of cells involved—proliferative one and motile one. The basic mechanical scheme of cell proliferation is modeled as in Kim et al. (2007) and the basic algorithm for

motile cells is introduced as in Dallon and Othmer (2004). The cells are treated as oriented ellipsoids and cytoplasm is considered as an incompressible, viscoelastic solid. When growth is off, their volume is constant under all deformations. However, growth component (u_g^a) is included in series the active response and the passive forces. (See Figure 2A.) We use the multiplicative form of the growth rate function for the i -th axis given by

$$(u_i^g)' = f(\sigma) P(M, A)$$

where σ is the force acting on the cell and P is a function of the miR-451 activity (M) and AMPK levels (A). The growth function $f(\sigma)$ is defined so that cells can grow under sufficiently small tensile and compressive forces (Kim et al., 2007, 2011b). The relationship between growth and stresses are complex and further detailed modeling work is needed. Cell proliferation may depend on up- or down-regulation of intracellular players that control the cell cycle. In the present work, we assume that the core system determines cell proliferation, i.e., a cell proliferates when miR-451 (AMPK) is up-regulated (down-regulated) at the cell site. Then, the function $P(M, A)$ is defined as

$$P(M, A) = \begin{cases} 1 & \text{if } M > th_M, A < th_A \\ 0 & \text{otherwise} \end{cases} \quad (2)$$

where th_M, th_A are threshold values of the miR-451 and AMPK levels that will be introduced in Section 2.3. The active force \mathbf{T}_i of cell i is given by

$$\mathbf{T}_i = \phi(M_i) \frac{\nabla C}{\sqrt{K_C + |\nabla C|^2}} \quad (3)$$

where C is the concentration of a chemoattractant. Here, the indicator function $\phi(M)$ is given by

$$\phi(M) = \begin{cases} r_n F_0 & \text{if } M < th_M, A > th_A, \text{ cell without} \\ & \text{physical constraints,} \\ 0 & \text{otherwise,} \end{cases} \quad (4)$$

where F_0 is the basal magnitude of the active force ($0 \leq |\mathbf{T}_i| \leq F_0$) and r_n is a random number in $[0.8, 1.2]$. Therefore, the active force is completely turned off for proliferative cells ($M_i > th_M, A < th_A$), cells under physical constraints (a cell completely surrounded by neighboring cells), or in the absence of chemotactic signal ($\nabla C = 0$).

2.2. REACTION-DIFFUSION

We let $G(\mathbf{x}, t)$, $C(\mathbf{x}, t)$, $\rho(\mathbf{x}, t)$, $P(\mathbf{x}, t)$ be the concentrations of glucose, a chemoattractant of glioma cells, ECM, and MMPs, respectively, at space \mathbf{x} and time t . Governing equations of all variables are given by

$$\begin{aligned} \frac{\partial G}{\partial t} = & \underbrace{D_G \Delta G}_{\text{Diffusion}} + \underbrace{\sum_{j=1}^{N_G} \lambda_{in}^G I_{[t_j^G, t_j^G + \tau_d^G]} \times \Omega_\epsilon}_{\text{Injection}} \\ & + \underbrace{\lambda_b \eta_1(x, G)}_{\text{Input}} - \underbrace{\lambda_c \eta_2(x, G)}_{\text{Consumption}} - \underbrace{\mu_G G}_{\text{Removal}} \text{ in } \Omega, \end{aligned} \quad (5)$$

$$\frac{\partial C}{\partial t} = \underbrace{D_C \Delta C}_{\text{Diffusion}} + \underbrace{\sum_{j=1}^{N_C} \lambda_{in}^C I_{[t_j^C, t_j^C + \tau_d^C]} \times \Omega_\epsilon}_{\text{Injection}} - \underbrace{\mu_C C}_{\text{Decay}} \text{ in } \Omega, \quad (6)$$

$$\frac{\partial \rho}{\partial t} = - \underbrace{\lambda_1 P \rho}_{\text{Degradation}} + \underbrace{\lambda_2 \rho (1 - \frac{\rho}{\rho_*})}_{\text{Release/reconstruction}} \text{ in } \Omega, \quad (7)$$

$$\frac{\partial P}{\partial t} = \underbrace{D_P \Delta P}_{\text{Diffusion}} + \underbrace{\lambda_3 \eta_3(x, P)}_{\text{Production by cells}} - \underbrace{\mu_P P}_{\text{Decay}} \text{ in } \Omega, \quad (8)$$

where D_G, D_C, D_P are the diffusion coefficients of glucose, chemoattractant, and MMPs, respectively, $\lambda_{in}^G (\lambda_{in}^C)$ is the glucose (chemoattractant) injection rate on a subdomain Ω_ϵ over time intervals $[t_j^G, t_j^G + \tau_d^G], j = 1, \dots, N_G$ ($[t_j^C, t_j^C + \tau_d^C], j = 1, \dots, N_C$) with a period $\tau^G (\tau^C)$ and duration $\tau_d^G (\tau_d^C)$ after the initial surgery at $t = t_S$ ($t_1^G > t_S$), λ_b is the glucose flux from a blood flow, λ_c is the consumption rate of glucose by tumor cells, λ_1 is the degradation rate of ECM by MMPs, λ_2 is the release/reconstruction rate of ECM, λ_3 is the secretion rate of MMPs by tumor cells, μ_G is the glucose removal rate from the system via blood flow and glucose consumption in the surrounding tissue (Chiro et al., 1982; Rozental et al., 1991; Goldman et al., 1996; Aronen et al., 2000; Valle-Casuso et al., 2012), μ_C, μ_P are decay rates of chemoattractant and MMPs, respectively. Here, indicator functions (η_1, η_2, η_3) are given by

$$\eta_1(x, G) = \begin{cases} 1 & \text{blood vessel} \\ 0 & \text{otherwise} \end{cases}, \quad \eta_2(x, G) = \begin{cases} 1 & \text{tumor} \\ 0 & \text{otherwise} \end{cases},$$

$$\eta_3(x, P) = \begin{cases} 1 & \text{invasive cells} \\ 0 & \text{otherwise.} \end{cases}$$

We also assume no flux (Neumann) boundary conditions $\frac{\partial G}{\partial \nu} = 0, \frac{\partial C}{\partial \nu} = 0, \frac{\partial P}{\partial \nu} = 0$, on $\partial\Omega$. The reaction-diffusion equations (5–8) are solved on the regular grid using the alternating-direction implicit (ADI) method and the non-linear solver *nksol* for algebraic systems. A typical spatial grid size used is $h_x = h_y = 0.01$ on a square domain $[0, 1] \times [0, 1]$. An adaptive time stepping method is used. **Table 1** lists parameter values and references values for the equations (5)–(8).

2.3. MATHEMATICAL MODELING OF miR-451-AMPK CONTROL

The core control model of miR-451 activity and AMPK levels introduced in Kim et al. (2011a) was integrated into the hybrid model. Based on biological observations, we write the phenomenological equations for the rate change of those key molecules (m, a) as follows:

$$\frac{dm}{dt} = \lambda_g g + \frac{\Lambda_1 \Lambda_2^2}{\Lambda_2^2 + \Lambda_5 a^2} - \mu_1 m, \quad (9)$$

$$\frac{da}{dt} = s + \frac{\Lambda_3 \Lambda_4^2}{\Lambda_4^2 + \Lambda_6 m^2} - \mu_2 a, \quad (10)$$

where g is the signaling pathways from glucose to miR-451, s is the signaling pathways to AMPK complex, Λ_1, Λ_3 are the auto-catalytic enhancement parameters for miR-451, AMPK complex, respectively, Λ_2, Λ_4 are the Hill-type inhibition saturation parameters from the counter part of miR-451 and AMPK complex, respectively, Λ_5 is the inhibition strength of miR-451 by the AMPK

Table 1 | Values of reference variables and parameters used in the hybrid model.

Var	Description	Value	Refs.
DIFFUSION COEFFICIENTS			
D_G	Glucose	$6.7 \times 10^{-7} \text{ cm}^2/\text{s}$	Jain (1987)
D_C	Chemoattractant (EGF)	$1.66 \times 10^{-6} \text{ cm}^2/\text{s}$	Thorne et al. (2004)
D_P	MMPs	$8.0 \times 10^{-9} \text{ cm}^2/\text{s}$	Saffarian et al. (2004)
PRODUCTION/DECAY/CONSUMPTION RATES			
λ_2	ECM reconstruction/remodeling rate	$5.6 \times 10^{-3} \text{ s}^{-1}$	TW
λ_3	MMP production rate	5.8	
λ_c	Glucose consumption rate by tumor	0.8 pg/cell/min	TW
μ_G	Removal rate of glucose in brain tissue	0.0034 min^{-1}	TW
μ_C	Decay rate of chemoattractant (EGF)	$8.02 \times 10^{-6} \text{ s}^{-1}$	Kudlow et al. (1986)
λ_1	ECM degradation rate by MMPs	$3.0 \times 10^4 \text{ cm}^3 \text{ g}^{-1} \text{ s}^{-1}$	TW
μ_P	Decay rate of MMPs	$5.0 \times 10^{-5} \text{ s}^{-1}$	TW
REFERENCE VALUES			
T	Time	1 h	
L	Length	2.0 mm	
G^*	Glucose concentration	$4.5 \times 10^{-3} \text{ g/cm}^3$	Deisboeck et al. (2001), Sander and Deisboeck (2002), Godlewski et al. (2010a)
C^*	Chemoattractant (EGF) concentration	$1.0 \times 10^{-8} \text{ g/cm}^3$	Boccardo et al. (2003), Sadlonova et al. (2005)
ρ^*	ECM concentration	$1.0 \times 10^{-3} \text{ g/cm}^3$	Kaufman et al. (2005), Stein et al. (2007)
P^*	MMP concentration	$1.0 \times 10^{-7} \text{ g/cm}^3$	Annabi et al. (2005)

complex, Λ_6 is the inhibition strength of the AMPK complex by miR-451, μ_1, μ_2 are microRNA/protein degradation rates of miR-451 and AMPK complex, respectively. **Table A1** in Appendix summarizes the dimensionless parameters. By taking the thresholds $th_M (=2.0)$ of miR-451 levels and $th_A (=2.0)$ of AMPK complex, we shall define the migratory region M_m by $M_m = \{(M, A) \in \mathbb{R}^2: M < th_M, A > th_A\}$ and the proliferative region M_p by $M_p = \{(M, A) \in \mathbb{R}^2: M > th_M, A < th_A\}$. See **Figure 2C** for a diagram for proliferative and migratory regions.

3. RESULTS

In this Section, we present analysis of the hybrid model and predictions for therapeutic strategies for eliminating invasive glioma cells.

3.1. DYNAMICS OF THE MODEL

In order to validate the mathematical model, we first investigated invasion patterns of glioma cells embedded in high and low glucose levels in the absence of blood supply of glucose ($\lambda_b = 0$), glucose injection ($\lambda_{in}^G = 0$) and chemoattractants, and by assuming cells on the surface of the spheroid are migrating toward the glucose gradient (∇G) [i.e., by replacing $\frac{\nabla C}{\sqrt{K_C + |\nabla C|}}$ with $\frac{\nabla G}{\sqrt{K_G + |\nabla G|}}$ in the active force form in the equation (3)]. **Figures 3A–C** show spatial profiles of tumor spheroids in response to high ($G_0 = 1.0$), intermediate ($G_0 = 0.5$), and low ($G_0 = 0.1$) glucose levels. **Figure 3D** shows relative miR-451 levels in response to high (*Glucose+*) and low (*Glucose−*) levels in simulations and experiments (U251 and LN229 cell lines) (Godlewski et al., 2010a). General patterns of tumor spheroids in response to high (**Figure 3A**) and low (**Figure 3C**) glucose levels in simulations are in good agreement with experimental observations in Godlewski et al. (2010a) where high (4.5 g/l) and low (0.3 g/l) levels of glucose induced over- and under-expression of miR-451 (see **Figure 3D**), leading

to proliferating (as in **Figure 3A**) and dispersed invasive (as in **Figure 3C**) patterns of tumor cells, respectively.

We investigate invasion dynamics of a growing tumor in response to glucose levels in the presence of blood supply. **Figures 4A–C** show spatial patterns of a growing/invading tumor in response to glucose supply ($G_0 = 10$) at time $t = 0, 20, 30$ h. Initial high glucose level is decreased due to glucose consumption by tumor cells at the center of the domain and nearby tissue (**Figures 4D–F**). The miR-451 activity at cell sites is decreased and AMPK levels creep up due to decreased glucose levels (**Figures 4M,N**). Cells on the surface of the tumor mass immediately respond to intracellular biochemical signals (miR-451 and AMPK levels) and begin to migrate when miR-451 level drops below the threshold ($M < th_M = 2.0$) and AMPK level is up-regulated ($A > th_A = 2.0$) due to decreased glucose level at the cell site (cf. **Figure 2C**). However, cells at the center of the tumor mass are surrounded by neighboring cells and stay inside the tumor due to physical constraints despite biochemical migration signals ($M < th_M, A > th_A$). **Figure 4N** shows time courses of miR-451 activities and AMPK levels in response to glucose levels in **Figure 4M** at two cell sites [cell id = 220 with initial location (108.2, 99.5); cell id = 160 with initial location (100.5, 99.8)]. The miR-451 levels for both cells drop below the threshold (th_M) and AMPK levels are above the threshold (th_A) around $t = 16$ h already, generating “migratory” signal. However, the cell (marked in “gray”; cell id = 220) in **Figure 4A** still stays in the tumor mass at $t = 20$ h (**Figure 4B**) and begins to shed off at later time ($t = 26$ h; arrow in **Figure 4N**) when free space is available. Another cell (cell id = 160) at the center of domain remains at the center of the tumor due to physical constraints until final time [$t = 40$ h; final location (100.3, 99.7)]. When glioma cells on the surface of the tumor mass migrate into surrounding brain tissue, proteinases (MMPs) are secreted in the invading front and ECM is degraded due to high levels of MMPs (proteolysis). See localized

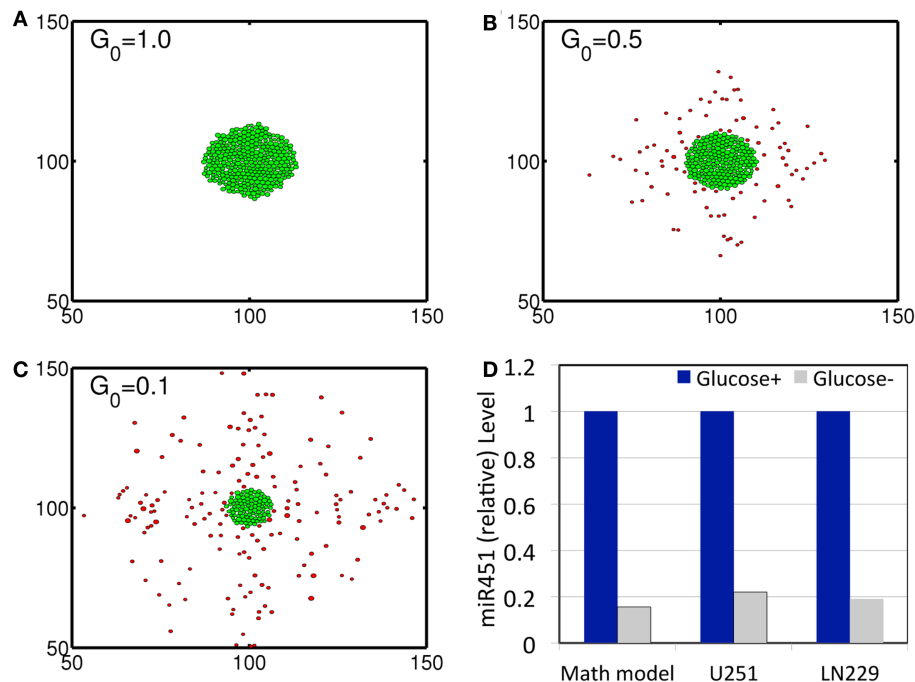


FIGURE 3 | (A–C) Profiles of tumor spheroid in response to high ($G = 1.0$), intermediate ($G = 0.5$), and low ($G = 0.1$) glucose levels at $t = 30$ h. Domain size = $[50 \mu\text{m}, 150 \mu\text{m}] \times [50 \mu\text{m}, 150 \mu\text{m}] = [0.25, 0.75]^2$ in the dimensionless domain $[0, 1]^2$. **(D)** Comparison between simulation results and experimental data. In response to high (Glucose+, blue) and low

(Glucose–, gray) glucose levels, miR-451 expression levels are quantified. Simulation results are in good agreement with experimental results on U251 and LN229 cell line in Godlewski et al. (2010a). * $\lambda_b = 0$, $\lambda_{in}^G = 0$. It was assumed that tumor cells respond to the glucose gradient for migration *in vitro* as in Godlewski et al. (2010a).

MMPs at cell sites and degraded ECM profiles in **Figures 4G–L**, respectively.

Figures 5A–D show cyclic tumor growth patterns at $t = 0, 20, 38, 46$ h in response to periodic glucose injection. When high doses ($G = 10.0$) of glucose are introduced into the system at $t = 0, 26$ h, fluctuating glucose values (**Figure 5E**) at a cell site (cell id = 220; arrowhead in **Figures 5A–D**) lead to a cycle of up-regulation and down-regulation of miR-451 (**Figure 5F**). Cells outside the tumor core respond to this stimulus by either proliferating or migrating. See **Figures 5A–D**. Cell phenotype changes between proliferative and migratory cells are more clear in **Figure 5G**. Initial proliferative cells due to high glucose levels change their phenotype to become migratory cells whenever glucose level lowered to induce migratory phase [$M > th_M$, $A < th_A$; $\sim t = 16$ h (black arrow) and $t = 42$ h (red arrow)]. These migratory cells change their phenotypes to proliferative cells ($\sim t = 26$ h; black arrowhead) when the high glucose level from glucose injection induces proliferative phase ($M > th_M$, $A < th_A$).

3.2. SENSITIVITY OF THE MODEL TO INHIBITION PARAMETERS (α , β) IN THE CORE SYSTEM

From now on, the *activation time for invasion* is defined to be time when a cell in proliferative phase ($M > th_M$, $A < th_A$) changes its phenotype to a migratory cell ($M < th_M$, $A > th_A$) due to a microenvironmental change (glucose fluctuation) and begins to migrate away from the main tumor aggregate for the first time among all other cells. In **Figure 6A** we show steady state values

of miR-451 (M^f) in response to different glucose levels for various inhibition strength (β) of AMPK complex by miR-451. See Appendix A.2 for definition and role of β (and α below) in the core system. As β is decreased the bifurcation curve shifts to the right (higher glucose levels). In the control case ($\beta = 1.0$), a relatively low glucose level ($G = 0.4$) is required for activation of cell invasion. When this inhibition strength is weakened (β small), a cell may begin to migrate for larger glucose levels. **Figure 6B** shows activation time for invasion as a function of inhibition strength of AMPK complex production (β). As β is decreased from control base parameter ($\beta = 1.0$), the rate of AMPK complex formation is increased and miR-451 level is decreased at earlier time, leading to early activation time for invasion. This might have biological implications. For example, one could totally use or partially block inhibition pathways from miR-451 to AMPK (decrease in β) in order to boost invasion activation under certain circumstances.

Figures 7A,B show effect of inhibition strength (α) of miR-451 production by AMPK complex on tumor population and activation time for cell invasion. As the inhibition strength α is increased, miR-451 levels are decreased at earlier time (**Figure 7B**) and more cells on the surface of the tumor mass migrate from the biochemical signal. See **Figure 7A**. This would have several implications. For example, cell migration or dispersion might be prevented by any drug that blocks inhibitory activity of AMPK complex to miR-451. This may generate faster growth of tumor mass since most of cells would be in proliferative phase. Therefore, this could be used

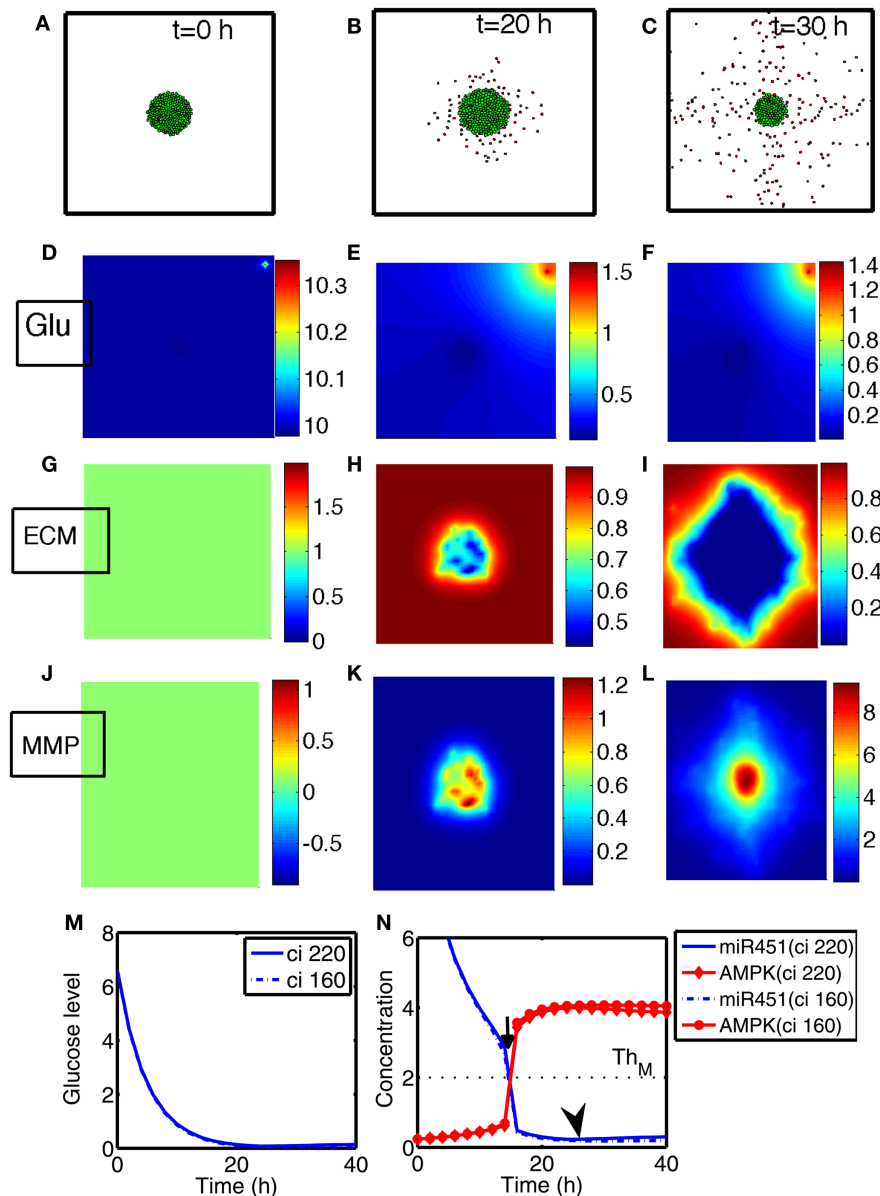


FIGURE 4 | (A–C) Tumor invasion pattern at time $t = 0, 20, 30$ h in response to glucose levels ($G_0 = 10$). Domain size $= [0.25, 0.75] \subset [0, 1]^2$. **(D–F)** Profiles of glucose concentration on the domain $[0, 1] \times [0, 1]$. Glucose flux from a blood vessel induces a peak value at the upper right corner. **(G–I)** Profiles of ECM on the subdomain $[0.25, 0.75] \times [0.25,$

$0.75] \subset [0, 1]^2$. ECM were degraded in the invasive region. **(J–L)** Profiles of MMPs on the subdomain $[0.25, 0.75] \times [0.25, 0.75] \subset [0, 1]^2$. MMPs are localized in tumor region. **(M)** Glucose levels at two cell sites (cell id = 220, 160). **(N)** Concentrations of intracellular variables, miR-451 and AMPK complex, at the cell sites in **(M)**.

as a temporary way of holding cell migration in order to not miss out single migratory cells for surgery.

3.3. PREDICTIONS OF THE MODEL FOR A POSSIBLE THERAPEUTIC APPROACH

In this section, we developed therapeutic strategies for eradicating *invisible* migratory glioma cells in the brain after conventional surgery where only *visible* parts of tumor mass are removed. Here we assume that invasive cells in surrounding tissue can sense and respond to the chemoattractant gradient (∇C).

Figures 8A–F show spatial profiles of the tumor cells at $t = 0, 17, 25, 32, 39, 44$ h, respectively. After first surgery (region inside red dotted circle in **Figure 8A**) at $t = 0$, a chemoattractant was injected at the center of the resected area. See **Figures 9D–F** for spatial profiles of chemoattractant at time $t = 0, 16, 18$ h. Invasive cells begin to migrate back to the surgical site. After waiting 17 h ($t_1^G = 17$), a high dose of glucose was introduced into the system at the center of surgical site and glucose molecule diffuses through the domain (**Figures 9A–C**). High glucose levels trigger the intracellular switch from the migratory phase to the proliferative mode

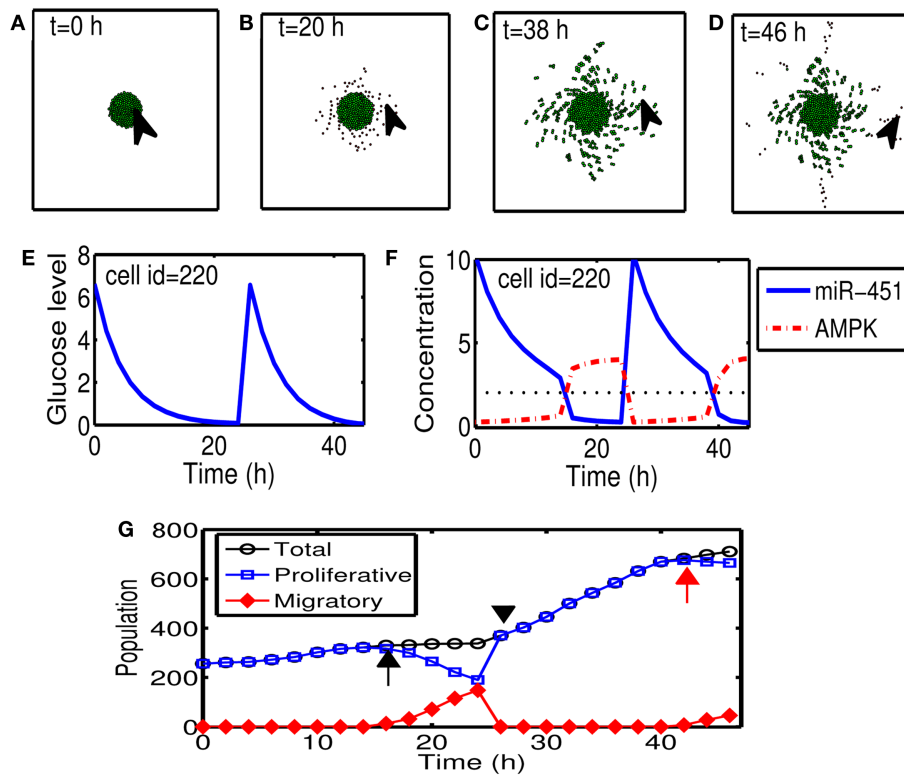


FIGURE 5 | (A–D) Tumor growth patterns at $t=0, 20, 38, 46$ h in response to glucose injection. Two cycles of proliferation-migration pattern are observed after initial ($t=0$ h) and second ($t=26$ h) injections of glucose ($G=10$). Domain size = $[0.2, 0.8] \times [0.2, 0.8] \subset [0, 1]^2$. **(E)** Glucose level at a cell site [cell id = 220; arrowhead in (A–D)]. **(F)** Time course of miR-451 activity and AMPK concentration at the cell site in (E). Dotted black line in the

middle = threshold value of miR-451 (th_M). **(G)** Time course of cell populations: proliferative (blue square), migratory (red diamond), and total (black circle) cells. Some of proliferative cells become migratory ones around $t=16$ h (black arrow) and $t=42$ h (red arrow) when miR-451 levels drop below threshold due to lowered glucose levels. All migratory cells enter the proliferative phase around $t=26$ (black arrowhead) in response to glucose injection.

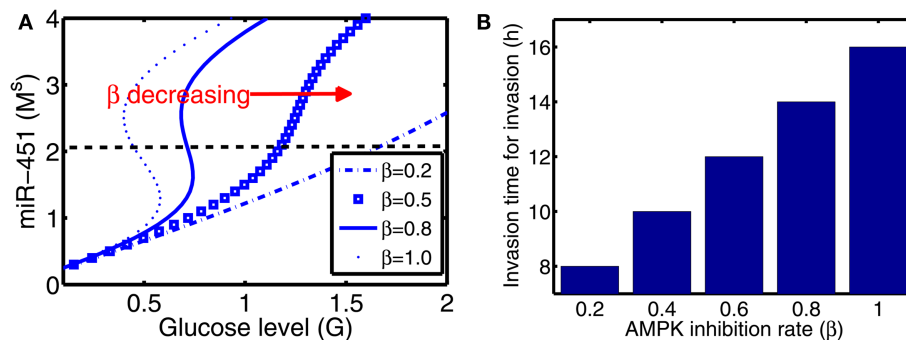


FIGURE 6 | (A) Steady state values of miR-451 (M^S) as a function of glucose level (G) for various inhibition strength of AMPK by miR-451 (β) in core control system. **(B)** Effect of the inhibition rate (β) on activation time

for glioma cell invasion in the hybrid model. As β is decreased, activation time for invasion is decreased. See Appendix A.2 for definition and role of β in the core system.

for invasive cells near the injection site (Figure 9G). Figure 9G shows time courses of miR-451 activity and AMPK level at two cell sites (cell id = 36, 37). A cell (cell id = 36) close to the center of the resection site is activated for proliferation at the earlier time ($\sim t=17$). Green cells inside the blue dotted circle in Figure 8B represent proliferative cells due to high glucose levels while red

cells outside the blue circle are still migratory cells in migratory phase ($M < th_M$, $A > th_A$) from low glucose levels. While infiltrative tumor cells after surgery may not be detected, regrown tumor mass may be detected by conventional screening tools such as MRI when tumor density is high enough. This may increase the probability of eliminating invasive cells.

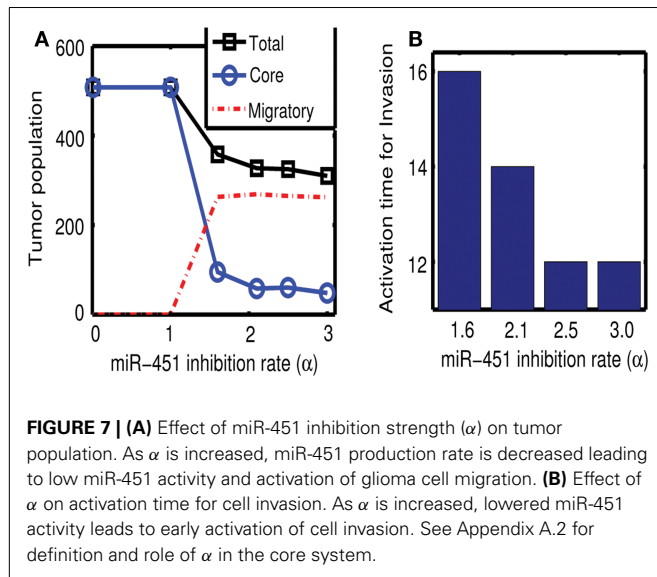


Figure 10 shows time courses of average cell speeds of migratory (solid circle, red) and proliferative (blue square) cells in **Figure 8**. From the beginning of the simulation, the average cell speed of cells in migratory phase maintained the values in the range of $27\text{--}33\text{ }\mu\text{m/h}$ until cell speeds begin to drop down around $\sim 17\text{ h}$ due to cell aggregation at the center of domain. Eventually all migratory cells become proliferative cells around $t = 19\text{ h}$. Proliferative cells (blue square, transformed from migratory cells around 9 h) show very low cell speeds due to absence of active force since their movement is due to growth not cell movement. Cell speeds have been reported to be in the range of $39\text{--}45\text{ }\mu\text{m/h}$ in 2D barrier-free culture condition and $15\text{--}20\text{ }\mu\text{m/h}$ in 3D glioblastoma cell culture in the absence/presence of EGF-stimulation (Kim et al., 2008), $15\text{--}25\text{ }\mu\text{m/h}$ in glioblastoma cells with/without α -actinin isoforms (Sen et al., 2009), $15\text{--}48\text{ }\mu\text{m/h}$ for cells embedded in collagen I matrix (Kaufman et al., 2005). So, the cell speed in our model is in good agreement with experimental data.

To test our hypothesis in a more realistic situation, we tested our hypothesis of attracting cancer cells back to the resection bed in a more realistic setting in **Figure 11**. Here we assume that a cell can sense the environment of the resection bed and stop moving on the edge of the resection bed. In our simulation, generation of active force of a migratory cell is turned off, i.e., active force \mathbf{T}_i in the equation (3) is set to be zero when the cell reaches periphery of the resection bed. The simulation begins immediately after initial surgery of the large tumor mass at the center of the domain again. **Figures 11A–H** show proliferation and migration patterns of tumor cells at $t = 0, 8, 16, 24, 32, 40, 48, 56\text{ h}$ in response to initial injection of a chemoattractant ($t = 0\text{ h}$) followed by glucose injection at $t = 17\text{ h}$. **Figures 11I, J** show time courses of miR-451 activity and AMPK level at a cell site (cell id = 22) and cell populations [proliferative (blue circle), migratory (red dotted), and total (green square) cells], respectively. Initially, there exist only a phenotype of migratory cells but these cells begin to aggregate on the periphery of the resection bed. However, these cells

switch their phenotype to proliferative ones via core control system (**Figure 11I**) in response to glucose injection at $t = 17\text{ h}$. These proliferative cells form a *visible* larger tumor mass which can be ready for the second follow-up surgery. Most of these proliferative cells enter the migratory phase ($M < th_M$, $A > th_A$) again around $t = 49\text{ h}$ due to lowered glucose levels.

3.4. THERAPEUTIC OPTIMIZATION

In **Figures 12A–F**, we investigate the effect of glucose injection time on tumor growth patterns for chemoattractant-induced second surgery under same conditions as in **Figure 8**. **Figures 12A–D** illustrate spatial growth patterns of tumor cells at final time ($t = 44\text{ h}$) when a high dose of glucose was injected at the center of the surgical site at different initial injection time ($t_1^G = 10, 12, 15, 17\text{ h}$). When glucose was injected at the earlier time ($t_1^G = 10\text{ h}$), more invasive cells enter the cell cycle ($M > th_M$, $A < th_A$) for higher flux of glucose before they reach the surgical site. For the case of glucose injection at later time ($t_1^G = 17\text{ h}$), more cells are localized at the center of the surgical site. **Figure 12E** shows tumor population at final time. Cells inside the bigger size of tumor mass are subject to slower growth (see mechanical aspects of the hybrid model). Initial glucose injection time decreases tumor population since more tumor cells are activated for proliferation and tumor cells grow faster without physical constraints. This injection time also decreases resection area for second surgery due to localized tumor cells at the original surgical site (**Figure 12F**). Therefore, choosing appropriate injection time is important for efficacy of tumor treatment. However, any further delay of second surgery would lead to larger size of tumor mass and one may face another possibility of tumor invasion.

Next, we investigate the effect of chemoattractant strength on efficacy of therapeutic strategies suggested in this paper. **Figures 13A–F** show migration-proliferation patterns of tumor cells at $t = 0, 17, 56\text{ h}$ in the presence of low ($\bar{\lambda}_{in}^C = \lambda_{in}^{C/10}$) and high (control) levels of a chemoattractant and glucose injection at $t = 17\text{ h}$ after initial surgery at $t = 0\text{ h}$. When the chemoattractant level is low, cells in the far away field do not effectively respond to the chemotactic signals (red arrows in **Figure 13B**) and do not move toward the resection bed easily, which induces further tumor growth later at the undesirable location (black arrowheads in **Figure 13C**). **Figures 13G, H** show populations of localized cells (cells with $d < 0.25$) and cells outside the localized domain (cells with $d > 0.25$), respectively. Here, $d = \sqrt{(x_i - 0.5)^2 + (y_i - 0.5)^2}$ is the distance from cell location (x_i, y_i) to the center (0.5, 0.5) of the domain. One can see that the low chemoattractant level leads to a moderate decrease in the population of localized cells (**Figure 13G**) but induces a significant increase in the population of cells in the far away field (**Figure 13H**) at $t = 17, 56\text{ h}$. These missed cells reduce efficacy of second surgery. These results effectively show that enough levels of chemoattractant need to be provided for the more efficient therapy.

4. DISCUSSION

One major challenge for treating glioblastoma is that by the time the disease is diagnosed cancer cells have already invaded other parts of the brain, inhibiting complete elimination of cancer cells. Blocking this critical invasion process or finding a

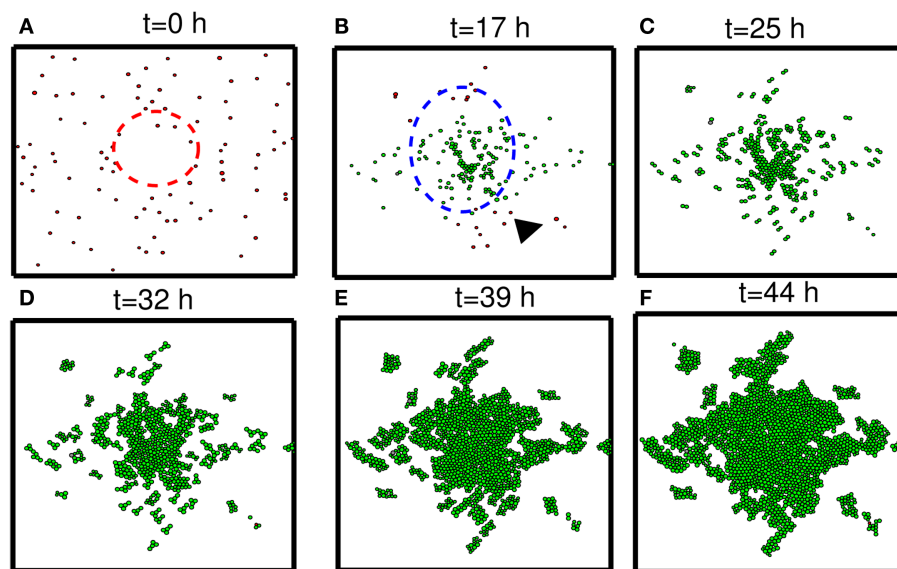


FIGURE 8 | Strategy of eradicating migratory cells after first surgery.

(A–F) Spatial profile of a surgically removed tumor at $t = 0, 17, 25, 32, 39, 44$ h. Detectable tumor core was surgically removed at $t = 0$ h (red dotted circle) and a chemoattractant was injected at the center of the removed area immediately after surgery ($t = 0$ h). After waiting 17 h, glucose was injected at

the center of the removed area again in order to turn the migratory switch ($M < th_M, A > th_A$) off and make these cells grow ($M > th_M, A < th_A$). This growing mass of tumor may be *visible* for secondary surgery, leading to eradication of *invisible* migratory cells. Domain size = $[0.25, 0.75] \times [0.25, 0.75] \subset [0, 1]^2$.

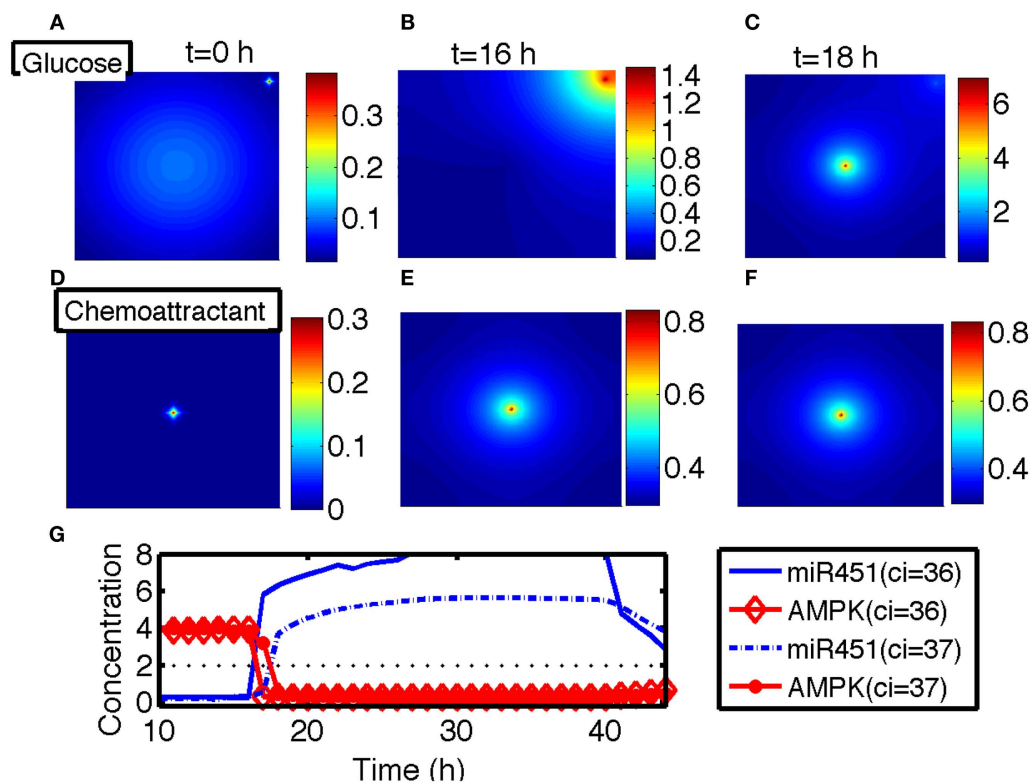


FIGURE 9 | (A–C) Spatial profiles of glucose at $t = 0, 16, 18$ h. Glucose was injected at the center of the domain around $t = 17$ h. Glucose flux from a blood vessel induces a peak value at the upper right corner. **(D–F)** Spatial

profiles of chemoattractant at $t = 0, 16, 18$ h. Chemotactic source was located at the center of the domain. **(G)** Time course of the miR-451 activity and AMPK level at two cell sites (cell id = 36, 37). *Domain size in (A–F) = $[0, 1]^2$.

way of eradicating invasive tumor cells would lead to better clinical outcomes. Godlewski et al. (2010a) recently identified a key miRNA, miR-451, and its target, AMPK complex, that

regulates a critical switch between cell migration and proliferation. Reduced miR-451 activity has been associated with cancers (Bandres et al., 2009) including glioma (Gal et al., 2008; Godlewski et al., 2010a). In the harsh microenvironment, glioblastoma cells shift their metabolic machinery toward a high level of glucose uptake, *Warburg effect* (Warburg, 1956; Kim and Dang, 2006; Heiden et al., 2009), and lowered glucose levels trigger active cell migration toward the better microenvironment. Some up-regulated miRNAs in brain tumors are believed to play a pro-oncogenic role via supporting growth, proliferation, migration, and survival of cancer cells while expression of other miRNA having anti-tumor effects is suppressed in gliomas. These miRNAs harbor a therapeutic significance as therapeutic agents in anti-cancer therapy (Lawler and Chiocca, 2009; Godlewski et al., 2010b; Chistiakov and Chekhonin, 2012). Godlewski et al. (2010a) illustrated glucose regulation of proliferation and migration of glioma cells: (i) low glucose \Rightarrow down-regulation of miR-451 and up-regulation of the AMPK complex \Rightarrow cell migration (ii) normal (high) glucose \Rightarrow up-regulation of miR-451 and down-regulation of AMPK complex \Rightarrow proliferation.

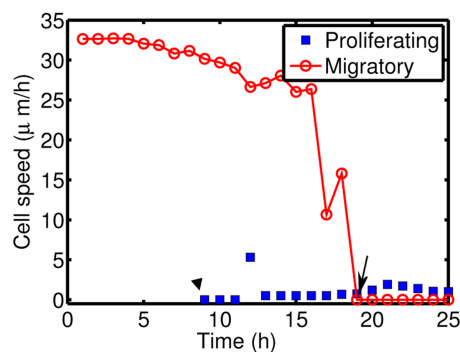


FIGURE 10 | Cell speeds of proliferative (blue square) and migratory (solid circle, red) cells in Figure 8.

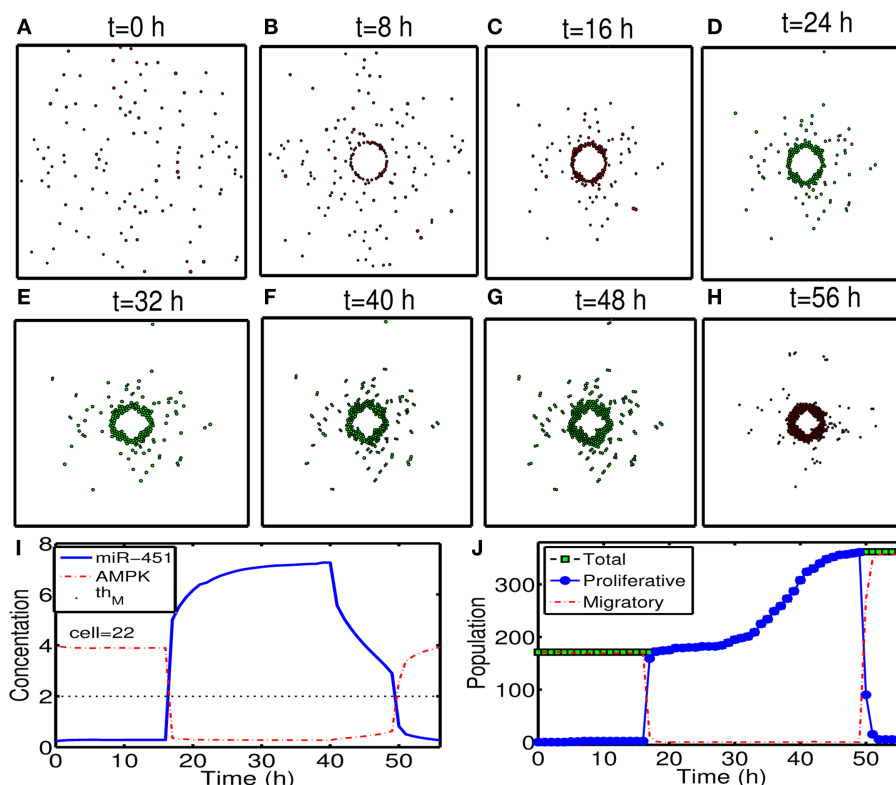


FIGURE 11 | (A–H) Tumor migration-proliferation patterns at $t = 0, 8, 16, 24, 32, 40, 48, 56$ h in response to injection of a chemoattractant at $t = 0$ h and glucose at $t = 17$ h after initial surgery at $t = 0$ h. Migratory cells switch to proliferative phenotype, forming a *visible* larger tumor mass, in response to glucose for second follow-up surgery. Migratory cells stop on the periphery of the resected area from the first surgery. It was assumed that a cell can sense the environment of the resection bed and the active force of a migratory cell is set to be zero when the cell reaches the periphery of the resection bed. Domain size = $[0.2, 0.8] \times [0.2, 0.8] \subset [0,$

$1]^2$. **(I)** Time course of miR-451 activity and AMPK level at a cell site (cell id = 22). Dotted black line in the middle = threshold value of miR-451 ($th_M = 2.0$). **(J)** Time course of cell populations: proliferative (blue circle), migratory (red dotted), and total (green square) cells. All migratory cells switch to proliferative ones around $t = 17$ h when low miR-451 levels jump to higher value [$M > 5$ in **(I)**] and the level stays above threshold ($th_M = 2.0$) due to glucose injection. Most of these proliferative cells enter the migratory phase ($M < th_M, A > th_A$) again around $t = 49$ h due to lowered glucose levels. Parameters used: $t_1^G = 17$ h, $\tau_d^G = 24$ h.

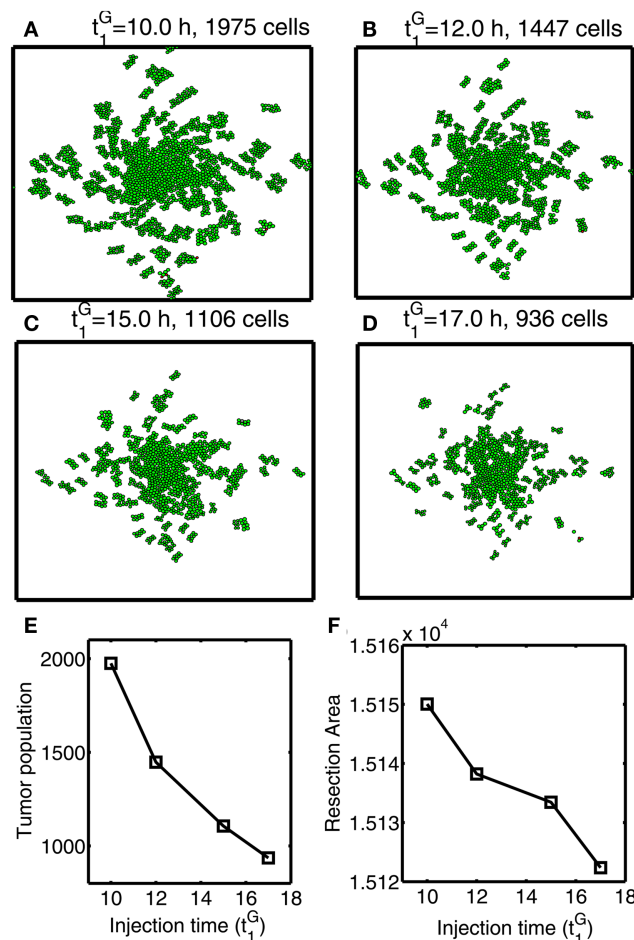


FIGURE 12 | Optimal strategy for glucose injection for second surgery after attracting invasive cells via chemotaxis. (A–D) Growth patterns at final time ($t = 33$ h) for various glucose injection time ($t_1^G = 10$ (A), 12 (B), 15 (C), 17 h (D)). Domain size = $[0.2, 0.8] \times [0.2,$

$0.8] \subset [0, 1]^2$. **(E)** Tumor population for different t_1^G . Tumor population is decreased as t_1^G is increased due to delay of growth signal.

(F) Resection area for second surgery for various t_1^G . Resection area is decreased as injection time is increased.

Conventional treatment options such as radiotherapy and chemo therapy after surgical resection of tumor mass lead to poor clinical outcome in many cases of glioblastoma due to invisible migratory cancer cells in the brain tissue. In the present paper we aimed at understanding a basic mechanism of proliferation and migration of glioma cells in response to fluctuating glucose levels and developing therapeutic strategies for eradicating *invasive* glioma cells after initial conventional surgery. The present paper develops a hybrid mathematical model of glioma cell migration and proliferation. The hybrid model considers proliferation and migration of individual tumor cells based on cell-mechanics, concentrations of glucose, chemoattractant, ECM, and MMPs in a spatio-temporal domain, and regulation of key intracellular molecules, miR-451 and AMPK complex, at each cell site. Mechanical stress and active forces acting on tumor cells were taken into account in the model. The spatial distribution of both proliferative and migratory cells in response to high and low glucose levels is in good agreement with experiments (Godlewski et al., 2010a).

We first considered the important role that the core control system (miR-451, AMPK) plays in regulation of the migratory phase and proliferative phase when cells on the surface of tumor mass begin to migrate away from the main core in the harsh microenvironment where glucose levels fluctuate. We analyzed the migratory behavior of cells in response to variations in two key parameters, inhibition strength of miR-451 (α) and inhibition strength of AMPK complex (β), that play a critical role in characterizing the invasion of glioma cells. Active migration of a cell depends on chemical signals from the core miR-451-AMPK system and their physical microenvironment in response to glucose injection. Growing tumor cells in the presence of abundant glucose switch their mechanism for cell migration when glucose is not available and cells are not subject to physical constraints. When glucose was introduced into the system in a periodic fashion, tumor repeat migration-proliferation cycle, which may lead to faster growth (Kim et al., 2011a).

For therapeutic strategies, the model suggested that (i) Introduction of chemoattractant at the surgical site may bring these

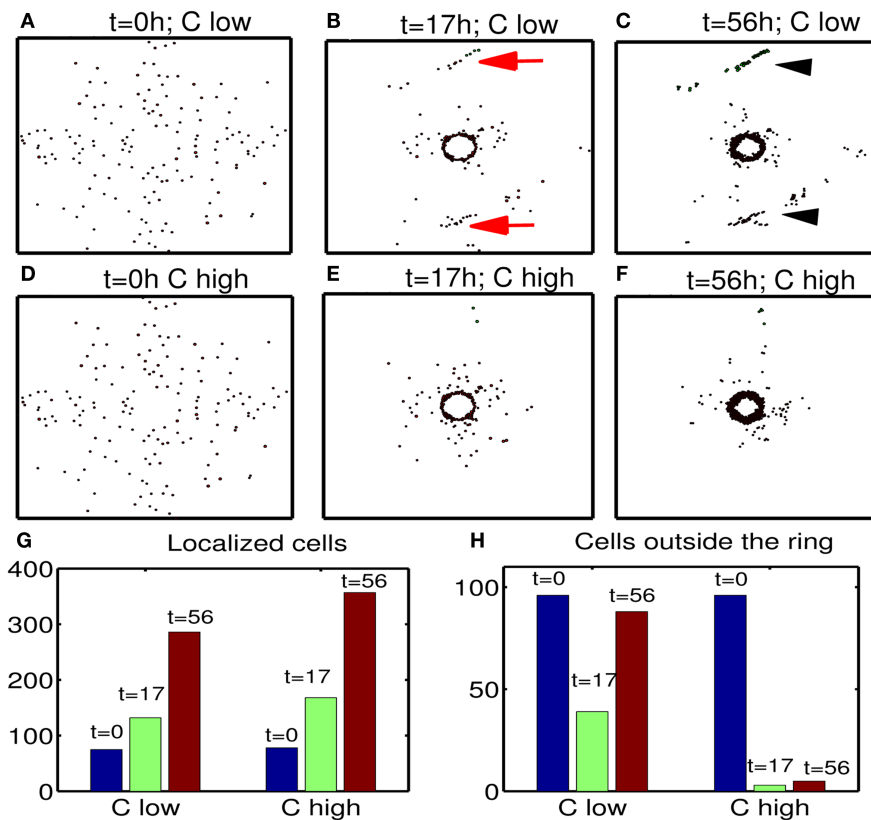


FIGURE 13 | Effect of chemoattractant strength (λ_{in}^C) on efficacy of the therapy. (A–F) Tumor migration-proliferation patterns for low ($\lambda_{in}^C = \lambda_{in}^{C/10}$) and high (control) levels of a chemoattractant at $t = 0, 17, 56$ h. A high dose of glucose was injected at $t = 17$ h after initial surgery at $t = 0$ h. When the chemoattractant level is low, cells in the far away field do not effectively respond to the chemoattractant (red arrows in (B)), which induces further

growth later at the undesirable location (black arrowheads in (C)). Domain size = $[0.1, 0.9] \times [0.1, 0.9] \subset [0, 1]^2$. (G) Populations of localized cells (cells with $d < 0.25$) for low (10-fold smaller) and high levels of chemoattractant. Here, $d = \sqrt{(x_i - 0.5)^2 + (y_i - 0.5)^2}$ is the distance from cell location (x_i, y_i) to the center $(0.5, 0.5)$ of the domain. (H) Same as in (G) but for cells outside the localized domain (cells with $d > 0.25$). Parameters used: $t_i^G = 17$ h, $\tau_d^G = 24$ h.

invasive tumor cells back to the tumor site. (ii) Glucose injection at the center of the surgical site would lead to up-regulation of miR-451 and down-regulation of AMPK complex, which induces cell proliferation. (iii) Follow-up surgery may eradicate the tumor cells that managed to survive from the first surgery. Multiple microsurgical resections for glioblastoma have been proven to be effective and useful (Hong et al., 2012). However, we also found that glucose injection at the wrong time may grow the tumor even before tumor cells gather together and this may lead to undesirable results, faster growth of dispersed tumor mass. Detecting appropriate time glucose injection and second surgery might also be a challenge. Tumor cells can be cultured from biopsies up to 4 cm away from the bulk tumor (Silbergeld and Chicoine, 1997). When cancer cells migrate too far from the original site, it may be difficult to attract these cells. For example, we found that too low chemoattractant may not be able to attract all migratory cells for second surgery (Figure 12) and these missed cells would decrease efficacy of the therapy. Therefore, in order to attract those invasive cells in the far away field (>4 cm away) one might need strong chemoattractants at the resection bed. However, this new strategy in this paper may be a novel way of eliminating all cancer

cells when an appropriate combination of chemoattractants and glucose is used.

The analysis and predictions of the hybrid model in this paper may serve as a starting point for experimentation and more detailed modeling. We indicate several aspects and directions for further development of *in vivo* and/or *in vitro* multi-scale models: (i) One might use a multi-phase approach to describe the inhomogeneity of the microenvironment (Byrne and Preziosi, 2004; Preziosi and Tosin, 2009; Preziosi and Vitale, 2011). See a review (Lowengrub et al., 2010) for further discussion. (ii) It has been suggested that some glioma cells may migrate while they grow. We could incorporate this aspect easily in this hybrid framework. Collective cell migration is also considered as a key aspect of tumor invasion (Friedl and Alexander, 2011). Creating a microtrack of locally digested ECM followed by generating a larger excavated macrotrack by proteolysis was suggested as a way of collective cell migration (Wolf et al., 2007; Friedl and Alexander, 2011; Ilina et al., 2011). In recent study, Sampetean et al. (2011) also illustrated the importance of collective migration along fiber tracts in glioma cell invasion, suggesting the need for anti-invasion approach. (iii) The simplified network of miR-451 and AMPK

complex can be extended to the more detailed network in order to take into account cell cycle and other anti-cancer molecules. (iv) Some important players such as immune cells and cytokines in the microenvironment should be included in the model (Cheng and Weiner, 2003; Rejniak and McCawley, 2010; Wiranowska and Rojiani, 2011). (v) It was observed that isoforms of myosin II are specifically required for an adaptation needed to squeeze through the dense network of other cells (Beadle et al., 2008). Detailed

modeling work is necessary to take into account deformation of cell body for cell motility. We hope to address these issues in future work.

ACKNOWLEDGMENTS

This work was supported by the Basic Science Research Program through the National Research Foundation of Korea by the Ministry of Education and Technology (2012R1A1A1043340).

REFERENCES

- Aguda, B. D., Kim, Y., Hunter, M. G., Friedman, A., and Marsh, C. B. (2008). MicroRNA regulation of a cancer network: consequences of the feedback loops involving miR-17-92, E2F, and Myc. *Proc. Natl. Acad. Sci. U.S.A.* 105, 19678–19683.
- Annabi, B., Bouzeghrane, M., Currie, J. C., Hawkins, R., Dulude, H., Daigneault, L., et al. (2005). A PSP94-derived peptide PCK3145 inhibits MMP-9 secretion and triggers CD44 cell surface shedding: implication in tumor metastasis. *Clin. Exp. Metastasis* 22, 429–439.
- Aronen, H. J., Pardo, F. S., Kennedy, D. N., Belliveau, J. W., Packard, S. D., Hsu, D. W., et al. (2000). High microvascular blood volume is associated with high glucose uptake and tumor angiogenesis in human gliomas. *Clin. Cancer Res.* 6, 2189–2200.
- Bandres, E., Bitarte, N., Arias, F., Agorreta, J., Fortes, P., Agirre, X., et al. (2009). MicroRNA-451 regulates macrophage migration and proliferation of gastrointestinal cancer cells. *Clin. Cancer Res.* 15, 2281–2290.
- Bartel, D. P. (2009). MicroRNAs: target recognition and regulatory functions. *Cell* 136, 215–233.
- Beadle, C., Assanah, M. C., Monzo, P., Vallee, R., Rosenfield, S. S., and Canoll, P. (2008). The role of myosin II in glioma invasion of the brain. *Mol. Biol. Cell* 19, 3357–3368.
- Boccardo, F., Lunardi, G. L., Petti, A. R., and Rubagotti, A. (2003). Enterolactone in breast cyst fluid: correlation with EGF and breast cancer risk. *Breast Cancer Res. Treat.* 79, 17–23.
- Byrne, H., and Preziosi, L. (2004). Modeling solid tumor growth using the theory of mixtures. *Math. Med. Biol.* 20, 341–360.
- Chauviere, A., Preziosi, L., and Byrne, H. (2010). A model of cell migration within the extracellular matrix based on a phenotypic switching mechanism. *Math. Med. Biol.* 27, 255–281.
- Cheng, J. D., and Weiner, L. M. (2003). Tumors and their microenvironments: tilling the soil commentary re: A. M. Scott et al., a phase I dose-escalation study of sibtuzumab in patients with advanced or metastatic fibroblast activation protein-positive cancer. *Clin. Cancer Res.* 9, 1590–1595.
- Chintala, S. K., Tonn, J. C., and Rao, J. S. (1999). Matrix metalloproteinases and their biological function in human gliomas. *Int. J. Dev. Neurosci.* 17, 495–502.
- Chiro, D. G., DeLaPaz, R. L., Brooks, R. A., Sokoloff, L., Kornblith, P. L., Smith, B. H., et al. (1982). Glucose utilization of cerebral gliomas measured by [18f] fluorodeoxyglucose and positron emission tomography. *Neurology* 32, 1323–1329.
- Chistiakov, D. A., and Chekhonin, V. P. (2012). Contribution of microRNAs to radio and chemoresistance of brain tumors and their therapeutic potential. *Eur. J. Pharmacol.* 684, 8–18.
- Choe, G., Park, J. K., Jouben-Steele, L., Kremen, T. J., Liao, L. M., Vinters, H. V., et al. (2002). Active matrix metalloproteinase 9 expression is associated with primary glioblastoma subtype. *Clin. Cancer Res.* 8, 2894–2901.
- Crute, B. E., Seefeld, K., Gamble, J., Kemp, B. E., and Witters, L. A. (1998). Functional domains of the alpha1 catalytic subunit of the amp-activated protein kinase. *J. Biol. Chem.* 273, 35347–35354.
- Dallon, J. C., and Othmer, H. G. (2004). How cellular movement determines the collective force generated by the *Dictyostelium discoideum* slug. *J. Theor. Biol.* 231, 203–222.
- Davis, F. G., and McCarthy, B. J. (2001). Current epidemiological trends and surveillance issues in brain tumors. *Expert Rev. Anticancer Ther.* 1, 395–401.
- Deisboeck, T. S., Berens, M. E., Kansal, A. R., Torquato, S., Stemmer-Rachamimov, A. O., and Chiocca, E. A. (2001). Pattern of self-organization in tumour systems: complex growth dynamics in a novel brain tumour spheroid model. *Cell Prolif.* 34, 115–134.
- Demuth, T., and Berens, M. E. (2004). Molecular mechanisms of glioma cell migration and invasion. *J. Neurooncol.* 70, 217–228.
- Esquela-Kerscher, A., and Slack, F. J. (2006). Oncomirs – microRNAs with a role in cancer. *Nat. Rev. Cancer* 6, 259–269.
- Friedl, P., and Alexander, S. (2011). Cancer invasion and the microenvironment: plasticity and reciprocity. *Cell* 147, 992–1009.
- Gabriely, G., Wurdinger, T., Kesari, S., Esau, C. C., Burchard, J., Linsley, P. S., et al. (2008). MicroRNA 21 promotes glioma invasion by targeting matrix metalloproteinase regulators. *Mol. Cell. Biol.* 28, 5369–5380.
- Gal, H., Pandi, G., Kanner, A. A., Ram, Z., Lithwick-Yanai, G., Amariglio, N., et al. (2008). Mir-451 and imatinib mesylate inhibit tumor growth of glioblastoma stem cells. *Biochem. Biophys. Res. Commun.* 376, 86–90.
- Gantier, M. P., McCoy, C. E., Rusinova, I., Saulep, D., Wang, D., Xu, D., et al. (2011). Analysis of microRNA turnover in mammalian cells following Dicer1 ablation. *Nucleic Acids Res.* 39, 5692–5703.
- Gatenby, R. A., and Gillies, R. J. (2004). Why do cancers have high aerobic glycolysis? *Nat. Rev. Cancer* 4, 891–899.
- Godlewski, J., Nowicki, M. O., Bronisz, A., Nuovo, G., Palatini, J., Lay, M. D., et al. (2010a). MicroRNA-451 regulates LKB1/AMPK signaling and allows adaptation to metabolic stress in glioma cells. *Mol. Cell* 37, 620–632.
- Godlewski, J., Newton, H. B., Chiocca, E. A., and Lawler, S. E. (2010b). MicroRNAs and glioblastoma; the stem cell connection. *Cell Death Differ.* 17, 221–228.
- Godlewski, J., Nowicki, M. O., Bronisz, A., Williams, S., Otsuki, A., Nuovo, G., et al. (2008). Targeting of the Bmi-1 oncogene/stem cell renewal factor by microRNA-128 inhibits glioma proliferation and self-renewal. *Cancer Res.* 68, 9125–9130.
- Goldman, S., Levivier, M., Pirotte, B., Brucher, J. M., Wikler, D., Damhaut, P., et al. (1996). Regional glucose metabolism and histopathology of gliomas. A study based on positron emission tomography-guided stereotactic biopsy. *Cancer* 78, 1098–1106.
- Hardie, D. G. (2007). Amp-activated/snf1 protein kinases: conserved guardians of cellular energy. *Nat. Rev. Mol. Cell Biol.* 8, 774–785.
- Harpold, H. L., Alvord, E. C. Jr., and Swanson, K. R. (2007). The evolution of mathematical modeling of glioma proliferation and invasion. *J. Neuropathol. Exp. Neurol.* 66, 1–9.
- Hatzikirou, H., Basanta, D., Simon, M., Schaller, K., and Deutsch, A. (2010). 'Go or grow': the key to the emergence of invasion in tumour progression? *Math. Med. Biol.* 27, 255–281.
- Heiden, M. G., Cantley, L. C., and Thompson, C. B. (2009). Understanding the Warburg effect: the metabolic requirements of cell proliferation. *Science* 324, 1029–1033.
- Hong, B., Wiese, B., Bremer, M., Heissler, H. E., Heidenreich, F., Krauss, J. K., et al. (2012). Multiple microsurgical resections for repeated recurrence of glioblastoma multiforme. *Am. J. Clin. Oncol.* (in press).
- Ilina, O., Bakker, G., Vasaturo, A., Hofmann, R. M., and Friedl, P. (2011). Two-photon laser-generated microtracks in 3d collagen lattices: principles of MMP-dependent and -independent collective cancer cell invasion. *Phys. Biol.* 8, 015010.
- Jaalinoja, J., Herva, R., Korpela, M., Hoyhtya, M., and Turpeenniemi-Hujanen, T. (2000). Matrix metalloproteinase 2 (mmp-2) immunoreactive protein is associated with poor grade and survival in brain neoplasms. *J. Neurooncol.* 46, 81–90.

- Jacobs, V. L., Valdes, P. A., Hickey, W. F., and De Leo, J. A. (2011). Current review of in vivo gbm rodent models: emphasis on the cns-1 tumour model. *ASN Neuro* 3, e00063.
- Jain, R. K. (1987). Transport of molecules in the tumor interstitium: a review. *Cancer Res.* 47, 3039–3051.
- Jia, Y., Zeng, Z. Z., Markwart, S. M., Rockwood, K. F., Ignatoski, K. M., Ethier, S. P., et al. (2004). Integrin fibronectin receptors in matrix metalloproteinase-1-dependent invasion by breast cancer and mammary epithelial cells. *Cancer Res.* 64, 8674–8681.
- Jones, R. G., and Thompson, C. B. (2009). Tumor suppressors and cell metabolism: a recipe for cancer growth. *Genes Dev.* 23, 537–548.
- Kaufman, L. J., Brangwynne, C. P., Kasza, K. E., Filippidi, E., Gordon, V. D., Deisboeck, T. S., et al. (2005). Glioma expansion in collagen I matrices: analyzing collagen concentration-dependent growth and motility patterns. *Biophys. J.* 89, 635–650.
- Kim, H. D., Guo, T. W., Wu, A. P., Wells, A., Gertler, F. B., and Laufner, D. A. (2008). Epidermal growth factor-induced enhancement of glioblastoma cell migration in 3d arises from an intrinsic increase in speed but an extrinsic matrix and proteolysis-dependent increase in persistence. *Mol. Biol. Cell* 19, 4249–4259.
- Kim, J. W., and Dang, C. V. (2006). Cancer's molecular sweet tooth and the Warburg effect. *Cancer Res.* 66, 8927–8930.
- Kim, Y., Lawler, S., Nowicki, M. O., Chiocca, E. A., and Friedman, A. (2009). A mathematical model of brain tumor: pattern formation of glioma cells outside the tumor spheroid core. *J. Theor. Biol.* 260, 359–371.
- Kim, Y., Roh, S., Lawler, S., and Friedman, A. (2011a). miR451 and AMPK/mark mutual antagonism in glioma cells migration and proliferation. *PLoS ONE* 6:e28293. doi:10.1371/journal.pone.0028293
- Kim, Y., Stolarska, M., and Othmer, H. G. (2011b). The role of the microenvironment in tumor growth and invasion. *Prog. Biophys. Mol. Biol.* 106, 353–379.
- Kim, Y., Stolarska, M., and Othmer, H. G. (2007). A hybrid model for tumor spheroid growth in vitro I: theoretical development and early results. *Math. Models Methods Appl. Sci.* 17, 1773–1798.
- Kudlow, J. E., Cheung, C. Y., and Bjorge, J. D. (1986). Epidermal growth factor stimulates the synthesis of its own receptor in a human breast cancer cell line. *J. Biol. Chem.* 261, 4134–4138.
- Lamszus, K., Schmidt, N. O., Jin, L., Lateral, J., Zagzag, D., Way, D., et al. (1998). Scatter factor promotes motility of human glioma and neuromicrovascular endothelial cells. *Int. J. Cancer* 75, 19–28.
- Lawler, S., and Chiocca, E. A. (2009). Emerging functions of microRNAs in glioblastoma. *J. Neurooncol.* 92, 297–306.
- Li, C. K. (1982). The glucose distribution in 9l rat brain multicell tumor spheroids and its effect on cell necrosis. *Cancer* 50, 2066–2073.
- Lowengrub, J. S., Frieboes, H. B., Jin, F., Chuang, Y. L., Li, X., MacKlin, P., et al. (2010). Nonlinear modelling of cancer: bridging the gap between cells and tumours. *Nonlinearity* 23, R1.
- Luca, A. D., Niccolo Arena, Sena, L. M., and Medico, E. (1999). Met overexpression confers HGF-dependent invasive phenotype to human thyroid carcinoma cells in vitro. *J. Cell. Physiol.* 180, 365–371.
- Lund-Johansen, M., Bjerkvig, R., Humphrey, P. A., Bigner, S. H., Bigner, D. D., and Laerum, O. D. (1990). Effect of epidermal growth factor on glioma cell growth, migration, and invasion in vitro. *Cancer Res.* 50, 6039–6044.
- Pham, K., Chauviere, A., Hatzikirou, H., Li, X., Byrne, H. M., Cristini, V., et al. (2012). Density-dependent quiescence in glioma invasion: instability in a simple reaction-diffusion model for the migration/proliferation dichotomy. *J. Biol. Dyn.* 6(Suppl. 1), 54–71.
- Platten, M., Wick, W., and Weller, M. (2001). Malignant glioma biology: role for TGF-beta in growth, motility, angiogenesis, and immune escape. *Microsc. Res. Tech.* 52, 401–410.
- Preziosi, L., and Tosin, A. (2009). Multiphase and multiscale trends in cancer modelling. *Math. Model. Nat. Phenom.* 4, 1–11.
- Preziosi, L., and Vitale, G. (2011). A multiphase model of tumor and tissue growth including cell adhesion and plastic reorganization. *Math. Models Methods. Appl. Sci.* 21, 1901–1932.
- Rejniak, K. A., and Anderson, A. R. A. (2011). Hybrid models of tumor growth. *Wiley Interdiscip. Rev. Syst. Biol. Med.* 3, 115–125.
- Rejniak, K. A., and McCawley, C. J. (2010). Current trends in mathematical modeling of tumor microenvironment interaction: a survey of tools and applications. *Exp. Biol. Med.* 235, 411–423.
- Rong, Z., Cheema, U., and Vadgama, P. (2006). Needle enzyme electrode based glucose diffusive transport measurement in a collagen gel and validation of a simulation model. *Analyst* 131, 816–821.
- Rozental, J. M., Levine, R. L., and Nickles, R. J. (1991). Changes in glucose uptake by malignant gliomas: preliminary study of prognostic significance. *J. Neurooncol.* 10, 75–83.
- Sadlonova, A., Novak, Z., Johnson, M. R., Bowe, D. B., Gault, S. R., Page, G. P., et al. (2005). Breast fibroblasts modulate epithelial cell proliferation in three-dimensional in vitro co-culture. *Breast Cancer Res.* 7, R46–R59.
- Saffarian, S., Collier, I. E., Marmer, B. L., Elson, E. L., and Goldberg, G. (2004). Interstitial collagenase is a Brownian ratchet driven by proteolysis of collagen. *Science* 306, 108–111.
- Sampetrean, O., Saga, I., Nakanishi, M., Sugihara, E., Fukaya, R., Onishi, N., et al. (2011). Invasion precedes tumor mass formation in a malignant brain tumor model of genetically modified neural stem cells. *Neoplasia* 13, 784–791.
- Sander, L. M., and Deisboeck, T. S. (2002). Growth patterns of microscopic brain tumors. *Phys. Rev. E Stat. Nonlin. Soft Matter Phys.* 66, 051901.
- Scianna, M., Merks, R. M., Preziosi, L., and Medico, E. (2009). Individual cell-based models of cell scatter of ARO and MLP-29 cells in response to hepatocyte growth factor. *J. Theor. Biol.* 260, 151–160.
- Sen, S., Dong, M., and Kumar, S. (2009). Isoform-specific contributions of a-actinin to glioma cell mechanobiology. *PLoS ONE* 4:e8427. doi:10.1371/journal.pone.0008427
- Silbergeld, D. L., and Chicoine, M. R. (1997). Isolation and characterization of human malignant glioma cells from histologically normal brain. *J. Neurosurg.* 86, 525–531.
- Stein, A. M., Demuth, T., Mobley, D., Berens, M., and Sander, L. M. (2007). A mathematical model of glioblastoma tumor spheroid invasion in a three-dimensional in vitro experiment. *Biophys. J.* 92, 356–365.
- Stella, M. C., and Comoglio, P. M. (1999). HGF: a multifunctional growth factor controlling cell scattering. *Int. J. Biochem. Cell Biol.* 31, 1357–1362.
- Stylli, S. S., Kaye, A. H., MacGregor, L., Howes, M., and Rajendra, P. (2005). Photodynamic therapy of high grade glioma – long term survival. *J. Clin. Neurosci.* 12, 389–398.
- Swanson, K. R., Alvord, E. C., and Murray, J. D. (2003). Virtual resection of gliomas: effect of extent of resection on recurrence. *Math. Comput. Model.* 37, 1177–1190.
- Tamagnone, L., and Comoglio, P. M. (1997). Control of invasive growth by hepatocyte growth factor (hgf) and related scatter factors. *Cytokine Growth Factor Rev.* 8, 129–142.
- Thorne, R. G., Hrabetova, S., and Nicholson, C. (2004). Diffusion of epidermal growth factor in rat brain extracellular space measured by integrative optical imaging. *J. Neurophysiol.* 92, 3471–3481.
- Trusolino, L., and Comoglio, P. M. (2002). Scatter-factor and semaphorin receptors: cell signalling for invasive growth. *Nat. Rev. Cancer* 2, 289–300.
- Valle-Casuso, J. C., Gonzalez-Sanchez, A., Medina, J. M., and Tabernero, A. (2012). HIF-1 and c-Src mediate increased glucose uptake induced by endothelin-1 and connexin43 in astrocytes. *PLoS ONE* 7:e32448. doi:10.1371/journal.pone.0032448
- Warburg, O. (1956). On the origin of cancer cells. *Science* 123, 309–314.
- Watters, J. J., Schartner, J. M., and Badie, B. (2005). Microglia function in brain tumors. *J. Neurosci. Res.* 81, 447–455.
- Wiranowska, M., and Rojiani, M. V. (2011). “Extracellular matrix microenvironment in glioma progression,” in *Glioma – Exploring Its Biology and Practical Relevance*, ed. Dr. Anirban Ghosh (Shanghai: InTech), 257–284.
- Wolf, K., Wu, Y., Liu, Y., Geiger, J., Tam, E., Overall, C., et al. (2007). Multi-step pericellular proteolysis controls the transition from individual to collective cancer cell invasion. *Nat. Cell Biol.* 9, 893–904.

- Xu, R. H., Pelicano, H., Zhou, Y., Carew, J. S., Feng, L., Bhalla, K. N., et al. (2005). Inhibition of glycolysis in cancer cells: a novel strategy to overcome drug resistance associated with mitochondrial respiratory defect and hypoxia. *Cancer Res.* 65, 613–621.
- Young, N., and Brocklyn, J. R. (2007). Roles of sphingosine-1-phosphate (S1P) receptors in malignant behavior of glioma cells. Differential effects of S1P2 on cell migration and invasiveness. *Exp. Cell Res.* 313, 1615–1627.
- Zhou, Y., Larsen, P. H., Hao, C., and Yong, V. W. (2002). Cxcr4 is a major chemokine receptor on glioma cells and mediates their survival. *J. Biol. Chem.* 277, 49481–49487.
- Conflict of Interest Statement:** The authors declare that the research was conducted in the absence of any commercial or financial relationships that could be construed as a potential conflict of interest.
- Received: 12 December 2012; accepted: 28 February 2013; published online: 18 March 2013.
- Citation: Kim Y (2013) Regulation of cell proliferation and migration in glioblastoma: new therapeutic approach. *Front. Oncol.* 3:53. doi: 10.3389/fonc.2013.00053
- This article was submitted to *Frontiers in Molecular and Cellular Oncology*, a specialty of *Frontiers in Oncology*. Copyright © 2013 Kim. This is an open-access article distributed under the terms of the Creative Commons Attribution License, which permits use, distribution and reproduction in other forums, provided the original authors and source are credited and subject to any copyright notices concerning any third-party graphics etc.

A. APPENDIX

A.1. PARAMETER ESTIMATION AND NON-DIMENSIONALIZATION

A.1.1. Tumor module

The characteristic distance is the maximum domain size ($L = 2$ mm) of growing glioblastoma within 48 h similar to the size of the migratory region in the experiments by Godlewski et al. (2010a) and we use $T = 1$ h to get dimensionless variables and parameters:

$$\begin{aligned}\bar{t} &= \frac{t}{T}, \bar{x} = \frac{x}{L}, \bar{G} = \frac{G}{G^*}, \bar{C} = \frac{C}{C^*}, \bar{\rho} = \frac{\rho}{\rho^*}, \bar{P} = \frac{P}{P^*}, \\ \bar{D}_G &= \frac{T}{L^2} D_G, \bar{D}_C = \frac{T}{L^2} D_C, \\ \bar{D}_P &= \frac{T}{L^2} D_P, \bar{\lambda}_{in}^G = \frac{T \lambda_{in}^G}{G^*}, \bar{\lambda}_b = \frac{T \lambda_b}{G^*}, \bar{\lambda}_c = \frac{T \lambda_c}{G^*}, \\ \bar{\lambda}_{in}^C &= \frac{T \lambda_{in}^C}{G^*}, \bar{\lambda}_1 = T \lambda_1 P^*, \\ \bar{\lambda}_2 &= T \lambda_2, \bar{\rho}_* = \frac{\rho_*}{\rho^*}, \bar{\lambda}_3 = T \lambda_3, \bar{\mu}_G = T \mu_G, \\ \bar{\mu}_C &= T \mu_C, \bar{\mu}_P = T \mu_P,\end{aligned}\quad (A1)$$

We estimate some of parameters and reference values in the following. (i) D_G : diffusion coefficients of glucose (G) were measured to be 6.7×10^{-7} cm²/s in the brain (Jain, 1987) and 1.3×10^{-6} cm²/s in collagen gel (Rong et al., 2006). We take $D_G = 6.7 \times 10^{-7}$ cm²/s as in Jain (1987). (ii) D_P : in experiments of the movement of MMP-1 in the collagen fibril, Saffarian et al. (2004) estimated the diffusion coefficient of MMPs as $(8.0 \pm 1.5) \times 10^{-9}$ cm²/s for inactive mutant and $(8.0 \pm 1.5) \times 10^{-9}$ cm²/s for wild-type activated MMP-1, respectively. For our simulation, we take $D_P = 8.0 \times 10^{-9}$ cm²/s. (iii) D_C : the diffusion coefficient of chemoattractant was taken from one of EGF, $D_C = 1.66 \times 10^{-6}$ cm²/s from Thorne et al. (2004). (iv) λ_c (glucose consumption rate): the measured level $\alpha = 1.6$ pg/cell/min for piecewise increasing linear consumption term $\alpha(G)n$ was used in a glioma invasion study (Sander and Deisboeck, 2002) along with a threshold value $G_1^{th} = 2.0 \times 10^{-4}$ g/cm³, taken from the work of Li (1982). We take $\lambda_c = 0.8$ pg/cell/min and use a sphere with a radius $r = 8\text{--}20$ μ m for estimation of cell volume. (v) G^* : Sander and Deisboeck (2002) used the characteristic concentration of glucose 2×10^{-4} g/cm³, and took the value 6×10^{-4} g/cm³ for glucose level far from the tumor (see also Deisboeck et al., 2001). Kim et al. (2009) took 6×10^{-4} g/cm³ as a reference value based on experimental observation. In *in vitro* experimental study (Godlewski et al., 2010a), high (4.5 g/l = 4.5×10^{-3} g/cm³) and low (0.3 g/l = 3.0×10^{-4} g/cm³) levels of glucose induced the up- and down-regulated miR-451 expression. We take the high glucose level, $G^* = 4.5 \times 10^{-3}$ g/cm³, as a reference value. (vi) ρ^* : collagen is one of main ECM components. ECM concentration was estimated to be $0.5\text{--}2.0$ mg/ml in an experimental study of growth patterns of glioma spheroids. Stein et al. (2007) investigated growth patterns of glioma cell lines in experiments where U87 wild-type and its mutant, U87DEGFR, were implanted into collagen I of concentration of 2.6 mg/ml. We take $\rho^* = 1.0$ mg/cm³ as our reference value of ECM. (vii) P^* : in a breast cancer cell invasion study, MMP concentrations

were measured to be 1.6×10^{-9} g/cm³ (Jia et al., 2004). On the other hand, it was shown that PCK3145 can down-regulate MMP-9 level in prostate cancer patients with up-regulated MMP-9 level of >100 μ g/l (Annabi et al., 2005). We take the high levels of MMPs ($P^* = 100$ μ g/l) as our reference value of MMPs.

Table 1 lists reference values and all parameter values above.

A.1.2. Core control system (miR-451, AMPK)

We use the following dimensionalization scheme to get the dimensionless key control parameters (Kim et al., 2011a).

$$\begin{aligned}\tau &= \mu_1 t, M = \frac{m}{m^*}, A = \frac{a}{a^*}, G = \frac{g}{m^*}, l_g = \frac{\Lambda_g}{\mu_1}, \\ S &= \frac{s}{\mu_2 a^*}, l_1 = \frac{\Lambda_1 \Lambda_2^2}{\mu_1 m^*}, l_2 = \Lambda_2, \\ l_3 &= \frac{\Lambda_3 \Lambda_4^2}{\mu_2 a^*}, l_4 = \Lambda_4, \alpha = \Lambda_5 (a^*)^2, \\ \beta &= \Lambda_6 (m^*)^2, \epsilon = \frac{\mu_1}{\mu_2},\end{aligned}\quad (A2)$$

and the dimensionless form of core control system

$$\frac{dM}{d\tau} = l_g G + \frac{l_1}{l_2^2 + \alpha A^2} - M, \quad (A3)$$

$$\epsilon \frac{dA}{d\tau} = S + \frac{l_3}{l_4^2 + \beta M^2} - A. \quad (A4)$$

Table A1 | Parameters that are used in the intracellular miR-451-AMPK system.

	Description	Value	Refs.
l_g	Glucose signaling rate	1.0	Kim et al. (2011a)
l_1	Autocatalytic production rate of miR-451	4.0	Kim et al. (2011a)
l_2	Hill-type coefficient	1.0	Kim et al. (2011a)
α	Inhibition strength of miR-451 by AMPK complex	1.6	Kim et al. (2011a)
th_M	Threshold of AMPK for proliferation/migration switch	2.0	Estimated
l_3	Autocatalytic production rate of AMPK	4.0	Kim et al. (2011a)
l_4	Hill-type coefficient	1.0	Kim et al. (2011a)
β	Inhibition strength of AMPK complex by miR-451	1.0	Kim et al. (2011a)
S	Signaling source of AMPK	0.2	Kim et al. (2011a)
ϵ	Scaling factor (slow dynamics) of AMPK complex	0.02	Crute et al. (1998); Aguda et al. (2008); Gantier et al. (2011); Kim et al. (2011a)
th_A	Threshold of AMPK for proliferation/migration switch	2.0	Estimated



Modeling tumor-associated edema in gliomas during anti-angiogenic therapy and its impact on imageable tumor

Andrea Hawkins-Daarud¹, Russell C. Rockne¹, Alexander R. A. Anderson² and Kristin R. Swanson^{1*}

¹ Department of Neurological Surgery, Northwestern University, Chicago, IL, USA

² Integrated Mathematical Oncology, Moffitt Cancer Center, Tampa, FL, USA

Edited by:

Heiko Enderling, Tufts University
School of Medicine, USA

Reviewed by:

Janusz Rak, McGill University, Canada
Kerri-Ann Norton, Johns Hopkins
University, USA

*Correspondence:

Kristin R. Swanson, Department of
Neurological Surgery, Feinberg School
of Medicine, Northwestern
University, 680 N Lake Shore Drive,
Suite 1500, Chicago, IL 60611, USA.
e-mail: kristin.swanson@
northwestern.edu

Glioblastoma, the most aggressive form of primary brain tumor, is predominantly assessed with gadolinium-enhanced T1-weighted (T1Gd) and T2-weighted magnetic resonance imaging (MRI). Pixel intensity enhancement on the T1Gd image is understood to correspond to the gadolinium contrast agent leaking from the tumor-induced neovasculature, while hyperintensity on the T2/FLAIR images corresponds with edema and infiltrated tumor cells. None of these modalities directly show tumor cells; rather, they capture abnormalities in the microenvironment caused by the presence of tumor cells. Thus, assessing disease response after treatments impacting the microenvironment remains challenging through the obscuring lens of MR imaging. Anti-angiogenic therapies have been used in the treatment of gliomas with spurious results ranging from no apparent response to significant imaging improvement with the potential for extremely diffuse patterns of tumor recurrence on imaging and autopsy. Anti-angiogenic treatment normalizes the vasculature, effectively decreasing vessel permeability and thus reducing tumor-induced edema, drastically altering T2-weighted MRI. We extend a previously developed mathematical model of glioma growth to explicitly incorporate edema formation allowing us to directly characterize and potentially predict the effects of anti-angiogenics on imageable tumor growth. A comparison of simulated glioma growth and imaging enhancement with and without bevacizumab supports the current understanding that anti-angiogenic treatment can serve as a surrogate for steroids and the clinically driven hypothesis that anti-angiogenic treatment may not have any significant effect on the growth dynamics of the overall tumor cell populations. However, the simulations do illustrate a potentially large impact on the level of edematous extracellular fluid, and thus on what would be imageable on T2/FLAIR MR. Additionally, by evaluating virtual tumors with varying growth kinetics, we see tumors with lower proliferation rates will have the most reduction in swelling from such treatments.

Keywords: glioma, edema, mathematical model, anti-angiogenic therapy

INTRODUCTION

Glioblastoma Multiforme (GBM) is a highly aggressive and invasive primary brain tumor. The standard treatment protocol is to surgically remove as much of the tumor as is reasonably safe, followed by a combination of chemotherapy with radiation. Despite aggressive treatment, the prognosis remains poor with a median survival time of 14 months (Stupp et al., 2005). The inability to accurately determine the extent of diffuse tumor cell infiltration of the normal brain affects the ability to assess response to treatment through clinical imaging, confounding clinical progress. Currently, clinicians rely primarily on three magnetic resonance imaging (MRI) modalities to monitor the development of the tumor, the T2 weighting, FLAIR, and T1 weighting with gadolinium contrast enhancement (T1Gd) sequences illustrated in **Figure 1**. However, it is known that none of these sequences are able to show the entire extent of the malignant cells (Silbergeld and Chicoine, 1997), since the abnormal regions highlighted in the MR images are as dependent on the microenvironment around the disease, particularly the vasculature, as on the tumor cells themselves.

Increased vasculature is a primary hallmark of GBM, and while angiogenesis is a hallmark of cancer in general, there are some important factors that separate GBMs from other tumors. First, the glioma cells inhabit an organ that is highly vascularized in its native state. Second, glioma cells are diffusely invasive and are known to co-opt the existing vasculature and migrate and grow along the vessels (Holash et al., 1999; Leenders et al., 2002). Nevertheless, GBMs can form hypoxic regions, often leading to regions of necrosis, and thus, downstream of this hypoxic signaling, emit an abnormally large amount of angiogenic factors such as vascular endothelial growth factor (VEGF) for the recruitment of additional vasculature, analogous to observations in solid tumors (Kerbel, 2000). This process results in the vasculature developing abnormally large vessel radial sizes and, unique to the brain, results in a breakdown of the blood brain barrier in the tumor region.

FEATURES CHARACTERIZING MR IMAGING OBSERVATION

In the case of GBM, the enhancing abnormalities on all of the primary MR imaging modalities, T1Gd, T2, and FLAIR primarily result from a compromised blood brain barrier. The T1Gd image

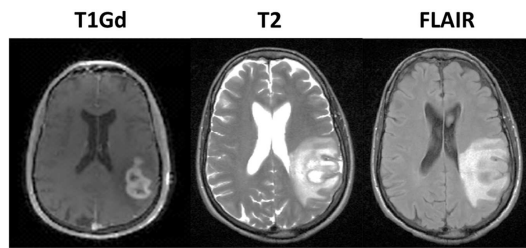


FIGURE 1 | Illustration of primary imaging modalities. The T1Gd image will show enhancement where the contrast agent has been able to diffuse into the extracellular space where the blood brain barrier has been compromised due to tumor-induced neo-angiogenesis. The T2-weighted and FLAIR images are associated with edema or swelling; FLAIR is different from T2 in that the signal from the cerebral spinal fluid (CSF) is removed. In the case of GBM, the non-CSF T2/FLAIR enhancement is primarily vasogenic edema, defined as fluid originating from blood vessels that accumulates around cells (Marmarou, 2007). The fluid leaves the vessels due to pressure and osmotic gradients induced by the breakdown in the blood brain barrier.

signal is enhanced where the contrast agent has been able to leak into the extracellular space through breakdowns in the blood brain barrier due to tumor-induced neo-angiogenesis. The T2-weighted and FLAIR images show edema or swelling; FLAIR is different from T2 in that the signal from the cerebral spinal fluid (CSF) is inverted. In the case of GBM, the non-CSF T2/FLAIR hyperintense signal is primarily vasogenic edema, defined as fluid originating from blood vessels that accumulates around cells (Marmarou, 2007). The fluid leaves the vessels due to pressure and osmotic gradients induced by the breakdown in the blood brain barrier. Thus, whilst changes in any primary imaging modality (T1Gd or T2/FLAIR) are often interpreted as corresponding to changes in tumor cell density, they may be artifacts of MR imaging.

THE ROLE OF ANTI-ANGIOGENICS IN GBM

The concept of anti-angiogenic treatment for cancer has been popular ever since the landmark paper by Folkman (1971) stating that malignant tumors were angiogenesis-dependent and has been used with some success for other solid tumors in combination with chemotherapy (Hurwitz et al., 2004; Sandler et al., 2006). Since a defining hallmark of GBM is increased vasculature through endothelial cell proliferation (Louis et al., 2007), this disease seems like an obvious candidate for vascular targeting treatment. However, the differences between the vasculature in GBMs and other solid tumors produce different treatment effects. In GBMs, one of the effects of anti-angiogenic treatments is to, at least transiently, repair the blood brain barrier and allow the vessels to return to their normal radial size, increasing their efficiency (Jain, 2005; Batchelor et al., 2007) – referred to as vascular normalization. Ostensibly, this improved efficiency of the vasculature is not the desired impact, though it may help in delivery of other therapeutic agents.

More concerning, however, is that this normalization may directly impact the efficacy of the MR imaging. It is possible for glioma patients with enhancing lesions on T1Gd and T2/FLAIR imaging to have decreased enhancement within a day

of anti-angiogenic treatment (Batchelor et al., 2007; Norden et al., 2008), as illustrated by patients 1 and 2 in Figure 2, but upon stopping treatment, the imageable lesion is even larger and more disperse than before (Iwamoto et al., 2009). However, responses are varied; a patient may see no deflection in growth but faster growth after treatment, such as the third patient in Figure 2, or see stabilized disease returning to the previous growth patterns after treatment, as illustrated by the fourth patient in Figure 2. These patients were consented to this study with approval by the local institutional review board at either the University of Washington or the University of California, Los Angeles, and their relevant demographic and therapeutic information is given in Table 1. These conundrums have led to two hypotheses: first, anti-angiogenic treatment has minimal cytotoxic effect but does influence the imaging so that the tumor cannot be effectively visualized, and second, that the treatment may be selecting for a more aggressively invasive phenotype (Verhoeff et al., 2009; Keunen et al., 2011).

Previous studies have shown the use of anti-angiogenic drugs, specifically bevacizumab (Avastin), tends to increase progression-free survival and reduce symptoms of recurrent GBMs, but they have failed to consistently show a significant increase in overall survival and there is concern that the measured radiographic responses do not reflect changes in tumor cell counts (Verhoeff et al., 2009; Deming, 2012). Additionally, animal studies have revealed that treatment with anti-angiogenic drugs may be creating an environment favorable for local invasion and metastasis (Ebos et al., 2009; Pàez-Ribes et al., 2009). Even though there is a lack of significant evidence for increased overall survival after bevacizumab, and it is possible that treatment selects for a more invasive phenotype, the increase in quality of life for some of the patients, due to the relief from edema-related symptoms, means anti-angiogenic therapy is an attractive and relevant treatment option. However, the inability to determine *a priori* which patients will receive more benefit than harm from anti-angiogenic therapy ultimately keeps clinicians wary (Deming, 2012).

In this paper, we aim to illustrate how a previous mathematical model of glioma growth can be extended to explicitly incorporate edema formation allowing us to directly characterize and potentially predict the effects of anti-angiogenics on imageable tumor growth. The ultimate goal of this model is to help the treatment planning process by identifying exactly those patients that would receive the most benefit from anti-angiogenic treatment.

MATERIALS AND METHODS

THE PROLIFERATION-INVASION-HYPOXIA-NECROSIS-ANGIOGENESIS-EDEMA MODEL

Over the last decade we have made a significant effort toward the development of patient specific mathematical models of GBM that are able to capture the growth kinetics of individual patients (Swanson, 1999; Swanson et al., 2000, 2002a,b; Harpold et al., 2007; Rockne et al., 2010). The simplest form of the model, referred to as the Proliferation-Invasion (PI) model is based on patient specific net rates of proliferation and invasion and has been successful in predicting untreated growth rates for individual patients (Harpold et al., 2007) and providing predictions of outcomes following surgical resections (Swanson et al., 2003), chemotherapy

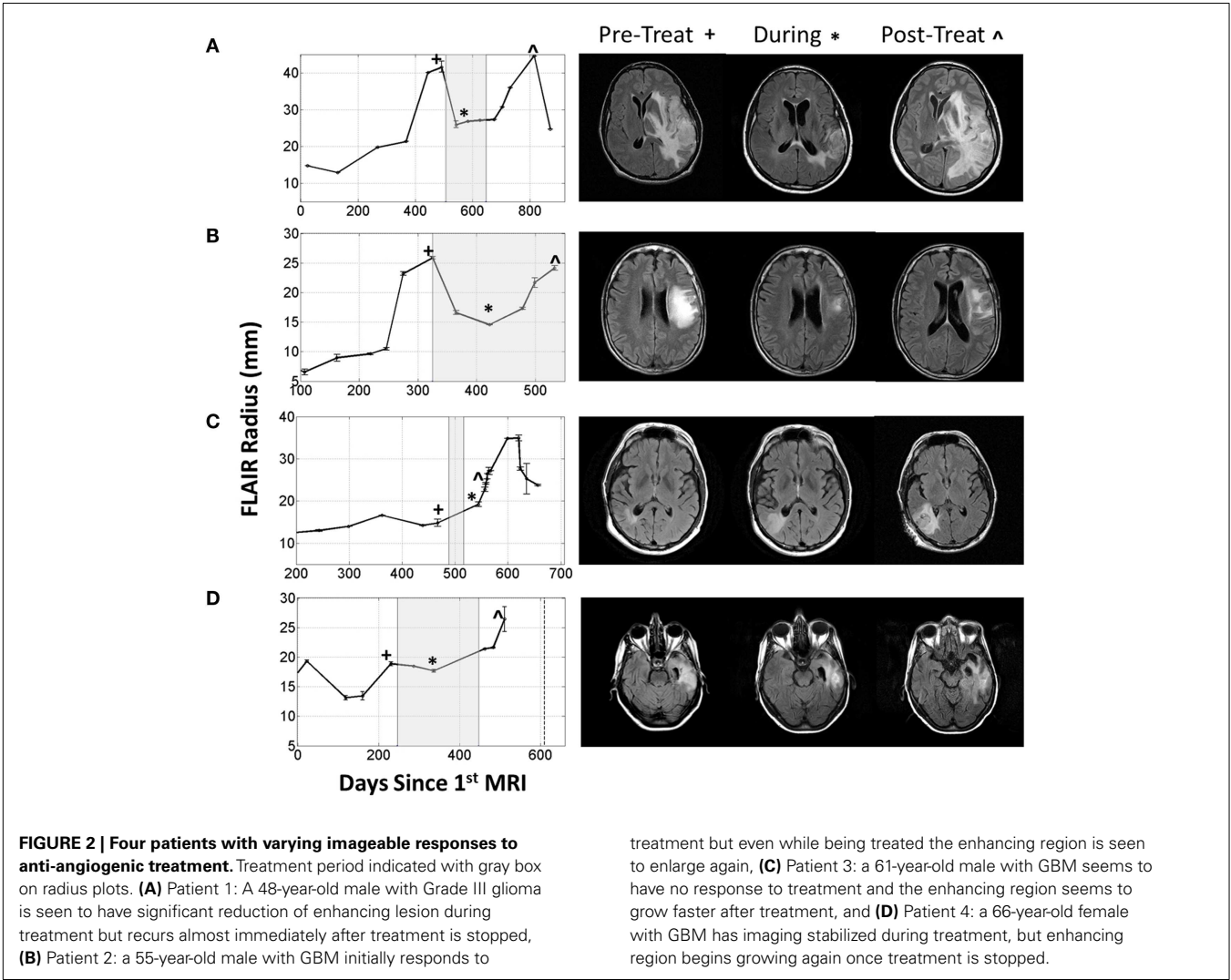


Table 1 | Demographic and treatment information corresponding to patients in Figure 2.

	Age	Sex	Grade	Race	XRT dose (cGy)	Concurrent TMZ	Bev given at recurrence	Concurrent therapies with Bev
Patient 1	48	M	III	Caucasian	Given, but unknown dosage	Y	Y	Irinotecan, dexamethasone
Patient 2	55	M	IV	Caucasian	6000	Y	Y	Carboplatin
Patient 3	61	M	IV	Unknown	6000	Y	Y	Irinotecan
Patient 4	66	F	IV	Caucasian	6120	Y	Y	Irinotecan

(Swanson et al., 2002a,b, 2003), and radiation (Rockne et al., 2010), while also providing insight into glioma ontogeny (Bohman et al., 2010).

A MATHEMATICAL MODEL OF THE ANGIOGENIC CASCADE IN GLIOBLASTOMA

The Proliferation-Invasion-Hypoxia-Necrosis-Angiogenesis (PIHNA) model first discussed in Swanson et al. (2011) incorporates the angiogenic cascade and characterizes malignant gliomas with relative proportions of well-oxygenated “normoxic” tumor

cells, (*c*), poorly oxygenated hypoxic tumor cells, (*h*), necrotic cells, (*n*), and vascular, or endothelial cells, (*v*), along with a generic population of angiogenic factors, (*a*) (Swanson et al., 2011). In words, it assumes the level of nutrients present in the local microenvironment, as inferred from the number of vasculature cells, determines whether the present tumor cells will exhibit normoxic or hypoxic phenotypes. That is, if there is a sufficient level of nutrients present, the cells will remain normoxic, but if the nutrient level falls below a given threshold, the cells will become hypoxic. If the nutrients provided by the vasculature fall below an even lower threshold value,

the hypoxic cells will undergo necrosis, at a rate of α_h (1/year) and remain in the necrotic cell population. Normoxic tumor cells are allowed to move (invade) and divide while, due to restricted amounts of nutrients, the hypoxic cells are only allowed to move. The hypoxic cells produce a large amount of angiogenic factors which ultimately cause an increase in the number of vasculature cells. The system is described with a mathematical model composed of the following five coupled reaction-diffusion equations:

$$\begin{aligned}
 \frac{\partial c}{\partial t} &= \underbrace{\nabla \cdot (D(x)(1-T)\nabla c)}_{\text{Net dispersal of normoxic glioma cells}} + \underbrace{\rho c(1-T)}_{\text{Net proliferation of normoxic glioma cells}} \\
 &+ \underbrace{\gamma h V}_{\text{Conversion of hypoxic to normoxic}} - \underbrace{\beta c(1-V)}_{\text{Conversion of normoxic to hypoxic}} \\
 &- \underbrace{\alpha_n n c}_{\text{Conversion of normoxic to necrotic}} \\
 \frac{\partial h}{\partial t} &= \underbrace{\nabla \cdot (D(x)(1-T)\nabla h)}_{\text{Dispersal of hypoxic glioma cells}} - \underbrace{\gamma h V}_{\text{Conversion of hypoxic to normoxic}} \\
 &+ \underbrace{\beta c(1-V)}_{\text{Conversion of normoxic to hypoxic}} - \underbrace{(\alpha_h h(1-T) + \alpha_n n h)}_{\text{Conversion of hypoxic to necrotic}} \\
 \frac{\partial n}{\partial t} &= \underbrace{\alpha_h h(1-V) + \alpha_n n(c+h+v)}_{\text{Conversion of hypoxic, normoxic, and vasculature to necrotic}} \\
 \frac{\partial v}{\partial t} &= \underbrace{\nabla \cdot (D_v(x)(1-T)\nabla v)}_{\text{Dispersal of vasculature}} + \underbrace{\mu \frac{a}{K_m+a} v(1-T)}_{\text{Net proliferation of vasculature}} \\
 &- \underbrace{\alpha_n n v}_{\text{Conversion of vasculature to necrotic}} \\
 \frac{\partial a}{\partial t} &= \underbrace{\nabla \cdot (D_a \nabla a)}_{\text{Net dispersal of angiogenic factors}} + \underbrace{\delta_c c + \delta_h h}_{\text{Net production of angiogenic factors}} \\
 &- \underbrace{q\mu \frac{a}{K_m+a} v(1-T) - \omega a v}_{\text{Net consumption of angiogenic factors}} - \underbrace{\lambda a}_{\text{Decay of angiogenic factors}}.
 \end{aligned} \tag{1}$$

In these equations, $D(x)$ is the net rate of invasion (mm^2/year). Glioma cells migrate faster along myelinated axons in the white matter than in the dense and less structured cortical gray matter. For this reason, we consider the net rate of invasion as piecewise constant, with non-zero values in the gray and white matter, D_g and D_w , respectively, with $D_w > D_g$, and zero in the regions of cerebral spinal fluid. Additionally, ρ (1/year) is the net proliferation rate of the normoxic cells, γ (1/year) and β (1/year) are the maximum conversion rates between the hypoxic and normoxic cell populations, α_n (1/year) is the rate at which cells undergo necrosis when in contact with necrotic cells (contact necrosis), α_h (1/year) is the rate of conversion of hypoxic cells to necrotic cells when nutrient levels fall too low, D_v (mm^2/year) is the rate of dispersal of vasculature cells, estimated from Sherratt and Murray

(1990), Levine et al. (2001) μ (1/year) is the vasculature proliferation rate, estimated from Xiu et al. (2006), $T = (c + h + n + v)/K$ (dimensionless), where K is the carrying capacity (cells/mm^3), and $V = v/(v + c + h)$ (dimensionless) and is a surrogate for the local vasculature efficiency. Angiogenic factors are produced by both normoxic and hypoxic cells with rates δ_c (1/year) and δ_h (1/year) respectively, with $\delta_h > \delta_c$ and are consumed by the vasculature for both regular vasculature maintenance [with rate ω (1/year)] and for vasculature proliferation [with rate q (1/year)]. Finally, the angiogenic factors are assumed to decay over time with rate λ (1/year) and disperse with rate D_v (mm^2/year). Values for parameters related to the angiogenic factors were derived in part from work done in Levine et al. (2001), Serini et al. (2003), Mac Gabhann and Popel (2004). The reader is referred to (Swanson et al., 2011) for further details.

It is known that GBM tumors are extremely genetically heterogeneous both within a single tumor and between different tumors (Dunn et al., 2012). A large effort has been put forth to identify subtypes of GBMs by their dominating genotype (Verhaak et al., 2010). While the model parameters do not directly try to capture effects of single mutations, it is our belief that the dominating genotypes characterizing subtypes of GBMs ultimately result in different net rates of proliferation and invasion which would be used in our model. For example, pro-neural tumors are more likely to have the IDH-1 mutation and be secondary GBMs. In our model, this would manifest as a low- D , low- ρ tumor which begins as low grade and progresses into higher grade/malignancy.

In this model, there are different cell populations, normoxic, hypoxic, and necrotic competing for space and each with differing phenotypes: normoxic cells proliferating and invading, hypoxic cells only invading, and necrotic cells which are dead and just taking up space. Since each cell population is evolving in space and time, there is an effective spatial heterogeneity of predicted proliferative activity across space and time which could be analogized to heterogeneous Ki67 labeling across glioma specimens. Thus, while this model is attempting to capture the overarching phenotype of different tumors and assumes global constants for individual tumors, spatial heterogeneity in behavior is possible due to regional levels of vasculature which may result in hypoxia and/or necrosis. We also remark the aim of this model is not to predict cell-level behaviors (ex. Ki67), rather, use information obtained from routine imaging to quantify and explain imaging scale behavior and evolution.

The PIHNA model only captures cellular species and angiogenic factors. While these all have an impact on what is ultimately seen on MR imaging, in and of themselves they are not sufficient to describe enhancing regions of T2 and T1Gd MR images. Here we extend the PIHNA model to capture the imaging responses post anti-angiogenic treatment. To achieve this, we add to the model one additional element: edema, (l), to create the merged proliferation-invasion-hypoxia-necrosis-angiogenesis-edema (PIHNA-E) model. A schematic of the six species interactions is shown in Figure 3.

A MATHEMATICAL MODEL FOR TUMOR-INDUCED EDEMA FORMATION

Generically, edema refers to a swelling phenomenon. While there are different types of cerebral edema, in the case of GBM, it is

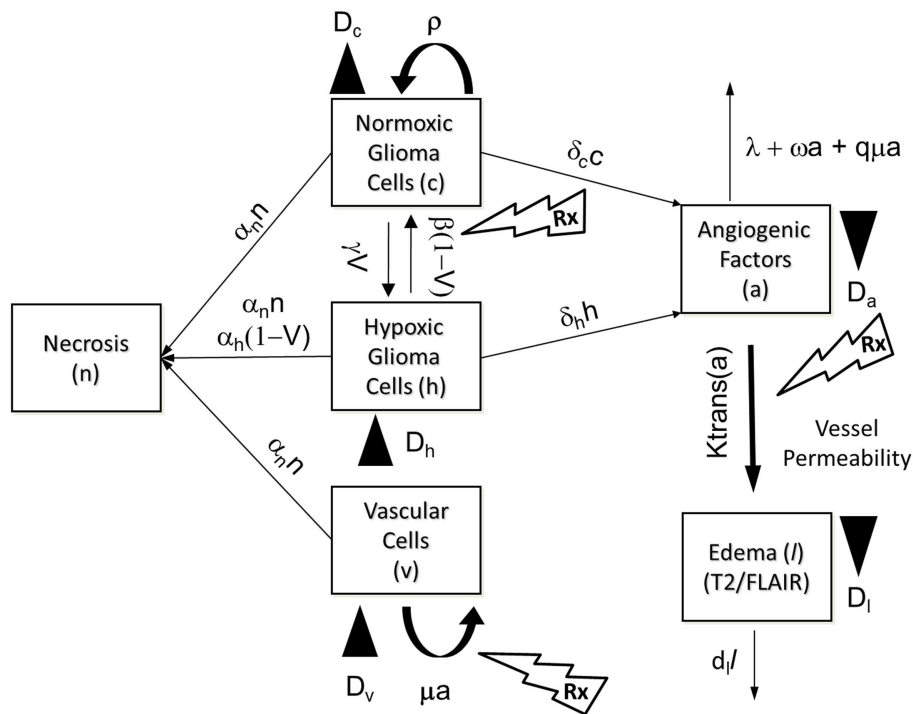


FIGURE 3 | Schematic of the PIHNA-E model. The main components of the model are seen in the flow chart: *c* represents the normoxic glioma cells, *h* the hypoxic gliomas cells, *v* the vascular endothelial cells, *n* the necrotic cells, *a*, the angiogenic factors, and *l* the edematous fluid. Depending on the level of oxygen, normoxic, and hypoxic cells will undergo phenotypic switching. If oxygen levels fall too far and are not compensated for by sufficient angiogenesis, the hypoxic cells will undergo necrosis. Additionally, all cells will undergo necrosis if in contact with

necrotic cells. Both hypoxic and normoxic cells release angiogenic factors into the extracellular space which recruit additional vasculature to increase the levels of oxygen. The angiogenic factors are removed from the system by interaction with vascular cells or natural decay. The local levels of angiogenic factors are indicative of the local degree of vessel permeability. Edematous liquid exits the vasculature where the permeability, $K_{trans}(a)$, allows and enters the extracellular space where it diffuses and will be removed at rate d_l .

almost exclusively vasogenic edema which results from fluid and protein leakage from the breakdown of the blood brain barrier (Marmarou, 2007). Over the last few decades, there have been quite a few attempts to model vasogenic edema (Rapoport, 1978; Kumagai, 1986; Nagashima et al., 1990) and its associated interstitial pressure and interstitial fluid velocity (Baxter and Jain, 1989, 1990). These models were primarily based on Starling's equation which describes fluid exchange between compartments due to pressure and osmotic gradients. These models are very detailed and are generally solved on shorter time scales, i.e., a few days versus months. In our efforts, while we do have interest in the specific mechanisms, we will take a coarser grained approach allowing us to approximate the phenomena over longer time scales relevant to tumor growth kinetics.

To begin, we make the simplifying assumption that the edema is only composed of fluid which has leaked into the extra-cellular space and has not yet been reabsorbed into the system. This fluid is assumed to leak into the extracellular space where the blood brain barrier has been compromised. From the PIHNA model, we can approximate these regions along with the degree of permeability from the local levels of present angiogenic factors. Once the fluid is in the extra-cellular space it moves via diffusion and is reabsorbed into the system at a constant rate. This process is written in the

form of a partial differential equation as:

$$\frac{\partial l}{\partial t} = \underbrace{\nabla \cdot (D_l \nabla l)}_{\text{Fluid diffusion}} + \underbrace{K_{trans}(a) \cdot (l_v - l)}_{\text{Leakage}} - \underbrace{\delta_l l}_{\text{Drainage}} \quad (2)$$

Here l is the concentration of edematous fluid, D_l (mm^2/year) is the diffusion rate of the edematous liquid which would be analogous to an Apparent Diffusion Coefficient, ADC, value derived from diffusion-weighted MRI (Moritani, 2009), l_v (fluid/mm^3) is the normal level of fluid in the vasculature, δ_l ($1/\text{year}$) is the reabsorption rate, and K_{trans} ($1/\text{year}$) is the transmission rate [analogous to the value K_{trans} measured on dynamic contrast enhanced MRI (DCE-MRI)], capturing the permeability surface area product per unit volume of tissue (Tofts, 1991) and is assumed to depend on the level of angiogenic factors, a , present. Homogeneous Neumann boundary conditions are assumed at the boundary of the brain to ensure no fluid leaves the brain.

The dependence of the K_{trans} coefficient on the angiogenic factors is assumed to take a Michaelis–Menten type I form:

$$K_{trans}(a) = K_{max} \frac{a}{a + K_{half}} \quad (3)$$

to reflect that VEGF (also known as vascular permeability factor, VPF) strongly influences vascular permeability (Bates, 2010). Here K_{\max} (1/year) is the maximum possible value of K_{trans} , the value of which is calibrated to Grade IV gliomas (Patankar et al., 2005), and K_{half} (angiogenic factors/mm³) is the concentration of a at which K_{trans} reaches half of its maximum value. Thus, as the concentration of the angiogenic factors increases, the degree of vessel permeability will also increase until saturated.

MODELING ANTI-ANGIOGENIC TREATMENT

The PIHNA-E model describes the evolution of the tumor and its microenvironment in an untreated context. By understanding the premise of how specific therapies are meant to alter the system, one can also model the effects of various treatments. Here we are interested in anti-angiogenic treatment and, while there are many different types of drugs for this action, will focus on the drug bevacizumab.

Bevacizumab is a drug specifically targeted at the molecule vascular endothelial growth factor A (VEGF A). This particular angiogenic factor stimulates the growth of new vessels by binding with the vascular endothelial growth factor receptor (VEGFR2) on endothelial cells. Bevacizumab inhibits angiogenesis by binding to the free molecules of VEGFA and preventing them from binding to VEGFR2. An unintended consequence of this drug, however, is that beyond preventing the growth of new vessels, it also “normalizes” pre-existing vasculature (Jain, 2005; Verhoeff et al., 2009). That is, once the levels of stimulating angiogenic factors are reduced, the vessels are able to repair their leakiness and return to a normal size – making them more efficient nutrient deliverers. In our model, both of these phenomena can be captured by requiring higher levels of angiogenic factor to be present to have the same level of “action” in the contexts of both vessel proliferation and vessel permeability. Additionally, since the treatment is making the vessels more efficient, the level of vasculature needed for a cell to be normoxic will decrease, which we can capture by modifying the cell conversion rates from hypoxic to normoxic and from normoxic to hypoxic. Treatment is approximated by decreasing the parameter for conversion from normoxic to hypoxic (β) by a factor of 10, increasing the parameter for conversion from hypoxic and normoxic (γ) by a factor of 10, and increasing the required levels of angiogenic factors for inducing vascular growth and vessel permeability by 2 as supported by the studies in Desjardins et al. (2007), Zhang et al. (2009). The treatment modification of β and γ is representative of a dramatic increase in the efficiency of the blood vessels, though exact changes are not available from experimental data.

SIMULATIONS OF GLIOBLASTOMA GROWTH AND RESPONSE TO ANTI-ANGIOGENIC THERAPY

For simplicity, we consider in all simulations here a two-dimensional tumor growing on one axial slice of the brain, with the brain geometry defined from the BrainWeb atlas (Cocosco et al., 1997). The brain is primarily composed of three different types of matter, CSF, gray matter, and white matter. Glioblastomas originate in gray or white matter and due to physical barriers will not enter into the regions of CSF. New mass will often deform the barriers, a phenomena called mass effect, and while there are some models that attempt to capture this (Clatz et al., 2005;

Mohamed and Davatzikos, 2005; Hoge et al., 2008), here the brain is considered a stationary domain.

In all simulations, the domain is taken to be a slice of human brain embedded in a grid $[0, 147] \text{ mm} \times [0, 185] \text{ mm}$ and the equations are spatially discretized on a grid with resolution of $1 \text{ mm} \times 1 \text{ mm}$ using first order accurate finite volumes. Time integration is done with an operator splitter technique utilizing backward Euler for the diffusion terms and the TR-BDF2 algorithm (Leveque, 2005) for the reaction terms with a time step size of 1 day. The simulations were initiated with a small amount of normoxic cells distributed as

$$c_0(x, y, t = 0) = 1000 * \exp\left(-\left(100\left[(x - x_0)^2 + (y - y_0)^2\right]\right)\right)$$

where $(x_0, y_0) = (103, 83)$. Vasculature is set at 3% of the cell carrying capacity in all gray and white matter based on estimates from Blinkov and Glezer (1968), and all other quantities in the PIHNA-E model are initiated to zero. Unless otherwise stated, parameter values used in simulations for the edema equation are in Table 2, the additional parameter values are taken as specified in Swanson et al. (2011).

RESULTS

DECOUPLING IMAGING CHANGES FROM TUMOR RESPONSE

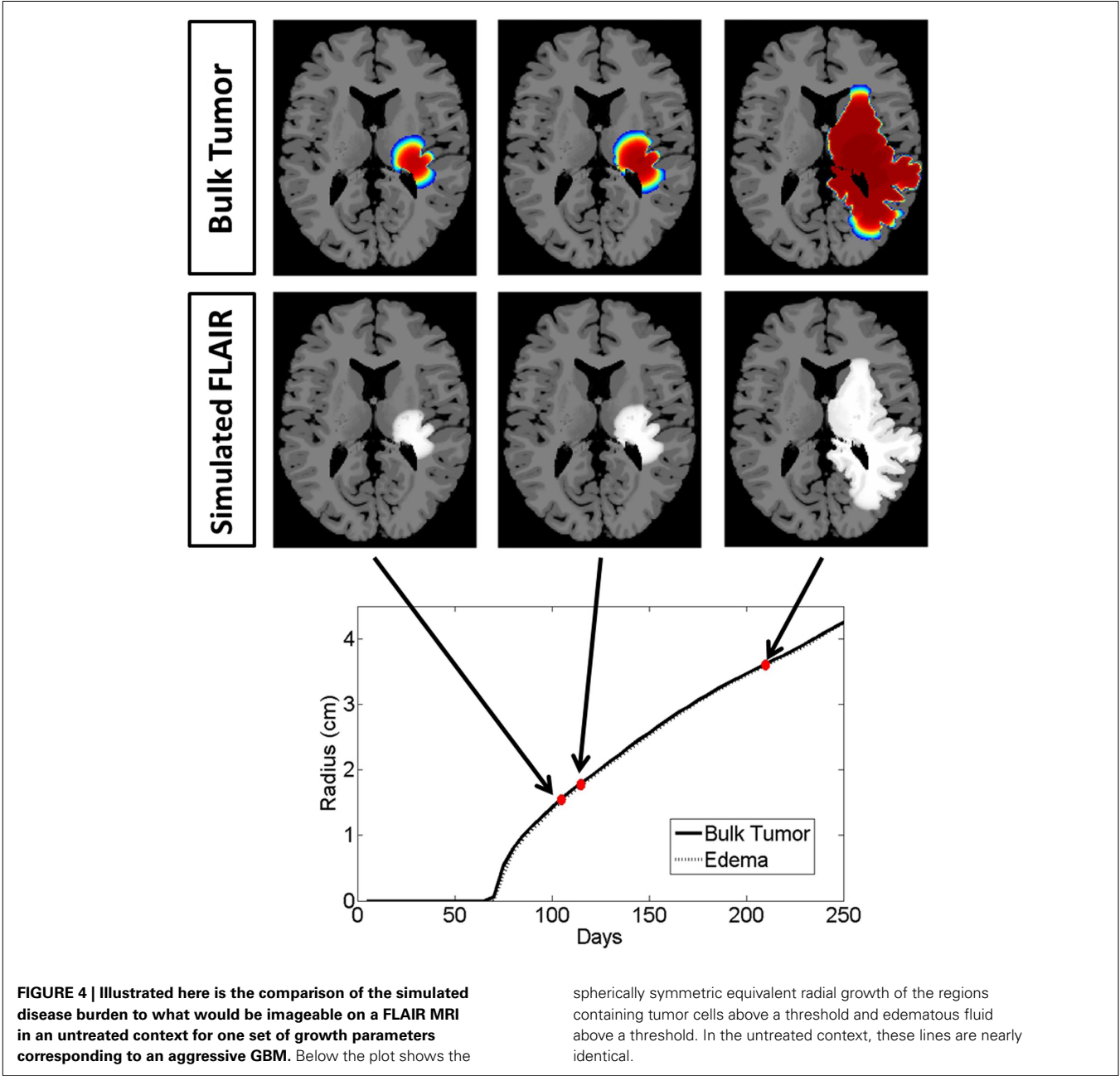
To highlight the real impact of anti-angiogenic treatment as captured by our model, we chose parameter values that represent a patient with an aggressive GBM (net invasion rates $D_w = 53 \text{ mm}^2/\text{year}$ and $D_g = 0.53 \text{ mm}^2/\text{year}$ and net proliferation rate $\rho = 75 \text{ 1/year}$) and simulate tumor growth without treatment (Figure 4) and then compare to tumor growth with treatment (Figure 5). For comparison to what was done in previous work (Swanson et al., 2008a, 2011; Rockne et al., 2010), we refer to the region with total cell density summing to 80% of the cell carrying capacity (K) to correspond to what would enhance on the T1Gd, and started treatment when the T1Gd spherically symmetric equivalent radius was equal to 1 cm and was terminated 100 days later. This is consistent with a typical size of an abnormality seen clinically for consideration of anti-angiogenic treatment. Although treatment length can vary, 100 days is representative of the length of a typical course of treatment with anti-angiogenics in human GBM.

Snapshots of the untreated case are shown in Figure 4 with the analogous snapshots corresponding to the same time points of the treated tumor being shown in Figure 5. The top row in both Figures 4 and 5 shows the density of the bulk tumor (the summed density of all the cell populations: normoxic, hypoxic, necrotic, and vasculature). The second row shows what the simulated FLAIR corresponding to the microenvironmental levels of edematous extracellular fluid. These figures also contain radial growth plots showing the equivalent spherical radii for the regions of interest corresponding to the tumor and the edema. The line representing the bulk tumor is calculated from the volume of tissue containing abnormal cells, normoxic, hypoxic, and necrotic, at levels greater than or equal to 16% of the carrying capacity, i.e., a density five times lower than what can be visualized on T1Gd (Swanson et al., 2008b). The edema radius was defined by considering the volume containing edematous fluid above 50% of the fluid level in the capillaries. There is no literature to guide

Table 2 | Parameter values for the edema equation used in all simulations unless stated otherwise in the text.

Parameter	Definition	Value	Reference
K_{half}	Michaelis–Menten half-max of response of ECs to angiogenic factors	$5.75e-7$ (mmol/cc tissue)	Derived from Mac Gabhann and Popel (2004)
D_I	Net rate of edematous fluid diffusion	$0.77e-3$ (mm ² /s)	Chosen as average ADC value in normal brain tissue as given in Moritani (2009)
K_{max}	Maximum K_{trans} value in response to angiogenic factors	36 (1/day)	Taken to match the maximum K_{trans} value observed in Grade IV gliomas in Patankar et al. (2005)
δ_I	Edematous fluid reabsorption rate	$0.3 \times K_{max}$ (1/day)	Assumed proportional to vessel permeability

All other parameter values are taken as described in Swanson et al. (2011).



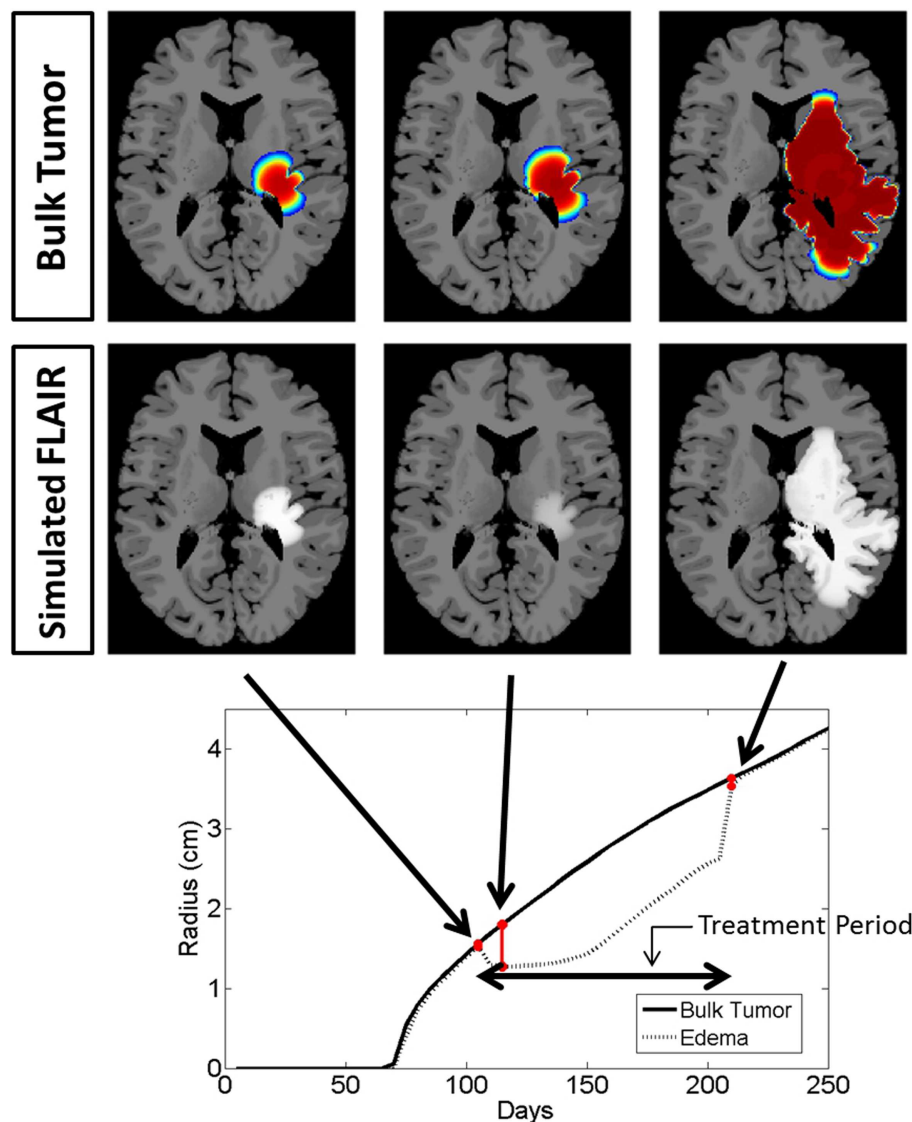


FIGURE 5 | Comparison of the simulated disease burden to what would be imageable on a FLAIR MRI in a treated context for the same set of growth parameters as shown in Figure 4. Below the plot shows the spherically symmetric equivalent radial growth of the regions containing

tumor cells above a threshold and edematous fluid above a threshold. Once treatment has begun, we see a drop in the levels of edema. Upon termination of the treatment, the edematous volume is seen to once again increase to the same size of the volume of tumorous cells.

the choice of the cutoffs for fluid volume constituting T2/FL visible edema. Thus, cutoffs were chosen to roughly match clinically observed behavior.

In the untreated case (Figure 4) the radial plot shows the size of the region impacted by edema evolves very similarly to the size of the region occupied by the bulk tumor throughout the entire course of growth. In the treated case (Figure 5), the edema grows at the same rate as the bulk tumor until the treatment begins at which point the edema begins to decline. Edema begins to increase again once the angiogenic factors have been able to accumulate at levels which overcome the impact of the anti-angiogenic drug. Once treatment is terminated the edema levels rise to again occupy a region of the same size as the bulk tumor.

These simulations support the hypothesis that anti-angiogenic treatment may not have a significant effect on the growth dynamics of the overall cell populations, while having a large impact on the level of edematous extracellular fluid and thus on what would be imageable on T2/FLAIR MRI. This is also in agreement with the current understanding that anti-angiogenic treatment serves as a surrogate to steroids for reducing swelling.

EXPLORING RESPONSE ACROSS TUMOR KINETICS

The virtual control experiment illustrated in Figures 4 and 5 is only providing insight into tumor/edema response for the case of one set of tumor growth kinetics. However, the range of radiographic response patterns seen clinically is broad, a few examples of which

are shown in **Figure 2**. Previous work has shown patient specific values of net proliferation and invasion range over many orders of magnitude (Tracqui et al., 1995; Harpold et al., 2007). To investigate if the different types and extents of radiographic responses could be explained by different underlying tumor growth kinetics, we simulated tumor growth and the associated edema under treatment for many different combinations of net proliferation rates, ρ , and net invasion rates, D_w and D_g .

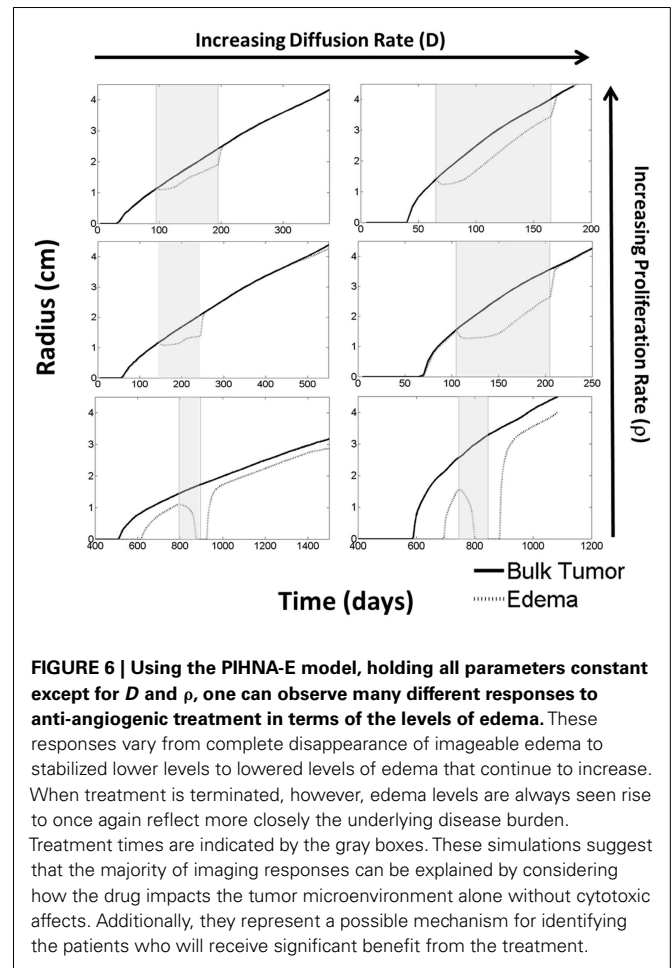
For all cases, treatment was started when the tumor reached a simulated 1 cm T1Gd radius for a total of 100 continuous days. Treatment was implemented in the same manner as the first case. Illustrative results are shown in **Figure 6** from simulations with $\rho = [5, 75, 125]$ (1/year) and $D_w = [5.3, 53]$ (mm^2/year) and $D_g = D_w/10$ consistent with the observed range hypothesized in human gliomas (Harpold et al., 2007) and since observed (Wang et al., 2009; Rockne et al., 2010).

From these six scenarios, summarized in **Figure 6**, we were able to observe a few trends. First, none of the simulations showed a significant change in the bulk tumor growth rate after treatment had begun. However, levels of edema were impacted and by different degrees in each of the simulations. In general, tumors with higher proliferative capacities (higher ρ 's), due to their higher metabolic needs, have larger regions of hypoxia and thus produce greater levels of angiogenic factors. Treatment of these tumors initially reduces the level of edema, however, the tumor quickly produces enough angiogenic factors to continue progressing under imaging. In contrast, the slower growing tumors (low ρ) produce low levels of angiogenic factors and treatment may result in a complete disappearance of the abnormality on imaging. Additionally, higher dispersion rates (high D_w and D_g) reduce the local metabolic needs and the production of angiogenic factors. Thus, the imaging of tumors with high D_w and high D_g improve for a longer time, however, ultimately the tumor does still produce enough angiogenic factors to be seen progressing on imaging. For all cases, once treatment is discontinued, the edema levels quickly rise to again reflect the underlying tumor burden.

What is particularly encouraging is that many of the different behaviors observed for the four patients illustrated in **Figure 2** can be connected to different simulation predictions. For example, the first patient's behavior is analogous to the moderate proliferation rate with a low invasion rate in that the imageable lesion initially decreased, stabilized, but after treatment dramatically increased. Additionally, the second patient can be compared to either the moderate or highly proliferative rate with a high invasion rate where the hyperintensity is seen to decrease at the beginning of treatment, but even while treatment is continuing, start growing again.

DISCUSSION

Anti-angiogenics remain a controversial form of treatment for GBM due to the difficulty in assessing tumor response using MR imaging. The resulting reduction in swelling and related symptoms for a subset of patients keeps it an attractive option despite the lack of evidence of an increase in overall survival and the possibility of the treatment selecting for a more aggressive phenotype (Ebos et al., 2009; Pàez-Ribes et al., 2009; Verhoeff et al., 2009; Keunen et al., 2011). It is unclear how anti-angiogenic treatment



impacts the cell phenotypes present and there is not yet a deep enough understanding or a unifying theory to provide explanation for all the different response patterns. Thus, *a priori* identification of patients who will receive a significant symptom-reduction benefit remains difficult. As there are other side effects and consequences from anti-angiogenic therapy, being able to make this early distinction would help remove the controversial nature of this therapy.

The model developed in this work, built on the PIHNA model for glioma proliferation and invasion (Swanson et al., 2011; Gu et al., 2012), is meant to illustrate a first step toward the creation of a tool for identifying patients who will receive the greatest benefit from anti-angiogenic treatment. It captures the formation of edema caused by leaky vasculature, and is thus able to decouple what would be seen on the T2/FLAIR MRI from the true underlying disease burden. In effect, this would help the clinicians to “turn the light back on” by being able to infer the disease burden that lies beyond what is captured by imaging alone. While this model is not meant to capture individual cell behavior, it does provide a map between overall tumor growth kinetics and treatment response on the imaging/continuum scale.

Many simplifying assumptions have been made in the creation of this model such as ignoring the possible direct impact of

anti-angiogenic therapy on cell proliferation, the likely presence of thrombosis (Tehrani et al., 2008), and that the hyperintensity on the T2/FLAIR image is entirely a result of fluid leaking from the vasculature. The model is clearly incomplete, and future modifications of the model will need to consider these other phenomena as well as other possible factors on T2/FLAIR hyperintensity, such as higher cell density and additional cytoplasm. However, even in its current state, it has been able to exhibit many of the types of response patterns observed clinically. It is particularly encouraging because the modeling effects of treatment were held constant and only varying the net dispersal and net proliferation rates, D and ρ , respectively, was sufficient to produce a wide range of imaging responses analogous to what is seen clinically. That is, by modeling the treatment in the exact same way for different values of proliferation and diffusion in the tumor growth model, the visible levels of edema are seen to respond in different ways. In general, the simulations predict edema (swelling) to decrease, supporting the role of these drugs as surrogates for steroids for reduction of symptoms, analogous to the most current understanding (Deming, 2012). Though, the model clearly illustrates that not all patients would receive the same benefit.

Another interesting implication from these simulations is that while different imaging responses to treatment were achieved for the same treatment conditions, in all cases the bulk tumor is seen to progress with little deflection in overall tumor growth rates. This result could be considered evidence against the cytotoxic effects of anti-angiogenic treatment when administered exclusively, also in agreement with current clinical understanding (Verhoeff et al., 2009). While this work is not directly speaking to survival outcomes, we remark that these results highlight the potential for the mathematical model paradigm to serve in evaluating clinical trial outcomes by analyzing relative benefit from anti-angiogenics,

especially in the case of low- N trials. As a particular example, such models may have the potential to be applied to patient cohorts for exploring how differential effects of anti-angiogenics on imaging may or may not relate to overall outcomes.

A drawback of this model is the large number of parameters required. In this document, we assumed the primary influential factor were the net rates of invasion and proliferation and thus held all other parameters constant. These other parameters are likely different patient to patient, however, as demonstrated here, changes in the small number of parameters are sufficient to produce a wide variety of imaging responses. While future sensitivity analysis is required, we believe the work is here is evidence that a complicated explanation for the different imaging responses to anti-angiogenic therapy may not be needed. Major next steps of this work will involve developing techniques for obtaining patient specific growth parameters from pre-treatment images which we believe will be successful from previous accomplishments with a simpler model capturing just the proliferation and invasion tumor characteristics PI (Swanson, 1999, 2002; Swanson et al., 2000, 2003, 2004, 2008a; Szeto et al., 2009; Wang et al., 2009; Rockne et al., 2010).

Also, modification of the model to capture the pressure induced from the vasogenic edema and possible herniation would allow for deeper understanding of the steroid-like reduction in swelling. For each new feature eventually added validation tests will be required, however, we believe the results presented here in and of themselves represent a significant step in overcoming clinical imaging restrictions with mathematical models.

ACKNOWLEDGMENTS

The authors would like to greatly acknowledge the funding of this work which was sponsored in part by NIH Grants: R01 CA 16437 and U54 CA 143970, along with the NSF Fellowship 1122322.

REFERENCES

- Batchelor, T. T., Sorensen, A. G., di Tomaso, E., Zhang, W. T., Duda, D. G., Cohen, K. S., et al. (2007). AZD2171, a pan-VEGF receptor tyrosine kinase inhibitor, normalizes tumor vasculature and alleviates edema in glioblastoma patients. *Cancer Cell* 11, 83–95.
- Bates, D. O. (2010). Vascular endothelial growth factors and vascular permeability. *Cardiovasc. Res.* 87, 262–271.
- Baxter, L. T., and Jain, R. K. (1989). Transport of fluid and macromolecules in tumors. I. Role of interstitial pressure and convection. *Microvasc. Res.* 37, 77–104.
- Baxter, L. T., and Jain, R. K. (1990). Transport of fluid and macromolecules in tumors. II. Role of heterogeneous perfusion and lymphatics. *Microvasc. Res.* 40, 246–263.
- Blinkov, S. M., and Glezer, I. I. (1968). *The Human Brain in Figures and Tables: A Quantitative Handbook*. New York: Basic Books.
- Bohman, L. E., Swanson, K. R., Moore, J. L., Rockne, R., Mandigo, C., Han-kinson, T. et al. (2010). Preoperative MRI characteristics of glioblastoma multiforme: implications for understanding glioma ontogeny. *Neurosurgery* 67, 1319–1327.
- Clatz, O., Sermesant, M., Bondiau, P. Y., Delingette, H., Warfield, S. K., Malandain, G., et al. (2005). Realistic simulation of the 3-D growth of brain tumors in MR images coupling diffusion with biomechanical deformation. *IEEE Trans. Med. Imaging* 24, 1334–1346.
- Cocosco, C., Kollokian, V., Kwan, R. S., and Evans, A. (1997). "Brainweb: online interface to a 3D MRI simulated brain database," in *Neuroimage, Proceedings of the Third International Conference on the Functional Mapping of the Human Brain*, Copenhagen.
- Deming, S. (2012). Bevacizumab for glioblastoma: symptom relief proven, overall survival benefit being studied. *OncoLog* 57. Available at: <http://www2.mdanderson.org/depts/oncolog/articles/pf/12/6-jun/6-12-2-pf.html>
- Desjardins, A., Barboriak, D. P., Herndon, J. E. II, Reardon, D. A., Quinn, J. A., Rich, J. N., et al. (2007). Dynamic contrast-enhanced magnetic resonance imaging (DCE-MRI) evaluation in glioblastoma (GBM) patients treated with bevacizumab (BEV) and irinotecan (CPT-11). *J. Clin. Oncol.* 25(Suppl.), abstr. 2029.
- Dunn, G. P., Rinne, M. L., Wykosky, J., Genovese, G., Quayle, S. N., Dunn, I. F., et al. (2012). Emerging insights into the molecular and cellular basis of glioblastoma. *Genes Dev.* 26, 756–784.
- Ebos, J. M., Lee, C. R., Cruz-Munoz, W., Bjarnason, G. A., Christensen, J. G., and Kerbel, R. S. (2009). Accelerated metastasis after short-term treatment with a potent inhibitor of tumor angiogenesis. *Cancer Cell* 15, 232–239.
- Folkman, J. (1971). Tumor angiogenesis: therapeutic implications. *N. Engl. J. Med.* 285, 1182–1186.
- Gu, S., Chakraborty, G., Champey, K., Alessio, A. M., Claridge, J., Rockne, R., et al. (2012). Applying a patient-specific bio-mathematical model of glioma growth to develop virtual [18F]-FMISO-PET images. *Math. Med. Biol.* 29, 31–48.
- Harpold, H. L., Alvord, E. C. Jr., and Swanson, K. R. (2007). The evolution of mathematical modeling of glioma proliferation and invasion. *J. Neuropathol. Exp. Neurol.* 66, 1–9.
- Hogea, C., Davatzikos, C., and Biros, G. (2008). An image-driven parameter estimation problem for a reaction-diffusion glioma growth model with mass effects. *J. Math. Biol.* 56, 793–825.
- Holash, J., Maisonpierre, P. C., Compton, D., Boland, P., Alexander, C. R., Zagzag, D., et al. (1999). Vessel cooption, regression, and growth in tumors mediated by angiopoietins and VEGF. *Science* 284, 1994–1998.
- Hurwitz, H., Fehrenbacher, L., Novotny, W., Cartwright, T., Hainsworth, J.,

- Heim, W., et al. (2004). Bevacizumab plus irinotecan, fluorouracil, and leucovorin for metastatic colorectal cancer. *N. Engl. J. Med.* 350, 2335–2342.
- Iwamoto, F. M., Abrey, L. E., Beal, K., Gutin, P. H., Rosenblum, M. K., Reuter, V. E., et al. (2009). Patterns of relapse and prognosis after bevacizumab failure in recurrent glioblastoma. *Neurology* 73, 1200–1206.
- Jain, R. K. (2005). Normalization of tumor vasculature: an emerging concept in antiangiogenic therapy. *Science* 307, 58–62.
- Kerbel, R. S. (2000). Tumor angiogenesis: past, present and the near future. *Carcinogenesis* 21, 505–515.
- Keunen, O., Johansson, M., Oudin, A., Sanzey, M., Rahim, S. A., Fack, F., et al. (2011). Anti-VEGF treatment reduces blood supply and increases tumor cell invasion in glioblastoma. *Proc. Natl. Acad. Sci. U.S.A.* 108, 3749–3754.
- Kumagai, Y. (1986). Mathematical model of brain edema and optimal control of intracranial pressure. *No To Shinkei* 38, 885–891.
- Leenders, W. P., Küsters, B., and de Waal, R. M. (2002). Vessel co-option: how tumors obtain blood supply in the absence of sprouting angiogenesis. *Endothelium* 9, 83–87.
- LeVeque, R. (2005). *Numerical Methods for Conservation Laws*, 2nd Edn. Basel: Birkhäuser.
- Levine, H. A., Pamuk, S., Sleeman, B. D., and Nilsen-Hamilton, M. (2001). Mathematical modeling of capillary formation and development in tumor angiogenesis: penetration into the stroma. *Bull. Math. Biol.* 63, 801–863.
- Louis, D. N., Ohgaki, H., Wiestler, O. D., Cavenee, W. K., Burger, P. C., Jouvett, A., et al. (2007). The 2007 WHO classification of tumours of the central nervous system. *Acta Neuropathol.* 114, 97–109.
- Mac Gabhann, F., and Popel, A. S. (2004). Model of competitive binding of vascular endothelial growth factor and placental growth factor to VEGF receptors on endothelial cells. *Am. J. Physiol. Heart Circ. Physiol.* 286, H153–H164.
- Marmarou, A. (2007). A review of progress in understanding the pathophysiology and treatment of brain edema. *Neurosurg. Focus* 22, E1.
- Mohamed, A., and Davatzikos, C. (2005). Finite element modeling of brain tumor mass-effect from 3D medical images. *Med. Image Comput. Assist. Interv.* 2005(Pt 13749), 400–408.
- Moritani, T. (2009). *Diffusion-Weighted MR Imaging of the Brain*. New York: Springer.
- Nagashima, T., Horwitz, B., and Rapoport, S. I. (1990). A mathematical model for vasogenic brain edema. *Adv. Neurol.* 52, 317–326.
- Norden, A. D., Young, G. S., Setayesh, K., Muzikansky, A., Klufas, R., Ross, G. L., et al. (2008). Bevacizumab for recurrent malignant gliomas: efficacy, toxicity, and patterns of recurrence. *Neurology* 70, 779–787.
- Pàez-Ribes, M., Allen, E., Hudock, J., Takeda, T., Okuyama, H., Viñals, F., et al. (2009). Antiangiogenic therapy elicits malignant progression of tumors to increased local invasion and distant metastasis. *Cancer Cell* 15, 220–231.
- Patankar, T. F., Haroon, H. A., Mills, S. J., Balériaux, D., Buckley, D. L., Parker, G. J., et al. (2005). Is volume transfer coefficient (K(trans)) related to histologic grade in human gliomas? *AJNR Am. J. Neuroradiol.* 26, 2455–2465.
- Rapoport, S. I. (1978). A mathematical model for vasogenic brain edema. *J. Theor. Biol.* 74, 439–467.
- Rockne, R., Rockhill, J. K., Mrugala, M., Spence, A. M., Kalet, L., Hendrickson, K., et al. (2010). Predicting the efficacy of radiotherapy in individual glioblastoma patients in vivo: a mathematical modeling approach. *Phys. Med. Biol.* 55, 3271–3285.
- Sandler, A., Gray, R., Perry, M. C., Brahmer, J., Schiller, J. H., Dowlati, A., et al. (2006). Paclitaxel-carboplatin alone or with bevacizumab for non-small-cell lung cancer. *N. Engl. J. Med.* 355, 2542–2550.
- Serini, G., Ambrosi, D., Giraudo, E., Gamba, A., Preziosi, L., and Bus-solino, F. (2003). Modeling the early stages of vascular network assembly. *EMBO J.* 22, 1771–1779.
- Sherratt, J. A., and Murray, J. D. (1990). Models of epidermal wound-healing. *Proc. Biol. Sci.* 241, 29–36.
- Silbergeld, D. L., and Chicoine, M. R. (1997). Isolation and characterization of human malignant glioma cells from histologically normal brain. *J. Neurosurg.* 86, 525–531.
- Stupp, R., Mason, W. P., van den Bent, M. J., Weller, M., Fisher, B., Taphoorn, M. J., et al. (2005). Radiotherapy plus concomitant and adjuvant temozolomide for glioblastoma. *N. Engl. J. Med.* 352, 987–991.
- Swanson, K. R. (1999). *Mathematical Modeling of the Growth and Control of Tumors. Applied Mathematics*. Ph.D. thesis, University of Washington, Seattle.
- Swanson, K. R. (2002). Serial imaging observations and postmortem examination of an untreated glioblastoma: a traveling wave of glioma growth and invasion. *Neuro-oncology* 4, 340.
- Swanson, K. R., Alvord, E. C. Jr., and Murray, J. D. (2000). A quantitative model for differential motility of gliomas in grey and white matter. *Cell Prolif.* 33, 317–329.
- Swanson, K. R., Alvord, E. C. Jr., and Murray, J. D. (2002a). Quantifying efficacy of chemotherapy of brain tumors with homogeneous and heterogeneous drug delivery. *Acta Biotheor.* 50, 223–237.
- Swanson, K. R., Alvord, E. C. Jr., and Murray, J. D. (2002b). Virtual brain tumours (gliomas) enhance the reality of medical imaging and highlight inadequacies of current therapy. *Br. J. Cancer* 86, 14–18.
- Swanson, K. R., Alvord, E. C., and Murray, J. D. (2004). Dynamics of a model for brain tumors reveals a small window for therapeutic intervention. *Discrete Continuous Dyn. Syst. Ser. B* 4, 289–295.
- Swanson, K. R., Bridge, C., Murray, J. D., and Alvord, E. C. Jr. (2003). Virtual and real brain tumors: using mathematical modeling to quantify glioma growth and invasion. *J. Neurol. Sci.* 216, 1–10.
- Swanson, K. R., Harpold, H. L., Peacock, D. L., Rockne, R., Pennington, C., Kilbride, L., et al. (2008a). Velocity of radial expansion of contrast-enhancing gliomas and the effectiveness of radiotherapy in individual patients: a proof of principle. *Clin. Oncol.* 20, 301–308.
- Swanson, K. R., Rostomily, R. C., and Alvord, E. C. Jr. (2008b). A mathematical modelling tool for predicting survival of individual patients following resection of glioblastoma: a proof of principle. *Br. J. Cancer* 98, 113–119.
- Swanson, K. R., Rockne, R. C., Claridge, J., Chaplain, M. A., Alvord, E. C. Jr., and Anderson, A. R. (2011). Quantifying the role of angiogenesis in malignant progression of gliomas: in silico modeling integrates imaging and histology. *Cancer Res.* 71, 7366–7375.
- Szeto, M. D., Chakraborty, G., Hadley, J., Rockne, R., Muzi, M., Alvord, E. C. Jr., et al. (2009). Quantitative metrics of net proliferation and invasion link biological aggressiveness assessed by MRI with hypoxia assessed by FMISO-PET in newly diagnosed glioblastomas. *Cancer Res.* 69, 4502–4509.
- Tehrani, M., Friedman, T. M., Olson, J. J., and Brat, D. J. (2008). Intravascular thrombosis in central nervous system malignancies: a potential role in astrocytoma progression to glioblastoma. *Brain Pathol.* 18, 164–171.
- Tofts, P. S. (1991). Measurement of the blood-brain barrier permeability and leakage space using dynamic MR imaging. 1. Fundamental concepts. *Magn. Reson. Med.* 17, 357–367.
- Tracqui, P., Cruywagen, G. C., Woodward, D. E., Bartoo, G. T., Murray, J. D., and Alvord, E. C. Jr. (1995). A mathematical model of glioma growth: the effect of chemotherapy on spatio-temporal growth. *Cell Prolif.* 28, 17–31.
- Verhaak, R. G., Hoadley, K. A., Purdom, E., Wang, V., Qi, Y., Wilkerson, M. D., et al. (2010). Integrated genomic analysis identifies clinically relevant subtypes of glioblastoma characterized by abnormalities in PDGFRA, IDH1, EGFR, and NF1. *Cancer Cell* 17, 98–110.
- Verhoeff, J. J., van Tellingen, O., Claes, A., Stalpers, L. J., van Linde, M. E., Richel, D. J., et al. (2009). Concerns about anti-angiogenic treatment in patients with glioblastoma multiforme. *BMC Cancer* 9:444. doi:10.1186/1471-2407-9-444
- Wang, C. H., Rockhill, J. K., Mrugala, M., Peacock, D. L., Lai, A., Jusenius, K., et al. (2009). Prognostic significance of growth kinetics in newly diagnosed glioblastomas revealed by combining serial imaging with a novel bi-mathematical model. *Cancer Res.* 69, 9133–9140.
- Xiu, M., Turner, S. M., Busch, R., Gee, T. A., and Hellerstein, M. K. (2006). Measurement of endothelial cell proliferation rate in vivo using 2H20 labeling: a kinetics biomarker of angiogenesis. *FASEB J.* 20, A718–A718.
- Zhang, W., Kreis, T. N., Solomon, J., Reynolds, R. C., Glen, D. R., Cox, R. W., et al. (2009). Acute effects of bevacizumab on glioblastoma vascularity assessed with DCE-MRI and relation to patient survival. *Proc. Intl. Soc. Mag. Reson. Med.* 17, 282.

Conflict of Interest Statement: The authors declare that the research was conducted in the absence of any commercial or financial relationships

that could be construed as a potential conflict of interest.

Received: 20 December 2012; paper pending published: 24 January 2013; accepted: 14 March 2013; published online: 04 April 2013.

Citation: Hawkins-Daarud A, Rockne RC, Anderson ARA and Swanson KR (2013) Modeling tumor-associated edema in gliomas during anti-angiogenic therapy and its impact on imageable tumor. *Front. Oncol.* 3:66. doi: 10.3389/fonc.2013.00066

This article was submitted to *Frontiers in Molecular and Cellular Oncology*, a specialty of *Frontiers in Oncology*.

Copyright © 2013 Hawkins-Daarud, Rockne, Anderson and Swanson. This is an open-access article distributed under the terms of the Creative

Commons Attribution License, which permits use, distribution and reproduction in other forums, provided the original authors and source are credited and subject to any copyright notices concerning any third-party graphics etc.